Cardiff School of Engineering

The Running-In and Incipient Micropitting of Ground Gear Surfaces Under Mixed Lubrication Conditions

William Britton

A thesis submitted in partial fulfilment for the degree of Doctor of Philosophy

August 2021

Summary

This thesis investigates the running-in and early-stage micropitting of ground surfaces operating in mixed elastohydrodynamic lubrication regimes representative of gear contacts. Micropitting is a common mode of fatigue failure for gears, for example those used in wind power or in the drivetrains of ships, however the mechanisms of micropitting are poorly understood. This work aims to better understand the role of contact conditions on micropitting. The effects of contact pressure, slide-roll ratio, and entrainment velocity were evaluated via a full factorial experimental programme with the aim of meeting three objectives:

1. To investigate their influence on surface modification during running-in
2. To investigate their influence on micropitting
3. To compare fatigue simulation results across a range of conditions to real tests

The experimental investigation showed pressure to be the strongest influencing factor on both running-in and micropitting, inducing greater surface modification during running-in and increasing the extent of micropitting. Increased entrainment velocity was shown to reduce surface modification during running-in and to oppose the initiation of micropitting, however its effect weakened later in the test - particularly for the slower surface. The slide-roll ratio was shown to have the strongest influence on micropitting initiation and retained a strong effect on the fast surface throughout the test. Both during running-in and micropitting, complex two- and three-factor interaction effects were observed.

Simulations of fatigue using rough surface profiles were performed for each experiment. Results indicate that accurate predictions of material failed may be

obtained if an appropriate depth is selected for analysis. A model was devised to predict this depth, however further testing is required to confirm its applicability.

Test disks which exhibited non-uniform micropitting behaviour were investigated using Scanning Electron Microscopy. Plastic deformation regions and areas of microstructural change were observed in the near-surface of the test disks.

This work made several novel contributions to the field, which will add to the understanding and prevention of fatigue in gears. These include:

- Assessment of the influence of pressure, slide-roll ratio and entrainment velocity on running-in and micropitting, without interference from confounded higher-order effects
- The application of a structured experimental approach for comprehensive analysis of running-in, fatigue, and simulation
- Development of an algorithm to detect micropits in surface scans
- SEM investigation of microstructure in a sample which underwent both wear and fatigue

Acknowledgements

I must first thank the EPSRC who funded this research project and who kindly and generously extended additional assistance when COVID struck during my third year. Thanks are also due to Cardiff University, which has been my school and workplace for seven of the past eight years.

I would like to thank my supervisors Dr Alastair Clarke and Professor Pwt Evans. During both my PhD and the undergraduate degree that preceded it both have been available for guidance and discussion whenever needed, but also allowed me the free reign and moral support to dive into whatever rabbit holes seemed appealing at the time.

Next, I would like to thank my incredible fiancé Kimberley, who frankly deserves a certificate of her own for putting up with me over the last few years. She has helped me through all the stress and anxiety that a PhD entails, and always been ready with the care, silliness, and occasional tough talks that were needed to get me through. She also probably knows more than she wants to about micropits.

I would also like to thank my family for their support during my extended stay in formal education. More specifically I would like to thank my Dad for always showing an interest in what I'm doing (occasionally more enthusiastically than myself!), my Mum for her emotional support and guidance when things got tough, and my sister Hannah for being a totally barmy distraction from all things PhD.

Last but by no means least, thanks are due to the chaps in the office and the tribology team; Dr Simon Hutt, Paul Revill, George Hunt-Pain, Adrien Monteil, Othman Al-Shatti, Dr Salem Al-Mail, Dr Hassneen Al-Asadi, and Salem El-Sheltat. Without you all I would doubtless have finished quicker and wasted less time, but I would have had a lot less fun and missed a few truly great friends.

Table of Contents

Summary ii

Acknowledgements iv

Nomenclature xii

1 Introduction and Literature Review 1

1.1 Motivation for this Work 1

1.2 Tribology 1

1.3 EHL & Mixed lubrication 2

1.4 Micropitting 6

1.4.1 Observations of Crack development and Micropit Morphology 7

1.4.2 Proposed Mechanisms 12

1.4.3 Surface Roughness, Topology, and Changes due to Running-In 21

1.4.4 Influence of Lambda Ratio and Film Thickness 33

1.4.5 Influence of Speed, Sliding Speeds and Slide-Roll Ratio 39

1.4.6 Influence of Load / Pressure 45

1.4.7 Further Literature 47

1.4.8 Summary 48

1.5 Thesis Objectives 49

2 Elastohydrodynamic Contact Theory and Simulation for Fatigue Analysis 50

2.1 Elliptical Hertzian Contacts 50

2.2 The Film Thickness Equation 54

2.3 The Hydrodynamic Reynolds Equation 57

2.4 The Eyring Model 62

2.5 The Coupled Solution Method..... 66

2.6 Fatigue Analysis..... 70

2.6.1 Recording Stress history..... 70

2.6.2 Fatemi and Socie model..... 70

2.6.3 Stress cycle counting – the rainflow counting method..... 72

3 Experimental Method and Equipment, Data Analysis Development, and Initial Investigations 74

3.1 Description of the Test Rig..... 74

3.1.1 Introduction..... 74

3.1.2 Application of Load 77

3.1.3 Supply of Lubricating Oil to the Test Head..... 79

3.1.4 Drive to Shafts and Setting of Slide-Roll Ratio..... 80

3.1.5 Measurement of Contact Voltage 81

3.1.6 Determining Contact Friction 83

3.1.7 Two-Dimensional Surface Profile Measurement Process..... 84

3.1.8 An Investigation into Relocation Error in 2D Profiles 87

3.2 Description of the Test Disks 89

3.2.1 Material Specification and Properties..... 89

3.2.2 Test Disk Geometry 89

3.2.3 Grinding the Surface Finish 90

3.2.4 Disk Material Comparison Test 92

3.3 Surface Replica Material Selection and Application 98
3.3.1 Selection of Surface Replica Material 98
3.3.2 Design of Replica-Taking Components 100
3.3.3 Procedure for Surface Replication 102
3.4 Surface Measurement 103
3.5 Results Analysis Software Development and Modification 105
3.5.1 Analysis of Two-Dimensional Profiles 105
3.5.2 Evaluation of Asperity Radii of Curvature 109
3.5.3 Evaluation of Running-in Parameters 110
3.5.4 Analysis of Areal Surface Scans 113
3.6 Evaluating Surface Replication 120
3.7 Estimation of Volume Removed by Micropitting 128
3.8 Selection of Variables 129
3.9 Experimental Design and Selection of Variable Settings 130
3.9.1 Selection of the Experiment Design 130
3.9.2 Scuffing Boundary Tests 137
3.9.3 Interpreting of Factorial Experiment Results 143
3.10 Error and Repeatability 148
3.11 Summary 149
4 Full-Factorial Experimental Investigation of Running-in 150
4.1 Introduction 150
4.2 Test 1 151

4.3 Test 2 156
4.4 Test 3 160
4.5 Test 4 162
4.6 Test 5 166
4.7 Centrepoint Test 169
4.8 Test 6 174
4.9 Test 7 177
4.10 Test 8 180
4.11 Individual Running-InTests Summary 184
4.12 Factorial Analysis of Running-in 185
4.12.1 Roughness: Ra and Rq 186
4.12.2 Mean Radius of Curvature 194
4.12.3 Extreme Profile Features: Rp, Rv, Rz, and Rt 200
4.12.4 Profile Element Measures: Rc, Asperity Height, and Asperity CSA. 212
4.12.5 Distribution of Heights: Rsk and Rku 225
4.12.6 Modelling of Running-in Behaviour 230
4.13 Discussion – Running-in 230
4.14 Summary – Running-in 234
5 Full-Factorial Experimental Investigation of Micropitting 235
5.1 Introduction 235
5.2 Test 1 236
5.3 Test 2 246

5.4 Test 3 255
5.5 Test 4 262
5.6 Test 5 271
5.7 Centrepoint Test 277
5.8 Test 6 284
5.9 Test 7 291
5.10 Test 8 298
5.11 Individual Micropitting Tests Summary 304
5.12 Factorial Analysis of Micropitting 309
5.12.1 Surface Micropitted at End of Test 309
5.12.2 Deepest Micropitted Points 315
5.12.3 Volume Removed 320
5.12.4 Cycles to Reach 3% Micropitted 325
5.12.5 Micropitting Rate During Load Stages 9 and 10 330
5.12.6 Early Stage Micropitting 335
5.12.7 Modelling Micropitting Response 343
5.13 Discussion – Micropitting Investigation 345
5.13.1 An Appraisal of the Two-Dimensional Analysis Approach 345
5.13.2 Influence of Wear and Running-in on Micropitting 346
5.13.3 Influence of Pressure, SRR and Entrainment on Micropitting 350
5.14 Summary - Micropitting 353
6 Simulation of Micropitting Fatigue Using Real Surface Profiles 355

6.1 Introduction 355
6.2 Process for Running Simulations 355
6.2.1 Determining appropriate input conditions 355
6.2.2 Selection of profile sections 357
6.2.3 Determining Fatigue Damage 362
6.2.4 Profile Changes due to Fatigue 362
6.3 Fatigue Analysis – Run-in Profiles Only 363
6.3.1 Percentage of Material Failed 363
6.3.2 Equivalent Depth 369
6.3.3 Discussion – Run-in profile simulations 378
6.4 Fatigue Analysis – Updating Profiles 380
6.5 Summary – Fatigue Simulations 388
7 Scanning Electron Microscopy of Disk Microstructure 389
7.1 Introduction 389
7.2 Preparation of Samples 389
7.3 Steel microstructure and transformations 391
7.4 Observations from Test 1 Analysis 392
7.4.1 Non-micropitted sections 392
7.4.2 Heavily micropitted sections 397
7.5 Discussion and Summary 402
8 Discussion and Conclusions 405
8.1 Discussion 405

8.1.1 Differences Between Fast and Slow Surface Effects 405

8.1.2 Progress against Objectives 410

8.1.3 How Robust is This Work? 411

8.2 Novelty 414

8.2.1 Conclusions 415

8.3 Future Work 418

9 References 420

Appendix 1. Running in Factorial 429

Appendix 2. Running-in Factorial Response Models 434

Appendix 3. Micropitting Factorial response Models 444

Appendix 4. R^2 values for micropitting outputs to roughness parameters 451

Appendix 5. Run-in Profile Simulation Results 453

Appendix 6. Factorial Response Models for Simulations Using Run-in Profiles 459

Appendix 7. Updating Profile Simulation Results 462

Nomenclature

The following nomenclature is not exhaustive but includes terms which are in common use or used repeatedly throughout this work. Isolated uses of variables and abbreviations not included here are defined at the point of use.

μ	Mean factorial result
a	Hertzian half-dimension in the entrainment direction
Asperity CSA	Mean cross-sectional area of asperities above the mean line
b	Hertzian half-dimension perpendicular to entrainment
CV	Contact Voltage
D5	Mean depth of the deepest 5% of micropitted points
DER	Dark Etching Region
E	Young's modulus
E'	Elastic modulus
EHL	Elastohydrodynamic Lubrication
FD	Fast Disk
h	Film thickness
k, F	Dimensionless parameters in contact dimension calculations
N3	Number of fast disk cycles taken to reach 3% micropitted
p	Pressure
PDR	Plastic Deformation Region
$\bar{R}$	Reduced radius of curvature
Ra	Arithmetical mean roughness
Rc	Mean height of profile elements
Rku	Kurtosis of the height distribution
Rp	Maximum profile peak height
Rq	Root-mean-square roughness
Rsk	Skewness of the height distribution
Rt	Total height of the roughness profile
Rv	Maximum profile valley depth
Rx, Ry	Radius of curvature of body
Rz	Maximum peak to valley height
SD	Slow Disk
SEM	Scanning electron microscopy
SRR	Slide-Roll Ratio

β	Factorial model coefficient
u	Surface velocity
U, V, W	Velocity of lubricant in x, y, and z directions respectively
w	Applied load
WEB	White Etching Bands
x, y, z	Contact axes
ZDDP	Zinc Dialkyl Dithio-Phosphate
α	Pressure-viscosity coefficient
η	Dynamic viscosity
Λ	Specific film thickness
v	Poisson's ratio
ρ	Lubricant density
τ	Shear stress

1 Introduction and Literature Review

1.1 Motivation for this Work

Fatigue is a common cause of failure for gears used across a range of applications. As fatigue occurs within the conventional design limits of the component and takes a long time to develop (unlike other failure types such as overloading to deformation or breakage) it is difficult to understand the relative importance of factors which contribute to fatigue. It is also believed that some fatigue behaviours may be influenced significantly by the surface modifications experienced during the running-in process, making it as important to understand the initial process of contact as it is to investigate the eventual failure. By investigating the influence of contact conditions on the initial surface modification and following fatigue behaviour in gear contacts, this work aims to make a contribution to the understanding of the problem and development of means to prevent it, for example through design best practise. Additionally, by comparing results to simulations, this work aims to contribute to making simulations more accurate and reflective of the systems they model, thus reducing the need for time-consuming and costly experimentation.

1.2 Tribology

Tribology is the scientific field concerning the friction, lubrication and wear of interacting surfaces in relative motion. In many ways this makes it a compound science including aspects of fluid mechanics, materials science and solid mechanics in its problem-solving toolbox.

Because of its compound nature, the coining of the term “tribology” and hence full recognition of what it constitutes is only a comparatively recent development – it has been said that the birth of tribology can be traced to a report published in March 1966. Despite this, humans have been making use of tribological principles

for thousands of years; in the building and moving of structures by the ancient Egyptians, or even prior to this in the making of primitive bearings during the stone age. (Dowson 1998)

In the modern era, proper tribological design is key to the survival and efficiency of components involved in the generation and transmission of power. For example, the gears used in wind turbines are vital to converting the harvested energy to useable electricity, while the rotating shafts on which those gears are mounted are reliant on efficient and durable bearings.

The survival and efficiency of components can be a trade-off from a tribological perspective. Thick lubricant films that separate surfaces entirely offer the best protection against wear and fatigue but inherently involve significant power losses as energy is wasted in shearing a thick, high viscosity lubricant. If thinner lubricant films are employed to improve efficiency the consequent contact between the surfaces can bring about wear and fatigue, risking eventual failure of the component.

In circumstances where contact between the surfaces is unavoidable the challenge has become to understand the mechanisms by which wear occurs, and from this to develop accurate means of wear prediction and effective strategies to reduce wear.

1.3 EHL & Mixed lubrication

Well over a century ago, Reynolds (1886) showed that hydrodynamic action could create a thick, pressurised film of fluid lubricant sufficient to completely separate two interacting surfaces; a situation which theoretically prevents wear entirely. This discovery, known as hydrodynamic lubrication, explained the operation of journal bearings and thrust bearings and applies to a great number of lubrication problems where there is a high level of geometrical conformity between surfaces.

Where contacts were non-conforming however, the mechanisms were not understood until the middle of the 20th century.

As is explained by Stachowiak & Batchelor (1993), components such as gears and bearings, which operate under immense loading with a fluid lubricant were something of a mystery. Their low level of wear suggested hydrodynamic lubrication, but the film thicknesses calculated by hydrodynamic theory could not possibly separate the surfaces fully. It was not until the late 1940s that models began to shed a light on the true mechanisms behind this: an elastic deformation of the surfaces and a pressure dependent increase in viscosity in combination with hydrodynamic theory. This is now known as Elastohydrodynamic Lubrication (EHL).

In this system the movement of the contacting surfaces draws the lubricant into the contact area, which is subjected to very high pressures. Because of the piezo-viscous qualities of the lubricant the viscosity increases drastically with pressure – to such an extent that the oil cannot be squeezed out of the contact area by the surfaces but instead becomes so "stiff" as to force the surfaces (even surfaces such as hardened gear steel) to elastically deflect to accommodate it. As such a lubricant film remains interposed between the two surfaces, with a near-constant film thickness throughout the equivalent dry contact area.

Where these conditions are present and the oil film remains sufficiently thick to prevent any direct contact between the surfaces, this state is referred to as "full film EHL" or often "full EHL". This reflects the fact EHL can be considered as a spectrum of states ranging from "dry" contact with no lubricant present through to full EHL. Between these two extremes are states of lubrication where the load is shared by a mixture of lubricant film and direct surface-to-surface interaction; this is referred to as "Mixed EHL" and this is the form of lubrication with which this thesis is concerned.

Mixed Lubrication:

Mixed lubrication is the term used to describe an EHL situation where the thickness of the lubricant film is of the same order as the surface roughness. This is often through use of lubricants that are insufficiently viscous to develop a full film, and through high levels of surface roughness. Mixed EHL is a very common operating condition for gears largely due to increased manufacturing cost to produce smoother surfaces, and because the higher viscosity lubricants needed to fully separate the surfaces leading to larger frictional losses and hence reduced efficiency. Typically, a set of ground gears for use in aerospace applications might have an average roughness (Ra) of around 0.4 μm and a maximum peak to valley height of 2 μm, but operate with a film thickness around 1 μm (Britton *et al*. 2000). In this situation, roughness features on the surfaces are of the same order of magnitude as the film itself, and hence surface asperities are sure to interact directly.

Describing the lubrication state using only the roughness average and film thickness is not the clearest means of indicating the conditions of the contact. The ratio Λ, proposed by Tallian (1967) is often used to define the lubrication condition:

$$\Lambda = \frac{h}{\sqrt{{R_{q1}}^2 + {R_{q2}}^2}} \qquad \textit{Equation 1}$$

This is the ratio of the EHL film thickness to the composite RMS (Root-Mean-Square) roughness of the two surfaces in contact, and is commonly referred to as the specific film thickness, or the Λ ratio. At Λ=0 there is no lubricant film present and hence this indicates dry contact, while values of $\Lambda \geq 4$ are generally taken to indicate full film lubrication. It is not uncommon for gears and bearings to operate at a Λ ratio much lower than this, often below unity under the most arduous conditions,

despite this being a state of lubrication in which significant direct surface interaction can take place.

When calculating Λ the roughnesses that should be used are those of the surface after running-in has occurred (assuming that the aim of the calculation is to obtain a value that is representative of the conditions under general running). Running-in is the modification of the contacting surfaces to better accommodate the loads experienced through the contact, and to adapt to the opposing surface roughness. Surfaces after running-in should be used for this calculation because running-in can result in a significant reduction in the surface roughness (Clarke *et al*. 2016a).

In addition to these changes in roughness it is of interest that the lubrication conditions are not uniform across the contact. Even under idealised conditions there is a constriction at the outlet of the contact, leading to the existence of separate central film thickness and minimum film thickness calculations for these conditions. To further complicate matters, under the rough surface conditions experienced in real contacts the valley features left by the grinding process can allow lubricant to leak from the sides of the contact area. Krantz (2005) found this effect to produce a channel of damage at the contact edge in ground gears, while superfinished gears with their much reduced surface roughness did not suffer from this. The simulations conducted by Holmes *et al.,* (2005) found that side leakage resulted in increased contact between asperities on opposing surfaces, potentially leading to this type of scuffing damage occurring.

The choice of which film thickness value should be used to define the specific film thickness varies through the literature. While minimum film thickness provides a worst-case value, some researchers have argued that the central film thickness is more representative of true behaviour in rough contacts.

1.4 Micropitting

Micropitting is a form of fatigue in which pits appear on the surface of the material on the micron scale, which can eventually result in catastrophic failure of the component. This occurs only within the realm of mixed lubrication, where the surface roughness is of the same order as the film thickness, however the mechanisms by which micropitting occurs are not fully understood. This is a significant and prevalent issue in many areas of engineering, but wind turbines provide a clear example of the issues raised by micropitting. The cost of wind energy is largely influenced by the cost of operating and maintaining the wind farm – in excess of 20% of the cost of wind energy is a direct result of operating and maintenance costs, and micropitting is the most prevalent cause of failure within wind turbine drivetrains (Keller *et al*. 2017). Although not the most prevalent form of failure (electrical equipment failures are most common) tribological components are often the most expensive to repair or replace, and can prove to be a significant logistical undertaking (Kotzalas and Doll 2010). There are currently standards in existence which attempt to provide a method for design which avoids micropitting (ISO 2014) however the methods used require either expensive further experimentation or comparison to standard experiment results (which may not be representative of the desired operating conditions) which can put severe limitations on their utility.

Although micropits are very small in size, it can be entirely possible to tell if a gear or disk is micropitted by the “Frosted”, or “grey stained” sliver-grey effect left on the surface. This grey stained appearance is given by the reflection of light from inside the cracks and micropits on the fatigued surface. This was confirmed by the Scanning Electron Microscopy (SEM) observations of Ariura *et al* (1983), who investigated what was then called “grey staining”, known to influence gear tooth profile and often be accompanied by spalling.

This section covers a number of elements – firstly the mechanisms by which micropitting is believed to occur, and some of the modelling work (both at Cardiff and elsewhere) aiming to numerically analyse and predict micropitting failure. Focus is then shifted towards a number of the operating conditions which influence micropitting, considering their effects and significance in determining whether micropitting will occur.

1.4.1 Observations of Crack development and Micropit Morphology

A number of consistent observations can be made across the literature with regard to the appearance of cracks and the shape and growth of micropits. These are often used as something of a benchmark against which to test the proposed mechanisms that will be discussed in Section 1.4.2, hence are introduced prior to addressing the proposed causes of micropitting. These observations are that:

- Pitting occurs along asperity ridges
- Cracks develop with a given directionality and angle
- Pits develop a shape which is defined by the direction of sliding or surface traction.

Location and Morphology of Micropits

Hardened gears are commonly finished by grinding, a process by which an abrasive wheel is used to remove material from the surface of the steel. This can be used to produce surfaces of varying quality, down to Ra≈0.2 μm if sufficient care is given to the process. In gears, grinding is performed transverse to the direction of motion of the gear surface, leaving a clear pattern of ridges and valleys on the surface. This can be seen in Figure 1.4.1.

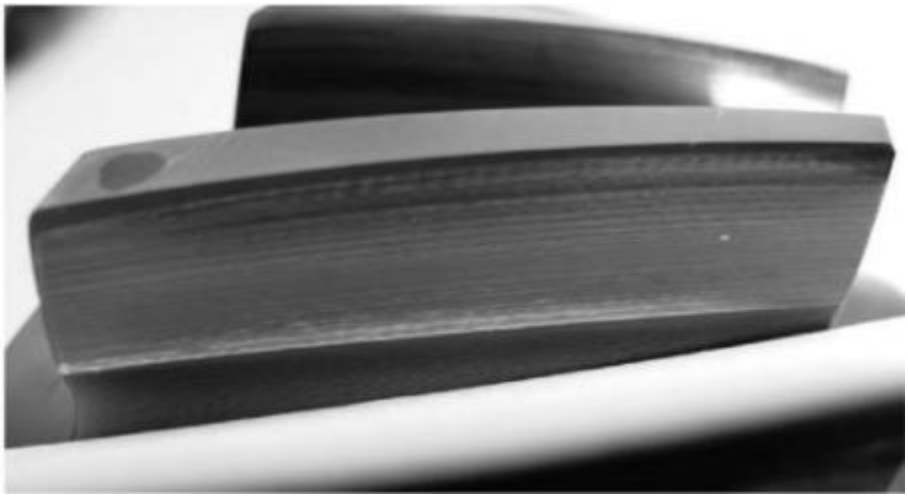

Figure 1.4.1 Image of a ground gear tooth after a period of operation in a gear test. The grinding marks can still be seen transversely across the tooth surface, as can an area of wear in the gear tooth flank. Image reproduced from Zhang and Shaw (2016).

Micropits are always seen to initiate at locations where there was initially an asperity, and there is a tendency for micropits to accumulate along prominent asperity ridges. The widely accepted explanation for this is that larger asperities protrude through the lubricant film and hence experience a greater number of stress cycles than other locations on the surface. These asperities also experience more stress as a disproportionate share of the load is carried by that asperity. The accumulation of micropits along a ridge can clearly be seen in Figure 1.4.2, a test disk used in the twin disk tests conducted by Weeks (2015). It is worth drawing the reader's attention to the fact that not all asperity ridges will develop micropits, as can also be seen in Figure 1.4.2. This is because the tallest asperity ridges protrude through the lubricant film more prominently and thus experience more severe loading, while smaller asperity ridges experience less severe conditions. In addition, relatively large asperity ridges can experience less fatigue than would be expected if they are shielded from contact by more prominent asperities in the locality.

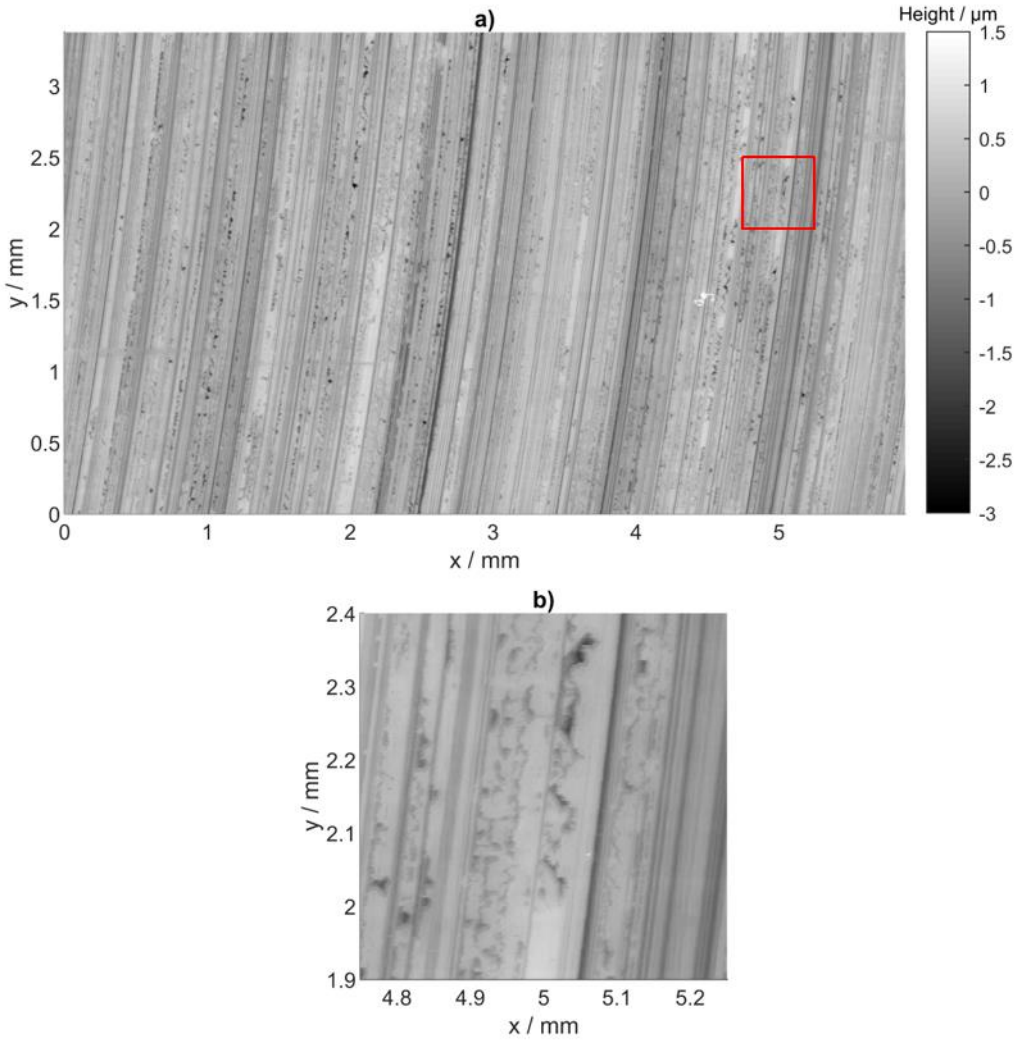

Figure 1.4.2 a) The surface of a micropitted, transversely ground disk. b) Close up image of the area shown in red showing micropits in chevron formation. Original figure produced using surface data from tests by Weeks (2015).

Notable in Figure 1.4.2 is the shape of the pits that appear as black spots. Some of these can be seen to take the form of chevrons, as was noted by Weeks. It can also be seen that where pits agglomerate along an asperity a common "flat edge" often occurs, with pits growing in the same direction from this flat edge. In an article discussing the morphology and development of micropits, Errichello (2012) highlighted that pits always develop in the opposite direction to sliding (and traction), beginning at the leading edge of the pit (the first part of the pit to reach

the contact) and progressing to an exit which is the last part of the pit in the contact with each cycle. The flat edge mentioned above is at the entry to the contact, with the ragged, rounded or chevron-shaped edges and features being the trailing edge or exit of the pit.

The discussion above covers the question of micropitting location on the micro-scale, but the location on the macro scale, i.e. on a gear tooth, is equally of interest. Both in operation and in micropitting tests, gears consistently show a preference for micropitting in the dedendum region of the gear tooth. The cause of this is difficult to isolate because of the combination of severe conditions which occur in this region. Firstly, the geometry of the teeth in this region leads to very aggressive contact conditions as the tip of one tooth comes into contact with the root of the other. This is more significant if the teeth have been designed with a tip relief – a deviation from the involute form at the tip to encourage smooth operation and prevent premature tooth contact. In addition, the greatest amount of sliding in a gear contact is experienced at the extreme ends of the contact path.

Directionality and Angle of Crack Growth

Consistent observations can also be made of crack growth behaviour, although with more difficulty than the micropit shape observations above. The best means of observing cracks is to section a test specimen – either removing teeth from a gear or cutting apart a test disk – and then view these specimens using Scanning Electron Microscopy (SEM). Figure 1.4.3 provides an excellent illustration of the characteristics of micropitting fatigue cracks. Clearly, the cracks in the figure are all growing in the same direction. In the same way as the direction of growth of the pits, the direction of propagation for cracks is related to the direction in which frictional and tractive forces act on the surface. A natural repercussion of this is

that the direction of crack propagation is reversed either side of the pitch point as the direction of sliding reverses.

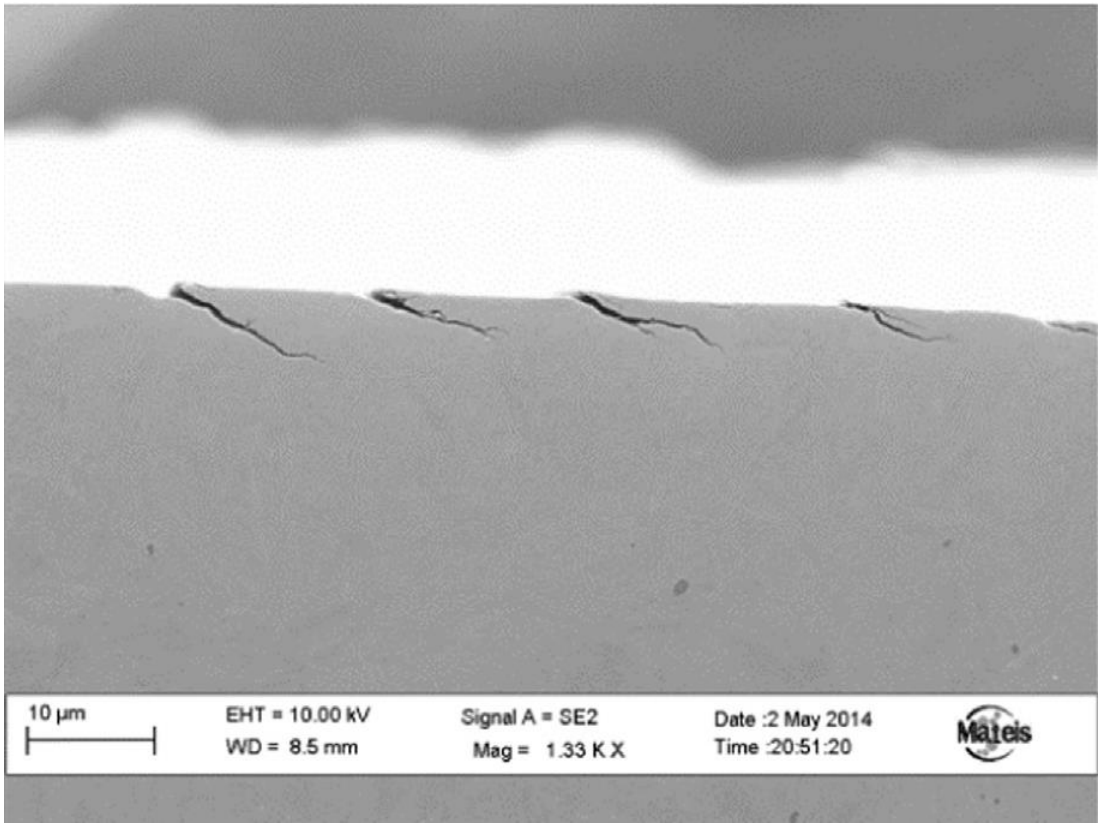

Figure 1.4.3 SEM image of a cross-section of a gear tooth, showing micro-cracks at the surface. Image reproduced from L'Hostis et al, (2017).

There is also general agreement reported regarding the angles between surface originated cracks and the free surface. Errichello (2012) reports that angles generally sit within the range of 10˚-30˚, with Olver (2005) and Kadiric and Rycerz (2016) in agreement, stating values of 20˚ and 30˚ respectively. What variation there is in this range could be accounted for by a dependency on the location on the gear tooth, where cracks are most steep (larger angles) in the addendum and dedendum regions of the tooth (at the extreme ends of the contact path) and become increasingly shallow towards the pitch point (L'Hostis *et al*. 2017).

In summary, observations of developing cracks and established micropits are very consistent throughout the literature, and can be used as a benchmark against which to assess possible causes and mechanisms for micropitting fatigue.

1.4.2 Proposed Mechanisms

The mechanisms by which micropitting is initiated and then progresses are still poorly understood, although several theories have been proposed. It is now accepted that the micropitting process begins with the development of micro-cracks in the near surface of the material which, by mechanisms yet to be universally agreed, progress to fully separating a small piece of material from the surface to form the observed micropit. The main potential mechanisms are now discussed in detail.

Fluid Entrapment and Hydraulic Pressure Mechanisms

It has long been proposed that the lubricant plays an active part in bridging the gap between the initiation of a crack and its development into a micropit. The investigations by Way (1935) into the development of macro-pits remain highly relevant for micropitting in this respect. This paper made a number of interesting findings, chief among these being that pitting could not occur in a dry contact. The tests were carried out in pure rolling under a range of conditions and were able to show that dry contacts did not pit. One interesting discovery was that rollers which began in lubricated conditions but were switched to dry operation when cracks began to appear, did not pit either. Also of particular interest was a test in which rollers operated without lubrication for 5,400,000 cycles before having lubricant added. Pitting then occurred within 160,000 cycles of this addition of lubricant.

These results, coupled with a clear directionality to crack growth and distinctive shape of pits led to the proposal of a mechanism where highly pressurised lubricant

is forced into the crack, creating a stress concentration at the tip and causing the crack to grow. It was also suggested that one of the factors which renders contacts lubricated with low viscosity oils more susceptible to this type of failure is the enhanced ability of less viscous oil to successfully penetrate the cracks in the surface.

This mechanism was one of three considered by the modelling work of Bower (1988), who considered hydraulic crack opening alongside a theory of lubricated crack faces allowing cyclic shear forces to drive crack growth, and of fluid becoming trapped inside the crack and forcing growth as the pressure rises. These mechanisms were analysed because they all have a key dependence on a lubricant being present (as deemed vitally important by Way), and were evaluated against two criteria: that stress at the crack tip should be influenced by direction – reflecting the established directional sensitivity to crack growth, and that the direction of tractive force on the surface should have an influence (reflecting the practical observation that pitting is always more severe on the driven component). The conclusions of this work were as follows:

- Growth by shear forces: Results showed this to be a plausible mechanism, however it was noted that in some experimental works it has proven difficult to grow cracks in this way. It was also noted in the review conducted by Olver (2005) that this mechanism would produce a much higher stress concentration for cracks perpendicular to the surface, calling into question why cracks at an angle would propagate most prevalently under this mechanism.
- Hydraulic Pressure: Did not exhibit the sensitivity to direction of contact that is seen in experimental tests, and also gave such severe stress

intensities that calculated fatigue life was much shorter than seen in real tests.

- Fluid Entrapment: Showed results most consistent with reality in terms of life, and direction of motion and traction effects acted to close the crack before fluid could enter when the direction was to oppose growth, showing agreement with directional sensitivity. The direction of crack growth was unclear however, due to the complexity of the stress patterns produced.

This therefore suggests that fluid entrapment is the most promising suggested mechanism analysed here. Two things should be noted however: Firstly, the assumptions made of linear elastic fracture mechanics being applicable may no longer be reasonable where the crack length is as small as those which cause micropits. Secondly, the two-dimensional geometry of the crack as modelled here cannot represent the characteristic shape of pitting cracks, nor can the much simplified lubricant properties truly represent the behaviour of a gear oil – this is a general criticism of these types of models which is best attested to by Olver (2005).

It is well established that the most serious micropitting damage on real world gear teeth occurs in the dedendum region of the teeth, where there is negative sliding (where sliding velocity is in the opposite direction to the rolling velocity). This is often cited as being a strong case for the fluid pressurisation effect (e.g. Errichello (2012)). In truth, this argument alone does not make this a more convincing mechanism than fluid entrapment, however it does make a good case that one of these two methods provides a contribution to crack propagation.

Changes in material properties

Changes in the microstructure of the gear material have long been a recognised phenomenon in rolling contact scenarios and are primarily a concern for bearings

operating under high loads for extended periods of time. This was first recognised by the work of Jones (1947) who noted that, in heavily loaded bearings, the martensitic structure below the surface begins to transform into 'troostite' or, as it is now known, tempered martensite. This work showed that there was a relationship between this phenomenon and the loading of the contact, highlighting that the patches of transformed material were larger and darker at higher load. Jones deduced that this phenomenon was related to the high levels of subsurface shear stress, suggesting that the heat resulting from the dissipation of shear strain energy caused this tempering.

Furthermore, Bush *et al*. (1961) was able to show that a threshold load exists below which no microstructural changes will occur in the material. They also found that, above this threshold, increasing the load further did not change the size of the affected area below the surface but instead resulted in a more complete change in that region. As with Jones' findings, this was shown by patches of tempered martensite being larger and darker (within the affected region) when the load was increased. Bush did not entirely agree with Jones however and proposed that the mechanism by which the martensitic decay process progressed was not thermal tempering of the material but an intrusion/extrusion method by which material is transported from carbide particles into the surrounding matrix along slip bands, or possibly by migration of carbon atoms induced by stress.

Because of its high practical relevance in the field of bearing fatigue this topic has gained a great deal of attention, and Warhadpande *et al*. (2013) performed a comprehensive literature review of the topic which provides good insight to the current understanding of martensitic decay in bearings. This review found many areas of general agreement:

- A threshold load exists which must be exceeded for decay to occur

- The extent of decay is dependent on the load and number of cycles
- Dark etching occurs first and is followed by white bands transversely parallel to the surface, at first oriented at angles of 20-30 degrees and later at 70-80 degrees (dependent on the bearing type). The white bands are “sandwiched” between discs of very high carbon content.
- The dark etched region is ferritic with excess carbon distributed through the matrix, while the white bands are ferritic with very low carbon content.

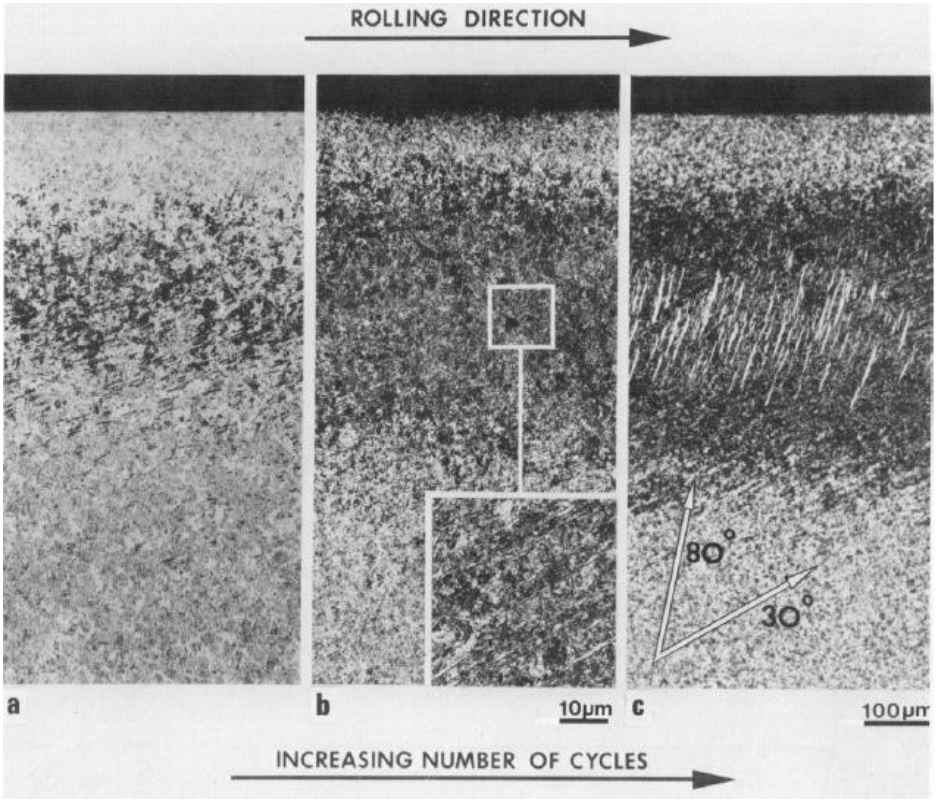

Figure 1.4.4 Image illustrating stages of martensitic decay. a) Early stage dark etching region, b) white bands oriented at 30°, c) bands oriented at 80° alongside further 30° bands. Reproduced from Swahn et al. (1976).

Despite this agreement across a great many areas it is concluded that the exact mechanism is still a matter for debate, however the most generally accepted proposal is the stress induced migration of carbon atoms as was first suggested as a possibility by Bush.

Martensitic decay in gears has received far less recognition than bearings, however it has been proposed as a possible cause for micropitting – perhaps most effectively put forward by Oila *et al*. (2005) and Oila and Bull (2005). Together these papers were able to show that martensitic decay does occur in gears, and that a semi-circular (in profile) non-martensitic Plastic Deformation Region (PDR) of very high hardness forms directly below particularly prominent asperities, bordered by the Dark Etching Region. It was concluded that cracks were initiated by stress concentrations at this boundary between materials of differing hardness and then propagated along this line resulting in pits as material becomes fully separated from the surface. Figure 1.4.5 shows an illustration of this process.

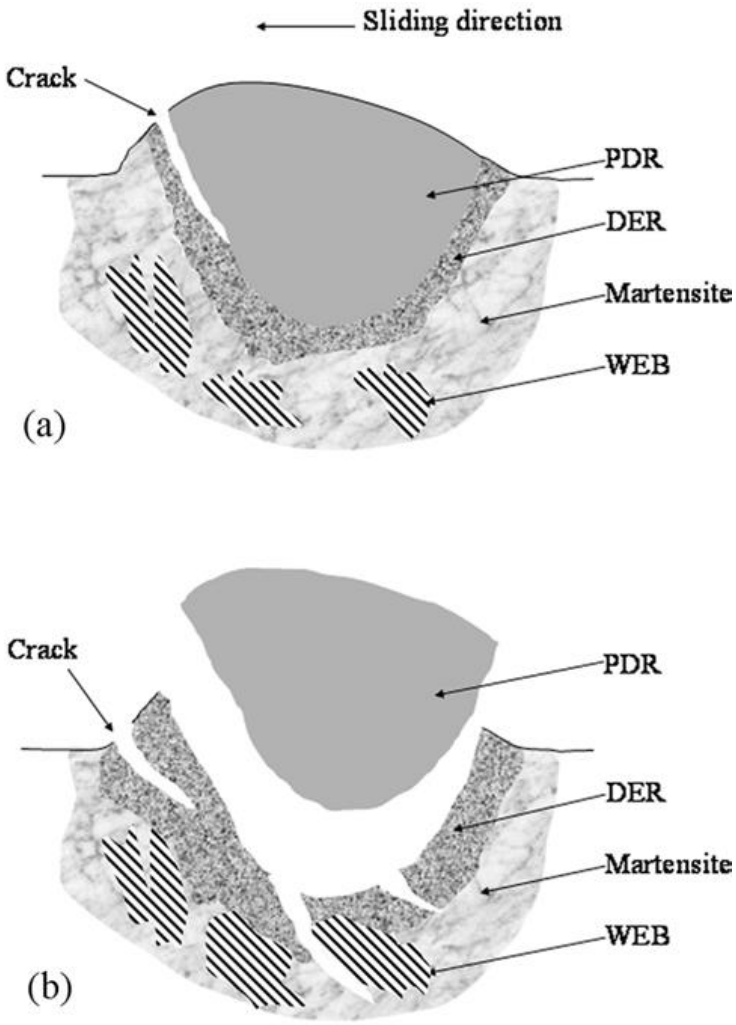

Figure 1.4.5 The initiation and propagation of a crack along the boundary where the Plastic Deformation Region and Dark Etching Region meet, resulting in the removal of material and creation of a micropit. Image reproduced from Oila et al. (2005).

Research conducted by L'Hostis *et al.* (2017) into the influence of lubricant additives on crack propagation used methods such as Tunnelling Electron Microscopy (TEM) and SEM to observe the formation of tribofilms and the interaction of additives with the steel surface. This also allowed observation of changes to the microstructure around microcracks. It was found that the microstructure became much more refined in the space between micro-cracks and the surface. These areas contained no austenite and did not exhibit the needle-like grain structure of

martensite, but rather were comprised of nano-scale ferrite grains with distributed carbide content. This holds a definite resemblance, both in shape of affected area and in microstructural change, to the PDR mentioned above. It is notable that these regions were only observed where microcracks were also found – leading to the suggestion that the cracks act as the root cause of this change as the strain between the micro-crack and the surface (arising from sliding at the crack faces) causes hardening and refinement of microstructure. It is not unreasonable to suppose that in this case too, the crack would propagate along the boundary of this region for the same reasons as the mechanism proposed by Oila *et al*. (2005).

Not all evidence is in support of this mechanism, however. For instance, the gear tests conducted by Mallipeddi *et al*. (2017) found no link between changes to the microstructure and the occurrence of micropitting. In addition, the review of rolling contact fatigue by Olver (2005) (although contemporary with the works of Oila mentioned above, and hence not benefitting from their findings) suggested that while transformed material can be found close to the surface in micropitting tests it does not necessarily follow that it is a *cause* of that micropitting. Instead it is proposed that phase transformation of the material may simply be a natural consequence of high amounts of energy being dissipated within a non-equilibrium structure – its coincidence with micropitting being of low significance.

Additionally, D'errico (2011) conducted an investigation into the mechanism of micropitting for steel with three different treatments; heat tempering, carburizing and nitriding. This work found no microstructural changes to have occurred in the hardened layers of the nitride and carburized specimens – instead cracks were found to start where there were oxide inclusions causing increased brittleness at a grain boundary. In the more ductile tempered surface cracks were found to initiate due to other forms of surface distress.

As with all proposed mechanisms for micropitting, the evidence to confirm or deny martensitic decay as a cause is still inconclusive and would certainly benefit from further investigation. At present there is comparatively little research into micropitting that looks in detail at the microstructure of the material, which is unsurprising when the practicalities of conducting this research are considered. In order to thoroughly examine the structure at this level a Scanning Electron Microscope is required; an expensive piece of equipment for which some level of expertise is required in the preparation of samples and interpretation of results if any useful information is to be gained from it. In addition, analysis of the results necessitates a comprehensive knowledge of the metallurgy and chemistry of steel which many tribologists may feel ill-prepared to undertake – however it is only through fresh investigation into this area that the effects of changing microstructure may be fully understood.

Summary & Areas for Development:

The mechanism of micropitting is still an area of broad debate. Beyond the fact that repeated stress cycling must undoubtedly play a part, there is little agreement as to the process by which micropits appear. It may be that in different conditions, or with dependence on the materials used, the mechanism by which micropitting develops may differ as well. Assessment of micropitting across a broad range of conditions with multiple changing variables may help to identify if this is the case. Additionally, the current work may be able to investigate whether changes in microstructure are present in the samples used as a result of contact. This is an area in which there is a lot of debate which can only be resolved by adding further investigations and data to the body of knowledge.

1.4.3 Surface Roughness, Topology, and Changes due to Running-In

The surface roughness is known to be a significant influence on the occurrence of micropitting in mixed EHL contacts, and is arguably the most significant factor determining whether micropitting will occur. The roughness of a surface influences the probability and frequency of direct contact between surfaces, and the stress concentrations arising from asperity-asperity loading.

The roughness and surface topology are changed significantly in the first period of loading – this process is termed "running-in" and involves significant surface modification. Most notably, larger asperities on the surface plastically deform and decrease in height. In the case of ground surfaces this has the effect of taking the essentially Gaussian height distribution (for the unrun surface) and negatively skewing it as high points are removed. It has also been shown that the radii of curvature of asperity tips increase through this process (Bishop and Snidle 1984) and that this process can cause an increase in the wavelength of the roughness (Kelly *et al*. 1998). This increased wavelength of roughness can shift the lubrication mode from mixed EHL toward micro-EHL, a mode of lubrication in which the direct contact between surfaces is reduced and localised hydrodynamic pressure is generated between asperity tips through the film.

It is predominantly the asperities which are influenced by the running-in process while the valley features of a surface are essentially unaffected, as was shown by Clarke *et al*. (2016a) through experiments using a twin disk rig. This is in agreement with the work of Sosa *et al*. (2015) who performed an in-situ analysis of the changing topology of gear teeth during the running-in process. They did this using a specially mounted profilometer and employing a sixth order polynomial function to remove the involute profile of the tooth. Considering that the peaks were the primary feature changing during the running-in process, Sosa *et al*. (2015) suggested that

Rpk (the average height of the roughness peaks) was the best way to characterize the running-in process (in two dimensions) as it gave a clearer output than Ra or RMS roughness (Rq) values. These effects are also clearly shown in the work of Clarke *et al.* (2016a) where Ra and Rq values remained largely unchanged while the Rpk responded strongly to the running-in process. Prajapati and Tawari (2019) investigated the change in three-dimensional topographical parameters, albeit using circumferentially ground disks which are less representative of gears. They found that Sa, Sq and Sz (the 3D equivalents of Ra, Rq and Rpk) did change with running-in, but that much more significant changes occurred in texture aspect ratio, autocorrelation length and RMS slope, which are much less commonly used parameters.

As was discussed by Wang *et al.* (2000), the rougher a surface is to begin with (in this case indicated by higher Ra) the greater the percentage change in roughness will be – or in other words the ratio of original to run-in roughness will be greater. The impact of stopping and starting tests, as is common practise to allow measurements to be taken, was also questioned. By comparing with a test where measurements were taken by an optical method without pausing the test, it was shown that this methodology can result in an increase in wear and a decrease in surface roughness not present in continuous operation. For the earliest measurements taken in using the start-stop method the optical method yields very similar results, indicating that both methodologies are comparable for measuring the surface. As more stops occurred the measured Ra was much reduced compared to that measured optically, implying that the stop-start process contributes to decreasing the roughness of the surface. It is not specified however whether disks were removed for profilometry during the start-stop tests or measured in-situ, and failure to preserve the kinematics when reinstalling the disks might be expected to have a similar effect.

The effect of running-in on asperities (and lack of effect on valley features) is most effectively illustrated by Figure 1.4.6 (Clarke *et al*. 2016a) where the significant flattening and rounding of asperities can be seen clearly after one load stage, while the valley features are largely unchanged.

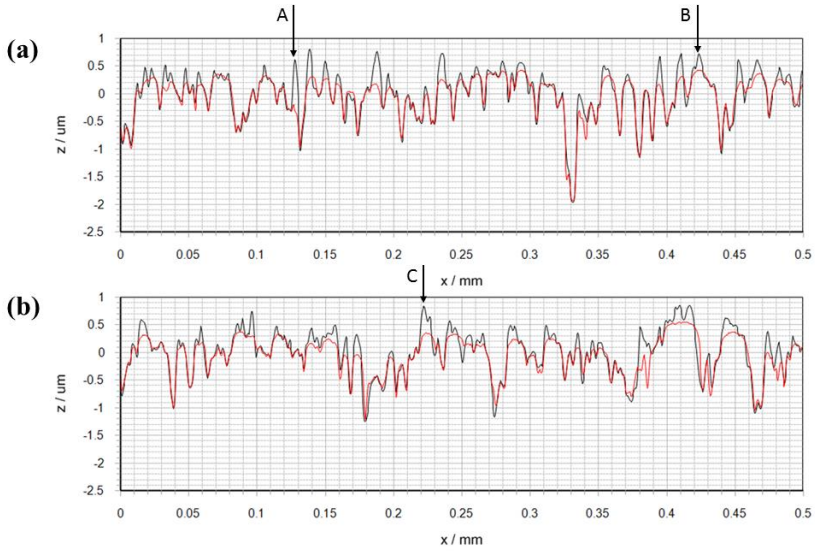

Figure 1.4.6 Shows the changes from the unrun (black) surface to the run-in (red) surface, for a) the fast disk and b) the slow disk. The points A, B and C indicate some notable points of change in the surface. Reproduced from Clarke (2016a).

Cabanettes and Rosén (2014) considered a number of linear and areal surface parameters in their analysis of running-in. They were able to obtain areal scans of surfaces through the use of soft replica materials which could be examined away from the experimental rig. Through analysis of the percentage change in these characteristics, they found that Ssc (mean summit curvature), Sdr (developed interfacial area ratio) and Sdq (mean slope) underwent the most significant changes during the running-in period. Their two-dimensional analysis methods suggested that wear affected asperities in the direction perpendicular to the rolling direction

regardless of the frequency of the features, while wear had a dependence on the frequency of features in the rolling direction.

The means of determining the end of the running-in period is a key point of discussion. Surface finish can provide useful information both during the running-in process and at other stages, however Blau (2005) questions whether the surface finish alone can be used to evaluate running-in. Blau suggests that friction, wear rate, and the time taken to reach a steady state condition for those parameters should also form a part of any models of the running-in process.

Lugt *et al*. (2001) used an entirely different approach to the running-in process. Using a two-disk rig equipped with contact voltage measurement, they evaluated the relationship between running-in, slide-roll ratio (SRR), and "lift-off speed" – defined as the sum speed of the disks at which the voltage reaches or exceeds 90% of its full separation value. They alternated the SRR between 2.8% slip and pure rolling, finding the initial take off speed before setting the speed to 40 rpm. Results showed that while running-in at 40 rpm, the lift-off speed for the disks decreased. If left for long enough then the lift-off speed eventually reduced to the running-in speed, which was taken to imply that running-in was complete for that set of conditions. It was seen that as the amount of sliding was alternated between the 2.8% and pure rolling settings the lift-off speed would initially increase before coming down to the running-in speed. As the magnitude of this increase appeared to lower the more times this was alternated (and eventually effectively no increase took place) it was hypothesised that continuing to alternate in this way would eventually result in the equalisation of lift-off speed and run-in speed across the range of slip speeds tested.

Other works have found running-in to be completed within the first few cycles of loading, through measurement of surface change (Sosa *et al*. 2016) or acoustic emission from asperity contacts (Hutt *et al*. 2018).

Surface roughness

That surface roughness plays a significant part in the micropitting process has been known for a long while – even before the terminology used to describe micropitting was made consistent and various terms including “grey staining”, “Peeling” and “microspalling” were used to describe the phenomenon. The theories proposed to describe the causes of initiation of micropitting have already been discussed, but the role of roughness within these theories is based on the roughness peaks providing locations for high pressure loading (where load is borne by the asperity) causing high cyclic subsurface stress concentrations, and acting as stress raisers at which cracks may form. In the case of martensitic decay, it has been proposed (Oila and Bull 2005) that these high pressures and temperatures provide the energy to drive this change in the material.

Ariura *et al*. (1983) noted a link between the roughness of the surface and the occurrence of micropitting. Gears with varying roughnesses were tested to investigate the occurrence of grey staining. Both finely and coarsely ground surfaces used in this paper developed micropits, however the surface that was polished with a buffing wheel did not succumb to micropitting, and only minor changes in the surface were observed after running for 10^7 cycles.

Many experiments conducted since have also agreed that very finely finished surfaces may forego micropitting entirely. For example, Ahlroos *et al*. (2009) conducted an investigation of surface roughness which produced similar results. This paper compared the effects of different roughnesses, lubricant types and

surface treatments through the means of twin disk testing and found the surface roughness to be the most dominant influence on micropitting by far. As part of these experiments the roughness was varied down to a minimum Ra of 0.04 μm, corresponding to a polished or super-finished surface. It was shown that at this Ra the surface would not micropit, irrespective of other parameters. Similarly, Krantz *et al.* (2001) and Krantz (2005) showed that reducing the Ra of gears by a factor of five (by superfinishing) can increase the fatigue life of the gear by four to five times.

Li and Kahraman (2013) conducted a series of eight experiments on a two-disk machine, designed to investigate the impact of roughness, rolling velocity, SRR and contact pressure in the context of wind turbine gearbox operating conditions. Again, it was shown clearly that surface roughness was the most significant influence on micropitting (the prevalence of which was gauged by percentage micropitted area in an areal scan), however all factors investigated were found to have a role to play; for example lower contact pressure and increased entrainment velocity were shown to reduce micropitting occurrence. A particularly interesting note was the attention paid to the running-in process. Results suggested that an aggressive running-in period of high load and low surface speed reduced micropitting. The authors postulated a number of possible causes for this, including residual compressive stress and work hardening, but also that severe conditions and wear at an early stage produced a polishing effect and reduced roughness. This is a point which will be revisited later in this section in the context of lubricant additives and their effects.

The topology of a surface evolves and changes throughout a test, and this was considered in detail in the work of Martins *et al.* (2011) who performed a number of stages of testing on a set of ground gears, increasing the torque with each loading

period. The surface topology was monitored using areal scans between each test stage, allowing more detailed observations to be made of the evolution of the surface and the different metrics used to quantify this. The majority of surface modification was found to occur in the first 200,000 cycles of testing, and surfaces were found to decrease in roughness until micropitting increased rapidly in severity in the closing, overloaded stage of the test. In this final stage, Rmax (the difference between minimum and maximum heights) increased, which suggests the possibility that features previously at mean height may start to become the new peaks of the profile.

Martins *et al*. (2011) considered a range of different metrics for quantifying the change in the surface topology. They concluded that the most effective parameters for showing the evolution of the surface through to the micropitting stage were the areal parameters St (height difference between the highest and lowest points) and Sv (largest valley depth). Bergseth *et al*. (2012) found that these parameters did indeed capture many of the changes in topology in their two-disk test, but they did not find the Sv parameter to grow larger than the unused surface as was found in the work of Martins. Bergseth *et al*. (2012) found that polished disks were more effectively separated and experienced little topological change, while all ground surfaces experienced micropitting. It should however be noted that the polished disks used in this instance had no crowning, and as a result operated at a lower pressure than the crowned ground disks, meaning that comparison between them is of limited value. They also found that for preheated disks an iron sulphide layer, formed as a result of a sulphurous additive used during the preheating process, can act as a sacrificial layer for wear. This resulted in reduced friction, but also significant mass loss from the disk. Despite this, preheating did not influence micropitting behaviour.

Some simulation work also has directly addressed the influence of surface topology on fatigue, one highly relevant example being that of Epstein *et al*. (2003) who considered eight different surface topologies generated by different manufacturing methods. A mixed EHL simulation was used, coupled with a fatigue calculation based on the work of Zaretsky (1987) and Ioannides and Harris (1985). These simulations showed that the roughness of the surface was not the only driver of fatigue failure: while dimpled and polished surfaces showed the most resistance to fatigue, ground surfaces (the roughest used) showed a middle-of-the-field performance. It was concluded that the driving factors were the pressure developed on asperities and the near surface shear stress, which were influenced by the textural qualities of the different surfaces, while the lubrication mode was also altered by roughness and surface texture.

Cao *et al* (2019) also applied the Zaretsky fatigue model to investigate the difference in predicted fatigue lives between surfaces in their run-in and unrun states. They found that the Rq and asperity radius of curvature both showed promise as indicators of surface improvement but did not universally show whether a surface was more fatigue resistant in of themselves. Combining these two metrics into Rq/asperity radius of curvature they found that there was a strong correlation with smaller Rq/asperity radius of curvature leading to longer fatigue life.

The dimpled surfaces used by Epstein *et al*. (2003) were not produced by shot peening, unlike the dimpled surfaces used in the experimental work of Rabaso *et al*. (2013). It was found that shot peening produced significant resistance to pitting, but perhaps not solely due to reduced roughness; residual compressive stresses and surface hardening were likely also to have a role in this reduction. The work of Shaw *et al*. (2003) (although considering the strength of gears in bending fatigue as opposed to rolling contact) demonstrated that the high compressive residual

stresses imparted by shot peening and similar processes impeded the development of fatigue cracks at oxide inclusions in the near-surface. It is likely that these considerations may also have some effect on surface initiated fatigue cracks in rolling/sliding contact.

Lubricant Additives and Interplay of Fatigue and Wear

A number of studies have shown that the use of anti-wear additives have some influence on fatigue behaviour. Benjayati *et al*. (2003) conducted micropitting tests on disks, comparing behaviour using lubricant with and without the Zinc Dialkyl Dithio-Phosphate (ZDDP) anti-wear additive. It was found that the anti-wear additive had the effect of preserving roughness features, whilst the roughness declined much more rapidly where no anti-wear additive was present. Consequently, micropitting occurred where ZDDP was present while the test conducted with no additive resulted in no micropitting at all. This relationship between anti-wear additives and increased micropitting has also been recreated in subsequent tests (Lainé *et al*. 2008). Benjayati *et al*. (2003) confirmed that increased micropitting is not directly caused by the additive (but instead indirectly by its preservation of the surface) by a second test where ZDDP was added after the running-in period with no observed increase in micropitting versus the tests with no additive.

Brizmer *et al*. (2013) compared experiments with a number of lubricants and additives with a theoretical model which predicts micropitting. Their model found good agreement with the experimental results, and showed that the amount of micropitted area on a disk decreased with increasing wear rate. It was thus concluded that the effect of anti-wear additives is purely mechanical in nature as

wear removes surface features and fatigue damaged layers at the surface, which is also in line with previous findings.

Further modelling work to simulate micropitting has more recently been undertaken by Morales-Espejel *et al*. (2018). These simulations included both a wear model and a fatigue model (based on the Dang Van criterion) and were able to account for removal of material from the surfaces as they accumulated damage. The wear coefficient could be changed in the program, and it was shown that the least amount of micropitting occurred where wear was highest, and the most where no wear occurred. The wear process was shown to remove asperity peaks, thus reducing the high stress concentrations and number of cycles which are the direct causes of fatigue. Further simulation work performed by Zhou *et al* (2019a) resulted in similar conclusions, but also made the interesting observation that reduction in stress cycles and amplitudes as the test goes on implies a reduction in micropitting risk as the test progresses.

Morales-Espejel (2020), added thermal damage estimation to the experimental model developed in Morales-Espejel *et al* (2018). This considered thermal softening of the steel resulting in smearing, and micro-scuffing. A key conclusion of this modelling work and the associated experimental validation was that while thermal failure can be catastrophic it can also develop gradually. Where a gradual onset occurs, thermal failure modes can join the existing competition between wear and fatigue processes.

Simulation work undertaken by Liu *et al* (2020) based upon the interaction of large wind turbine gear teeth also included removal of material due to wear. Their analysis suggested that, while an amount of wear may restrain micropitting, the location of peak accumulated damage moved further into the subsurface as wear progressed. The eventual fatigue failure location was an order of magnitude further

below the surface than the initial peak of damage in the early stages, leading the authors to suggest that while wear may outcompete surface-initiated fatigue (such as micropits), subsurface fatigue may then become the dominant failure mechanism.

Similarly to the impact of lubricant additives, it has been shown that some coatings can prevent micropitting at the expense of an increase in wear processes. A number of Diamond-Like-Carbon (DLC) coatings were compared to uncoated gears by Moorthy and Shaw (2012) and from this the BALANIT® C and Nb-S coatings received further in-depth investigation (Moorthy and Shaw 2013). In the case of BALANIT® C one surface lost its coating in the dedendum region leaving the other hard-coated surface to wear the surface away to a polished appearance. This same effect was seen in all coatings explored other than Nb-S, and the wear processes were shown to cause significant deviation from the gear tooth profile. Zhang and Shaw (2016) also found reduced micropitting from the WC/C coating (the same type of coating as BALANIT® C) at the expense of wear. In contrast to this, Singh *et al*. (2016) investigated the use of a soft, Highly Hydrogenated Diamond-Like Carbon (H-DLC) coating in a 3 disk, 1 roller micropitting rig. They found that the coating markedly increased resistance to fatigue, with no coated specimens failing within 100 million cycles whilst uncoated specimens failed within 32 million cycles. It was also suggested that the coating made a transition to graphite under operating conditions and was able to transfer between surfaces, explaining how specimens were able to survive to 100 million cycles even when only one surface was coated. It is possible, therefore, that some coatings may aid in the avoidance of micropitting.

Although the literature has shown that allowing some wear can reduce micropitting, it should not be forgotten that wear can be a damaging process in itself. It may be that, as shown by Li and Kahraman (2013) and Benjayati *et al*. (2003), allowing a

limited amount of wear to occur before then restraining it (either through lubricant additives or operating conditions) is one way of achieving a comfortable balance between these processes.

Summary & Areas for Development

Roughness and topology are likely the most extensively researched influences on micropitting fatigue behaviour. It is known that improving the surface finish of gears (i.e. reducing the roughness) results in improved fatigue performance – and hence cost is the primary reason that this is not more widely done outside of safety-critical components. This work does not include surface roughness as a variable, however it is vital to keep in mind the effect that surface roughness and texture have upon gears.

The relationship between wear and fatigue discussed in this section is of particular relevance to this work however, as the primary variables in considered here are all known to have influences on wear through adding to or opposing abrasive contact. By considering these variables across a range of settings it may be possible to evaluate how they individually and collectively effect the balance between fatigue and wear behaviours.

A fair amount is present in the literature regarding running in, however much of it falls into either being concerned with which parameters best indicate how much the surface has been changed, or when running in has finished and normal operation has begun. Quantitative analysis of how contact conditions influence different aspects of surface modification has been limited, and the current work aims to perform an extensive investigation of this to fill this gap.

1.4.4 Influence of Lambda Ratio and Film Thickness

A major purpose of the lubricant film in an EHL contact is the separation of the opposing surfaces, a primary reason being to prevent wear and damage being done to the surfaces. Using the film thickness alone as a metric is insufficient to describe its effectiveness when surface roughness features have heights of the same order as the lubricant film thickness. While a lubricant film may appear to be thick, a sufficiently rough surface may still result in partial failure to separate the surfaces. The specific film thickness or Λ ratio serves to quantify this effectiveness of surface separation.

It has been long appreciated that where the asperities of the opposing surface are able to protrude through the film (i.e., where the film thickness is less than the height of the asperities) the probability of micropitting failure is increased. This was noted as far back as the work of Littmann and Widner (1966) relating to peeling failure. This work was prior to the introduction of the specific film thickness term, but their results show that low Λ values result in damage to the surface. Notable also in this work is the appreciation of local film thinning and pressure loss effects caused by deep grinding marks, scratches, and features that enable side leakage. Figure 1.4.7 gives an example of how this local depressurisation and film thinning may lead to surface failure.

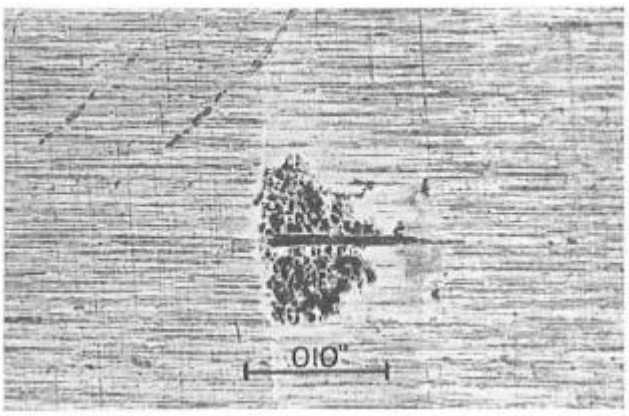

Figure 1.4.7 A cluster of micropits caused by loss of film thickness and pressure in the region of the very deep grinding mark in the centre. Figure reproduced from Littmann and Widner (1966).

More recent papers have also discussed the propensity for ground surfaces to allow lubricant to escape the sides of the contact area through roughness valley features. This was shown, in simulations conducted by Holmes *et al*. (2005), to result in an increase in the contact count at the transverse edges of the contact area. Although Holmes' work was concerned with scuffing, this increased contact count can be extrapolated to imply increased fatigue damage and the occurrence of fatigue failure in a shorter operating time. Krantz (2005) found that a channel like wear feature was developed at the edge of the contact area for ground gears, which was suspected to be linked to lubricant starvation due to leakage at the edge of the contact. This was contrasted with the results for superfinished gears which did not have this channel-like feature, this being attributed to the lack of valley features through which leakage could occur.

The Λ ratio can in many ways be seen as a product of the operating conditions as opposed to a separately controllable independent variable. The film thickness is affected by the load, temperature, lubricant viscosity, and contact geometry, and in calculating Λ the roughness is also introduced as a factor. This gives good reason

to ask whether all Λ ratios are created equal: can a value of Λ be deemed a "safe" value, or must the specific conditions which contribute to that value be taken into account?

Webster and Norbart (1995) compared the wear depth measured in a series of roller disk tests at constant load to the calculated specific film thickness for that test. All tests but one were carried out at a load of 2.1 GPa, an SRR of 0.2, and an average entraining velocity of 5.43 m/s. The roughness of the surfaces, the supply temperature and the lubricant were varied. These tests effectively showed no relationship between the value of Λ and the resultant depth of wear – the most severe wear occurred at Λ=1.06, and the second most at Λ=1.87. The supposedly worse cases of Λ=0.46 gave a middle-of-the-field performance, while the second-best performance was given by a test at lower load and SRR with a Λ of 0.47. The wild variability in these results strongly argues against any suggestion that Λ can be used in isolation to define the resistance of a system to damage.

The experimental work of Wellauer and Holloway (1976) tested gears using petroleum and ester-based lubricants at different specific film thicknesses. This did not look specifically at micropitting but investigated the influence of Λ on surface distress – defined as *"surface pitting or wear which might be destructive or could shorten the gear drive life"*. Nevertheless the findings of this paper were that a larger value of Λ is needed to prevent surface damage when the operating speed is higher. This would suggest that the exact conditions contributing to a particular value of Λ are highly relevant, and this was directly discussed by Olver (2002), who identified a number of factors in this discussion. Notably, the high speeds introduce a number of (thermal) film-thinning effects which if not considered can often result in an overestimate of the true thickness of the film (and hence the calculated Λ needed to avoid damage at high speed may be an overestimate). It was also

discussed however, that the increased cycle rate and greater speed of sliding (which in turn generates higher temperatures) may have significant influence on the propensity for failure at a given Λ. The influence of competing wear effects is also relevant, as it has been shown (Morales-Espejel *et al*. 2018) that micropitting increases as Λ is reduced only up to a point where wear processes become dominant over fatigue.

In an attempt to address the lack of comparability between studies, Krantz (2015) combined previous results and a number of new gear tests to create a dataset of 258 comparable tests ranging from Λ=0.47 to Λ=5.2. The study investigated the relationship between fatigue failure of the surface and the specific film thickness, and found a nonlinear trend of increasing fatigue life with increasing specific film thickness. Tests showed significant increase in life with specific film thickness as Λ increased from just below Λ=1 to around Λ=2, and a levelling off of this increase with Λ>2. Under full film conditions, gear tests (aborted when vibration triggered a stop) lasted 8-10 times longer than those in a mixed regime, and some superfinished gear sets did not fail in over 300 million cycles. It should be noted that none of the end-of-test failures in this study were due to micropitting; all failures resulting from macropitting or spalling. This is likely to be due to very high speed of operation (10,000 rpm / pitch line velocity 46.5 m/s) and high hertzian contact pressure of 1.9GPa used as standard operating conditions for these tests.

In much lower Λ conditions than those investigated by Krantz (0.06-0.23), Zhou *et al* (2019b) found that the extent of micropitting increased nonlinearly from Λ=0.06 to 0.16 before decreasing. This is likely a further manifestation of the competition between wear and fatigue processes discussed in Section 1.4.3.

One means of investigating the specific film thickness while holding the majority of other effects constant is to change the viscosity of the lubricant fluid. This is not

practical to do in a single physical experiment, however numerical simulations allow this method to be used, and this was the procedure adopted by Sharif *et al*. (2012) using fatigue models and the results of mixed-EHL simulations using measured roughness profiles. They found that as the Λ ratio was increased from 0.1 to 2 there was a decrease in calculated subsurface damage of three orders of magnitude, coinciding with a large reduction in the occurrence of direct solid contact between the surfaces. It was also suggested that the mixed lubrication range could be considered to extend across the whole range considered. Figure 1.4.8 shows an example of the results obtained in this work, corresponding to the surface of the wheel. This work has particular relevance to the current trend of decreasing viscosity of lubricants being used in real engineering applications in the name of increased efficiency. Keeping in mind the question raised already in this section regarding the 'equality' of Λ ratios, it would be interesting to see this same test performed with a few other sets of constant operating conditions. This might then help to more comprehensively classify the true impact of the specific film thickness.

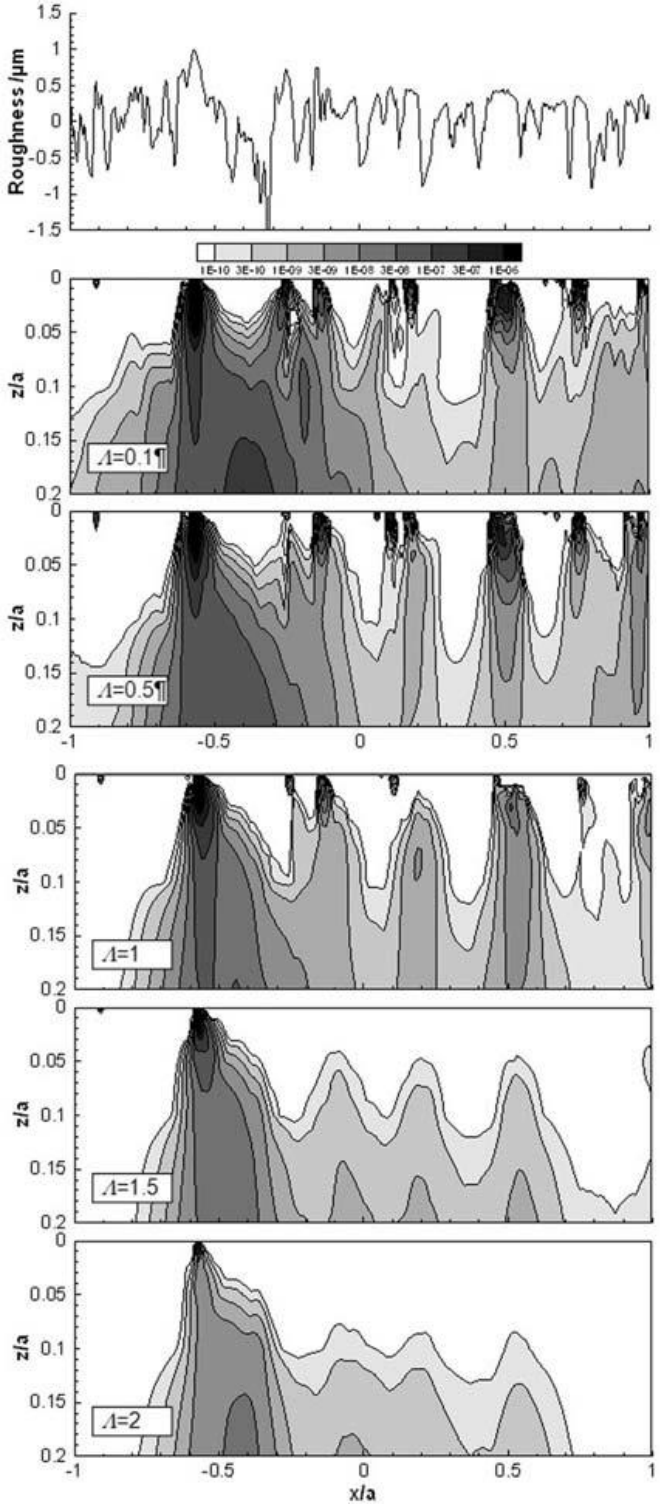

Figure 1.4.8 Contour plots of predicted subsurface damage on the wheel gear at a range of Λ ratios produced by changing the viscosity of the lubricant. Note that the most severe damage is located very close to the surface, and that the damage predicted for the surface decreases notably as Λ is increased.

Summary & Areas for Development

The literature regarding film thickness is broadly in agreement that film thickness alone is a comparatively meaningless term, and must be qualified in some form. The widely-accepted means of doing so is via the ratio Λ, which considers film thickness in the context of surface roughness to determine how thick a film needs to be to effectively separate roughness features. This is considered by some to be the end of the matter – separate the surfaces and damage will be prevented. In some ways this may be a simplification however, as other inputs to the contact may have their own influence which either cause deviation from the predicted film thickness, or demand a greater film thickness to mitigate them. This is not extensively considered in the literature, and remains an unanswered question.

The current work will conduct experiments under a range of conditions, including a range of Λ ratios – albeit all well within the "mixed" bracket of Λ values. In doing so this will produce new data from which the interaction of calculated Λ conditions with other variables can be evaluated.

1.4.5 Influence of Speed, Sliding Speeds and Slide-Roll Ratio

The SRR is a key parameter describing the amount of sliding which takes place in a contact. It is commonly used to describe conditions in both real gearing systems (where the SRR is dependent on the current point in the meshing cycle) and in twin-disk experiments (where the SRR can be controlled). The SRR is calculated as the ratio between the sliding speed and the entrainment (or mean) velocities as follows, where u_1 and u_2 are the velocities of each surface and S is the Slide-Roll ratio:

$$SRR = \frac{2|u_1 - u_2|}{u_1 + u_2} \qquad \textit{Equation 2}$$

The role of the SRR and of sliding in the micropitting process has been investigated in a number of studies, with several differing conclusions about the effect of sliding. Despite this, the SRR is clearly a significant parameter in the micropitting process. In his comprehensive review of gear lubrication, Olver (2002) noted research into sliding and SRR of high importance, with particular interest in unravelling why some systems operating with supposedly sufficient film thickness to avoid micropitting can fall victim to this failure under high speed conditions. Also noted was the fact that gear teeth often do not micropit at the location which experiences the most severe loading, but actually at the locations of highest sliding speed.

The shearing of the fluid between two surfaces moving at different speeds does, of course, cause shear heating which can result in a thinner lubricant film and a much smaller Λ ratio, the impact of which has already been discussed. It is likely one of the key components in answering Olver's question of pitting at high speed. The impact of speed and SRR on temperature have also been directly noted as a possible cause for micropitting in cases where martensitic decay has been suggested as a mechanism (Oila and Bull 2005).

Despite this suggestion that sliding is a propagation mechanism for micropitting, more applicable once pits have already appeared, there has been little investigation into the effect of sliding on an already-present micropit. One exception to this is provided by Olver *et al*. (2004) who observed the behaviour of a micropit in an EHL contact against a glass plate. They found that under a negative SRR (pit on the slower moving surface, which is always the more severely micropitted) the pit is opened by the frictional forces in the contact, allowing lubricant to leak through the crack network through the pit and consequently reducing the film thickness. In positive sliding the pit was closed by the frictional forces. As the micropit exited the contact, fluid was expelled. It is not beyond the realms of imagination therefore

that lubricant starvation caused by the presence of a pit might assist in the development of further pits.

As a fatigue process, micropitting is driven by the cyclical loading of asperities. The numerical models of Qiao *et al*. (2008) and Morales-Espejel *et al*. (2018) have both directly shown that fatigue damage can become more severe as a result of an increase in asperity loading cycles. Figure 1.4.9 shows the impact of increasing SRR on fatigue resulting from increased cycles of loading.

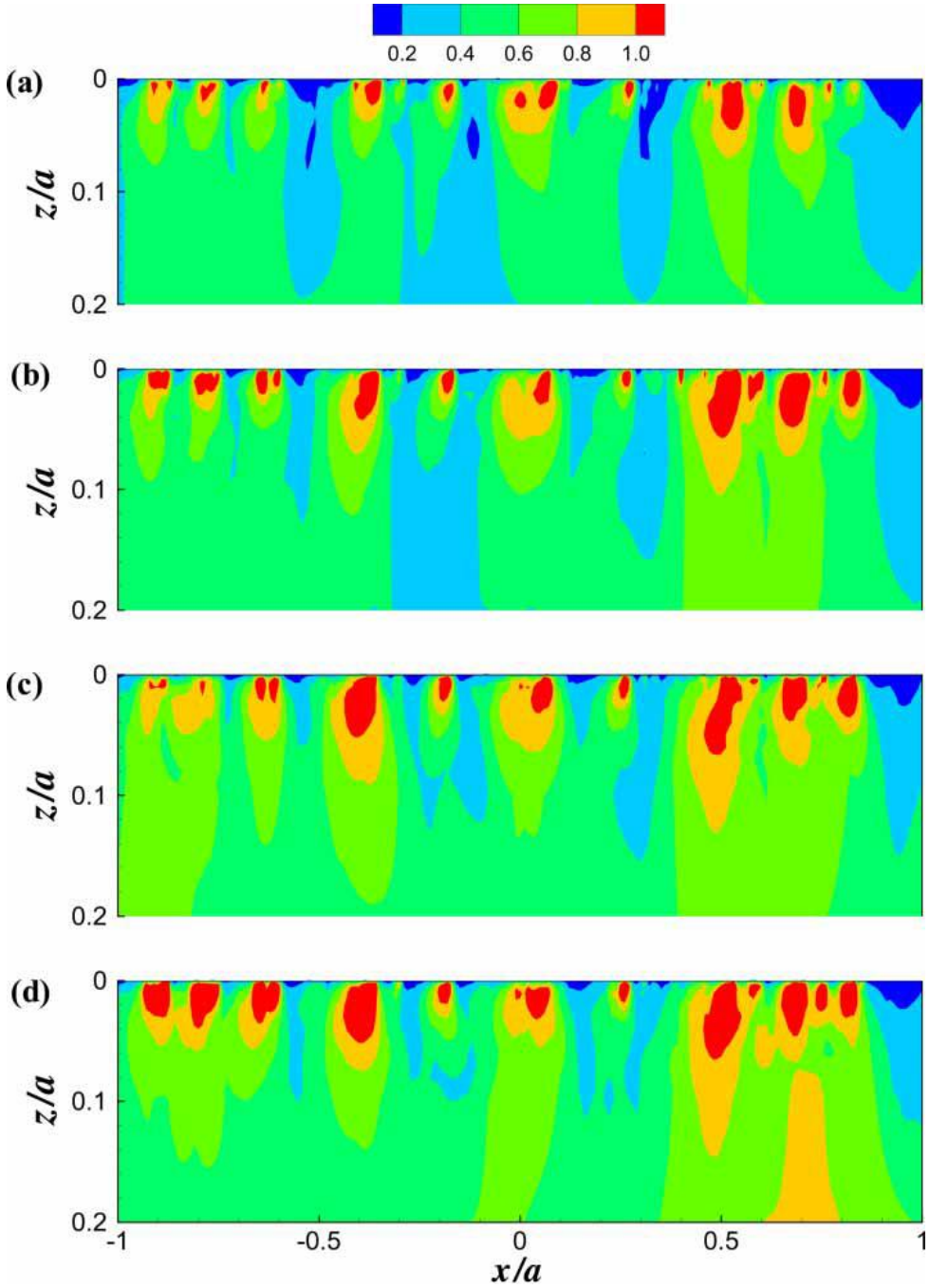

Figure 1.4.9 Influence of increasing SRR on the fatigue parameter for the slow surface assessed using the Dang Van criterion at 10^7 cycles. Slide roll ratios are: a) SRR=0.25, b) SRR=0.5, c) SRR=0.75, d) SRR=1.0 calculated in that paper as (u1-u2)/(u1+u2). Reproduced from Qiao et al. (2008).

The experimental work of Kadiric and Rycerz (2016) further expounds the theory that the increased asperity stress cycles are the dominant effect of sliding on micropitting. A three disk micropitting rig was used with the temperature of the inlet oil modified so as to control the bulk temperatures of the roller and disks, and thus maintain the same oil thickness and Λ ratio for all three tests. By maintaining the same load and entrainment speeds for all tests the SRR could then be isolated, with SRRs of 0.05, 0.15 and 0.3 tested. The severity of micropitting was gauged in this paper by the depth of micropitting wear – an unusual means of measuring micropitting severity. One might consider the percentage of micropitted area a more intuitive and robust gauge of micropitting severity, and a similar experiment conducted with these parameters used would be very interesting for their greater comparability to other tests. Regardless of this, their findings suggested that the amount of micropitting is very highly dependent on the sliding distance (which in turn is directly linked to the number of asperity stress cycles) but independent of the SRR or sliding speed. This is shown in Figure 1.4.10.

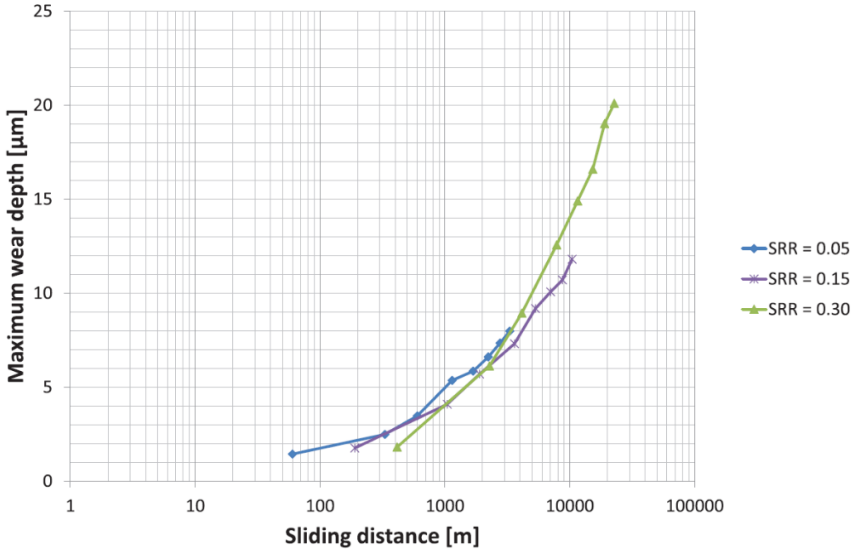

Figure 1.4.10 The amount of micropitting wear has been shown to be directly related to the distance slid (and therefore the number of asperity stress cycles) regardless of the SRR used. Figure reproduced from Kadiric and Rycerz (2016)

A second test was performed with a ball on a sapphire disk to test the effect of increasing sliding on film thickness, aiming to refute decreased film thickness arising from increased temperature caused by sliding as a predominant effect. It was found that the central film thickness only began to decrease from 100% sliding (SRR=1) and above, and this is taken as showing that the impact of sliding on film thickness is only prevalent at very high levels of sliding. This seems contrary to the primary experiment, where oil supply temperature was changed by 23 ºC between SRR=0.05 and SRR=0.3 to maintain film thickness. One must remember however, that the overall thermal behaviour of a ball on sapphire test is very different from the more realistic steel roller test. Further in-depth investigation of the influence of sliding on the film thickness would therefore be very interesting, as there is relatively little available in the literature to confirm or contrast with these findings.

Despite this effect of increasing asperity cycles, Morales-Espejel *et al*. (2018) and the earlier works of Morales-Espejel and Brizmer (2011), Rabaso *et al*. (2013) and Cen *et al*. (2018) have shown that the micropitting will not necessarily increase with sliding – all of these papers identifying sliding as a parameter that can increase wear, influencing the balance of wear and fatigue processes that was discussed in Section 1.4.3.

Guegan *et al*. (2016) investigated the impact of the slide roll ratio on friction in a contact. They found that the friction in smooth contacts is dependent on the SRR, and that in rough contacts the friction may be split into two components - a smooth component (equivalent to a smooth surface under the same operating conditions) dependent on the SRR, and a rough component which is independent of the SRR. It is suggested that this rough component could be due to direct solid contact or to limiting shear stress of lubricant at asperity tips. The rough component was shown

to also have some dependence on the specific film thickness, and friction was shown to level off as speed increases due to shear heating in the lubricant film.

Summary & Areas for Development

The influence of sliding on micropitting and fatigue is an area of debate in the literature, although many have observed that the locations of greatest micropitting on gear teeth also coincide with the areas of greatest sliding. It has been suggested variously that sliding may influence micropitting through increased asperity cycles, increased shearing driving thermal effects, or indirectly through its influence on the balance of wear and fatigue effects. Certainly no broadly accepted influencing effects or mechanisms seem to have been adopted by the wider research community.

The current work will aim to address this by considering slide-roll ratio as a variable across running-in and micropitting tests and simulations. From this, the understanding of both the direct effects of sliding and its interactions with other variables including speed can be investigated.

1.4.6 Influence of Load / Pressure

It is well agreed that the Hertzian pressure experienced as a result of the load is a key influence on the micropitting behaviour of the contact. Both Oila and Bull (2005) and Li and Kahraman (2013) found the load to have a significant impact on the micropitting behaviour. Higher load during normal running (i.e. not during the running-in phase) resulted in an increase in the number of pits in the tests run by Li and Kahraman, and Oila and Bull found that the load was the most significant factor in the initiation of micropits.

It is notable however that Li and Kahraman considered the load during running-in to be a distinct variable, with analysis of the results indicating that a higher running-

in load at a slower speed (in other words, very harsh conditions) had a polishing effect on the disks which reduced the amount of micropitting. In contrast with this, Mallipeddi *et al*. (2017) found that a high load during the running-in process increased micropitting despite a smoothening of surface asperities. Micropitting was instead found to be associated with the higher levels of near surface residual stress resulting from the higher load during running-in.

The load increasing tests conducted by Webster and Norbart (1995) provided interesting results when compared to the constant load tests which were initially conducted in their experimental programme. Under constant load conditions the rate of micropitting slowed in the later stages of the test, but in the load increasing tests the rate of micropitting increased with the load. This was common across all slide roll ratios and lubricants, strongly indicating that increased Hertzian pressure acts as a driving factor in micropitting.

Zhou *et al*. (2019b) found the applied pressure to be a very significant factor in micropitting. Under a load of 1 GPa, mild micropitting was observed on the surface at the test cut-off limit of 100 million cycles. As the pressure was increased to 1.5 GPa, 1.9 GPa and 2.5 GPa, micropitting became more severe and total failure occurred earlier in the test – the highest pressure causing failure just 12 million cycles into the test. This paper contested the statement made by Oila and Bull (2005) that the pressure only significantly affected micropitting initiation, finding that the propagation of micropitting was also strongly influenced by the pressure.

Prajapati and Tiwari (2020) did not directly change the applied load, but changed the radius of curvature of one test disk in the direction perpendicular to entrainment while maintaining a constant load. The primary consequence of this was that the smaller radius of curvature had a raised pressure (1.96 GPa) relative

to the larger radius of curvature (1.5 GPa). They showed that pits were deeper and micropitting more severe in the case of disks with a smaller radius of curvature.

As is ever the case, not all experimentation is in agreement that higher load results in an increase in micropitting. The twin disk tests conducted by Rabaso *et al,* (2013) found that changing the Hertzian pressure in the range 1.5 GPa to 2.5 GPa had no effect at all on the extent of micropitting in either pit depth or percentage of surface pitted.

Summary & Areas for Development

The general understanding of the effect of load in the literature is that increasing the pressure within the contact results in increased micropitting. This is likely through increased stress on asperities causing cracks to initiate and grow. Some literature has suggested that the effects of pressure on fatigue are not necessarily linear – that effects may lessen above a certain pressure, or (discussed in reference to proposed mechanisms) that a threshold load may cause material to transform.

One gap in the literature that the current work aims to investigate is the interaction effects between pressure and other variables. Previous works which included pressure effects did include confounding, hence interactions observed previously need to be considered with caution. By looking at pressure effects without these issues this thesis can add a more robust understanding of the relationship between pressure and other variables.

1.4.7 Further Literature

In many real-world gear systems a “hunting ratio” is selected as the gear ratio. This refers to a ratio of gear teeth which have no common factors other than 1 – the result of this being that each gear tooth on one gear makes contact with every tooth of the opposing gear. This is in contrast to other ratios in which each gear tooth

comes into contact with only a small set of teeth on the mating gear. The benefit of this system is that no gear tooth experiences contact under better or worse conditions than any other, therefore all teeth should wear at the same rate. Ishibashi and Tanaka (1981) compared the effect of using a hunting gear ratio versus a unity gear ratio with respect to pitting. Running at a range of loads with a number of steels of different hardness it was found that gears with a hunting ratio of 1.08 are susceptible to pitting at a lower load and suffer a greater amount of fatigue damage compared to gears with a ratio of 1. This work also suggested that the influence of this effect is reduced as the surface finish is improved, although all surface roughnesses considered are comparatively rough by modern standards. It is possible that this increase in susceptibility to pitting is due to poorer conformity between surfaces under the hunting ratio arrangement, while under conditions where each tooth sees only a small number of other teeth the running-in process can "tailor" the modified surface to accommodate the smaller number of loading scenarios to which it is subjected.

1.4.8 Summary

The literature review conducted here has helped to identify where the collective understanding of the field is quite deep but also where further research can provide useful contributions. It is fairly well established that increased roughness, poorer lubrication relative to that roughness, and higher loads all cause a trend to greater micropitting. Understanding of the influence of sliding on micropitting has been less extensively explored, however literature suggests that increased asperity loading cycles may cause greater amounts of fatigue. There is a general understanding of how surface appearance is modified through the running-in process, however there has been little exploration of how contact conditions influence running-in – most research concerning how to best determine the conclusion point of running-in. For both running-in and micropitting fatigue, interaction effects between factors

influencing the contact conditions have been neglected, or at best may be difficult to reliably determine from confounded experimental designs.

1.5 Thesis Objectives

The goals of this thesis can be distilled into three primary objectives, which form the basis of this thesis structure. These objectives are as follows:

1. To investigate the influence of operating conditions on early-stage micropitting behaviour for contacts representative of those in highly loaded ground gears.
2. To investigate the influences of operating conditions on the running-in behaviour of ground gear surfaces.
3. To perform computational simulations of fatigue using real gear surface profiles and compare the influence of operating conditions on fatigue simulation output with experimental data.

These objectives will be revisited in the conclusions of this work.

2 Elastohydrodynamic Contact Theory and Simulation for Fatigue Analysis

This chapter discusses some of the fundamental theory and equations governing the contact between two surfaces such as gear teeth or disks, as seen in the experimental work in this thesis. It begins with an explanation of Hertzian contacts, followed by an introduction to the two equations governing EHL contacts; the hydrodynamic Reynolds equation and the film thickness equation.

The theory behind the EHL contact simulation and fatigue analysis is then discussed.

The application of theory to the simulation as discussed here was not developed in this work, and is employed here as in previous works at Cardiff (Holmes 2002; Davies 2005; Qiao 2005). Novel developments in the approach to simulation in this work concern the selection of input profiles and processing of results as discussed in Chapter 6: Simulation. This model has previously been shown to correlate well with individual experimental results such as Al-Mayali et al (2018), however has not been previously tested against a range of experimental conditions.

2.1 Elliptical Hertzian Contacts

Heinrich Hertz famously gave birth to Hertzian contact theory (and by extension, the field of contact mechanics) whilst attempting to calculate the deformation of stacked optical lenses over the course of his Christmas break. These models, while not originally intended for this purpose, are now routinely used by tribologists as a starting point for the analysis of concentrated tribological contacts because of their reliable predictions of contact dimensions and pressures. It should be noted that Hertzian contact theory is applied to ‘smooth’ surfaces, however it can also be used to provide reasonable estimates for ‘rough’ contacts. Figure 2.1.1 shows the contact between two curved surfaces resulting in an elliptical contact area.

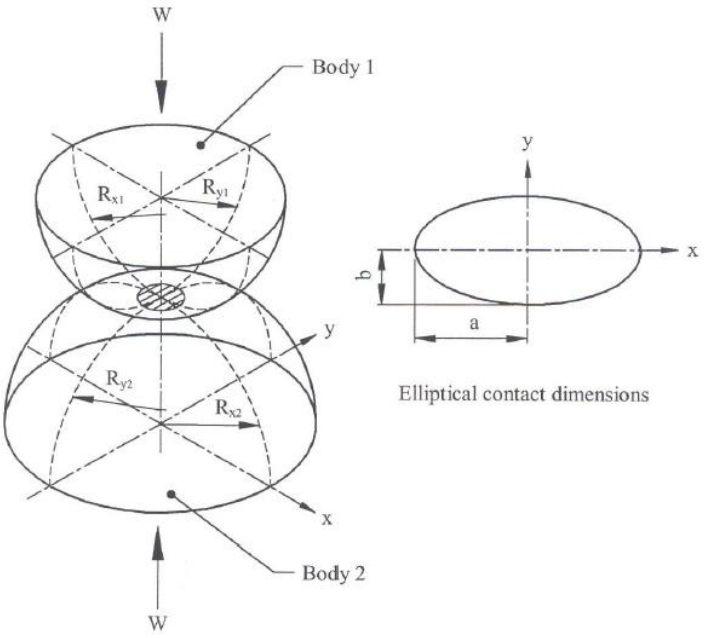

Figure 2.1.1 Two curved surfaces in contact under load, with the resultant elliptical contact area shown on the right. Figure reproduced from Holmes (2002).

The dimensions *a* and *b* illustrated above are referred to as the contact dimensions. Elliptical contacts occur where the radii of relative curvature in the two principal axes are not equal. The radii of relative curvature in the x and y axes (as per Figure 2.1.1) are calculated as:

$$\frac{1}{R_x} = \frac{1}{R_{x1}} + \frac{1}{R_{x2}} \qquad \textit{Equation 2-1}$$

$$\frac{1}{R_y} = \frac{1}{R_{y1}} + \frac{1}{R_{y2}}$$

The contact at the interface between the disks used in the twin disk tests conducted in this thesis are elliptical, as is the case between a ball bearing and its raceway and is often the case between gear teeth, for example spur gears with axial crowning. In gears the contact dimensions and pressure are dependent on the current point in the meshing cycle. This is a result of changes in loading as the

number of teeth in contact changes, but also because the radius of curvature for each surface changes as the contact moves along the involute profile. Figure 2.1.2 illustrates this.

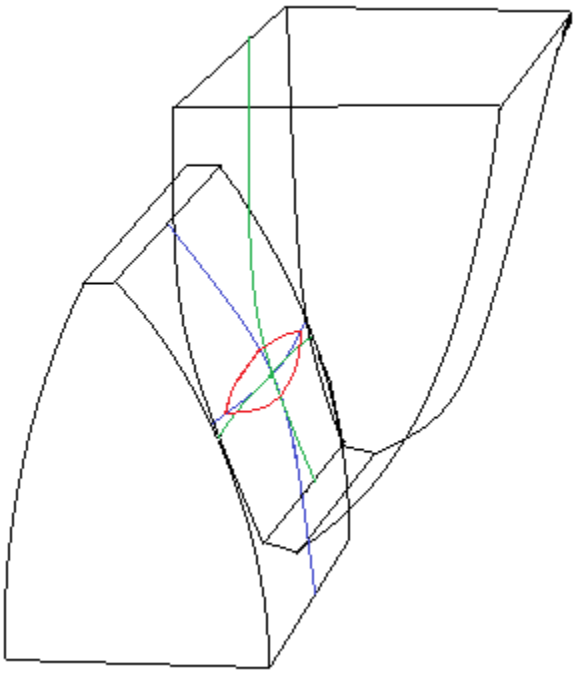

Figure 2.1.2 An illustration of two contacting gear teeth with an elliptical contact area between them. It can be easily visualised that the radii of curvature would be drastically different at different stages of the meshing cycle.

A full derivation for determination of contact pressures and dimensions can be found in Timoshenko and Goodier (1970). The derivation shown in that reference makes use of two dimensionless parameters *m* and *n*, however these parameters are used here in their more commonly encountered form as *k* and *F*, obtained graphically from Figure 2.1.3 using the ratio $\frac{R_x}{R_y}$ computed from values obtained from Equation 2-1.

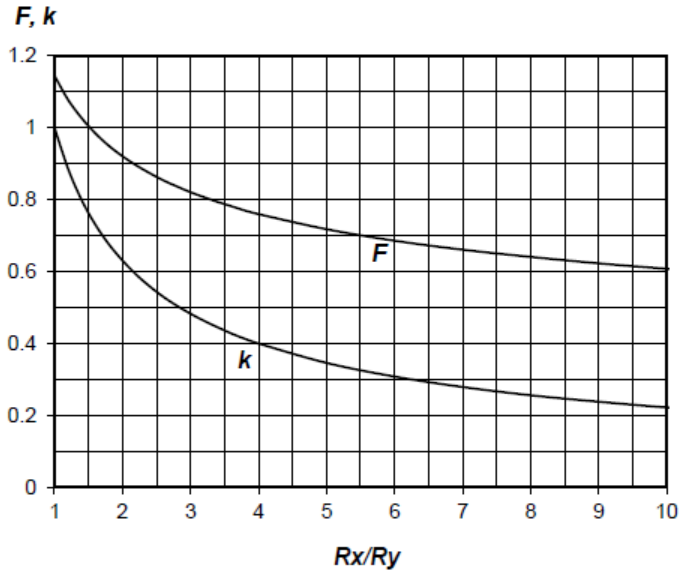

Figure 2.1.3 Dimensionless parameters k and F.

The reduced radius of curvature, $\bar{R}$ can be calculated from R_x and R_y as shown below:

$$\frac{2}{\bar{R}} = \frac{1}{R_x} + \frac{1}{R_y} \qquad \textit{Equation 2-2}$$

The material properties of the two contacting bodies must also be accounted for. The parameter *E'* is calculated from the Young's modulus and Poisson ratio of each material, as shown in Equation 2-3.

$$\frac{2}{E'} = \frac{1-\nu_1^2}{E_1} + \frac{1-\nu_2^2}{E_2} \qquad \textit{Equation 2-3}$$

The necessary parameters have now been obtained to allow calculation of the pressures and dimensions within the contact when load *w* is applied. Firstly, the contact dimension *b* (the half-width of the contact in the y direction, perpendicular to entrainment) is found as:

$$b = F\left(\frac{\bar{R}w}{E'}\right)^{\frac{1}{3}}$$ *Equation 2-4*

The contact half-width in the x direction can then be found from *b* using Equation 2-5.

$$a = \frac{b}{k}$$ *Equation 2-5*

The maximum pressure can then be calculated from the load and the contact dimensions found above.

$$P_0 = \frac{3}{2}\frac{w}{\pi ab}$$ *Equation 2-6*

The mean pressure in the contact is then equal to two-thirds of the maximum contact pressure.

$$P = \frac{2}{3}P_0$$ *Equation 2-7*

2.2 The Film Thickness Equation

In an EHL contact, the surfaces of the contacting bodies are forced to elastically deflect in order to accommodate the lubricant film which has been entrained into the contact area. A typical centreline section in the entrainment direction is shown in Figure 2.2.1. In this illustration surface 2 is taken to be a rigid surface, hence all deformation is applied to surface 1.

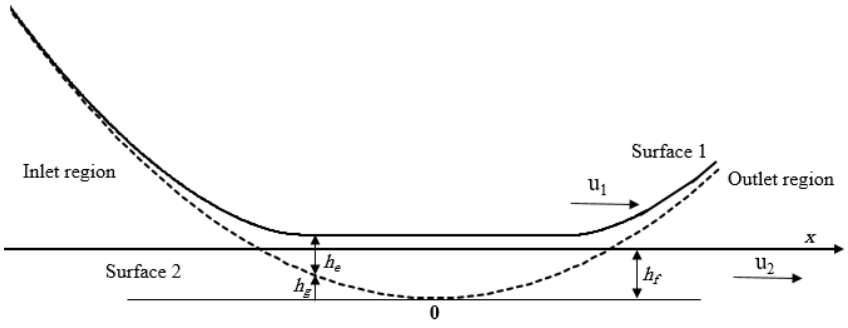

Figure 2.2.1 Geometry of lubricant film in a centreline section of a contact.

The elastic film thickness equation is therefore:

$$h(x,y) = \varphi(x,y) + h_g(x,y) + h_e(x,y) - h_f \qquad \text{Equation 2-8}$$

Where φ contains the combined roughness of the two surfaces, h_f is a constant value for the separation of the surfaces, h_e is the elastic deformation of the surfaces under load, and h_g is the gap between the undeformed surfaces whose geometry is assumed to be given by a parabola as below:

$$h_g = \frac{x^2}{2R_x} + \frac{y^2}{2R_y}$$

The contacting bodies are assumed to be semi-infinite, an assumption based on the small relative size of the contact when compared to the rest of the body. As given by Timoshenko and Goodier (1970), the elastic deflection perpendicular to the surface due to pressure is:

$$h_e(x,y) = \frac{2}{\pi E'} \int\int \frac{p(s,v)}{\sqrt{(s-x)^2 + (v-y)^2}} dsdv \qquad \textit{Equation 2-9}$$

As the lubricant film fills the gap between the two surfaces, the film thickness at a given node in the mesh during a rough surface simulation can therefore be considered as shown in Equation 2-10. This consists of the film thickness at the point of application of the equation, the undeformed geometry, the elastic deformation as above, and an additional term φ containing the combined roughness of the two surfaces.

$$h(x,y) = h_0 + \frac{x^2}{2R_x} + \frac{y^2}{2R_y} + \varphi(x,y) + \frac{2}{\pi E'}\int\int \frac{p(s,v)}{\sqrt{(s-x)^2 + (v-y)^2}} dsdv \qquad \text{Equation 2-10}$$

A differential form of this equation (Equation 2-11) is used to take full benefit of the work of Evans and Hughes (2000), whose use the Laplacian of the deflection to exploit the rapid decay of the weighting functions (f_{ij}) which result from this method.

$$\frac{\partial^2 h(x_i y_i)}{\partial x^2} + \frac{\partial^2 h(x_i y_i)}{\partial y^2} = \frac{\partial^2 \varphi(x_i y_i)}{\partial x^2} + \frac{\partial^2 \varphi(x_i y_i)}{\partial x^2} + \frac{1}{R_x} + \frac{1}{R_y} + \frac{2}{\pi E'} \sum_{all\ k,l} f_{k-1,l-j} p_{k,l} \qquad \text{Equation 2-11}$$

This is employed within the point contact EHL simulation as per Equation 2-12 or within the line contact simulation as Equation 2-13. In this formulation, the most influential mesh points nearest to the point of application are part of the coupled solution updated with every iteration (the “near” contributions), however the “close” and “far” contributions (removed from the point of application by a distance) need only be updated periodically as they have significantly less

influence. This reduces the required computing time significantly when compared to other formulations. The $\bar{E}_{ij}$ term contains the roughness and undeformed geometry terms and remains constant for the duration of each timestep.

$$\frac{\partial^2 h(x_i y_i)}{\partial x^2} + \frac{\partial^2 h(x_i y_i)}{\partial y^2} - \frac{2}{\pi E'} \sum_{near} f_{k-i,l-j} p_{k,l} = \bar{E}_{ij} + \frac{2}{\pi E'} \sum_{close} f_{k-i,l-j} p_{k,l} + \frac{2}{\pi E'} \sum_{far} f_{k-i,l-j} p_{k,l} \quad \text{Equation 2-12}$$

$$\frac{\partial^2 h(x_i)}{\partial x^2} - \frac{2}{\pi E'} \sum_{near} f_{k-i} p_k = \bar{E}_{ij} + \frac{2}{\pi E'} \sum_{far} f_{k-i} p_k \quad \text{Equation 2-13}$$

It has been shown by Holmes (2002) that this can be reduced to Equation 2-14 where $C_{i,j}$ and $D_{i,j}$ are coefficients of the pressure and film thickness at the location i,j, while $E_{i,j}$ contains all remaining terms, including the undeformed geometry and near, close and far contributions to the deflection.

$$C_{i,j} p_{i,j} + D_{i,j} h_{i,j} = \bar{E}_{i,j} \quad \text{Equation 2-14}$$

2.3 The Hydrodynamic Reynolds Equation

The hydrodynamic Reynolds equation is used to calculate pressures in a lubricant film. It is simplified from the Navier-Stokes equations by the introduction of several assumptions:

1. Flow is laminar
2. Inertia terms are negligible
3. No slip occurs at the surfaces

4. The fluid is Newtonian, hence shear stress is proportional to shear strain (although this may be relaxed)
5. Pressure, density and viscosity do not vary through the thickness of the film
6. Body Forces are negligible

The Equation is derived by application of equations of motion and continuity to a small element of fluid as shown in Figure 2.3.1.

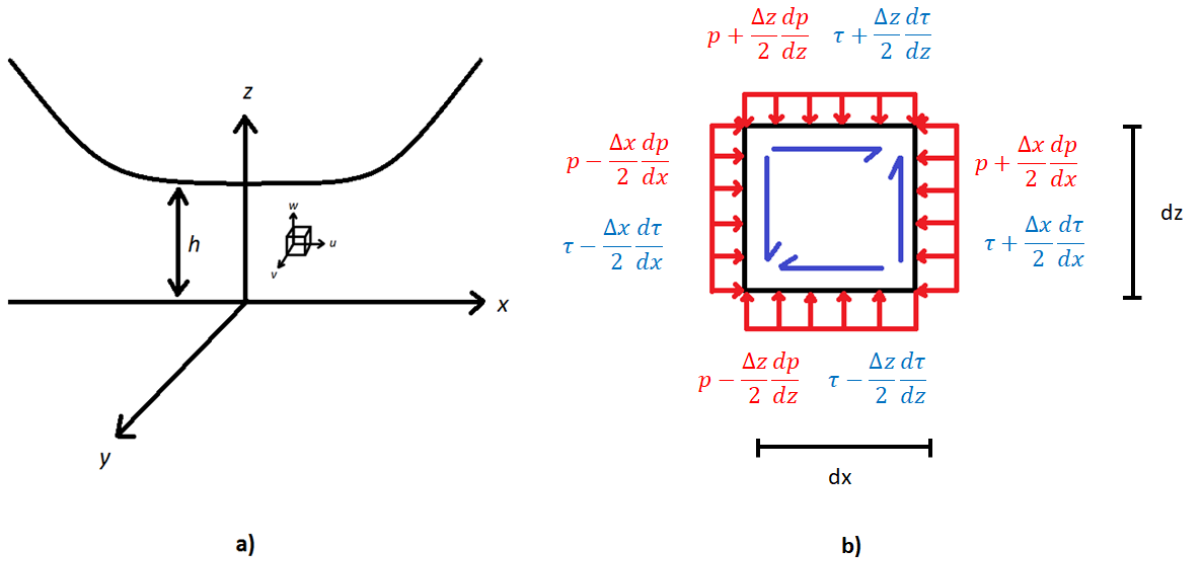

Figure 2.3.1 a) Shows an element of fluid in the lubricant film between two surfaces. b) Shows the pressures and shear stresses acting upon that element in the x-z plane. Similar diagrams can be made for the y-z plane, however the x-z alone is shown for simplicity.

Considering the forces acting in each direction in the whole elemental volume gives:

$$x\ direction: \qquad \frac{\partial \tau_{zx}}{\partial z}+\frac{\partial \tau_{yx}}{dy}=\frac{dp}{dx}$$

$$y\ direction: \qquad \frac{\partial \tau_{zy}}{\partial z}+\frac{\partial \tau_{xy}}{dx}=\frac{dp}{dy}$$

For both the x direction and y direction, the shear stress in the x-y plane is negligible compared to the other shear stress term, hence this term can be neglected. Hence the remaining identities are:

$$x\ direction: \qquad \frac{\partial \tau_{zx}}{\partial z} = \frac{dp}{dx}$$

$$y\ direction: \qquad \frac{\partial \tau_{zy}}{\partial z} = \frac{dp}{dy}$$

On the assumption of a Newtonian fluid (assumption 4), the shear stress is proportional to the velocity gradient. Substituting this in gives:

$$x\ direction: \qquad \frac{\partial}{\partial z}\left(\eta \frac{\partial U}{\partial z}\right) = \frac{\partial p}{\partial x} \qquad \textit{Equation 2-15}$$

$$y\ direction: \qquad \frac{\partial}{\partial z}\left(\eta \frac{\partial V}{\partial z}\right) = \frac{\partial p}{\partial y}$$

Integrating twice with respect to z then yields:

$$U = \frac{z^2}{2\eta}\frac{\partial p}{\partial x} + Az + B$$

$$V = \frac{z^2}{2\eta}\frac{\partial p}{\partial y} + Cz + D$$

Because of the assumption of no slip at the surfaces, the fluid velocity is equal to the velocity of the surfaces. Therefore, the following boundary conditions can be applied:

$$At\ z = h; \qquad U = U_1\ and\ V = V_1$$

$$At\ z = 0; \qquad U = U_2\ and\ V = V_2$$

Using these boundary conditions the values of the constants A, B, C, and D can be obtained and the expressions for U and V become:

$$U = \frac{1}{2\eta}\frac{\partial p}{\partial x}(z^2 - zh) + \frac{z(U_1 - U_2)}{h} + U_2$$

$$V = \frac{1}{2\eta}\frac{dp}{dy}(z^2 - zh) + \frac{z(V_1 - V_2)}{h} + V_2$$

Equation 2-16

Thus far only conservation of momentum has been considered, however conservation of mass must also be accounted for. Figure 2.3.2 shows the flow of lubricant into an elemental volume. The only flow in the z direction (perpendicular to the surfaces) is the squeeze film term, which arises due to compression of the lubricant.

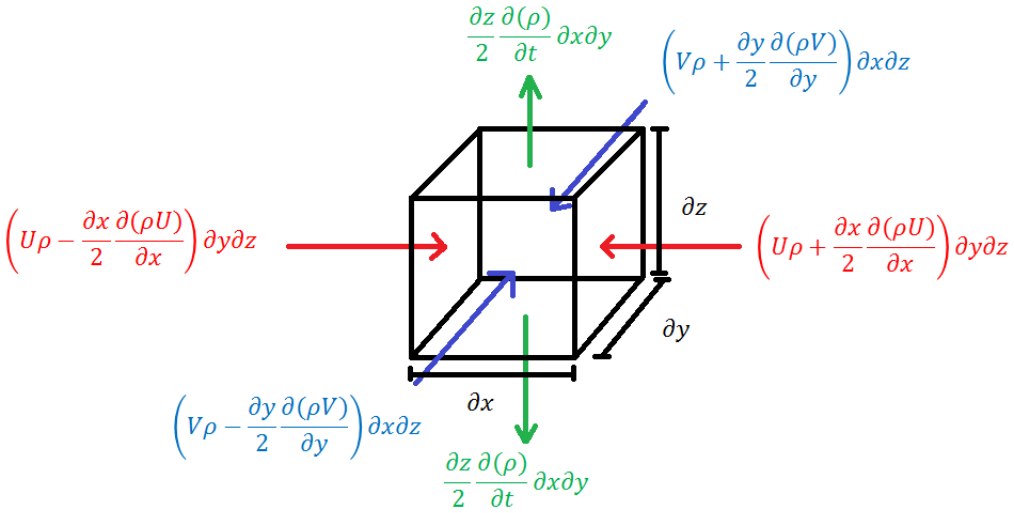

Figure 2.3.2 Lubricant flow into a volume element

The sum of the flow into and out of the element must be equal to zero for continuity of mass to be satisfied. Summing the flows in Figure 2.3.2 gives the continuity equation for a single element to be:

$$\frac{\partial \rho U}{\partial x}\partial z + \frac{\partial \rho V}{\partial y}\partial z - \frac{\partial \rho}{\partial t}\partial z = 0 \qquad \text{Equation 2-17}$$

This can be extended to the entire column of fluid by integrating between the two surfaces with respect to z. For a column of fluid, the equation of continuity becomes:

$$\frac{\partial}{\partial x}\int_0^h \rho U \, dz + \frac{\partial}{\partial y}\int_0^h \rho V \, dz - \int_0^h \frac{\partial \rho}{\partial t} \, dz = 0$$

Substituting in the expressions for U and V from Equation 2-16:

$$\frac{\partial}{\partial x}\rho \int_0^h \left[\frac{1}{2\eta}\frac{\partial p}{\partial x}(z^2 - zh) + \frac{z(U_1 - U_2)}{h} + U_2\right]$$

$$+ \frac{\partial}{\partial y}\rho \int_0^h \left[\frac{1}{2\eta}\frac{dp}{dy}(z^2 - zh) + \frac{z(V_1 - V_2)}{h} + V_2\right] - \int_0^h \frac{\partial \rho}{\partial t} \, dz = 0$$

This then becomes:

$$\frac{\partial}{\partial x}\left(\frac{\rho h^3}{12\eta}\frac{\partial p}{\partial x} - \frac{\rho h}{2}(U_1 + U_2)\right) + \frac{\partial}{\partial y}\left(\frac{\rho h^3}{12\eta}\frac{\partial p}{\partial y} - \frac{\rho h}{2}(V_1 + V_2)\right) - \frac{\partial}{\partial t}(\rho h) = 0$$

Letting $\overline{U} = \frac{U_1 + U_2}{2}$ and $\overline{V} = \frac{V_1 + V_2}{2}$ and separating pressure and velocity terms, and finally substituting $\sigma_x = \sigma_y = \frac{\rho h^3}{12\eta}$ as the flow factors (which can be adapted to take

into account Non-Newtonian lubricant rheology) the hydrodynamic Reynolds equation in two dimensions is obtained:

$$\frac{\partial}{\partial x}\left(\sigma_x \frac{\partial p}{\partial x}\right) + \frac{\partial}{\partial y}\left(\sigma_y \frac{\partial p}{\partial y}\right) - \frac{\partial}{\partial x}(\rho \bar{U} h) - \frac{\partial}{\partial y}(\rho \bar{V} h) - \frac{\partial}{\partial t}(\rho h) = 0 \qquad \text{Equation 2-18}$$

This may be simplified depending on the case. For line contacts, terms relating to flow in the y-direction may be removed. In smooth, steady state conditions the squeeze film term may be removed.

Within the simulation program the Reynolds equation is expressed in the form of Equation 2-19. In this formulation, the pressure terms and their coefficients (*A*) for n_c points are summed, along with film thickness terms and their coefficients (*B*). The right hand side R_{ij} contains the squeeze film term which is zero under steady state conditions.

$$\sum_{k=1}^{k=n_c} A_k p_k|_{i,j} + \sum_{k=1}^{k=n_c} B_k h_k|_{i,j} = R_{ij} \qquad \text{Equation 2-19}$$

2.4 The Eyring Model

The lubricant used in the experimental work in this thesis exhibits non-Newtonian behaviour, and hence a model must be adopted to approximate this non-Newtonian behaviour in simulations so that they remain applicable to the problem. In order to achieve this, the Eyring shear thinning rheological model was adopted and applied

through modifications to the flow factors. This model relates shear stress to shear strain as:

$$\dot{\gamma} = \frac{du}{dz} = \frac{\tau_0}{\eta} \sinh\left(\frac{\tau}{\tau_0}\right) \qquad \text{Equation 2-20}$$

Considering a force balance on an elemental volume in the x direction (assuming no flow in the y direction) has been shown to yield Equation 2-21:

$$\frac{d\tau}{dz} = \frac{dp}{dx} \qquad \textit{Equation 2-21}$$

Assuming pressure does not vary through the film thickness, this can then be integrated with respect to z to give:

$$\tau = \tau_m + z\frac{dp}{dx} \qquad \textit{Equation 2-22}$$

Substituting this into Equation 2-20 then gives:

$$\frac{du}{dz} = \frac{\tau_0}{\eta} \sinh\left(\frac{\tau_m + z\frac{dp}{dx}}{\tau_0}\right)$$

Which can be simplified as follows by introducing $\lambda_E = \frac{\tau_m}{\tau_0}$ and $\Sigma_E = \frac{h}{2\tau_0}\frac{dp}{dx}$ to give

$$\frac{du}{dz} = \frac{\tau_0}{\eta} \sinh\left(\lambda_E + \frac{2\Sigma_E}{h} z\right) \qquad \text{Equation 2-23}$$

The velocity of the fluid can then be determined by integrating with respect to z:

$$u = \frac{\tau_0 h}{2\Sigma_E \eta} \cosh\left(\lambda_E + \frac{2\Sigma_E}{h} z\right) + constant$$

Based on the assumption of no slip at each surface, limits of $u = u_1$ at $z = \frac{h}{2}$ and $u = u_2$ at $z = -\frac{h}{2}$ can be applied. This gives a velocity profile *u* and sliding velocity u_s as below:

$$u = u_2 + \frac{\tau_0 h}{2\Sigma_E \eta}\left[cosh\left(\lambda_E + \frac{2\Sigma_E}{h} z\right) - \cosh\left(\lambda_E - \Sigma_E\right)\right]$$

$$u_s = \frac{\tau_0 h}{\Sigma_E \eta} sinh(\lambda_E) sinh(\Sigma_E)$$

Making λ_E the subject:

$$sinh(\lambda_E) = \frac{\eta u_s}{\tau_0 h} \frac{\Sigma_E}{\sinh\left(\Sigma_E\right)} \qquad \textit{Equation 2-24}$$

Now the mass flow in the x direction must be considered (assuming density to be constant). This is given by:

$$Q = \int_{\frac{-h}{2}}^{\frac{h}{2}} \rho u dz = \rho \bar{u} h - \int_{\frac{-h}{2}}^{\frac{h}{2}} \rho \frac{du}{dz} z dz$$

In which the first term is the Couette flow, and the term in the integral is the Poiseuille flow. It can be shown that substituting in $\frac{du}{dz}$ from Equation 2-23, solving the Poiseuille integral and substituting for τ_0 gives the mass Poiseuille flow as:

$$Q_p = -\frac{\rho h^3}{12\eta} \frac{dp}{dx} \left\{ \frac{3[\Sigma_E \cosh(\Sigma_E) - \sinh\left(\Sigma_E\right)]}{{\Sigma_E}^3} \cosh\left(\lambda_E\right) \right\}$$

This can be used to redefine the flow factors applied in Equation 2-18 to become applicable to the non-Newtonian case as:

$$\sigma = \frac{\rho h^3}{12\eta} S \qquad \textit{Equation 2-25}$$

Where S is:

$$S = \frac{3[\Sigma_E \cosh(\Sigma_E) - \sinh(\Sigma_E)]}{{\Sigma_E}^3} \cosh(\lambda_E)$$

Which can be written in its final form by applying hyperbolic identities and substituting in Equation 2-24 to give:

$$S = \frac{3[\Sigma_E \cosh(\Sigma_E) - \sinh(\Sigma_E)]}{{\Sigma_E}^3} \sqrt{1 + \left[\frac{\eta u_s}{\tau_0 h} \frac{\Sigma_E}{\sinh(\Sigma_E)}\right]^2} \qquad \textit{Equation 2-26}$$

S then serves as a non-Newtonian correction to the viscosity, allowing the effective non-Newtonian viscosity to be defined as:

$$\eta_{eff} = \frac{\eta}{S}$$

This means of accounting for non-Newtonian behaviour was incorporated into the simulation by Davies (2005), based on a method developed by Conry *et al*. (1987). The benefit of this method is that the Reynolds equation can be applied exactly as it would be for a Newtonian lubricant (or for any other non-Newtonian model using this method) with only the definition of the flow factor being changed. This avoids unnecessary complexity in the program design and enables easier application of different rheological models if desired – although only the Eyring model is applied in this work.

2.5 The Coupled Solution Method

In all simulations, whether point or line contact, the simulation begins by establishing the pressure distribution and film thickness under the input conditions for a smooth, steady state problem. An initial set of conditions must be calculated as a starting point for the smooth simulation. This starting condition is achieved using the well-known film thickness equation developed by Dowson and Higginson (1977) (line contacts) or Chittenden *et al*. (1985) (point contacts) and applying the corresponding Hertzian pressure distribution. The pressure and film thickness are then converged before roughness profiles can be introduced, in the case of the line contact simulation for the research reported in this thesis.

For both smooth and rough surfaces, Equation 2-14 and Equation 2-19 are applied in the form below, in which the coefficients and unknowns p_0 and h_0 for the point at which the equations are applied are alone on the left hand side while all other information (including the contributions at near, close and far points) is moved to the right hand side.

$$C_0 p_0 + D_0 h_0 = \hat{E}_{i.j} \left\{ = \bar{E}_{i,j} + \sum_{k=1}^{n_c} C_k p_k + \sum_{k=1}^{n_c} D_k h_k \right\}$$

$$A_0 p_0 + B_0 h_0 = \hat{R}_{i.j} \left\{ = R_{i,j} + \sum_{k=1}^{n_c} A_k p_k + \sum_{k=1}^{n_c} B_k h_k \right\}$$

These can then be solved simultaneously to provide new values for the film thickness and pressure in a pair wise Gauss Seidel iteration as:

$$h_{i,j}^{new} = \frac{\hat{E}_{i,j}A_0 - \hat{R}_{i,j}C_0}{A_0D_0 + B_0C_0} \qquad \textit{Equation 2-27}$$

$$p_{i,j}^{new} = \frac{\hat{R}_{i,j}D_0 - \hat{E}_{i,j}B_0}{A_0D_0 + B_0C_0} \qquad \textit{Equation 2-28}$$

This solution method was developed by Holmes (2002) who found that the alternative approach of solving for pressure and then using that result to obtain a corresponding film thickness was unstable. Instead, the coupled approach begins with the assumed pressure and film thickness, and calculates all contributions (including far and, if applicable, close). Then, holding close and far contributions the same but including the near contributions as part of the iterative solution, the calculation is repeated until pressure and film thickness values have converged. The close contributions are then updated and the far ones are updated periodically. This process is repeated until the pressure and film thickness have completely converged. The simulation then progresses to the next timestep.

One final note is that, within the rough line contact simulations in this thesis, mixed and boundary lubrication conditions are encountered. Under these conditions, asperities may make direct contact which results in calculation of a negative or zero film thickness. As the film thickness cannot be negative this must be corrected for, and hence the value of film thickness at the current point, h_0, must be set to zero. This provides a boundary condition at the point that replaces the Reynolds

equation. The unknown pressure at the point is then obtained from the elastic deflection equation (1-25) which with h^{new} = 0 reduces to (Holmes *et al*. 2005).

$$p_0 = \frac{\hat{E}_{i,j}}{C_0} \qquad \textit{Equation 2-29}$$

The rough surface simulation process is summarised in Figure 2.5.1. The pressure, film thickness, stress state, and rough surface positions at each timestep are recorded and included in the outputs. The stress history the material is then input to the fatigue analysis as described in Section 2.6.

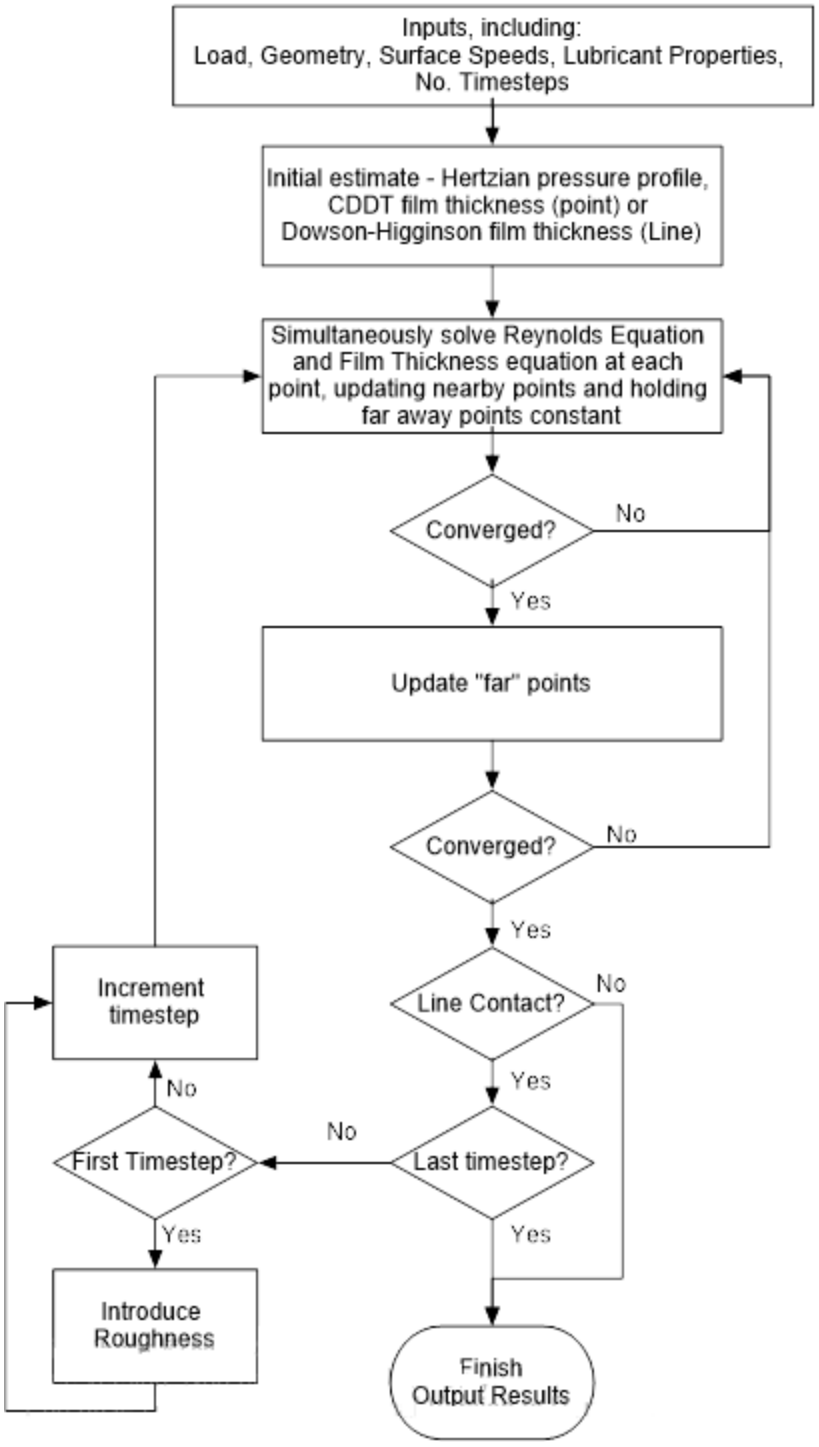

Figure 2.5.1 Flow chart of the simulation process for both smooth point and rough line simulations.

2.6 Fatigue Analysis

2.6.1 Recording Stress history.

During the simulation stress is calculated at each point of a material mesh encompassing the full length of the profile section and specified depths from the profile surface. This mesh travels through the contact with the profile as illustrated in Figure 2.6.1, and the stress state of the material at each timestep provides a stress history of the profile. It is from this stress history that the fatigue damage in each contact cycle is calculated.

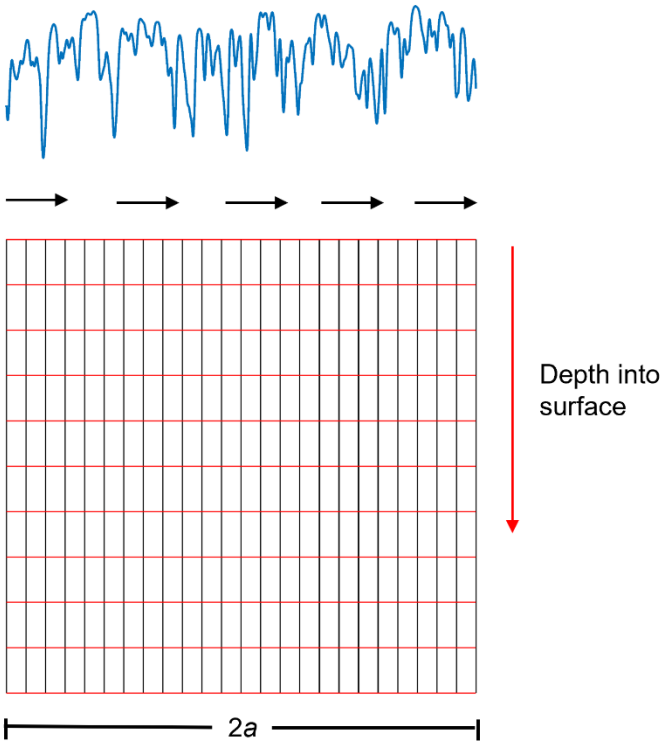

Figure 2.6.1 Profile with an associated mesh moving through the contact together. Mesh spacing is significantly increased for clarity.

2.6.2 Fatemi and Socie model

A number of models exist for predicting fatigue failure, however no model has yet reached the point of general acceptance. This task is complicated by the fact that some influences on fatigue are probabilistic in nature – for example fatigue cracks

tend to originate at defects (such as voids or inclusions) in the material, the occurrence and distribution of which can only be determined statistically.

Most models utilise a cumulative damage approach which has its roots in the Palmgren-Miner rule, initially developed by Palmgren in 1924 and built upon by Miner in 1945. The Palmgren-Miner rule effectively proposes that each stress cycle applied to a material element contributes an amount of damage to the material related in some way to the magnitude of stress experienced. These damage contributions accumulate until a value of unity is reached, at which point a fatigue crack has initiated and the material failed. The key complication of this process lies in the conversion of applied loads and stresses into a value of damage.

Previous work at Cardiff university (Qiao *et al*. 2008) performed comparisons of a number of critical plane fatigue criteria including those of Findley (1959), Matake (1977), Dang Van (1989) and Fatemi and Socie (1988), of which the Dang Van and Fatemi and Socie models are probably in the most common usage.

The Findley, Matake and Dang Van methodologies are applied by calculation of a fatigue parameter, with failure occurring when this value reaches unity. Fatigue properties of the material are accounted for using constants determined from results of fully reversed bending and torsional fatigue tests. The fatigue parameter is taken from the critical plane, the criteria for which (whether the plane of highest fatigue parameter or highest shear stress for example) depends on the model used. These fatigue parameters can then be converted to statistical evaluations of probability of failure through models such as those developed by Ioannides and Harris (1985) or Zaretsky (1987).

The Fatemi and Socie model uses a cumulative damage approach building upon earlier critical plane work developed by Brown and Miller (1973). On the basis that

fatigue cracks initiate on the plane of maximum shear strain, this method assumes that the shear strain drives the process of fatigue, with some contribution from normal stress. The use of normal stress in place of normal strain (as used by Brown and Miller) is the defining element of the Fatemi and Socie model, as this allows cyclic hardening effects to be accounted for.

This study found that these methods yielded similar results for fatigue failure, and since this time the Fatemi and Socie model has been adopted as the standard methodology applied for fatigue analyses at Cardiff. The results of simulations performed as part of this work will be compared to the experimentally obtained results to assess the validity and effectiveness of this approach.

The Fatemi and Socie model can be written as in Equation 2-30 (Bannantine and Socie 1992).

$$\gamma\left(1+K\frac{\sigma_n}{\sigma_y}\right)=\frac{\tau'_f}{G}\left(2N_f\right)^b+\gamma'_f\left(2N_f\right)^c \qquad \textit{Equation 2-30}$$

In this equation γ is the maximum shear strain amplitude, σ_n is the mean stress normal to the plane of maximum shear strain, σ_y is the yield stress of the material, τ'_f is the torsional fatigue stress coefficient, G is the shear modulus, γ'_f is the torsional ductility coefficient. K is a material coefficient between 0.6 and 1, b is a shear fatigue strength exponent and c is a shear fatigue ductility exponent.

2.6.3 Stress cycle counting – the rainflow counting method

In order to make use of any fatigue model the stress cycles experienced by a given location must be evaluated. As the material passing through the contact is loaded with variable stress amplitude and may undergo successive loadings without returning to an un-stressed state, this becomes a complex problem. The Cardiff

fatigue simulation overcomes this issue by applying the widely-used rainflow counting method, often deemed the method which gives the most accurate fatigue life predictions (Socie 1992). This was initially developed by Matsuishi and Endo, and so named for the useful visualisation of rain cascading between pagoda roofs which can help in applying the method (as is expertly explained by Lee and Tjhung (2012)). The method has since been built upon by a number of researchers, including Downing and Socie (1982).

In essence, the rainflow method extracts closed stress-strain hysteresis loops from a complex loading history. It aims to do so in such a way that maximises the ranges of stress cycles that are encountered, thus weighing more importance on the difference between the highest and lowest stresses experienced as opposed to smaller intermediate fluctuations.

3 Experimental Method and Equipment, Data Analysis Development, and Initial Investigations

The test rig as described in this chapter was used to conduct experiments to meet objectives 1 & 2, and to provide rough surface data to meet objective 3. As is expanded upon below, the twin disk rig allows contacts representative to those between gears to be investigated with much reduced cost and complexity. The rig was designed and developed in previous works and was not significantly modified in this work, except for the addition of a 0.375 SRR gear pair. Novel developments in this section include:

- Quantification of error in measurement relocation
- Comparison of disk material fatigue performance
- Application of surface replicas
- Development of 2d and 3d micropit programs
- Application of a full-factorial test programme

3.1 Description of the Test Rig

3.1.1 Introduction

Twin-disk test rigs are a well-established apparatus for experimental testing of rolling contact fatigue. The origins of this testing method can be found in the work of Merritt (1935) who developed an apparatus where two disks of differing diameters (one four inches, the other eight inches) could be run against each other under load. The load was applied by a lever and jockey weight which pressed the smaller disk, which was mounted in a swinging frame, against the larger one. A variable speed motor provided drive to the fixed disk, with gears or a chain transmitting drive to the smaller disk shaft at the speed ratio required. Merritt found that this design was able to provide a good two-dimensional representation of the worm gear behaviour he was trying to recreate, and disk-based test rigs have

since become a standard experimental set up used throughout the literature to investigate lubricated concentrated contacts.

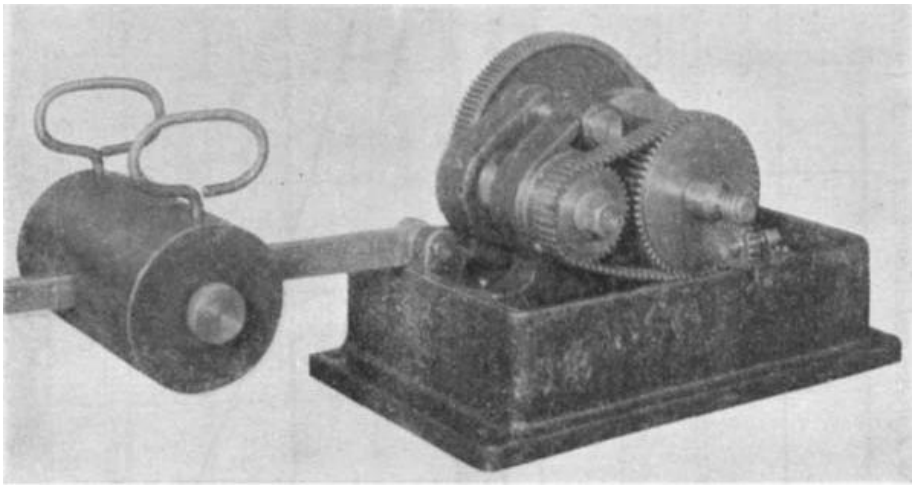

Figure 3.1.1 The first disk machine, designed to simulate worm gear contacts. Image reproduced from Merritt (1935).

There are clear advantages to testing using disk rigs to simulate gear contacts as opposed to using actual gears. The primary benefit of using disks is that they provide a constant set of conditions allowing specific aspects of the contact conditions to be investigated – unlike in true gear contacts where the SRR, entrainment velocity and load all vary with position along the contact path and number of teeth in contact. Not only does this mean that the factors which contribute to micropitting can be investigated independently as per the aim of this thesis, it also means that laborious gear calculations can be avoided. A secondary benefit is the much-reduced financial cost of disks when compared to gears.

The twin-disk rig used in this work was first developed by Alanou (2005), and was first employed experimentally by Davies (2005) to investigate the process of running-in and the amount of metallic contact between the surfaces. Projects by Weeks (2015) and Hutt (2018) further utilised this apparatus, each making modifications and improvements – for example changing all driving gears from spur

to helical designs for smoother operation, and complete re-writing of the control software with the optional inclusion of acoustic emission sensors.

Figure 3.1.2 shows a schematic of the twin-disk rig as used in this work. The fast shaft is shown on the left of the image, and the slow shaft is shown on the right. Disks were pressed onto the shafts and then secured with locking nuts. Cabling for thermocouples and contact voltage measurement was routed to the slip rings through the centre of each shaft.

Each shaft was supported by two rolling element bearings which were securely clamped into place in bearing housings, as can be seen in the figure. Flexible couplings were used to attach the shafts in the test head to the shafts at the drive end of the test area - these allowed some misalignment due to the applied load to be accommodated.

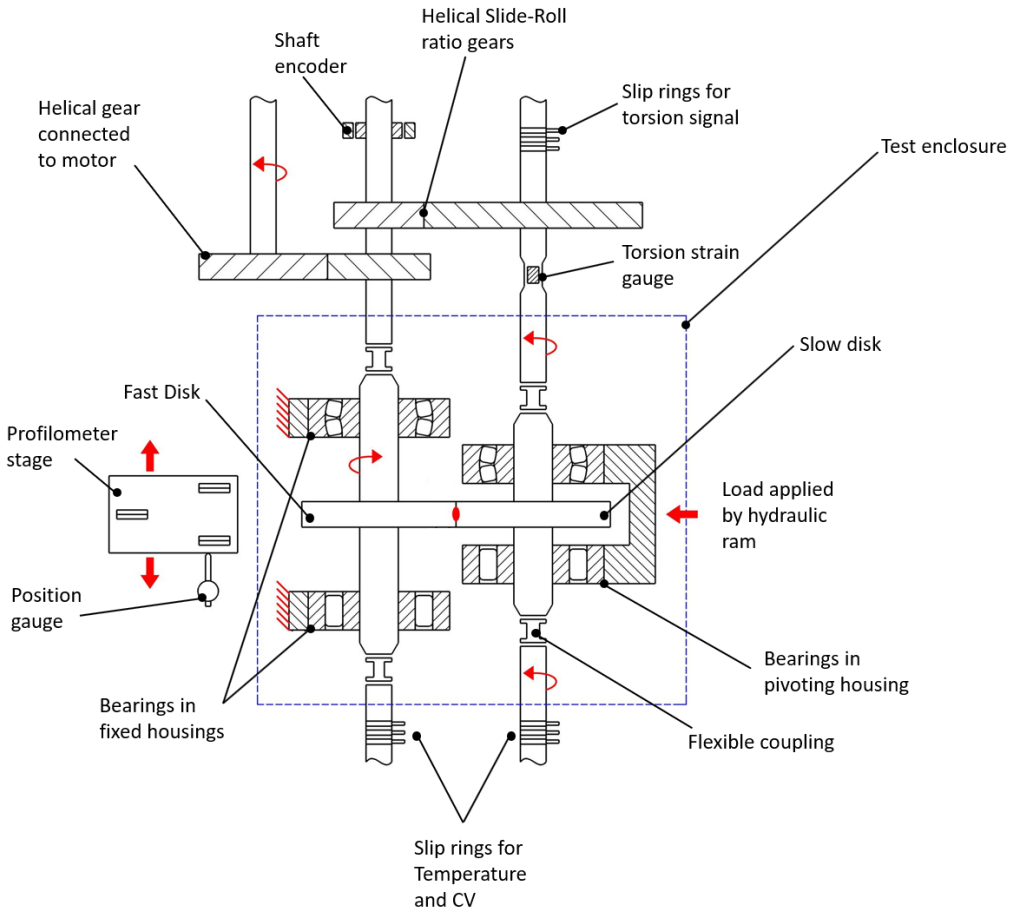

Figure 3.1.2 Schematic of the twin-disk micropitting test rig

3.1.2 Application of Load

As can be seen in Figure 3.1.2 the load was applied to the test disks via the slow shaft. Both the fast and slow shafts were supported with self-aligning bearings, however while the fast shaft bearings were mounted in a stationary housing, the housing in which the slow shaft bearings were mounted was able to pivot about a point near the bottom of the housing assembly.

Force was supplied via a hydraulic ram and push-rod assembly. The OEP-80 oil used to lubricate the disks also served as the hydraulic fluid, and this was supplied via a centrifugal pump which drew from the main oil tank. A maximum force of 8kN could be supplied which equates to a maximum Hertzian contact pressure of 2.1 GPa with

the disk geometry used. A force transducer on the loading face of the hydraulic ram was used to record the applied force at the point of application.

Load was applied and removed by manual operation of a butterfly valve on the return line. The disks were loaded approximately two seconds after closing the valve, however load was removed instantly upon reopening of the return valve. The hydraulic loading mechanism was able to reduce shock loading effects which can occur when using a lever arm to apply the load (as in the original twin disk design by Merritt (1935)). Figure 3.1.3 provides an illustration of how the load was applied to the pivoting housing.

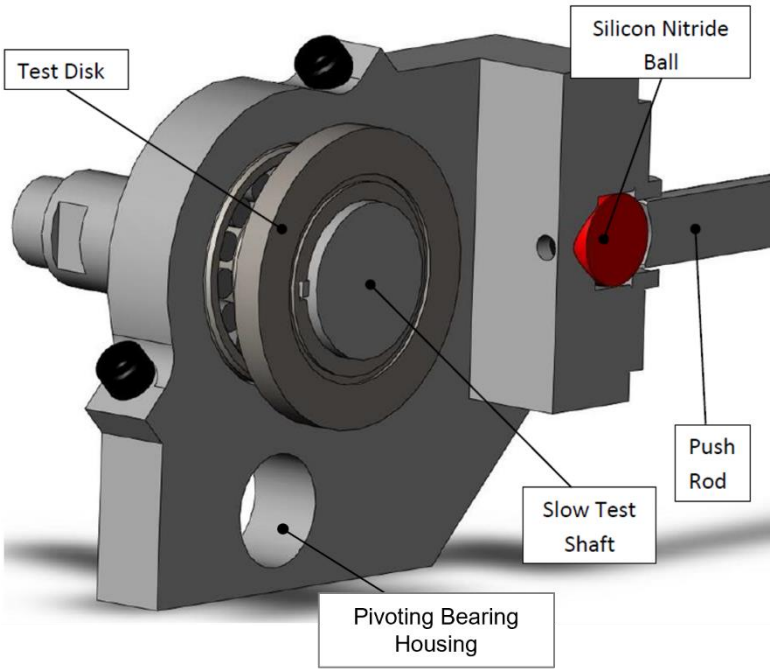

Figure 3.1.3 3D CAD model showing the slow shaft bearing housing and load application mechanism. Figure reproduced from Weeks (2015).

3.1.3 Supply of Lubricating Oil to the Test Head

The lubricating oil used in this work was OEP-80, the characteristics of which are specified in DEFSTAN 91-74. This is a mineral oil containing extreme pressure (EP) additives which act to oppose wear effects under highly-loaded conditions. The EP additives used are not specified either by the DEFSTAN or lubricating oil suppliers, so the constituents must can only be assumed. Anti-wear and extreme pressure additives include phosphate esters and dithiophosphates (such as ZDDP – a likely candidate), sulphur compounds, sulphur-phosphorus derivatives (Frene et al. 1990).

A Grant Instruments heating bath HE10 was used as an oil storage tank and was located directly below the test head. This was fitted with a 2 kW UH2 high temperature heater, however to reach and maintain the 80 ºC supply temperature used in these tests this was used in concert with a Grant Instruments TC120 Heating Circulator. From Test 3 onwards the UH2 high temperature heater was removed due to an electrical fault and replaced with a second Grant Instruments TC120 Heating Circulator.

Lubricant was drawn from the tank by a centrifugal pump (powered by an electric motor). The intake nozzle was attached to a coarse wire mesh filter to remove any large debris. The oil was then pumped through an inline filter to remove any particles greater than 3 μm in size. The lubricating oil flow was divided between a number of spray nozzles supplying lubricating oil to the disk contact (from above and below), all bearings within the test head area, the speed increasing gears from motor to fast shaft, and the SRR gears. The supply temperature of the oil was measured using a J-type thermocouple attached to the oil supply nozzle above the disk contact, which provided readings directly to the rig control interface.

Lubricant was returned to the tank under gravity through a series of drainage lines located in the base of the test head and gearboxes.

3.1.4 Drive to Shafts and Setting of Slide-Roll Ratio

The drive to the test rig was provided by a Marathon Electric 5.5kW three-phase asynchronous six pole motor. The shaft from the motor fed directly to a pair of speed increasing helical gears with a gear ratio of 2:1, providing drive to the fast shaft.

An encoder connected to the fast shaft was used to monitor the speed. The achievable range of fast shaft speeds was 200 rpm – 2000 rpm, and the required speed could be set in the rig control program. The program then output a signal of 0 V – 10 V corresponding to the desired speed. The shaft encoder allowed the control system to assess the true speed of the shaft to confirm that the target speed was reached. The encod er also controlled the sampling of in-test data such as temperatures, contact voltage and load, which were sampled once per fast disk rotation.

A second pair of helical gears was located aft of the speed increasing gears, connecting the fast and slow shafts. These gears provided drive to the slow shaft and set the SRR for the test. Four pairs of these gears (henceforth referred to as the SRR gears) were used in this work, corresponding to SRR values of 0.25, 0.375, 0.5 and 0.75. Table 3.1.1 gives details of the tooth numbers on each gear pair and the achievable range of contact entrainment speeds.

Table 3.1.1 Shows the tooth numbers on the pinion and wheel gears of each SRR gear pair used in this work. Minimum and Maximum contact entrainment speeds are calculated at fast disk speeds of 200 and 2000 rpm respectively.

SRR	Pinion Teeth No.	Wheel Teeth No.	Min. achievable entrainment speed / ms^{-1}	Max. achievable entrainment speed / ms^{-1}
0.25	35	45	0.71	7.09
0.375	39	57	0.67	6.72
0.5	30	50	0.64	6.38
0.75	25	55	0.58	5.80

3.1.5 Measurement of Contact Voltage

It has long been known that the resistance and voltage between the two bodies in a tribological contact can provide valuable information about the nature of that contact. For instance, the work of Bowden and Tabor (1939) used evaluations of electrical conductance to reveal that the true area of contact between two surfaces was in reality much smaller than it appears (as in reality contact occurs between the tips of asperities, not across a larger smooth surface). Other early works were able to illustrate the influence of various parameters on the amount of direct contact – for example showing that high entrainment speeds result in more effective separation of the surfaces (Courtney-Pratt and Tudor 1946). Other researchers have attempted to relate the contact voltage, contact resistance or capacitance to the true film thickness in the contact with varying levels of success (Crook 1957; Guangteng *et al*. 1999; Lord and Larsson 2008).

Use of contact voltage in EHL is predicated on the lubricant film separating two surfaces serving as an electrical insulator, preventing electrical flow between the two bodies. If the film is insufficient to completely separate asperities, electricity is able to flow from one surface to the other via direct asperity contacts. The greater the area of direct asperity contact, the lower the resistance to electrical flow becomes and hence the voltage between the two surfaces decreases in the potentiometer circuit used in this work.

Contact voltage measurement was first incorporated into this test rig by Davies (2005) and was further developed by Weeks (2015) and Hutt (2018). In this thesis, V_{DC} and the resistors R_1 and R_2 were the same as used by Hutt (2018), to give a maximum contact Voltage of 45 mV.

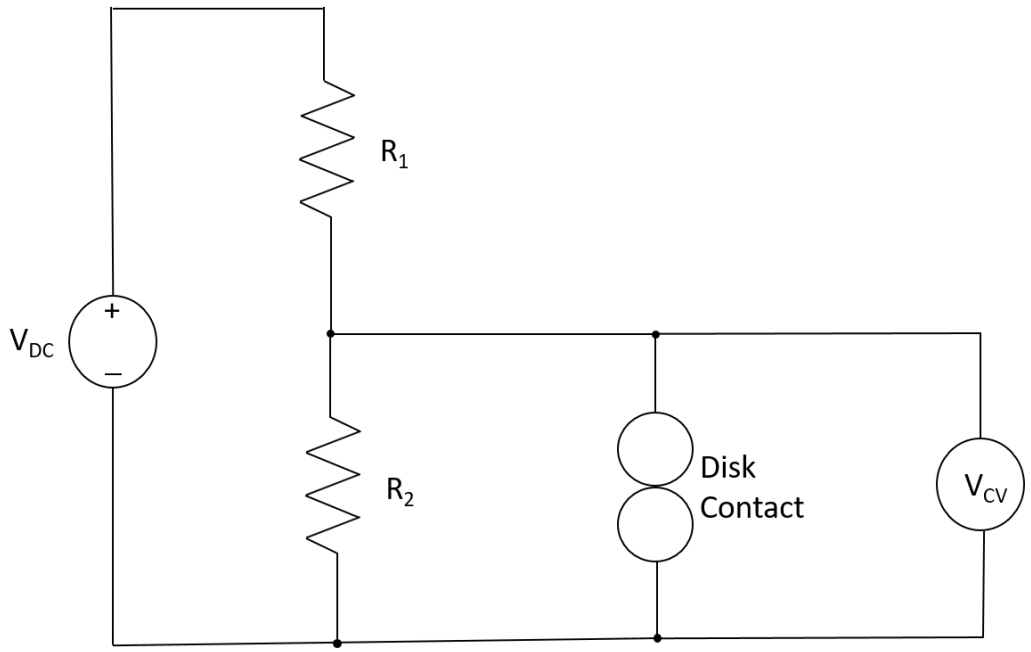

Figure 3.1.4 Circuit diagram of the contact voltage system.

To prevent electrical flow occurring through any route other than at the contact, the slow shaft was electrically isolated from the rest of the rig. A Polytetrafluoroethylene (PTFE) coupling provided electrical isolation at the slip ring

end, while the flexible coupling at the drive end of the test head clamped on to a PolyEther Ether Ketone (PEEK) bush, preventing electrical flow in the other direction. Both the ball connecting the pivoting housing and push rod assembly, and the rolling element bearing rollers supporting the slow shaft were made of Silicon Nitride, providing insulation through both of those routes.

Values for contact voltage were recorded once per revolution of the fast disk, with the recorded value being the average contact voltage for 270° of the rotation (270° used due to hardware constraints on data recording). Contact voltage data acquisition was triggered by a digital pulse from the shaft encoder on the fast shaft.

3.1.6 Determining Contact Friction

The friction at the contact cannot be directly measured, but may be found as the result of a series of steps. The slow shaft flexible coupling at the drive end of the test head was connected to a quill shaft to which a strain gauge was applied. This enabled the deformation due to torsion to be found, and from this the total torque in the shaft was calculated.

The torque in the shaft is equal to the total amount of torsion required to overcome the friction at the contact, plus the friction in the rolling element bearings on the slow shafts.

Weeks (2015) conducted an experiment to determine the bearing friction at each setting of his test programme by disconnecting the fast shaft from the input coupling and operating in pure rolling at each speed and load condition. From this he was able to determine the bearing friction on both shafts and, as the bearings are identical on each shaft, use this to find the slow shaft bearing friction. Subtracting this from the measured friction in-test gave contact friction alone. It was not possible to conduct the corresponding test for this experimental

programme, hence in this work the friction data recorded constitutes the contact friction plus slow shaft bearing friction. Windage losses were accounted for by subtracting the unloaded friction reading at test speed from the values in-test. The largest value of bearing friction recorded by weeks was approximately 6.2 N at 2000 rpm and 1.4 GPa. Based on Weeks' calibration data, at the lower speeds and higher loads used in the current work, bearing friction would not be expected to exceed this value.

3.1.7 Two-Dimensional Surface Profile Measurement Process

Two dimensional profiles were taken between each test stage using a Taylor Hobson Talysurf Intra 2 portable surface profilometer. The profilometer was mounted on a stage located to the side of the test area, as shown in Figure 3.1.5. The stage was made of thick steel plate, securely fixed to the test rig frame. These sturdy mounting arrangements minimised vibrations experienced by the measuring apparatus. Two sets of holes were machined into the surface of the stage for the feet of the profilometer to sit securely and to ensure that the measurement (x) axis of the profilometer is perpendicular to the shafts. These two sets of holes correspond to the profilometer being placed in the forward or rear measuring positions used for the slow and fast disks respectively.

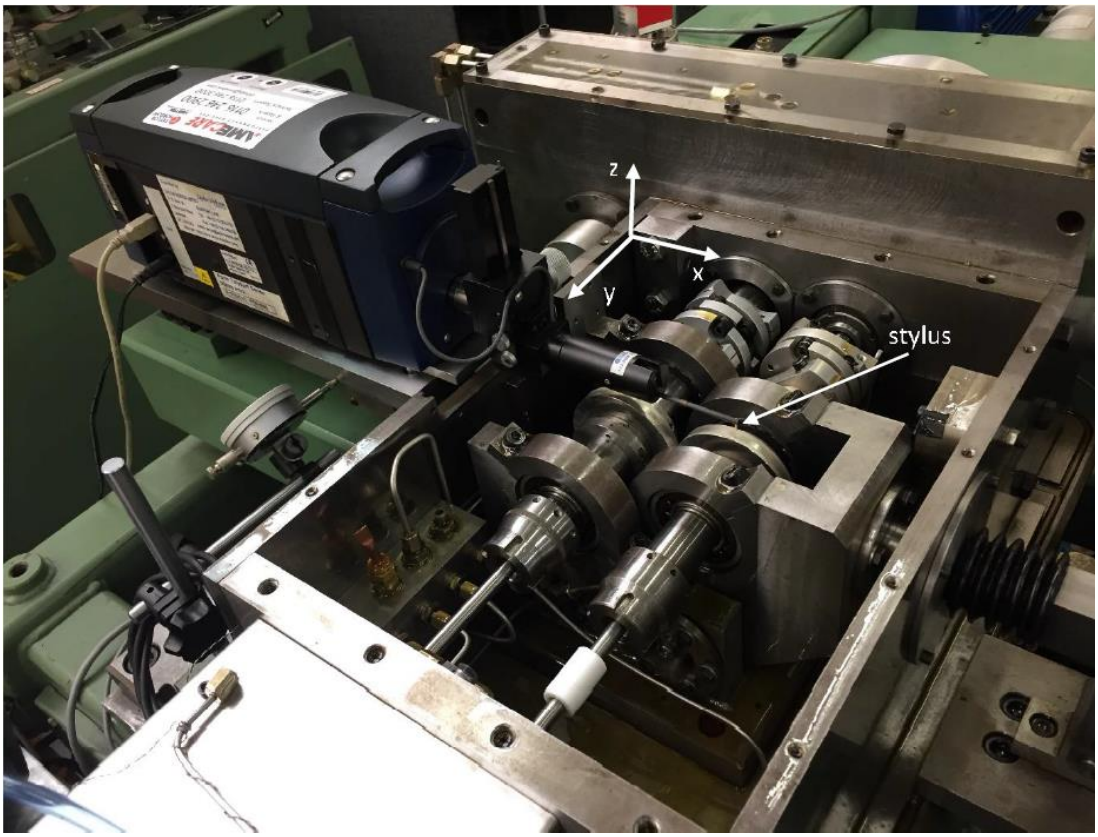

Figure 3.1.5 Portable profilometer mounted on the disk measurement stage, shown in the forward position measuring the slow disk surface.

The stage allowed movement in the y axis (transversely across width of the disks) by means of a manually operated lead screw. The position of the stage was indicated by a Mitutoyo dial gauge with a range of 10 mm.

For each load stage, nine two-dimensional profiles (as shown in Figure 3.1.6) were obtained for each disk. The intervals for these measurements were determined from the Hertzian contact dimensions. Each profile was 12 mm in length with a point spacing of 0.5 μm. The procedure for taking two-dimensional profiles is outlined below:

- The surface of the disks was thoroughly degreased in the area to be measured, indicated by an engraved line on the side of each disk to allow repeated measurements at the same nominal circumferential position.

- The profilometer was placed on the stage in the rear position to measure the fast disk. The stylus was brought to the approximate centre of the disk width by eye, and then lowered into contact with the disk surface. The autocrest function was used to locate the highest point of the disk along the x axis (around the disk circumference).
- The profilometer was moved in the positive y direction using the stage lead screw until the profilometer reading decreased by 60 microns. This position was taken to be the right-hand edge of the disk, and the dial gauge was set to 9.5 mm. The disk was then adjusted to ensure that the engraved line was exactly in line with the stylus.
- The profilometer was moved to the rightmost measuring location using the leadscrew and the stylus was lowered until the reading was near the maximum of the gauge range. The stylus was then moved -6 mm in the x axis (along the circumference of the disk, away from the user).
- A 12mm surface profile was then measured and the results saved. A Gaussian filter with a 0.8 mm cutoff length was applied to the measured profile. 0.8 mm was selected as the cutoff wavelength to exclude any features larger than the contact dimension but to ensure that any significant features within the contact area were retained.
- The stylus was then returned to the start position (-6 mm from the disk crest) and the profilometer translated using the stage to the next measuring position. The process was then repeated until all profiles on both disks had been obtained.

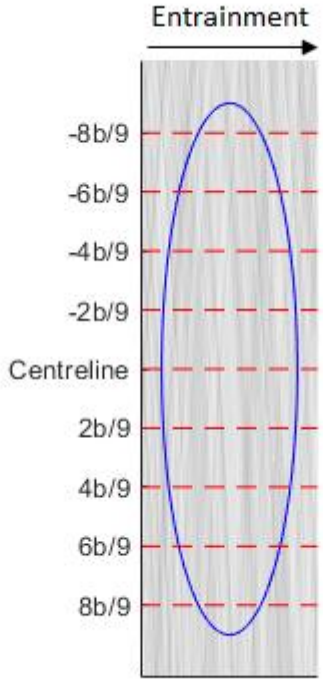

Figure 3.1.6 Measuring positions for two-dimensional profiles measured in situ, shown with a corresponding contact ellipse.

3.1.8 An Investigation into Relocation Error in 2D Profiles

The analysis of two-dimensional profiles measured in-situ in the rig requires the profiles taken between each load stage to be measured at the same set of axial positions on the disks each time. As the surface profilometer must be removed from the test rig while each load stage is running, this is difficult to achieve. The procedure outlined in Section 3.1.7 attempts to use the edge of the disk as a reference each time the profilometer is set up, and all measurements are then made relative to the location of the edge.

The error in axial relocation can therefore be quantified by repeating the set up procedure of lowering the profilometer stylus into contact in the approximate centre of the disk, and then traversing width of the disk until the reading drops by 60 μm. The spread of readings on the position gauge for the y-stage indicates the

error in this relocation method. The process was performed ten times for relocation to the left side of the disk, followed by a further ten relocations to the right side of the disk. Results are shown in Table 3.1.2.

Table 3.1.2 Results for axial relocation error test

Repeat	Left side reading /mm	Right side reading /mm
1.000	0.000	9.350
2.000	0.020	9.360
3.000	0.055	9.335
4.000	0.080	9.360
5.000	0.020	9.410
6.000	0.025	9.465
7.000	0.000	9.390
8.000	0.110	9.410
9.000	0.095	9.345
10.000	0.160	9.420
Mean:	**0.057**	**9.385**
Range:	**0.160**	**0.130**
Standard Deviation	**0.0506**	**0.0393**

The results for the investigation were very similar when conducted for both disk edges. In both cases the range was greater above than below the mean, however the ranges of 0.16 mm and 0.13 mm for the left and right sides of the disk respectively were both of the same order.

When it is recalled that the typical diameter of a micropit is between 10 – 30 μm these ranges of values are highly significant - as any detection of micropits using height history from two-dimensional scans must not be able to revoke the designation of a point as micropitted, the addition of pits from different axial locations has the potential to lead to overestimation of pitting.

3.2 Description of the Test Disks

3.2.1 Material Specification and Properties

The test disks used in this work were manufactured from case hardened steel meeting the specifications for 655M13 steel. The British Standard BS9701:1996 outlines the requirements for this material (BSI 1996). This type of case-hardened steel is widely used in gears due to its ability to withstand very high stresses and its resistance to surface wear. The acceptable range of chemical content can be seen in Table 3.2.1.

Table 3.2.1 Chemical composition of 655M13 steel by % Mass. (BSI 1996).

C %	Mn %	Cr %	Ni %
0.10-0.16	0.35-0.60	0.70-1.00	3.00-3.75

The case hardened (by carburising) surface of the disks had a specified Rockwell C hardness of 60-63, with a case depth of 1 mm (±0.1 mm).

3.2.2 Test Disk Geometry

The test disks had a nominal diameter of 76.2 mm [3”] and a width of 9.53 mm [3/8”]. The contacting surfaces of the disks were ground using a conical abrasive wheel which resulted in an axial finish (grinding marks run transverse to the entrainment direction of the contact, see Figure 3.1.6). This also imparted a crown to the disk surface, resulting in elliptical contact between the disks.

A keyway was cut into the disk, corresponding to a key on the shaft. The disk had a bore of 41.28 mm which provided an interference fit to the shaft. Disks were pressed on and off the shafts using a hydraulic press.

A 2.2 mm diameter, 6.6 mm depth hole was drilled 3.17 mm below the contacting surface of the disk, above the keyway. This allowed a thermocouple to be installed to measure the near surface temperature of the disk during operation.

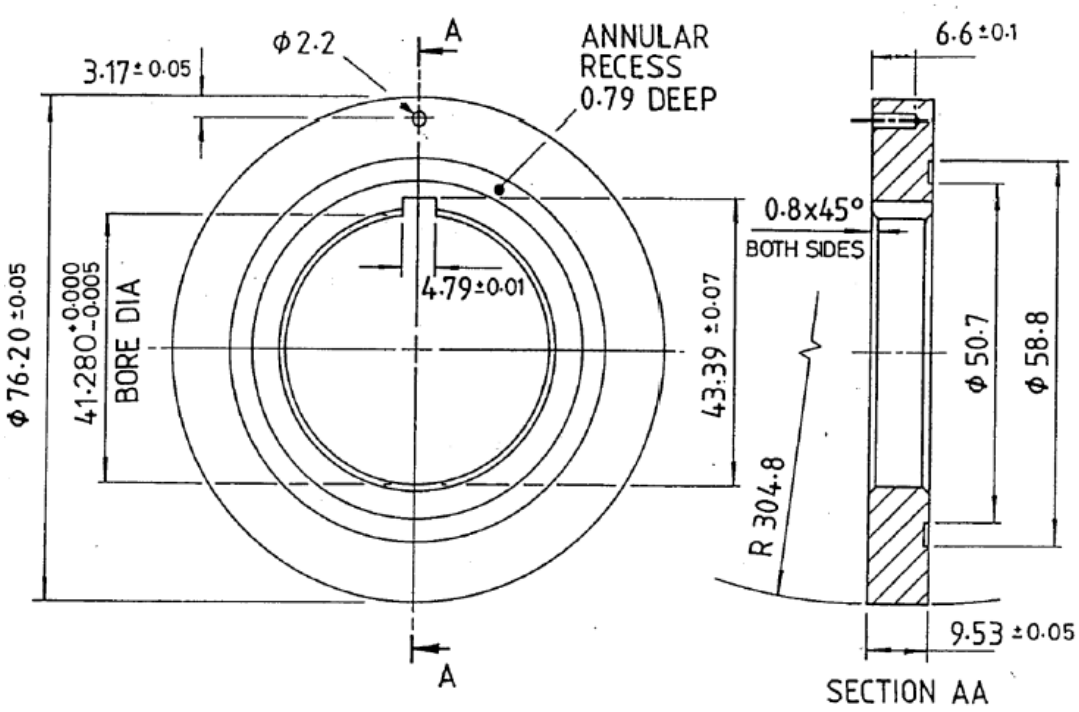

Figure 3.2.1 Diagram of a test disk. Image reproduced from Weeks (2015).

3.2.3 Grinding the Surface Finish

For the surfaces of the disks to be representative of a true gear tooth surface it was necessary to replicate the transverse lay of the grinding marks found on gear teeth. This required an unconventional grinding arrangement originally devised at Cardiff University for the work of Patching *et al*. (1995). In this arrangement (See Figure 3.2.2 and Figure 3.2.3) the disk is ground against the side of an abrasive wheel, dressed to take the form of an internal cone at a 15-degree angle. This setup yields

the desired lay of grinding marks, but also imparts a crown on the disks, helping to centre the contact and avoid edge effects.

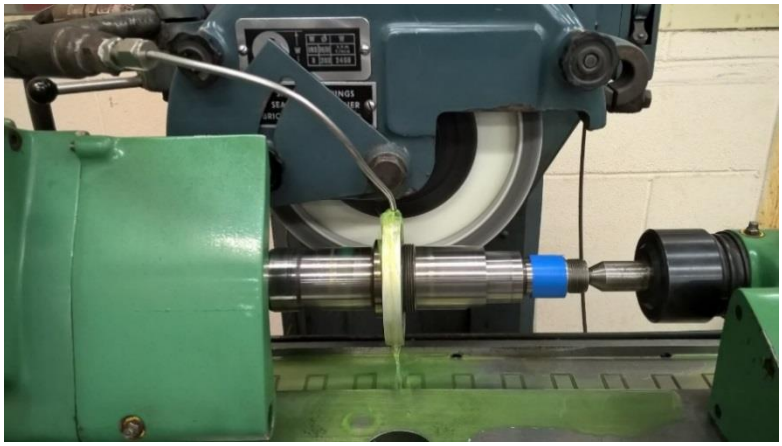

Figure 3.2.2 The process of grinding a disk. The grinding wheel rotates clockwise while the blank test disk rotates toward the reader.

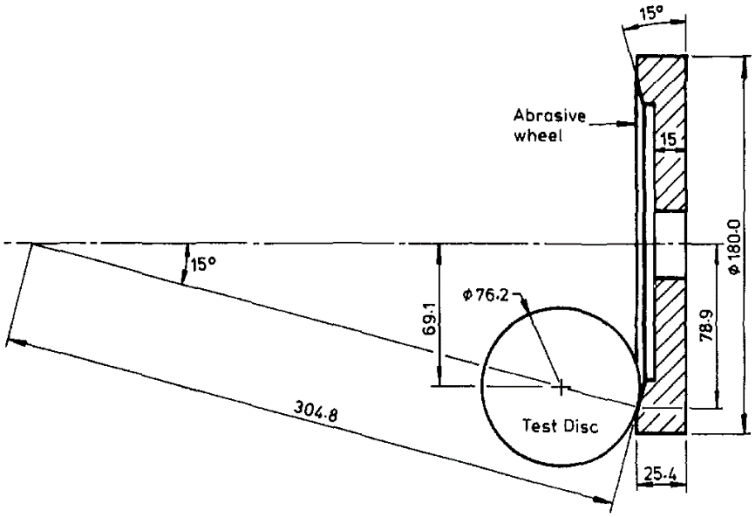

Figure 3.2.3 A diagram of the grinding arrangement

Disks of two different Ra values were ground, although due to scuffing encountered using Ra=0.6 μm disks, only Ra=0.4 μm disks were used in micropitting tests. Disks of 0.2μm roughness were also planned, but not ground prior to the decision to remove roughness as a variable. These roughnesses were chosen to provide a sensible range of roughnesses that would be encountered in real gears. A roughness

of Ra=0.6μm is a fairly coarse grind for gears in modern applications, but is not so exceptionally coarse as to be unrealistic. A roughness of Ra=0.2μm is a fine grind, but achievable where sufficient care is taken in the grinding process - however as roughness is known to be a key factor in micropitting aiming for a finer finish than this (e.g. by superfinishing) would likely prevent any micropitting within the test window. The roughness of Ra=0.4μm between these two is a realistic average for ground gear surfaces.

These roughnesses were achieved by varying the grit of the abrasive wheel and the rotational speed of the test disk. Due to the range of factors which influence the surface finish produced, even once the correct settings had been achieved some variation in the roughness produced persisted. As a result, a bracket of ±0.05 μm on the target Ra value was deemed acceptable.

Table 3.2.2 Settings used to achieve each Ra

Target Ra / μm	Abrasive wheel grit	Rotational speed of test disk / rpm	Grinding duration
0.6	60	100	Until runout
0.4	100	200	Until runout

3.2.4 Disk Material Comparison Test

The steel specification for the disks used in this work differed slightly from that which was used previously (for example, in the referenced work of Clarke *et al* (2016a) and Al-Mayali *et al* (2018)). The steel used in these previous studies was manufactured to Rolls Royce specification 6010. As noted in Section 3.2.1 the

current work uses more readily-available 655M13 steel made according to British Standard BS9701:1996. This specification was chosen for this work on the basis of being a similar steel grade to that used in previous work that is commercially available. Table 3.2.3 shows a comparison of the elemental components of these steels.

Table 3.2.3 Specified elemental components of RR6010 and 655M13 steel for comparison. (BSI 1996; Weeks 2015).

Element	C	Si	Mn	P	S	Ni	Cr	Mo
% by mass RR6010	0.14-0.18	0.10 - 0.35	0.25-0.55	0.00-0.015	0.00-0.015	3.80-4.30	1.00 - 1.40	0.20-0.30
% by mass 655M13	0.10 – 0.16	Not Specified	0.35 - 0.60	Not Specified	Not Specified	3.00 – 3.75	0.70 – 1.00	Not Specified

When preparing disks for testing it was noted that while the specified hardness of the disks remained the same, the measured hardness was found to be lower for 655M13 than for the previous disk material. The mean hardness of the Rolls-Royce 6010 specification disks was found to be 755 Hv, while the mean hardness of the new 655M13 disks was found to be 712 Hv. For this reason, and to better understand the impact of any other differences between these steel grades, it was decided to run a micropitting test at the same set of conditions as used in the experiments recorded in Al-Mayali *et al* (2018) for the purposes of comparison.

Results

The conditions used in this test duplicate the experimental test conditions employed by Al-Mayali *et al* (2018) other than in the disk material specification. These conditions are shown in Table 3.2.4.

Table 3.2.4 Settings for Disk Material Comparison Test

Variable	**Value**
Maximum Hertzian Contact Pressure	1.2 GPa
Fast Disk Ra	0.39 μm
Slow Disk Ra	0.38 μm
Entrainment Velocity	3.2 m/s
SRR	0.5
Oil Supply Temperature	80°C

Al-Mayali *et al* (2018) used the mean height at each test stage for points which had pitted by the conclusion of the test to indicate the progress of pitting on the surface. This data was obtained from two-dimensional profiles taken from the disks in-situ. The mean was initially high as the surface positions which went on to pit during the test began as asperities. The running-in process causes an initial decrease in height as the asperities are plastically deformed but then stabilises. The mean height of pitted points then decreased as the test progressed and asperities were removed and replaced with deep pits.

Figure 3.2.4 presents the data from the comparison test alongside the two corresponding tests given in Al-Mayali *et al* (2018). For both the fast and slow surfaces of the comparison test the mean height was slightly higher although these disks were of the same nominal roughness as those used in the previous tests. Both tests with initial running-in data showed the same behaviour with a similar initial height decrease of 0.14 – 0.16 µm occurring in both. All tests then entered the period of pitting at the same point in the test, before the pitting later arrested by 1 million fast disk cycles. The final values for height of pitted points on the fast disk were very similar for all tests, while the comparison test finished with a higher value on the slow disk compared to the tests in the paper. This could mean that the pits were less deep on the slow disk in the comparison test, or may be an effect of the locations the stylus passed through (i.e. the edge of pits as opposed to the centre) due to the limited sample size offered by 9 relocated profiles.

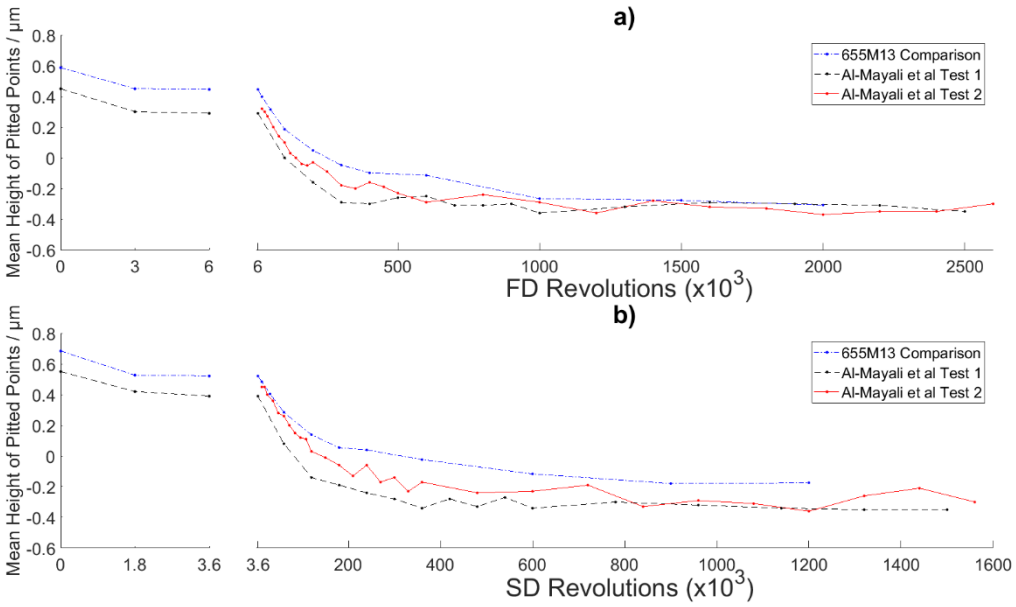

Figure 3.2.4 Comparison of mean heights of pitted points for a) the fast disk and b) the slow disk. Profiles were vertically aligned to the final profile in each test as in Al-Mayali et al. (2018).

A comparison of the fast disk surfaces for a) the comparison test and b) Al-Mayali's Test 2 at end of test can be seen in Figure 3.2.5. At end of test, 3.6% of the contact area on the comparison test fast surface was found to be pitted. This is very similar to the previous test, where 3.9% of the surface was pitted. It should also be noted that Al-Mayali's test underwent a further $6x10^5$ fast disk cycles than the comparison test, however Figure 3.2.4 suggests that the pitting rate had slowed significantly before two million Fast Disk cycles was reached.

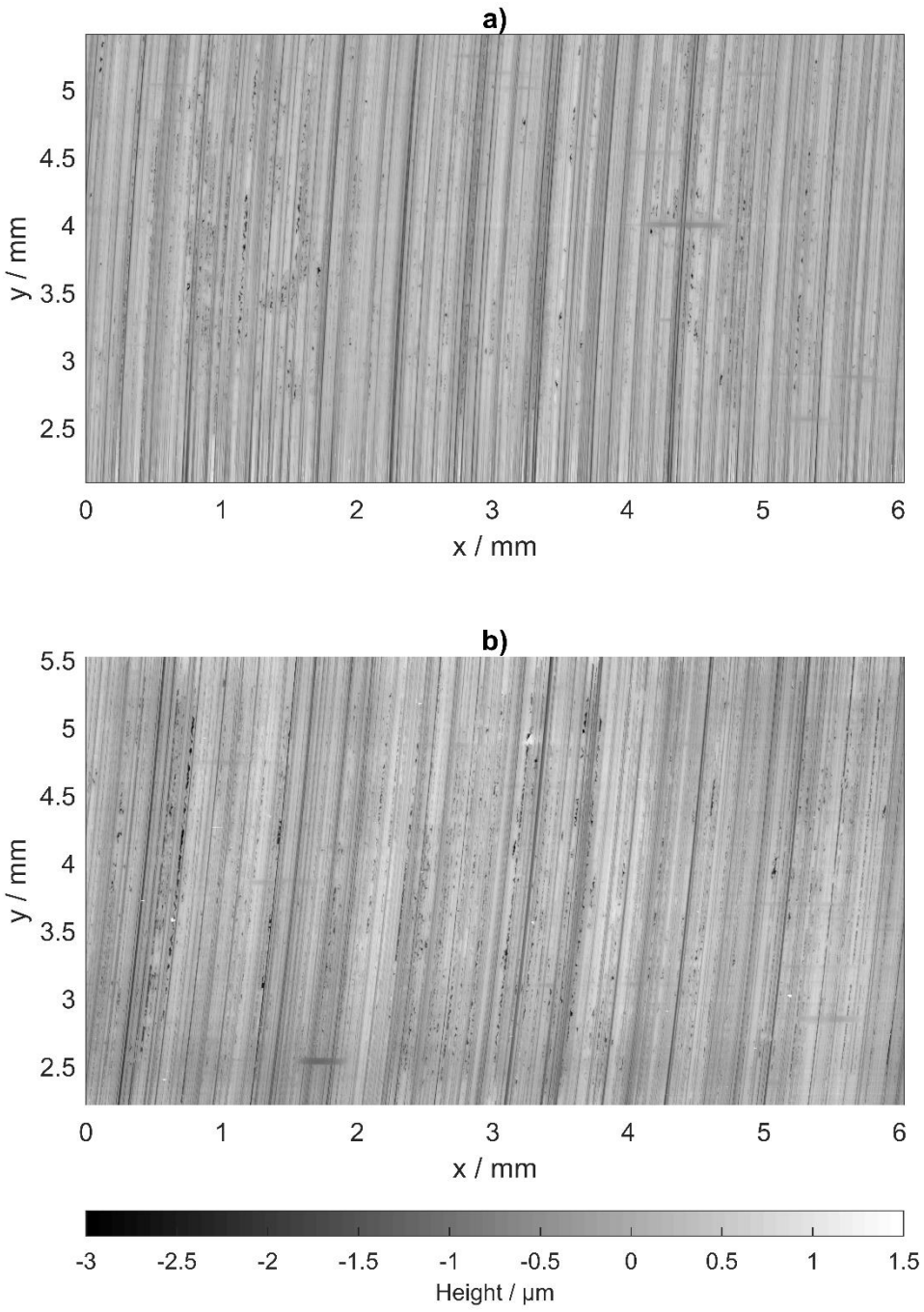

Figure 3.2.5 Fast disk surfaces at end of test for a) the comparison test and b) Test 2 in Al-Mayali et al. (2018)

Conclusion regarding disk material

The disk material comparison test was able to establish that disks made using steel to both Rolls Royce specification 6010 and 655M13 grade exhibit very similar behaviour under these conditions. Pitting began at the same point in all tests and

progressed at a comparable rate. In all tests pitting was arrested or significantly slowed before 1 million fast disk cycles was reached. Based on this result it is concluded that valid comparisons can be made between experiments in this thesis using 655M13 steel and previous work using steel under Rolls Royce specification 6010.

3.3 Surface Replica Material Selection and Application

3.3.1 Selection of Surface Replica Material

The experimental rig as detailed above could only be used to obtain two-dimensional profiles of the disk surface in-situ, due to the manually operated stage on which the Talysurf profilometer was mounted. Two-dimensional profiles can impose limitations on the analysis of micropitting for several reasons:

- Misalignment error is significant – it is very difficult to ensure that two-dimensional measurements are being taken in the same axial position each time. Using the methods available for this test rig as employed by Hutt (2018) there is inherent error in finding the edge of the disk, which then becomes a reference point on which the rest of the readings are based. The relocation error was investigated in Section 3.1.8.
- Micropits do not develop on the disk with uniform density but can develop with higher density on some surface features and much lower density on others. This, coupled with the small size of micropits and the fact that a profilometer stylus can easily miss pits in the vicinity, means that the low sample size achievable with in-situ measurements can result in non-representative evaluations of pitting.
- A large amount of data is “left on the disk” when only two-dimensional scans are used. The shape of pits as they develop, for example, is not quantifiable but can provide useful insights to the micropitting process.

Considering these limitations, it was decided that the addition of areal scans to the testing process would make the results more robust and allow far more data to be extracted from the tests. Two-dimensional profiles provided a more convenient means of observing the surface behaviour during the test due to the much-reduced processing time, while areal scans could then be used to analyse the surface changes in more detail after the testing was complete.

Two options were available to introduce areal scans during testing. The first option was to modify the profilometer mounting platform to incorporate an automated stage. Alternatively, surface replicas could be made in-situ and taken for measurement using another profilometer already equipped with an automated stage.

The second option was chosen for two reasons. Firstly, taking scans in-situ would require the rig to be stopped for the duration of two scans (approximately two working days), during which time no further testing could be carried out. In contrast, taking replicas required the rig to be stopped for only a few hours and replicas could be scanned elsewhere while testing continued. Secondly, a re-design of the platform would be both more time consuming and costly than taking replicas, which requires minimal design work and only the cost of the replica materials. An additional benefit of using surface replicas was that a physical copy of the surface at a given point is stored and can re-scanned at any time, while the surface of the real disk continues to change.

Several different replica materials capable of capturing the required level of detail are available, with varying properties and curing times which influence their applicability to these experiments. As measurements of the replica surface would need to be made with a contact profilometer this further limited the options, ruling out softer replica materials such as silicon- or rubber-based options.

George (1979) provided some guidance in this selection process. This paper compared the performance of several replica materials suitable for analysis using a surface profilometer. The most highly recommended replica was a form of araldite mixed with aluminium powder – however the curing time of 3 days made this wholly unsuitable and this was rejected. Acrulite Microtech Type A had the next best performance in this analysis and was recommended for scenarios with limited access to the work area due to its short setting time (quoted as 20 minutes in this paper, however the proportions for mixing were not disclosed - hence this differs from the setting time for the rest of this thesis). Acrulite was found to suffer from bowing, however as the replication area was significantly smaller in this test programme than that used by George this was deemed to be of minimal concern.

3.3.2 Design of Replica-Taking Components

Mixed Acrulite takes the form of a thick liquid with a viscosity similar to that of PVA glue. A dam must therefore be created around the replication area to keep the Acrulite in place as it sets. This is most commonly achieved using Plasticine, or alternatively George (1979) suggests using a "lifting collar". While Plasticine is suitable for this application - in that it does no damage to the surface of the disk - it is difficult to ensure a consistent size and shape to the dam construction using this method. Conversely, the lifting collar ensures consistent replica dimensions, but the design proposed by George (featuring lifting screws which push against the surface to free the cured replica) was unacceptable due to the risk of damage to the surface. A bespoke design was adopted instead, ensuring the consistent dimensions of the latter method but avoiding the risk of damage.

Figure 3.3.1 shows the design of an arch made of stainless steel, a pair of which were used on each disk. The radius of the arch was equal to the outside radius of the disk, allowing the curved protrusion of the arch to sit atop the disk surface on

the un-run region of the disk. The angled face provided wedge-shaped edges to facilitate easier removal of the replica from the disk. Either side of this, slots 2 mm wide by 2 mm deep were machined into the arch with a separation of 20 mm. Endplates cut from 1.5 mm acrylic sheet were placed in these slots, resting upon the disk surface between the two arches. The arches were then clamped to the disk by means of two 5 mm bolts. This arrangement can be seen in Figure 3.3.2. Plasticine was used to pack the outside of the endplates and the sides of the disk under the arch to prevent leakage.

The length of arc between the endplates was 20.2 mm, and the replication area was nominally 7.5 mm wide across the centre of the disk surface (each arc sitting upon 1 mm of the disk surface). This resulted in a nominal total replicated surface area of 152 mm^2.

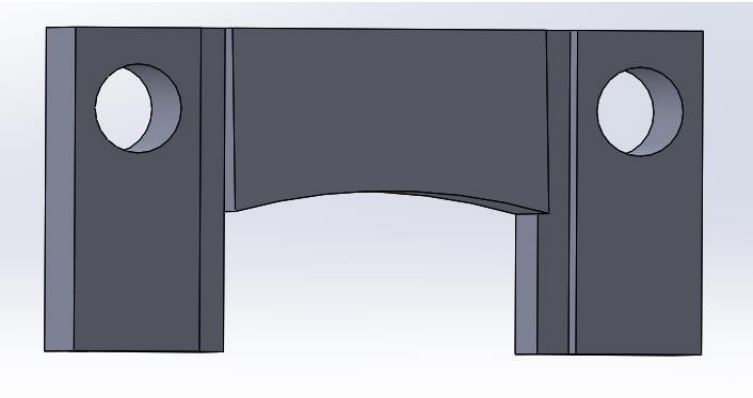

Figure 3.3.1 CAD model of one of the arches described above. The curved face sits at the edge of the disk surface and an arch is clamped to either side of the disk using two bolts. Acrylic endplates sit in the grooves either side of the area of interest.

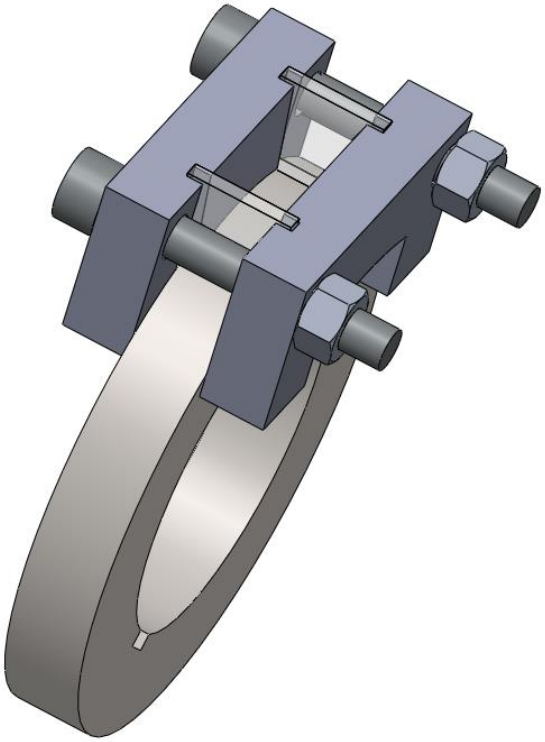

Figure 3.3.2 CAD model of arch arrangement applied to a disk. Plasticine is then packed behind each endplate and beneath each arch.

3.3.3 Procedure for Surface Replication

The disk surfaces were first thoroughly degreased using a fast-drying solvent. The arch components as described above were then attached to the disks and endplates were inserted, ensuring that the engraved line on the side of the disk indicating the area of interest was centrally located in the replication area. The outside of the arch components was then packed with plasticine.

The resin was then mixed. The Acrulite used in this work was supplied by Rubert & Co and consisted of a liquid (predominantly of methyl methacrylate), and a powder which initiates polymerisation to form solid Poly Methyl Methacrylate (PMMA). A ratio of five parts powder to two parts liquid by volume was employed, with an

allowed curing time of approximately 1 ¼ hours[1]. The constituents were measured out using measuring cylinders. The liquid was poured into a plastic cup and the powder was then added to the liquid and stirred for approximately thirty seconds, to ensure all powder was absorbed into the liquid. The mixture was then poured into the replication areas on each disk and left to cure for 75 minutes.

Once cured, the bolts were removed and the arches were then forced apart until one or both of the arches became separated from the acrulite replica. The replica could then be cleanly removed from the surface by means of a sharp impact from the side. If still attached to one arch the replica could then be freed by knocking the endplates free of the slots. This method was found to be the most successful in preventing damage to the replica surface, while simply forcing the arches upwards similarly to the lifting collar mentioned previously frequently resulted in cracks and fractures.

Once removed from between the arches, the Acrulite casting (with plastic endplates attached) was inspected under an optical microscope for any signs of damage or air bubble formation on the surface. If any such issues were observed, the replication process was repeated.

3.4 Surface Measurement

In order to analyse the micropitting behaviour of the test disks, measurements of the disk surface were collected between load stages, both in-situ and via replication. Two Surface Profilometers were used for this purpose. For two-dimensional measurements of the disks in-situ a Taylor Hobson Form Talysurf 50 mm Intra was used. This portable profilometer was operated from a specifically designed platform on the test rig, the process for this being described in section

[1] The author is indebted to Dr Jishan Zhang of Newcastle University for his guidance on preparing a suitable Acrulite mixture to replicate features of this scale.

3.1.7. For areal measurements of replicas, and disks pre and post-test, a Form Talysurf Series 2 was used (as shown in Figure 3.4.1). This features an automated stage for the y-direction, allowing areal scans to be made for the entire surface using a large number of offset two-dimensional profile measurements. Both profilometers use a conical diamond stylus with a 2 μm tip radius and a range of 1 mm, connected to an inductive gauge with a resolution of 16nm.

The surface profilometer moves the stylus over the surface at a known rate, recording the vertical displacement of the stylus tip as it does so. In these experiments the displacement was sampled every 0.5 μm of stylus movement for both two-dimensional and areal measurements. For areal scans, spacing in the y-direction (perpendicular to the direction of profile measurement) was 3 μm, chosen to provide high resolution whilst keeping file sizes manageable and scan times practical. Full width disk scans (6 x 9.53 mm) took approximately 26 hours to complete, measuring across the full disk width. Replica scans (approx. 6 x 7 mm) took up to 16 hours as a reduced area was scanned – sufficient to fit the full contact area, hardness marks and some unrun surface each side of the contact.

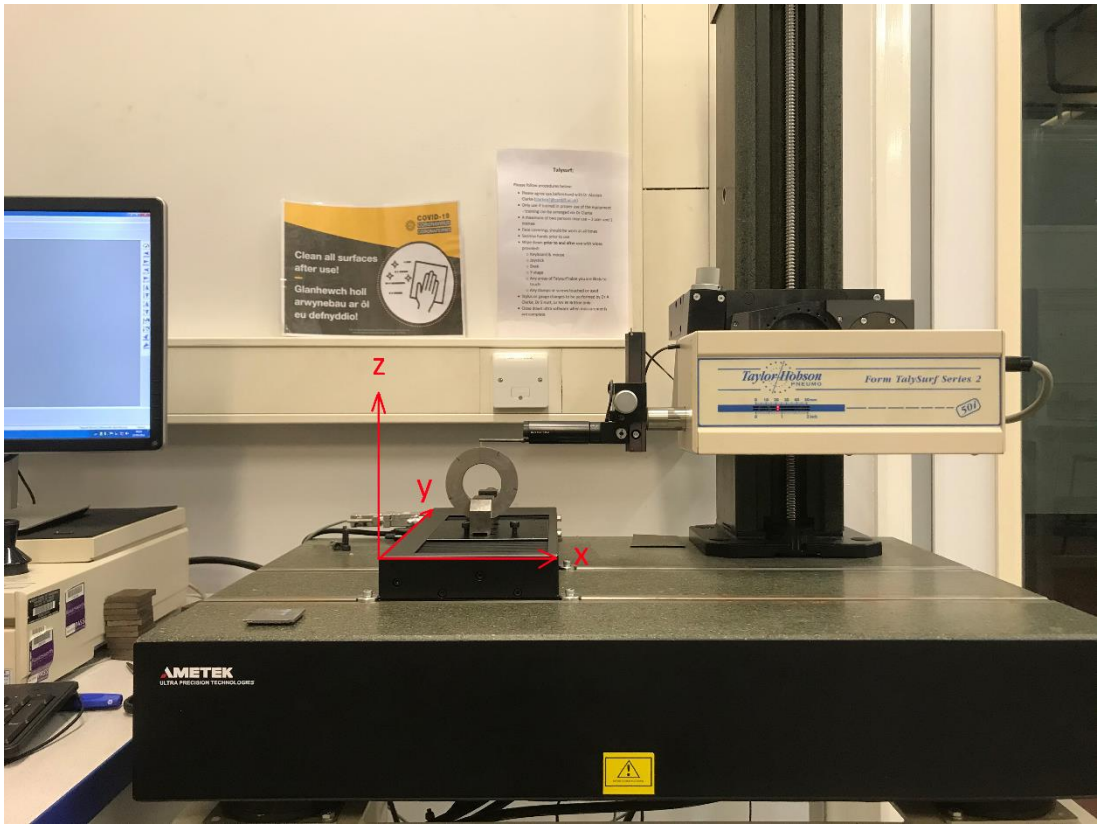

Figure 3.4.1 Talysurf surface profilometer with automated stage, used to obtain areal surface scans. Shown here with a disk in place for measurement.

3.5 Results Analysis Software Development and Modification

3.5.1 Analysis of Two-Dimensional Profiles

A bespoke piece of software was developed in MATLAB to enable the analysis of two-dimensional profiles. This software built upon the approach developed by Hutt (2018), who detected micropits using the standard deviation of recorded heights at a given point. Where material is removed from the surface through micropitting a large change in height occurs, widening the range of data and markedly increasing the standard deviation.

Because Hutt's method evaluated the standard deviation for all profiles at the end of testing it suffered from two limitations which the new software sought to overcome. Firstly, it was not possible to determine when in a test a pit occurred –

only whether a location was pitted at the end of testing. The extent of pitting at a given time could be inferred from the mean heights at each stage for locations which pitted, but not directly assessed. Secondly, there was an inherent bias for detecting points that pitted early in the test. This arises as error in axial relocation means that after a pit appears, profiles may go through the middle or edge of a pit or miss it entirely – the most likely outcome being a mix of these possibilities all occurring for the remainder of the test. This then raises the value of the standard deviation. If a point pits near the end of a test there are very few pitted readings amongst a large group of non-pitted readings, thus resulting in a smaller spread of data.

As a solution to this, the new analysis program required the user to indicate at which load stage the surface could be considered run in (taken throughout this work as six thousand fast disk cycles), and to provide a moving window size in test stages. Considering each measuring position in turn, profiles from the specified number of test stages were considered, the earliest profile being the run-in profile. The standard deviation of height values at each relocated point in the current group of profiles was calculated, and any points exceeding a threshold value were designated as pitted.

If a point was deemed to be pitted, the software would then search around this point to include all points where the standard deviation was above average – thus including the whole of the detected pit. Once each window of profiles was analysed the earliest profile would be discarded and the next profile chronologically would be added to the set. This process was then repeated until the end of the test was reached. If a pit was detected, the last test stage included in the window was identified as the stage in which it occurred. The exception to this was pits found during the first window. Instead, these were analysed on an individual basis,

designating either the largest negative change in height or earliest stage to exceed a set threshold height decrease as the stage in which pitting occurred (with the latter overriding the former).

These changes allowed significantly more information to be obtained than was previously possible. While the pitting behaviour could previously only be estimated from the mean heights of pitted and non-pitted points at each stage, this new method enabled the number of pits, pitted points and percentage of profile that is pitted at each stage to be assessed directly.

There are two key influences on the effectiveness of this method which remain; the alignment of profiles, and the setting of a threshold. These processes are elaborated on below.

Alignment of Profiles

As this analysis method is based on the comparison of values from sequential profiles, ensuring that these profiles are correctly aligned is of the utmost importance. Without correct alignment, both vertically and horizontally, artificial variation in the measurements leads to false micropit detection.

The horizontal alignment of profiles was achieved using the same methods as Hutt (2018), who performed a cross correlation between the first profile and each other profile in turn. The offset which results in the highest agreement between the two signals can then be determined, and once this has been done for every profile the offsets can be applied and the signals truncated to result in a complete set of aligned profiles of the same length.

While the loss of horizontal alignment is due to inherent error in the circumferential relocation of the measured location, the loss of vertical alignment results from

changes to the topology which occur during running. As asperities are removed, reduce in height or develop into pits the mean line of the profiles after Gaussian filtering is applied becomes lower, artificially shifting the profiles upwards.

To resolve this, the mean of the final profile was set as zero (the final profile was chosen for easier comparison to previous work). For the profile immediately prior to this all points above its own mean line were rejected, thus avoiding attempting to align asperities that have since become micropits. The offset between each remaining point and the corresponding point in the final profile was calculated to the nearest 10 nm. The most frequently occurring value was then selected and the profile was offset by that amount. The process was then repeated between this profile and the one preceding it, and so on until all profiles had been vertically aligned.

Setting the Threshold

The threshold (the value of the standard deviation in the current window which a given location must exceed to be declared a pit) was originally input by the user and modified based on whether the software was over- or under-identifying pits. An alternate method was therefore developed to remove subjective decisions from the process.

It was noted during development that, for measuring positions where there was a large amount of change (even if that change was predominantly due to micropitting) a higher threshold was needed to avoid false detections when compared to those measuring positions where only a small number of pits occurred. This is likely due to increased difficulty in achieving exact alignment of the profiles.

As an attempt to capture this effect, the mean value of the standard deviations for the entirety of each profile at the current measuring position was trialled as a

threshold value. This was found to perform very well at identifying pits, and hence this was retained as the means of obtaining a threshold.

3.5.2 Evaluation of Asperity Radii of Curvature

It has long been known that asperities are flattened and reduced in height as both surfaces adjust to better conform to each other (Østvik and Christensen 1968). As was illustrated by Bishop and Snidle (1984) the radius of curvature of asperities serves as a good means of quantifying this change. A method developed by Roberts (2017) was employed to evaluate the radii of curvature using the two-dimensional profiles measured in-situ in the test rig.

As only asperities could be considered valid, all points which were below the mean line were automatically discarded. A further threshold minimum height of 0.5 μm was applied on the basis that these are the peaks likely to come into direct contact, and that this reduced false peak identification. Further criteria were then applied to consider only remaining points which neighboured three consecutive valid points in both the positive and negative x-directions, and where the central point was higher than both of its neighbours and those points in turn were higher than their remaining neighbour. This ensured that the calculated radius would always be that of a true asperity and could not be calculated as negative.

The five-point mean sagitta method was then employed. In this method two circles are drawn; one passing the through the peak and both neighbours to its left, and one between the peak and its neighbours to the right (As shown in Figure 3.5.1). For each circle a sagitta (shown as *S1* and *S2* in the figure below) is drawn from the central data point to intersect the chord between the peak and left- or right-most point. The length of the sagitta for each circle can be determined trigonometrically. The mean of the two sagittas was then calculated, and assuming that the peak of

the asperity was located above the centre of the circle, the radius could be simply calculated using Pythagoras' theorem with the mean sagitta length and sample spacing dx, as shown in Equation 3.5-1

$$r = \frac{dx^2 + {s_{mean}}^2}{2s_{mean}}$$ Equation 3.5-1

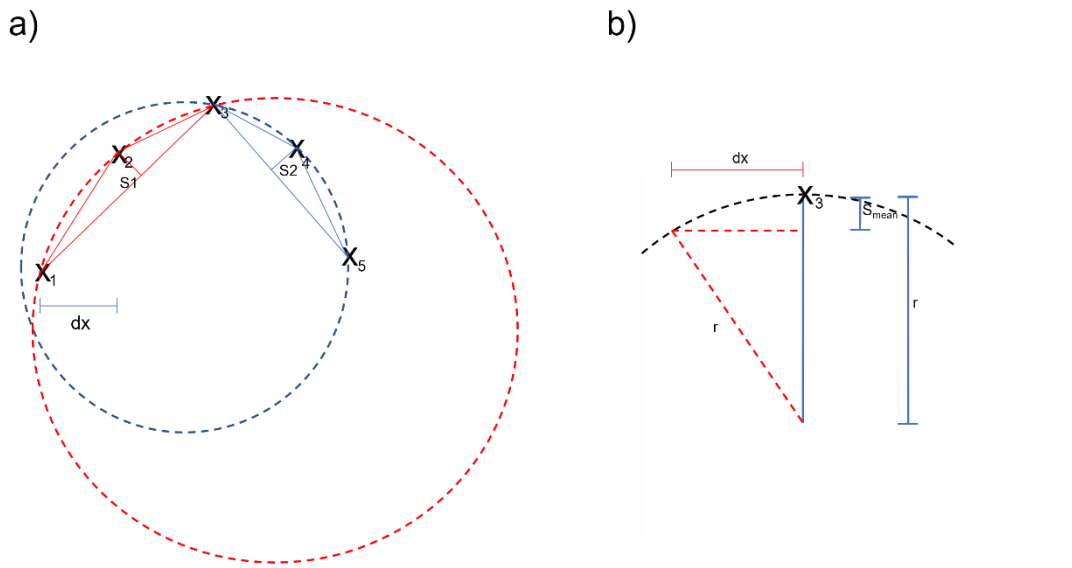

Figure 3.5.1 a) Two circles created as part of the 5 point mean sagitta method, b) illustration for the calculation of radius r from mean sagitta length S_{mean}.

3.5.3 Evaluation of Running-in Parameters

The parameters used to evaluate running-in in this work were those detailed in Table 3.5.1 below:

Table 3.5.1 Parameters used for evaluation of running-in

Rp	Maximum profile peak height
Rv	Maximum profile valley depth
Rz	Maximum peak to valley height
Rc	Mean height of profile elements
Rt	Total height of the roughness profile
Ra	Arithmetical mean roughness
Rq	Root-mean-square roughness
Rsk	Skewness of the height distribution
Rku	Kurtosis of the height distribution
Radius of Curvature	Radius of curvature of asperity peaks
Asperity Height	Mean height of asperities above the mean line
Asperity CSA	Mean cross-sectional area of asperities above the mean line

The first nine parameters listed in the table above were evaluated using the Talymap software according to ISO 4287, and the evaluation of radius of curvature was discussed in the previous section. Both the Asperity Height and Asperity CSA parameters were determined separately using an algorithm written in MATLAB, as will be explained here.

Similarly to Rc, both Asperity height and Asperity CSA were determined by dividing the profile into elements, each containing an asperity bounded by valleys on each side. These elements were determined through use of turning points. Valleys were identified as minima located below the mean line, with a height change of at least -0.2 µm from the previous peak, while peaks were identified as maxima above the mean line with at least 0.2 µm height change above the previous valley. Once a valley was detected the algorithm searched for the next peak (and vice versa). The aim of this was not to identify the highest or lowest point of a given asperity or valley, but to segment the profile into asperities with a valley on each side.

The Asperity height metric was then calculated as the mean of the maximum heights of all elements from the mean line. The Asperity CSA metric was the mean of the areas bounded by the profile and mean line for all elements. This is illustrated in Figure 3.5.2.

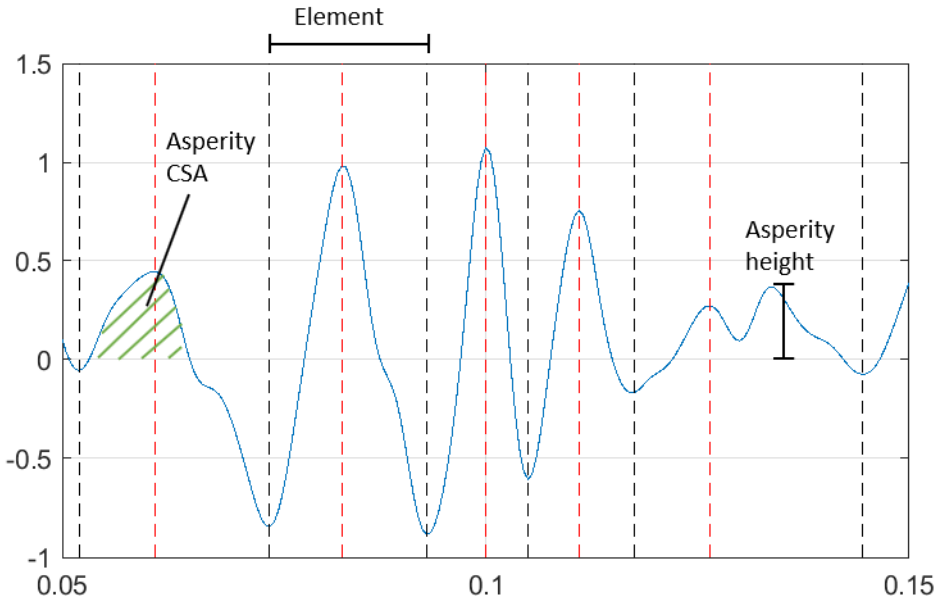

Figure 3.5.2 Profile section with identified valleys (black dashed lines) and peaks (red dashed lines) indicated. Elements are defined as the sections between two valleys, with asperity height and asperity CSA found as indicated on the figure.

3.5.4 Analysis of Areal Surface Scans

In order to take full advantage of the data from the replica surfaces, it was necessary to develop a software tool to analyse the areal scans obtained – MATLAB was chosen for this purpose. Initially, a method similar to the two-dimensional profile analysis described above was attempted by realigning the surfaces in sequence and using the standard deviation of the heights obtained for successive surfaces at each grid point as an indication that micropitting had taken place.

Two Vickers hardness indentations were made on the surface of each disk outside of the contact area to act as markers in the areal scans. The depth of these marks far exceeds that of any existing features on the surface, hence these were easily detectable. The surface was first translated such that one hardness mark was aligned on each surface. The surface was then rotated such that the angle between the y axis and the vector connecting the hardness marks was equal to that on the reference surface. The rotated surface was then interpolated onto the same grid as the reference surface.

This method was found to be unsuccessful however, yielding unreliable results. Differing temperatures in the laboratory when casting replicas, induced waviness due to variable shrinkage and porosity in replicas, temperature differences when scanning, and error introduced through interpolation were most likely contributing factors.

It was instead concluded that a method capable of detecting micropits within a single image was required. Valley features resulting from the grinding process presented the first obstacle, as their depth and steep edges make them difficult to programmatically differentiate from pits. It was therefore required to first remove the valley features from the surface prior to pit detection.

To achieve this the grinding marks were first 'straightened' by performing a cross correlation between each profile and its neighbour. This yielded the required lag for each profile to be offset in the x direction to remove the 'swept' character from the surface. Following straightening, the surface was truncated to leave a rectangular evaluation area. An example is shown in Figure 3.5.3. Once straightened, the surface could then be thought of as an extruded surface where the height values along each asperity and valley, now lines of constant x, should remain relatively constant. Any localised negative deviations were therefore almost certainly due to fatigue or wear effects. For clarity, this straightened surface is referred to as *h*.

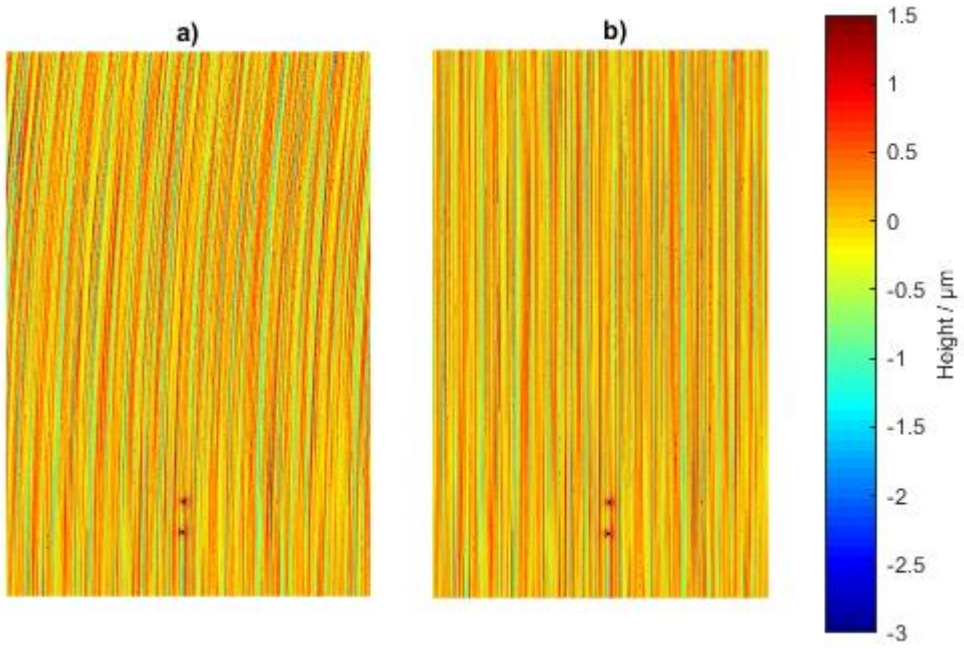

Figure 3.5.3 An unrun surface a) as measured and b) after straightening (h).

A zero-phase mean filter with a window size of 20 points (therefore 60 µm – twice the diameter of a typical micropit as described by Clarke *et al* (2016b)) was applied to each line of constant x in surface *h* – and therefore the length of each asperity or valley feature. The result was then subtracted from the straightened surface to give surface *f* - a high pass filtered surface with very short wavelength features and

their locations preserved. Figure 3.5.4 illustrates this process. It can be seen in Figure 3.5.4c that valley features have been removed from the surface while features due to pits remain prominent.

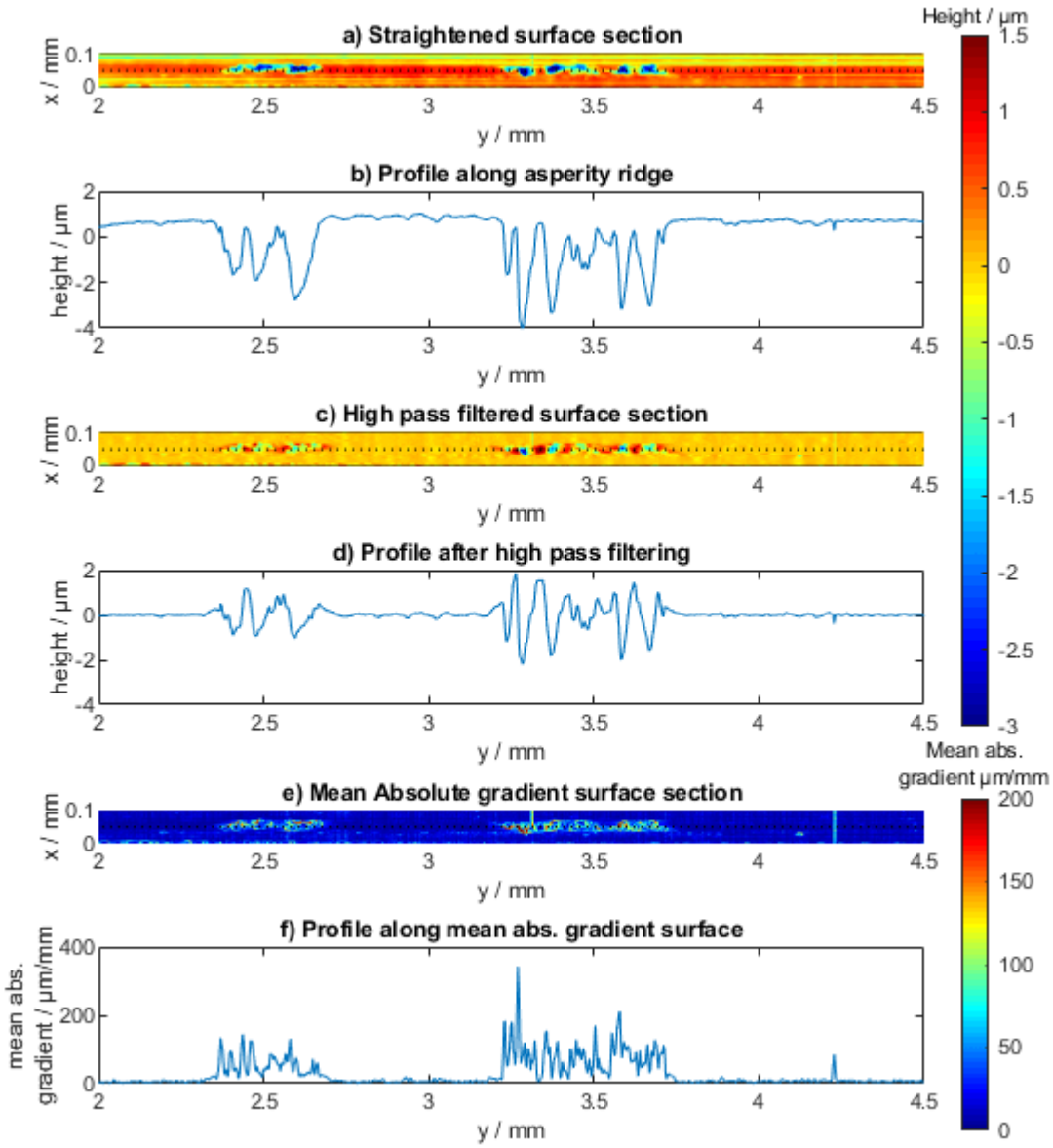

Figure 3.5.4 A small section of micropitted surface before and after the high-pass filtering process. a) section of straightened surface, dotted line indicates profile b) extracted from surface. c) A section of filtered surface f and d) extracted profile. e) Surface s section (as below), and f) extracted profile.

Initially a simple height threshold was applied to the surface *f* to detect pits, however while this was found to be largely effective it did suffer from noise and false detection. To overcome this, a method was devised to detect points by the mean of the absolute gradients between the current point and each of its neighbours. This exploits the fact that the walls of a micropit are the steepest features in the contact area. Figure 3.5.5 provides an illustration of the gradient calculation. The surface when all points are expressed as the mean value of absolute gradients with all neighbours in *f* is referred to henceforth as surface *s*. An example section can be seen above in Figure 3.5.4e.

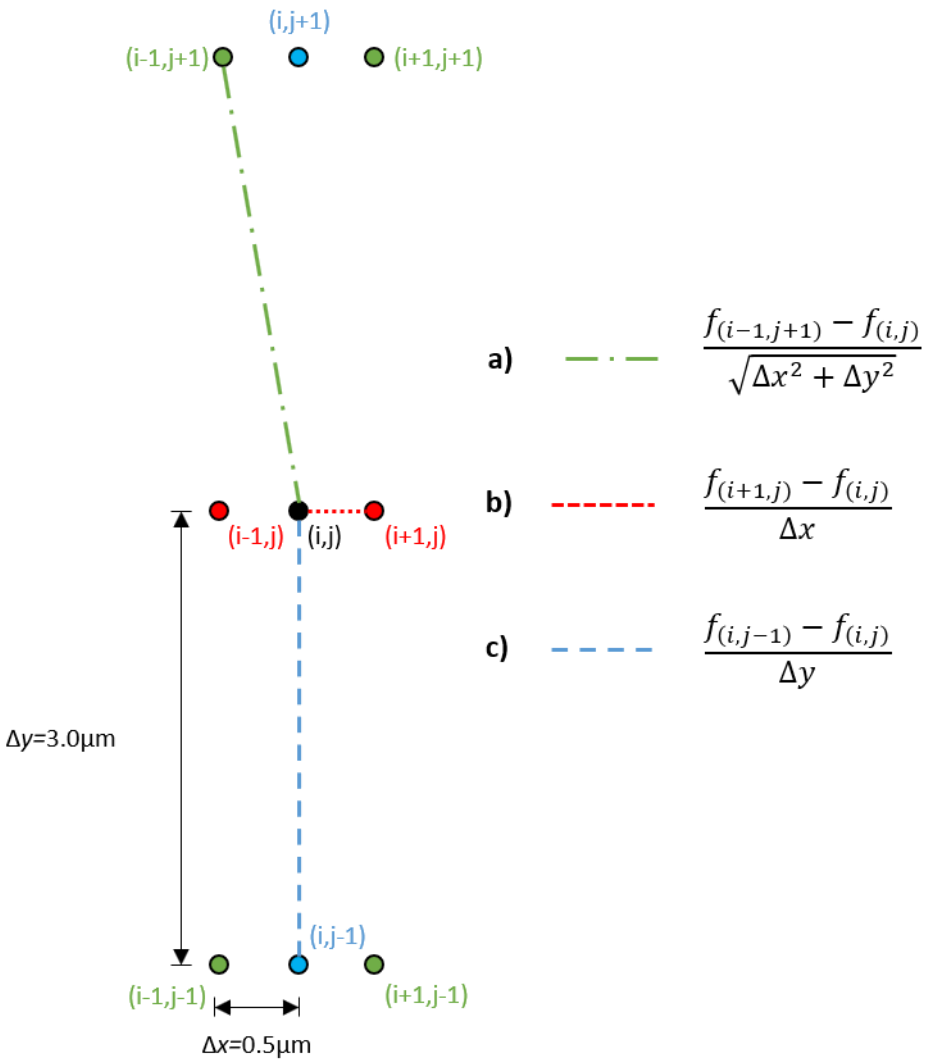

Figure 3.5.5 Illustration of gradient calculation. The current point under evaluation is point (i,j). Gradient between diagonally neighbouring points are as in a), while examples in the x and y directions are given by b) and c) respectively.

Unsurprisingly, this method tended to detect the edges of micropits and miss out the centres, however detection of micropit edges was very good with only a small amount of detection of residual valley features and scratches. As the required threshold was found to change with the surface, a constant value threshold was ineffective. Through systematic testing it was found that a value of three times the median value of points in *s* gave comparable results across all surfaces and was able

to adapt to the surface currently under analysis. An additional requirement was that the point should also be below 0 μm in surface *h*.

To fill in the centre of micropits a micropit filling procedure was introduced to allow points which neighboured pitted locations and had a value in *f* below a set threshold to also be designated as pitted points. This was called iteratively until no further points were added.

In some end of test surfaces subject to heavy micropitting, this was found to be insufficient for filling the largest pits on the surface. This was the result of amalgamations of pits reaching a size exceeding the wavelength of the high pass filter, such that only the edge features of these pits remained in *f*. To correct this, a final pit-filling stage was included to detect points which neighboured pitted points and had very low height values in the straightened surface *h*.

Initially, constant value thresholds of -0.1 μm in *f* and -1.0 μm in *h* were chosen as the thresholds for the pit-filling stages as the result of a systematic process of adjusting the threshold and evaluating the result. This process showed the selection of these values to be subjective, but the values chosen provided effective filling of points in pits whilst minimising false detection.

These values worked well over all surfaces tested, but to improve the robustness of the method and design for application to surfaces of differing roughness it was decided to express these thresholds as a multiple of the mean absolute height of the as-measured surface in the contact area. The coefficient was selected as the average coefficient required across a range of surfaces to give the constant thresholds already employed. The final values for these thresholds were -0.281Sa in *f* and -2.81Sa in *h*. Surfaces tested with scaled heights to simulate rougher and smoother surfaces were found to give identical pit detection behaviour.

Modifications were also made to disqualify detected pits which were insufficiently thin in the y direction or excessively long in the x direction as scratches or score marks. The stages of the detection process are illustrated by Figure 3.5.6.

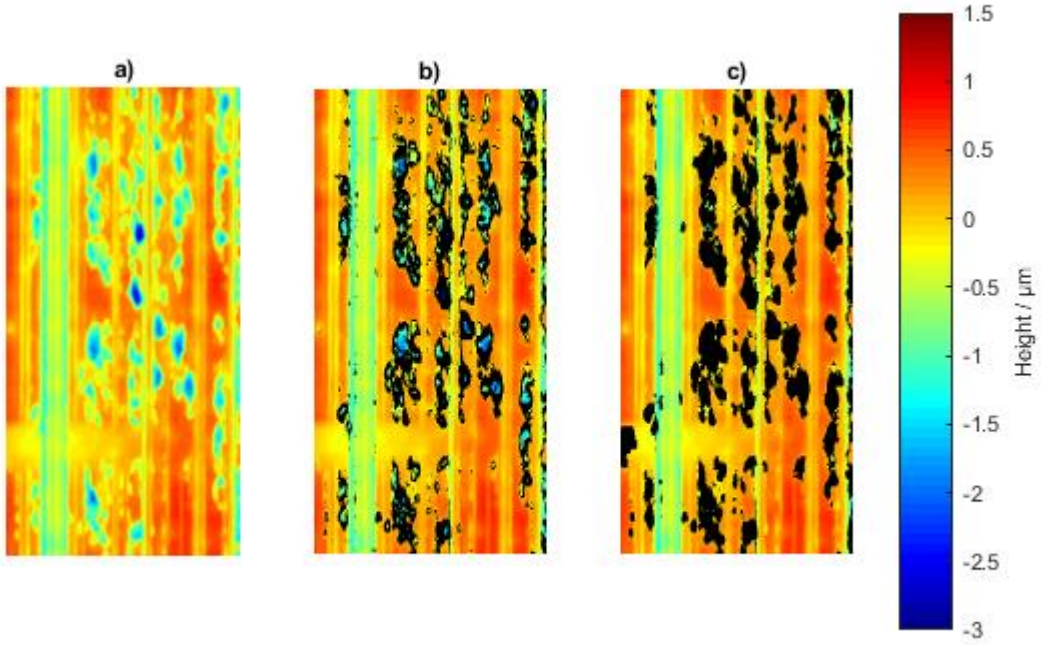

Figure 3.5.6 Stages of pit detection – Black overlay indicates detected pit. a) section of straightened surface h prior to detection, b) Detected points by mean absolute gradient in f only, c) after pit filling and removal of scratches and lone points.

Once processed, each surface was manually checked, and any clear false detections were removed. Common causes of false detections were residual short wavelength valley features or 'bleeding' of a large detected pit into a valley, or small defects in the replica surface.

3.6 Evaluating Surface Replication

For Acrulite surface replicas to be utilised in this experimental work, it was vital to ensure that the true surface of the disk was replicated to a suitable standard. Figure 3.6.1 shows a section of the disk and corresponding replica surface scan at the end of a test. Features on the disk surface are reproduced in the Acrulite replica with the correct shape and location, and can be easily located on the replica surface. It was also clear that the heights of features are exaggerated on the Acrulite replica, with pits being notably deeper and asperities appearing taller.

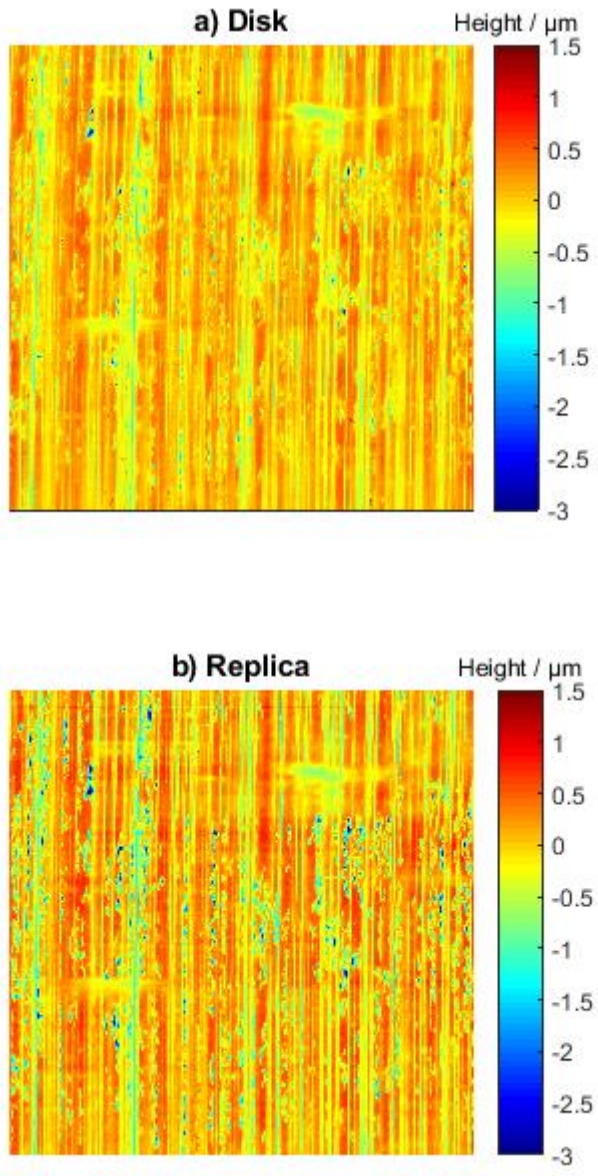

Figure 3.6.1 Matching 2x2 mm sections of scans taken from a) the disk and b) the replica at the end of a test.

This difference in measured heights is clearer in Figure 3.6.2, which shows the height distributions for the disk and replica surfaces. The range of heights in the replica surface is greater than in the original surface, and the peak of the height distribution is offset to the right (although this will be partly influenced by the shift in the location of the mean line after filtering).

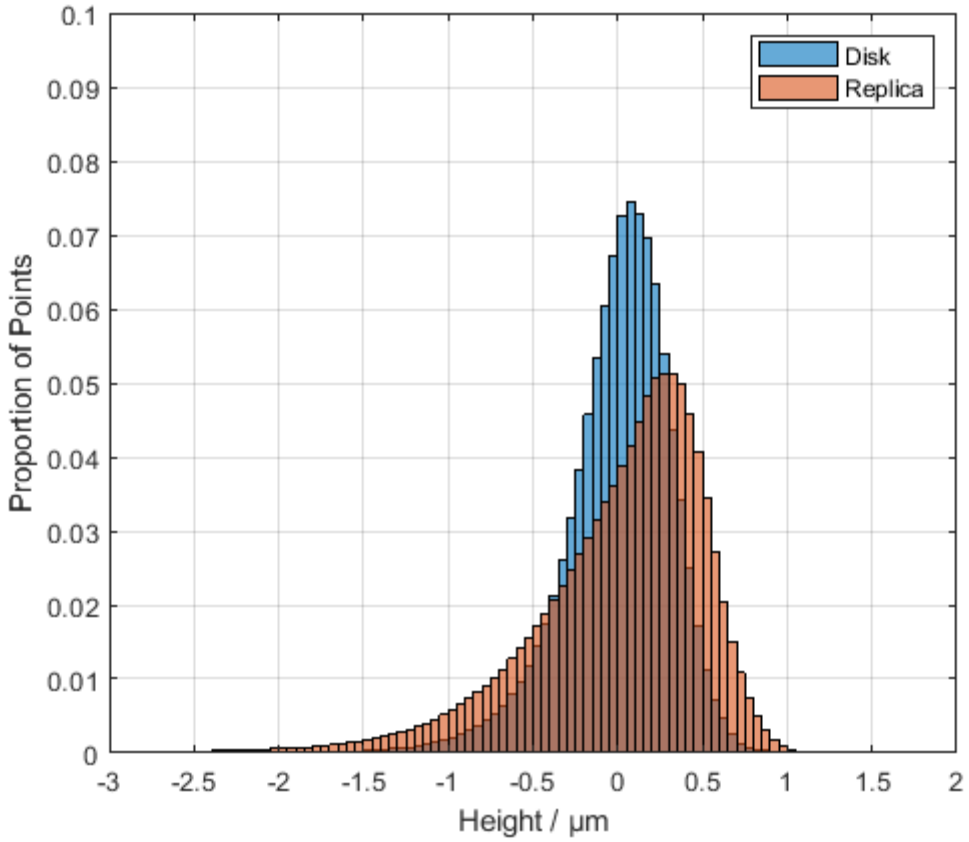

Figure 3.6.2 Height distributions in the running track at end of test for the disk and replica.

There are several possible causes for this difference in measured heights. As the replica surface is an inverse copy of the disk surface that is programmatically returned to the correct orientation, it was considered that the inverted surface may be interpreted differently due to the geometry of the profilometer stylus. Applying a tip deconvolution function to the surfaces using the TalyMap software was found to make a negligible difference to the surfaces. A MATLAB program was written to pass the stylus geometry over two-dimensional profiles and compare differences between the normal and inverted surfaces. The recorded profiles were identical for the majority of the profile length, however small differences were observed at very steep features. These could not account for the differences seen above, and were

not large enough to hold any significant influence on micropit detection. Figure 3.6.3 shows an example of this.

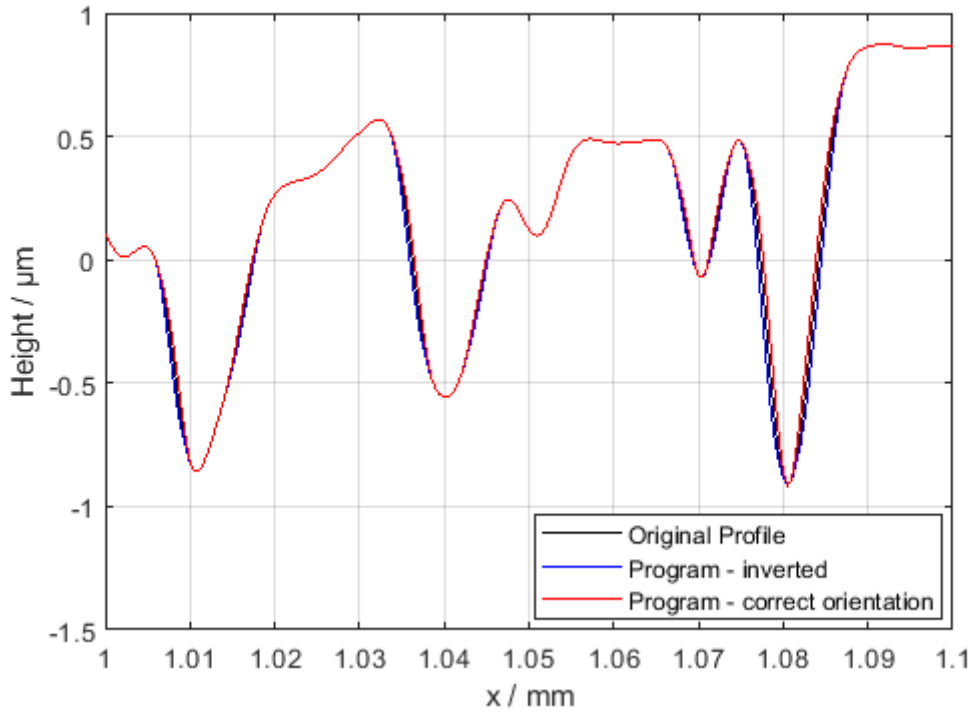

Figure 3.6.3 Comparison of profiles programmatically "Measured" using a MATLAB function. On the inverted surface valley / pit features become marginally wider than on the true profile, while they become narrower when oriented as on the disk and the stylus must descend into the feature.

Another possible cause for the difference in heights is expansion of the replica in the z-direction during the curing process. Expansion and contraction are commonly encountered difficulties with surface replication, and George (1979) noted shrinkage (and the consequent bowing) to be an issue with Acrulite. The replicas used in the current work did not exhibit bowing behaviour - perhaps due to their small size and large relative thickness - and no notable offset of features was identified in the x or y directions.

Regarding heights, shrinkage (i.e. contraction) of the replica would be more likely to cause the opposite change in height distributions to that seen above. It is unlikely that differences in mixing ratios between this work and previous studies would cause a change from contraction to expansion, however this should not be ruled out.

Another possibility is that, due to the rough texture and strong adhesion to the surface, the replica features stretch slightly as the replica is removed from the disk. Once cured, Acrulite is brittle and more prone to fracturing than deforming, however considering the very small distances of stretching for any point and the comparatively small amount of material available in these features to resist the forces this may be the most likely possible cause.

To better understand the replication of micropit features, it is helpful to look closely at individual micropits, as in Figure 3.6.4. The features on the disk are easily recognisable on the replica surface, with shape still well preserved. The depths are exaggerated however, as is easiest to see by considering the very shallowest micropits which become more substantial in the corresponding replica. The pit boundaries in the replicas also appear to have expanded outward slightly. This may be due to expansion of the replica material, however a stretching of the material as it is removed could also create this appearance.

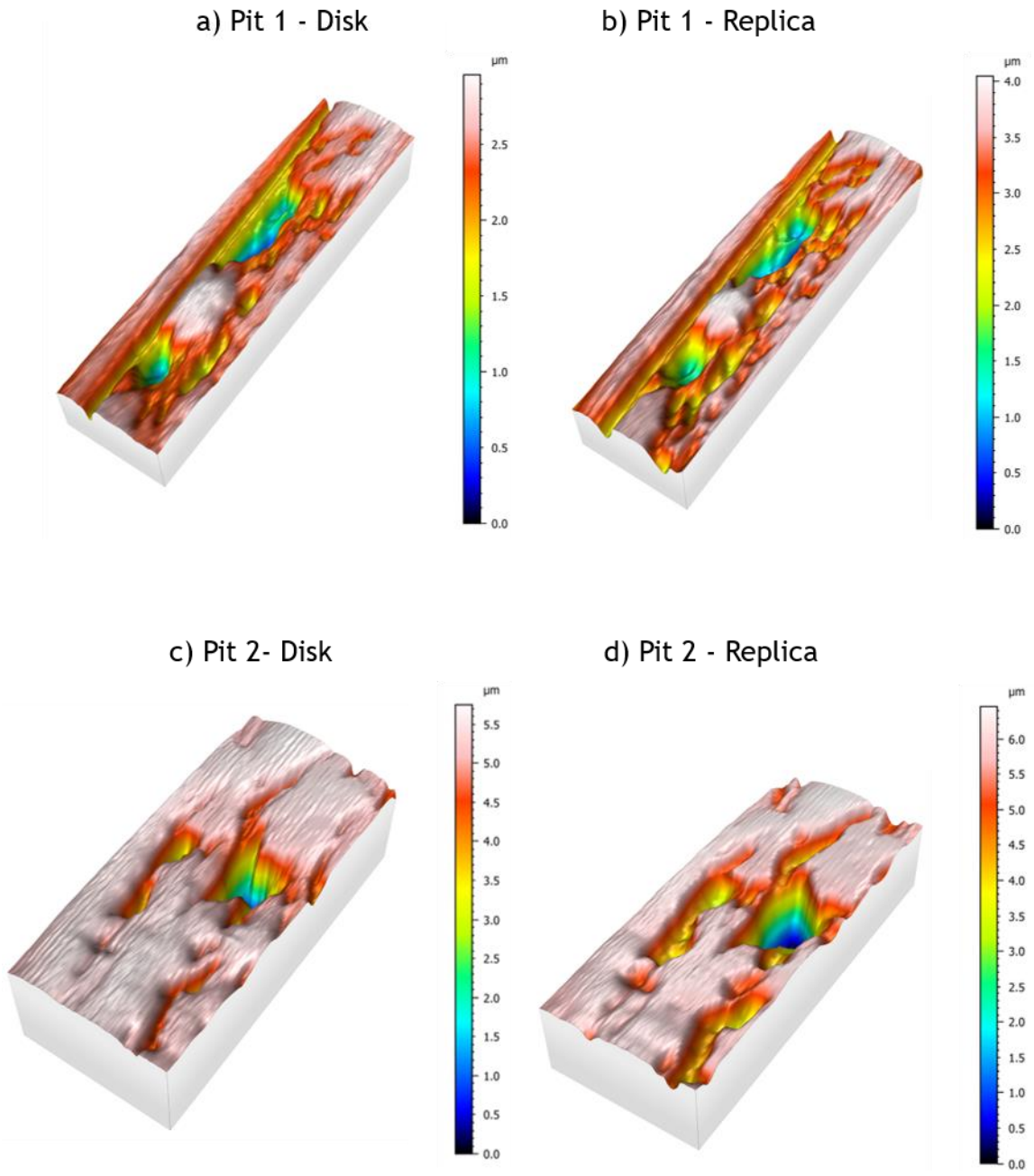

Figure 3.6.4 3D visualisations of pits produced using TalyMaps software. a) and b) are taken from the fast disk of Test 4, while c) and d) are taken from the slow disk of Test 3.

Impact on micropitting analysis

The modification of heights in the surface replicas presents challenges with respect to surface analysis. Lacking a reliable function to convert heights between the

replica and disk, numerical data such as roughness or pit volume cannot be reliably collected from replicas. As such, numerical data of this nature must be collected from two-dimensional profiles.

Application of the areal micropit detection algorithm to replica surfaces consistently gives a higher result for the pitted area than when applied to the equivalent disk scan. In overlay images such as those in Figure 3.6.5 the same pits are clearly detected on both surfaces but the boundaries of the pits in the replica images are slightly expanded.

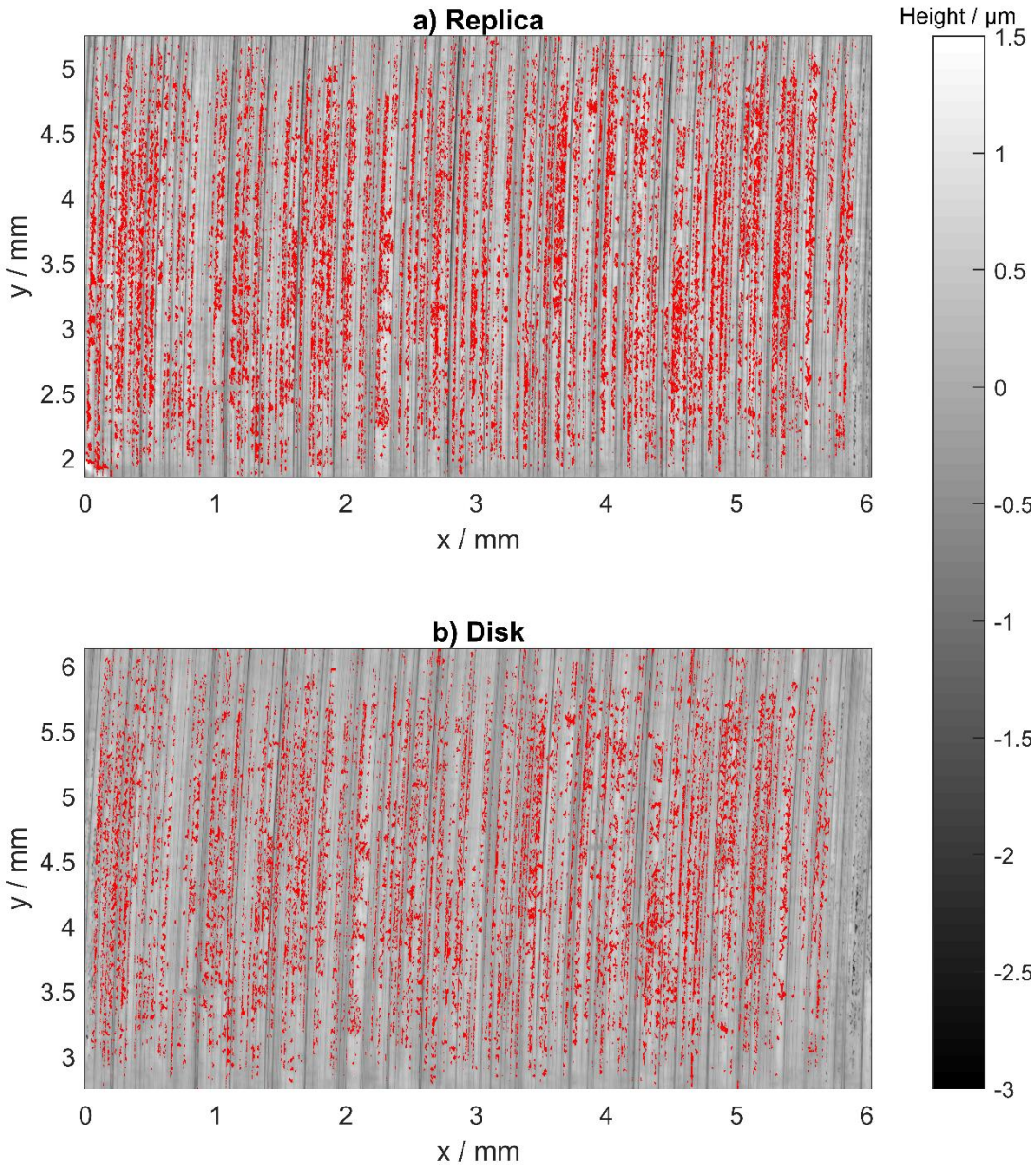

Figure 3.6.5 Comparison of micropit detection on a) the replica and b) the corresponding disk surface. Regions on the far right and left of the images are excluded from the analysis due to straightening requirements. Red overlay shows detected pits.

In order to investigate this overestimation, the micropit detection algorithm was applied to scans of disks at the end of test and to their corresponding replicas. A

scatter chart of the evaluated percentage of surface micropitted on the disk versus on the replica showed that there was a very consistent relationship between the determined values, as can be seen in Figure 3.6.6. The best fit line through the origin had an R^2=0.9941 indicating a very close fit to the data, and thus a coefficient of 0.7427 was adopted throughout this work to convert in-test percentage pitted values determined using replicas to the equivalent disk value. This is not claimed to be universally applicable for roughnesses outside of the scope of this work, but is demonstrably effective for the conditions used here.

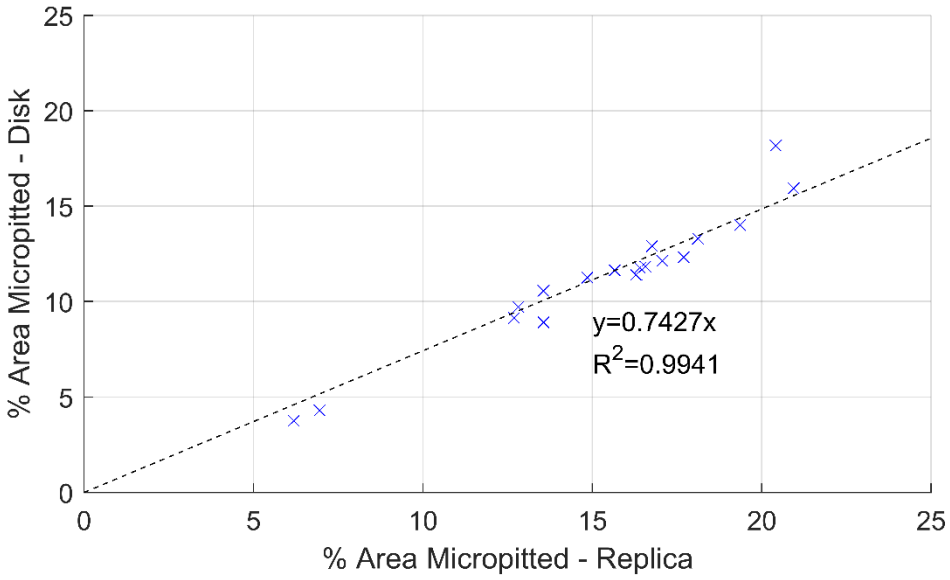

Figure 3.6.6 The percentage of area micropitted as detected on corresponding disk-replica pairs.

3.7 Estimation of Volume Removed by Micropitting

The result of micropitting is the removal of material from the surface, and it is interesting to try and quantify this. It is impossible to achieve a reasonable estimation using the two-dimensional profiles, but the development of micropit detection in areal scans provides a new opportunity to evaluate the volume removed.

Firstly, the micropit detection must be applied to the end of test true-disk surface - replica surfaces are not appropriate for this purpose due to the height modification issues discussed above. The locations of the micropitted points in the straightened surface (*h* as defined in section 3.5.4) are then found. By using the straightened surface, the extruded quality of the surface across the disk width can be exploited.

For each line of constant x (across the disk width) the average height of non-pitted points was calculated. If it is assumed that the height of any pitted points along that line would otherwise be at the calculated mean height, the volume removed at that point can be calculated by multiplying the difference between the pitted height and average height by the scan spacing in the x and y directions. Once this is performed for the whole surface, the total volume of material removed is the summation of the volumes removed at each pitted point.

3.8 Selection of Variables

The experimental element of this work aims to perform micropitting tests under a broad range of conditions to better understand the effects of the variables with the most impact on micropitting. As evidenced in Chapter 1, the effects which contribute to micropitting appear to be many and varied, however evidence to this point indicates that surface roughness, SRR, load, and speed (either of sliding or entrainment) may have a significant level of influence.

Load and surface roughness are both well established as having a notable effect on rolling contact fatigue. With respect to roughness, superfinishing gears has been established as the most effective means to prevent micropitting, and is therefore a common choice for gears used in safety critical applications. With regard to load, the works of Oila and Bull (2005) and Li and Kahraman (2013) both found the load

to have the most influence on micropitting behaviour in their experimental programmes.

The final two variables to be considered in this work are the SRR and entrainment velocity. Some studies have found sliding to be an influence on micropitting, however there remains to be little understanding of how. It is unclear whether sliding distance is the driving factor as suggested by Kadiric and Rycerz (2016), or whether the influence of SRR comes as a result of increased stress cycles or through some other effect entirely. The combined influence of speed and sliding - as discussed by Olver (2002) – is also of interest; both in terms of unravelling the separate effects of these variables and attempting to observe whether an interaction effect results in an effect separate to the sum of each individually.

3.9 Experimental Design and Selection of Variable Settings

3.9.1 Selection of the Experiment Design

The experimental program described in this thesis initially aimed to investigate the influence of 4 key variables on micropitting. Due to the duration of fatigue tests the test programme had to be carefully selected to ensure that useful data could be obtained in an achievable timeframe. Statistically, the most time efficient test program to comprehensively assess a number of variables is a full factorial experimental design. These designs allow the effects of individual variables to be investigated as well as the interaction effects (effects of two or more variables which are additional to the sum of the effects of the parts) between all combinations of variables.

The number of experiments required for a full factorial design can be calculated as n^k, where n is the number of levels at which one intends to set the variables (e.g. one high and one low setting for each gives n=2), and k is the number of variables

to be investigated. The number of levels at which the variables are set influences the types of relationships that can be analysed. For example, using three levels for each factor (high, medium and low) allows the quadratic relationships to be analysed - however for investigation of four variables this requires 3^4 (81) experiments which is clearly unfeasible. A two-level design where each variable has a high and low setting allows only linear effects to be analysed, however this design would require 2^4 (16) experiments which is still a very sizeable test program when the duration of fatigue tests is considered.

It was therefore necessary to look at the various options for designing experiments which allow fewer measurements than this to be taken while still yielding statistically valid results. The criteria for an acceptable design were:

a) The main test program should require no more than 12 tests, with the expectation that each test would take approximately 1 month to prepare and run
b) The primary effects of each variable should be easily and reliably obtainable from the results
c) It should be possible to identify nonlinear effects

Firstly, a Box-Behnken design was considered. These designs allow variables to be investigated at 3 levels in a highly efficient manner, meaning that quadratic effects can be analysed. Additionally, as a well-established experimental design, ample resources are available to assist in this analysis. This method, while fulfilling criteria b) and c) fails criterion a) as 27 tests would be required for a 4 variable design.

The other options consisted of various forms of fractional factorial designs. These designs are based on reducing the number of experiments in a factorial design at the expense of “confounding” some variables or interaction effects. Confounded

variables or interactions are indistinguishable from one another. For example, were variable A confounded with interaction CD then the calculated effect for variable A would in fact be A+CD. As it is impossible to say to what extent each contributes to the output the required assumption in these cases is that the interaction effect is negligible, which becomes a more reasonable assumption the more variables involved in the interaction. Fractional factorial designs are described as $n^{(k-p)}$ where p indicates the reduction in resolution that will occur. The greater the value of p the fewer tests required but the more severely confounded the results.

A $3^{(4-2)}$ three-level fractional factorial design consists of 9 experiments and would be capable of identifying quadratic effects, however there are significant disadvantages to this design; not only much increased complexity of analysis but also the limitations imposed by the relatively high level of confounding inherent in a resolution III fractional factorial design.

While it is possible to construct a mixed-level design where some variables have two levels and others have three, this is best avoided due to the complexity of analysis (as advised by Montgomery (2009)) and was therefore dismissed.

The final design considered was a variation of the $2^{(4-1)}$ fractional factorial design, a common two level fractional factorial design often used in screening experiments. This uses a high and low setting for each variable and hence only linear effects can be observed. As a resolution IV design criterion b) is fulfilled as main effects are confounded only with three-factor interactions (which are of low likelihood). In addition, this design consists of 8 tests - leaving sufficient time for additional "centre point" tests which can enable criterion c) to be met.

The term "centre point" comes from the graphical representation that is sometimes used for factorial experiments, where a two-level, 3 variable experiment can be

represented as a cube. The centre point involves setting the variables halfway between their respective high and low values and allows the *presence* of nonlinear effects to be detected. This is a simple concept; the mean of the high and low outputs for a given variable or interaction gives the value halfway between the two outputs. For a linear relationship this should be equal to the result of setting that variable halfway between the high and low values. The centrepoint run would therefore be expected to be approximately equal to the average of the high and low values. Any significant difference between the result and prediction indicates that there is nonlinearity in the true response – the one limitation of this method being that nature of that nonlinear response cannot be analysed.

A $2^{(4-1)}$ test programme was started with the most aggressive conditions intentionally placed at the start of the programme to allow the maximum limits to contact severity to be established and allow time to adapt the programme if severe wear was encountered. These severe conditions were found to consistently provoke scuffing failure, and hence further modification of the programme was required (these tests are discussed in detail in Section 3.9.2.

The maximum SRR in the original test plan (SRR=0.75) was reduced to 0.5 as it was found that neither Ra=0.6 μm or Ra=0.4 μm disks could avoid scuffing under the original conditions with SRR=0.75. To allow a wide spread of conditions for speed and load without inducing scuffing, it was decided to hold the roughness constant at 0.4 μm in the main experimental programme as it is the most well understood of the four variables considered. The maximum pressure applied was also reduced from 1.8 GPa to 1.6 GPa. The final test plan thus became a 2^3 full factorial experiment with the variables of speed, maximum Hertzian contact pressure, and SRR, including centrepoint tests for detection of nonlinearity and with two separate tests to examine the influence of roughness.

Two level fractional factorial designs have previously been employed with respect to micropitting in the work of Li and Kahraman (2013) and Oila and Bull (2005) whose results have been discussed in detail already in this thesis. These papers performed valuable analysis, however the fact that both addressed the influence of 7 variables in 8 experiments ($2^{(7-4)}$ design – resolution III) necessarily led to some fundamental assumptions in both works. As "resolution III" designs, the main effects were confounded with two-factor interactions. As a result, any conclusions drawn regarding main effects are made assuming that two-factor interactions are negligible, yet there is good cause to suspect that this may not be the case (for example, each variable investigated in the current thesis contributes to the complex feedback loop formed between film thickness and frictional heat generation).

In contrast to those tests discussed above, the full factorial design selected for the main test programme in this thesis involves no confounding, hence all interaction effects between SRR, Speed and Pressure can be examined. This serves as a natural progression, using the knowledge gained from these previous works to focus more intently on the variables of interest.

The final experimental design is shown below in Table 3.9.1. Tests 1 and 2 were intentionally conducted first as these were thought to be at most risk of scuffing failure or severe wear, and this would allow time to adapt if necessary. Tests 3, 4 and 5 were taken from the same fractional factorial group as Test 1, but chosen in random order. This allowed a fractional factorial programme to be complete by the halfway stage. Following the centrepoint test, the remaining tests from the second fractional factorial test were performed in a randomised order.

Table 3.9.1 The partially-randomised experimental programme employed in this research.

Test	Max. Hertzian Contact Pressure / GPa	Entrainment Velocity / ms^{-1}	SRR
1	1.6	4.0	0.500
2	1.6	2.0	0.500
3	1.6	2.0	0.250
4	1.2	2.0	0.500
5	1.2	4.0	0.250
Centrepoint Test	1.4	3.0	0.375
6	1.6	4.0	0.250
7	1.2	2.0	0.250
8	1.2	4.0	0.500

Each test in the experimental programme consisted of 12 load stages, reaching 2 million fast disk cycles. The only exception to this was Test 1, which was run for an additional 2 million fast disk cycles across four additional load stages. The load stages are shown in Table 3.9.2. Prior to running and between each test stage, two-dimensional profiles were measured and replicas were cast for both fast and slow disks. Due to their long duration, areal scans could not feasibly be made for both disks for all load stages. Surface scans were therefore made for each disk before running, and after load stages 2, 4, 5, 6, 8, 10, and 12 (plus 14 and 16 for Test 1).

Table 3.9.2 Number of fast disk cycles per load stage.

Load Stage	Fast Disk Cycles This Stage x 10^3	Cumulative Fast Disk Cycles x 10^3
1	3	3
2	3	6
3	14	20
4	30	50
5	50	100
6	100	200
7	100	300
8	100	400
9	200	600
10	400	1000
11	500	1500
12	500	2000
13 (Test 1 only)	500	2500
14 (Test 1 only)	500	3000
15 (Test 1 only)	500	3500
16 (Test 1 only)	500	4000

3.9.2 Scuffing Boundary Tests

As was discussed in Section 3.9.1 several tests were performed at the start of the experimental programme to establish the limits to the contact conditions that could be used. These tests induced scuffing failure, a severe wear mechanism thought to be the result of a failure of the lubricant to separate the surfaces, possibly as a result of side leakage effects and thinning of the lubricant film due to thermal effects (Holmes *et al*. 2003; Holmes *et al*. 2005). In all cases the disks scuffed at one of the contact edges, such as can be seen in Figure 3.9.1.

Figure 3.9.1 Image of a scuffed disk from the fourth scuffing test. Scuffing occurred at one side of the contact in all cases, resulting in the band of destroyed surface at the top edge of the running track.

First Scuffed Test

The test conditions for the first test are shown in Table 3.9.3.

Table 3.9.3 Settings for first scuffed test

Parameter	Value
Pressure / GPa	1.8
Entrainment Velocity / ms^{-1}	5.5
SRR	0.75
Ra / μm	0.6
Lubricant Supply Temperature / °C	80

This test was performed for two test stages, each consisting of 3,000 fast disk cycles. The load was pre-set and directly applied to the disks at the target value. The spikes in the friction data could imply that a small scuff may have occurred when the load was applied in the first test, however this was not supported by the disk temperature readings and the test was continued as a higher friction value is common at the start of a test. Both friction and temperature can be seen in Figure 3.9.2. In the second stage severe scuffing failure was encountered immediately upon applying the load.

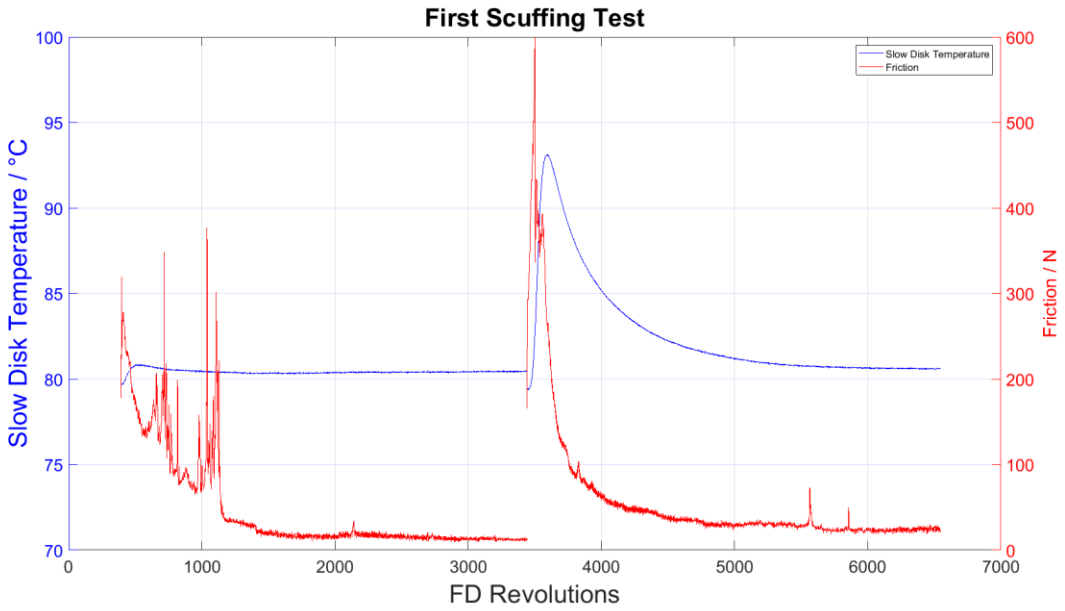

Figure 3.9.2 Friction and Slow Disk Temperature during the first scuffed experiment.

In both test stages it was noted that the circumferential alignment of the disks had been lost (i.e. the measured areas no longer met in the contact area every five rotations as enforced by the SRR of 0.5). For the second test stage several tell marks were drawn on the shafts and couplings, which showed this to be the result of slipping between the fast shaft and the flexible coupling connecting it to the drive. The most likely sequence of events is that the high contact friction force overcame the friction force clamping the flexible coupling to the shaft, causing slip and allowing the rotation of the fast shaft to slow. This then temporarily lowered the sliding speed, arresting the scuffing mechanism.

Second Scuffed Test - Gradual Load Application

In the second test a lower load was initially applied, and the pressure was then increased up to the target value. This test aimed to determine whether shock loading effects influenced the first scuffed test and whether the true scuffing load was below the applied load in the first test.

The pressure control valve was set to apply an initial pressure of less than 1 GPa, and the load was manually increased until the target load was reached. As can be seen in Figure 3.9.3 scuffing (indicated by the sharp increase in friction) occurred early in the test, when the applied maximum Hertzian contact pressure was approximately 1.3 GPa. This was significantly below the target pressure and sufficiently delayed from the initial application to rule this out as a result of shock loading. Once again slippage occurred at the fast shaft flexible coupling, which may be a factor in the arresting of the scuffing mechanism.

Figure 3.9.3 Applied maximum Hertzian contact pressure (calculated from applied load) and recorded friction during the second scuffed test.

Third Scuffed Test - Rolling Run-In

The first two tests both scuffed during the running-in stages, meaning the surfaces had not yet had an opportunity to fully complete the process of deforming to better accommodate the roughness on the opposing surface. This leads to higher friction and may provide more opportunity for side leakage of the oil than if the surfaces

had already run in. It was decided to allow the surfaces to complete their running-in process at full load but under near-rolling conditions.

This was achieved by removing the SRR gear from the fast shaft, therefore disconnecting the slow shaft from the drive. A small load was then applied to the disks while stationary, after which the motor was turned on. The load was then increased up to 1.8 GPa. The entrainment speed under pure rolling would be 5.5 m/s, however by allowing the slow shaft to roll freely against the fast (as opposed to using pure 1:1 gears) a small amount of slip may occur to allow the surfaces to better run in against multiple regions of the opposing surface.

After two running-in stages totalling 3,000 load cycles the SRR gear was returned to the fast shaft to restore an SRR of 0.75. Once again a low load was applied and then gradually increased, until scuffing occurred at a pressure of approximately 1.5 GPa. This was an increased scuffing pressure compared to that observed in the second test, however further experimentation would be needed to confirm whether this was due to the running-in process applied or a variation brought on by other factors (such as variation in roughness within the nominal Ra=0.6 μm ±0.05 bracket).

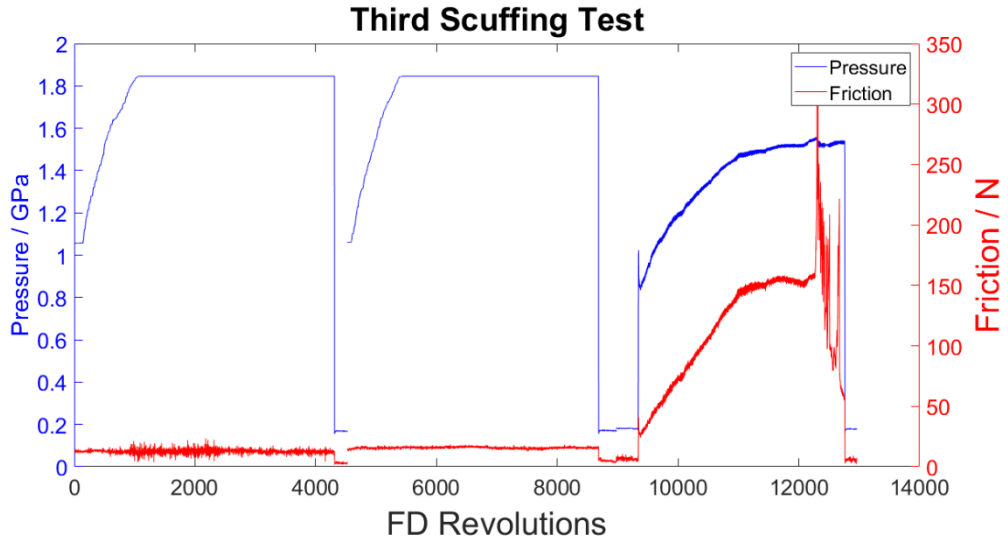

Figure 3.9.4 Applied pressure and measured friction for the third scuffing test.

Fourth Scuffed Test – Reduced Roughness

The results from the previous tests established that the scuffing limits at an Ra of 0.6 µm were too low to allow for fatigue at an SRR of 0.75, and so one further test was carried out to find the scuffing load for disks with an Ra of 0.4 µm. This reduction in roughness was expected to raise the scuffing load due to the reduced potential for side leakage effects thought to contribute to scuffing. The aim of this was to ascertain whether a load greater than 1.6 GPa could be used with a 0.75 SRR at a lower roughness. As the rolling run in technique used in the third test had been unsuccessful, it was decided to return to a gradual application of load with the test SRR applied throughout as before.

Scuffing occurred at a load of 1.6 GPa, before the target load of 1.8 GPa could be reached. This showed that simply reducing the roughness did not provide a sufficient increase in the scuffing limit to allow a broad range of loads to be applied in the test programme.

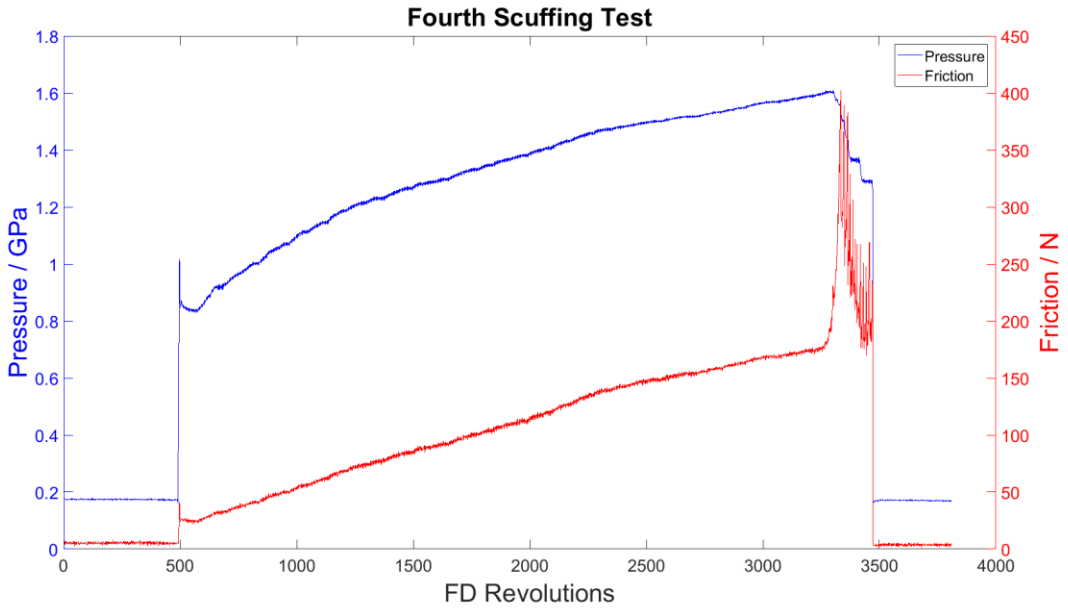

Figure 3.9.5 Applied pressure and measured friction during a scuffing test using disks of Ra=0.4 µm.

Scuffing Test Summary and Conclusion

This series of tests was able to help define an upper bound to the severity of conditions that could be applied during fatigue testing. It was shown that testing at 0.75 SRR was unfeasible for disks of 0.6 μm Ra as the scuffing load was reached at contact pressures far below the desired levels. For disks of 0.4 μm Ra the scuffing load was reached when a maximum Hertzian pressure of 1.6 GPa was applied, showing that reducing the roughness alone was not a suitable option if a range of pressures representative of gears were to be used.

As a result of these scoping tests a maximum SRR of 0.5 was adopted, along with a maximum applied Hertzian pressure of 1.6 GPa. As a further safety factor it was decided to run the full factorial experimental program with disks of Ra=0.4 μm only.

3.9.3 Interpreting of Factorial Experiment Results

The interpretation of factorial experiment results can be complex and confusing, hence a brief explanation of the way these results can be understood is presented here.

The influence of each factor or two-factor interaction in a two-level factorial experiment requires careful analysis to determine, as the experimental programme is a complex network of factors. The process is most easily understood by considering the experimental programme in a standard “coded” fashion, where “1” indicates a variable at its high setting (e.g. for pressure a 1 corresponds to 1.6 GPa) and “-1” indicates a variable at a low setting (hence for pressure a -1 represents 1.2 GPa) (Box *et al*. 1978; NIST/SEMATECH 2013).

This convention allows the two-factor interaction states to be easily established for each test by multiplying the settings of the constituent factors. A result of 1 shows where the two factors are both in the high or low setting, while a result of -1 shows

where the two factors are at different settings. The three-factor interaction settings can be determined by multiplying any two-factor interaction setting by the remaining main factor setting. The experimental programme used in this thesis is shown in this fashion in Table 3.9.4.

Table 3.9.4 Coded test settings and two-factor interactions

Test	Main Factors			Two-Factor Interactions			Three-Factor Interaction
	P	SRR	Ū	P x SRR	P x ū	SRR x ū	P x SRR x ū
Test 1	1	1	1	1	1	1	1
Test 2	1	1	-1	1	-1	-1	-1
Test 3	1	-1	-1	-1	-1	1	1
Test 4	-1	1	-1	-1	1	-1	1
Test 5	-1	-1	1	1	-1	-1	1
Test 6	1	-1	1	-1	1	-1	-1
Test 7	-1	-1	-1	1	1	1	-1
Test 8	-1	1	1	-1	-1	1	-1
Centrepoint	0	0	0	0	0	0	0

The influence of main factors on a given output may be assessed by separately taking the means of that output when a factor is in its low and high states. The difference between those means gives the average effect of the factor. These may be illustrated on graphs such as in Figure 3.9.6. The distance of the centrepoint

test value (shown here as a magenta cross) from the line can help to indicate whether the relationship is linear or nonlinear. The strength of interaction effects can be assessed in the same way as the main effects.

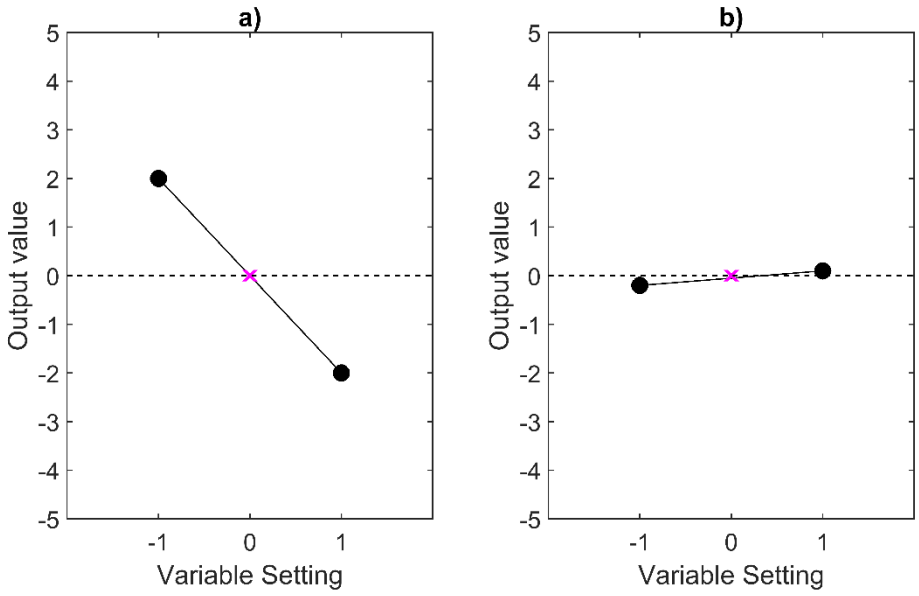

Figure 3.9.6 Example of main effect plots. In a) the variable has a strong effect on the output, while in b) the variable has a small-to-negligible effect.

While this approach can give a good indication of the influence of a factor, in both cases this should be investigated further using interaction plots. One of the interacting factors is represented on the x-axis, while one line each represents the high and low settings of the other factor. The four data points correspond to the four possible combinations of settings for the two interacting variables in question. Examples are shown in Figure 3.9.7.

Where lines are parallel such as in Figure 3.9.7a there is no interaction effect present, while if lines cross (or would cross if extended further) an interaction effect is present. If the heights of points consistently increase or decrease from left to right for each variable 2 setting, as in Figure 3.9.7a and d, then a main effect of variable 1 (the x axis variable) is present. Where the two lines have a relative offset

in height, such as in as in Figure 3.9.7a or b, then there is a main effect of variable 2 (in d the mean of points on each line is the same, hence no main effect of variable 2). In the case of Figure 3.9.7c, there is no main effect present from either variable, but there is a significant interaction effect. A deeper explanation of this analysis process can be found in Crump *et al.* (2019)

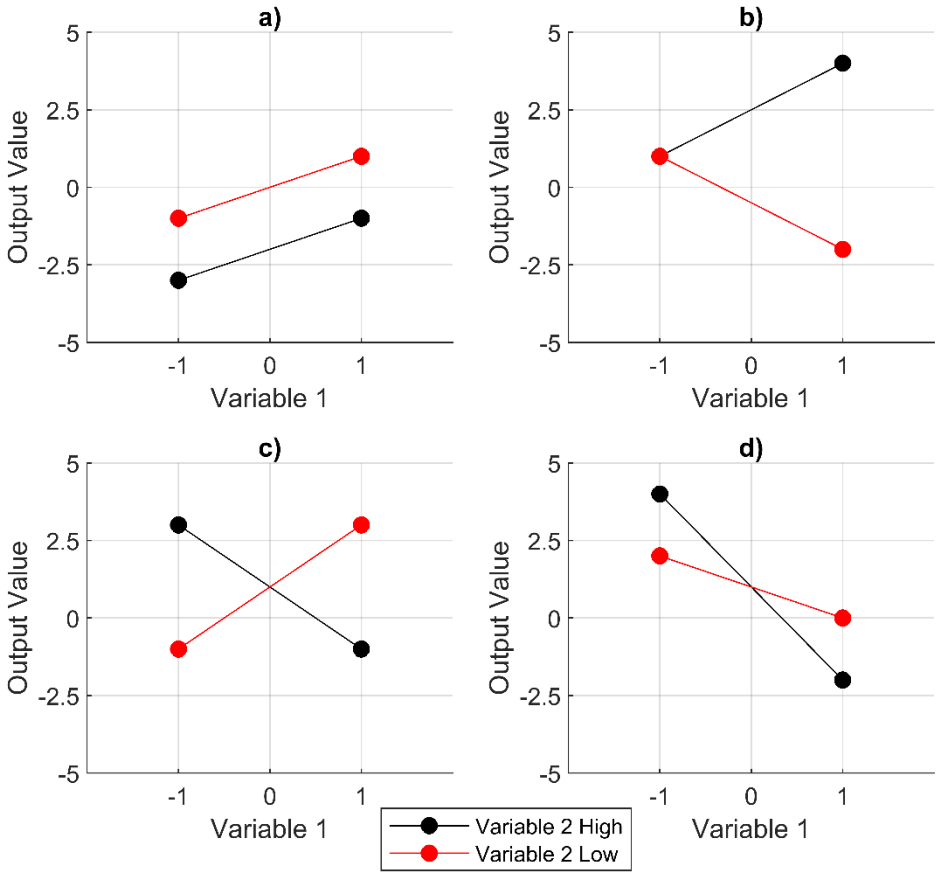

Figure 3.9.7 Examples of interaction plots for two variables.

Looking at the interactions in this way allows the nuances of the interactions to be better understood – for example variables may have shown inconsistent behaviour under specific scenarios that do not carry through to the rest of the test, such as shown in Figure 3.9.8. Without further inspection this type of behaviour can be disguised as a main effect.

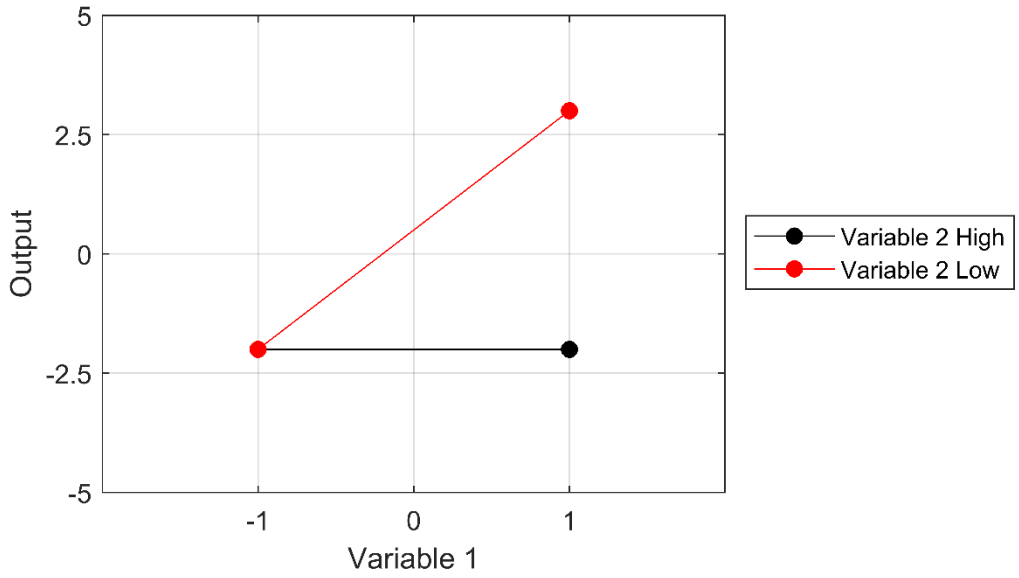

Figure 3.9.8 An example of an interaction where an effect was only measured with one specific combination of variables. This complexity is missed without inspecting interaction plots.

In exactly the same way as for the calculation of main effects, the interaction effects of factors can be calculated as the difference between the mean of results for tests where an interaction is coded as 1 and the mean of results for tests where an interaction is coded as -1 (see Table 3.9.4).

Three-factor interactions are highly complex, however these may also be investigated using a further variation on interaction plots. Two interaction plots can be made for the interaction between variables 1 and 2, one for the four tests where variable 3 is high, and one for those where variable 3 is low. If the two-factor interaction is the same in both cases then there is no 3-factor interaction. If the angle between the two-factor interaction lines is substantially different in each then a three-factor interaction is present. Again, the magnitude of a three-factor interaction can be calculated as the difference between the means of results from tests coded as 1 and -1.

Models may also be constructed from factorial experiment results to give a result for a given set of input conditions. Equation 3.9-1 shows the factorial effects model used here, where μ is the mean of the experimental outputs and *P*, *S* and *U* are the coded settings (as in Table 3.9.4) for Pressure, SRR and Entrainment respectively (NIST/SEMATECH 2013).

$$output = \mu + \beta_1 P + \beta_2 S + \beta_3 U + \beta_{12} PS + \beta_{13} PU + \beta_{23} SU + \beta_{123} PSU \quad \text{Equation 3.9-1}$$

The coefficients for each main and interaction effect denoted by β are obtained from the experimentally determined effects. As each variable is evaluated between coded settings -1 and 1, the magnitude of each coefficient is equal to the corresponding effect divided by 2 (the difference in coded units from the high to low setting).

3.10 Error and Repeatability

In conducting this experimental work, it is vital to maintain an appreciation of the repeatability of the experiment and the influence of error on the results. As previously stated, both profilometers used in this work had a measurement resolution of 16 nm or 0.016 μm. For some of the parameters investigated in this work, particularly in the case of running-in parameters, the change observed through running-in is on the order of tens of nanometers, meaning that error due to the resolution can have an influence on the result. Further still, some average effects were very close to or smaller than this value, and some caution must be allowed for in the use of these values.

To improve reliability, obtaining two-dimensional profiles from each disk at a number of offset locations across the contact width ensured that the result was not influenced excessively by a single outlying profile. For both the micropitting and running-in tests there is a risk that measuring at a single circumferential location (as mandated by time restrictions) does not account for different behaviours around the disk circumference. As the surface for the whole disk was produced on the same grinding wheel in a single-stage process, this risk is considered to be small.

The use of a well-practised process for grinding disks, and use of a test rig with parameters which are easily set, verified and calibrated means that the tests performed in this work are highly repeatable. Some variation in results would be expected in that grinding can only ever be performed to within a certain allowable bracket of roughness values, and pairs of disks selected at random may fall into different areas of this bracket – however with repeat testing similar results would be expected.

3.11 Summary

This chapter has detailed the equipment used in the experimental work conducted in this thesis, the techniques and analysis methods used to interpret the results, and the design of the experimental programme employed. The following Running-in Results and Micropitting Results chapters (Chapters 0 and 5 respectively) apply this work to a series of micropitting tests, which are also analysed in terms of their initial running-in behaviour

4 Full-Factorial Experimental Investigation of Running-in

4.1 Introduction

This chapter concerns the running-in behaviour observed in this programme of tests. Each test is first analysed individually. The influence of each variable on the running-in process is then investigated through analysis of the tests as a collective group.

Each fatigue test in the experimental programme began with an initial running-in process, which was deemed to be complete after six thousand fast disk cycles. The running-in phase was completed across two load stages consisting of three thousand fast disk cycles each.

The primary source for running-in analysis was the two-dimensional profiles taken between each stage as discussed in Section 3.1.7. The previously discussed relocation error (Section 3.1.8) has minimal influence on the result of running-in analysis as changes are much less localised than in the case of micropitting – hence two-dimensional profiles are preferred over replication methods as no intermediate surface is required.

All tests were conducted with a supplied oil temperature of 80°C and with surfaces of nominal Ra=0.4 μm. As roughness is difficult to control closely during manufacture, the surfaces used were between Ra values of 0.37 and 0.46 μm. Conditions for each test, alongside the initial Ra for each surface, are shown in Table 4.1.1.

Table 4.1.1 Test conditions for each test – note Ra values are a mean of 9 measured profiles prior to running.

Test	Max Pressure /GPa	SRR	Entrainment Velocity / ms^{-1}	Fast Disk Ra / μm	Slow Disk Ra / μm
Test 1	1.6	0.500	4.0	0.42	0.43
Test 2	1.6	0.500	2.0	0.39	0.40
Test 3	1.6	0.250	2.0	0.37	0.44
Test 4	1.2	0.500	2.0	0.41	0.41
Test 5	1.2	0.250	4.0	0.41	0.38
Centrepoint	1.4	0.375	3.0	0.46	0.41
Test 6	1.6	0.250	4.0	0.45	0.46
Test 7	1.2	0.250	2.0	0.45	0.46
Test 8	1.2	0.500	4.0	0.43	0.46

4.2 Test 1

A distinctive change in the surfaces of both Test 1 disks was apparent to the naked eye after the running-in stages, with the contact area clearly divided into a central region with a polished appearance and two edge regions with a dull appearance. This contrast can be seen in Figure 4.2.1, taken mid-way through the test but with visual appearance much the same as at six thousand fast disk cycles.

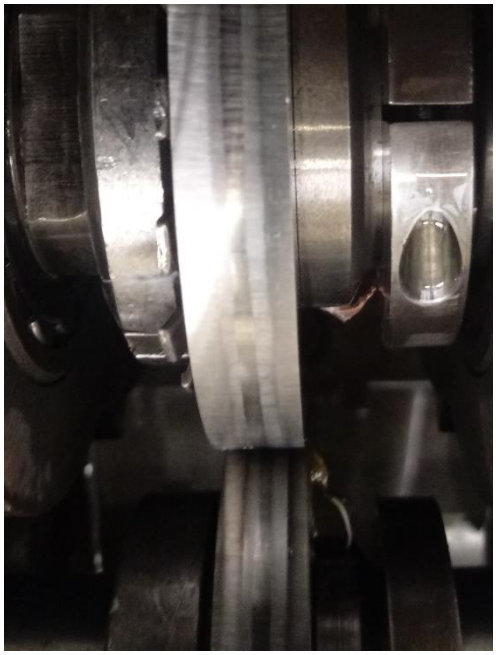

Figure 4.2.1 Photograph of the test disks showing the separate regions which developed during running-in.

Two-dimensional profilometry provides a much clearer view of the difference between these regions after the conclusion of the running-in stages. Figure 4.2.2 shows a series of profiles taken from each disk surface at the centreline and 1 mm removed from the centreline, which sits outside of the area that developed a polished appearance. For clearer comparison, the same asperity features are shown for each axial location. The profiles at the centreline of each disk both experienced an initial deformation up to three thousand fast disk cycles, however between three and six thousand fast disk cycles a significant second phase of height reduction occurred giving many of the asperities a table-top profile. For the profiles taken 1 mm from the centreline there was again an initial decrease in height up to three thousand cycles, however between three and six thousand cycles the surface either remained constant at that height, or a much smaller height reduction occurred.

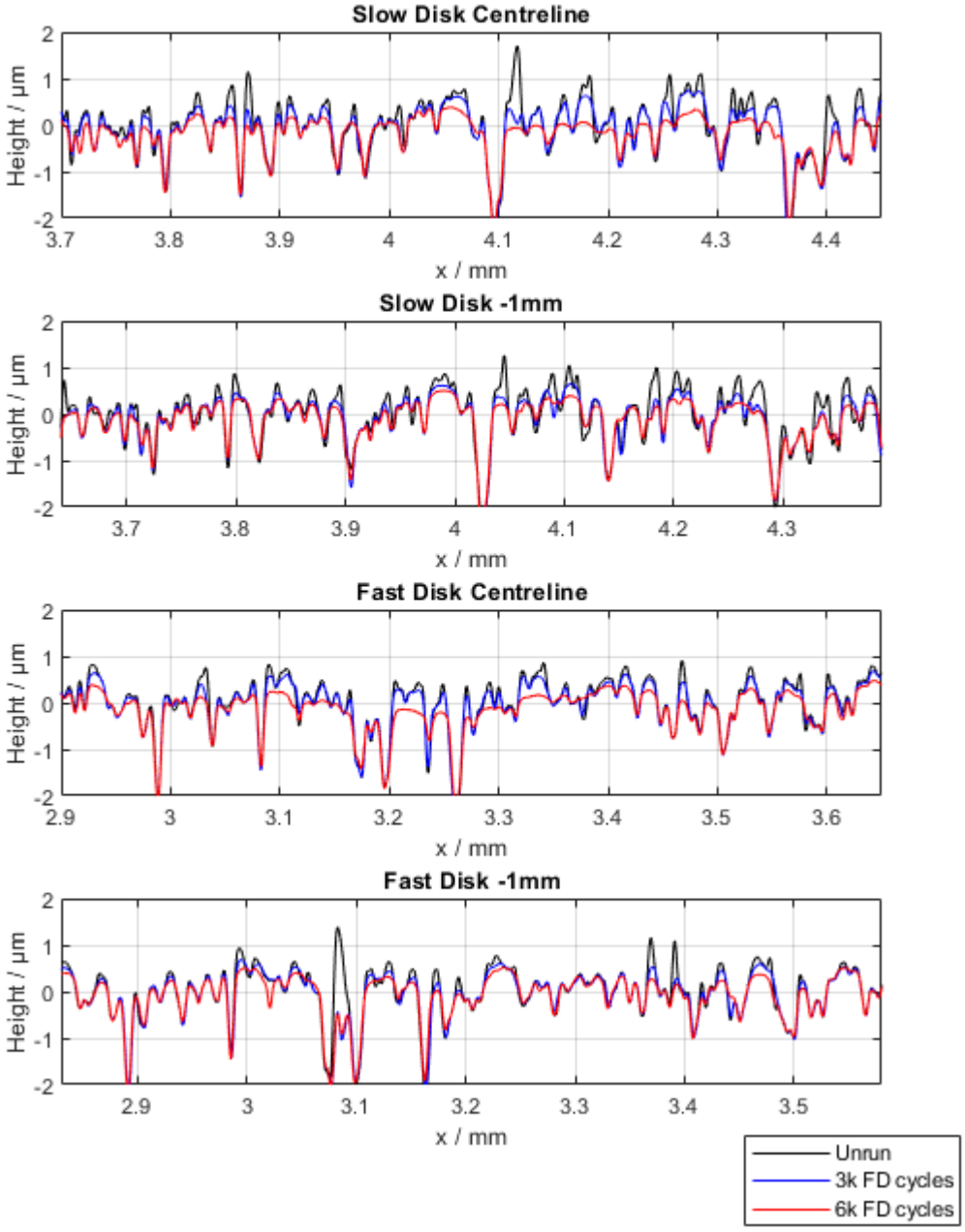

Figure 4.2.2 Test 1 profiles along matching surface features at the centreline and 1 mm from the centreline during running-in.

The change in radius of curvature of asperities was able to capture this difference in behaviour between the central band and the areas outside of it. It can be seen in Figure 4.2.3 that for profiles both inside and outside of the central band the initial increase in radius of curvature was very similar after the first load stage (i.e.

zero to three thousand cycles). Then during the second load stage the asperities in the central band became much more significantly flattened than those outside of this region. This disparity then remained until the final stages of the test. The same behaviour could also be observed on the slow disk.

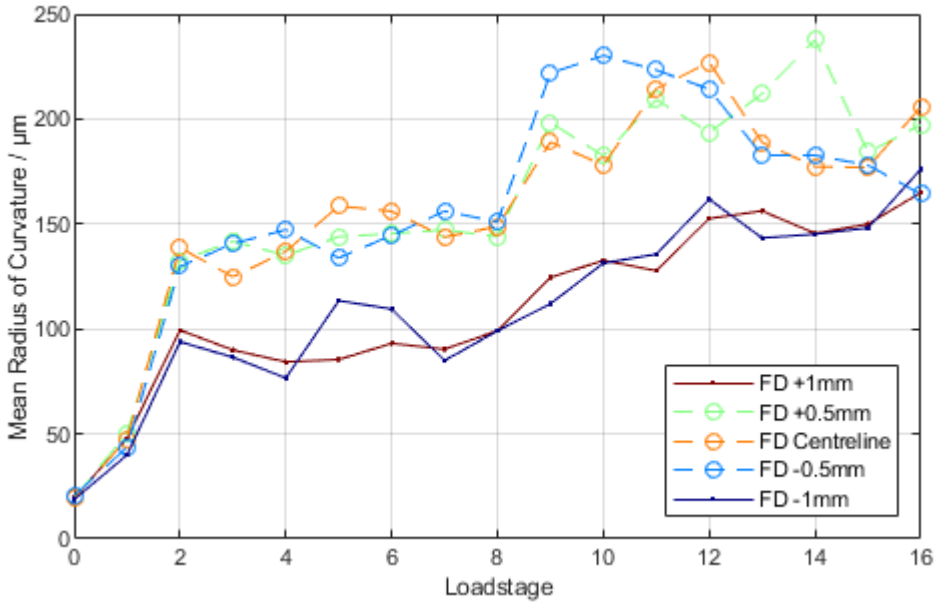

Figure 4.2.3 The mean radius of curvature of asperities on the fast disk, taken at a number of axial positions. Dashed lines show measurements taken within the central region while solid lines show measurements from outside of this area.

The aggressive levelling of the surface in the central region and the polished appearance within this region suggests that the change in that area of the surface is not due solely to plastic deformation but also to some form of wear. The profiles taken outside of this area will therefore be used as the basis for analysing the running-in behaviour, as this more aggressive wear is not representative of the majority of the tests in this programme.

Surface metrics evaluated for the disks during running-in are shown in Figure 4.2.4. Roughness parameters Rp, Rz, and Rt indicate the removal or significant

deformation of prominent asperity features – especially when the comparatively small change in Rv is considered. Also illustrative of this is the significant increase in negative skew shown by Rsk, indicating the Modification of points in the upper region of the height distribution – particularly for the slow surface. Both surfaces experienced similar magnitudes of decrease in roughness (Ra and Rq), mean height of profile elements (Rc), mean asperity height and mean asperity Cross-Sectional Area (CSA). The change in mean radius of curvature of asperity peaks was also very similar for both surfaces.

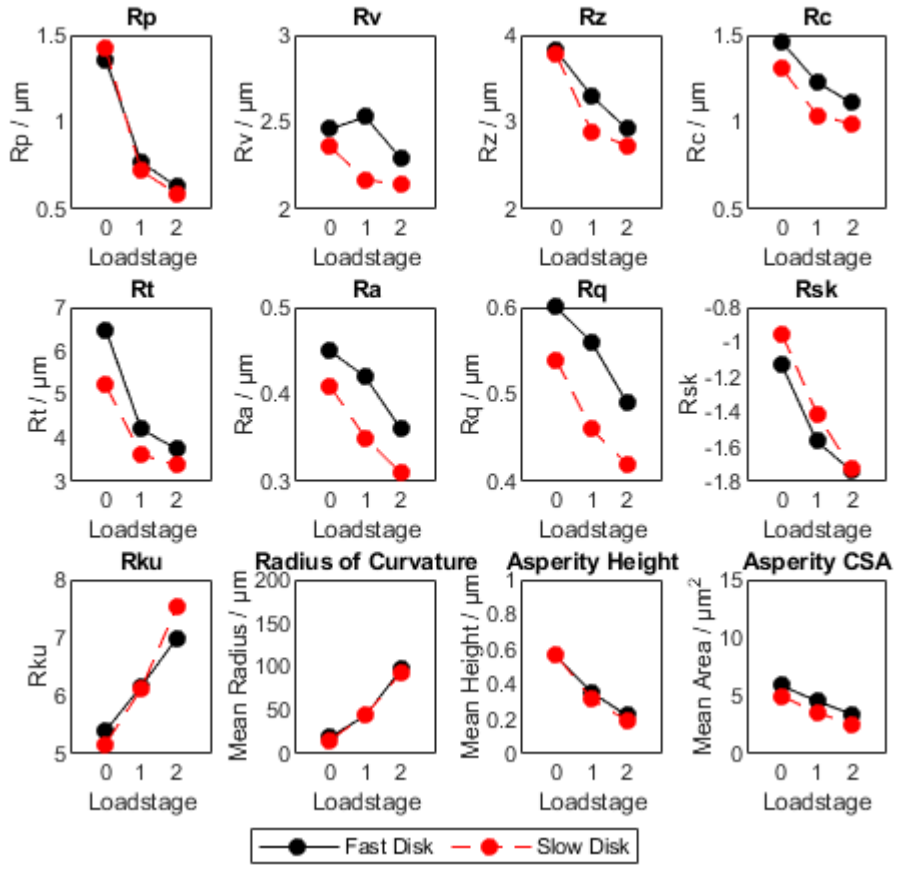

Figure 4.2.4 Surface metrics indicating changes in mean values of standard surface texture parameters, asperity radius of curvature, asperity height, and asperity Cross-Sectional Area for both the fast (black) and slow (red) surfaces at each load stage of running-in for Test 1.

4.3 Test 2

Similarly to Test 1, this test exhibited unusual running-in behaviour likely attributable to wear mechanisms. A key difference between these behaviours is that while Test 1 developed a continuous central band with a polished appearance, the disks in test 2 took on a patched appearance with islands of this polished finish appearing, as can be seen after load stage 2 (six thousand fast disk cycles) in Figure 4.3.1.

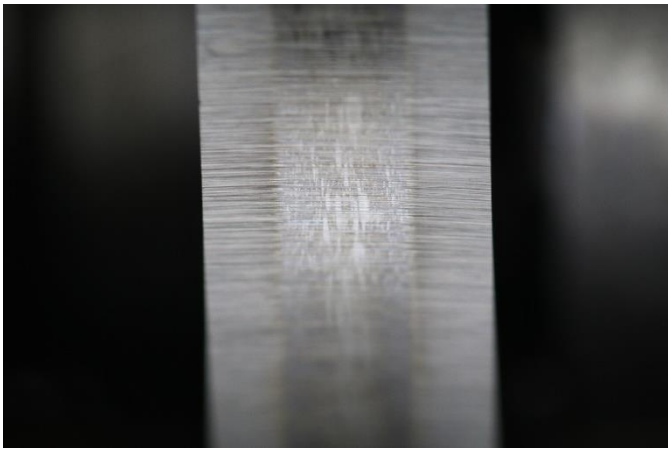

Figure 4.3.1 Photograph of a Test 2 test disk after running-in.

As can be seen in the photograph, these islands of shiny appearance were larger in the central region of the contact and were in all cases longer in the circumferential direction than the axial direction. Towards the edges of the contact area the islands became much thinner and reminiscent of score marks or micro-scuffs. This hints strongly at a possible source of the wear behaviour, and within the areas scanned on the fast and slow disk surfaces islands of wear could be seen with these marks at their centre. An example of these marks can be seen in Figure 4.3.2, which shows these marks inside a wear 'island'. The wear island is almost impossible to discern from this areal scan section and was more clearly seen in two-dimensional profiles at this stage. Later micropitting behaviour made these worn areas much clearer, as will be seen in Section 5.3.

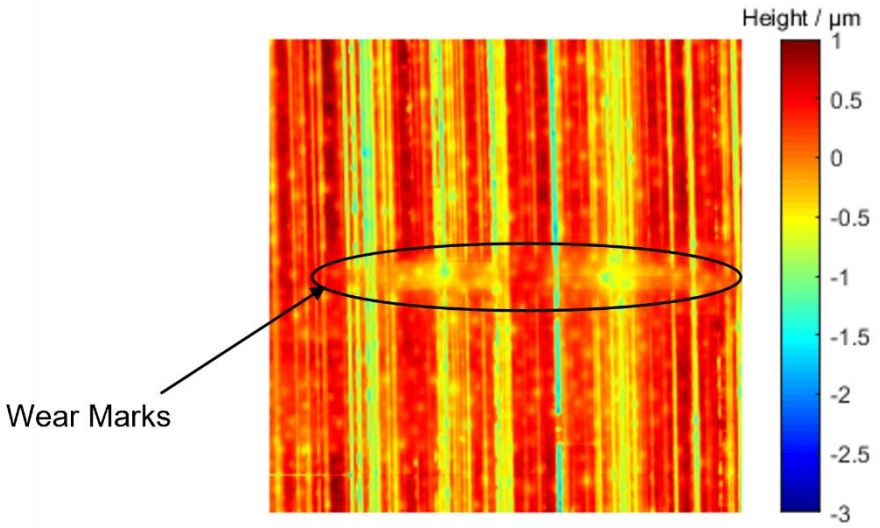

Figure 4.3.2 A 1 mm^2 section of an areal scan of the Test 2 fast disk replica surface after running-in that shows a wear mark which is located in the centre of a larger "island" of shiny appearance.

Examples of two-dimensional profile sections taken from inside and outside of these islands can be seen in Figure 4.3.3. The contrast between these regions is less stark than seen in the same analysis of Test 1, however there are still differences to be seen. Only the profile inside an island on the slow disk went through a second stage of height reduction (such as locations marked a), while the other profiles had reached their run-in heights after three thousand fast disk cycles. On the fast disk the difference is more subtle, but where double-peaked features were present inside the worn island they were reduced to single asperities with flattened tops (such as the locations indicated at b). Outside of these regions small remnants of these features remain.

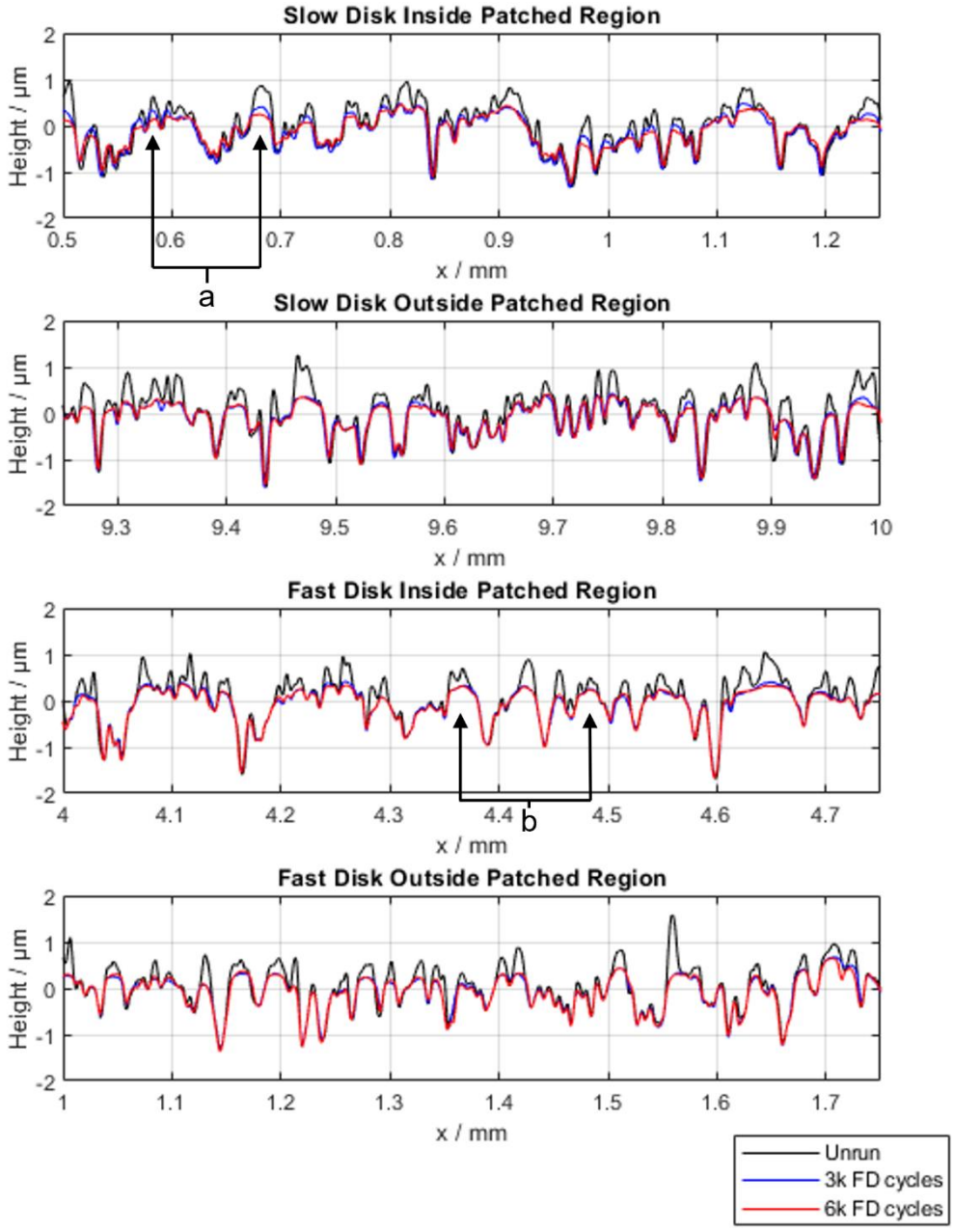

Figure 4.3.3 Two dimensional profile sections from both disks taken from inside and outside of the islands of wear.

Comparison of the profile sections which are inside these islands against those that are not shows that roughness after running-in was lower in these regions, and the mean radius of curvature of asperities was once again much larger. On this basis, running-in will again be assessed based on profile sections located outside of these worn areas.

Figure 4.3.4 shows the changing parameters for both the slow and fast disks in Test 2. These show that the process of running-in was largely complete at the conclusion of load stage 1 and the surface then remained stable through load stage 2. Running-in behaviour for each surface was largely identical for a number of parameters. Both surfaces experienced a 0.07 µm decrease in Ra to give the same final value, and experienced only 0.01 µm difference in decrease in Rq. The increase in mean radius of curvature was less for the slow disk, however for both disks was greater than that in Test 1. Mean asperity height and mean asperity CSA decreased by approximately the same amount on each surface, however the offset in values prior to testing was retained through running-in.

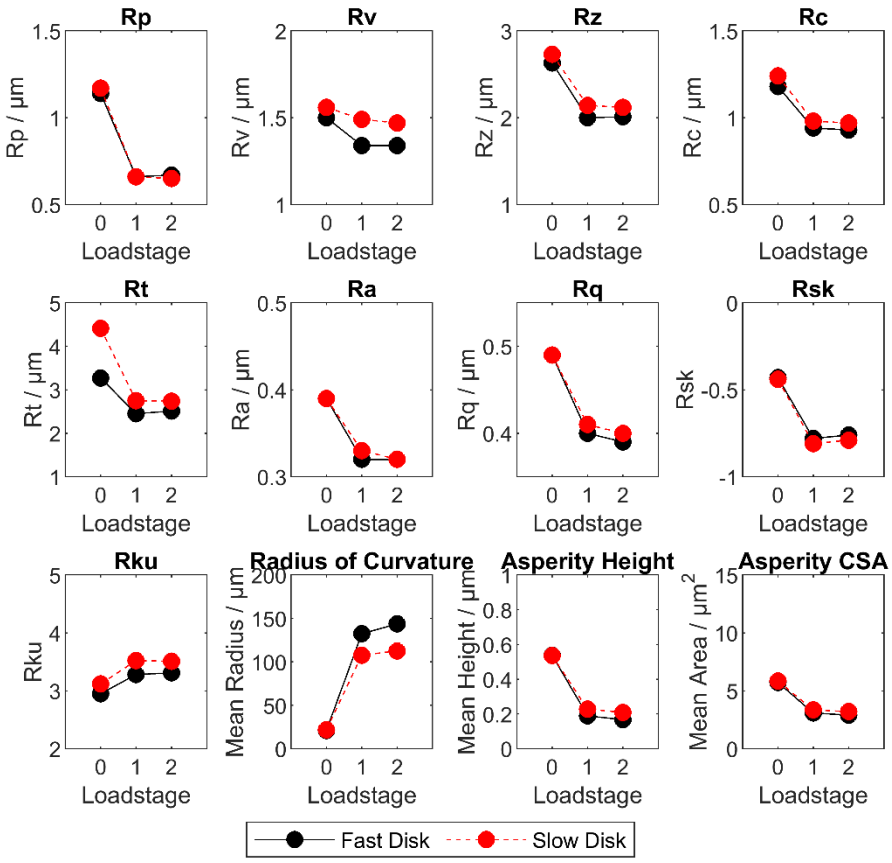

Figure 4.3.4 Surface metrics during running-in for the fast (black) and slow (red) surfaces in Test 2.

4.4 Test 3

The Test 3 disks ran in with no signs of the polished or worn areas of surface that were observed in earlier tests. The samples shown in Figure 4.4.1 show representative sections of centreline profiles from Test 3 during the running-in process. It is clearly visible from this image that both surfaces experienced substantial plastic deformation of asperity peaks in the first three thousand fast disk cycles, but had fully stabilised before the second running-in stage began.

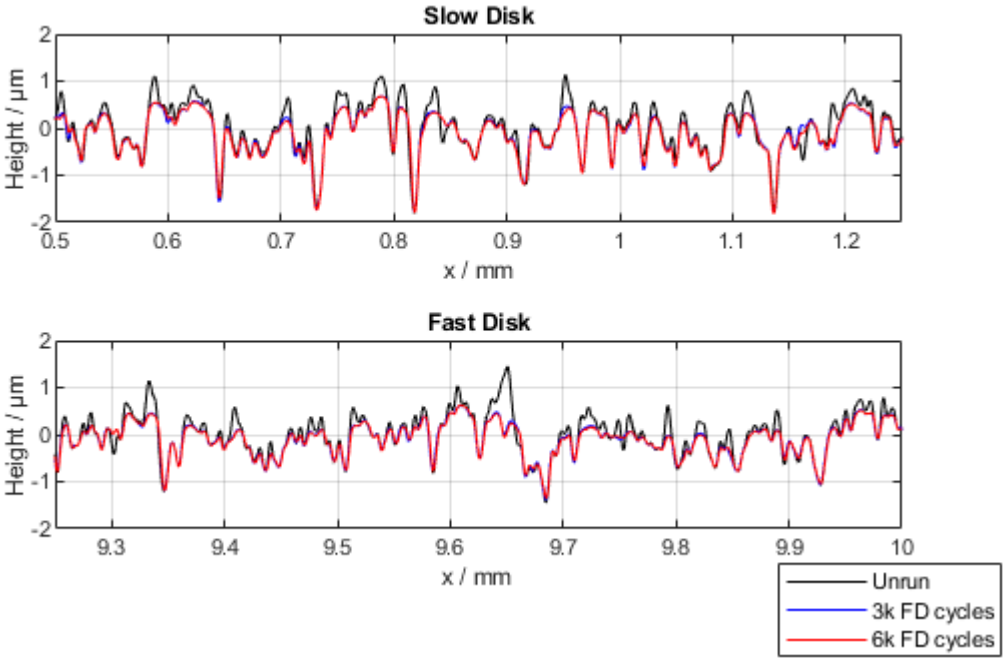

Figure 4.4.1 Two dimensional profile sections taken from the centrelines of the Test 3 disks during running-in.

As would be expected, the mean radius of curvature of asperity peaks increased through running-in. Interestingly, the magnitude of this change varied with axial position in this test, as can be seen in Figure 4.4.2. This shows that for both disks the mean radius of curvature of asperities increased significantly – in most axial locations this increase occurred largely during the first load stage followed by a minor increase during load stage 2. The increase in radius of curvature was most

significant at the measuring locations $\frac{6}{9}b$ from the contact centre, with the outermost measuring locations ($\frac{1}{9}b$ from the contact edge) generally exhibiting substantially less of an increase. On the slow disk the mean radius of curvature followed a u-shaped profile with the minimum value occurring at the centreline. The fast disk followed this profile on only one side of the contact, but also decreases to its minimum value at the centreline – albeit a minimum value that was significantly higher than that of the slow disk.

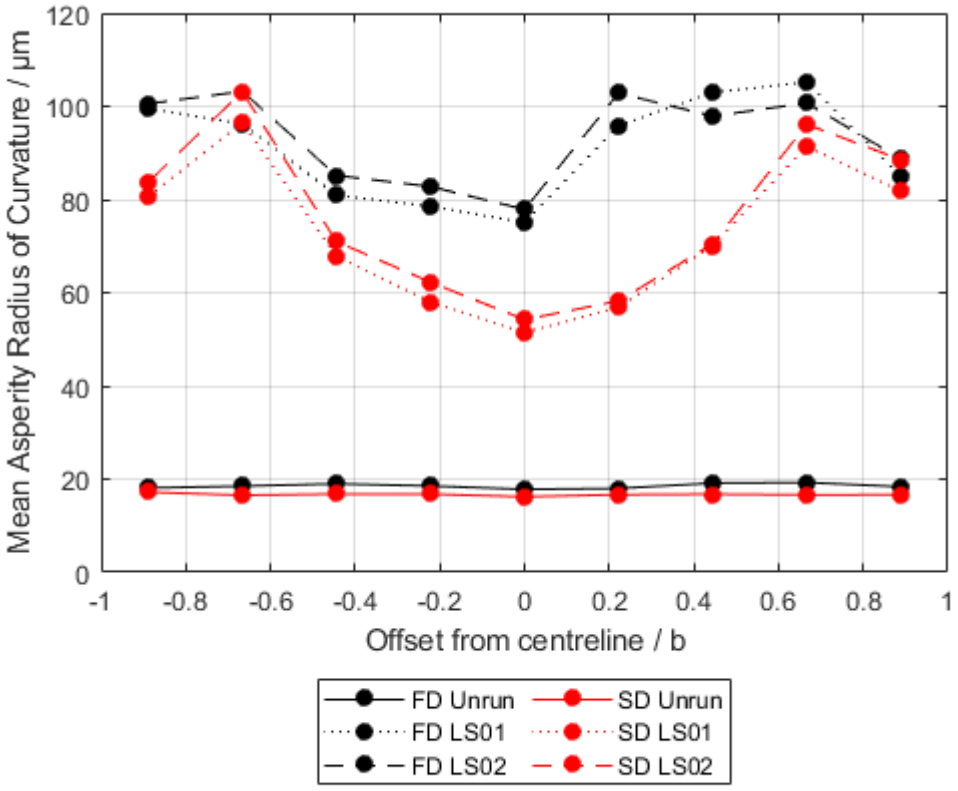

Figure 4.4.2 Mean radius of curvature of asperities at each measuring location on the fast and slow disks during Test 3 running-in.

The surface parameters assessed for Test 3 are shown below (Figure 4.4.3). Again, the parameters for each surface changed in largely the same way through the running-in process. While it can be seen that the initial Ra value of the slow surface

was on the upper bound of the acceptable level, the general pattern across the spectrum of metrics assessed was that the slow and fast surfaces experienced approximately equal magnitudes of change, retaining the same offset between the values as was present prior to testing. The shape of the change in the mean radius of curvature metric matches that seen in Test 2, and again the slow surface experienced a smaller increase in radius of curvature than the fast – although the magnitude of increase was much less than that seen in Test 2.

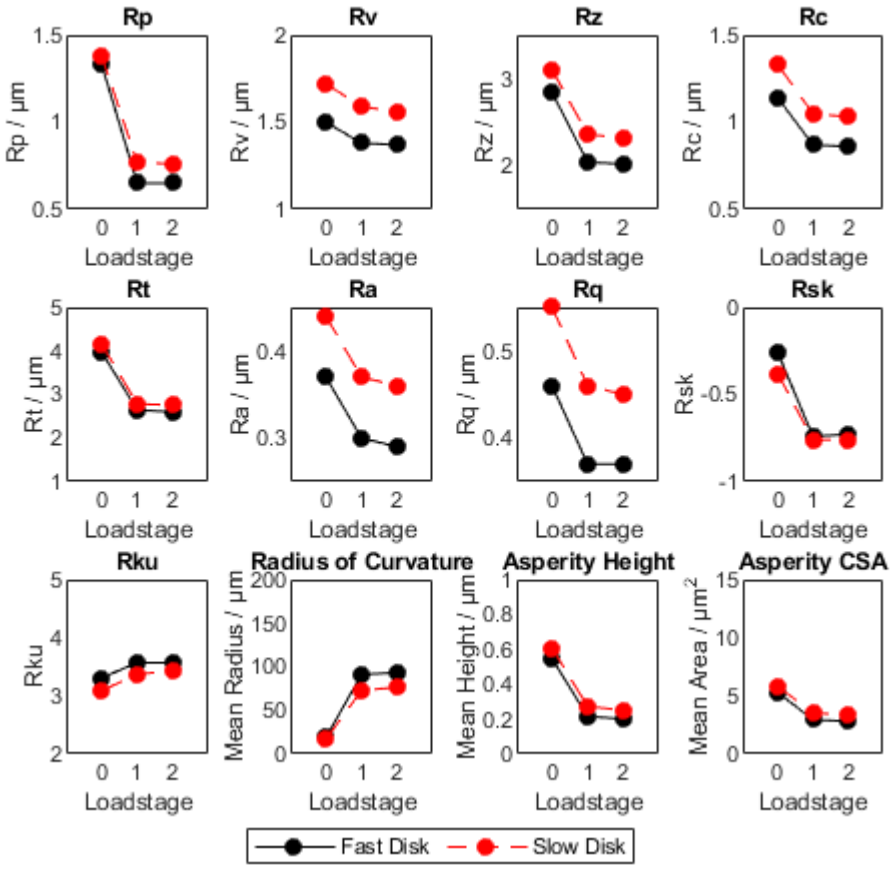

Figure 4.4.3 Surface metrics for the fast (black) and slow (red) disks of Test 3 during running-in.

4.5 Test 4

As in the previous test there were no significant visual observations for the running-in of the disks in Test 4, with the naked eye only able to identify the establishment

of a running track in the contact area of each disk. Figure 4.5.1 provides a representative illustration of the changing appearance of the centreline profiles from each disk.

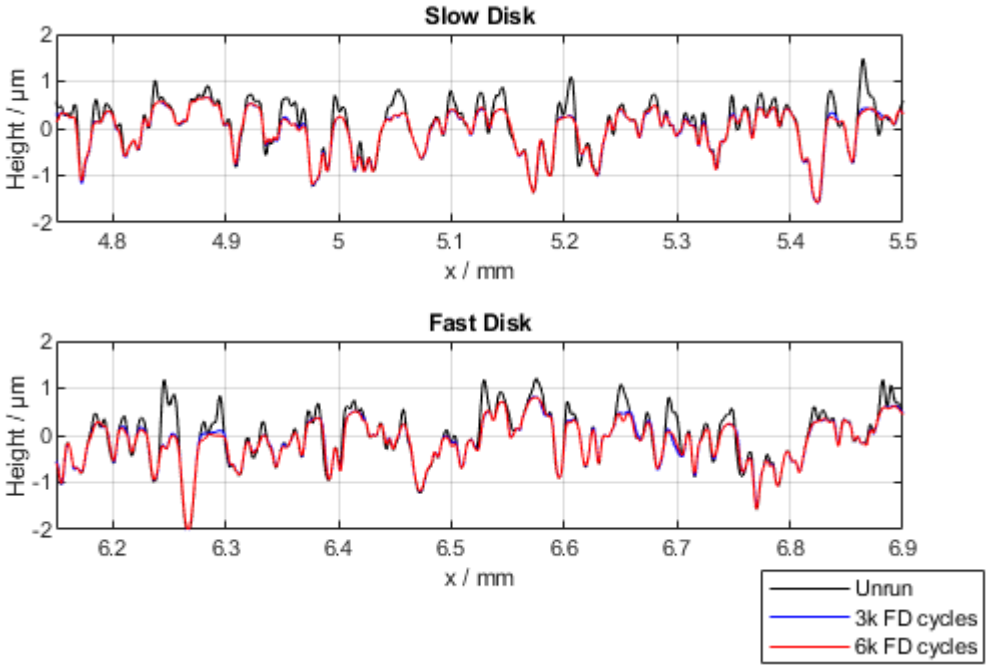

Figure 4.5.1 Representative profile sections from the centrelines of each disk in Test 4.

Consideration of the metrics extracted from the two-dimensional profiles indicated some element of non-uniform running-in behaviour for the slow surface. As can be seen in Figure 4.5.2 there was a significant increase in mean radius of curvature at each position on the fast disk, and while one side of the disk exhibited slightly more variation in values none deviated drastically from the mean. The slow surface however underwent an increase of only 26 µm on one edge, then followed a general upward trend across the disk width to a maximum increase of 94 µm.

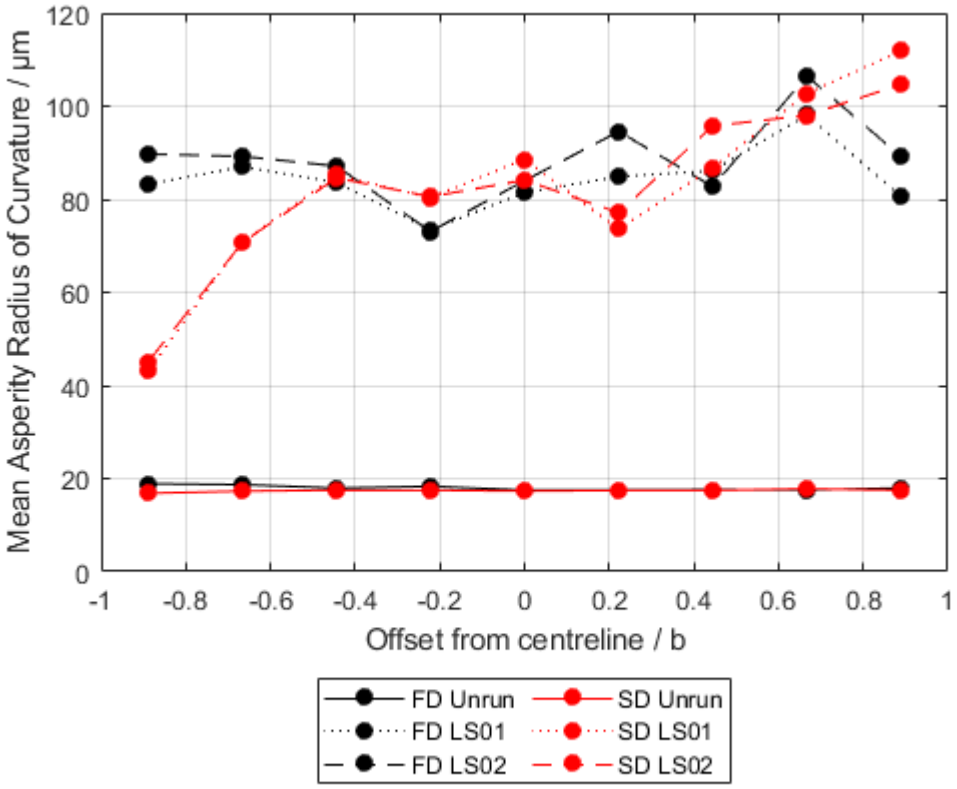

Figure 4.5.2 Mean radius of curvature of asperities at each measured axial location on the fast disk and slow disk during running-in.

Consideration of other parameters such as Ra, Rq and Rp (as shown in Figure 4.5.3) indicated that while the most profiles on the slow disk experienced a similar magnitude of change through running-in, the profile at $-\frac{8}{9}b$ was less influenced by the running-in process. This profile was measured close to the expected edge of the contact, and it is possible that a small misalignment in the contact (e.g. due to rig assembly or an off-centre crown) or in the measuring positions (which are located relative to the disk edge) could place this profile in the extreme edge region of the contact. This could possibly account for the difference in surface behaviour at this location. As this profile was not representative of the surface behaviour, this has been excluded from the remaining analysis of the contact.

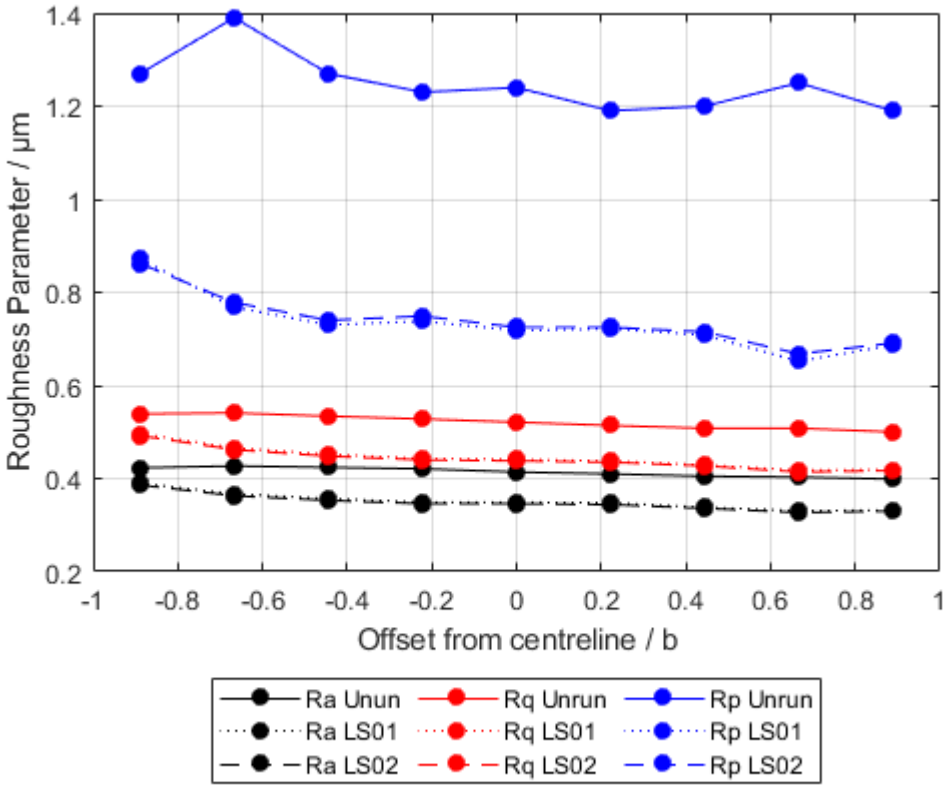

Figure 4.5.3 Values of Ra, Rq, and Rp for each position on the slow disk during the running-in process, showing the smaller magnitude of change for the profile at $-\frac{8}{9}b$

Figure 4.5.4 shows the assessed surface metrics for Test 4. The two disks used in this test began with identical Ra and Rq values - however the decrease in Rq was slightly smaller for the slow disk than the fast. Additionally, while the final Ra value for both surfaces was the same, the fast disk value had stabilised by the end of the first load stage while the slow disk value had not. Additionally, the value of Rp for the fast surface underwent a marginally larger decrease than did the slow disk. All remaining metrics exhibited nearly identical behaviour on both surfaces, with most metrics having stabilised by the end of the first load stage. Interestingly, both fast

and slow surfaces in this test show a maximal decrease in skewness at the end of the first load stage followed by a small increase during the second load stage.

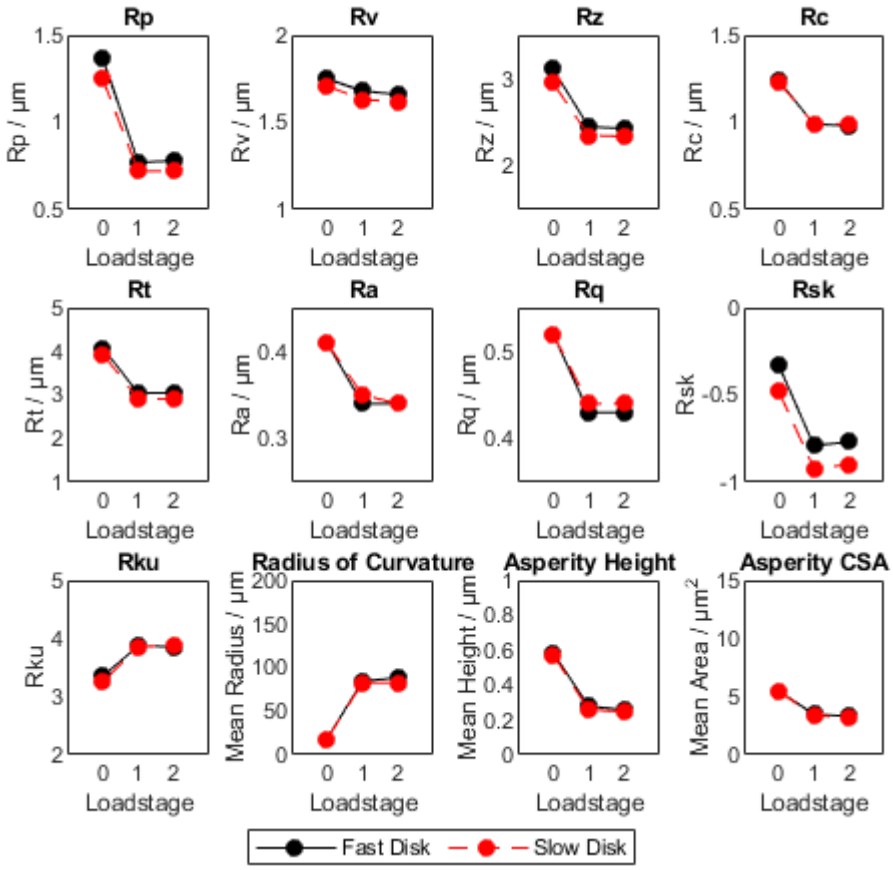

Figure 4.5.4 Surface parameters during running-in for the fast (black) and slow (red) surfaces in Test 4.

4.6 Test 5

By visual inspection the surfaces used in Test 5 developed a uniform appearance throughout the contact area. The representative centreline profile sections shown in Figure 4.6.1 illustrate the changes observed in the surface through the running-in process. As is very clear from these profiles, the extent of deformation seen in this test was significantly reduced in comparison to the previous tests.

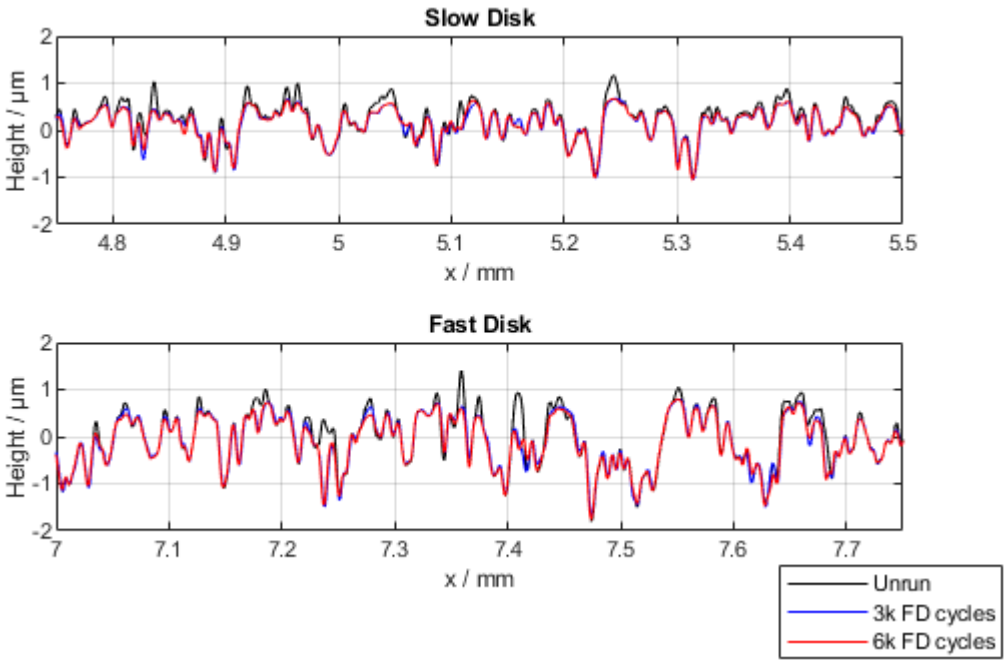

Figure 4.6.1 Representative centreline profile sections taken from the slow and fast disks of Test 5 during running-in.

It can clearly be seen in the figure above that even where plastic deformation can be observed in an asperity, more of the peak feature is preserved than in previous tests. This leads inevitably to a much smaller increase in radius of curvature of asperity peaks, while more aggressive deformation or wear results in rounded or flattened tops. In line with this observation, the mean radius of asperity curvature at a given axial location only increased by between 40 and 70 µm on both disks – the average increase being higher on the slow surface (Figure 4.6.2).

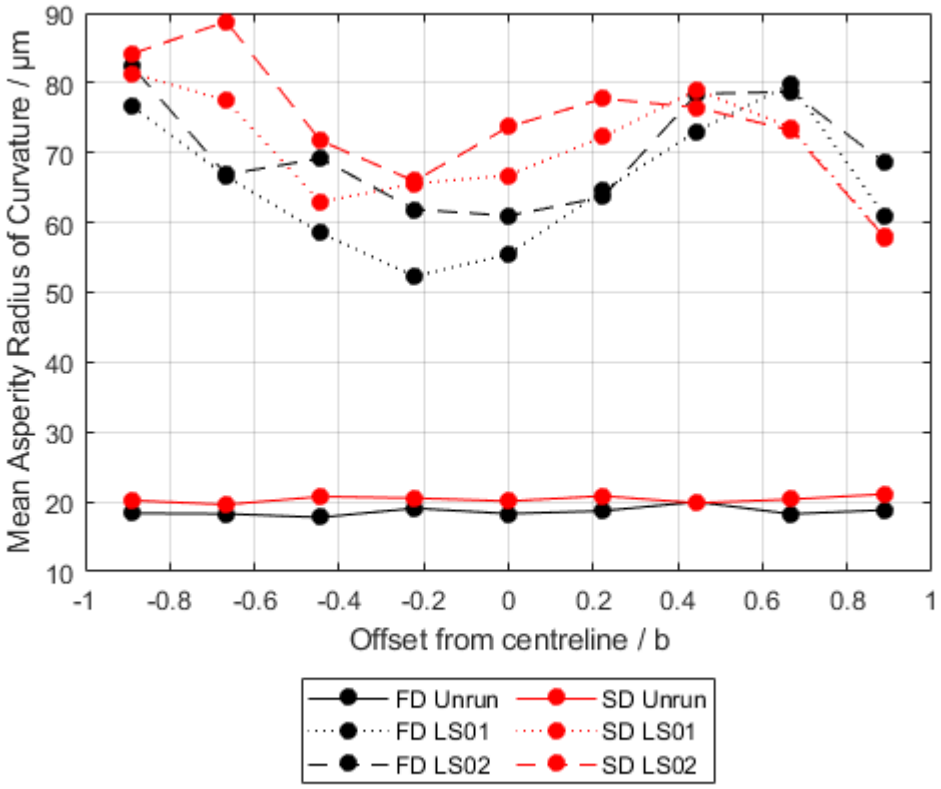

Figure 4.6.2 Mean radius of curvature of asperities by axial location on each disk during running-in.

The distinctive shapes of the radius of curvature profiles developed during running-in Figure 4.6.2 (above) are closely matched by both surfaces, which was not the case for the changes seen in previous tests. This is presumed to be the result of a complex interaction between roughness features and film thickness, as no parameters on either surface feature any similar profiles across the disk width that might be transferred to the radius of curvature.

Surface parameters for Test 5 during running-in are shown in Figure 4.6.3. This figure provides clear evidence to show that the surfaces had largely stabilised prior to the conclusion of the first load stage. It can be seen from many of these parameters that the slow surface underwent a more significant change during the

running-in process than the fast disk. The Rp parameter shows a greater decrease in the height of the highest peaks on the slow disk, and this carries through into Rz, Rc and Rt which are all influenced by peak heights. Additionally, the movement towards more negative skewness was significantly larger for the slow surface than the fast – showing the more drastic reduction in points on the right of the height distribution.

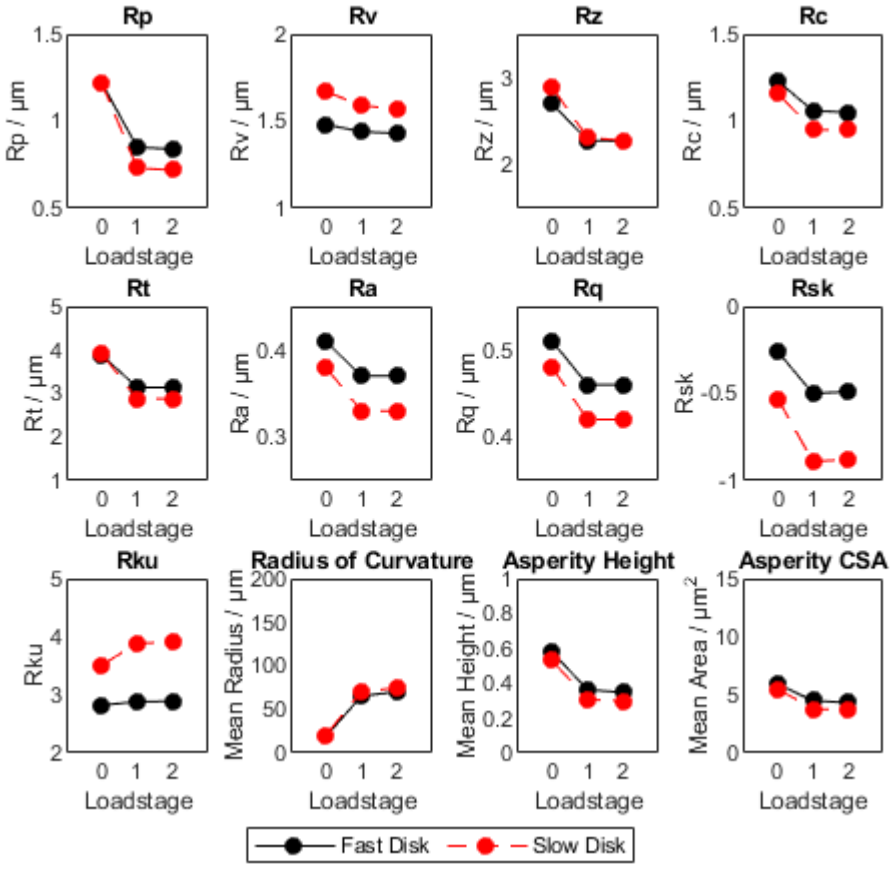

Figure 4.6.3 Surface parameters during running-in for Test 5 on the fast (black) and slow (red) surfaces.

4.7 Centrepoint Test

The contact area of the disks developed a uniform appearance after running-in for this test. The contact was not perfectly centred in this test, likely due to an off-centre crown on the disks. As a result, the intended $-\frac{8}{9}b$ measuring location fell

outside the contact and an additional measuring position was added from load stage 1 onwards at what would (if centred) be $+\frac{11}{9}b$. The unrun surface data for the $-\frac{8}{9}b$ location was representative of the rest of the surface and thus used in the averaged unrun parameters but not for any analysis from load stage 1 onwards. The profiles obtained at $+\frac{11}{9}b$ were valid for all data from load stage 1 onwards and used within the average parameters for the run in surface. Neither of these locations are used in the analyses across width below. The centreline of the contact was approximately located at the original $+\frac{2}{9}b$ location, and henceforth all locations referenced in this test will be given using that as the centreline location, 0.

The profiles shown in Figure 4.7.1, taken at the centrelines of each disk and $\frac{4}{9}b$ away from the centreline show the running-in behaviour on the same asperity features at different axial locations. The magnitude of deformation experienced at both locations is clearly very similar for both disks.

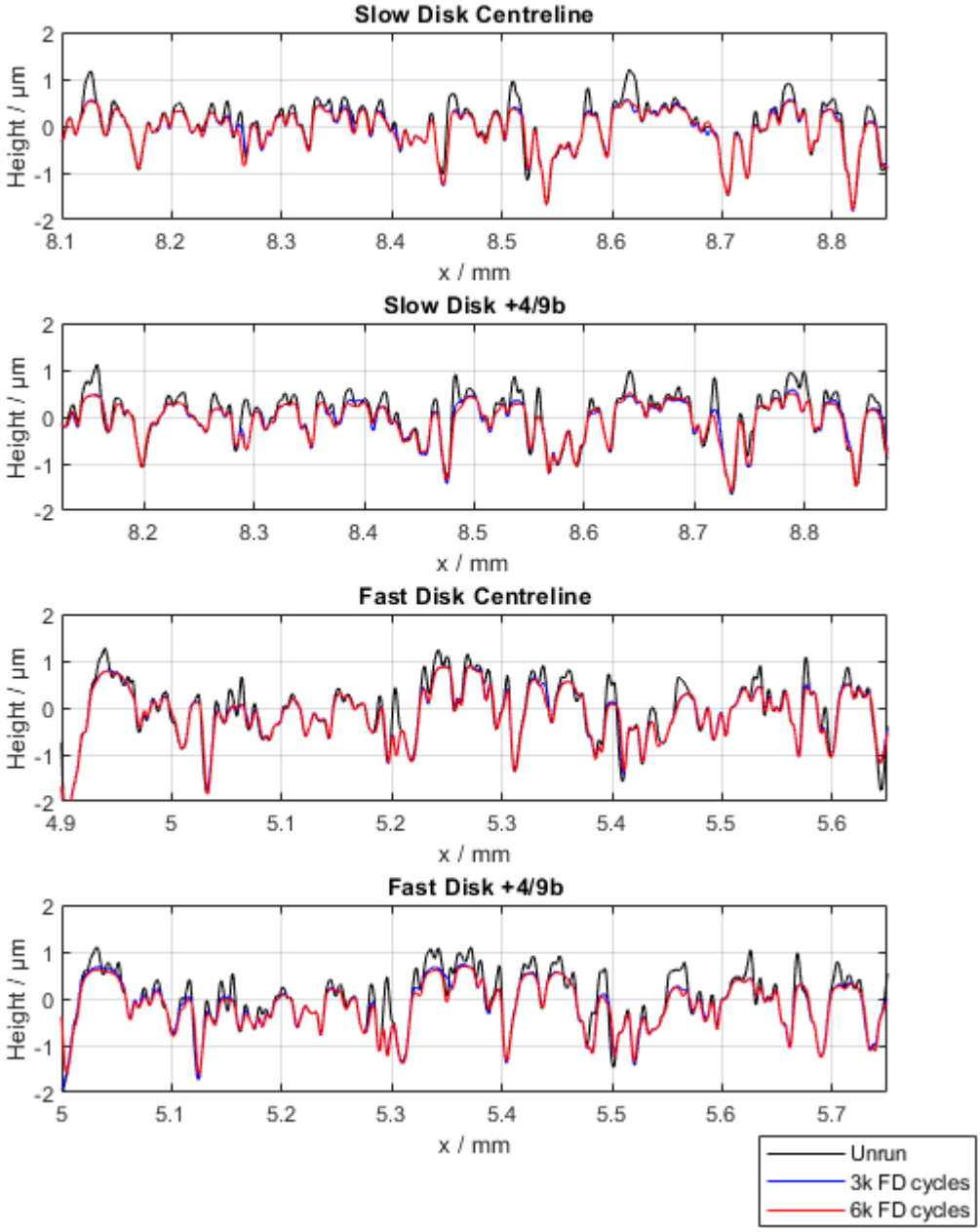

Figure 4.7.1 Representative sections from profiles taken at each stage of the running-in process at the centreline and $+\frac{4}{9}b$ *from the centreline on each disk.*

Most surface parameters considered across the contact width are largely unremarkable, either showing a largely constant value across the disk or an offset of the form found for the unrun surface. Two exceptions can be seen to this: Firstly, the mean radius of curvature of asperities was much smaller in the centre of the

contact for the fast disk, while the slow disk did not exhibit this form and showed a larger radius of curvature than the fast disk at all but one location. This can be seen in Figure 4.7.2.

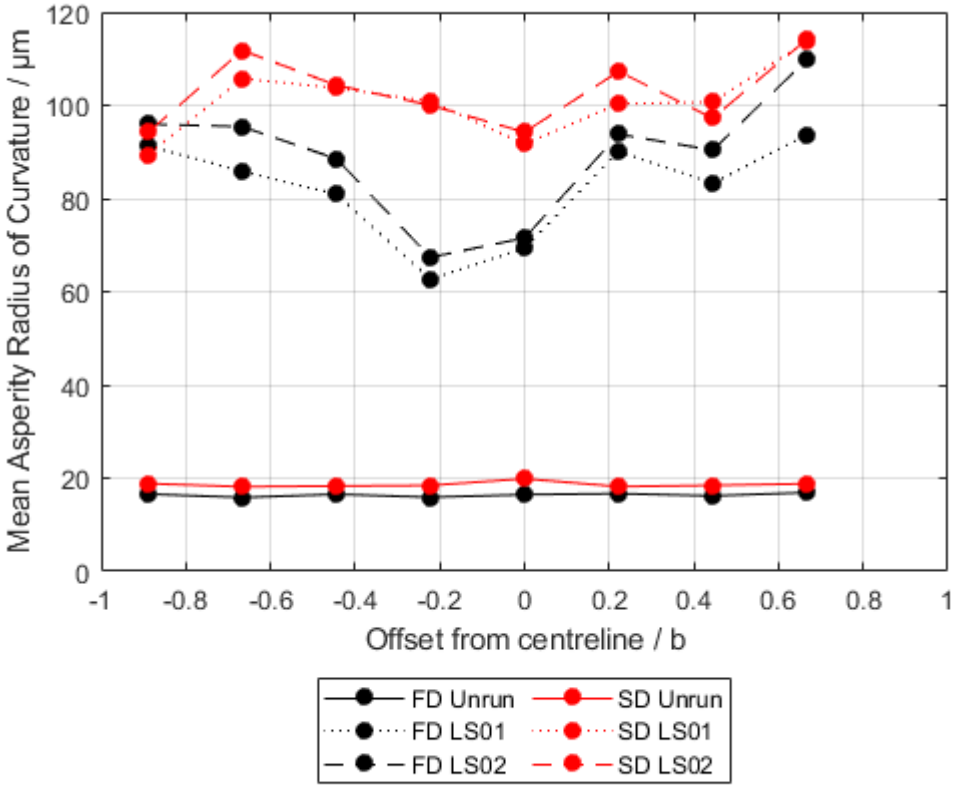

Figure 4.7.2 Mean radius of curvature across the contact width for the Centrepoint test.

The second exception is the skewness, which on both disks developed a dip at the measuring position $-\frac{6}{9}b$ from the centreline when no dip was present on either surface prior to testing. This suggests a common factor at that location causing removal of more material on both disks.

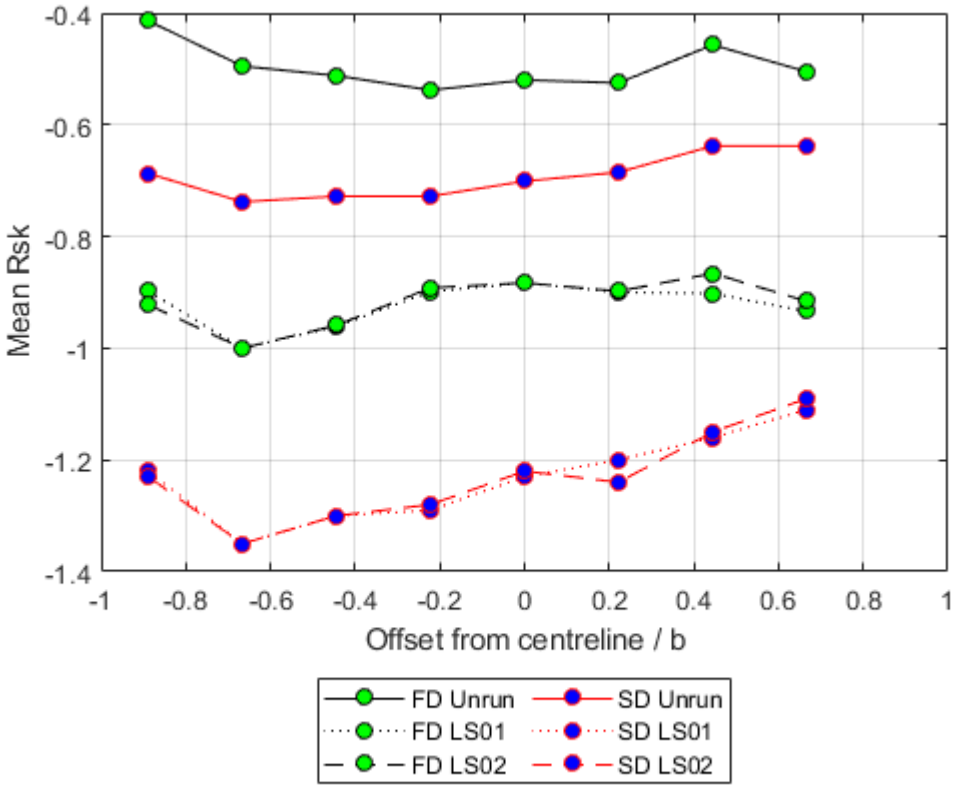

Figure 4.7.3 Variation in Skewness (Rsk) across the contact width through running-in during the Centrepoint test. A dip is developed at the second measuring position from the left edge of the contact ($-\frac{6}{9}b$) on each disk.

The surface parameters evaluated for the Centrepoint test can be seen in Figure 4.7.4. The measures influenced by peak values (Rp, Rz, Rt, and Rc) all show significant decreases for the fast disk during load stage 1, particularly Rp and Rt. For both Ra and Rq each surface decreased by the same magnitude, maintaining the same offset as was present in the unrun surfaces. Through the course of running-in the slow surface distribution developed a larger magnitude change in skewness, and more than 3 times larger increase in kurtosis than the opposing surface.

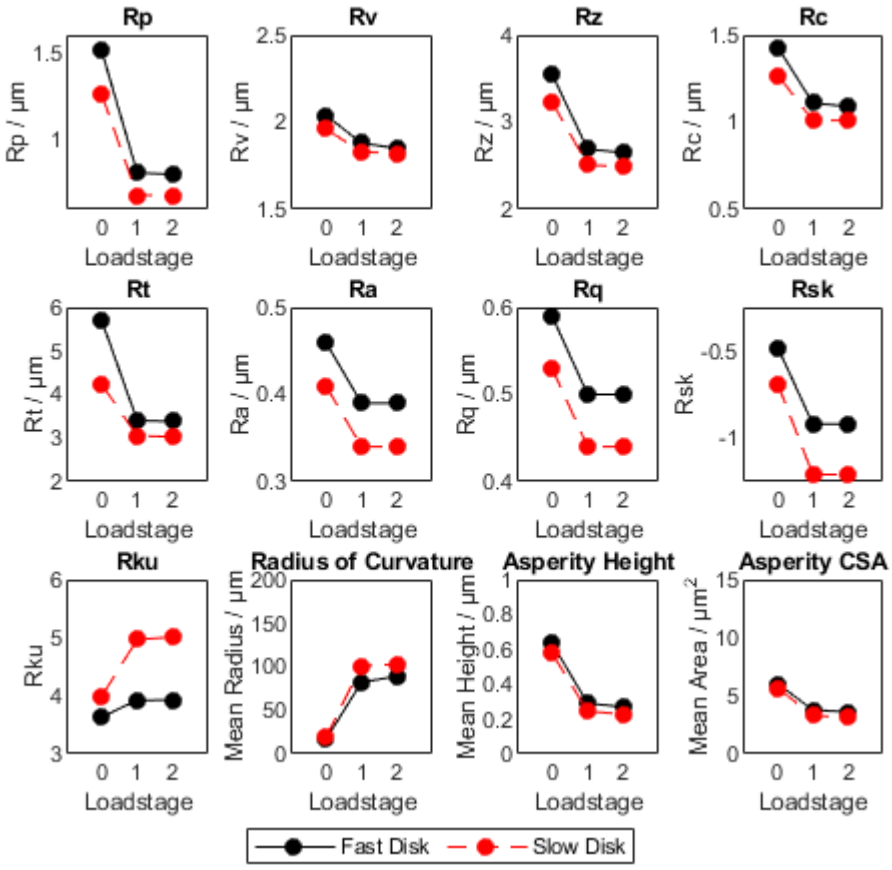

Figure 4.7.4 Surface parameters assessed on the fast (black) and slow (red) disks through running-in for the Centrepoint test.

4.8 Test 6

As with the centrepoint test the contact in this test was not perfectly centred, however as in that test an additional measuring position at $+\frac{11}{9}b$ from the centre of the disk was able to capture the full extent of the contact from the first load stage onwards.

Considering the variation of roughness parameters across the contact area, for both disks the profiles of roughness parameter variation across the contact width were maintained from the unrun through to run-in surface, albeit offset in value. This was the case for Ra, Rq, Rc, Rku and Rsk on both disks, and Rp on the fast disk.

For the remaining parameters on the fast disk, a dip in the profile on the negative side of the centreline was found, while on the opposite side of the centreline the peak values were shifted towards the contact edge. On the slow disk, values for Rp, Rz and Rt became essentially constant across the width of the contact, excepting a slight increase from $-\frac{6}{9}b$ to the contact edge. This suggests a largely uniform peak height after running-in on the slow disk. Both of these observations were in addition to larger offsets induced by running-in. Example plots of Ra and Rz below illustrate these behaviours (Figure 4.8.1).

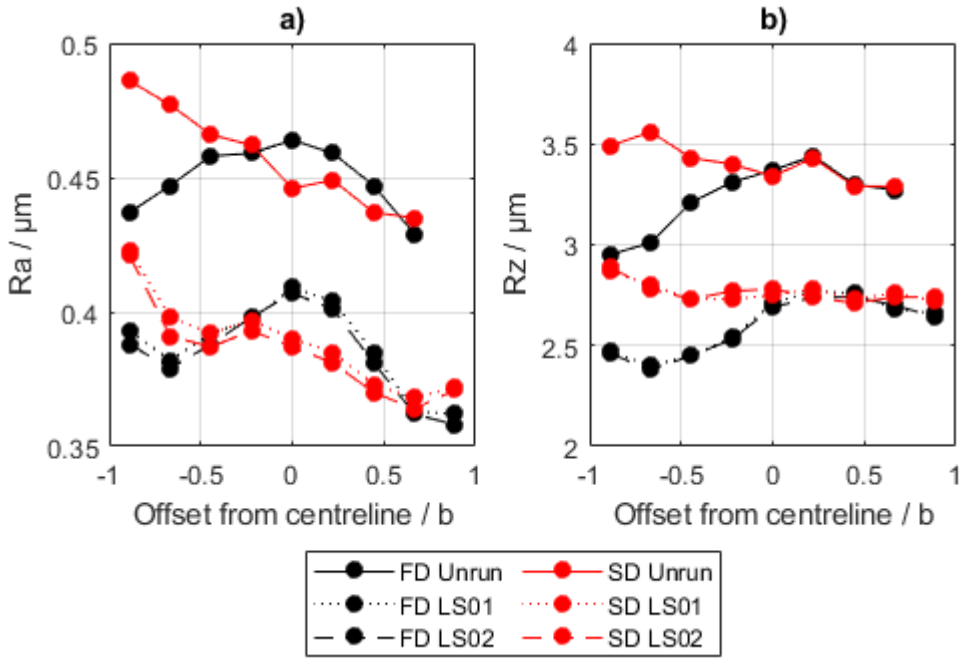

Figure 4.8.1 Variation of a) Ra and b) Rz across the width of the contact through running-in for both the fast and slow disks.

The changes in radius of curvature observed through running-in of Test 6 were similar to that seen previously in Test 3, which was conducted with the same contact pressure and SRR but a lower entrainment velocity. As with that test the radius of curvature (Figure 4.8.2) increased across the entire width of the contact, but notably less so in the contact centre. In the current test the fast disk and slow

disk were both limited to mean radii of curvature in the contact centre of approximately 60 µm, indicating that the fast disk centreline was more effectively protected from deformation and wear in this test than in Test 3.

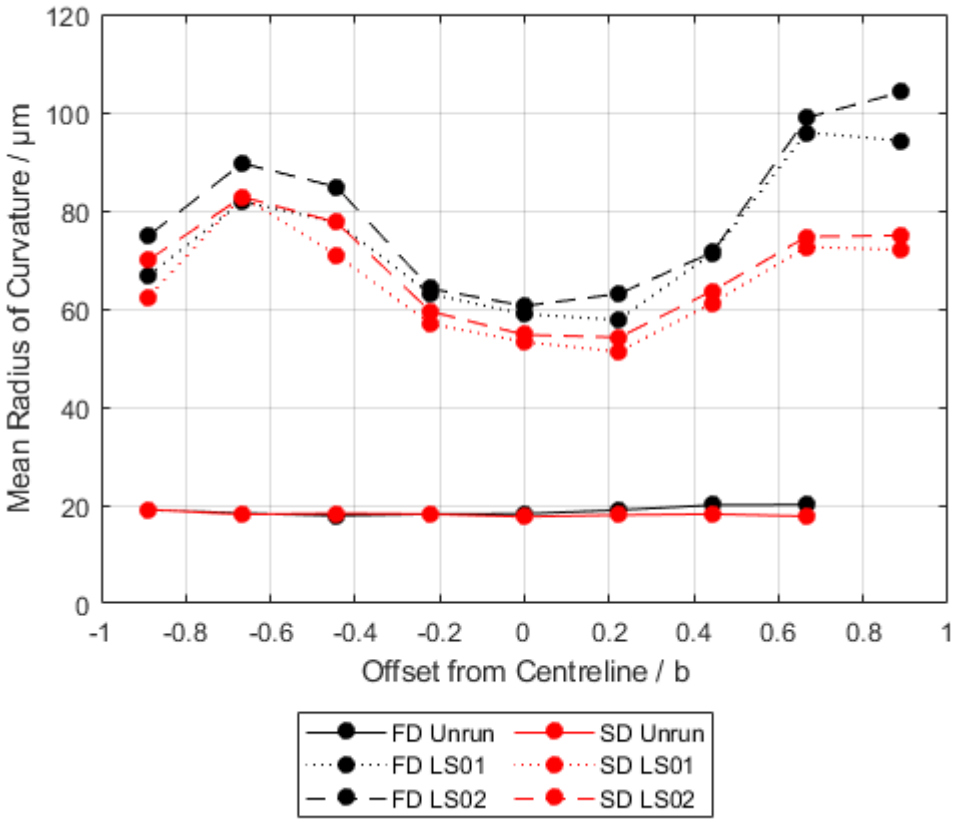

Figure 4.8.2 Variation in Radius of Curvature across the contact width in Test 6

Figure 4.8.3 shows the evolution of roughness metrics through the running-in process of Test 6. Roughness peaks were effectively reduced on both disks with the Rp parameter decreasing by 0.53 and 0.54 on the fast and slow surfaces respectively. Additionally, Rv showed a slight decrease on both surfaces and the compound effect of this can be seen in Rz and Rt. As in previous tests, the removal of high points from the surfaces resulted in an increase in negative skewness shown by Rsk. This decrease was larger on the slow surface than on the fast. This was accompanied by an increase in kurtosis for both disks, again with a larger magnitude

change for the slow surface than the fast. Considering the roughness parameter Ra, the slow surface had stabilised by the conclusion of load stage 1, while the fast surface decreased slightly further during load stage 2. This was not reflected in the values for Rq.

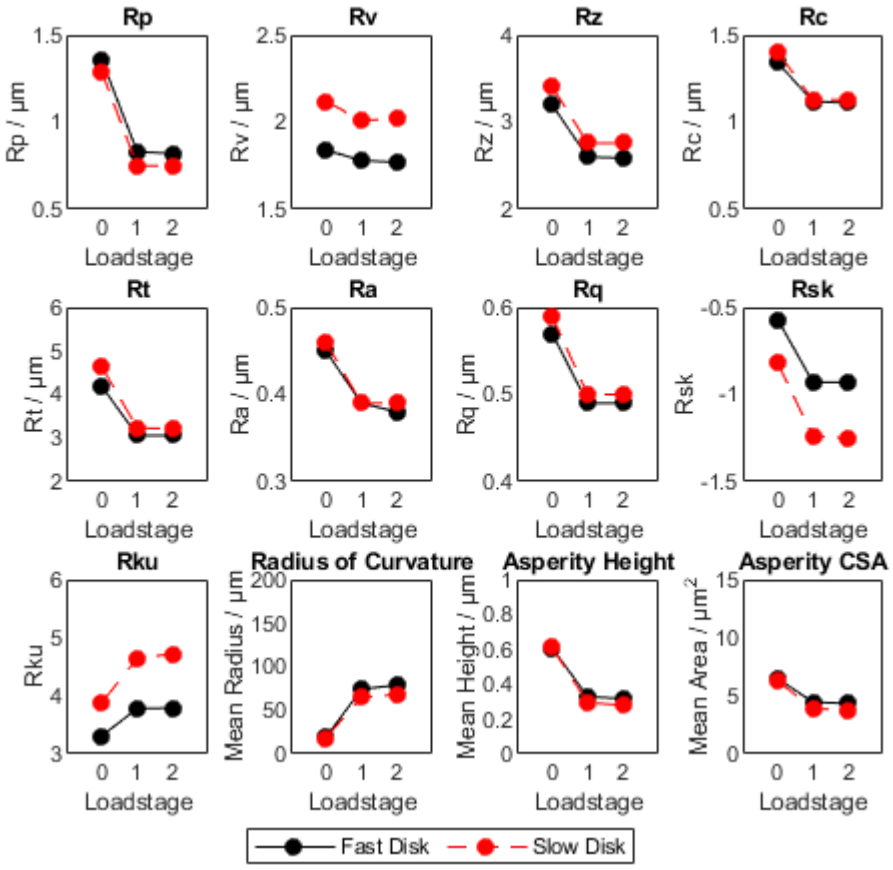

Figure 4.8.3 Running-in metrics for the fast and slow surfaces in Test 6

4.9 Test 7

Visually, the Test 7 surfaces appeared uniform across the contact area after running-in. On the fast disk, most roughness parameters influenced by peak heights (Ra, Rq, Rp, Rc, and Rz) showed a general trend of decreasing magnitude across the contact after running, excepting a slight upturn in roughness for the final profile. Prior to running all of these parameters had the same decreasing trend across the disk width but without the upturn at the opposing edge – suggesting that

much of this is likely an offset applied to the original values, but also that the conditions for asperities at the 'upturned' edge of the contact were less aggressive than elsewhere in the contact. A general trend toward less negative skewness across the contact width seen in the unrun profiles was maintained after running, albeit with a negative offset.

On the slow surface, most roughness parameters after running-in took on a profile of increasing roughness across the contact width. This trend already existed for some of the roughness parameters in the unrun surface such as Ra and Rq, but for parameters more strongly influenced by peak values, the initial profiles showed a pronounced u-shape in values on the negative side of the centreline – suggesting a region on that side had lower peaks on average. These behaviours on both surfaces are illustrated in Figure 4.9.1.

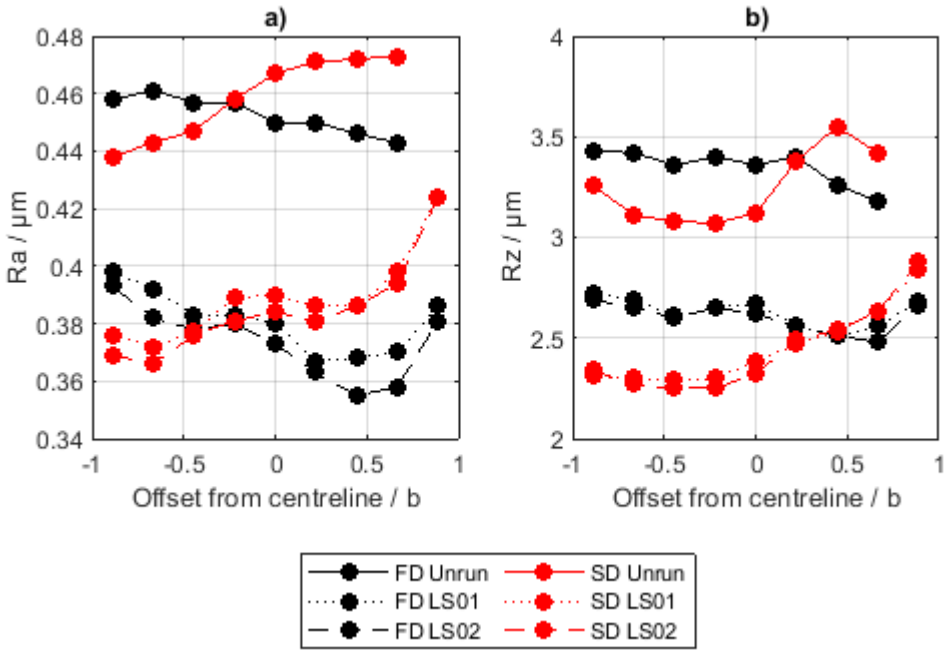

Figure 4.9.1 The variation in a) Ra and b) Rz across the width of the contact for the unrun surfaces of Test 7 and at each running-in stage.

As in all cases, the mean radius of curvature of asperities increased significantly during the running-in process. On the fast surface, the change in radii of curvature was reflected in the Ra curve above, with lower Ra profiles developing larger radii of curvature, and less significant increases being seen where Ra remained higher. There was a significant range to this with the largest mean radius of curvature reaching 97 μm, and the lowest reaching 58 μm. On the slow surface the mean radius of curvature at the conclusion of running-in was between 60-80 μm across the whole contact, with the exception of one profile at the far edge which increased to only 47 μm.

The running-in metrics assessed for Test 7 can be seen in Figure 4.9.2. It is clear from these metrics that the decrease in maximum peak height and valley depth was smaller on the fast surface than the slow. This carried through to Rz and Rt as expressions of extreme peak-valley height, but was not reflected in the Rc which represents mean of height differences on an element-wise basis.

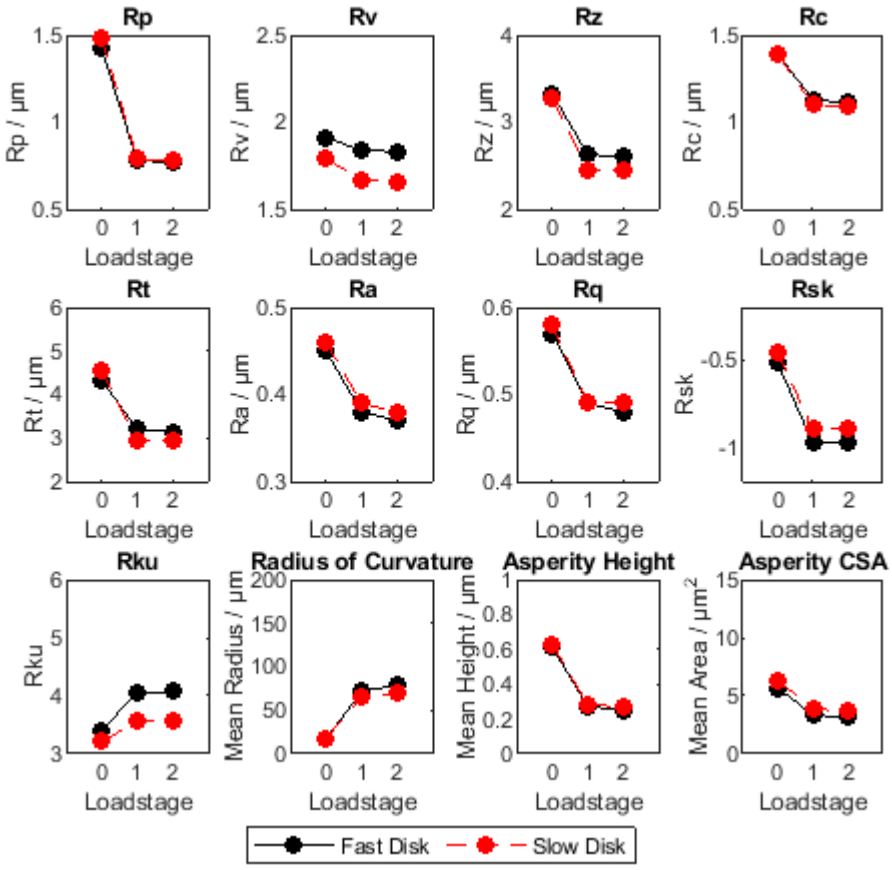

Figure 4.9.2 Running-in metrics for the fast and slow surfaces in Test 7

4.10 Test 8

Visual inspection of the Test 8 disks showed a uniform appearance across the contact width as expected, and inspection of the two-dimensional profiles measured through the running-in process were also indicative of largely uniform running-in behaviour as can be seen in Figure 4.10.1.

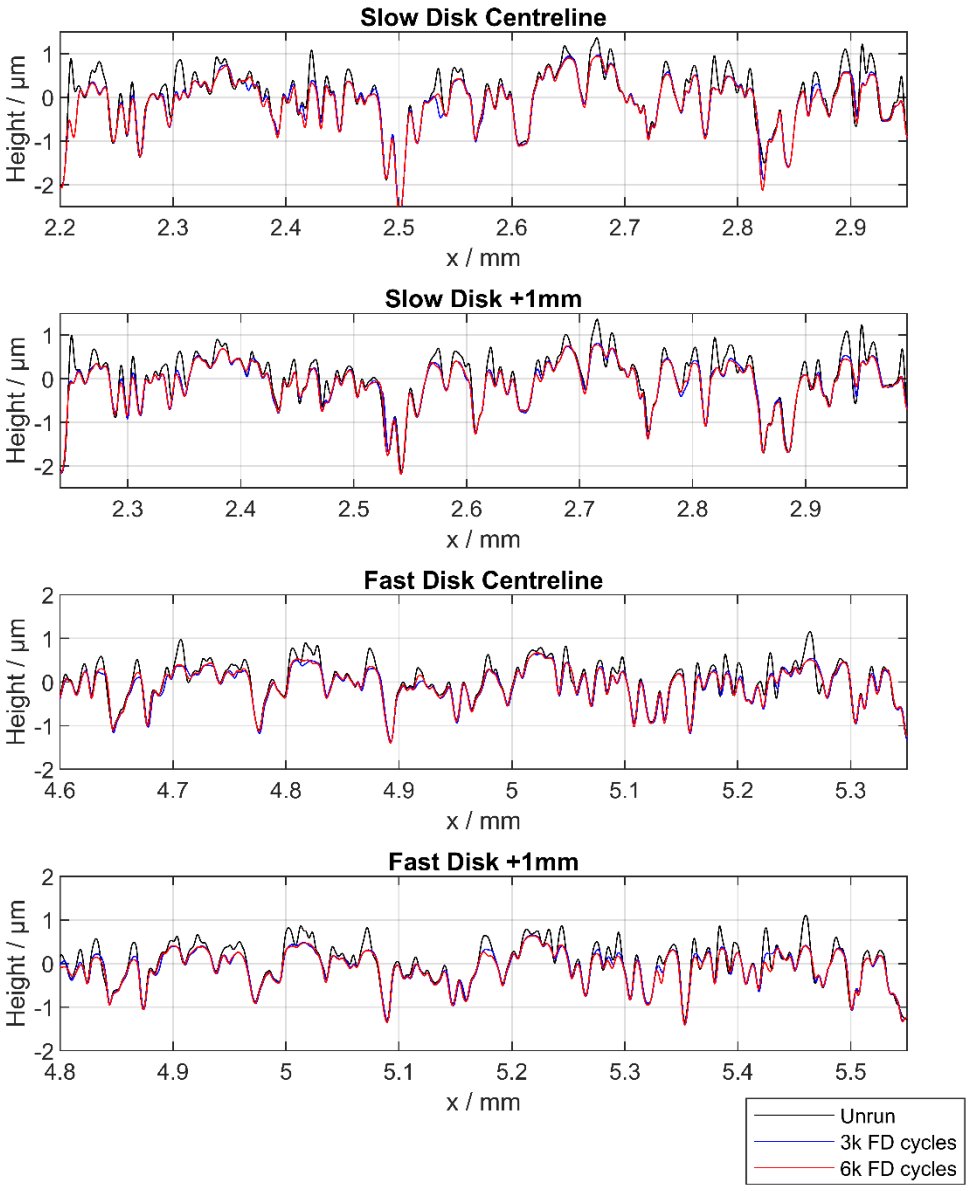

Figure 4.10.1 Test 8 Running-in profiles for the slow and fast disk surfaces at centreline and +1 mm from the centreline

Figure 4.10.2 shows run in metrics Ra, Rp and mean radius of curvature evaluated for each profile across the contact width. In Figure 4.10.2a it is clear that variation in the Ra across the slow disk width before running is maintained through the running-in process. While a slightly larger reduction is seen on the negative side of the contact, the magnitude of decrease is similar across the contact width. For the

fast surface, a less aggressive decrease in Ra is seen on one side of the contact, but the reduction is consistent across the rest of the contact.

Rp decreased significantly for both surfaces, but a smaller decrease could be seen at the extreme contact edges on both disks. Interestingly, the fast surface Rp decreased markedly more than the slow, yielding lower final values across the width despite its higher initial Rp values. Inspection of the Radius of Curvature change in Figure 4.10.2c shows that the radius of curvature of asperities on the fast surface underwent a significantly larger increase than on the slow surface.

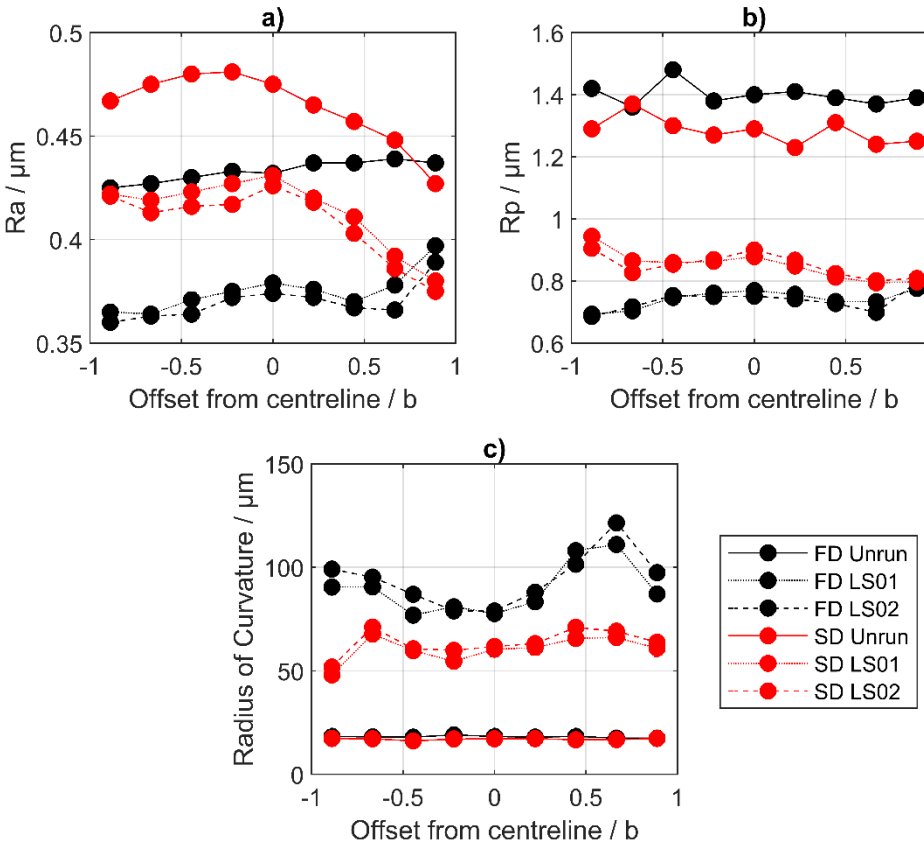

Figure 4.10.2 a) Ra, b) Rp, and c) mean radius of curvature across the contact width for Test 8 disks.

Figure 4.10.3 shows the parameters evaluated through the running-in process for Test 8. The Rp parameter indicates that the extreme peaks of the fast surface

underwent a significantly greater reduction than on the slow surface, however this difference is not reflected in the total height parameter Rt or in the similar mean height and mean element height parameters Rz and Rc. This is likely because a more significant decrease in Rv on the slow disk compensates for this. The reduction in Ra during the first stage of the running-in process was similar for both surfaces, however during the second stage a further reduction in Ra occurred for the fast surface. During both stages the Rq decreased faster on the fast surface than the slow, indicating that higher points were again being reduced more effectively on the fast surface.

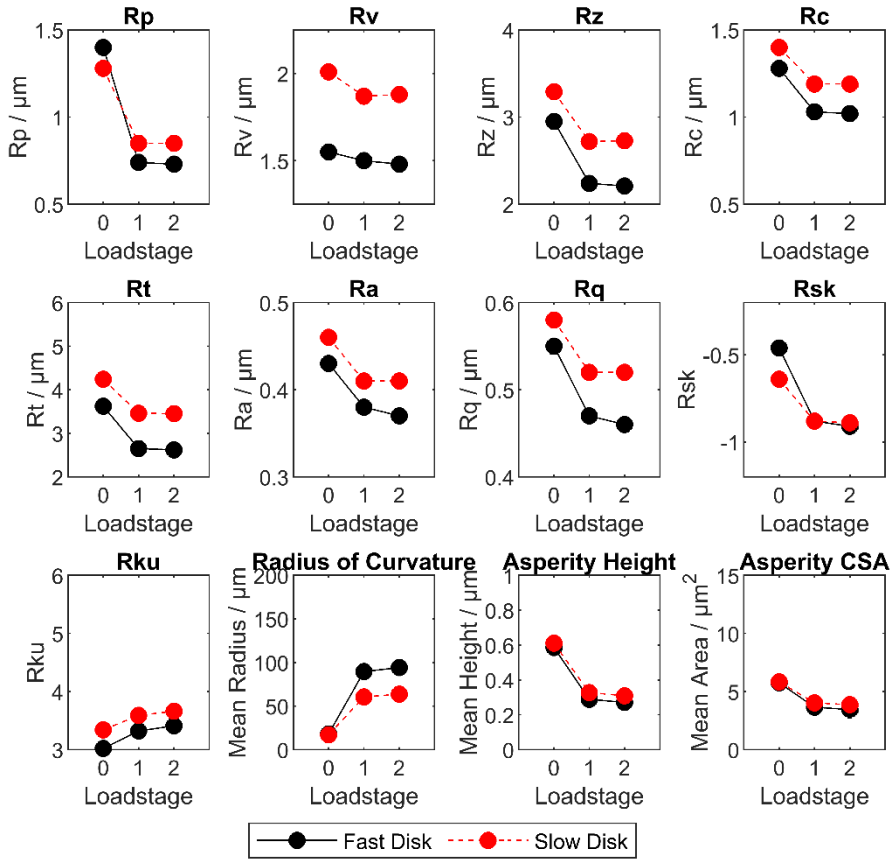

Figure 4.10.3 Running-in metrics for the fast and slow surfaces in Test 8

4.11 Individual Running-InTests Summary

The results for all tests are shown together below for the fast surface (Figure 4.11.1) and slow surface (Figure 4.11.2) respectively. These graphs highlight that similar behaviour was followed for most tests through the running in process, but also that some tests did act as outliers in some cases – most notably Test 1 as will be discussed further in the following sections.

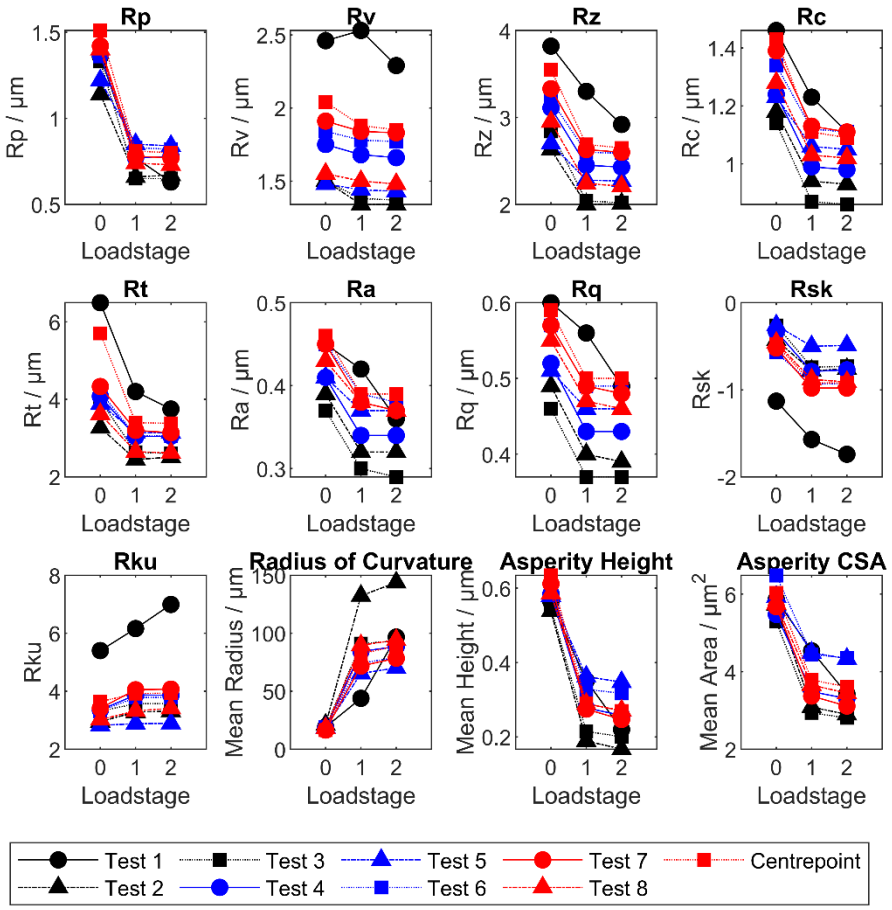

Figure 4.11.1 Surface parameters through the running-in process for the fast surfaces

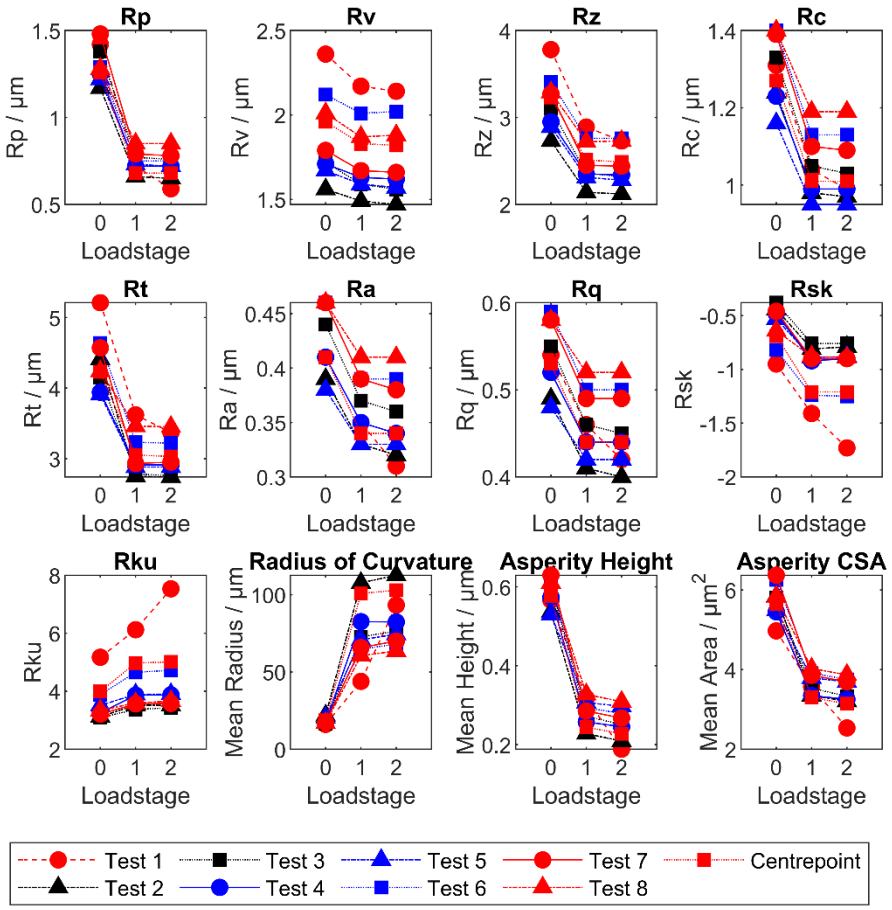

Figure 4.11.2 Surface parameters through the running-in process for the slow surfaces

4.12 Factorial Analysis of Running-in

In this section the effect of each variable and interaction is investigated to assess their influence on the running-in process.

For this section, the parameters investigated have been subdivided into several groups with shared characteristics. Ra and Rq are considered together as different evaluations of general surface roughness, and radius of curvature is considered alone. Variables that consider extreme features dependent on the highest and lowest points of the profiles are then investigated, followed by measures which consider the surface on an asperity-by-asperity basis. Finally, parameters concerning the statistical distribution of heights are considered.

This section primarily concerns the results, while discussion of possible mechanisms of each factor is considered in Section 4.13.

4.12.1 Roughness: Ra and Rq

The changes observed for both Ra and Rq were very similar. Figure 4.12.1 shows the main effects of each variable on the change in Ra through running-in. Clearly, each factor influenced the outcome in the same direction on both fast and slow surfaces. Pressure had the largest effect (i.e. the change in pressure induced the greatest change in the parameter in question) and acted to decrease Ra. SRR also decreased Ra, although the effect was very small and there was significant overlap in values at high and low SRR. Increasing entrainment provided a protective effect however, and lessened the decrease in Ra through running-in. Each of the factors considered resulted in Ra changes that were almost the same on both surfaces (differing by less than 0.0025 um). The changes due to pressure were larger on the slow surface whilst the changes due to SRR and the changes due to entrainment were larger on the fast surface.

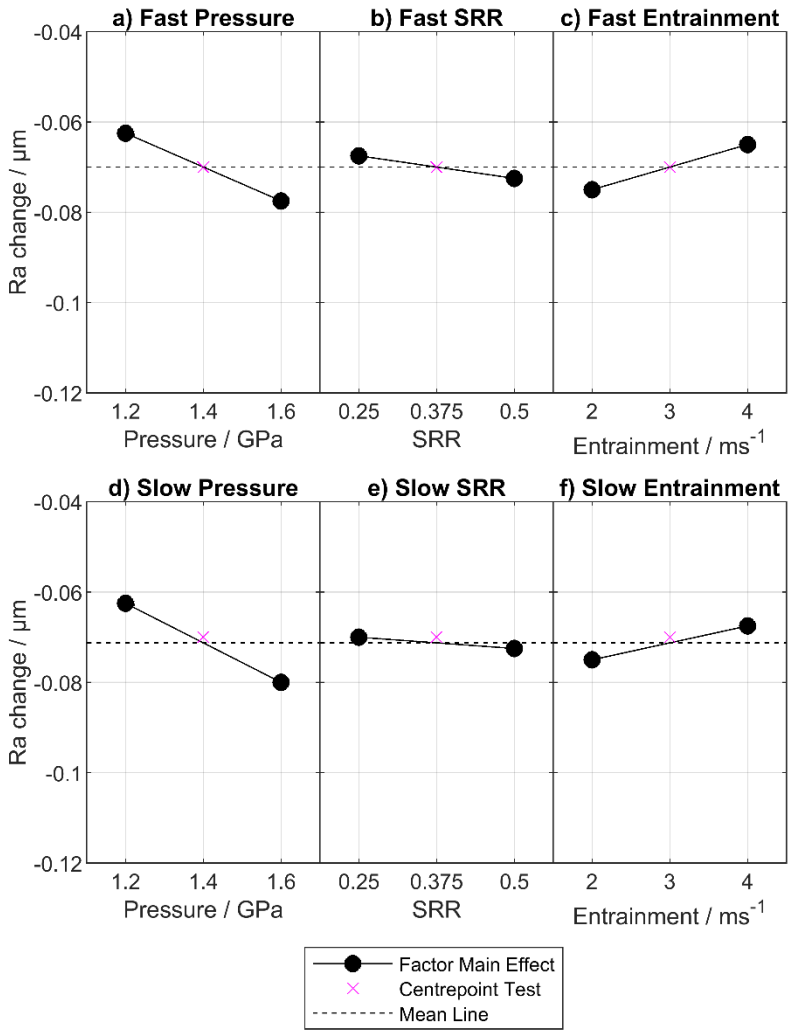

Figure 4.12.1 Main Effects of Pressure, SRR, and Entrainment on Ra (mean absolute roughness) for the fast (a-c) and slow (d-f) surfaces.

The main effect of each factor on Rq is shown in Figure 4.12.2. Again, each factor displayed the same direction of effect on both surfaces, but the magnitudes differ between the two surfaces. Pressure exhibited a larger Rq-reducing effect on the slow surface, while on the fast surface SRR was a considerably stronger influence than on the slow where is had only a very small effect. Entrainment was a marginally stronger factor on the fast surface.

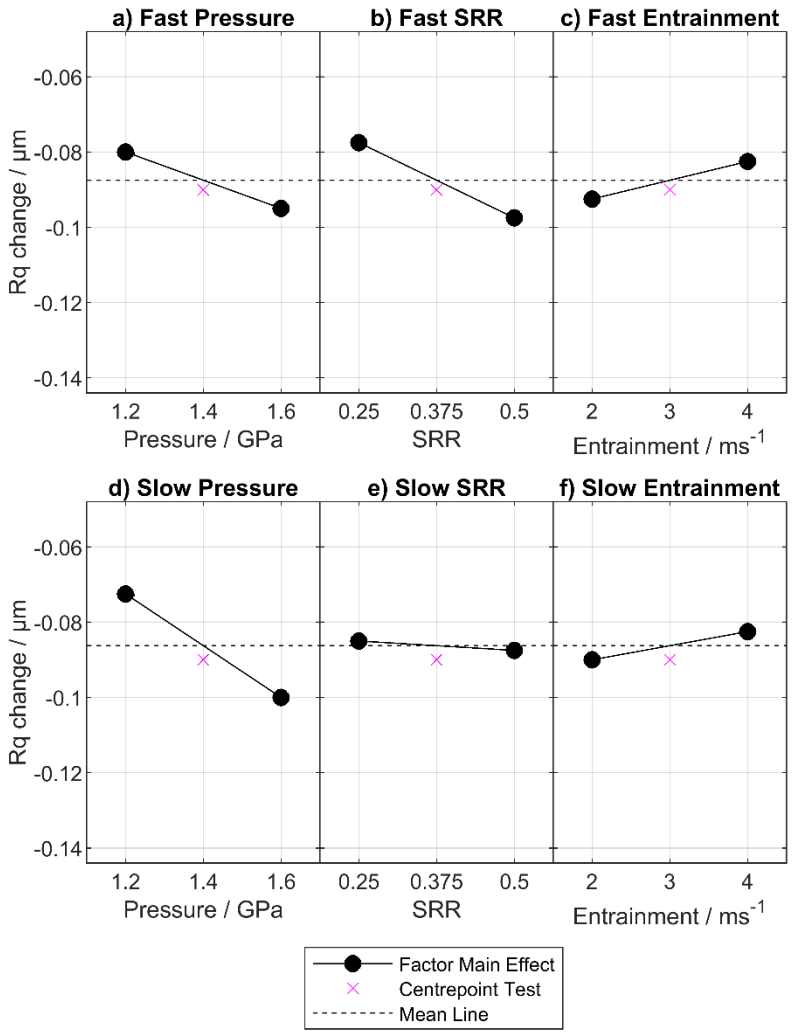

Figure 4.12.2 Main Effects of Pressure, SRR, and Entrainment on Rq (RMS roughness) for the fast (a-c) and slow (d-f) surfaces.

A comparison of note between the Ra and Rq main effects figures above is that the main effect lines for Ra pass directly through or extremely close to the centrepoint result, which provides good evidence for linear effects of the main variables on the change in Ra. For the Rq main effects, the centrepoint is slightly removed from the line, which may allude to the presence of minor nonlinear effects.

Figure 4.12.3 shows interaction effects plots for change in Ra on both surfaces. The interactions on each surface are remarkably similar, except between pressure and SRR. These showed no interaction on the fast surface but did on the slow, where

pressure had a stronger effect at higher sliding conditions, and where the pressure setting changed the direction of influence of SRR.

For both surfaces increased entrainment protected the surface at low pressure but led to greater Ra reduction at high pressure, while the transition from low to high pressure showed the strongest effect when entrainment was high. SRR and entrainment also interacted strongly, the influence of each changing direction entirely based on the setting of the other.

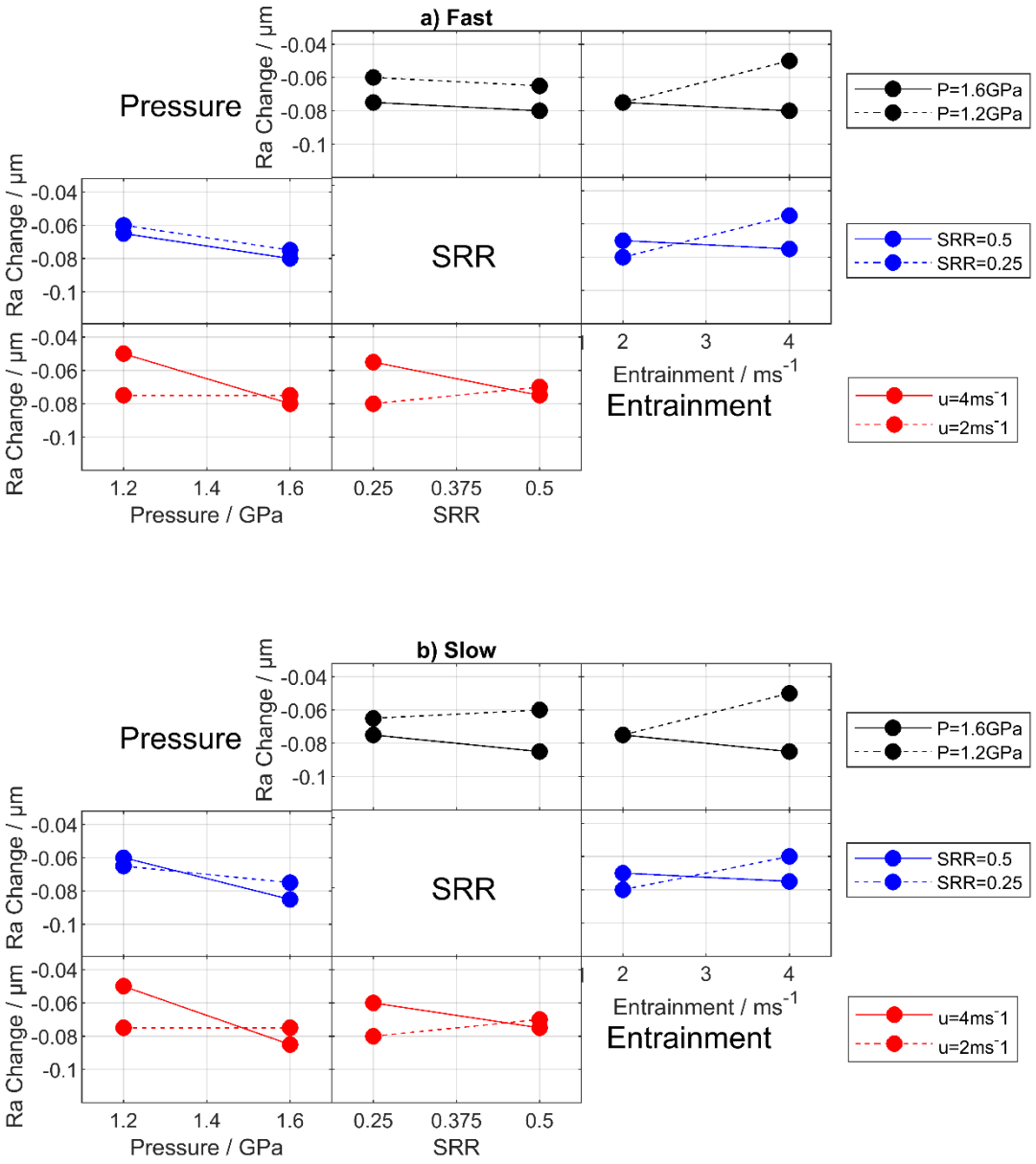

Figure 4.12.3 Two-factor interaction plots for pressure, SRR and entrainment on change in Ra through running-in for the fast and slow disks.

The interaction effects on Rq very closely matched the those for the Ra in both effect and magnitude, as can be seen in Figure 4.12.4.

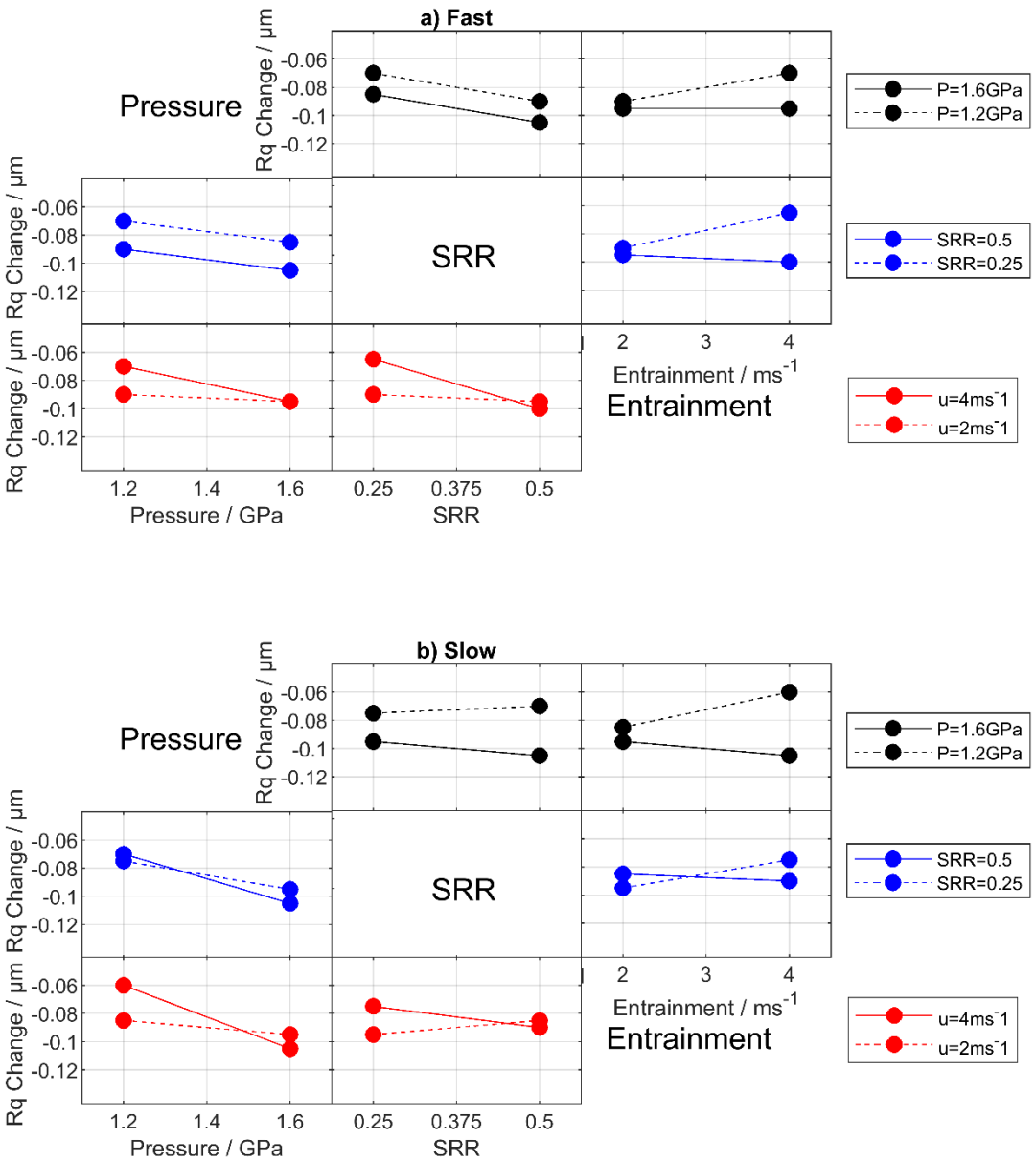

Figure 4.12.4 Two-factor interaction plots for pressure, SRR and entrainment on change in Rq through running-in for the fast and slow disks.

Changes in a two-factor interaction when a third variable is changed are indicative of a three-factor interaction. The plots shown in Figure 4.12.5 indicate that for the fast disk, there was no three-factor interaction present as the two lines (which are on top of each other in a)) remain parallel in both a) and b). On the slow surface a

three-factor interaction was present as pressure and SRR did not interact at low entrainment but did at high entrainment.

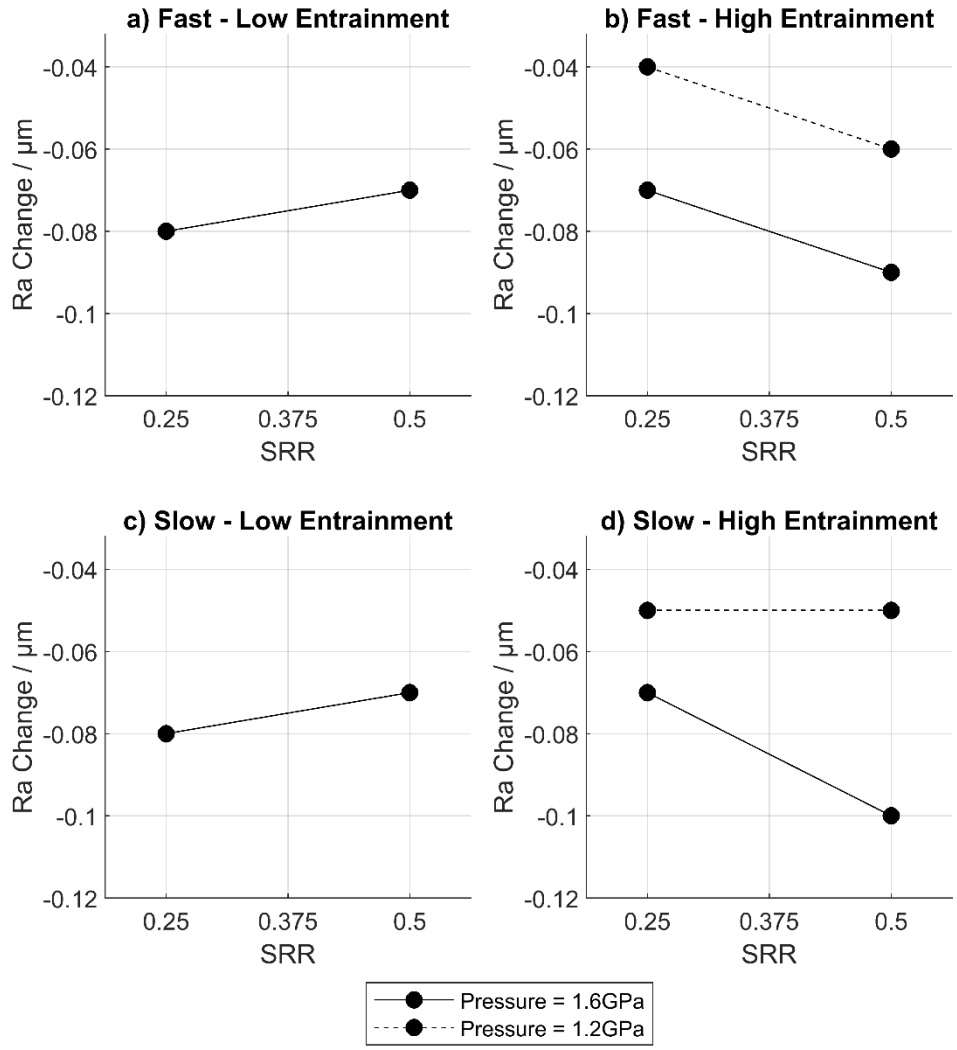

*Figure 4.12.5 Pressure*SRR interaction plots of change in Ra for the a) fast and b) slow surfaces at low and high entrainment.*

For Rq, three-factor interactions were present on both surfaces, acting in opposite directions. As can be seen in Figure 4.12.6, for the fast surface a two-factor interaction was present at both high and low entrainment, but the nature of this interaction changed with velocity. On the slow surface no two-factor interaction could be seen at low entrainment, but a clear interaction was present when entrainment was high.

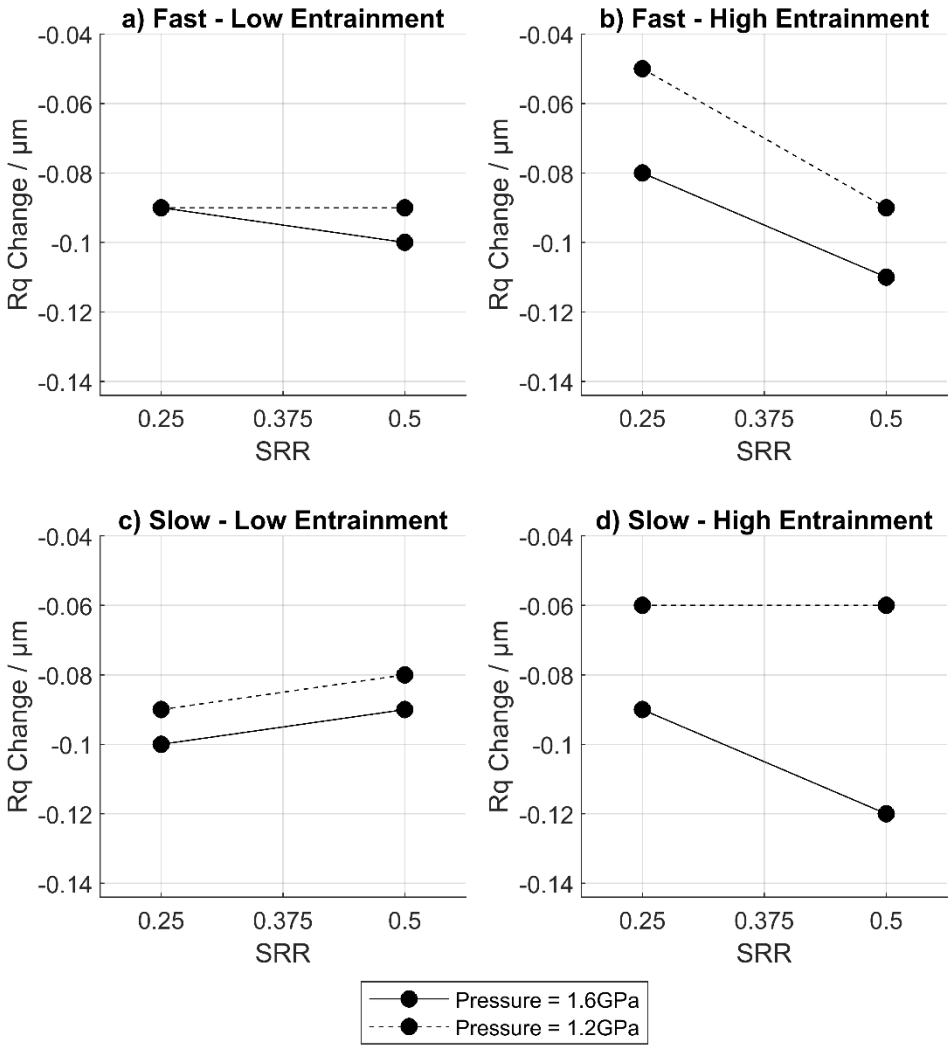

*Figure 4.12.6 Pressure*SRR interaction plots of change in Rq for the a) fast and b) slow surfaces at low and high entrainment.*

The effects of each variable and interaction on the running-in changes in Ra and Rq are shown in Table 4.12.1 and Table 4.12.2 respectively.

Table 4.12.1 Main and interaction effects for Ra

Factor / Interaction	Fast Surface change in Ra			Slow Surface change in Ra		
	Low average / µm	High Average / µm	Effect / Δµm	Low average / µm	High Average / µm	Effect / Δµm
Pressure	-0.063	-0.078	-0.015	-0.063	-0.080	-0.018
SRR	-0.068	-0.073	-0.005	-0.070	-0.073	-0.002
Entrainment	-0.075	-0.065	0.010	-0.075	-0.068	0.007
Pressure*SRR	-0.070	-0.070	0.000	-0.068	-0.075	-0.007
Pressure*Entrainment	-0.063	-0.078	-0.015	-0.063	-0.080	-0.018
SRR*Entrainment	-0.063	-0.078	-0.015	-0.065	-0.078	-0.013
Pressure*SRR*Entrainment	-0.070	-0.070	0.000	-0.075	-0.068	0.007

Table 4.12.2 Main and interaction effects for Rq

Factor / Interaction	Fast Surface change in Rq			Slow Surface change in Rq		
	Low average / µm	High Average / µm	Effect / Δµm	Low average / µm	High Average / µm	Effect / Δµm
Pressure	-0.080	-0.095	-0.015	-0.073	-0.100	-0.028
SRR	-0.078	-0.098	-0.020	-0.085	-0.088	-0.002
Entrainment	-0.093	-0.083	0.010	-0.090	-0.083	0.007
Pressure*SRR	-0.088	-0.088	0.000	-0.083	-0.090	-0.007
Pressure*Entrainment	-0.083	-0.093	-0.010	-0.078	-0.095	-0.018
SRR*Entrainment	-0.080	-0.095	-0.015	-0.080	-0.093	-0.013
Pressure*SRR*Entrainment	-0.085	-0.090	-0.005	-0.090	-0.083	0.007

4.12.2 Mean Radius of Curvature

The radius of curvature determined from the two-dimensional profiles as outlined in Section 3.5.2 provides a measure of how the geometry of asperity tips modifies to accommodate the load applied. The main effects of each factor on the mean radius of curvature of asperities are shown in Figure 4.12.7.

On both fast and slow surfaces increased pressure and SRR both increased mean radius of curvature, while higher entrainment opposed the increase in mean radius of curvature. For the parameter change levels adopted in these experiments, SRR was the strongest effect on both surfaces, followed by pressure and entrainment. For all three variables the effect observed was stronger on the fast surface than on the slow. A particularly striking difference between the fast and slow results is that while the fast surface results appear to have an essentially linear response, the slow surface centrepoint is indicative of highly nonlinear behaviour.

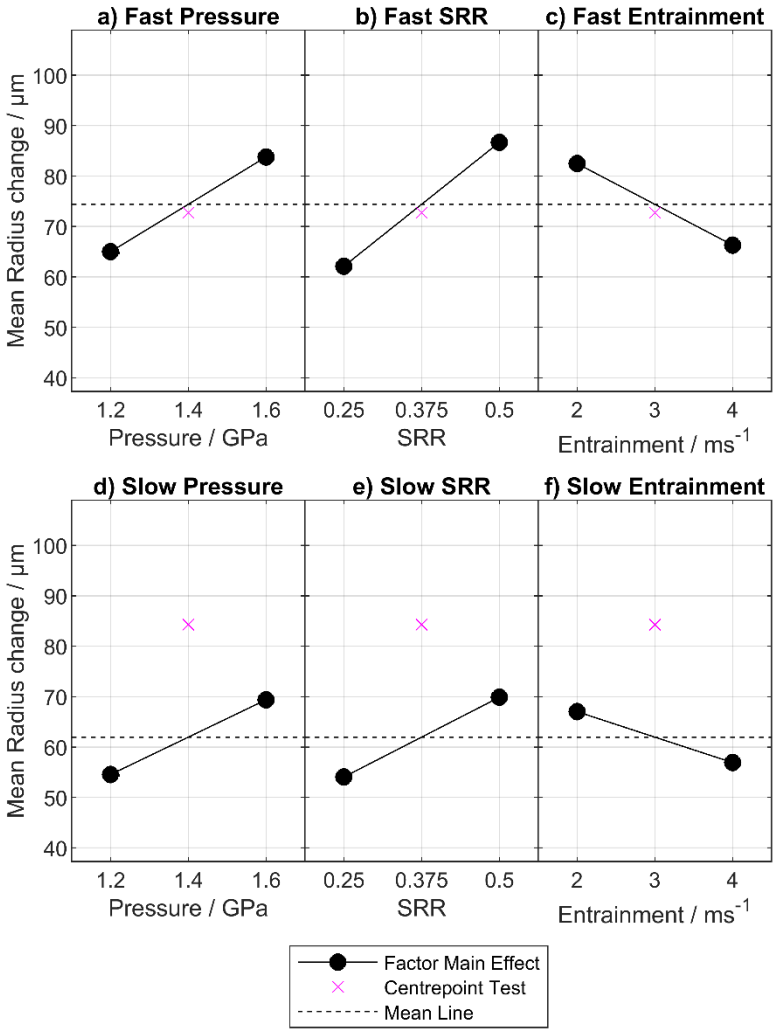

Figure 4.12.7 Main Effects of Pressure, SRR, and Entrainment on mean radius of curvature of asperity tips for the fast (a-c) and slow (d-f) surfaces.

Two- factor interaction plots for change in mean radius of curvature of asperities are shown in Figure 4.12.8. On the fast surface, pressure and SRR interacted weakly, increases in SRR or pressure having a greater effect when the other variable was also set high. On the slow surface however the mean radius of curvature was only elevated when both pressure and SRR were high. This behaviour can make a false contribution to the pressure and SRR main effects and so these main effects should be considered with caution.

Entrainment and pressure interacted strongly on the fast surface, pressure having a stronger radius-increasing effect where entrainment was low and entrainment having a stronger radius-reducing effect where pressure was high. Similarly to the slow disk pressure*SRR interaction, this type of inconsistent effect should be considered cautiously. On the slow surface the lines for pressure and entrainment were near-parallel indicating little to no interaction.

SRR and entrainment interacted only very weakly on the fast surface, but on the slow surface SRR had a stronger effect where entrainment was low and entrainment had a stronger effect where SRR was high.

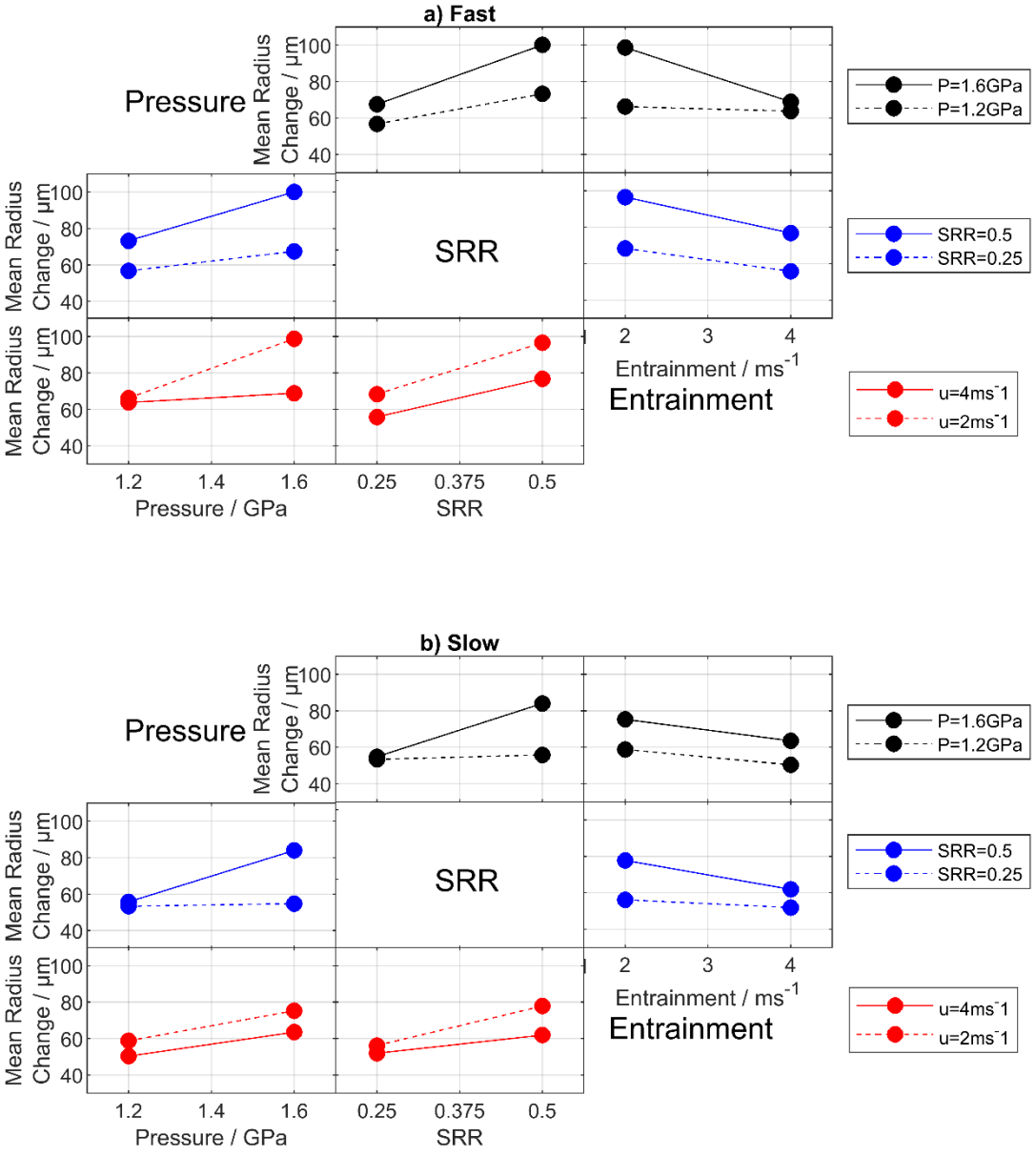

Figure 4.12.8 Two-factor interaction plots for pressure, SRR and entrainment on change mean radius of curvature of asperities through running-in.

Two-factor interactions at low and high entrainment for the fast and slow surfaces are shown in Figure 4.12.9. On both surfaces the two factor interactions seen at

low entrainment are different to those seen at high entrainment, indicating the presence of three-factor interactions.

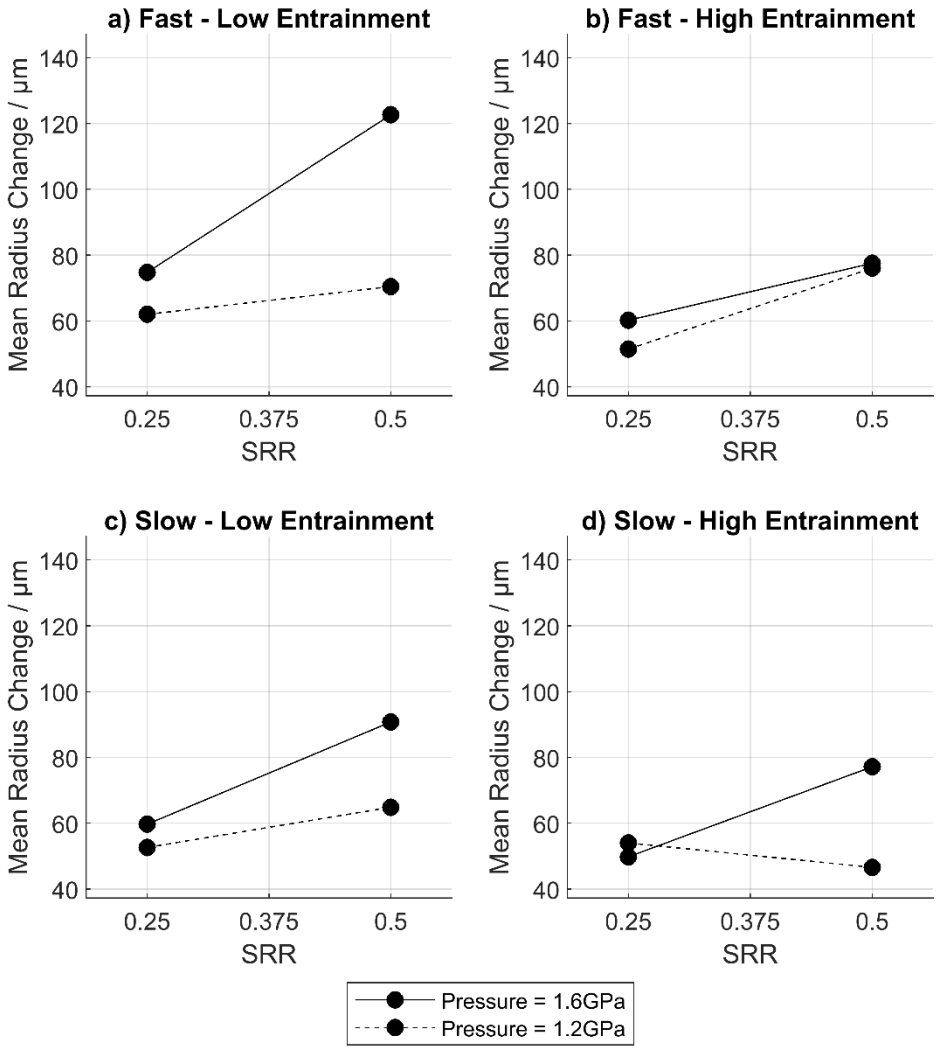

*Figure 4.12.9 Pressure*SRR interaction plots of change in mean radius of curvature of asperities for the a) fast and b) slow surfaces at low and high entrainment.*

Inconsistent main effects

As noted above, some two-factor interactions in this analysis appear to show an effect only occurring in one specific situation – for example the pressure*SRR interaction on the slow surface. From these plots alone it can appear that only when

pressure and SRR are both at their high settings is there a significant increase in mean radius. In that case, a contribution of this interaction can become attributed to a main effect when it is not a universally applied property of that main factor.

In this case the three-factor interaction plots and other two-factor interaction plots can help to separate the contributions of both tests where pressure and SRR are set high. From these we can see that there are main effects of pressure and SRR that persist aside from this strong interaction effect.

Interestingly, the tests in which pressure and SRR are both set high were those which provoked clear wear processes, and this may be a component of the radius of curvature interaction effects seen here.

The strengths of variable main and interaction effects on the change in mean radius of curvature through running-in are shown in Table 4.12.3.

Table 4.12.3 Main and interaction effects for mean radius of curvature of asperities.

	Fast Surface change in mean radius of curvature			Slow Surface change in mean radius of curvature		
Factor / Interaction	Low average / μm	High Average / μm	Effect / Δμm	Low average / μm	High Average / μm	Effect / Δμm
Pressure	64.99	83.79	18.80	54.55	69.38	14.83
SRR	62.11	86.68	24.57	54.06	69.87	15.81
Entrainment	82.47	66.31	-16.16	67.01	56.91	-10.10
Pressure*SRR	70.37	78.42	8.05	55.25	68.67	13.42
Pressure*Entrainment	81.24	67.55	-13.69	62.79	61.14	-1.65
SRR*Entrainment	76.19	72.60	-3.59	64.88	59.05	-5.83
Pressure*SRR*Entrainment	68.55	80.23	11.68	63.95	59.97	-3.98

4.12.3 Extreme Profile Features: Rp, Rv, Rz, and Rt

The roughness parameters considered in this section relate to the highest and lowest points in a profile, and the distance between them. It is worth noting however that, although nominally a measure of the depth of the deepest points on a surface, Rv in this context more effectively functions as a measure of the change in the location of the mean line through running-in. This is because the valleys are largely unaffected by the running-in processes, and micropit formation has not yet begun significantly enough to produce new deep points.

Main Effects

The most immediately noticeable change in a surface through the running-in process is the reduction in the height of asperities, the tallest of which are captured by the Rp parameter. The main effects plots for Rp are shown in Figure 4.12.10. This shows that increased pressure gives a greater reduction in Rp on both surfaces, however the effect is larger on the slow surface than the fast. SRR had the strongest influence of all variables on the fast surface, but minimal influence on the slow surface. Entrainment showed a very small peak-preserving effect on each surface.

It is also notable that while the slow surface lines passed directly through the centrepoint result, the centrepoint result was far removed from the main effect lines on the fast surface.

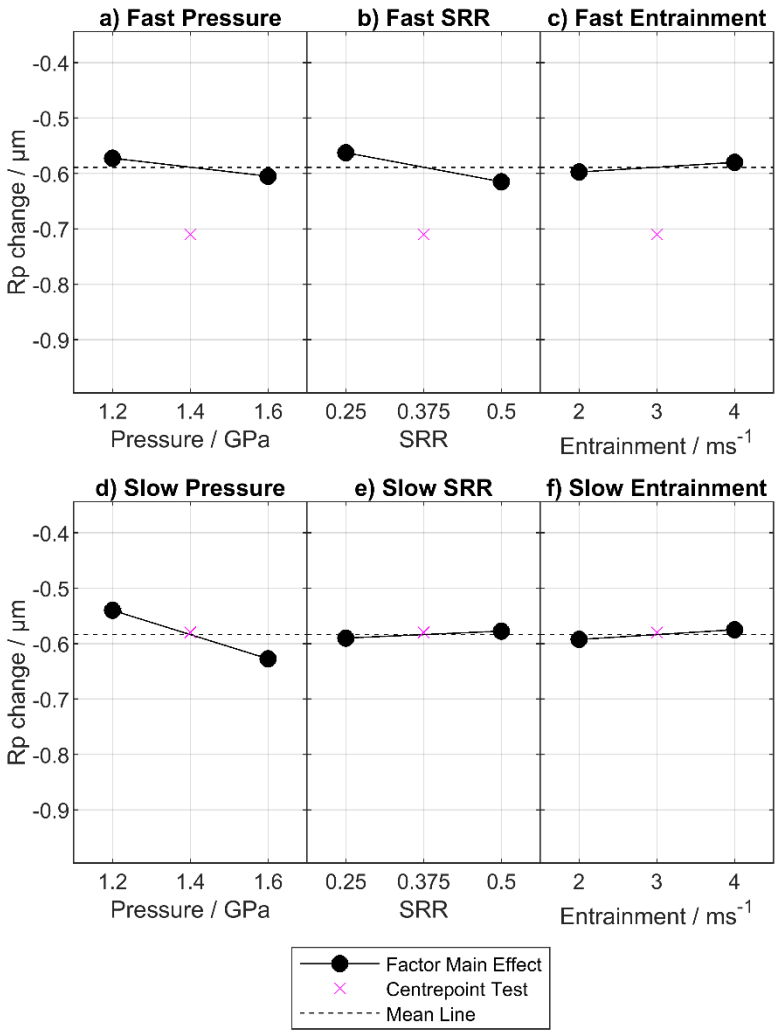

Figure 4.12.10 Main Effects of Pressure, SRR, and Entrainment on Rp for the fast (a-c) and slow (d-f) surfaces.

This is very similar to the main effect plots for Rz, shown in Figure 4.12.11. The fast surface effects were all larger in magnitude than their counterparts in Rp, as was the slow surface pressure effect - however the directions of influence, relative magnitudes, and lack of influence of SRR and entrainment relate closely to the effects seen for Rp.

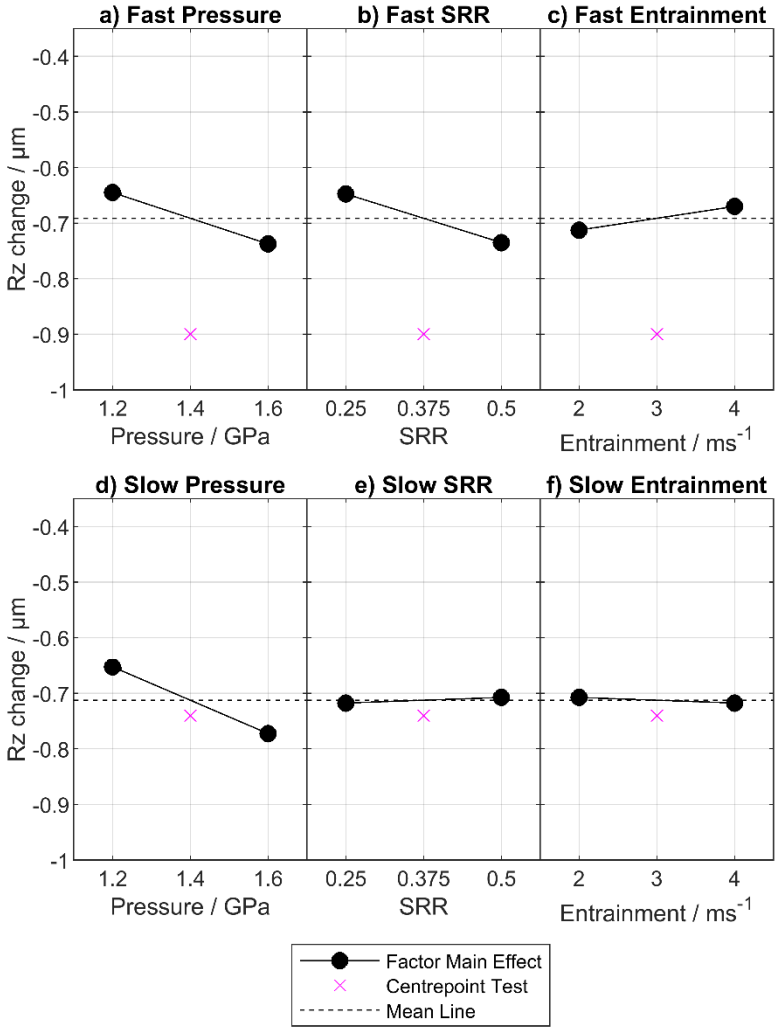

Figure 4.12.11 Main Effects of Pressure, SRR, and Entrainment on Rz for the fast (a-c) and slow (d-f) surfaces.

As would be expected, the change in Rv accounts for the difference between the changes in Rz and Rp values. As the peaks are reduced the mean line of the profile moves downwards, reducing the Rv value. The main effects for Rv are shown in Figure 4.12.12.

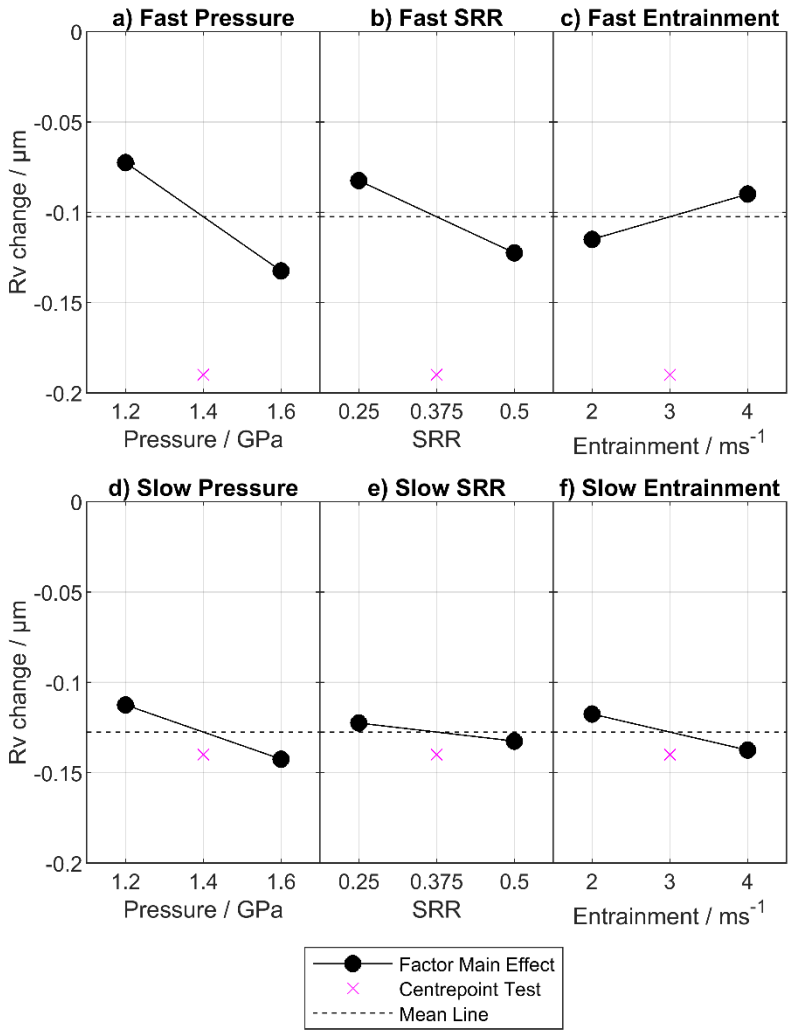

Figure 4.12.12 Main Effects of Pressure, SRR, and Entrainment on Rv for the fast (a-c) and slow (d-f) surfaces.

The final variable considered that is based on extreme profile features was Rt, the difference in height between the highest peak and lowest valley in the whole of the measured profile. This would be expected to reflect the same changes as seen in Rz, which is a mean of distances between a number of the highest peaks and lowest valleys, but was notably different as can be seen in Figure 4.12.13.

The magnitudes of change in Rt were much greater than seen in Rz, and the direction of influence of entrainment was seen to be in the opposite direction than seen for Rz on both surfaces. Crucially, the value of Rt varied by the greatest

amount of all variables on the initial surface before running, as can be seen in the parameter summary figures for each test. Because of its dependence on a single extreme peak and valley pair, the change in Rt is only able to convey a limited amount of information and provides minimal information on the status of the surface as a whole. As such, Rt shall not be discussed further, although two- and three- factor interaction plots for Rt can be found in Appendix 1.

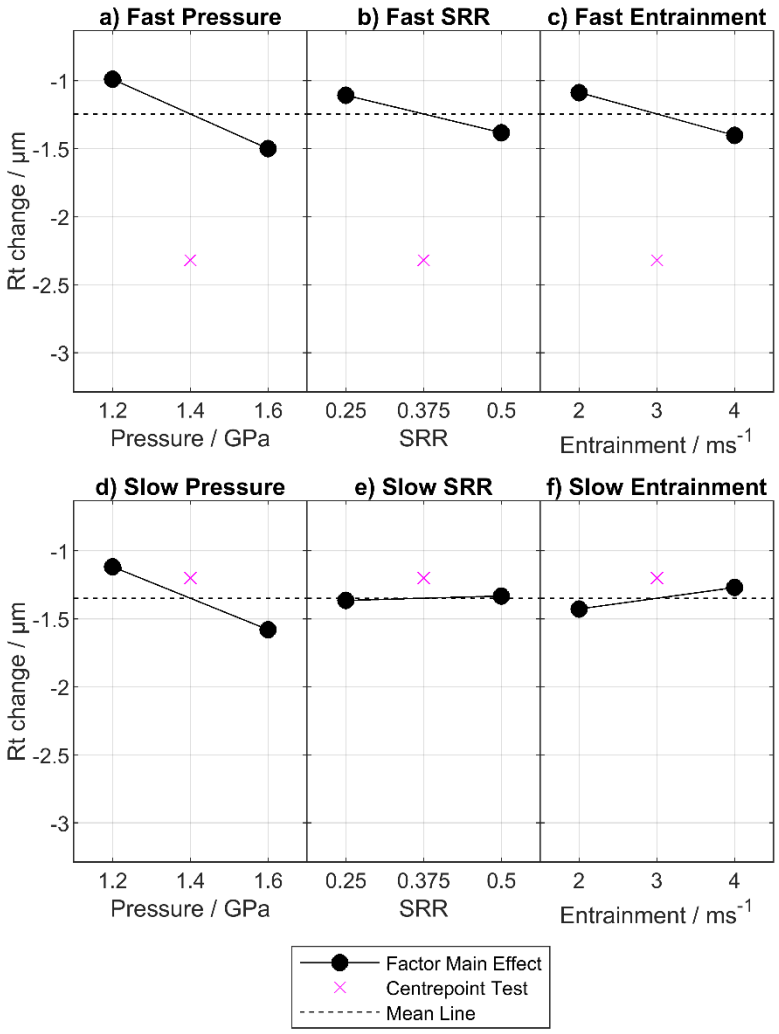

Figure 4.12.13 Main Effects of Pressure, SRR, and Entrainment on Rt for the fast (a-c) and slow (d-f) surfaces.

Two-Factor Interaction Effects

Further illustrating the dominance of peak height on the Rz parameter, the interaction effects seen for both Rp and Rz match very closely in all cases. Both Rp and Rz are discussed here alongside the interaction plots for Rp, while the Rz interaction plots can be seen in Appendix 1.

As can be seen in Figure 4.12.14 Rp (and hence also Rz) was influenced by two-factor interactions on both surfaces and between all three variables.

On both surfaces, a greater reduction in Rp resulted when entrainment and sliding were both set high or low, with a lesser reduction in Rp when the setting on each was different. The same was also true for the relationship between pressure and entrainment.

The interaction between pressure and SRR differed between the fast and slow surfaces. On the fast surface sliding had minimal influence when pressure was high, but at low pressure higher sliding led to a greater reduction in Rp while low sliding gave a smaller reduction in Rp. On the slow surface however, pressure had minimal influence at low sliding but showed a strong Rp reducing effect when sliding was high.

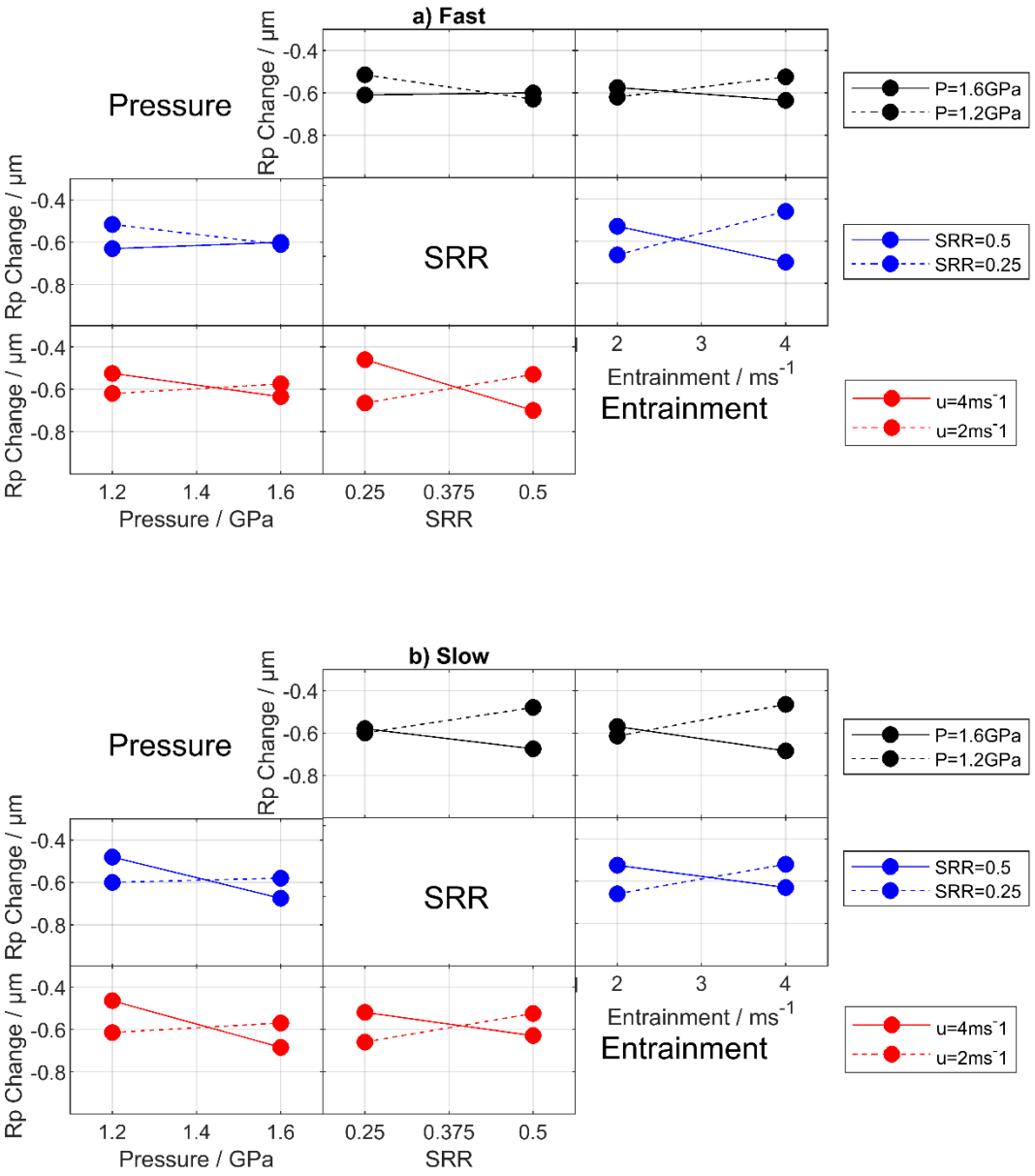

Figure 4.12.14 Two-factor interaction plots for pressure, SRR and entrainment on change in Rp through running-in for the fast and slow disks.

The two-factor interaction effects on Rv are shown in Figure 4.12.15.

Pressure and SRR interacted on both surfaces. On the fast surface both pressure and SRR were seen to have a greater Rv-reducing effect when the other was at its

high setting. The slow surface showed a similar effect, however only a marginal effect of SRR was seen when pressure was low.

Entrainment and pressure did not interact on the fast surface, while an interaction was seen on the slow surface where increasing entrainment or pressure had stronger Rv-reducing effects where the other variable was set high.

Both surfaces exhibited interactions between SRR and entrainment. On the fast surface, entrainment had a stronger effect to protect the surface (and thus reduce change in Rv) when sliding was low. On the slow surface, having both entrainment and SRR at the high or low setting produced a greater reduction in Rv than when they were at different settings.

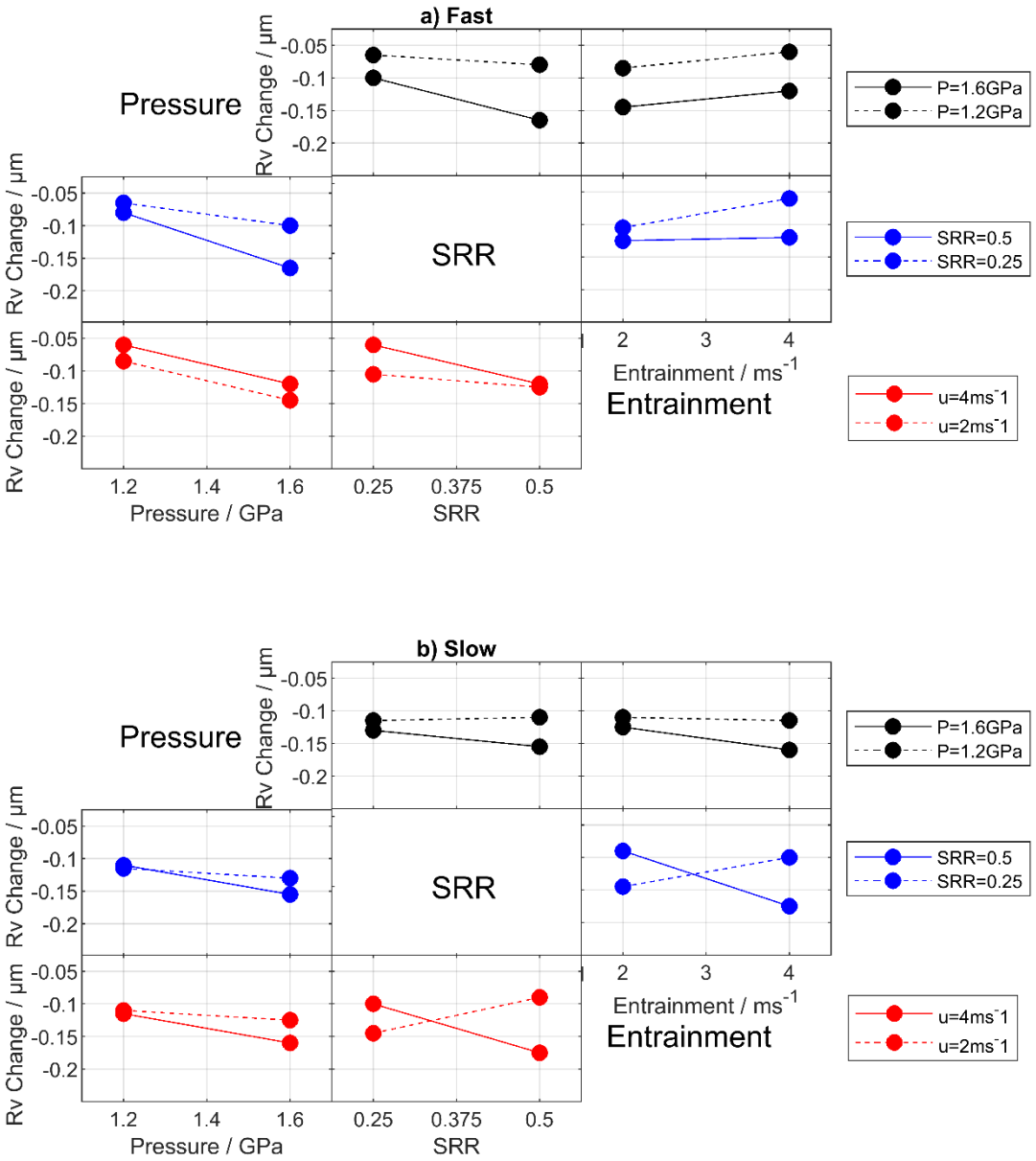

Figure 4.12.15 Two-factor interaction plots for pressure, SRR and entrainment on change in Rv through running-in for the fast and slow disks.

Three-Factor Interaction Effects

Three-factor interactions for Rp and Rz once again showed the same relationships, hence three-factor interaction plots for Rz can be found in Appendix 1 and only the Rp shall be used here, shown in Figure 4.12.16.

This clearly shows that for Rp (and hence also Rz) two-factor interactions were changed significantly by the third variable – hence three-factor interactions had an influence on Rp.

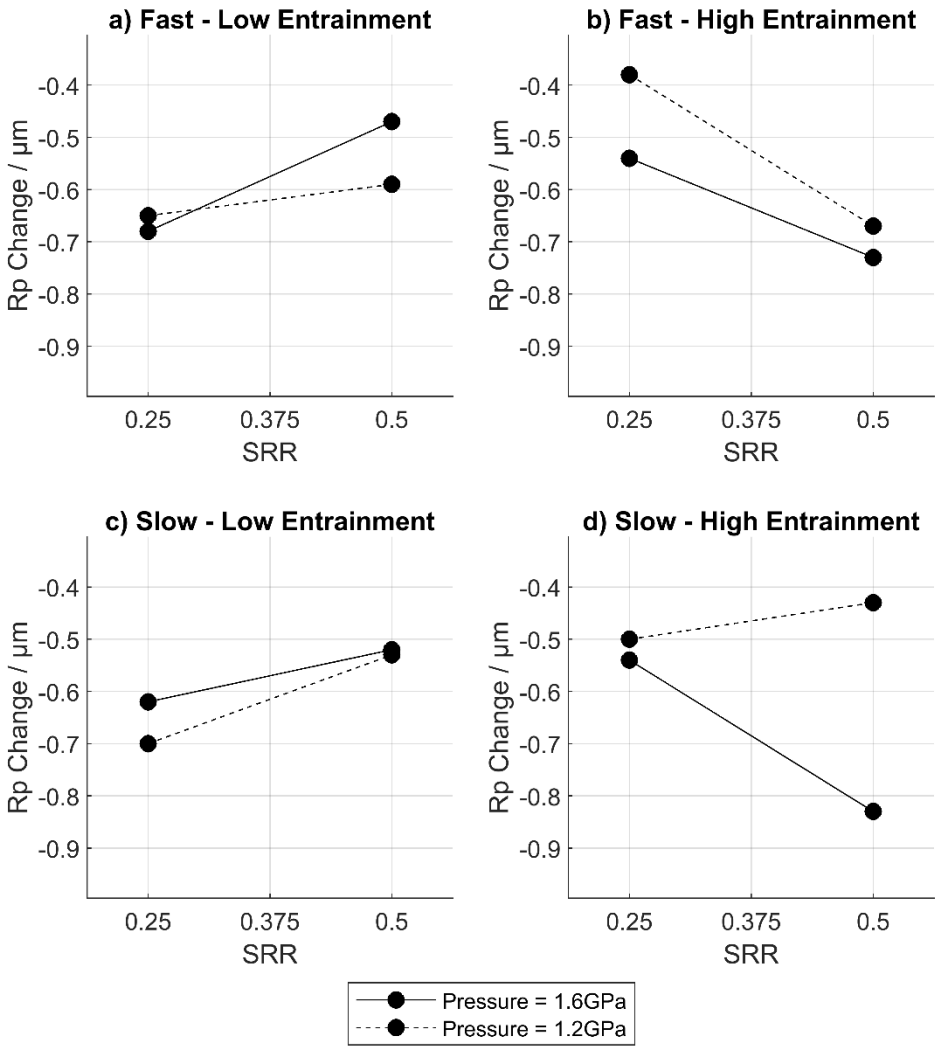

*Figure 4.12.16 Pressure*SRR interaction plots of change in Rp for the a) fast and b) slow surfaces at low and high entrainment.*

Figure 4.12.17 shows the pressure*SRR two factor interactions for each surface at low and high entrainment. On the fast surface there was only a very small interaction present at low entrainment, however the interaction effect became

much stronger when entrainment speed was increased. The interaction on the slow surface changed entirely when entrainment was increased, SRR influencing in the opposite sense compared to the low entrainment interaction and change in Rv showing pressure-dependence when SRR was high instead of low. As such, three-factor interactions were shown to have an influence on Rv.

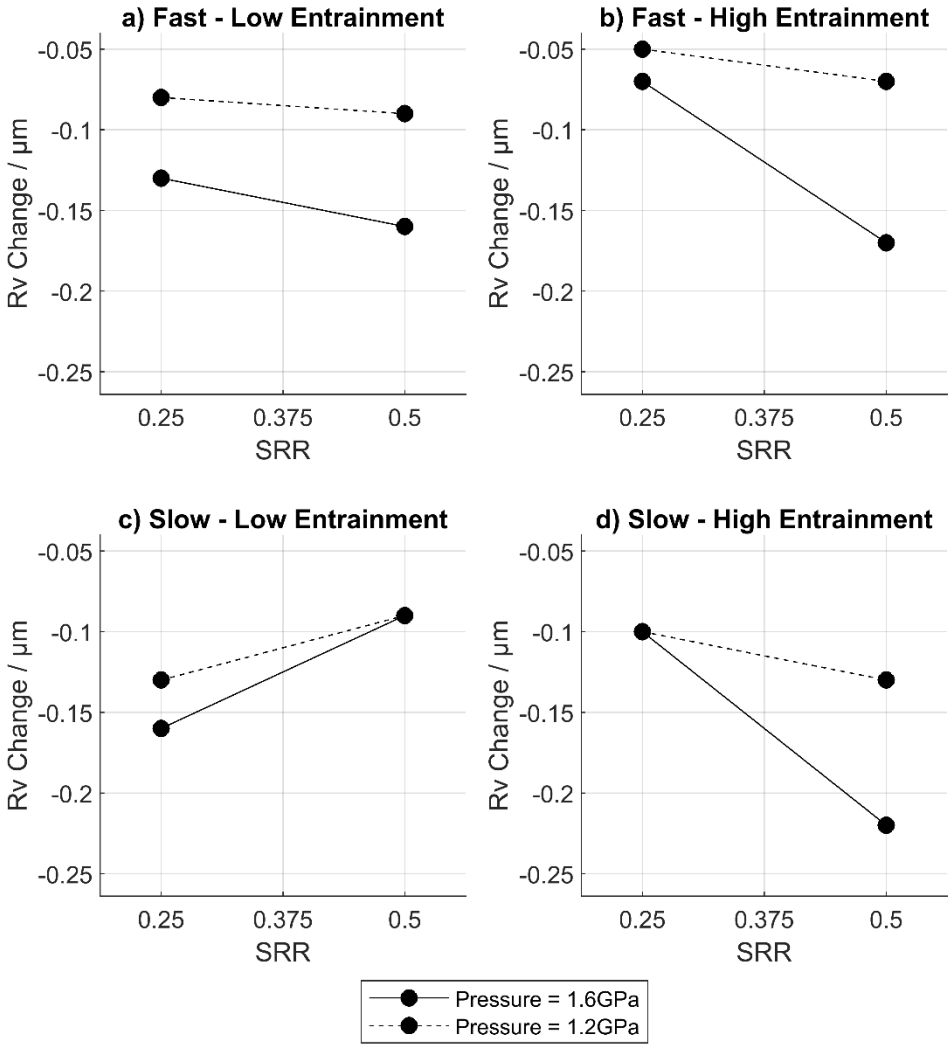

*Figure 4.12.17 Pressure*SRR interaction plots of change in Rv for the a) fast and b) slow surfaces at low and high entrainment.*

Strength of Effects

The following tables show the strengths of factor main and interaction effects on Rp, Rv, and Rz respectively. For completeness, the table showing effects for Rt is located in Appendix 1.

Table 4.12.4 Main and interaction effects for Rp

	Fast Surface change in Rp			Slow Surface change in Rp		
Factor / Interaction	Low average / µm	High Average / µm	Effect / Δµm	Low average / µm	High Average / µm	Effect / Δµm
Pressure	-0.573	-0.605	-0.033	-0.540	-0.628	-0.087
SRR	-0.563	-0.615	-0.053	-0.590	-0.578	0.013
Entrainment	-0.598	-0.580	0.018	-0.593	-0.575	0.018
Pressure*SRR	-0.620	-0.558	0.063	-0.530	-0.638	-0.108
Pressure*Entrainment	-0.550	-0.628	-0.077	-0.518	-0.650	-0.133
SRR*Entrainment	-0.495	-0.683	-0.188	-0.523	-0.645	-0.123
Pressure*SRR*Entrainment	-0.595	-0.583	0.013	-0.620	-0.548	0.073

Table 4.12.5 Main and interaction effects for Rv

	Fast Surface change in Rv			Slow Surface change in Rv		
Factor / Interaction	Low average / µm	High Average / µm	Effect / Δµm	Low average / µm	High Average / µm	Effect / Δµm
Pressure	-0.073	-0.133	-0.060	-0.113	-0.143	-0.030
SRR	-0.083	-0.123	-0.040	-0.123	-0.133	-0.010
Entrainment	-0.115	-0.090	0.025	-0.118	-0.138	-0.020
Pressure*SRR	-0.090	-0.115	-0.025	-0.120	-0.135	-0.015
Pressure*Entrainment	-0.103	-0.103	0.000	-0.120	-0.135	-0.015
SRR*Entrainment	-0.093	-0.113	-0.020	-0.095	-0.160	-0.065
Pressure*SRR*Entrainment	-0.110	-0.095	0.015	-0.143	-0.113	0.030

Table 4.12.6 Main and interaction effects for Rz

Factor / Interaction	Fast Surface change in Rz			Slow Surface change in Rz		
	Low average / µm	High Average / µm	Effect / Δµm	Low average / µm	High Average / µm	Effect / Δµm
Pressure	-0.645	-0.738	-0.093	-0.653	-0.773	-0.120
SRR	-0.648	-0.735	-0.088	-0.718	-0.708	0.010
Entrainment	-0.713	-0.670	0.043	-0.708	-0.718	-0.010
Pressure*SRR	-0.713	-0.670	0.043	-0.650	-0.775	-0.125
Pressure*Entrainment	-0.653	-0.730	-0.078	-0.640	-0.785	-0.145
SRR*Entrainment	-0.585	-0.798	-0.213	-0.620	-0.805	-0.185
Pressure*SRR*Entrainment	-0.708	-0.675	0.033	-0.763	-0.663	0.100

4.12.4 Profile Element Measures: Rc, Asperity Height, and Asperity CSA

The parameters considered in this section relate to profile elements, each an asperity feature bounded by valleys. Rc is a standard measure of roughness corresponding to the mean height difference from the bottom of valleys to the highest point in their neighbouring asperities. Asperity CSA and asperity height were defined in Section 3.5.3 and concern the mean cross-sectional area of asperities above the mean line, and the mean height of asperities above the mean line.

Main Effects

The main effects on Rc are shown in Figure 4.12.18. Pressure showed an Rc-reducing effect on both surfaces, however this was stronger on the slow surface. SRR showed an Rc-reducing effect on the fast surface that was marginally stronger (-0.005 µm) than the fast surface pressure effect. On the slow surface however, increasing SRR mildly reduced the change in Rc. Entrainment exhibited a protective effect on both surfaces.

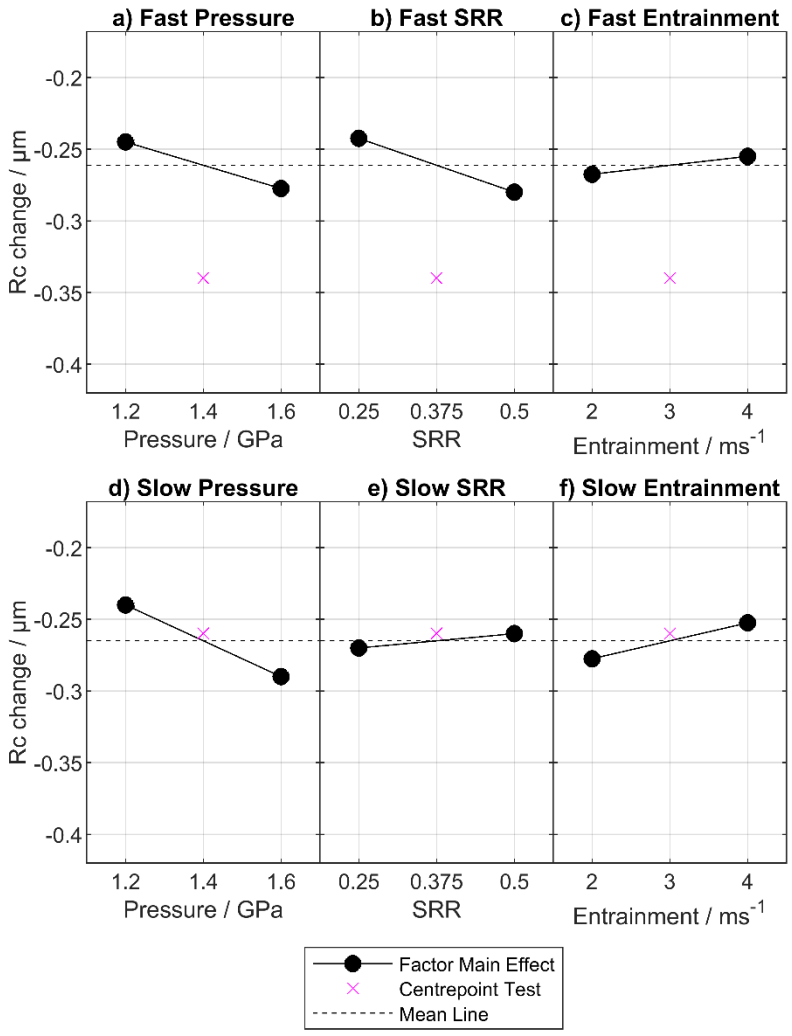

Figure 4.12.18 Main Effects of Pressure, SRR, and Entrainment on Rc for the fast (a-c) and slow (d-f) surfaces.

The mean asperity heights parameter was largely in agreement with Rc, as can be seen in Figure 4.12.19. Pressure had height-reducing effects on both surfaces, slightly smaller in magnitude than the change seen for Rc. On the fast surface a height-decreasing effect was seen for SRR, and again this was of smaller magnitude than the effect seen for Rc. The slow surface SRR showed a small height-decreasing effect – the opposite direction to the effect seen for Rc.

Entrainment had a stronger effect to lessen the decrease in asperity height on both surfaces than was seen for Rc.

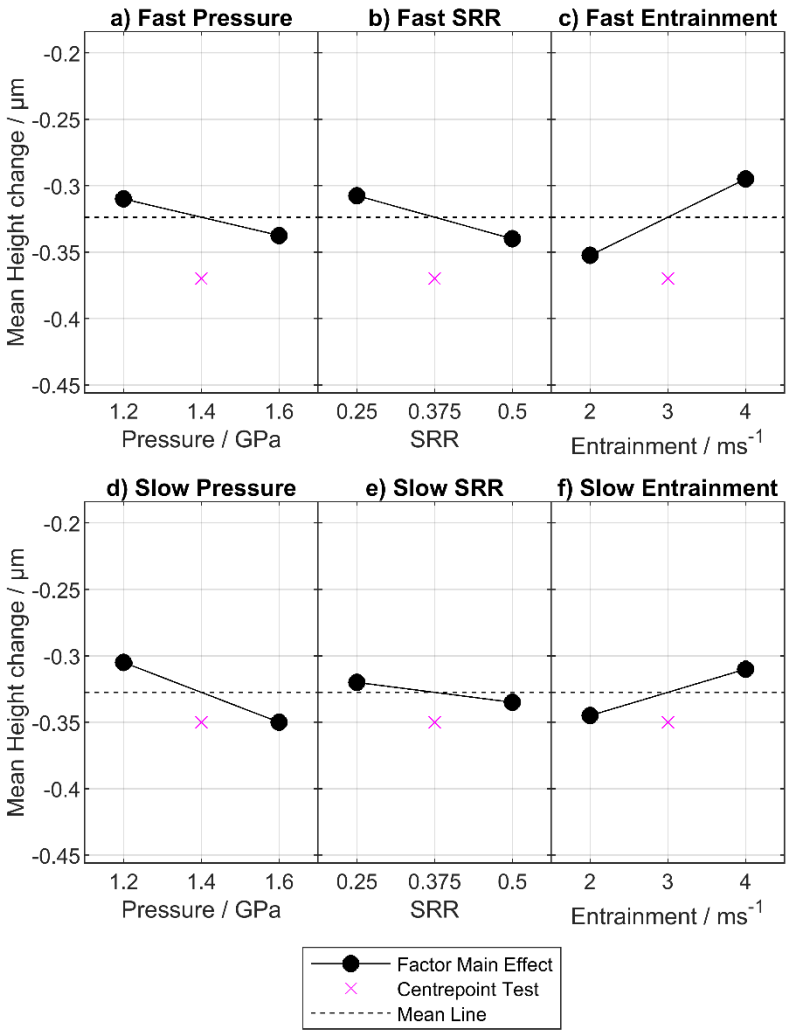

Figure 4.12.19 Main Effects of Pressure, SRR, and Entrainment on the mean asperity height parameter for the fast (a-c) and slow (d-f) surfaces.

The Asperity CSA parameter main effects aligned with the main effects for Rc in all senses other than that the relative magnitude of the entrainment effect (compared to pressure and SRR effects) on both surfaces was larger than seen for Rc. This is can be seen in Figure 4.12.20.

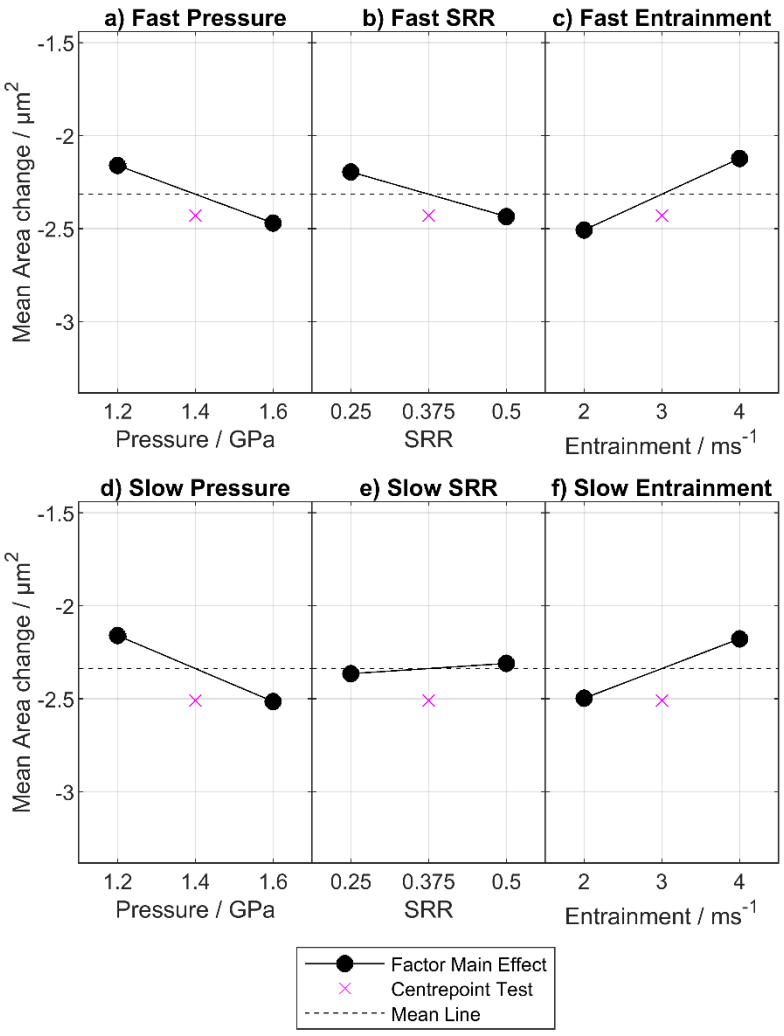

Figure 4.12.20 Main Effects of Pressure, SRR, and Entrainment on the mean cross-sectional area of asperities for the fast (a-c) and slow (d-f) surfaces.

It is notable that the centrepoint was located near the line between points for the slow surface Rc effects only, with all other parameters and surfaces indicating significantly nonlinear behaviour.

Two-Factor Interaction Effects

All three of the profile element measures are broadly similar again when their two-factor interaction effects are considered, but had a small number of differences in each case. The two-factor interaction effects on Rc are shown in Figure 4.12.21.

On the fast surface, a negligible interaction was seen between pressure and SRR, while both pressure and SRR interact strongly with entrainment. For both of these interactions, having both variables at the same setting (high or low) led to a greater reduction in Rc.

On the slow surface the interaction between pressure and SRR was more pronounced, with increased SRR reducing change in Rc at low pressure only, while increasing pressure reduced Rc only at high SRR. The remaining interactions on the slow surface matched the fast in effect, but were lower in magnitude.

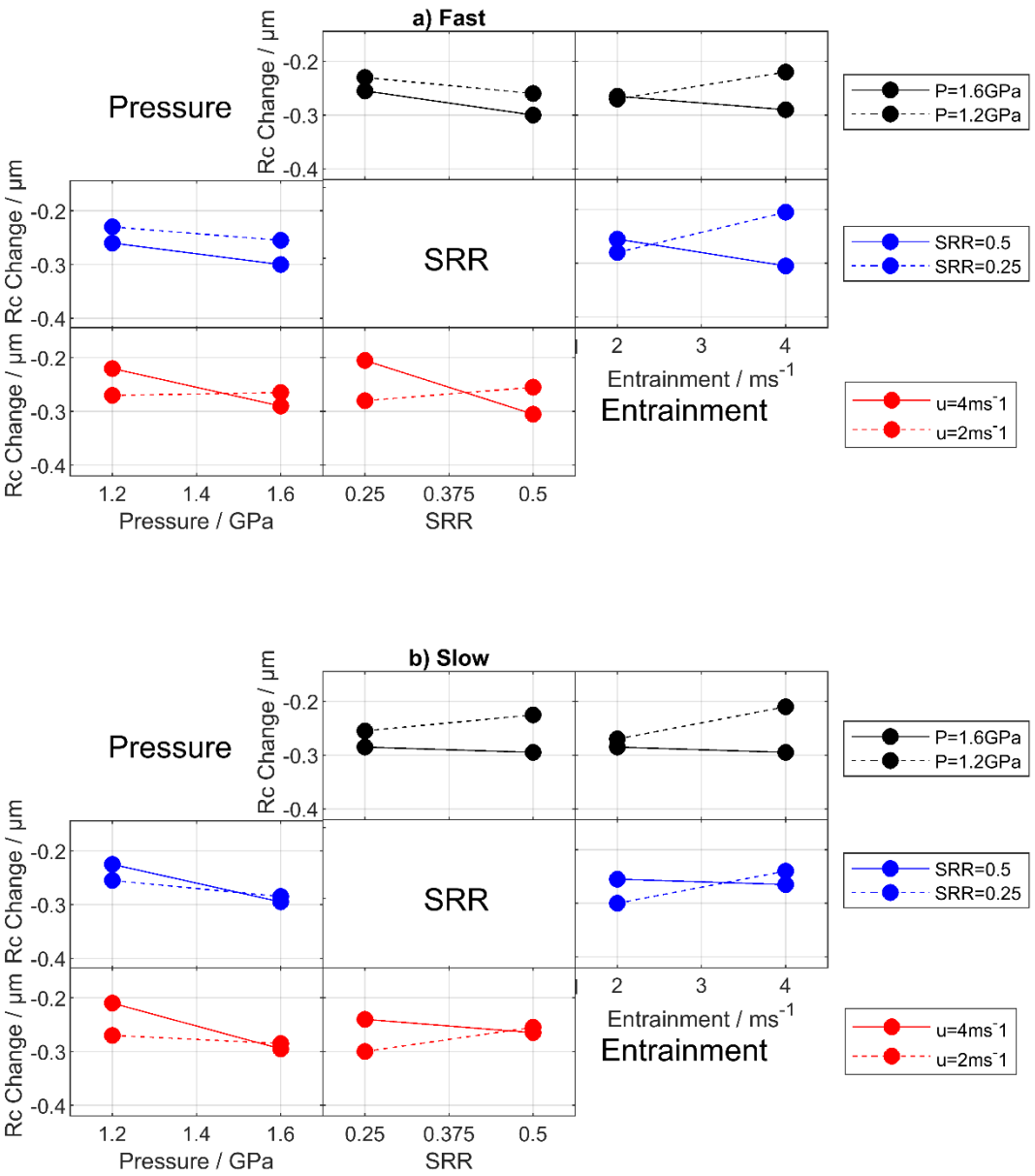

Figure 4.12.21 Two-factor interaction plots for pressure, SRR and entrainment on change in Rc through running-in.

The two-factor interaction effects for mean asperity height and mean cross sectional area of asperities are shown in Figure 4.12.22 and Figure 4.12.23 respectively.

On the fast disk, these closely matched the Rc interactions for pressure*SRR and SRR*entrainment, but the interaction between pressure and entrainment was in both cases much weaker than seen for Rc.

On the slow surface, the change in mean asperity height showed a much weaker interaction between pressure and SRR but otherwise was in agreement with Rc. The mean cross-sectional area of asperities meanwhile showed a weaker interaction between entrainment and SRR.

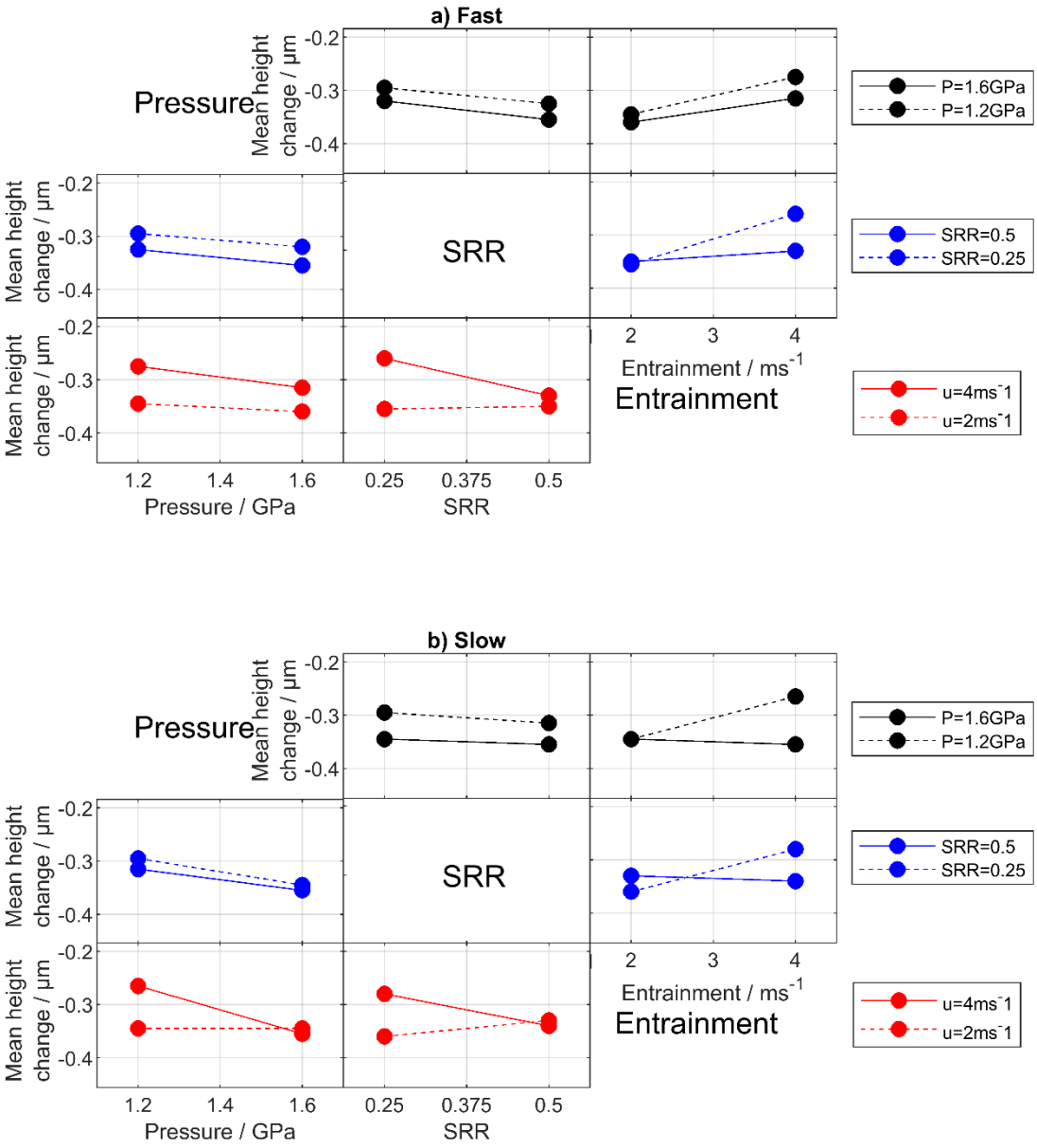

Figure 4.12.22 Two-factor interaction plots for pressure, SRR and entrainment on change in mean asperity height through running-in.

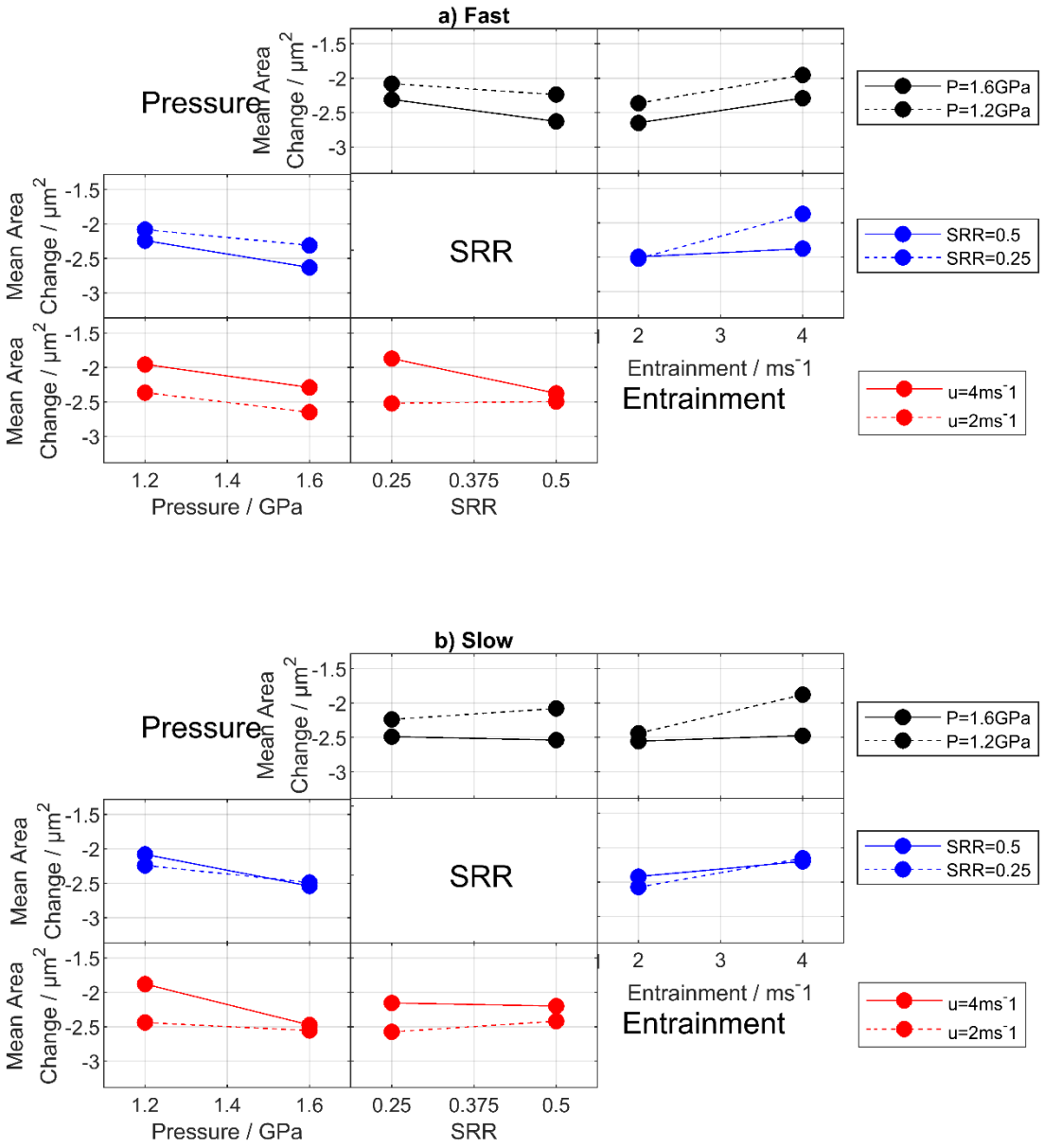

Figure 4.12.23 Two-factor interaction plots for pressure, SRR and entrainment on mean cross-sectional area of asperities through running-in.

Three-Factor Interaction Effects

Analysis of the change in the pressure*SRR interaction with entrainment showed that three-factor effects were present for all three parameters. The sole exception to this was the height change analysis for the slow surface only, which showed

negligible three-factor interaction. Plots showing the changing two-factor interactions for Rc, mean asperity height, and mean cross-sectional area of asperities are shown below.

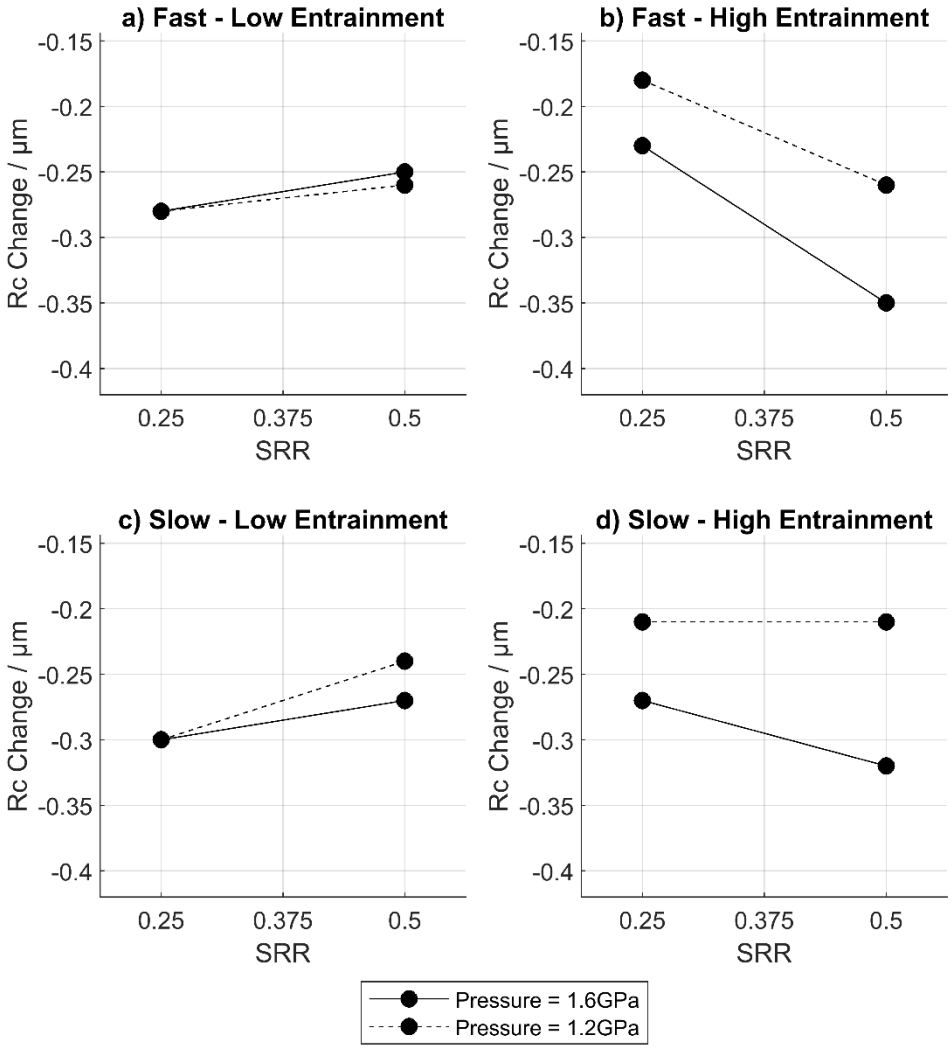

*Figure 4.12.24 Pressure*SRR interaction plots of change in Rc the a) fast and b) slow surfaces at low and high entrainment.*

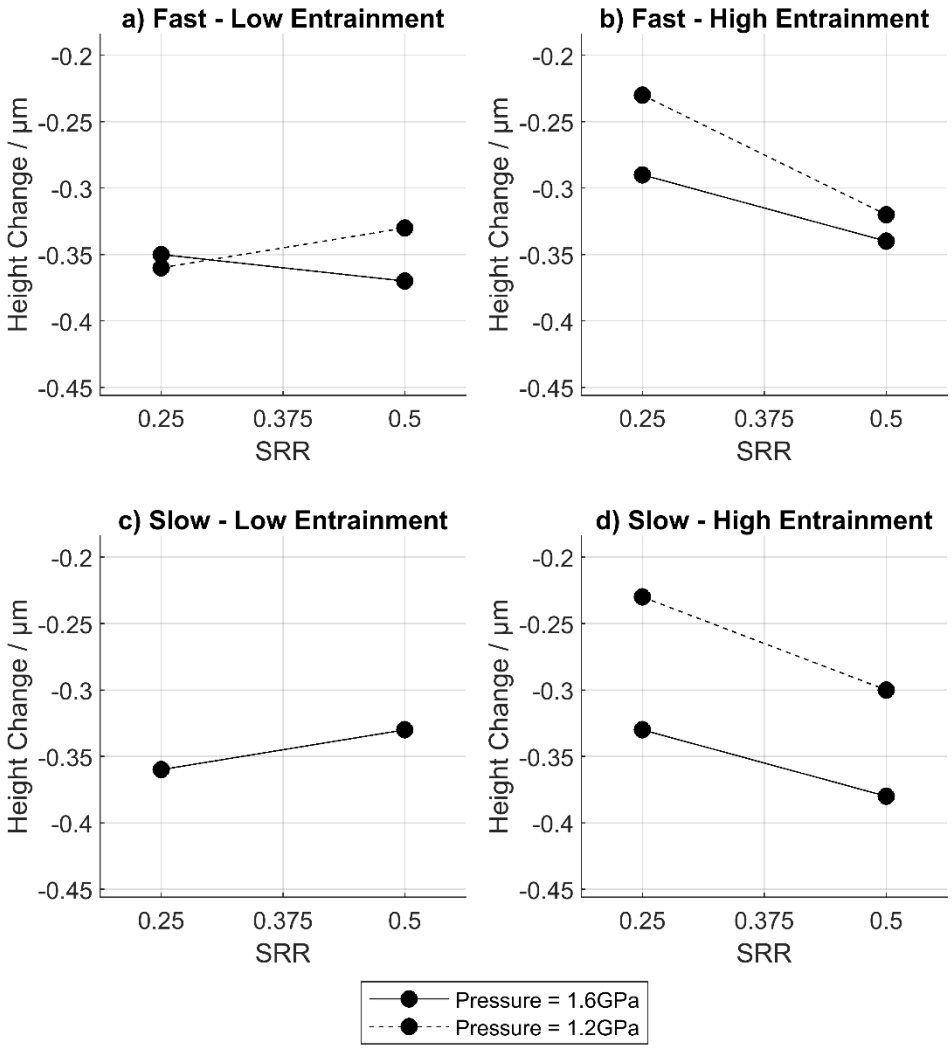

*Figure 4.12.25 Pressure*SRR interaction plots of change in mean height of asperities for the a) fast and b) slow surfaces at low and high entrainment.*

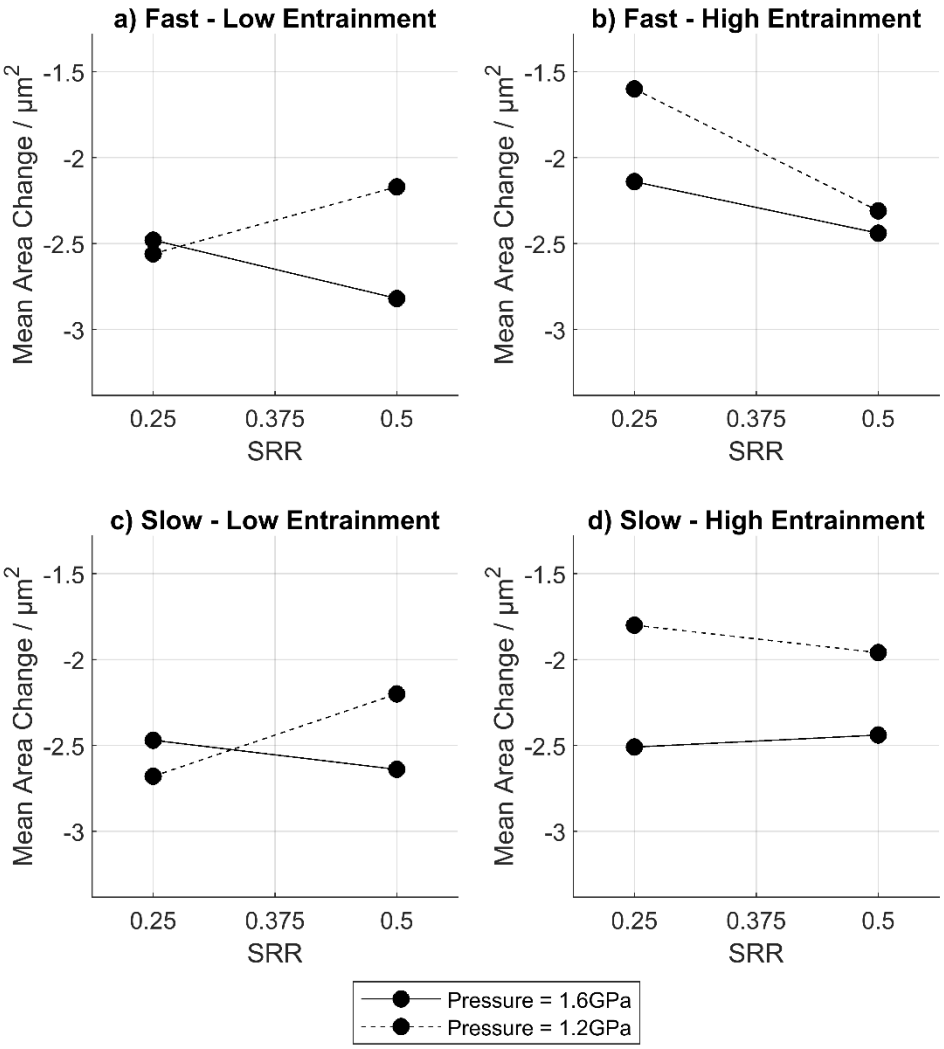

*Figure 4.12.26 Pressure*SRR interaction plots of change in mean cross-sectional area of asperities for the a) fast and b) slow surfaces at low and high entrainment.*

Strength of Effects

The strengths of main and interaction effects for the Rc, mean asperity height, and mean cross-sectional area of asperities are shown in Table 4.12.7, Table 4.12.8, and Table 4.12.9 respectively.

Table 4.12.7 Main and interaction effects for Rc

Factor / Interaction	Fast surface change in Rc			Slow surface change in Rc		
	Low average / µm	High Average / µm	Effect / Δµm	Low average / µm	High Average / µm	Effect / Δµm
Pressure	-0.245	-0.278	-0.033	-0.240	-0.290	-0.050
SRR	-0.243	-0.280	-0.038	-0.270	-0.260	0.010
Entrainment	-0.268	-0.255	0.013	-0.278	-0.253	0.025
Pressure*SRR	-0.258	-0.265	-0.008	-0.255	-0.275	-0.020
Pressure*Entrainment	-0.243	-0.280	-0.038	-0.248	-0.283	-0.035
SRR*Entrainment	-0.230	-0.293	-0.063	-0.248	-0.283	-0.035
Pressure*SRR*Entrainment	-0.268	-0.255	0.013	-0.268	-0.263	0.005

Table 4.12.8 Main and interaction effects for mean asperity height

Factor / Interaction	Fast surface change in asperity height			Slow surface change in asperity height		
	Low average / µm	High Average / µm	Effect / Δµm	Low average / µm	High Average / µm	Effect / Δµm
Pressure	-0.310	-0.338	-0.028	-0.305	-0.350	-0.045
SRR	-0.308	-0.340	-0.033	-0.320	-0.335	-0.015
Entrainment	-0.353	-0.295	0.058	-0.345	-0.310	0.035
Pressure*SRR	-0.323	-0.325	-0.003	-0.330	-0.325	0.005
Pressure*Entrainment	-0.318	-0.330	-0.013	-0.305	-0.350	-0.045
SRR*Entrainment	-0.305	-0.343	-0.038	-0.305	-0.350	-0.045
Pressure*SRR*Entrainment	-0.313	-0.335	-0.023	-0.325	-0.330	-0.005

Table 4.12.9 Main and interaction effects for mean cross-sectional area of asperities

Factor / Interaction	Fast surface change in asperity cross-sectional area			Slow surface change in asperity cross-sectional area		
	Low average / μm^2	High Average / μm^2	Effect / $\Delta\mu m^2$	Low average / μm^2	High Average / μm^2	Effect / $\Delta\mu m^2$
Pressure	-2.160	-2.470	-0.310	-2.160	-2.515	-0.355
SRR	-2.195	-2.435	-0.240	-2.365	-2.310	0.055
Entrainment	-2.508	-2.123	0.385	-2.498	-2.178	0.320
Pressure*SRR	-2.275	-2.355	-0.080	-2.285	-2.390	-0.105
Pressure*Entrainment	-2.303	-2.328	-0.025	-2.218	-2.458	-0.240
SRR*Entrainment	-2.183	-2.448	-0.265	-2.288	-2.388	-0.100
Pressure*SRR*Entrainment	-2.173	-2.458	-0.285	-2.228	-2.448	-0.220

4.12.5 Distribution of Heights: Rsk and Rku

The Rsk and Rku parameters give the skewness and kurtosis of the distribution of measured heights on the surface. The skewness property relates to the symmetry of the distribution and whether the peak is negatively or positively offset from that of a normal distribution. The kurtosis property relates to the "tails" of the distribution, a positive kurtosis indicating a sharp peak with long, thick tails, and negative kurtosis indicating a rounded peak with shorter, thinner tails.

Consideration of the unrun values of Rsk and Rku, shown in Table 4.12.10, reveals difficulties with analysis of Rsk and Rku: the values for both fast and slow surfaces of Test 1 are outliers compared to the values used for other tests.

Table 4.12.10 Unrun Rsk and Rku values for each test in the experimental programme

	Fast		Slow	
Test	Rsk	Rku	Rsk	Rku
1	-1.13	5.40	-0.95	5.17
2	-0.43	2.95	-0.44	3.12
3	-0.26	3.31	-0.38	3.09
4	-0.33	3.35	-0.48	3.25
5	-0.26	2.82	-0.53	3.51
Centrepoint	-0.48	3.64	-0.69	3.99
6	-0.57	3.31	-0.82	3.88
7	-0.52	3.41	-0.46	3.21
8	-0.46	3.02	-0.64	3.34

The Test 1 disks were part of a small initial batch of disks ground at the beginning of the testing process, the remainder of this batch being used in tests which scuffed during the scoping phase of the programme. While the grinding process and grit of the grinding wheel were the same as used for the other disks in the programme (as detailed in Section 3.2.3), minute differences in conditions and the use of a new (though nominally identical) grinding wheel appear to have produced differences in these measures of the distribution. Other roughness parameters remained comparable to other tests in both initial value and behaviour and hence are still considered valid.

Considering these initial values, and the larger changes recorded for Rsk and Rku for Test 1, it is likely that inclusion of Rsk and Rku in the analysis would falsely influence the calculated effects. By design, Tests 2, 6, 7, and 8 represent a $2^{(3-1)}$ factorial test programme, and do not include the values from Test 1. Analysing the results using only these tests allows an estimation of the effects of pressure, SRR,

and entrainment on Rsk and Rku. The main effects are however confounded with two-factor interaction effects, which must be kept in consideration when interpreting the results.

Effects of Factors

The effects on Rsk and Rku are shown in Figure 4.12.27 and Figure 4.12.28 respectively. In each of these, the main variable in question is confounded with the interaction effect of the remaining two variables – for example, plot a) shows the pressure effect, plus the interaction of SRR and entrainment.

In both cases both pressure and entrainment appear to influence the parameter in different directions on each surface, while the SRR influences in the same direction on both – albeit with a different magnitude. In all cases the centrepoint value is located a significant distance from the line, indicating nonlinear behaviour.

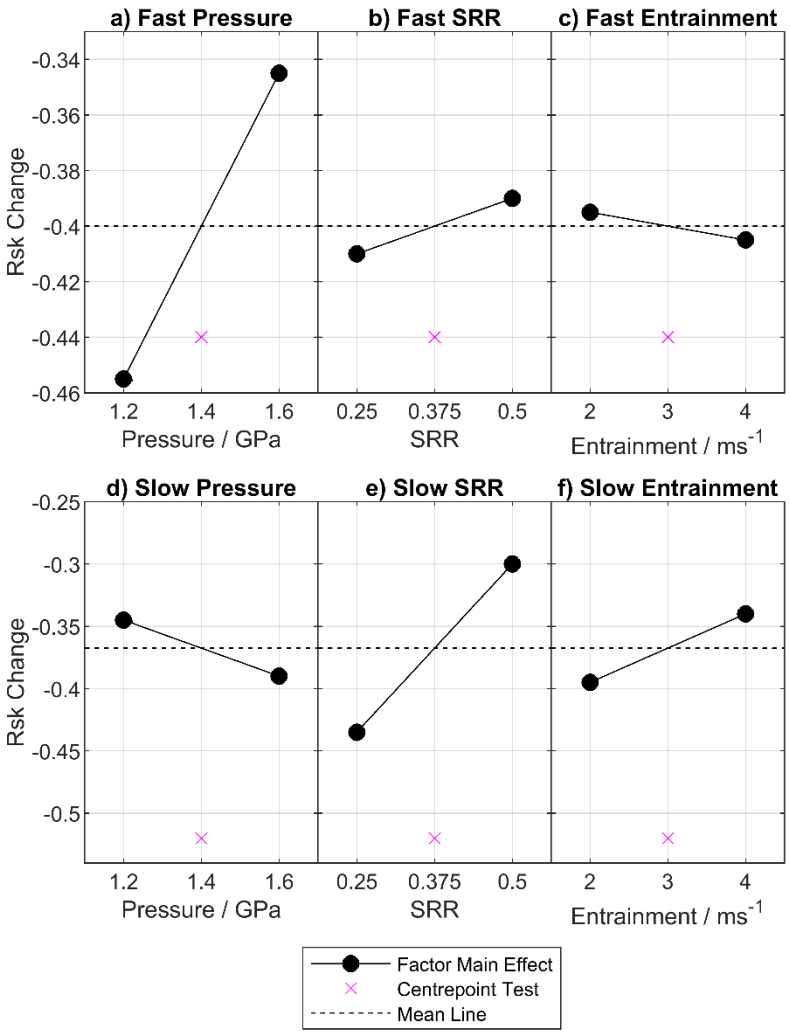

Figure 4.12.27 Effects of Pressure, SRR, and Entrainment on Rsk (mean absolute roughness) for the fast (a-c) and slow (d-f) surfaces.

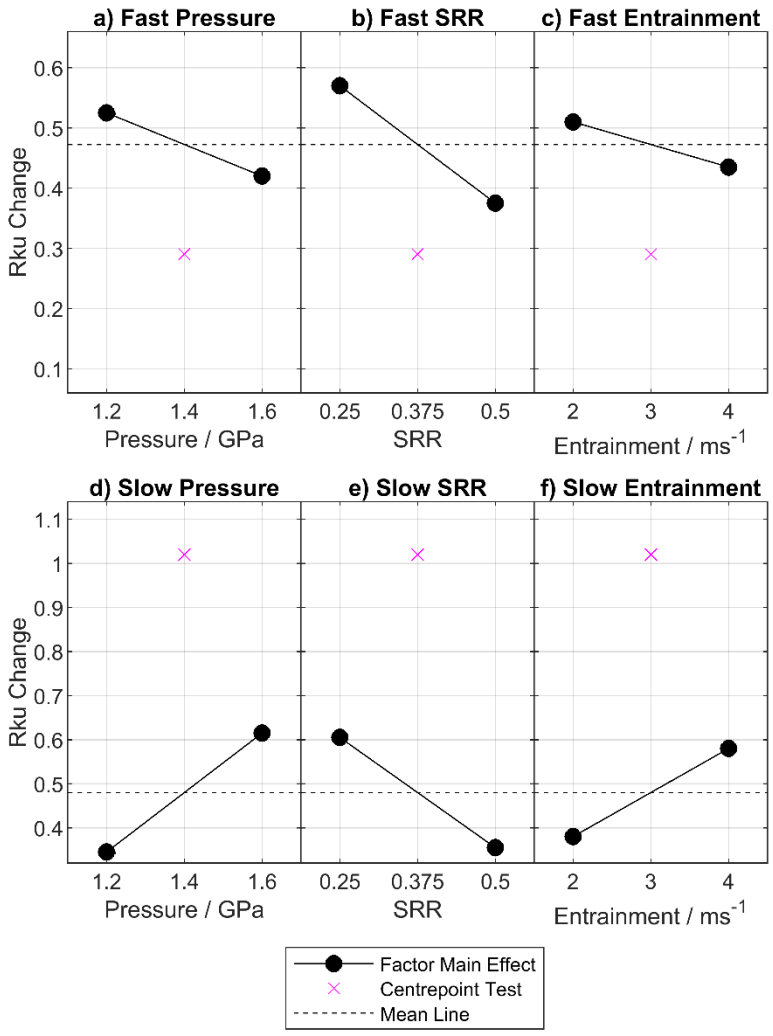

Figure 4.12.28 Effects of Pressure, SRR, and Entrainment on Rku (mean absolute roughness) for the fast (a-c) and slow (d-f) surfaces.

Very little information can be gathered from the results for Rsk and Rku shown here. The presence of interaction effects in all running-in processes investigated suggests that interaction effects are likely present in these results too, although they cannot be discerned from this fractional factorial analysis. Considering that there is still considerable range in the Rku and Rsk initial values even after the outlying Test 1 results are removed, it is quite possible that initial values still have an ongoing effect in the results.

Two things can still be gathered from these results however:

Firstly, Rsk decreases with running-in. This confirms an expected outcome as the removal of peak features reduces the number of points on the positive side of the distribution, while valleys remain on the negative side.

Secondly, Rku increases with running-in. Rku is a complex feature to relate to the physical changes in the surface, but likely results from the shortening of the positive tail of the distribution and thickening of the earlier part of that tail as the highest peaks are deformed into shorter, flatter asperities.

4.12.6 Modelling of Running-in Behaviour

The results of a full factorial experiment can be used to create models to predict the values of an output as detailed in Section 3.9.3. This modelling process assumes linear behaviour, which was only indicated in a small number of cases for the running-in shown here – although repeats of the centrepoint test would be able to confirm this. Specifically, the Ra appeared to change linearly for both surfaces, as did Rp for the slow surface only, and radius of curvature of asperities for the fast surface only.

Factorial response models for running-in can be found in Appendix 2 along with a summary of the coefficients used to produce them.

4.13 Discussion – Running-in

Influence of Pressure, SRR and Entrainment Velocity

The analysis of running-in performed in this work has been able to identify several trends in the running-in behaviour of surfaces. Moreover, it has been able to show that pressure, sliding, and entrainment velocity have both individual and combined

influences on the way in which surfaces adapt to contact during the earliest stages of operation.

The most reliable main effect was that of pressure, which consistently resulted in a greater change in roughness parameters through running-in on both the fast and slow surfaces. This is an expected outcome as the increased load induces greater amounts of plastic deformation on asperities, and increases frictional effects which encourage wear processes to round off or remove high points from the surfaces.

Entrainment velocity typically protected the surface and reduced the amount of change seen through running-in. The method by which this is achieved is almost certainly through generation of a thicker lubricant film to separate the two surfaces more effectively. The effect of entrainment velocity was less certain for the parameters that concerned "extreme profile features" – i.e. for Rp, Rz, Rv, and Rt.

The influence of entrainment on Rp was shown to be very small. This can, however, be easily reconciled with the strong protective effects seen for general roughness and element-wise parameters: The thicker lubricant films formed through increased entrainment more effectively protect average-sized asperities, while the tallest outliers still protrude through the film and are hence still aggressively reduced in height.

The influence of entrainment on Rv was much more complex and appeared to act in opposite directions on each surface. On the fast surface increased entrainment resulted in a smaller decrease in Rv; an expected result as the increased entrainment would protect the surface and result in a smaller decrease in the height of the mean line. On the slow surface the mean result would suggest that increased entrainment resulted in a greater reduction in Rv. The majority of results were very closely grouped for the slow surface however, and the high entrainment result was

heavily influenced by a single outlier from a test in which wear was induced. It is possible that the action of wear lowered the mean line a slightly greater amount for this test, creating the appearance of a larger effect on an otherwise small-to-negligible influence from entrainment. This cannot be confirmed without test repeats, however.

Rz was largely governed by the change in peak height, and the smaller decrease in Rz (compared to Rp) on the fast surface when entrainment was high was accounted for by the change in Rv. The apparent negligible effect of entrainment on slow surface Rz may again be the influence of the outlying Rv result discussed above.

The result for the fast surface does however beg the question of whether the Rz parameter is a more robust means of evaluating change in during running-in than Rp. The Rp must in a sense be qualified by concurrent inspection of the Rv to separate the contributions from peak height reduction and change in mean line height. The Rz parameter has this comparison in-built, hence if the valley features are known not to change, Rz may provide the more robust approach.

SRR, the final main factor investigated, exhibited complex behaviour that was not consistent between the fast and slow surfaces. Fast surface results typically showed the SRR to have main effects acting to induce a greater change in each output through running-in, while the slow surface results typically showed minimal/negligible influence from SRR. In cases such as the “profile element measures” grouping of output variables, the slow surface SRR appears to affect the surface by small amounts in different directions depending on the output. Close inspection of the values contributing to these effects shows considerable overlap between the high and low setting values - making it very possible that with more repeats, the slow surface may exhibit no influence from SRR on these factors.

On the fast surface the SRR effects were stronger, and even where groups overlapped there was sufficient offset between them to imply genuine effects - although the SRR main effect on Ra is perhaps on the border of these states.

Significantly though, one output for which SRR shows strong effects on both the fast and slow surfaces is the change in mean radius of curvature of asperities. On both surfaces there is a clear trend of increasing SRR leading to greater increase in radius of curvature, likely due to increased abrasive action and interface heat generation arising from the increased sliding.

Multi-Factor Effects

The full factorial analysis performed here indicated not only the presence of the main effects of factors on the running-in process, but also the presence of several two- and three-factor effects.

These influences varied depending on the parameter in question, though perhaps the most commonly-seen interaction showed entrainment velocity having a stronger protective effect at low pressure than high (Seen on both surfaces for Ra, Rq, Rp, Rz, Rc, and Asperity Heights). Another commonly seen interaction was between entrainment and SRR, where having both set high or low produced a greater change in the surface than having one each high and low (both surfaces: Ra, Rq, Rp, Rz, Rc).

The presence of these interactions (and the still more complex three-factor interactions) shows that the running-in process is the product of many interconnected inputs. The mechanisms through which these influence the surface may take several forms - such as frictional, thermal, and chemical effects, the number of loading scenarios (contact points between disks), or the specific film thickness.

4.14 Summary – Running-in

This investigation into the influence of contact conditions on running-in was able to identify a number of influences on running-in behaviour. Pressure was found to increase surface modification for all metrics across both surfaces, with a greater influence apparent on the slow surface. Entrainment exhibited the opposite effect, with increased entrainment resisting modification of the surface through running-in. SRR was found to have very little effect on the slow surface, while increasing fast surface modification – although SRR was a driving influence on radius of curvature for both surfaces. Two- and three-factor effects were present for all parameters investigated, indicating that a complex network of individual and multi-factor interactions drives the modification of the surface during running-in.

5 Full-Factorial Experimental Investigation of Micropitting

5.1 Introduction

This chapter concerns the micropitting behaviour observed in this programme of tests. Each test is first discussed individually before then analysing all tests together as a full factorial experimental programme to assess the influence of each variable on micropitting behaviour.

The conditions under which each test was conducted can be seen in Table 4.1.1, while Table 5.1.1 shows the calculated Λ for each test in the experimental programme. It should be noted, as discussed in Section 3.10, that a resolution of 0.016μm in the profilometer gauge may introduce a small amount of error into the raw profile heights used to calculate Rq. Additionally, film thickness values from simulation do not account for any side leakage effects, which may reduce the film thickness in a rough-surface elliptical contact. Cycles per load stage are shown in Table 3.9.2.

Table 5.1.1 Specific film thickness for each test, calculated using Rq values after running-in, and central film thickness from smooth point simulations performed using real test temperatures for lubricant properties.

Test	Fast Surface Rq / μm	Slow Surface Rq / μm	Smooth Point Central Film Thickness / μm	Specific Film Thickness, Λ
1	0.49	0.42	0.149	0.156
2	0.39	0.40	0.104	0.117
3	0.37	0.45	0.139	0.153
4	0.43	0.44	0.164	0.176
5	0.46	0.42	0.271	0.289
Centrepoint	0.50	0.44	0.178	0.184
6	0.49	0.50	0.205	0.206
7	0.48	0.49	0.179	0.182
8	0.46	0.52	0.246	0.248

5.2 Test 1

As was discussed in Section 4.2, the first test in the programme exhibited unusual behaviour during the running-in period, the contact area becoming divided into two side regions and a shiny central band. This was likely the result of a combination of plastic deformation and wear processes acting upon the surfaces.

In-test data for the contact voltage, contact friction, and disk temperature in Test 1 are shown in Figure 5.2.1. Data did not record correctly during the first running-in stage of the test (0 – $3x10^3$ fast disk cycles), hence data is not displayed for this period. In the second phase of running-in the recorded friction rose to a peak where maximum values reached 217 N. The friction value then decayed through the remainder of the test, the rate of this decay decreasing as the test progressed - mean values of friction from load stage 6 until the end of test decreased by less than 3 N.

As the friction decreased, a rise was seen in the contact voltage. Initial readings averaging 0.2 mV during the second running-in stage indicated considerable direct asperity contact between the surfaces. This began to increase at around $1x10^4$ total fast disk cycles, indicating that through plastic deformation, wear, and fatigue, the most severe asperities had been removed or reduced in size. This increase continued through the test, with the average reading during load stage 7 ($2x10^5$ – $3x10^5$ fast disk cycles) reaching 35.5 mV out of a possible 45 mV. The average value during the final load stage (not shown below) reached 40.2 mV.

Throughout the test the disk temperature stabilised to 111 ±1.5°C.

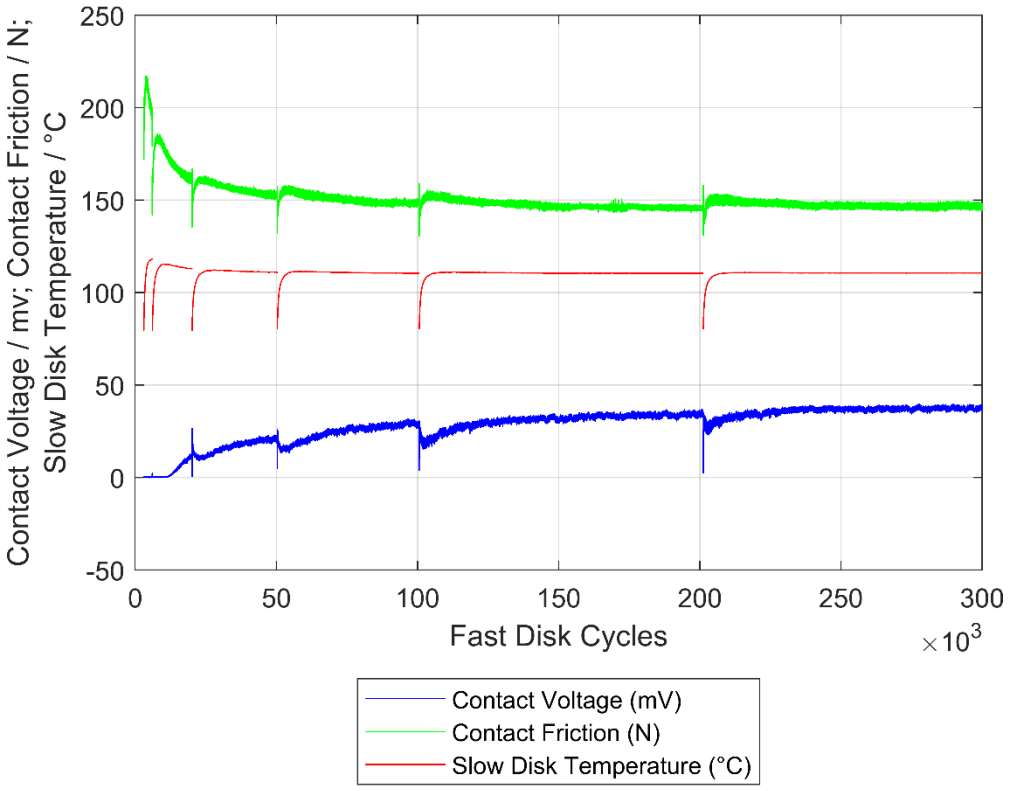

Figure 5.2.1 In-test data for the first 3x10^5 cycles of Test 1.

In Figure 5.2.2, showing the fast disk surface after running-in, a clear observation is that while the different appearance of the central band was clear to the naked eye it was not obvious in replica surface scans. Very close inspection of the Test 1 surfaces at this test stage showed that a very small amount of pitting had already taken place. These pits have been highlighted in the figure. On both surfaces, these pits typically formed in clusters along asperities, with the occasional lone pit. One asperity on the left side of the fast surface scan showed quite aggressive pitting for such an early point in the test, while most pits were shallow and small.

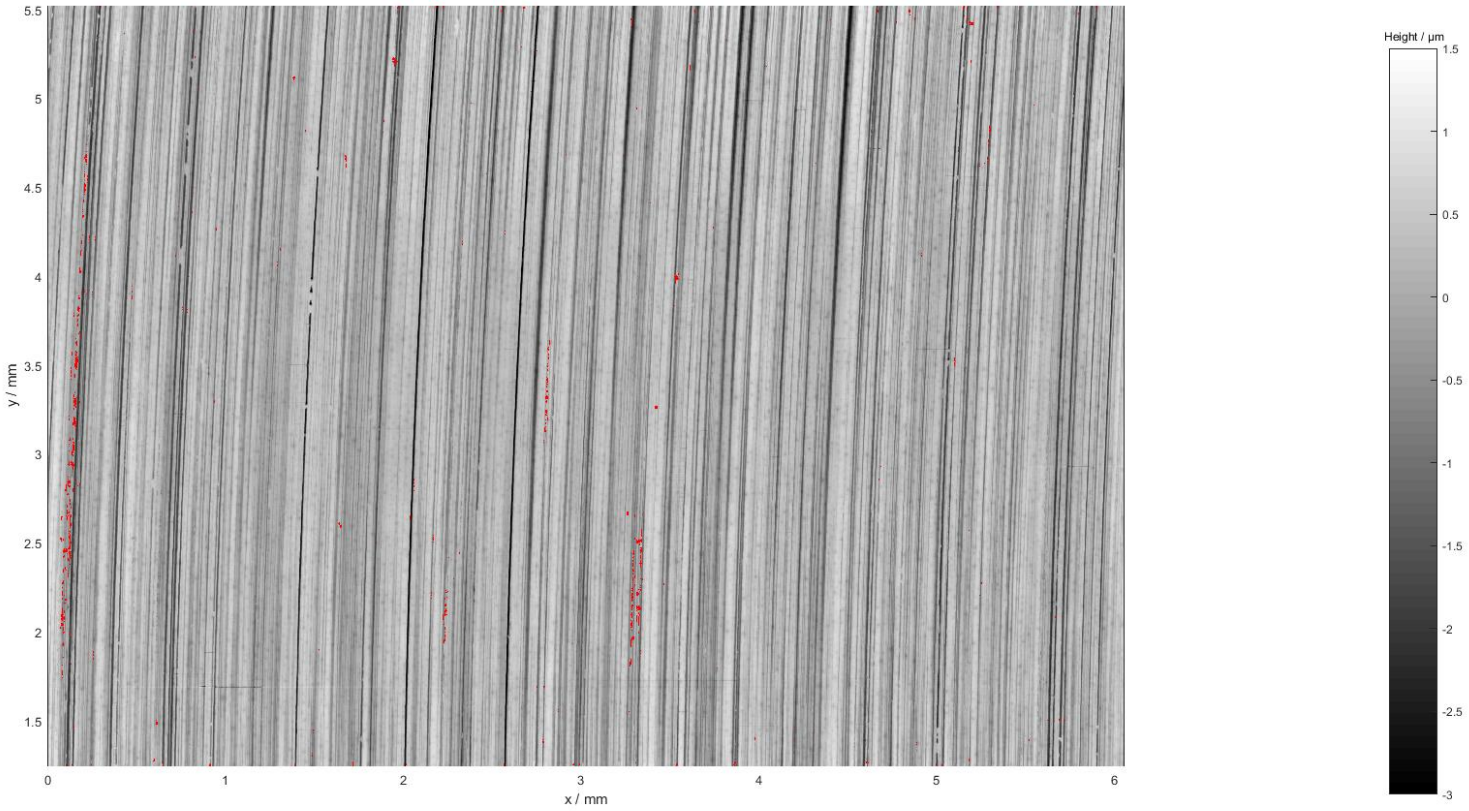

Figure 5.2.2 Fast surface in Test 1 after running-in, with pits overlaid in red

At the close of running-in, the small number of micropits that had formed did so both inside and outside of the central band. This did not remain the case as the test progressed. Instead, the central band exhibited a resistance to micropitting, while the regions either side of this band micropitted extensively.

Figure 5.2.3 showing the surfaces after load stage 12 illustrates this behaviour. While some pits can still be seen in the central region, the development of micropitting was very effectively limited in this central region. It is notable that the border between the heavily pitted and non-pitted regions is very clearly defined; i.e. there is not a gradual decrease in the concentration of micropits from the side regions to the central band, but a sudden change between heavy micropitting and unaffected surface.

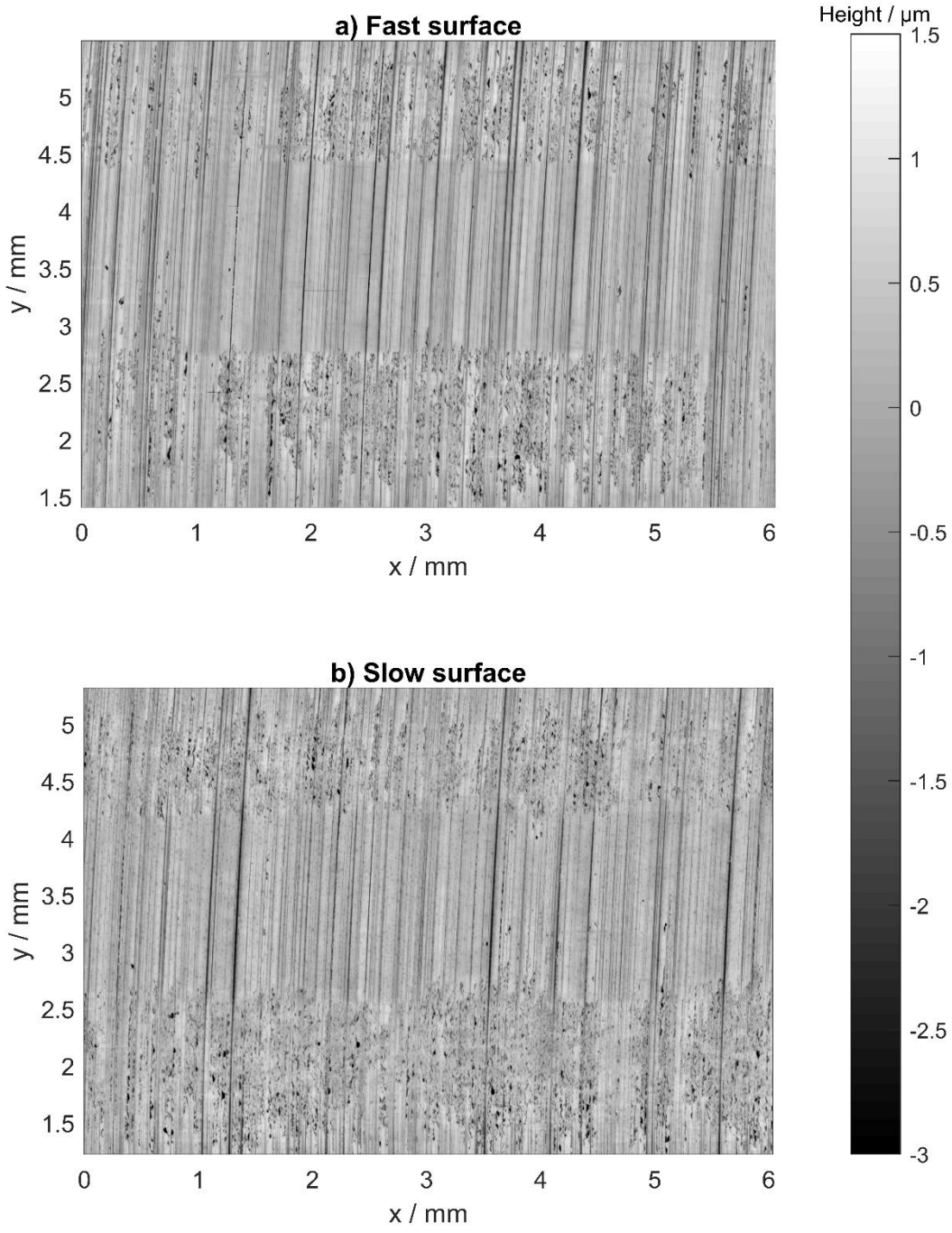

Figure 5.2.3 a) Fast and b) slow disk surfaces of Test 1 after load stage 12. On each surface a central band is seen to be only very mildly micropitted, while heavy micropitting is clear outside of this central region.

The formation of this fatigue resistant central band influences the analysis of micropitting, as consideration of the whole contact width is no longer representative of the of the influence of the three factors considered. Although the location of peak hertzian pressure and nominal location of thickest film fall inside the area of the central band, it is not unreasonable to assume that if one were able to "switch off" the mild wear processes that produced that band it would likely look very similar to the regions either side. Therefore, the side regions alone are used in the factorial analysis of micropitting.

Figure 5.2.4 shows the percentage of area pitted on the Test 1 surfaces, considering the whole surface together, as well as separately presenting the central band and side regions alone. Due to the low density of micropitting, the central bands are more strongly influenced by slight differences in alignment of the surface in the scan. This allows micropitted asperities on the edges of the measured region in the centre to be included or missed in the scan.

The micropitted area grew very rapidly in the early stages of the test if the side regions alone are considered, and by $5x10^4$ fast disk cycles the percentage micropitted area had reached 3.49% and 4.61% for the fast and slow surfaces respectively. The slow disk surface exceeded 5% micropitted area shortly after load stage 4, while the fast disk did not surpass this value until approximately $4x10^4$ further fast disk cycles had passed. The slow disk maintained a larger micropitted area than the fast disk throughout the test, reaching 14.80% pitted surface at the conclusion of load stage 12 (the standard test length), while the fast disk reached 12.67%. An additional 2 million fast disk cycles were run after load stage 12 across four further load stages. This was in order to see whether the defined bands would remain as such over a longer test – this was found to be the case.

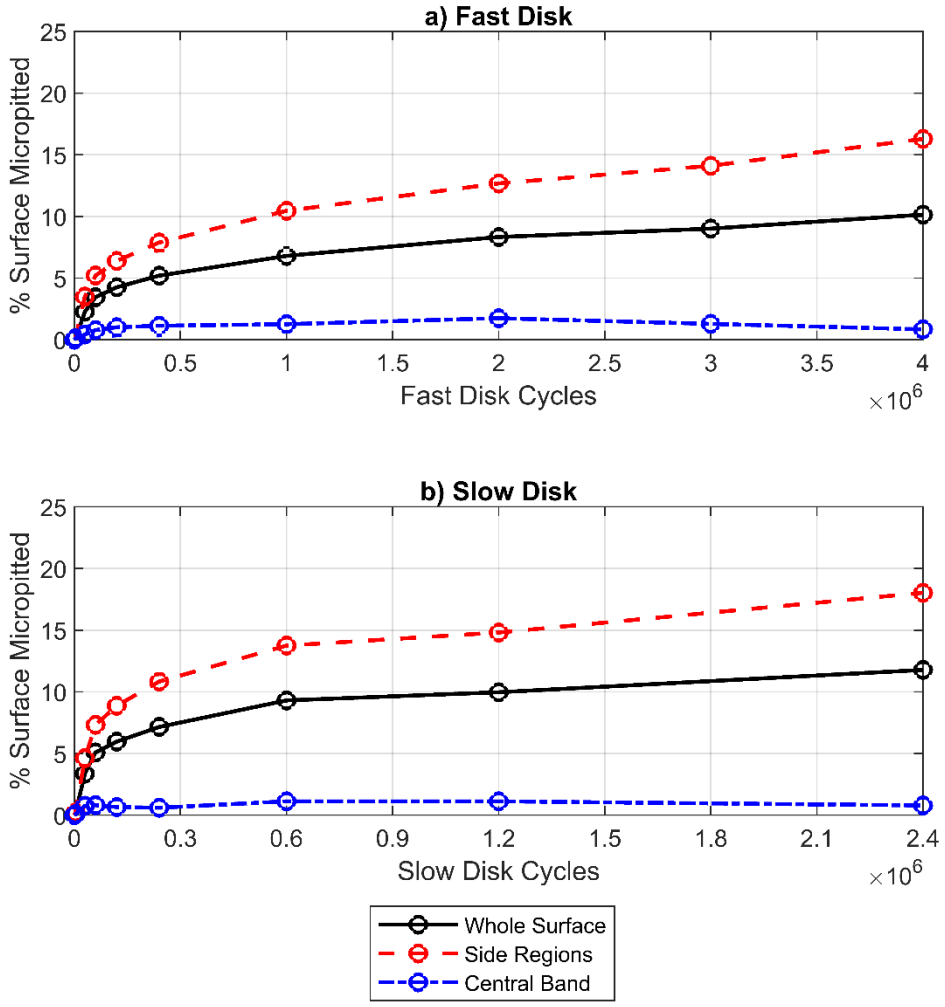

Figure 5.2.4 Percentage of surface area micropitted on the a) fast and b) slow surfaces. The slow disk replica at the conclusion of load stage 14 (1.8 x 10^6 slow disk cycles) was omitted due to damage.

Figure 5.2.5 shows the percentage of surface pitted evaluated for the side regions only, both by the areal analysis and by the two-dimensional profile analysis. It is clear from this that the two-dimensional profile method very significantly underestimated the micropitting on the surface early in the test. The slow surface two-dimensional analysis meets the areal analysis value at the end of load stage 8, while on the fast surface this happens mid-way through load stage 7. On both surfaces the two-dimensional analysis value continued to increase more rapidly than

the corresponding areal analysis, growing the gap between the two methods. At the close of load stage 12 (2 million fast disk cycles) the fast and slow two-dimensional analyses showed 21.05% and 20.17% micropitted respectively. These differed from the areal analysis by factors of 1.7 and 1.4 respectively.

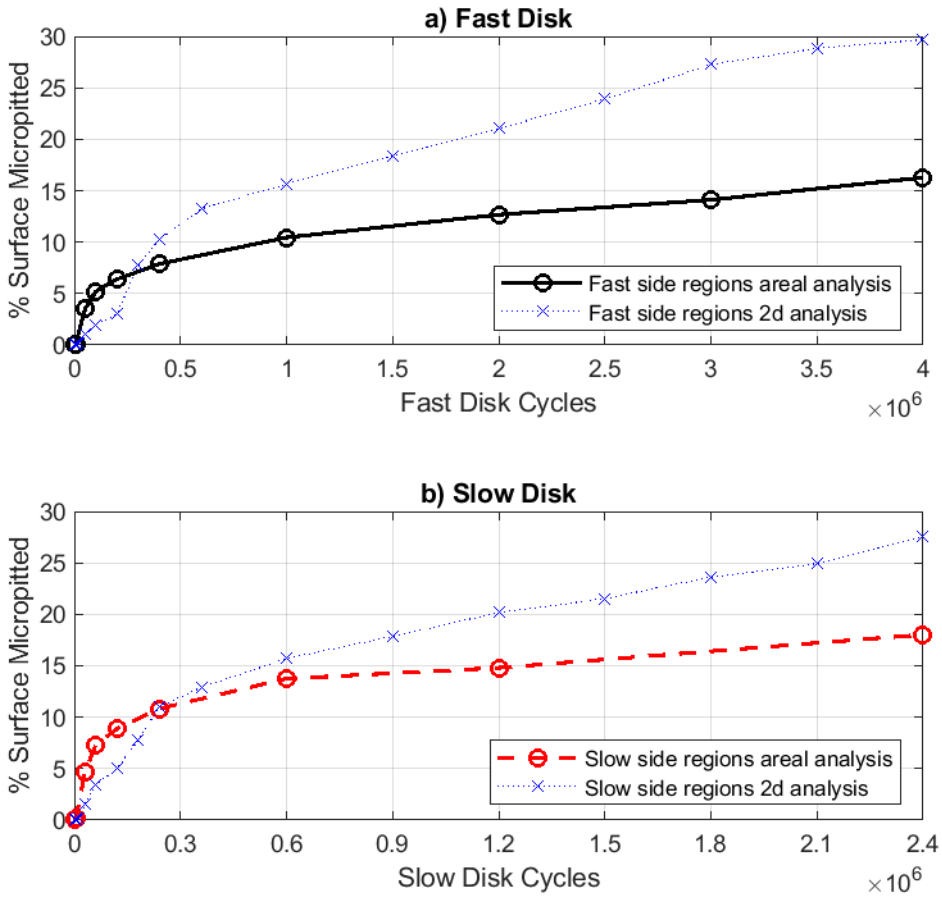

Figure 5.2.5 The percentage of surface pitted for the side regions of the a) fast and b) slow surfaces of Test 1, evaluated by both areal and two-dimensional profile analysis methods.

Large differences were seen in the rates at which micropitting progressed on each surface, particularly in the early stages of the test. While this can be observed in the figure above, Figure 5.2.6 provides a clearer representation of the micropitting

rate up to load stage 12. These graphs show the average rate of increase (in % area per cycle) between subsequent surface scans. The peak rate of increase of micropitting per cycle of the slow surface was 2.17 times the peak rate of increase per cycle on the fast surface. For both surfaces the peak rate occurred between load stages 2 and 4, after which it decayed to a much lower rate.

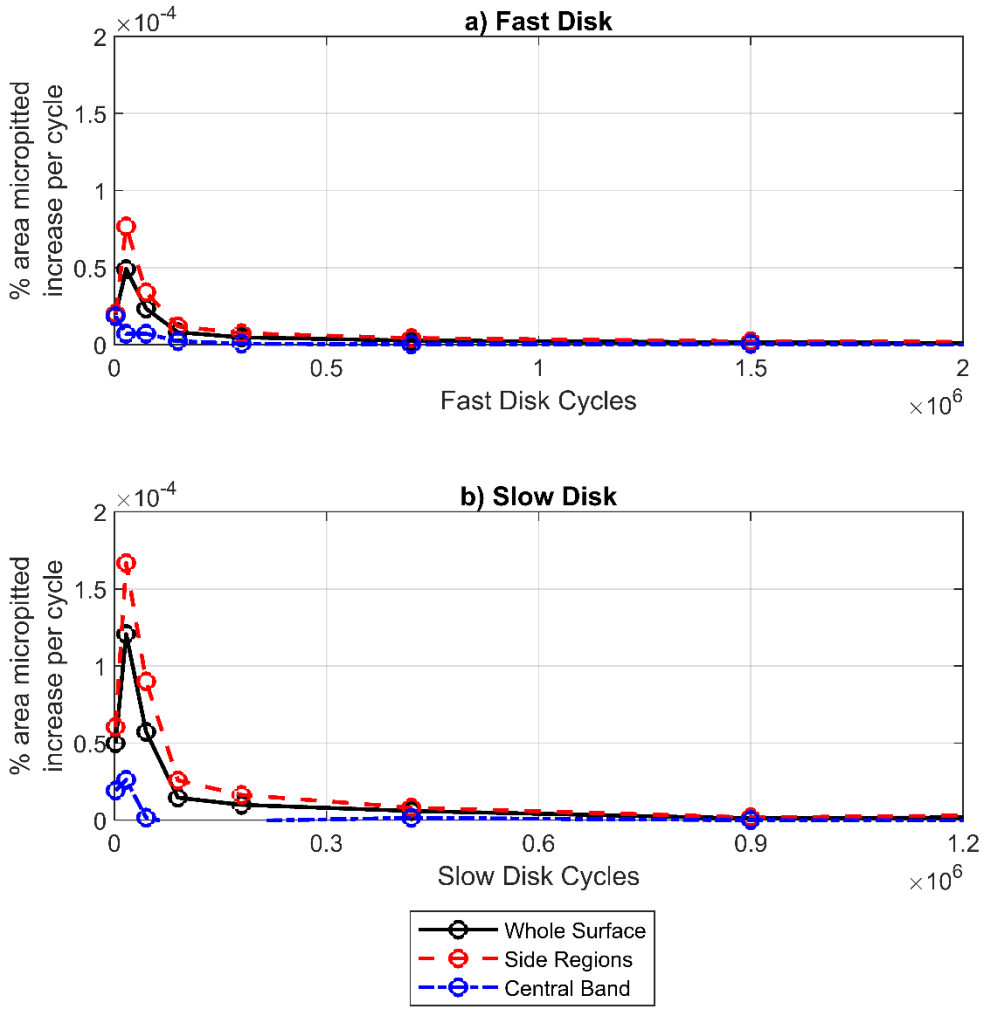

Figure 5.2.6 Rate of increase of micropitted area for the a) fast and b) slow surfaces. Each data point represents the average rate between two measured replicas, with the data point located halfway between these on the graph. Data is shown up to load stage 12 to allow early test data to be seen.

Also of interest is the volume of material removed from each surface. Using the methodology discussed in Section 3.7 the material removed from the surfaces by micropitting after load stage 16 was calculated. At this stage of the test the volume of material removed from the slow disk per unit area ($95.7x10^3$ $\mu m^3/mm^2$) was very similar to that on the fast disk ($92.3x10^3$ $\mu m^3/mm^2$), while the percentage of slow disk surface area pitted was 1.1 times that on the fast disk at this stage. The implication of this is that the average volume of a pit on the fast disk after load stage 16 was greater than on the opposing surface. Considering the mean height for the deepest 5% of micropitted points, referred to henceforth as D5, it would appear that this is not due to significantly deeper pits on the fast surface, and differences in pit shape must account for some of this.

To estimate the volume removed after load stage 12 (to allow comparison with other tests as part of the factorial test design), it was assumed that the volume removed scales linearly with % area pitted and calculated from the volume removed at the end of the test. The results of this analysis are shown in Table 5.2.1 along with the other fractional factorial metrics for Test 1. Parameter N3 is the number of cycles to reach 3% pitted (assuming linear variation between data points). The value of D5 is calculated for the end of test surfaces. For all tests, micropitting parameters are determined from the areal analysis results. The results of the two-dimensional approach are discussed in Section 5.13.1

Table 5.2.1 Factorial evaluation metric values for Test 1

Parameter	Fast Surface	Slow Surface
% Micropitted at conclusion of load stage 12	12.67	14.80
N3 / FD cycles	43,515	33,817
Peak rate of micropitting %/cycle	76.73×10^{-6}	166.70×10^{-6}
Average rate of micropitting between LS08 and LS10 %/cycle	4.28×10^{-6}	8.09×10^{-6}
Volume removed $\mu m^3/mm^2$	71.8×10^3	78.0×10^3
D5 / µm	-1.77	-1.73
% Micropitted at $1x10^5$ FD cycles	5.20	7.32

5.3 Test 2

As with the previous test, the disks in Test 2 exhibited unusual running-in behaviour attributable to wear processes. These left the disks with shiny "islands" of wear, giving the disks a patched appearance. This is discussed at length in Section 4.3. Within the measured area of the fast surface there was one large island of wear, while the slow disk measured area instead included three smaller areas of wear.

Figure 5.3.1 shows the in-test data recorded during Test 2. The contact voltage during the running-in stages of the test again showed very high levels of direct contact between the two surfaces, with mean values of 0.84 mV and 0.67 mV. The

contact voltage then began to increase rapidly through load stage 3, climbing to 15 mV at the conclusion of the stage, indicating a lubrication regime that is still mixed but with much reduced direct contact. A slow increase in contact voltage continued through the test, reaching a mean value of 37.8 mV during the final stage.

The disk temperature reached an initial peak during the first load stage of 104°C, and then in subsequent stages stabilised at 101 ±0.5°C for the remainder of the first 1 million fast disk cycles. A gradual rise of approximately 1.5°C was observed across the final 1 million fast disk cycles.

Friction data failed to record correctly during the first load stage due to a faulty cable which was subsequently replaced. Figure 5.3.1 shows a friction value of approximately 208 N at the start of the load stage 2, which rapidly decreased to a stable 180 N by $5x10^4$ fast disk cycles. After $6x10^5$ fast disk cycles this began to gradually increase, reaching a value of 200 N by the end of test. This likely accounts for the rise in temperature over these later stages. Friction spikes which are visible at the start of each test recording are due to thermal effects, and the thicker lubricant film present in the contact before the temperature increases.

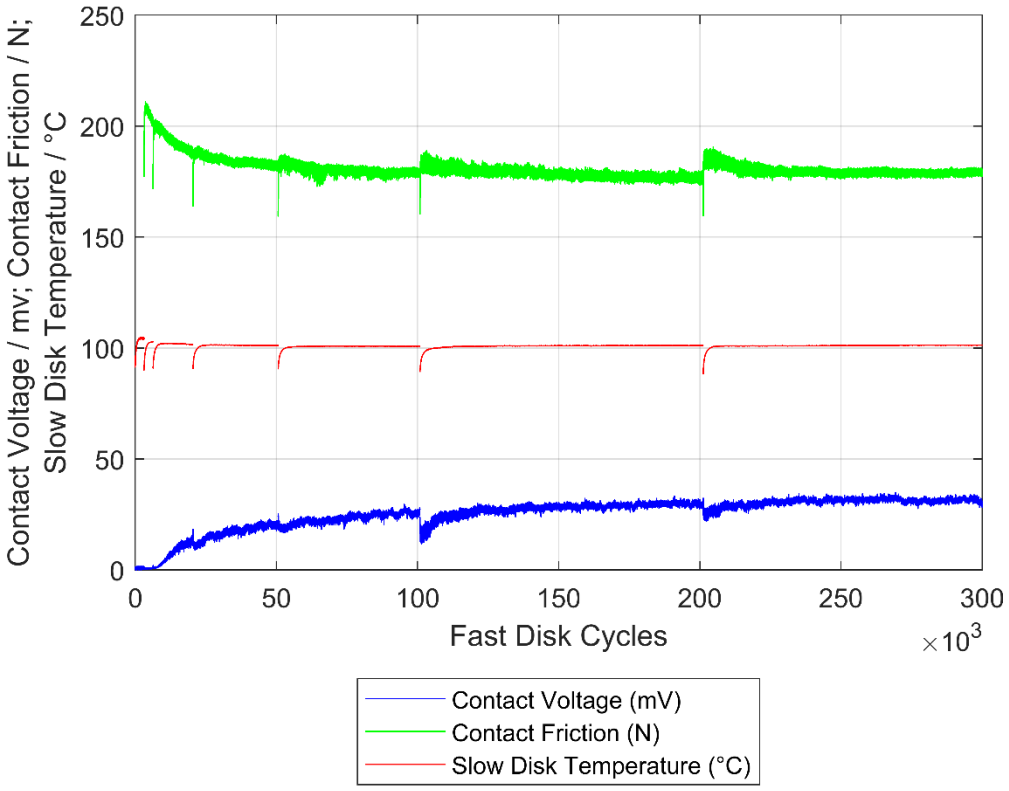

Figure 5.3.1 In-test data recorded for the first 300k fast disk cycles of Test 2

Again, micropitting began on both the fast and slow surfaces in the earliest stages of the test with the first micropits detected after load stage 2. Similarly to the previous test, these micropits were in their infancy and only visible under very close inspection due to their small size and shallow depth. The extent of micropitting at this stage was greater on the fast surface than on the slow surface with values of 0.40% and 0.19% respectively.

At the conclusion of load stage 4, micropitting was well established on both surfaces. The micropit-resistant wear island on the fast surface was already very clear (refer to Figure 4.3.3), however due to their much smaller size the wear areas on the slow disk were harder to distinguish in areal scans at this point, becoming clearer as the micropit density on the rest of the surface increased. Figure 5.3.2

shows the fast and slow surfaces after load stage 4. Pits at this stage of the test are not as developed as later in the test, making the smaller pits harder to distinguish – therefore pits have been overlaid in red in this figure for clarity.

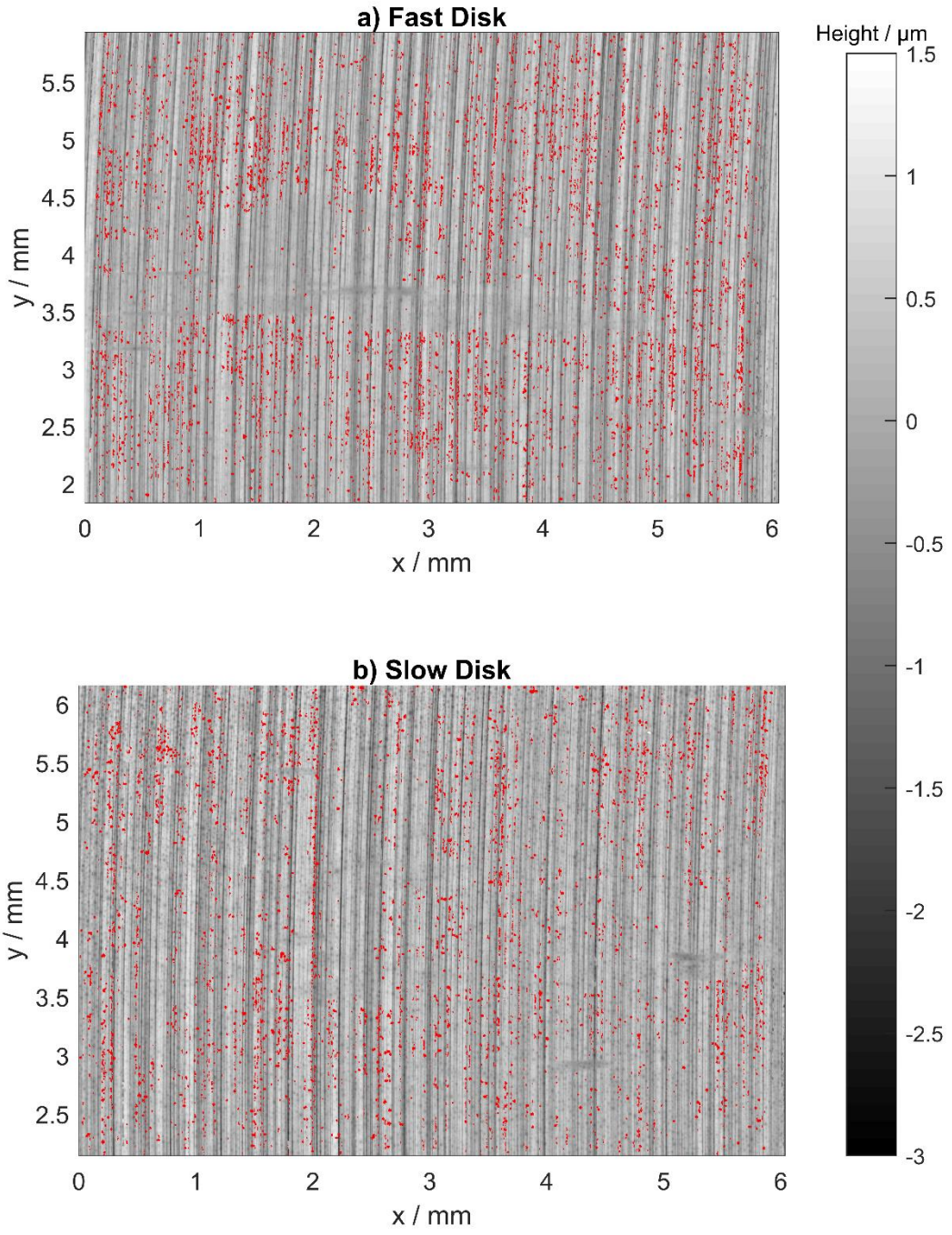

Figure 5.3.2 a) Fast and b) slow surfaces after load stage 4 ($5x10^4$ fast disk cycles and $3x10^4$ slow disk cycles) with pits overlaid in red.

At the end of test, both fast and slow surfaces had pitted extensively. In the fast disk surface shown in Figure 5.3.3a, micropitting can be clearly seen to decrease at the extreme edges of the contact area, yet the same effect cannot be seen in the slow surface in Figure 5.3.3b. Observation of the progress of micropitting on the fast surface through the test reveals that from load stage 4 onwards micropits were initially larger and more densely packed toward the centre of the contact, with shallower more widely spaced pits towards the edges. This more severe micropitting gradually progressed towards the edges as the test progressed.

Conversely the slow surface exhibited largely uniform micropitting density across the contact width, but a clearly lower density of micropits on the right side of the measured area (i.e. x>3 mm) than the left, even where the worn areas are ignored. As the wear patches on the slow surface are predominantly on the right half of the measured area, this may be an effect of these wear processes and consequent lubrication changes across a wider area – although there is no sign of a similar effect on the fast surface. Alternatively, the features on the right side of the slow measured area may simply be less aggressive, or come into contact with less aggressive features on the fast surface. Regardless of the cause, this highlights that there will always be some slight variation in the extent of pitting around the circumference of the disk.

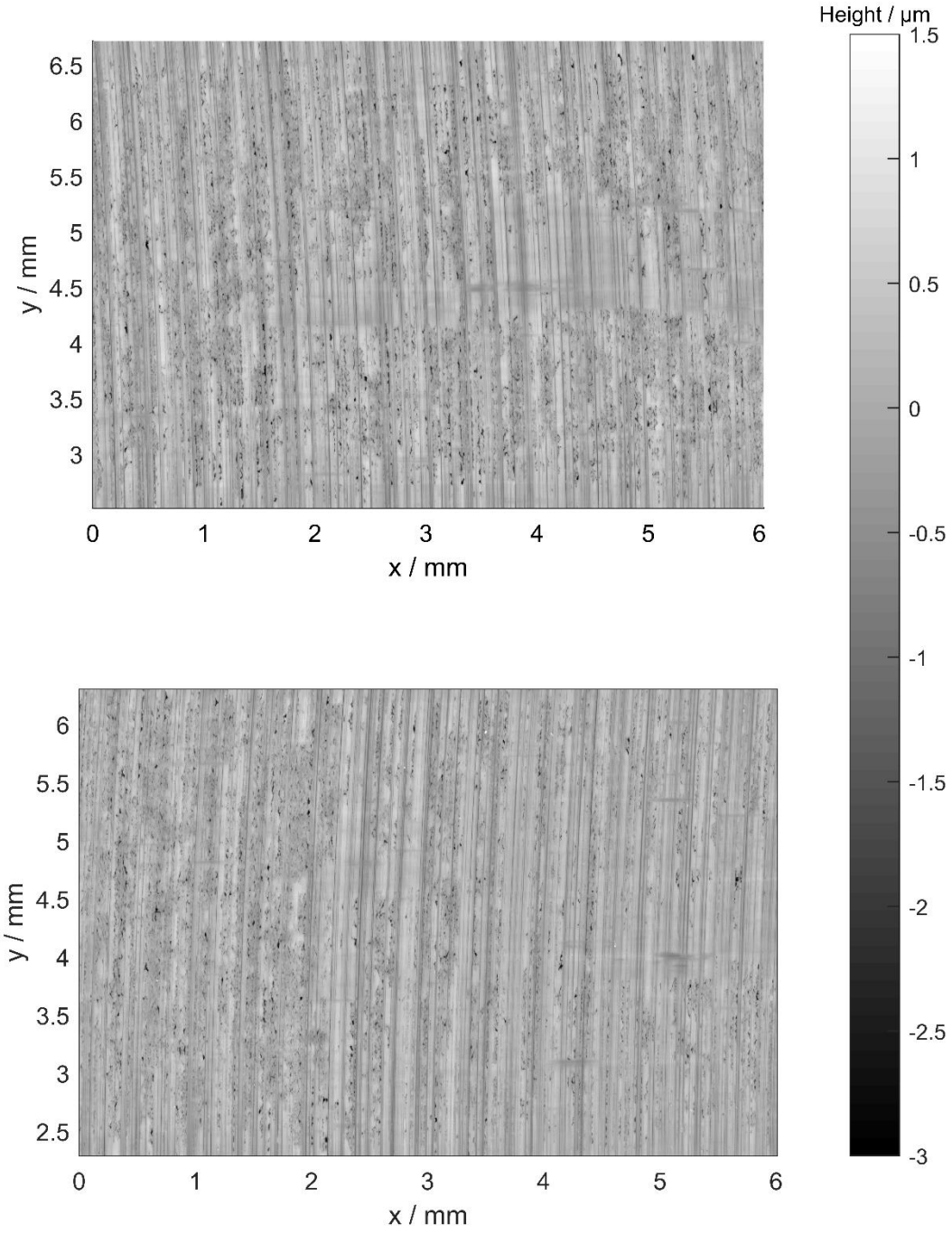

Figure 5.3.3 a) Fast and b) slow surfaces for Test 2 at the end of test.

For both the fast and slow surfaces the percentage of area micropitted was calculated with the wear islands excluded. Polygonal areas to be discounted on each surface were manually defined for each surface at the end of test (at which

point these areas are most clearly distinguishable) and a reference point was used to relocate these areas in each scan of that test.

Figure 5.3.4 shows the percentage pitted area through the test for the fast and slow surfaces of Test 2. The slow surface areal analysis data point at load stage 5 was discarded due to poor replica quality. The amount of micropitting on the fast surface exceeded that on the slow surface throughout the test, reaching a final percentage pitted area of 15.34%. This was 2.58% contact area pitted greater than the final slow surface value of 12.76%.

On both surfaces the two-dimensional profile analyses initially under-evaluated the percentage of surface micropitted, the two-dimensional analyses for the fast and slow surfaces crossing the areal analyses at load stages 6 and 8 respectively. For the fast surface the two-dimensional analysis continued to rise steadily until a final value of 26.22% was reached. The slow surface two-dimensional analysis remained much closer to the areal analysis line during load stages 9 and 10, differing by only 2.58% of surface pitted at load stage 10. It then rose very steeply through the final two load stages to reach a final slow surface two-dimensional analysis value of 22.78%. This differed from the areal analysis results by factors of 1.7 and 1.8 for the fast and slow surfaces respectively.

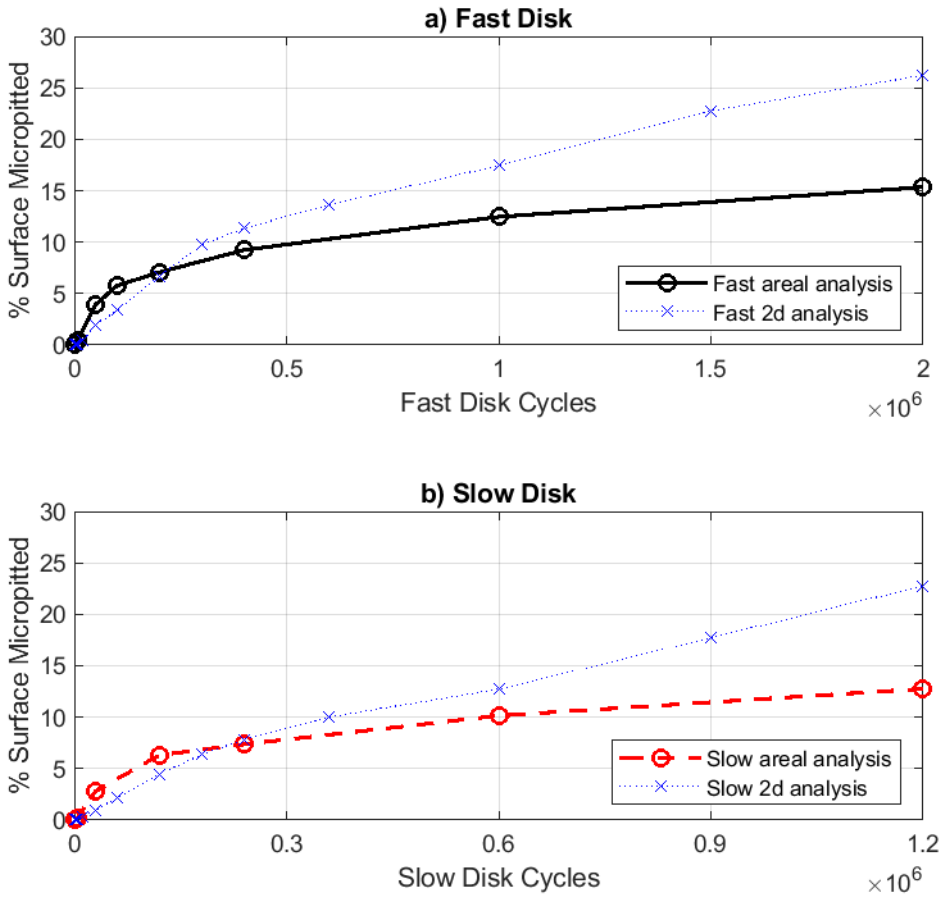

Figure 5.3.4 Percentage of surface pitted (excluding wear regions) for the a) fast and b) slow surfaces in Test 2.

The rate of micropitting on both surfaces is shown in Figure 5.3.5. It is much clearer in this image that while micropitting on the slow disk progressed at a lower rate than the fast with respect to time, the peak rate of micropitting per disk revolution was higher on the slow disk. The fact that the slow disk underwent only three revolutions for every five revolutions of the fast surface mitigated this higher rate of micropitting.

The rate of micropitting evaluated on the fast disk during load stages 7 and 8 was briefly higher than the equivalent slow disk micropitting rate, before dropping

below the rate of the slow disk for the remainder of the test. The final slow disk micropitting rate, although low, was evaluated at 1.51 times the final value on the fast surface.

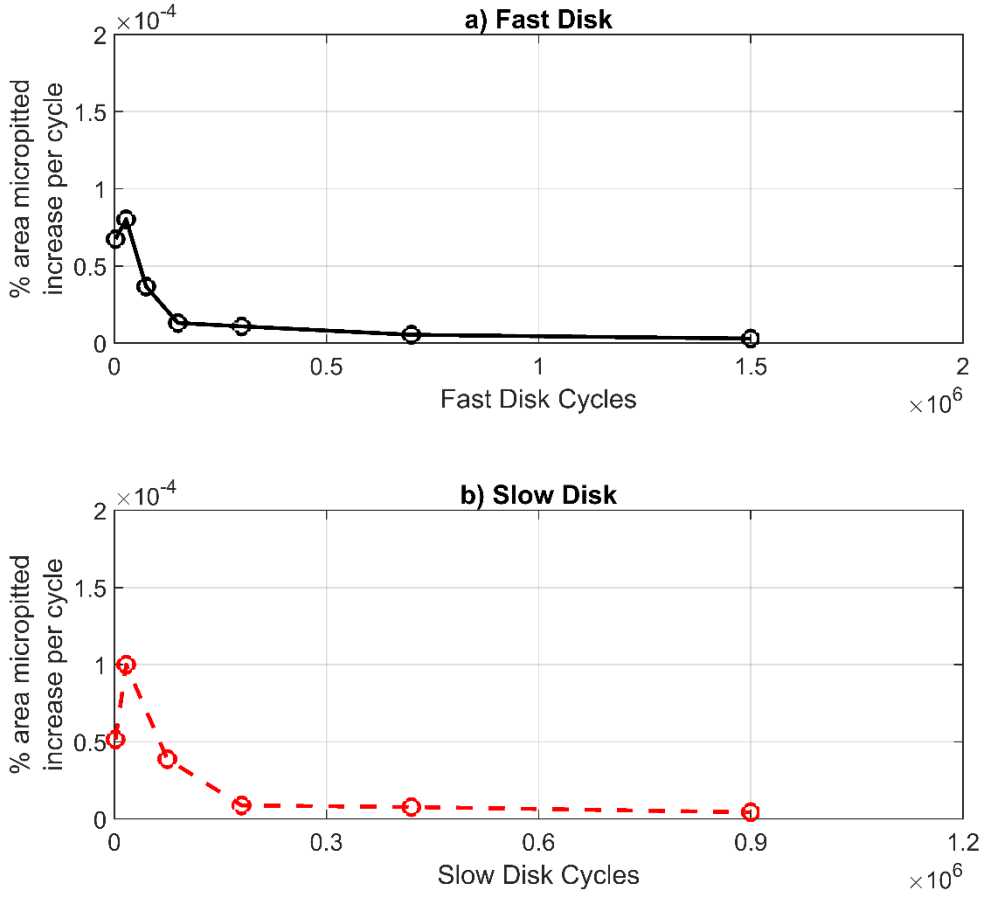

Figure 5.3.5 Rate of increase of micropitted area per cycle for the a) fast and b) slow surfaces of Test 2, evaluated by areal analysis

The metrics extracted from Test 2 are shown in Table 5.3.1. Notably, the volume of material removed by micropits per mm^2 on the slow disk was significantly less than on the fast surface, more so than might be expected from the difference in percentage of area micropitted between the two surfaces alone. i.e. If the fast surface volume removed were scaled by the percentage pitted, a volume removed

of 71.03x10^3 µm^3/mm^2 would be expected for the slow surface. The D5 values show that the bottoms of fast disk pits are 0.11 µm deeper on average which, combined with the difference in micropitted area can explain the difference in volume (multiplying 71.03x10^3 by $\frac{1.58}{1.69}$ gives 66.4 µm^3/mm^2, much closer to the value determined for the slow surface).

Table 5.3.1 Factorial evaluation metric values for Test 2

Parameter	Fast Surface	Slow Surface
% Pitted at conclusion of test	15.34	12.76
N3 / Fast Disk cycles	38,348	57,594
Peak rate of micropitting %/cycle	80.22 x 10^{-6}	99.92 x 10^{-6}
Average rate of micropitting between LS08 and LS10 %/cycle	5.38 x 10^{-6}	7.72 x 10^{-6}
Volume removed µm^3/mm^2	85.9 x 10^3	62.0 x 10^3
D5 / µm	-1.69	-1.58
% Micropitted at 1x10^5 FD cycles	5.77	N/A (due to discarded load stage 5 replica)

5.4 Test 3

Test 3 was the first test to employ the lower SRR setting of 0.25, alongside using a high max. pressure of 1.6 GPa and a low entrainment velocity of 2 ms^{-1}. Unlike the two previous tests, the Test 3 conditions did not provoke significant wear processes

during running-in. Due to the absence of visible wear on the surface a lower friction value might have been expected, however this was not the case as is shown in Figure 5.4.1. The friction during the initial contact of the first stage reached 240 N. The friction value decreased rapidly from this initial value as seen previously but did not decrease to the levels seen in previous tests. There was some variability in the mean recorded friction for each test, but values were typically from 190 – 200 N. Despite the higher friction the Test 3 temperatures were notably lower than the previous two tests, stabilising consistently around 92.5°C.

The measured contact voltage began around 1 mV at the start of the first load stage but had begun to rise from the initial contact reaching 2 mV by the conclusion of the first running-in stage and 5 mV by the conclusion of load stage 2. During load stage 7 (the last stage shown on the figure) the contact voltage averaged 28.0 mV, and this rise continued to a final stage average of 37.3 mV.

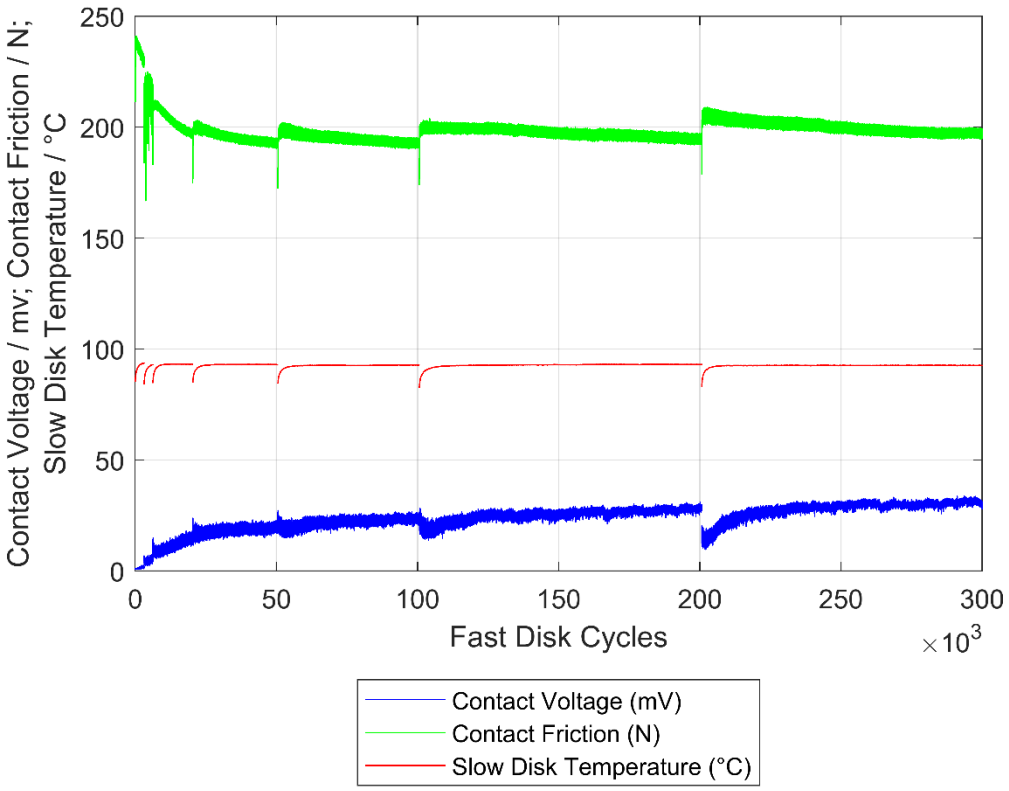

Figure 5.4.1 In-Test data recorded for the first 3x10^5 fast disk cycles of Test 3

Both surfaces in this test exhibited significant micropitting, however the micropitting observed on the slow surface was notably more severe than on the fast. Considering the fast surface at the end of the test, micropits were clearly lined along asperity ridges with some non-micropitted or less aggressively micropitted asperities interspersed amongst the heavily micropitted asperities. For the slow surface this was only the case for the left side of the measured area. In the central and right-hand regions of the measured area micropitting became so severe that the asperities began to lose their definition within the micropitted region, representing the early stages of manufacturing marks effectively being removed by the micropitting process. Figure 5.4.2 shows the surfaces at the end of Test 3.

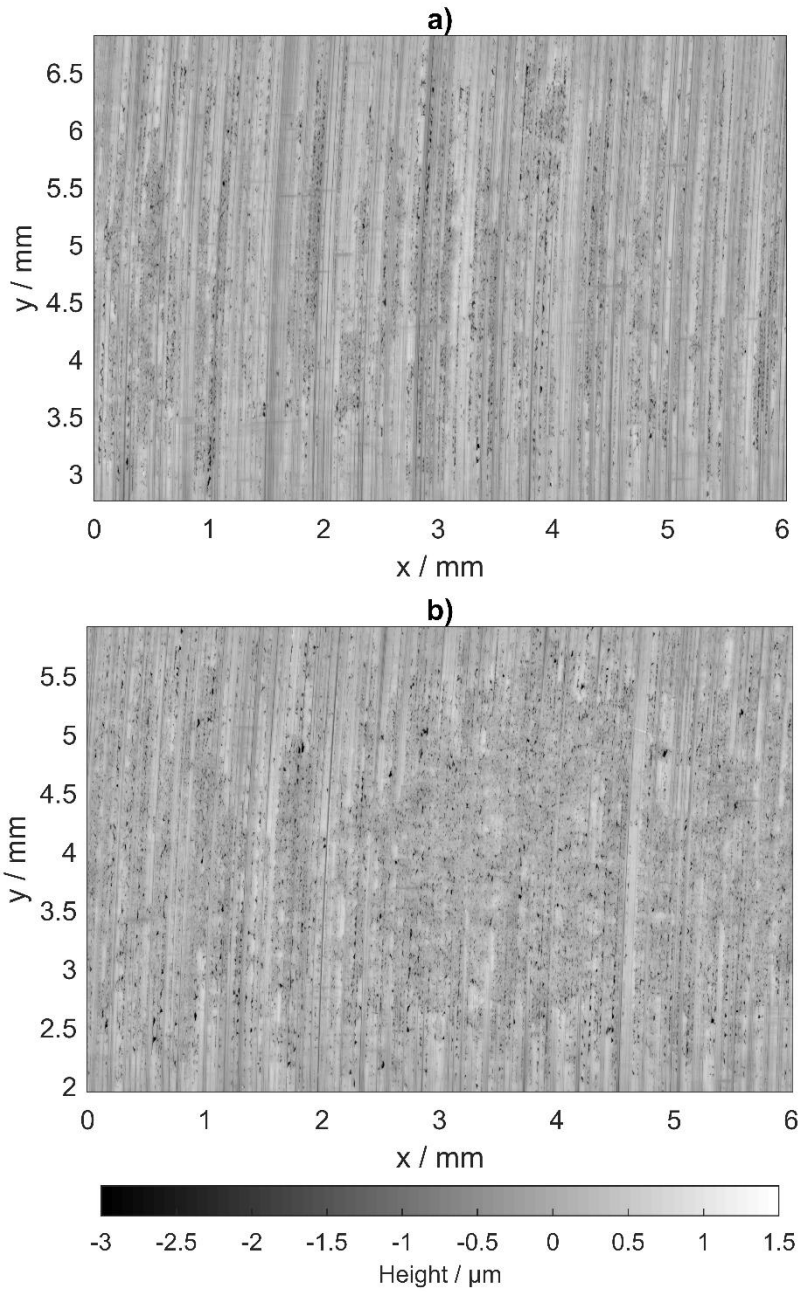

Figure 5.4.2 a) Fast and b) slow surfaces at the conclusion of Test 3

The evaluations of the percentage of area pitted are shown in Figure 5.4.3. Throughout the test a greater micropitted area was recorded on the slow surface than the fast, with final values of 17.46% and 12.59% area micropitted respectively using the areal analysis.

The two-dimensional profile analysis on both surfaces again showed an under-evaluation of micropitting in the first $2x10^5$ fast disk cycles, before going on to significantly exceed the final evaluation found by the areal analysis – particularly so for the slow surface. The final values for the fast and slow two-dimensional percentage micropitted analyses were 22.21% and 38.30% respectively, factors of 1.3 and 3.0 larger than the areal analysis results.

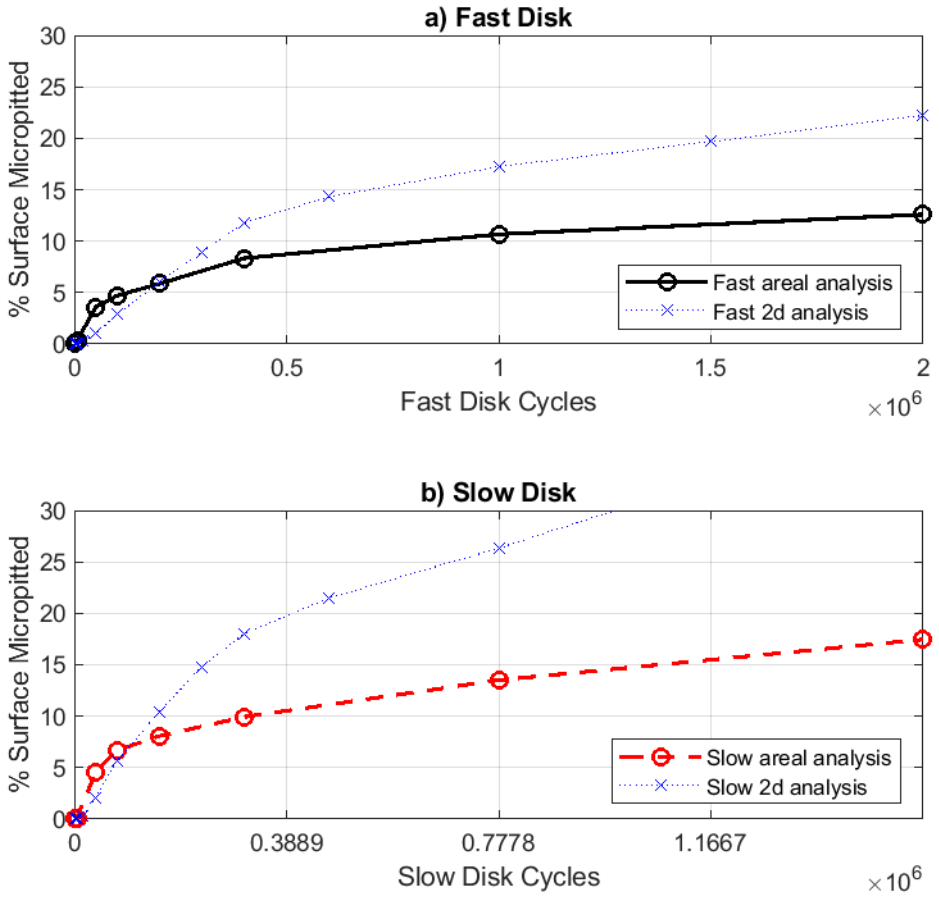

Figure 5.4.3 Percentage of area micropitted during Test 3 for the a) fast and b) slow surfaces.

The rates of micropitting on each surface through the test can be seen in Figure 5.4.4. The slow surface of Test 3 exhibited the highest peak rate of micropitting of

the first three tests, and as in the previous tests this value greatly exceeded that seen on the fast surface. After the peak the fast surface pitting rate appears to decrease to a temporarily stable rate, before a second decrease occurs between load stages 8 and 10. This behaviour was not observed on the slow surface.

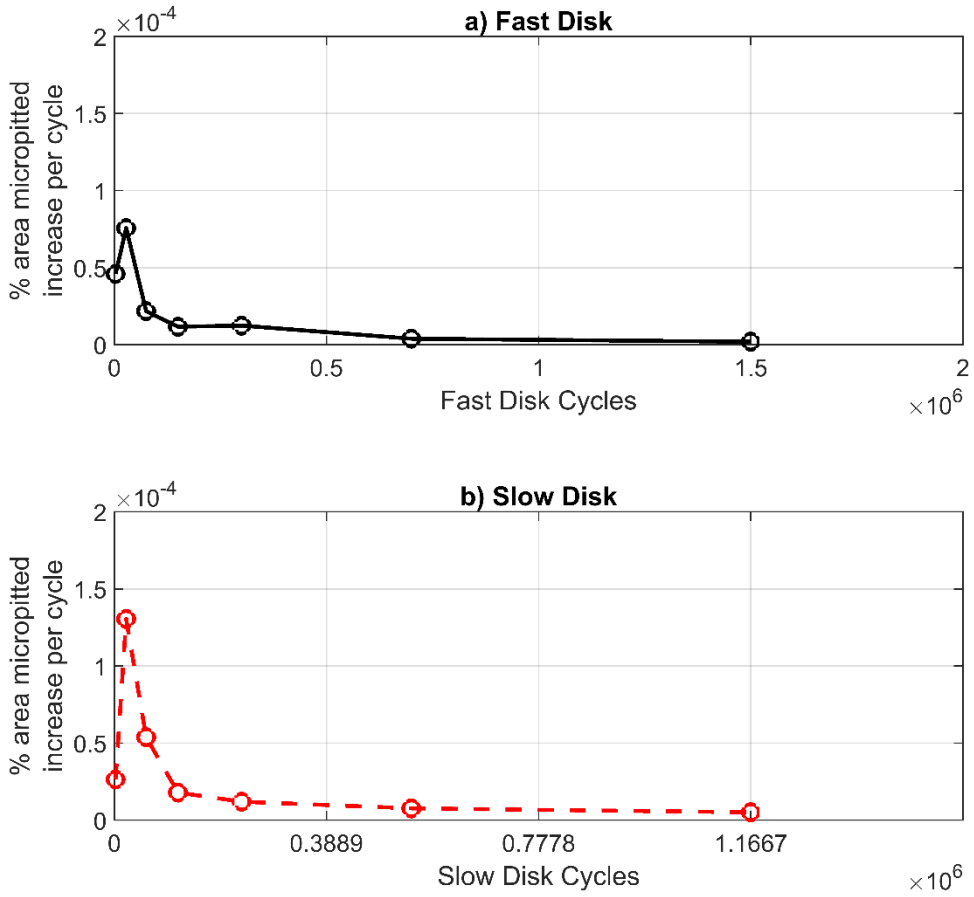

Figure 5.4.4 Rate of increase of pitting for the a) fast and b) slow surfaces of Test 3, as evaluated by the areal micropitting analysis.

On both surfaces micropits developed at locations across the contact width from the earliest stages of micropitting. A lower density of micropits was observed at the extreme contact edges where the pressure was markedly decreased, but micropits were still present in these regions.

Table 5.4.1 shows the evaluated metrics for micropitting behaviour in Test 3. The value of D5 evaluated for the slow surface is significantly deeper than that for the fast surface. Additionally of interest is the fact that the volume removed per unit area on each surface did not scale with percentage micropitted, with micropits on the fast disk being of greater volume than the slow if adjustment is made for the micropitted area. Therefore, while the deepest points in micropits on the slow surface are deeper than on the fast, the fast surface micropits appear to have a larger average depth to facilitate a greater volume removed per pit.

Table 5.4.1 Factorial evaluation metric values for Test 3

Parameter	Fast Surface	Slow Surface
% Pitted at conclusion of test	12.59	17.46
N3 / FD cycles	42,030	34,355
Peak rate of micropitting %/cycle	75.62×10^{-6}	130.44×10^{-6}
Average rate of micropitting between LS08 and LS10 %/cycle	3.89×10^{-6}	7.66×10^{-6}
Volume removed $\mu m^3/mm^2$	68.4×10^3	86.5×10^3
D5 / µm	-1.63	-1.79
% Micropitted at 1×10^5 FD cycles	4.69	6.68

5.5 Test 4

The fourth test in the experimental programme was the first to operate at the low load setting, the maximum Hertzian pressure in the contact being 1.2 GPa. The in-test data in Figure 5.5.1 shows much lower friction readings when compared to the previous tests, the peak friction recorded in the first test reaching approximately 102 N. This then decreased to an average of 70 N from load stage 5 onwards. Due to a component failure the rig was unable to record in-test data beyond Test 8.

The contact voltage reading at the start of the test indicated less severe direct contact between surfaces than seen previously, beginning around 10 mV and rising to an average of 24.7 mV in the second running-in stage. The continued steady increase of contact voltage led to an average value of 37.9 mV at the end of load stage 8. Once stabilised, the average disk temperature was reliably 88.7±0.1°C throughout the test.

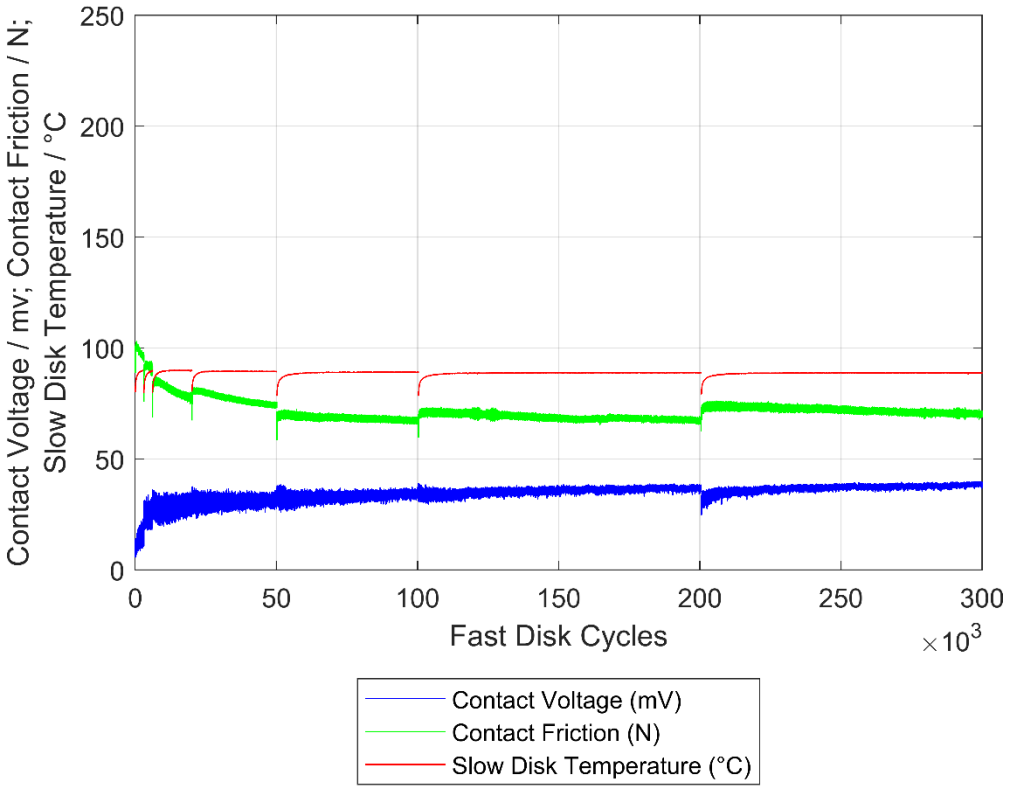

Figure 5.5.1 In-test data recorded during the first 3x10^5 fast disk cycles of Test 4.

Very minor micropitting developed on both surfaces during the running-in process, visible only under very close inspection of the surface scans. These pits were all both small in area and shallow in depth, constituting only 0.14% of the fast surface and 0.07% of the slow surface.

By the conclusion of load stage 4 this had progressed to widespread micropitting on both surfaces, as can be seen in Figure 5.5.2 and Figure 5.5.3.

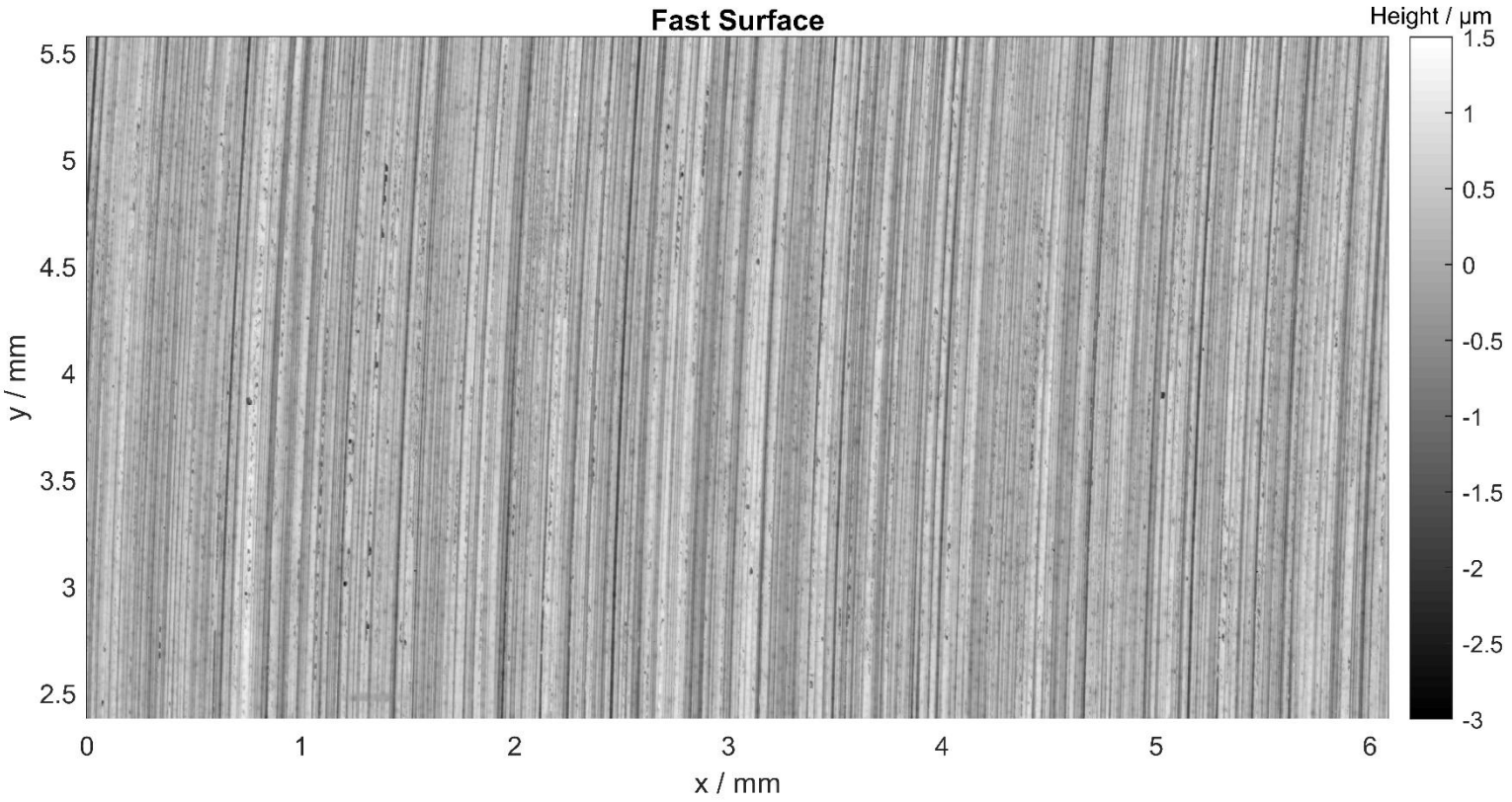

Figure 5.5.2 Test 4 Fast surface at the conclusion of load stage 4 ($5x10^4$ fast disk cycles).

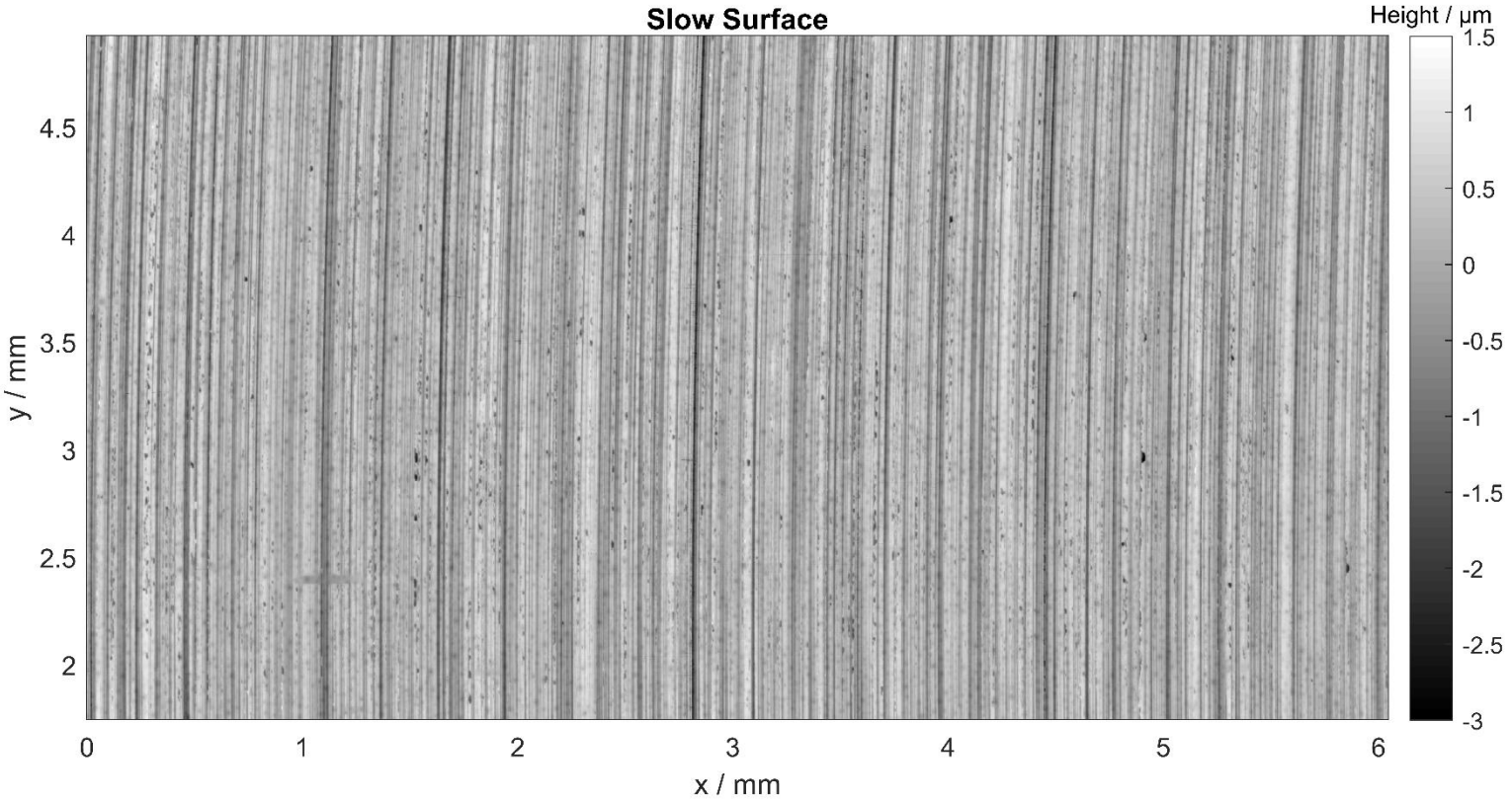

Figure 5.5.3 Test 4 Slow surface at the conclusion of load stage 4 ($3x10^4$ slow disk cycles).

These images clearly illustrate that micropitting developed across the full contact width at a similar time, although it appears that there is a decrease in the extent of micropitting at the extreme edge of the contact on both surfaces – locations where the pressure in the contact will be significantly lower than at the centre.

Figure 5.5.4 shows the same surfaces at the end of testing, demonstrating that this less aggressive micropitting at the edges persisted throughout the experiment. On both surfaces micropitting behaviour was again very orderly, and micropits developed along asperity ridges in lines allowing for the valleys and asperities to be easily distinguished, even where heavy micropitting occurred.

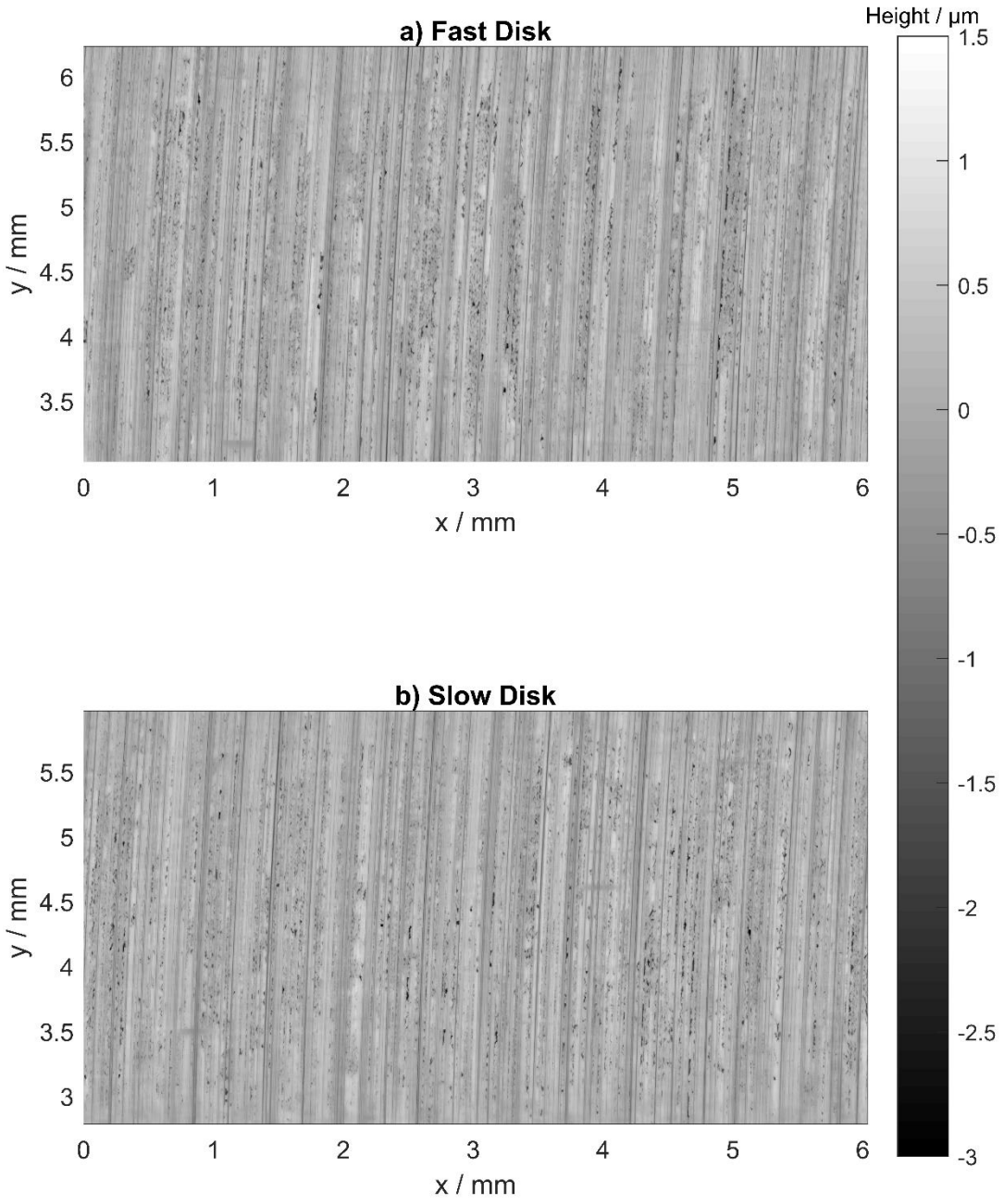

Figure 5.5.4 The a) fast and b) slow surfaces at the conclusion of Test 4.

The progress of micropitting can be seen in Figure 5.5.5 showing the percentage of surface pitted on each surface through the test. The micropitting behaviour on both surfaces was similar throughout the test, with the percentage micropitted at most

data points differing by less than 1% of the contact area. The difference between these surfaces only exceeded this at the conclusion of load stage 8, where the slow surface exhibited 8.79% area pitted versus 7.59% on the fast surface. After load stage 10 this difference had reduced once more to 0.53% of area pitted, and at the conclusion of the test the two surfaces had a difference in percentage area micropitted of 0.11% - the slow surface again being the more micropitted. This is interesting as it also shows that while the slow surface had the higher rate of micropitting by time (as opposed to by disk cycles as used in the micropitting metrics) in the early stages of the test, the rate of micropitting by time on the fast surface was higher in the mid- to late-test.

The results of the two-dimensional profile micropitting analyses can also be seen in Figure 5.5.5. For both surfaces the two-dimensional analysis evaluates a lower amount of micropitting than the areal analysis early in the test, in both cases the two-dimensional result crossing the areal analysis at the end of load stage 6 ($2x10^5$ fast disk cycles). The fast surface two-dimensional analysis increased much more rapidly than the slow during load stages 7 and 8 before slowing again, finishing with values of 20.85% micropitted on the fast surface (1.8 times the areal analysis result) and 17.53% (1.5 times the areal result) on the slow surface. Considering the very close values for micropitted area on each disk by areal analysis, and the similar way in which micropits are distributed on both surfaces, it is interesting that a significant difference can be seen between the values found by the two-dimensional analyses.

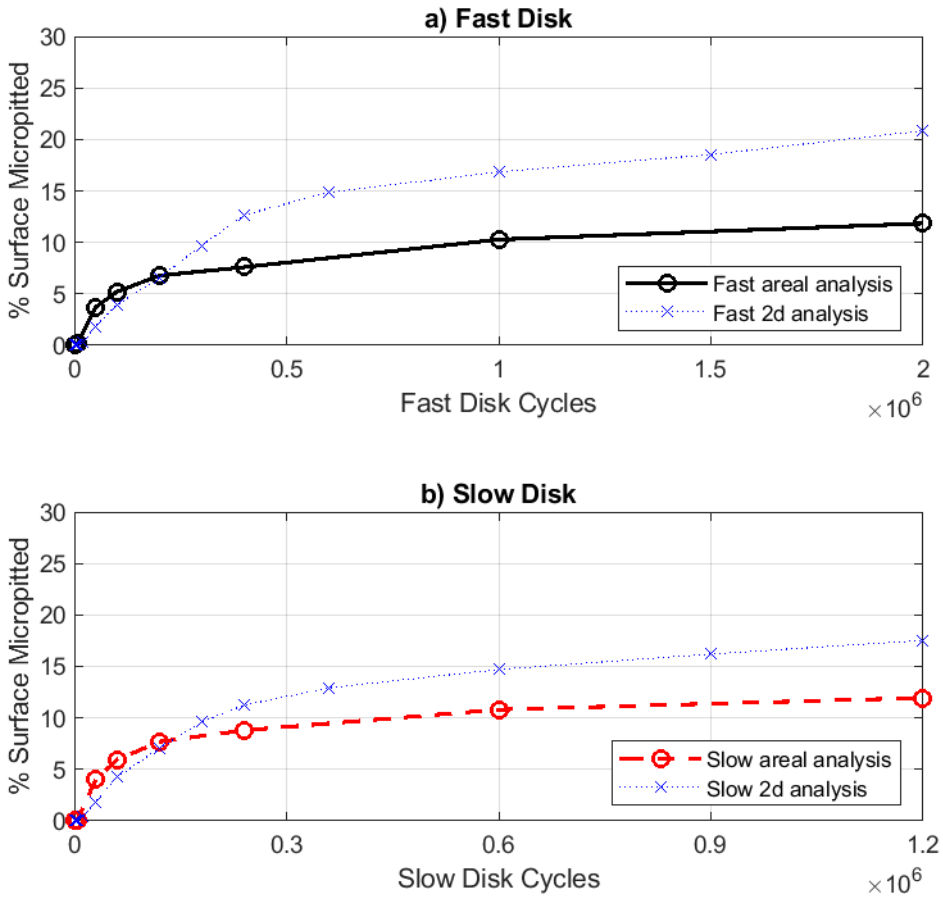

Figure 5.5.5 Percentage of contact area micropitted on the a) fast and b) slow surfaces of Test 4.

As can be seen in Figure 5.5.6, the rate of micropitting per cycle was higher for the slow surface throughout the test, reaching a higher initial peak and then maintaining at least double the rate seen on the fast surface until the conclusion of load stage 8. Due to the higher speed of the fast surface however, the rate of micropitting per cycle at an SRR of 0.5 need only exceed 60% of the slow surface value for the rate of pitting per unit time to be higher on the fast surface. It is this that allows the percentage area micropitted on the fast surface to overtake that of the slow surface in the late test, with the fast surface averaging 80% of the slow

surface micropitting rate during load stages 9 and 10, and 83% of the slow surface pitting rate in load stages 11 and 12.

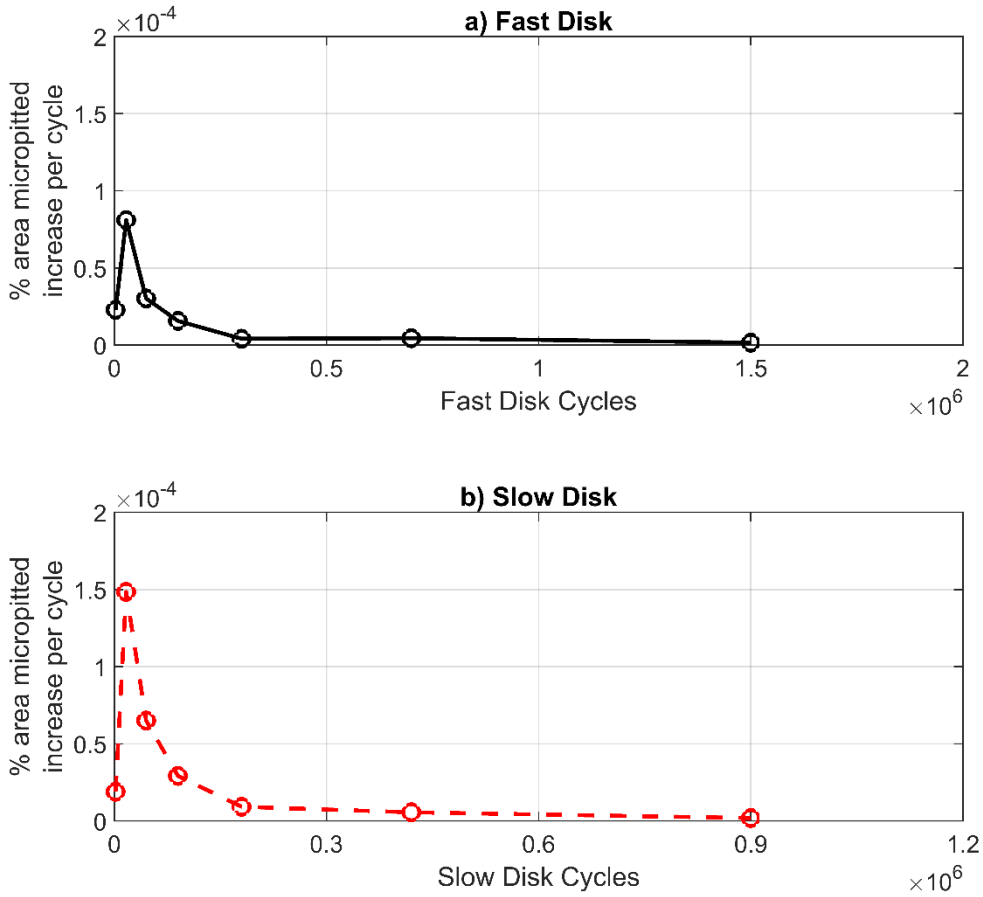

Figure 5.5.6 Rate of micropitting per cycle on the a) fast and b) slow surfaces during Test 4 as evaluated by the areal analysis.

The micropitting parameters evaluated for the Test 4 surfaces are shown in Table 5.5.1. The volume removed per mm^2 on the fast surface is higher than on the slow surface, despite the very similar percentage pitted and D5 values. From this it can be interpreted that the pitted points on the fast surface are deeper on average, while still having comparable extremes – perhaps suggesting flatter-bottomed pits.

Table 5.5.1 Factorial evaluation parameters for Test 4

Parameter	Fast Surface	Slow Surface
% Pitted at conclusion of test	11.84	11.95
N3 / FD cycles	41,328	38,929
Peak rate of micropitting %/cycle	81.03×10^{-6}	148.38×10^{-6}
Average rate of micropitting between LS08 and LS10 %/cycle	4.47×10^{-6}	5.60×10^{-6}
Volume removed $\mu m^3/mm^2$	58.7×10^3	53.6×10^3
D5 / µm	-1.46	-1.49
% Micropitted at $1x10^5$ FD cycles	5.21	5.94

5.6 Test 5

The conditions applied in Test 5 were expected to produce the least aggressive lubrication conditions in the test programme. The maximum contact pressure and SRR were both at 'low' settings; 1.2 GPa and 0.25 respectively. This was expected to result in less frictional heating. The entrainment velocity was at the 'high' setting of 4 ms^{-1} which, while resulting in a higher sliding velocity, is also the dominant factor in drawing a greater amount of lubricant into the contact and producing an effective lubricant film.

In-test monitoring confirmed these expectations, as the mean Contact Voltage (CV) measurement at the initial contact in load stage 1 was approximately 17 mV, rising

to 28 mV by the end of the first stage – a very high initial value and a rapid rise indicating less aggressive initial contact and a rapid decrease in direct contact over the initial load stage. The increase in contact voltage continued throughout the test, exceeding an average of 40 mV during load stage 6, reaching an average of 42.5 mV out of a maximum of 45 mV in the final stage. Further illustrating these mild conditions, the disk temperature rose to an average of 87.3°C. Friction began with an initial value of approximately 67 N during the first stage before decreasing to a stable 53 – 55 N in load stages 4 through 7. A slight further decrease was seen in the later stages reducing the average friction reading in the final load stage to 47.7N.

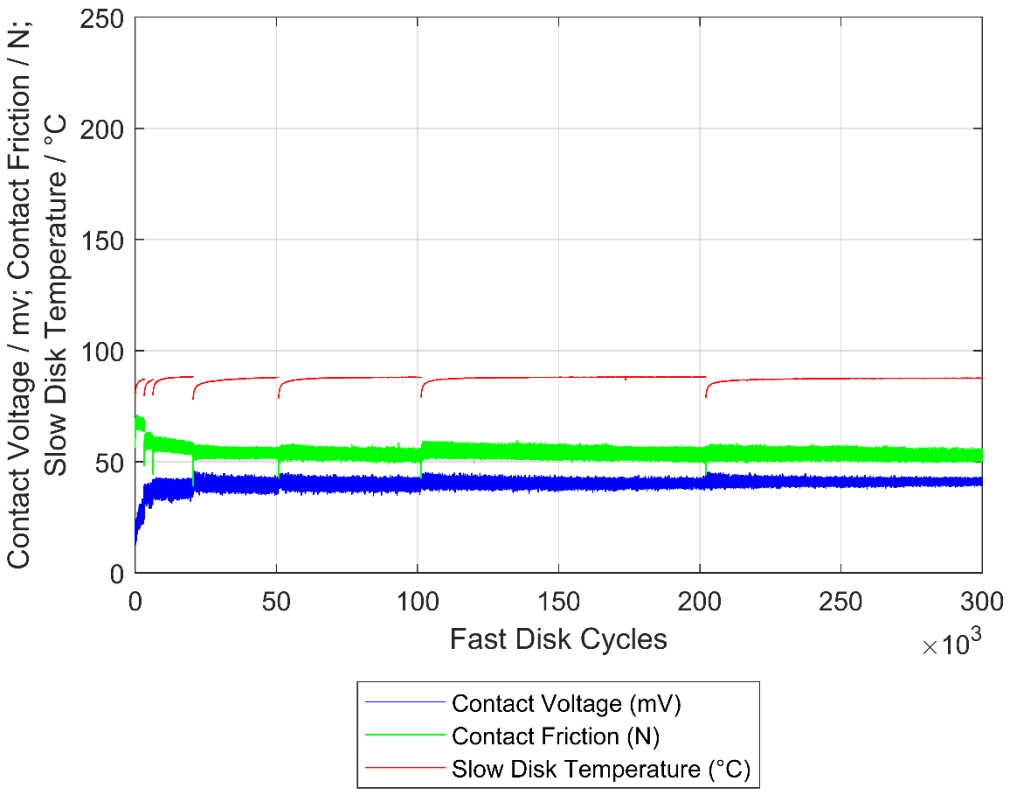

Figure 5.6.1 In-test data recorded for the first 3x10^5 fast disk cycles of Test 5.

Minimal micropitting was observed after running-in, with only a handful of identifiable pits on each surface, constituting 0.04% and 0.11% of the fast and slow

surfaces respectively. Micropitting then developed rapidly on the surface as expected, before levelling off in both cases. Micropits developed uniformly across the full width of the surfaces, with many asperities developing micropits along a significant portion of their length, as can be seen in the end of test surfaces shown in Figure 5.6.2.

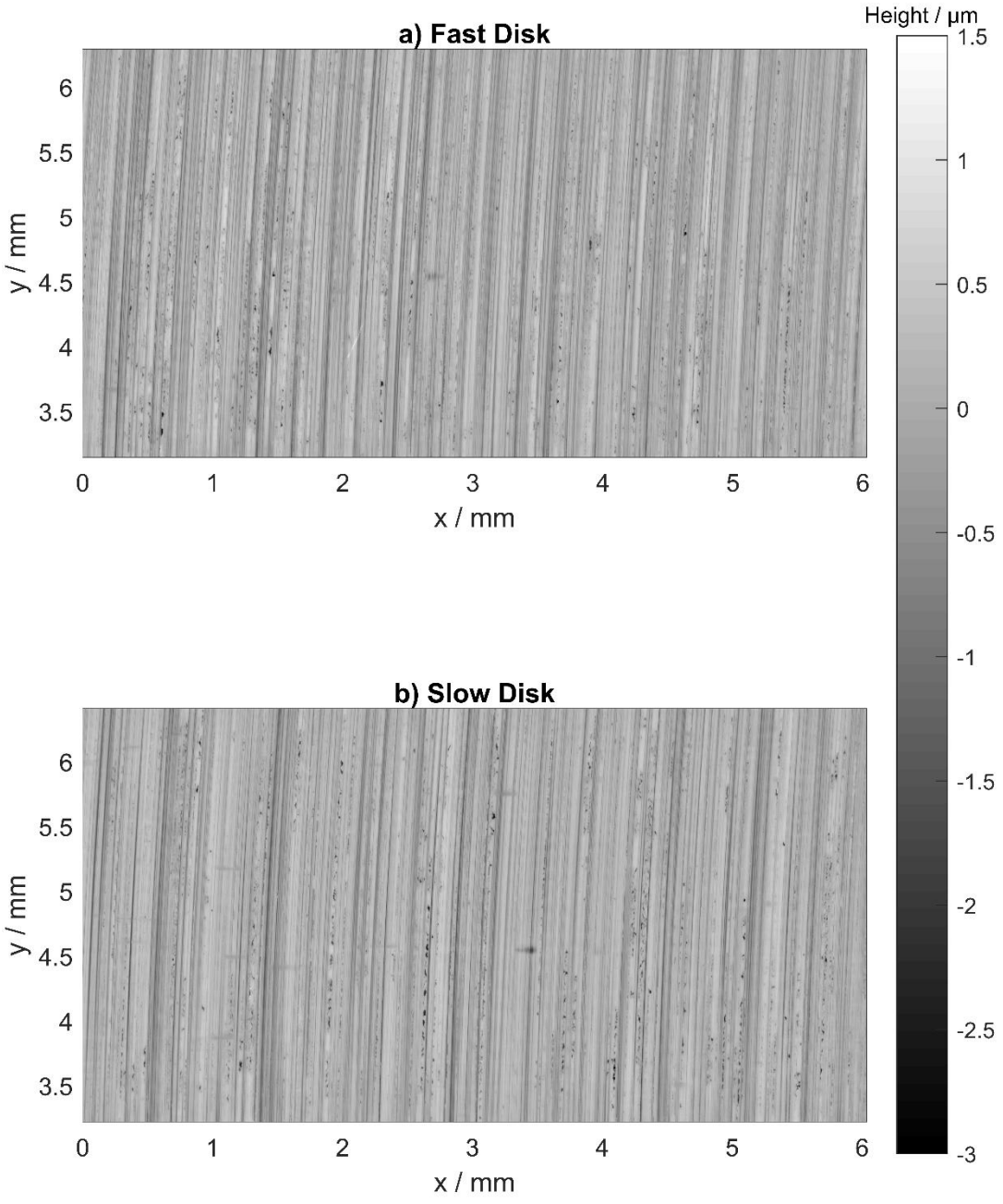

Figure 5.6.2 a) Fast and b) slow surfaces at end of test for Test 5.

The levelling-off of micropitting was very clear in the later stages of this test. Figure 5.6.3 shows the percentage of surface micropitted on the fast and slow surfaces of Test 5. In both surfaces there is an apparent decrease in micropitting at the end of the test, which is of course not possible. The low density of micropitting in this test and the tendency for micropits to form along single asperities made the scans of this test very susceptible to minor offsets in the x-positioning of the scanned area. In addition to this there is a contribution made by the transition from the adjusted replica values used in-test to the true disk values used for the final data point.

As with the previous tests the two-dimensional analysis yields lower values for percentage of area micropitted early in the test on both surfaces. While the fast surface evaluation crosses the areal analysis during load stage 7, the slow surface two-dimensional profile analysis does not significantly exceed the slow areal analysis, instead closely matching it for the remainder of the test. The final result for the slow surface two-dimensional analysis is a comparatively small-over estimation to give a final result of 5.85% micropitted, differing from the areal result by a factor of 1.3. The final fast surface two-dimensional analysis result of 8.70% is 2.2 times the corresponding areal analysis result.

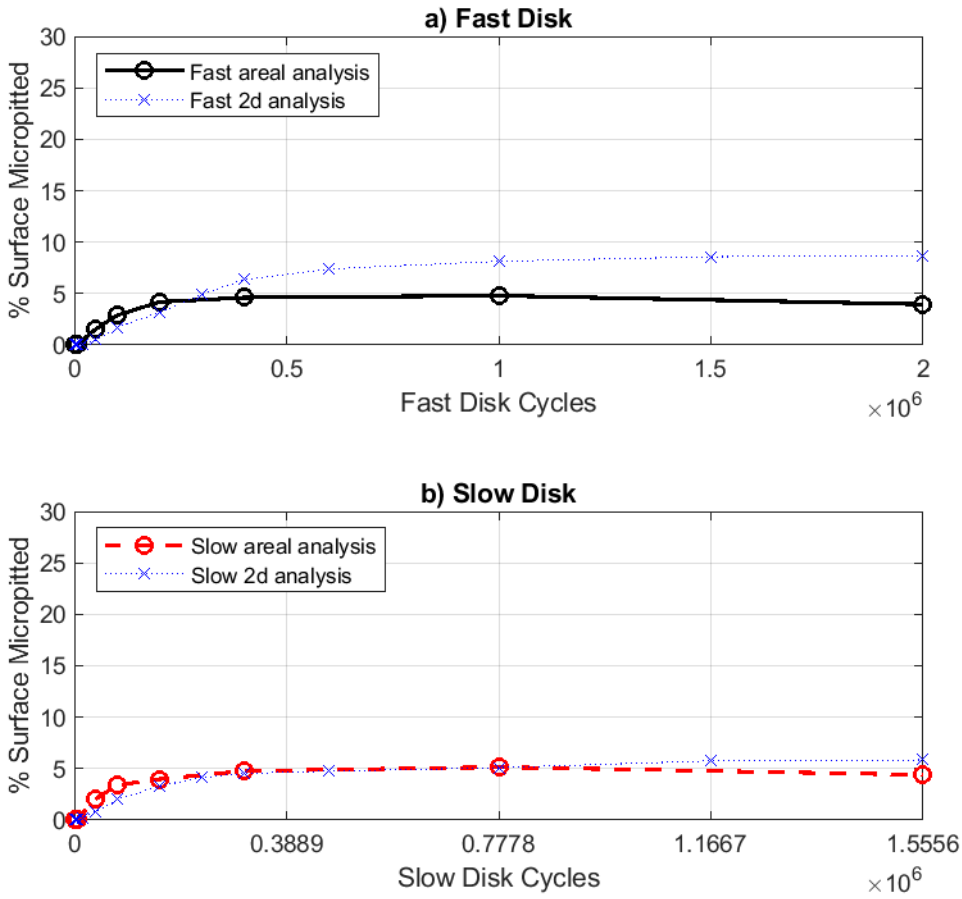

Figure 5.6.3 Percentage of contact area micropitted on the a) fast and b) slow surfaces during Test 5.

The slow surface initially micropitted at a higher rate than the fast surface, both in terms of cycles and time. The micropitting process also slowed earlier on the slow surface, however the fast surface micropitted at a higher per-cycle rate than the slow only during load stage 6. Both surfaces continued at a very low rate until the end of the test. The previously discussed apparent decrease to the final

surface lead to an artificially negative rate of micropitting during load stages 10 and 12.

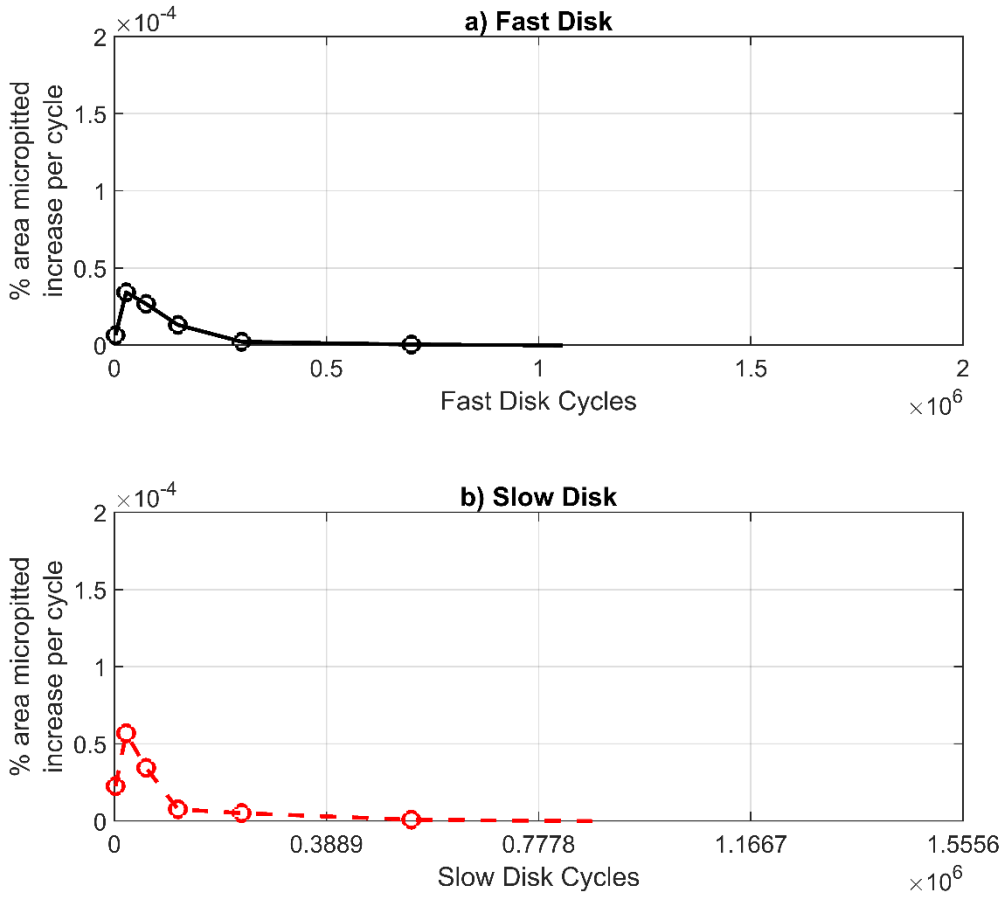

Figure 5.6.4 Rate of micropitting per cycle on the a) fast and b) slow surfaces of Test 5

Table 5.6.1 shows the micropitting parameters evaluated for Test 5.

Table 5.6.1 Factorial evaluation parameters for Test 5

Parameter	Fast Surface	Slow Surface
% Pitted at conclusion of test	3.96	4.40
N3 / cycles	109,543	85,518
Peak rate of micropitting %/cycle	34.21×10^{-6}	56.82×10^{-6}
Average rate of micropitting between LS08 and LS10 %/cycle	0.31×10^{-6}	0.82×10^{-6}
Volume removed $\mu m^3/mm^2$	18.6×10^3	20.0×10^3
D5 / µm	-1.32	-1.48
% Micropitted at $1x10^5$ FD cycles	2.88	3.39

5.7 Centrepoint Test

As was previously discussed, the centrepoint test was conducted with all test variables halfway between those used in the other eight tests of the programme. As with all tests, micropitting began early and by the conclusion of load stage 4 both surfaces showed micropits developing in all areas of the surface as can be seen in Figure 5.7.1. A red overlay is used on pits in the figure as many of the pits were small and shallow and required very close inspection, particularly on the fast surface.

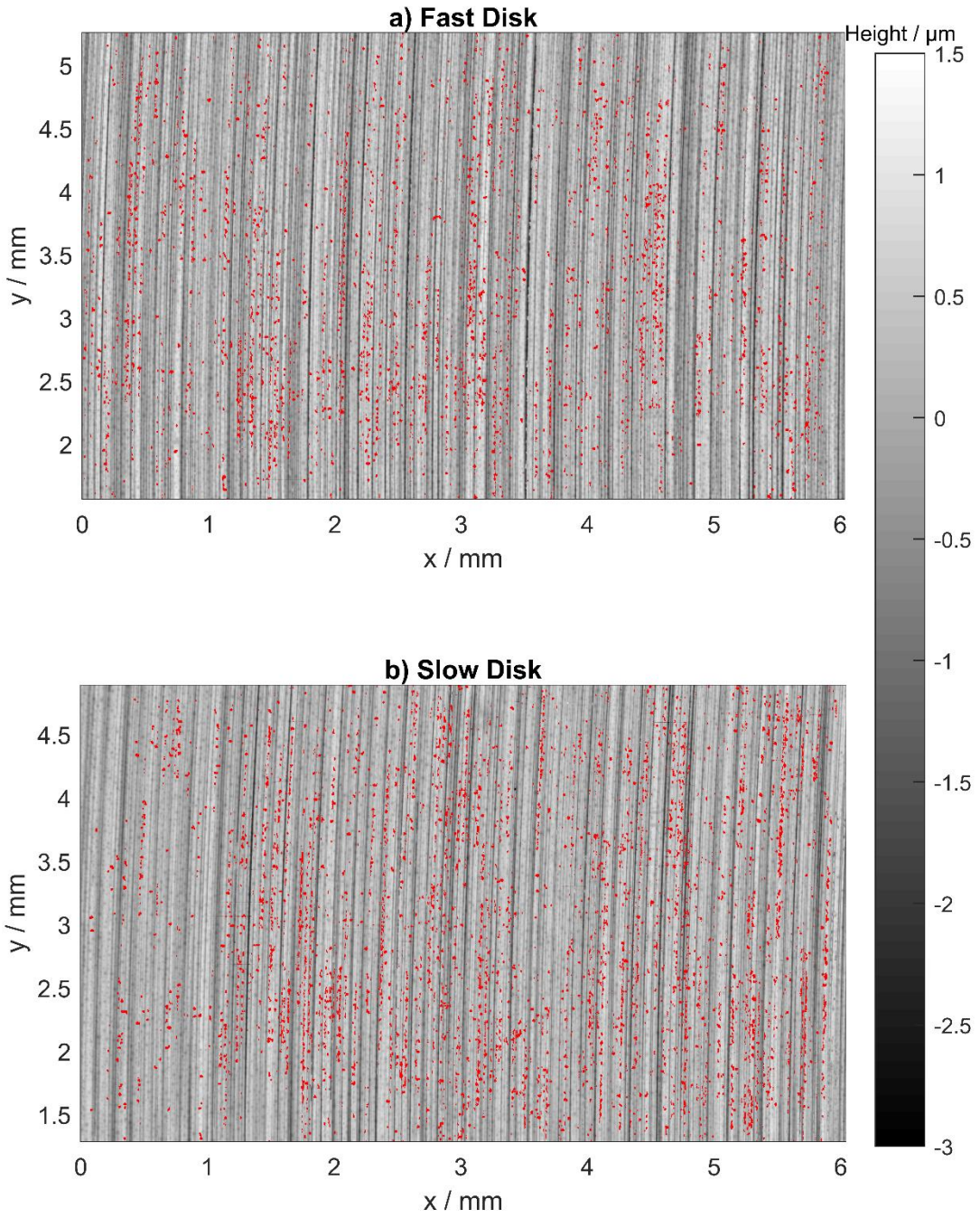

Figure 5.7.1 a) Fast and b) Slow centrepoint test surfaces after 5x10^4 fast disk cycles

The surfaces at the end of testing can be seen in Figure 5.7.2. At the conclusion of the test most asperities had micropitted to some extent, however there was a wide

range in how aggressively different regions had micropitted on both surfaces. While most asperities were heavily micropitted, only a handful of micropits can be seen on other asperities or regions of asperities. On both surfaces a lower density of micropits was maintained at the edges of the contact than the central region.

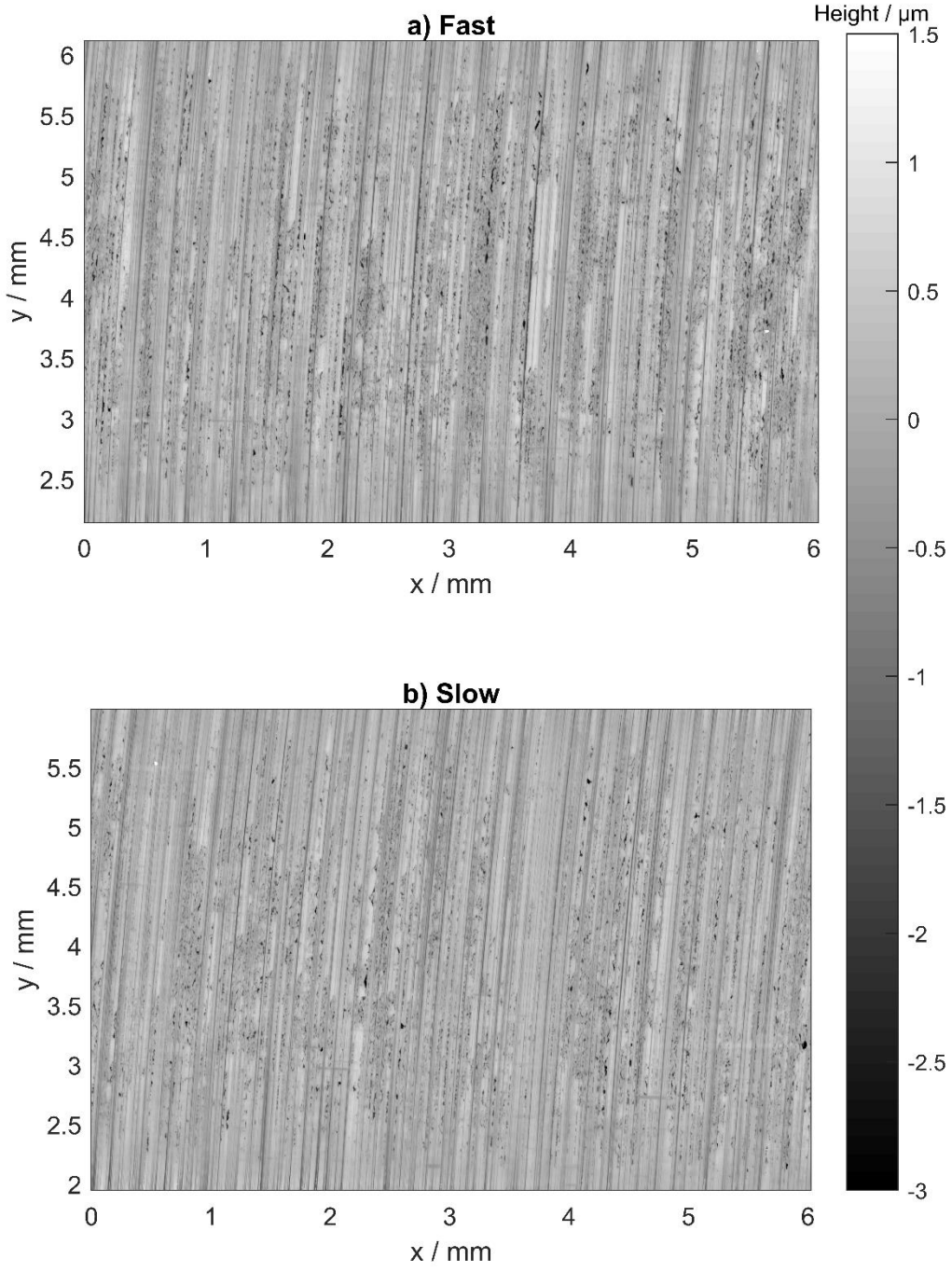

Figure 5.7.2 a) Fast and b) Slow centrepoint test surfaces after 2x10^6 fast disk cycles

The contact voltage measurement indicated a very rapid reduction in direct surface contact, as can be seen in Figure 5.7.3, which shows the first $3x10^5$ cycles of the test. This figure shows that the mean contact voltage had already risen to an average of 36 mV in load stage 3, 80% of its maximum possible value of 45 mV. The contact voltage maintained a steady average value around 39 mV for much of the test but climbed to an average of 40 mV during the final $7.5x10^5$ cycles.

The recorded friction in the test decreased markedly during the first $5x10^4$ cycles but remained in the 90 – 105 N range from $5x10^4$ cycles onwards.

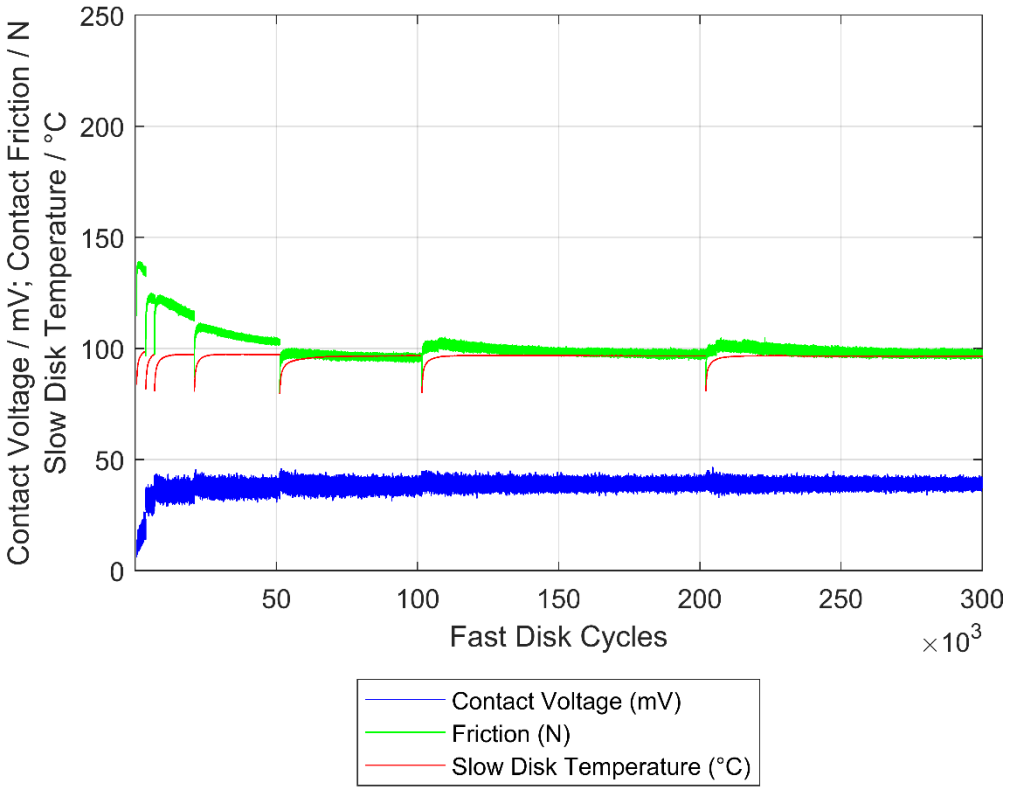

Figure 5.7.3 In-test data recorded for the first $3x10^5$ fast disk cycles of the centrepoint test.

Figure 5.7.4 shows the percentage of area micropitted on each surface through the course of the centrepoint test. The slow surface displayed more micropitting than the fast at all evaluated points other than at the end of test. The largest difference (0.87% of contact area) occurred at the end of load stage 4, after which the difference between the two evaluations became smaller at each evaluated point up to the conclusion of load stage 10. The fast surface micropitted at a much higher rate than the slow during the final 1 million fast disk cycles, finishing with 14.16% area micropitted. The slow surface showed 12.79% area micropitted at the end of test.

In terms of two-dimensional profile analysis, the fast surface analysis in this test did not significantly underestimate during the initial stages of the test but closely matched the development of micropitting seen by the areal analysis. During load stages 7 and 8 however, the rate of micropitting as appraised by the areal analysis began to slow to a greater extent than on the two-dimensional analysis, and hence the two-dimensional evaluation began to significantly overestimate in comparison. While the slow surface two-dimensional analysis did underestimate slightly in the early stages of the test, the following overestimation was less than on the fast surface. The fast and slow surface two-dimensional analyses concluded with 21.29% and 16.00% micropitted respectively. This was a factor of 1.5 greater than the areal analysis for the fast surface, and a factor of 1.3 greater for the slow.

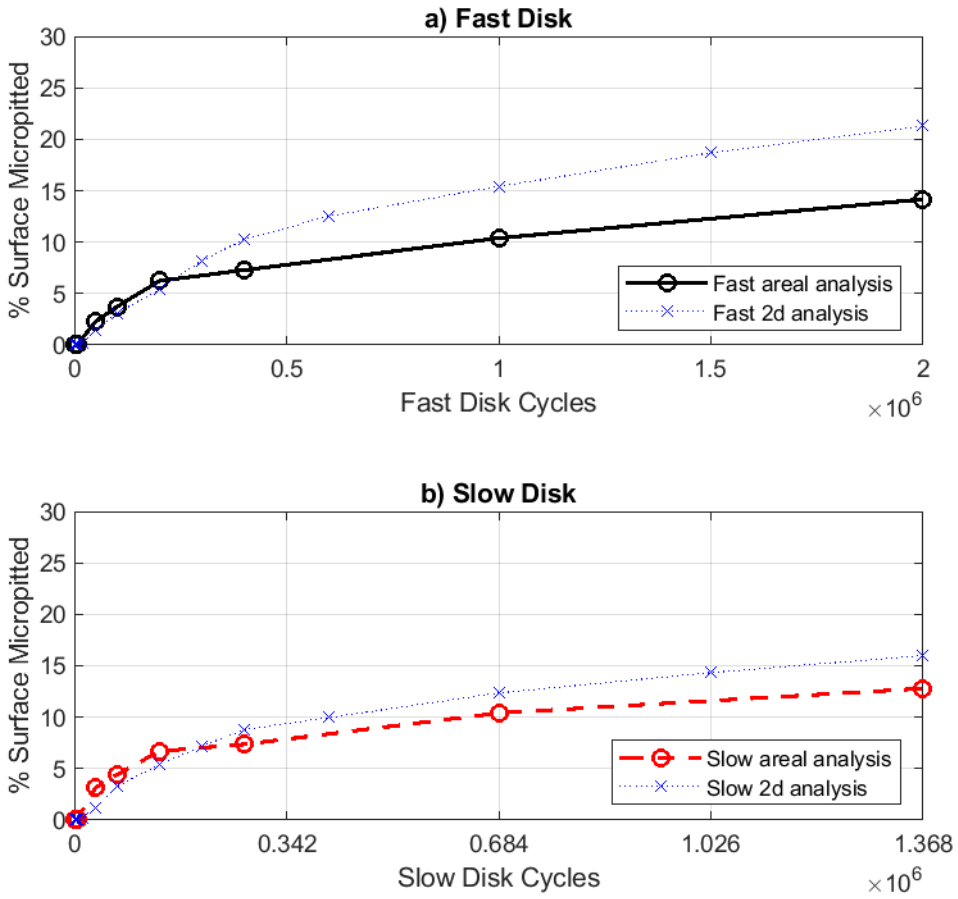

Figure 5.7.4 Percentage of surface micropitted for the a) fast and b) slow surfaces in the centrepoint test.

The rate of micropitting during the test for each surface can be seen below in Figure 5.7.5. It is notable that on both surfaces the peak values occurring during load stages 3 and 4 are followed by a lower 'ledge', which maintained an elevated rate of micropitting through load stages 5 and 6. This contrasts with all previous tests in

which a continuous decrease was seen from the peak value until a steadier, low rate of micropitting was established.

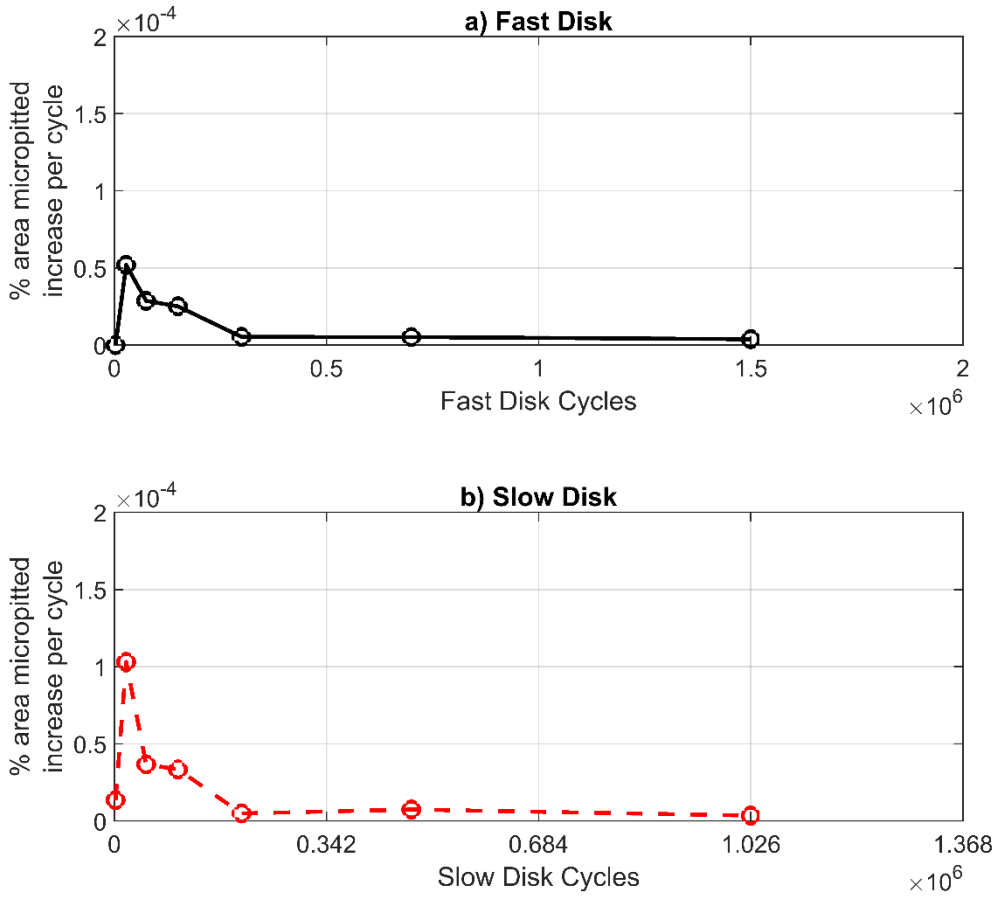

Figure 5.7.5 Rate of micropitting for the a) fast and b) slow surfaces of the centrepoint test as assessed by the areal analysis.

The values of the micropitting factorial analysis parameters for the centrepoint test are shown below in Table 5.7.1.

Table 5.7.1 Micropitting factorial evaluation parameters for the centrepoint test.

Parameter	Fast Surface	Slow Surface
% Pitted at conclusion of test	14.17	12.79
N3 / cycles	74,960	47,796
Peak rate of micropitting %/cycle	51.92×10^{-6}	103.00×10^{-6}
Average rate of micropitting between LS08 and LS10 %/cycle	5.18×10^{-6}	7.41×10^{-6}
Volume removed $\mu m^3/mm^2$	82.5×10^3	65.8×10^3
D5 / µm	-1.76	-1.61
% Micropitted at $1x10^5$ FD cycles	3.72	4.41

5.8 Test 6

Test 6 was carried out under conditions of high load and speed with a low SRR setting. In-test data in Figure 5.8.1 shows high amounts of friction during the initial running-in stages reaching almost 200 N. This decreased to a steady value between 150 – 160 N from load stage 7 until the conclusion of the test. The mean contact voltage for each fast disk revolution rose rapidly during the first phase of running-in, and by the second running-in stage had already reached an average of 34.7 mV, 77% of the maximum value. This continued to climb for the remainder of the test, averaging 37 mV during load stage 4 and then slowly increasing to a mean contact voltage reading of 39.6 mV during the final stage. The clearest interpretation of

this is that most of the reduction in direct surface contact was achieved during the initial running-in stage, but that further small reductions in asperity contact were achieved through fatigue and wear as the test continued. The disks did not reach a stable temperature during the short initial running-in stages, but once stabilised in each stage the mean disk temperature remained at 97 ±0.5°C throughout Test 6.

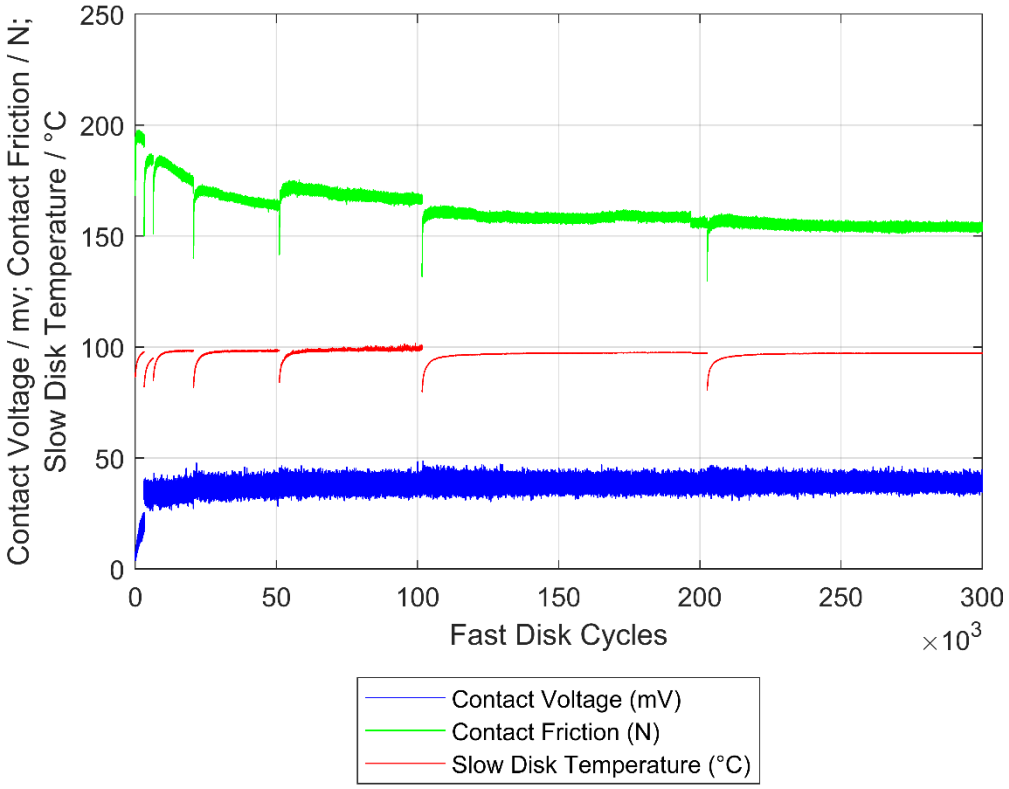

Figure 5.8.1 In-Test data recorded during Test 6.

The surfaces in Test 6 both developed very severe micropitting, the slow surface becoming the most heavily micropitted surface of the testing programme at the conclusion of the test. As can be seen in Figure 5.8.2a fast surface micropitting covered most asperities completely in the central region of the contact, although a small number of asperities survived with only mild micropitting. The density of micropitting decreased towards the edges of the contact. The slow surface, shown

in Figure 5.8.2b, includes two large regions (one of which occupies the whole of the central right half of the measured area) in which asperities have become almost impossible to distinguish due to the micropitting severity. A number of score or micro-scuff marks can be seen on the fast surface, although unlike in Test 2 where these were located in areas which appeared resistant to micropitting, there is no indication that these areas developed micropit resistance. On the slow surface a smaller number of these marks can be seen, mostly toward the contact edges, although one prominent mark can be seen in a heavily micropitted central area. While fewer of these marks appeared in the slow surface contact area, some marks were removed or obscured in the final surface by the micropitting process.

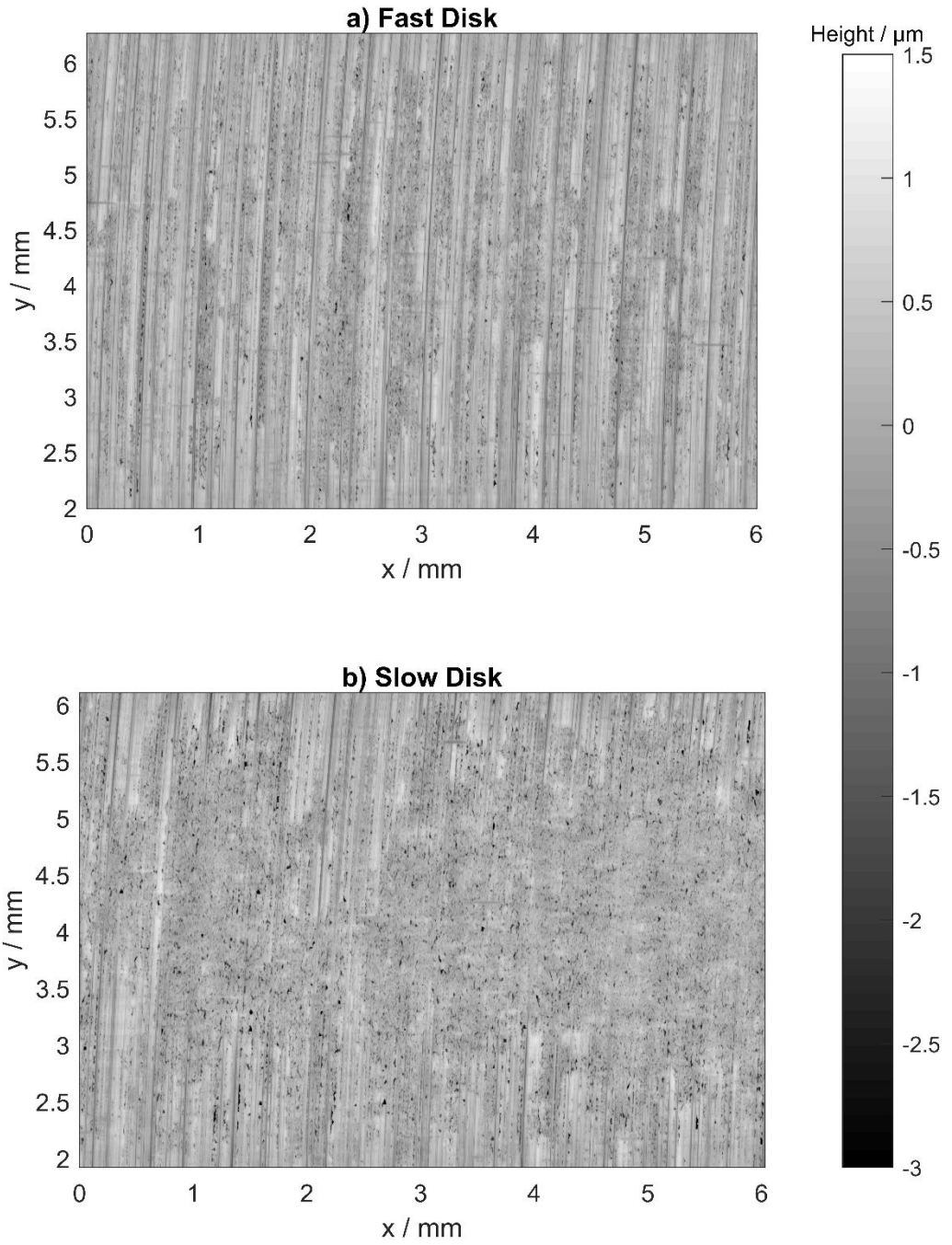

Figure 5.8.2 The a) fast and b) slow surfaces from of Test 6 at the conclusion of the test.

The percentage of the surface micropitted as evaluated through the test is shown in Figure 5.8.3. This shows that the slow surface exceeded 5% surface micropitted

before the conclusion of load stage 5 ($1x10^5$ fast disk cycles). By contrast the fast surface did not exceed 5% micropitted until approximately $3x10^5$ fast disk cycles had passed.

The two-dimensional analysis underestimated initial micropitting in the earliest stages on the fast surface, before exceeding the areal analysis from $3x10^5$ fast disk cycles onwards. The final fast surface value as assessed by the areal analysis was 13.63%, while the two-dimensional profile analysis reached a value of 23.30%, differing by a factor of 1.7. The slow surface two-dimensional profile analysis exceeded the areal analysis from load stage 6 onwards and continued to reach a final value of 46.90%, 2.41 times the final value of 19.43% assessed by the areal analysis.

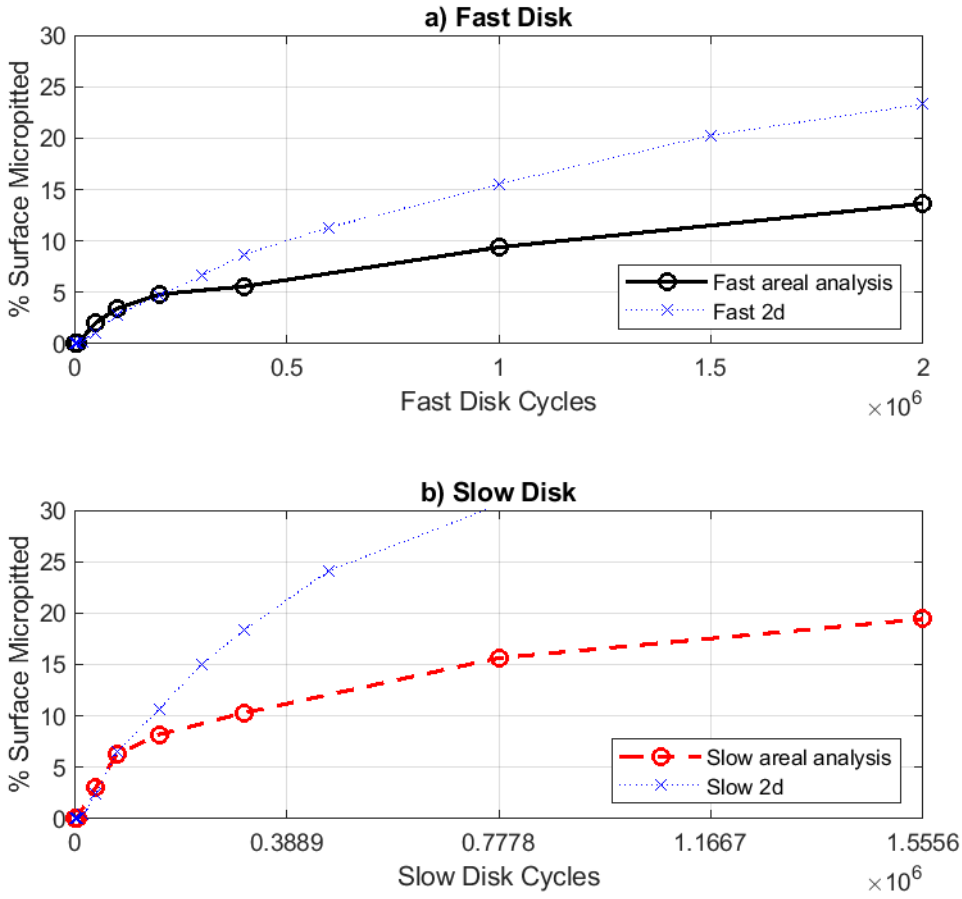

Figure 5.8.3 The a) fast and b) slow surface micropitting analyses for the Test 6 surfaces.

Analysis of the rate of micropitting shown in Figure 5.8.4 yields that the slow surface micropitted at a higher per-cycle rate than the fast surface in all stages of the test, and at a higher rate with respect to time throughout the first million cycles of the test. Across the final two load stages which go from 1 million to 2 million fast disk cycles the fast surface micropitted at a marginally higher rate with respect to time.

The peak rate of micropitting for the fast surface was reached between $6x10^3$ and $5x10^4$ fast disk cycles, followed by a rate which decreased at each of the next 3 evaluations. In contrast the slow surface experienced a sustained high peak of micropitting rate from $6x10^3$ to $1x10^5$ Fast disk cycles.

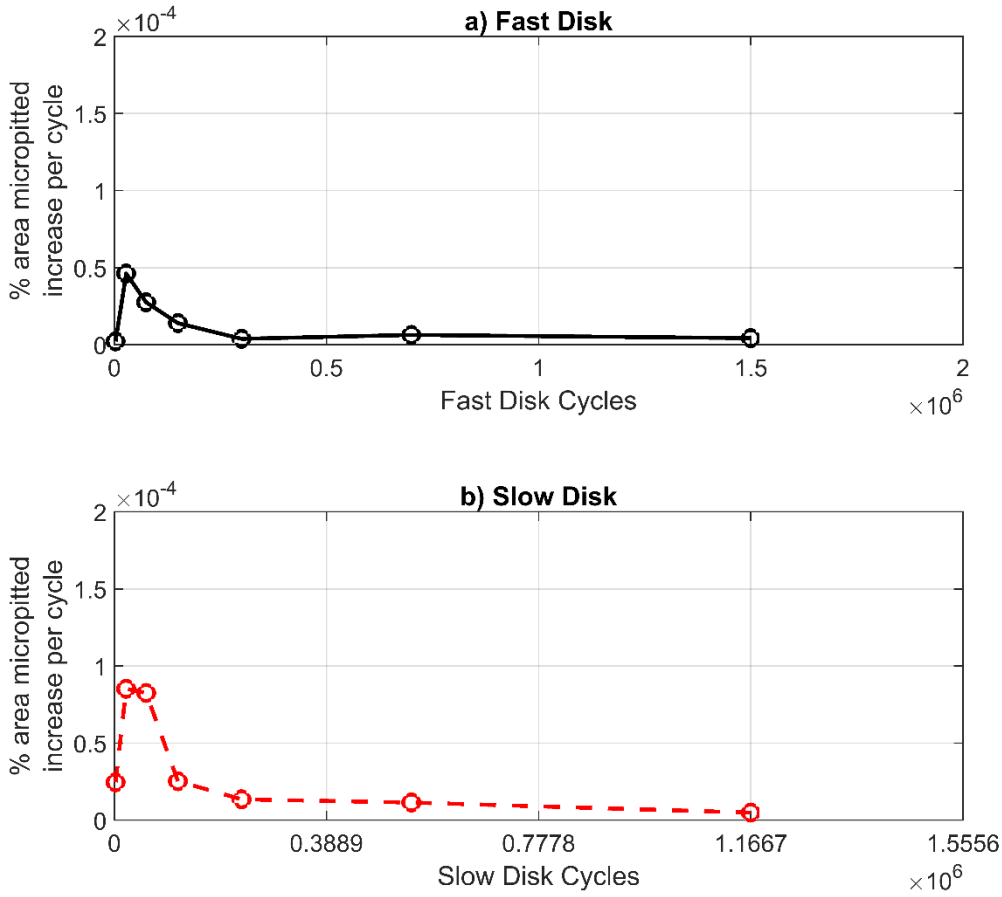

Figure 5.8.4 Micropitting rate for the a) fast and b) slow surfaces of Test 6.

The parameters for the factorial analysis of micropitting are shown in Table 5.8.1 below. From these it is clear that the micropitting experienced on the slow surface was more severe than on the fast in all respects.

Table 5.8.1 Micropitting factorial analysis parameters for Test 6.

Parameter	Fast Surface	Slow Surface
% Pitted at conclusion of test	13.63	19.43
N3 / cycles	84,730	49,549
Peak rate of micropitting %/cycle	46.17×10^{-6}	85.19×10^{-6}
Average rate of micropitting between LS08 and LS10 %/cycle	6.34×10^{-6}	11.4×10^{-6}
Volume removed $\mu m^3/mm^2$	70.4×10^3	112.9×10^3
D5 / µm	-1.45	-1.84
% Micropitted at $1x10^5$ FD cycles	3.42	6.24

5.9 Test 7

Test 7 operated under conditions in which each variable in the programme was at its low setting. As can be seen in Figure 5.9.1 the contact voltage initially began at approximately 7 mV in the first load stage, before decreasing to average 2.4 mV during load stage 2. The contact voltage then rose back to 7 mV by the conclusion of the third load stage. The gradual rise in contact voltage continued, but there was a wide range of values for each rotation from the start of load stage 3 which gradually decreased over the following $1x10^5$ fast disk cycles. This indicates a variability in the amount of direct contact depending on the exact regions of the surface in contact. As fatigue began to change the surface, it appears that the

amount of direct contact not only decreased but also became more uniform through each configuration of the surfaces. In the final load stage a mean contact voltage of 41.9 mV was recorded.

An initial friction reading of 99 N was observed at the first contact of the surfaces, however this decreased rapidly and was followed by a step-change of approximately 10 N between load stages 1 and 2. The friction stabilised at averages of 72 – 74 N during load stages 4 through 8. During load stages 9 through 12 noise due to a poor connection began to appear in the signal, hence these stages are not discussed further. Throughout the test, the disks reliably stabilised at a temperature of 84.5°C, giving the smallest temperature rise observed in the test programme.

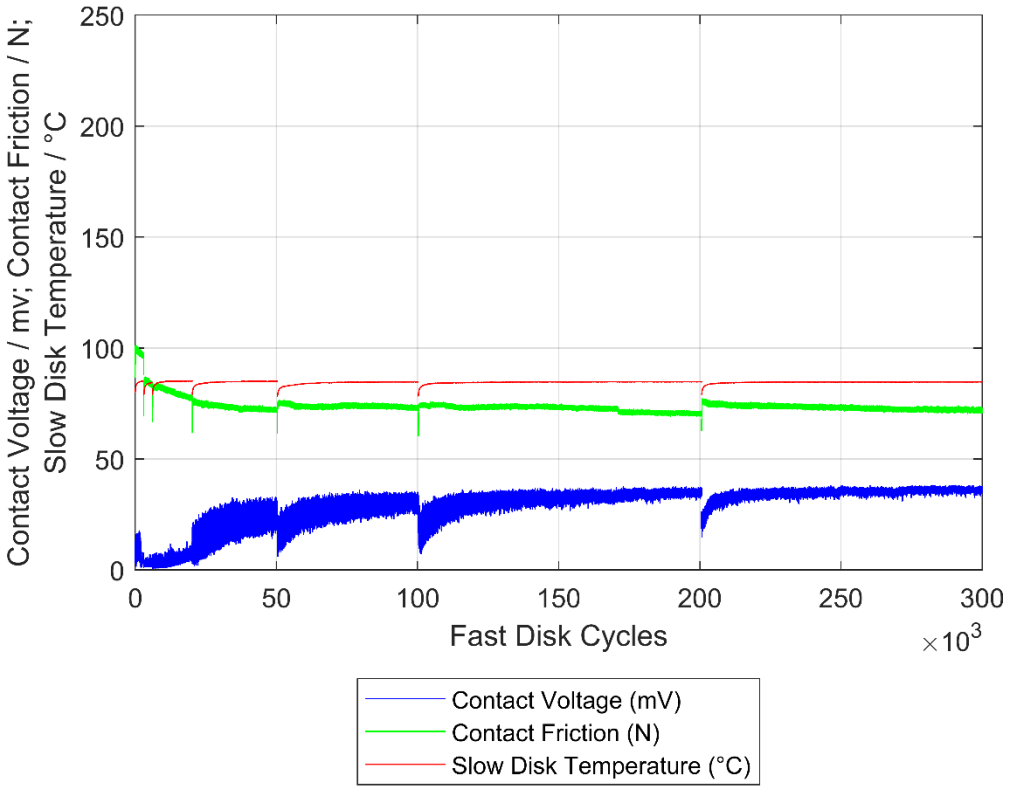

Figure 5.9.1 Test data recorded during the first 3x10^5 fast disk cycles of Test 7.

The surfaces in Test 7 exhibited the second-lowest amount of pitting in the experimental programme, although each surface still developed greater than double the percentage of contact area micropitted seen in Test 5. The way in which these micropits were distributed on the surface can be seen in the end of test surfaces shown in Figure 5.9.2. Micropits are distributed quite evenly across both surfaces, with neither showing any notable regions which resisted pitting and only very few small-sized groups of tightly clustered pits seen at the end of the test. On both surfaces both shallow and deep pits can be seen.

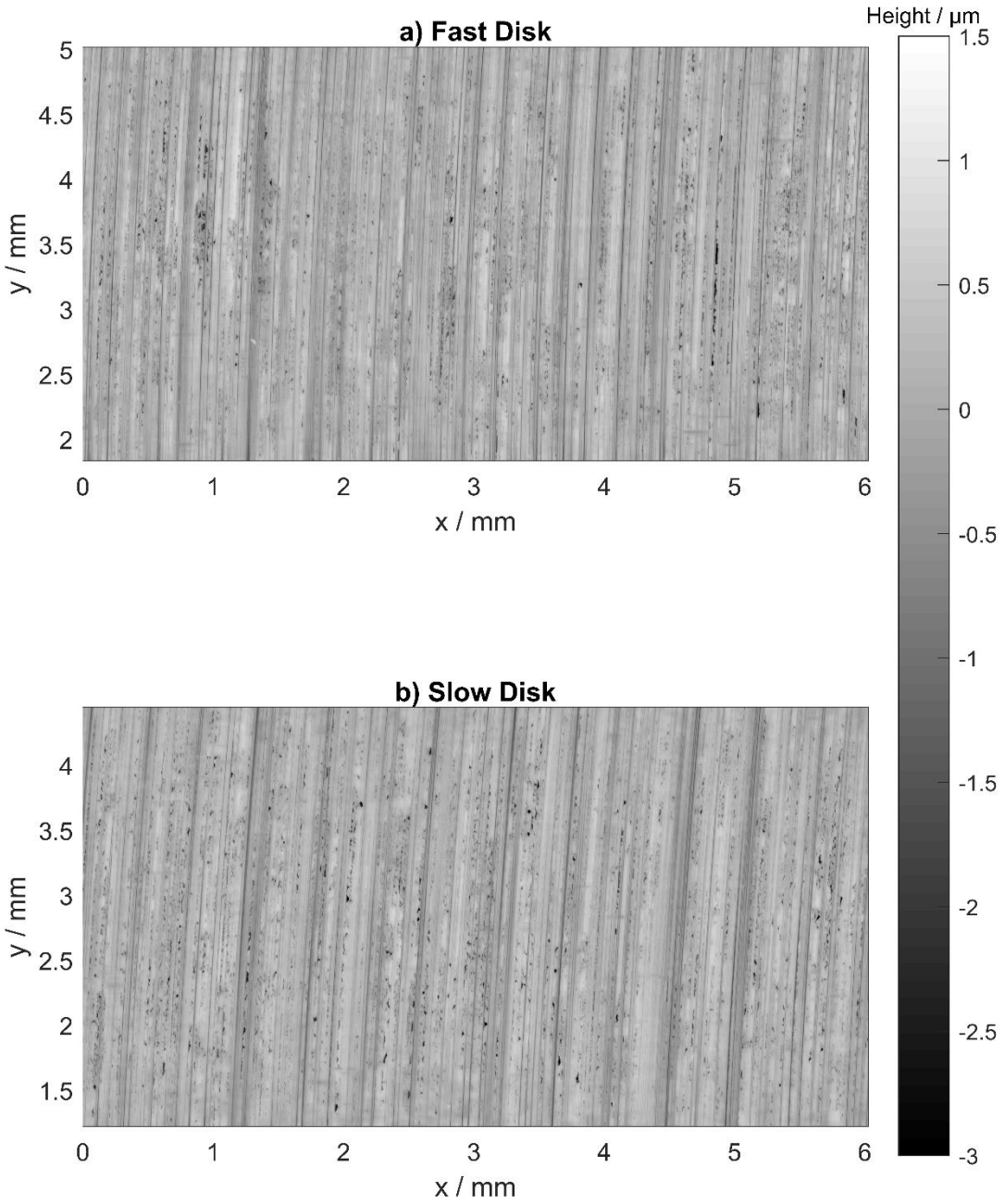

Figure 5.9.2 The a) fast and b) slow surfaces of Test 7 at the end of testing

The evaluations of percentage of surface pitted through the test can be seen in Figure 5.9.3. As in all tests the surfaces micropitted most rapidly in the early stages, the slow surface surpassing 5% micropitted at the start of load stage 6 ($1x10^5$ – $2x10^5$

fast disk cycles) with the fast surface passing this milestone later in the same load stage. The percentage of the fast surface micropitted continued to increase throughout the test, reaching a final value of 9.23% micropitted, while the slow surface effectively ceased to micropit further by the commencement load stages 11 and 12. The final value of micropitting recorded by the slow surface areal analysis was 9.63%.

The two-dimensional profile analysis on both Test 7 surfaces remained very close to the areal analysis from the start of the test to the conclusion of load stage 6, the slow surface two-dimensional and areal analyses being almost identical to this point. After this the two-dimensional analysis continued to rise at a faster rate than the areal analysis on both surfaces, with the two-dimensional analyses determining 14.74% micropitted on the fast surface and 19.68% on the slow surface. These differ from the areal analysis by factors of 1.6 and 2.0 respectively.

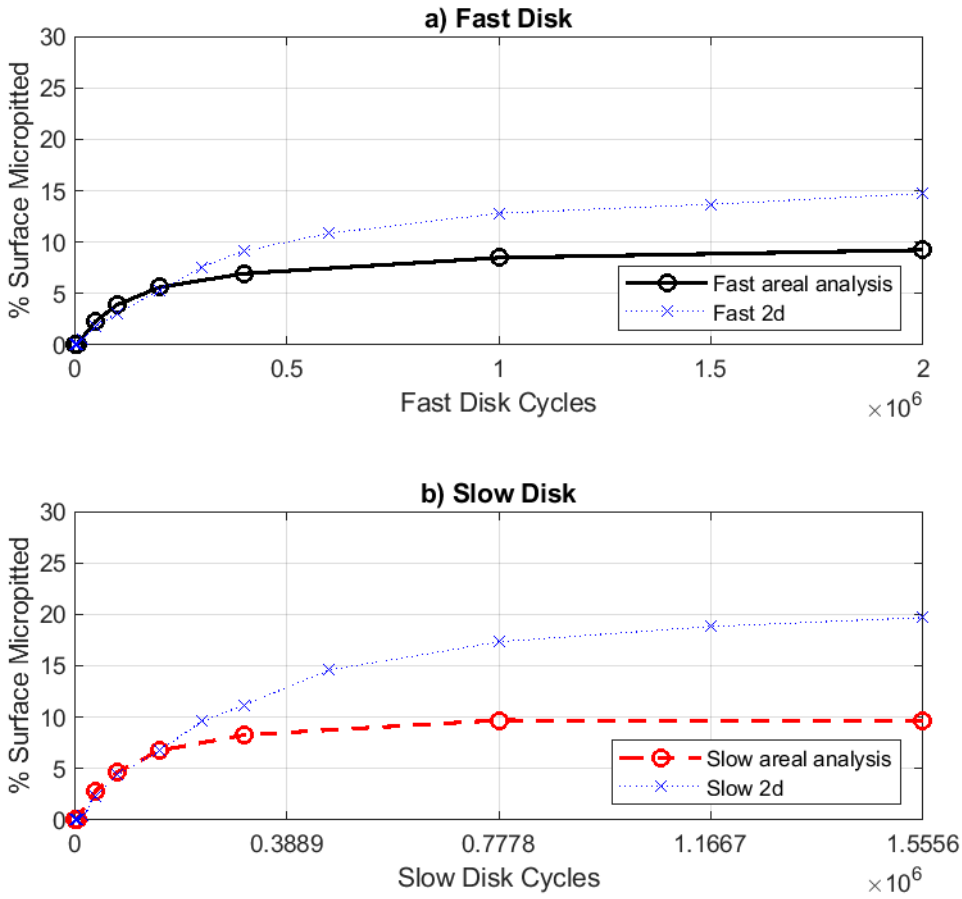

Figure 5.9.3 Percentage micropitted analyses for the a) fast and b) slow surfaces of Test 7

The rate of micropitting on each surface can be seen in Figure 5.9.4. Both surfaces displayed peak rates of micropitting during load stages 3 and 4 (between $6x10^3$ and $5x10^4$ fast disk cycles) followed by a rapid decay in micropitting rate which continued to decline until the test's conclusion.

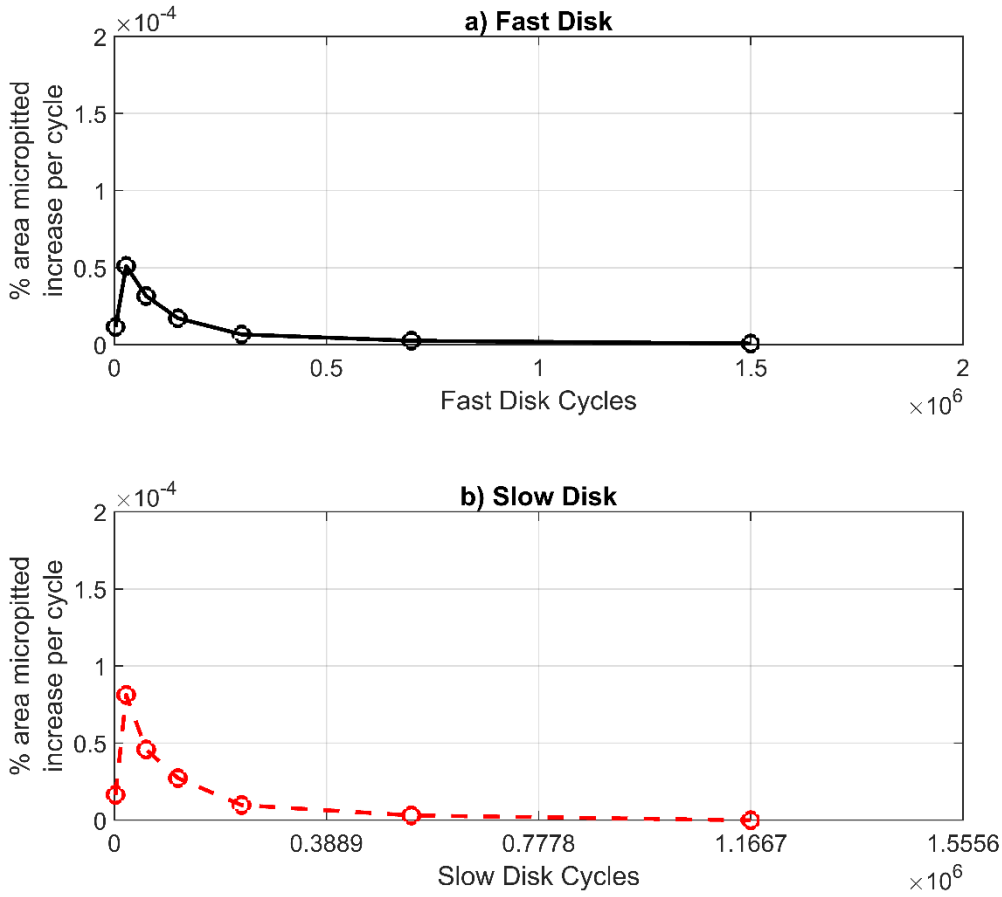

Figure 5.9.4 Micropitting rate for the a) fast and b) slow surfaces of Test 7, as evaluated by the areal analysis.

The micropitting parameters used for Test 7 in the factorial analysis are shown in Table 5.9.1 below.

Table 5.9.1 Micropitting factorial analysis factors for Test 7

Parameter	Fast Surface	Slow Surface
% Pitted at conclusion of test	9.23	9.63
N3 / cycles	71,581	54,028
Peak rate of micropitting %/cycle	51.1×10^{-6}	81.2×10^{-6}
Average rate of micropitting between LS08 and LS10 %/cycle	2.56×10^{-6}	3.07×10^{-6}
Volume removed $\mu m^3/mm^2$	41.8×10^3	43.7×10^3
D5 / µm	-1.52	-1.65
% Micropitted at 1×10^5 FD cycles	3.90	4.64

5.10 Test 8

The final test in the factorial programme, Test 8 was conducted at the low pressure setting of 1.2 GPa, with both entrainment and SRR at their high settings. Due to a faulty electrical connection, the contact voltage did not record correctly during this test, however the friction and temperature data recorded during Test 8 are shown below in Figure 5.10.1. The friction initially peaks to approximately 72 N during the first load stage, but decreased over the course of load stages 1 through 6 to settle in the 44 – 50 N range. The disk temperature consistently stabilised to a value of 92°C.

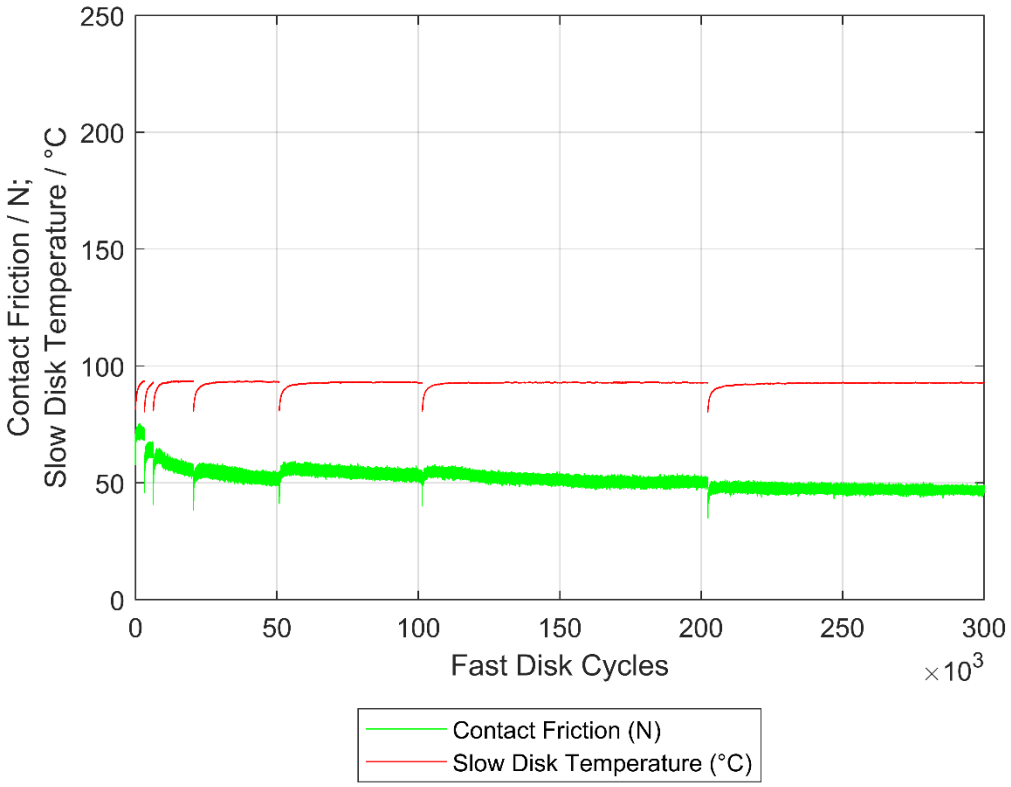

Figure 5.10.1 In test data recorded during the first 3x10^5 fast disk cycles of Test 8.

Both fast and slow surfaces in Test 8 micropitted extensively, as can be seen in Figure 5.10.2. While both surfaces were very similar in their micropitting density in the central area of the contact, the fast disk exhibited more micropitting at the edges of the contact than was seen for the slow surface.

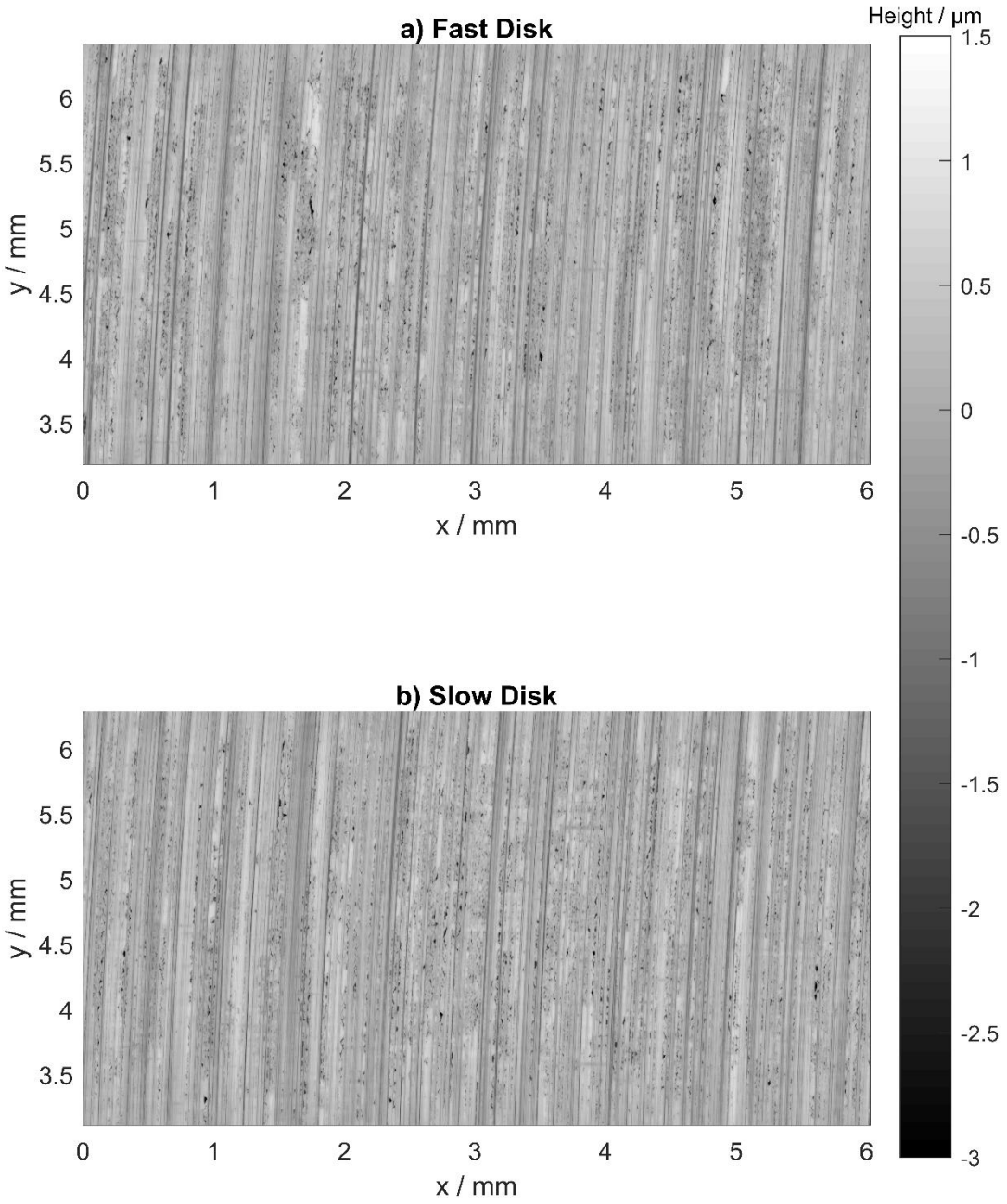

Figure 5.10.2 The a) fast and b) slow surfaces at the end of Test 8.

As is shown in Figure 5.10.3 both surfaces finished Test 8 with similar amounts of micropitting – 11.26% and 10.57% for the fast and slow surfaces respectively. The fast surface led in percentage micropitted throughout the test, the maximum

difference of 1.16% surface micropitted at the close of load stage 6. The rate of micropitting on the slow surface accelerated during the final two load stages, while the rate of micropitting decreased on the fast surface, reducing the difference between the surfaces. The fast surface replica taken after load stage 4 ($5x10^4$ fast disk cycles) had to be discarded due to poor replica quality and is not included in this analysis.

For both surfaces the two-dimensional analysis was extremely similar to the areal analysis during the first six load stages. The two-dimensional profile analysis increased at a faster rate than the areal analysis after this point however, continuing to finish with final values of 19.46% and 15.76% micropitted on the fast and slow surfaces at the end of testing. This differed from the areal results by factors of 1.7 and 1.4 for the fast and slow surfaces respectively.

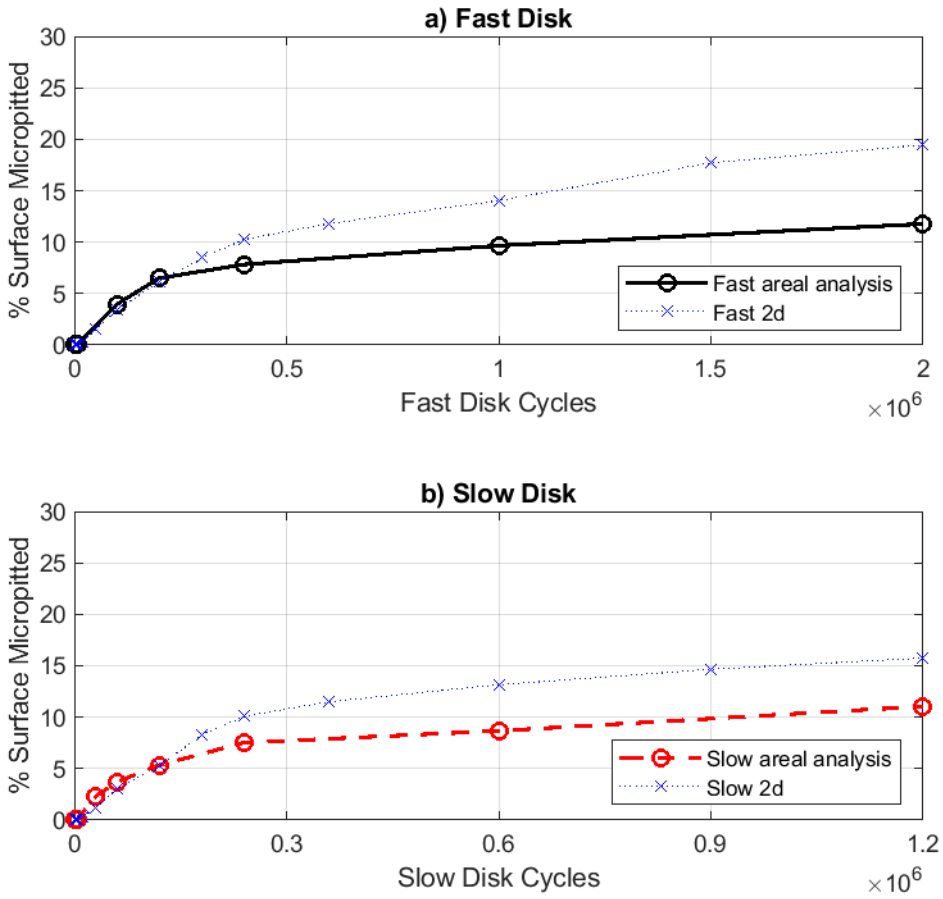

Figure 5.10.3 Percentage of contact area micropitted on the a) fast and b) slow surfaces of Test 8.

Figure 5.10.4 shows the rate of micropitting evaluated for the surfaces in Test 8. In both cases the peak of micropitting rate was inside the first $1x10^5$ cycles. In the case of the fast surface the peak is artificially lowered due to the need to discard the replica at $5x10^4$ fast disk cycles - which tended to hold the highest rate of pitting in the tests in this programme. It is clear from the graphs that the rate of micropitting on the slow surface decreased more slowly from the initial peak than the fast surface. During load stages 9 and 10 the fast surface micropitted at a higher

rate by time, but the slow surface micropitting rate increased during the final 1 million fast disk cycles while the fast surface rate fell.

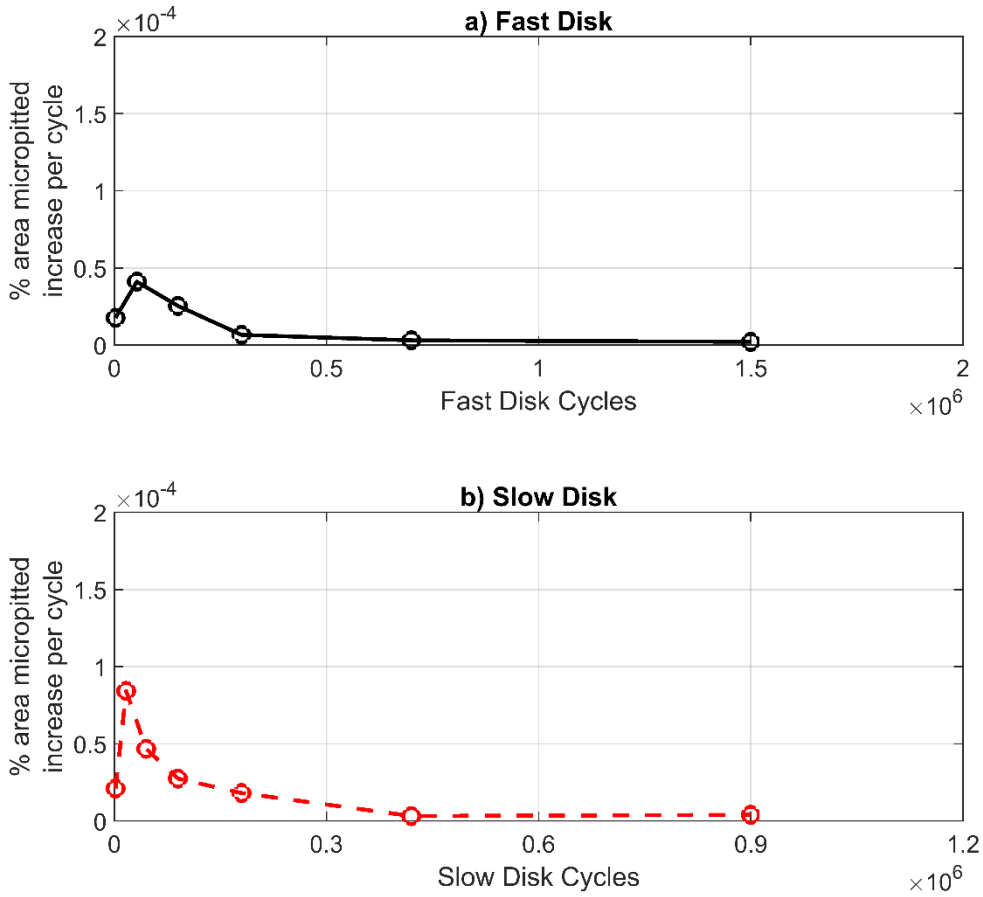

Figure 5.10.4 Rate of micropitting on the a) fast and b) slow surfaces of Test 8 as evaluated using the areal analysis.

The micropitting parameters for the Test 8 surfaces are shown below in Table 5.10.1.

Table 5.10.1 Micropitting factorial analysis parameters for Test 8.

Parameter	Fast Surface	Slow Surface
% Pitted at conclusion of test	11.77	11.05
N3 / cycles	52,850	74,924
Peak rate of micropitting %/cycle	41.07×10^{-6}	84.27×10^{-6}
Average rate of micropitting between LS08 and LS10 %/cycle	3.05×10^{-6}	3.20×10^{-6}
Volume removed $\mu m^3/mm^2$	61.6×10^3	53.9×10^3
D5 / µm	-1.55	-1.60
% Micropitted at $1x10^5$ FD cycles	3.97	3.70

5.11 Individual Micropitting Tests Summary

Figure 5.11.1 below shows the progress of percentage surface micropitted throughout the test duration as evaluated by the areal analysis for all tests, up to 2 million fast disk cycles. Figure 5.11.2 shows the micropitting rates through all tests up to 2 million fast disk cycles. Note that, as previously, for the micropitting rates the datapoints are evaluated halfway between measured areal scans – hence only the line for Test 1 continues beyond the point shown at Load Stage (LS) 11, which is actually the mean rate of increase between areal scans at Load Stages 10 and 12. On both graphs, the x-axis markers indicate the conclusion of the stage

marked, with the x axis markers for the conclusion of Load Stages 1 and 2 omitted for legibility.

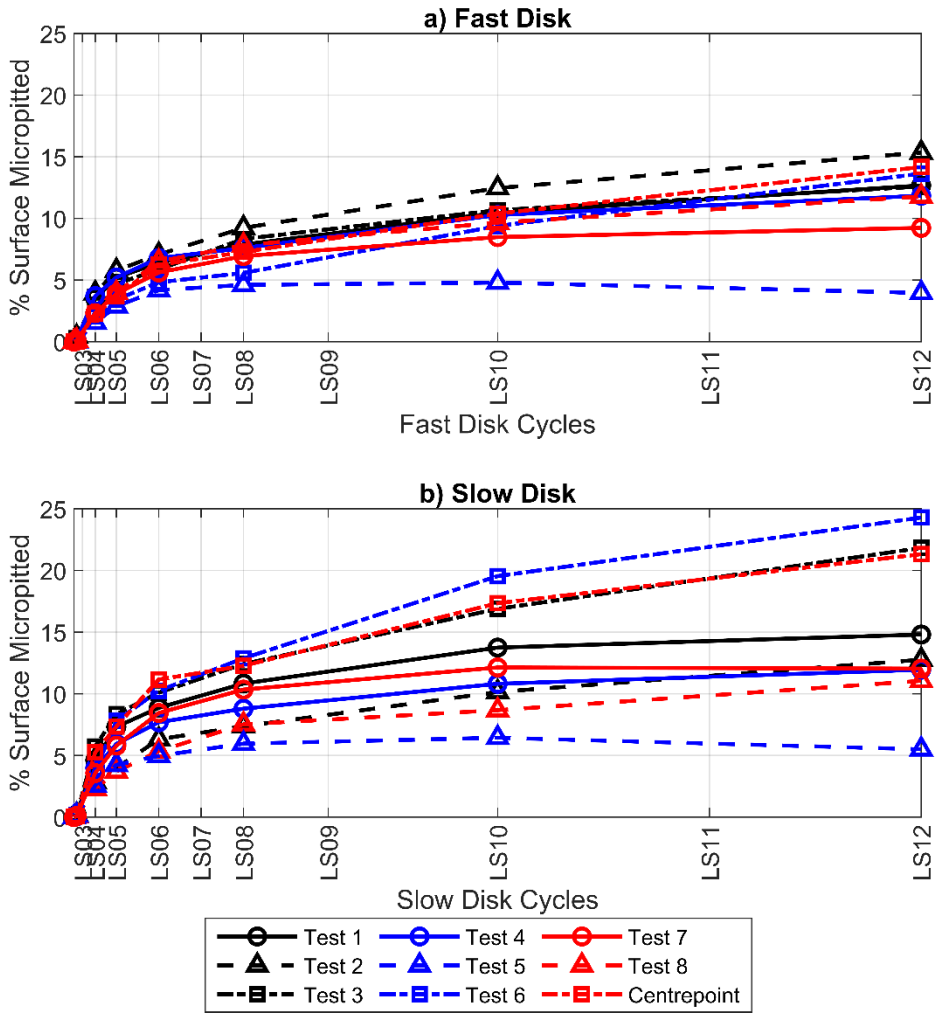

Figure 5.11.1 Percentage micropitted throughout all tests for the a) fast disk and b) slow disk.

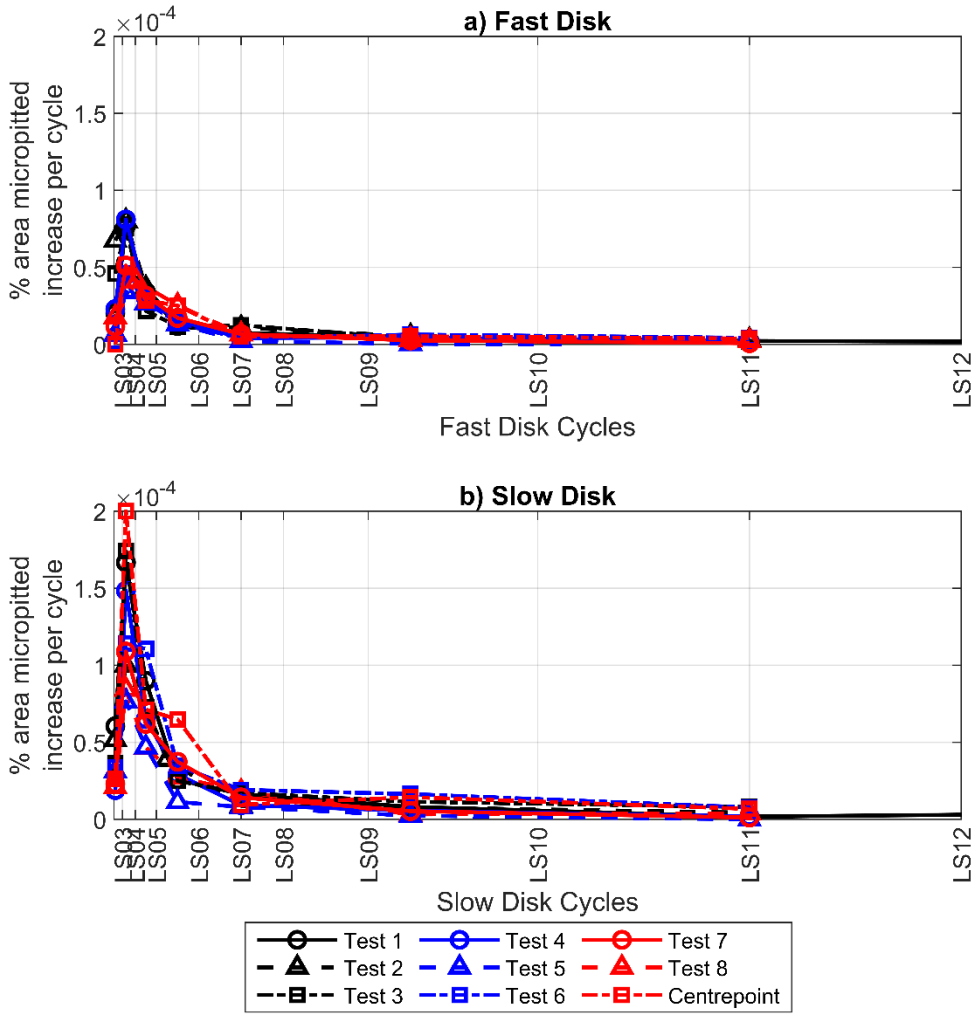

Figure 5.11.2 Micropitting rate throughout all tests for the a) fast disk and b) slow disk.

Micropitting parameters for all tests are summarised in Table 5.11.1 and Table 5.11.2 for the fast and slow surfaces respectively.

Table 5.11.1 Micropitting parameters recorded in each test for the fast disk.

Test	% Pitted at Conclusion of Test	N3 / Cycles	Peak rate of micropitting / %/Cycle	Average rate of micropitting between LS08 & LS10 / %/cycle	Volume removed / $\mu m^3/mm^2$	D5 / µm	% Micropitted at 1 x 10^5 FD cycles
Test 1	12.67	43,515	76.73×10^{-6}	4.28×10^{-6}	71.8×10^3	-1.77	5.20
Test 2	15.34	38,348	80.22×10^{-6}	5.38×10^{-6}	85.9×10^3	-1.69	5.77
Test 3	12.59	42,030	75.62×10^{-6}	3.89×10^{-6}	68.4×10^3	-1.63	4.69
Test 4	11.84	41,328	81.03×10^{-6}	4.47×10^{-6}	58.7×10^3	-1.46	5.21
Test 5	3.96	109,543	34.21×10^{-6}	0.31×10^{-6}	18.6×10^3	-1.32	2.88
Centrepoint Test	14.17	74,960	51.92×10^{-6}	5.18×10^{-6}	82.5×10^3	-1.76	3.72
Test 6	13.63	84,730	46.17×10^{-6}	6.34×10^{-6}	70.4×10^3	-1.45	3.42
Test 7	9.23	71,581	51.1×10^{-6}	2.56×10^{-6}	$41.8 X 10^3$	-1.52	3.90
Test 8	11.77	52,850	41.07×10^{-6}	3.05×10^{-6}	61.6×10^3	-1.55	3.97

Table 5.11.2 Micropitting parameters recorded in each test for the slow disk.

Test	% Pitted at Conclusion of Test	N3 / Cycles	Peak rate of micropitting / %/Cycle	Average rate of micropitting between LS08 & LS10 / %/cycle	Volume removed / $\mu m^3/mm^2$	D5 / µm	% Micropitted at 1 x 10^5 FD cycles
Test 1	14.80	33,817	166.70 x 10^{-6}	8.09 x 10^{-6}	78.0 x 10^3	-1.73	7.32
Test 2	12.76	57,594	99.92 x 10^{-6}	7.72 x 10^{-6}	62.0 x 10^3	-1.58	N/A
Test 3	17.46	34,355	130.44 x 10^{-6}	7.66 x 10^{-6}	86.5 x 10^3	-1.79	6.68
Test 4	11.95	38,929	148.38 x 10^{-6}	5.60 x 10^{-6}	53.6 x 10^3	-1.49	5.94
Test 5	4.40	85,518	56.82 x 10^{-6}	0.82 x 10^{-6}	20.0 x 10^3	-1.48	3.39
Centrepoint Test	12.79	47,796	103.00 x 10^{-6}	7.41 x 10^{-6}	65.8 x 10^3	-1.61	4.41
Test 6	19.43	49.549	85.19 x 10^{-6}	11.4 x 10^{-6}	112.9 x 10^3	-1.84	6.24
Test 7	9.63	54,028	81.20 x 10^{-6}	3.07 x 10^{-6}	43.7 x 10^3	-1.65	4.64
Test 8	11.05	74,924	84.27 x 10^{-6}	3.2 x 10^{-6}	53.9 x 10^3	-1.60	3.70

5.12 Factorial Analysis of Micropitting

In this section the parameters collected for each micropitting test are analysed to investigate the influence of each variable and their interactions on the output parameter.

5.12.1 Surface Micropitted at End of Test

The first parameter to be investigated is the extent of micropitting at the end of the standard 12 load stage test, containing 2 million fast disk cycles. This was considered as the percentage of contact area micropitted. The main effects of each variable for the fast and slow surfaces are shown below in Figure 5.12.1.

For both surfaces the pressure had the largest influence on the micropitting recorded at the end of the test, in both cases increased pressure resulting in increased micropitting. On the fast surface a similar effect was seen for the SRR, which exhibited an effect of only slightly lesser magnitude than seen for the pressure. In contrast, SRR had a negligible effect on the percentage of the slow surface micropitted at the end of test. On the fast surface, increased entrainment showed a protective effect, however this effect was negligible for the slow surface which showed considerable overlap between high and low entrainment results.

For the slow surface the centrepoint result was located on the line between mean results for all factors, which is indicative of a linear response. This was not the case for the fast surface, for which the centrepoint result was significantly distanced from the line in all cases.

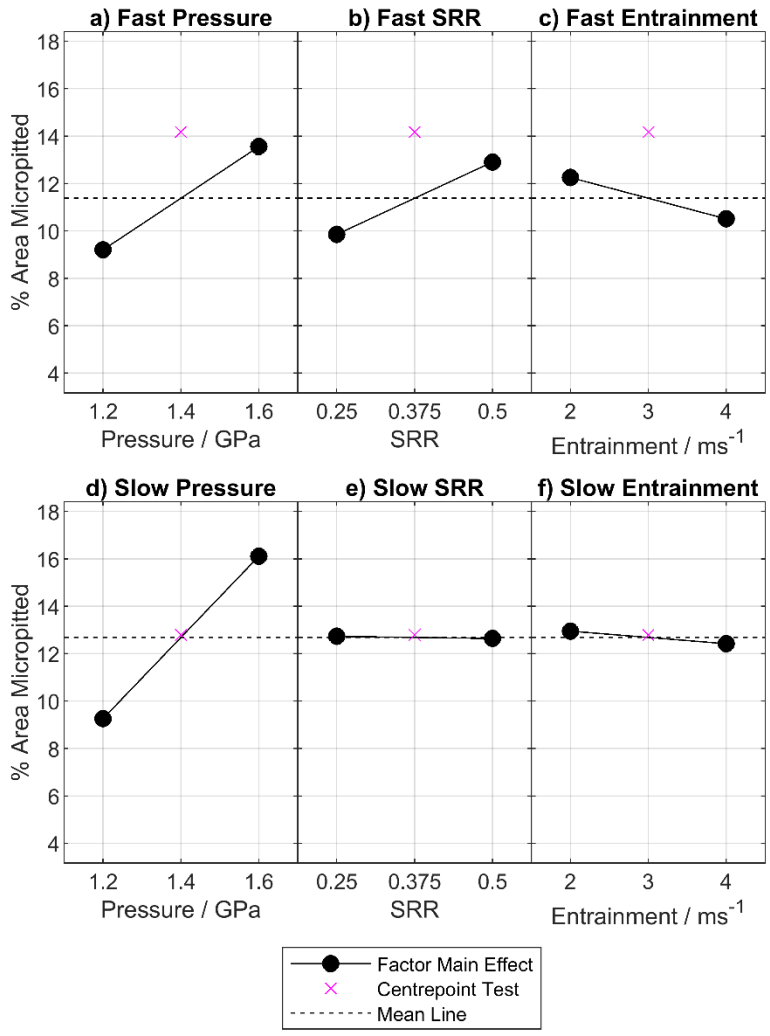

Figure 5.12.1 Main effects for the percentage of area micropitted at the end of test.

The main effects should not be considered in isolation however, but alongside inspection of two- and three- factor interactions. The two-factor interaction plots for percentage of surface micropitted are shown in Figure 5.12.2 below.

Both surfaces exhibited strong pressure-SRR interaction effects. On the fast surface, increases in pressure or SRR both had a greater micropitting-increasing influence when the other variable was at its low setting. On the slow surface, pressure was again seen to have a greater influence at low sliding. At high pressure, increasing

the SRR was shown to have the effect of decreasing the amount of micropitting – the opposite effect to when the pressure was low.

Pressure and entrainment also interacted on both surfaces, although only very mildly on the fast surface. In both cases, increased entrainment showed a protective effect at low pressure. On the fast surface, a lesser micropit-reducing effect was seen when pressure was high, but on the slow surface high entrainment coupled with high pressure worsened the micropitting outcome.

Entrainment and SRR did not interact strongly on the fast surface, but a small interaction effect was seen on the slow surface, where both variables at the same setting produced more micropitting than when one was high and the other low.

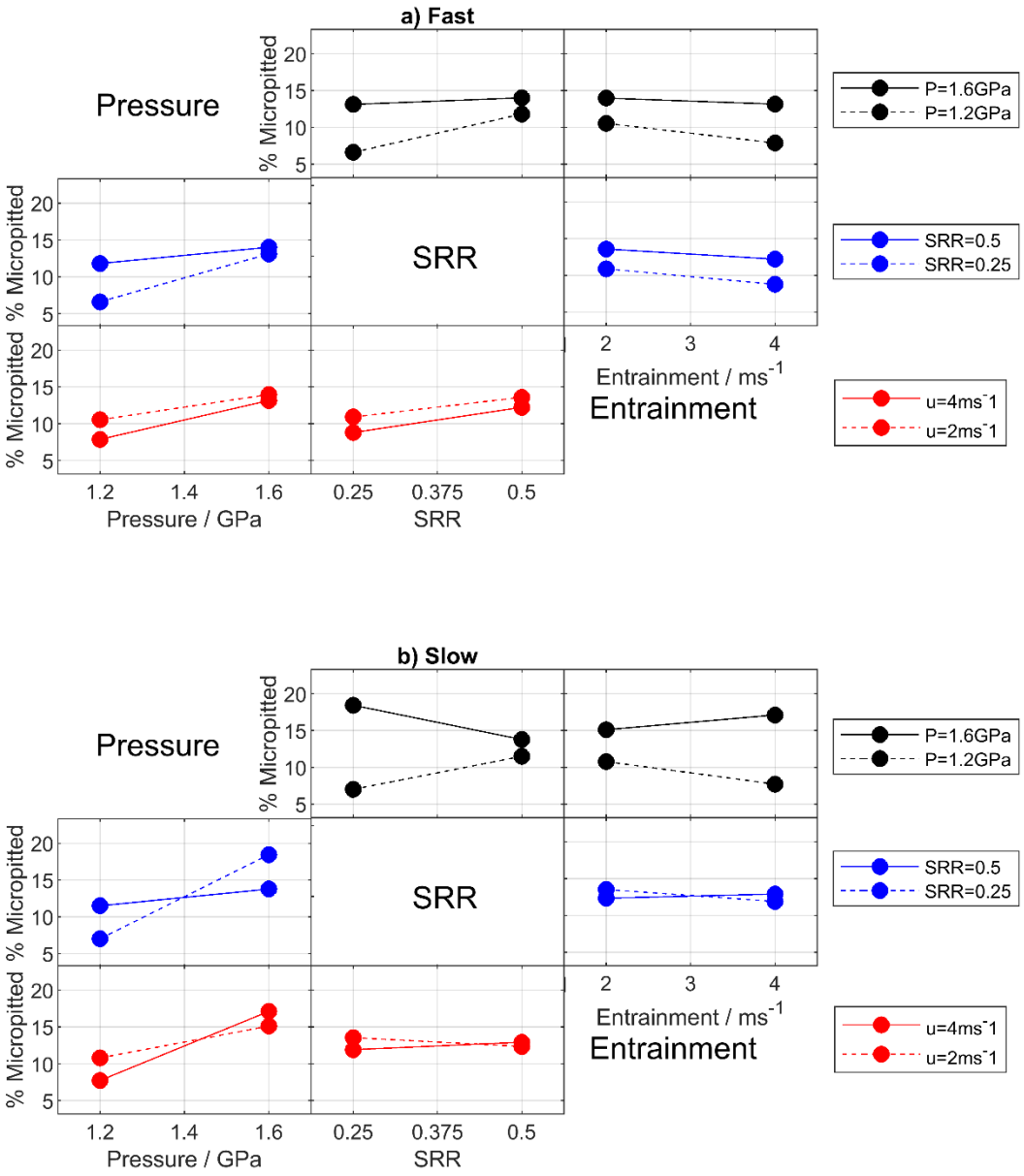

Figure 5.12.2 Two-factor interaction plots for % surface micropitted at end of test on the a) fast and b) slow surfaces.

By considering the changes in each two-factor interaction at the high and low setting of the third variable, the three-factor interactions can be investigated. The changes in the Pressure-SRR interaction with entrainment are shown below in Figure 5.12.3.

Considering Figure 5.12.3a and b it is clear that there was no interaction between SRR and pressure when the entrainment was low, but at high entrainment a clear interaction was present – the gradient of the low pressure line increased and the high pressure line had a negative gradient. Therefore, a three-factor interaction is present on the fast surface.

Figure 5.12.3c and d show the same interactions for the slow surface. There is a clear two-factor interaction in both, and the interaction is of a similar nature although the gradient of the low pressure line increases markedly from c to d. This suggests that there is also a three-factor interaction present on the slow surface but that the magnitude is less than the interaction seen on the fast surface.

The strengths of main factors and interaction effects for the percentage micropitted at end of test are shown in Table 5.12.1.

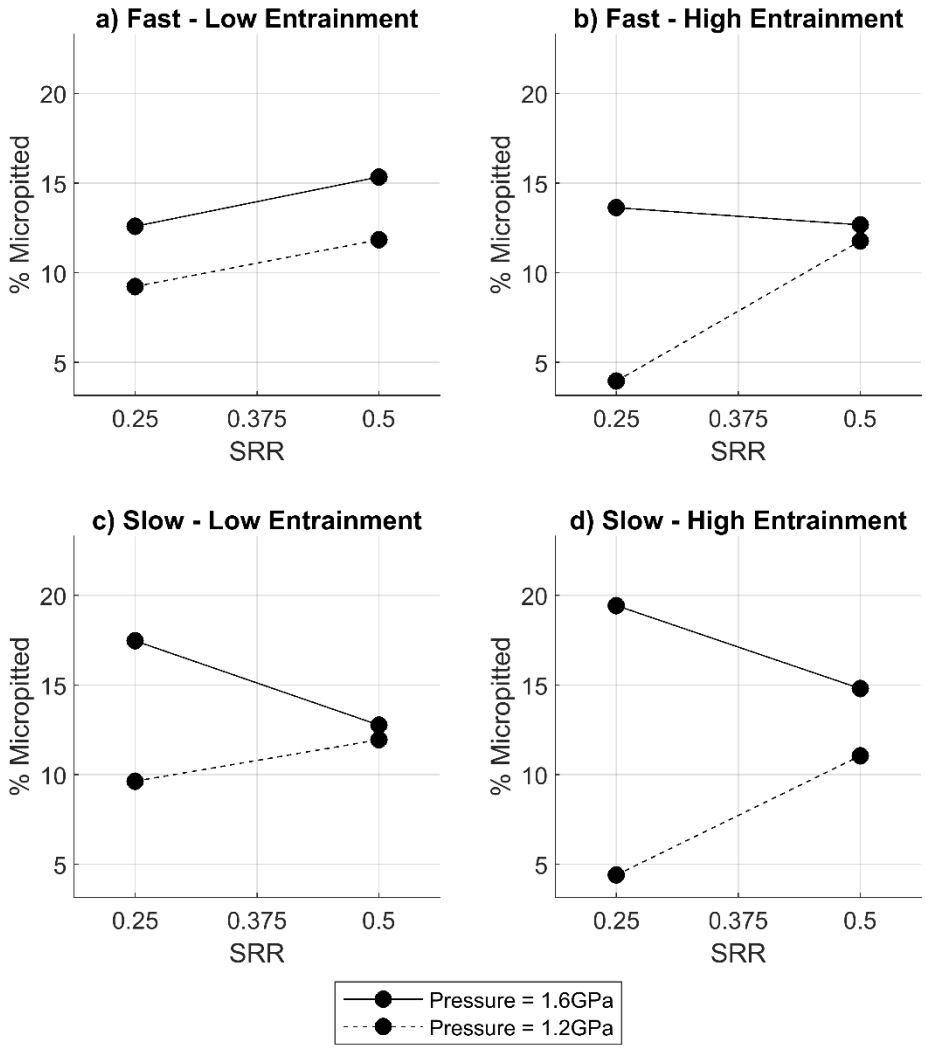

Figure 5.12.3 Two-factor interaction plots for pressure-SRR on each surface at low and high entrainment, for three-factor interaction analysis of micropitted area.

Table 5.12.1 Effects of main factors and interactions on % pitted at end of test.

	Fast Surface			Slow Surface		
Factor / Interaction	Low average / %	High Average / %	Effect / Δ%	Low average / %	High Average / %	Effect / Δ%
Pressure	9.20	13.56	4.36	9.26	16.11	6.85
SRR	9.85	12.91	3.06	12.73	12.64	-0.09
Entrainment	12.25	10.51	-1.74	12.95	12.42	-0.53
Pressure*SRR	12.46	10.30	-2.16	14.97	10.40	-4.57
Pressure*Entrainment	10.91	11.84	0.93	11.42	13.95	2.53
SRR*Entrainment	11.19	11.57	0.37	12.13	13.23	1.10
Pressure*SRR*Entrainment	10.26	12.49	2.23	12.15	13.22	1.07

5.12.2 Deepest Micropitted Points

For each surface the heights of all micropitted locations at the end of testing were recorded. The parameter referred to in this thesis as D5 was then calculated as the mean of the deepest 5% of micropitted points. This is reflective of the extreme depths of the micropits, ignoring the transitional points on the micropit walls.

The main effects of each parameter on D5 are shown in Figure 5.12.4. For both the fast and slow surfaces, pressure was again the main factor with the largest effect, increased pressure resulting in a lower value for D5 (i.e. deeper micropits). The SRR was the second largest influence for both surfaces, however the SRR appeared to influence micropit depth in opposite directions on the two surfaces. Closer inspection of the values used to calculate the SRR effect on the fast surface showed a clear offset between the high and low SRR data, however the high and low SRR data on the slow surface entirely overlapped. It is possible that the SRR effect on the slow surface is smaller than calculated, however further experimentation would be required to confirm this.

On the slow surface entrainment had minimal effect, and inspection of the high and low entrainment values confirmed this, showing complete overlap at each setting. There is an apparent small effect from entrainment on the fast surface however inspection of the range of values at the low and high settings again showed significant overlap. It is therefore possible that this effect is fact smaller than shown.

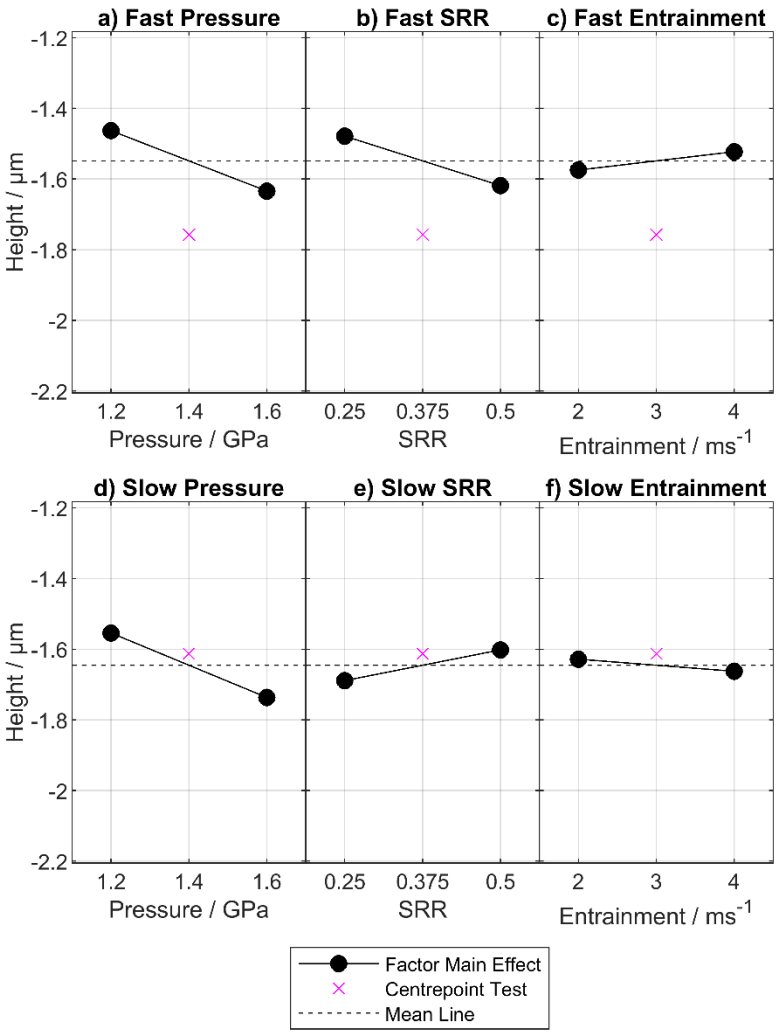

Figure 5.12.4 Main effects for depths of deepest 5% of pitted points at end of test

Two-factor interaction effect plots are shown in Figure 5.12.5.

The pressure*SRR interactions in Figure 5.12.5a show only a weak interaction present on the fast surface with increases in both SRR and Pressure increasing pit depth more when the other variable was set high. On the slow surface the interactions were more pronounced. While SRR had no influence at low pressure, increased SRR at high pressure deepened micropits. Increasing pressure deepened micropits at both high and low SRR, but had a larger effect when SRR was at the low setting.

No interaction was seen for pressure*entrainment on the fast surface, as illustrated by the parallel lines. On the slow surface, pressure deepened pits by a greater amount when the entrainment was high.

Interactions were seen for SRR*entrainment on both surfaces, with the opposite effects being seen on each surface. On the fast surface, high entrainment deepened pits when SRR was high but resulted in shallower micropits when SRR was low. SRR had minimal influence when entrainment was low. Conversely, on the slow surface low entrainment led to shallower pits when SRR was high and deeper pits when SRR was low, with SRR showing minimal influence under high entrainment conditions.

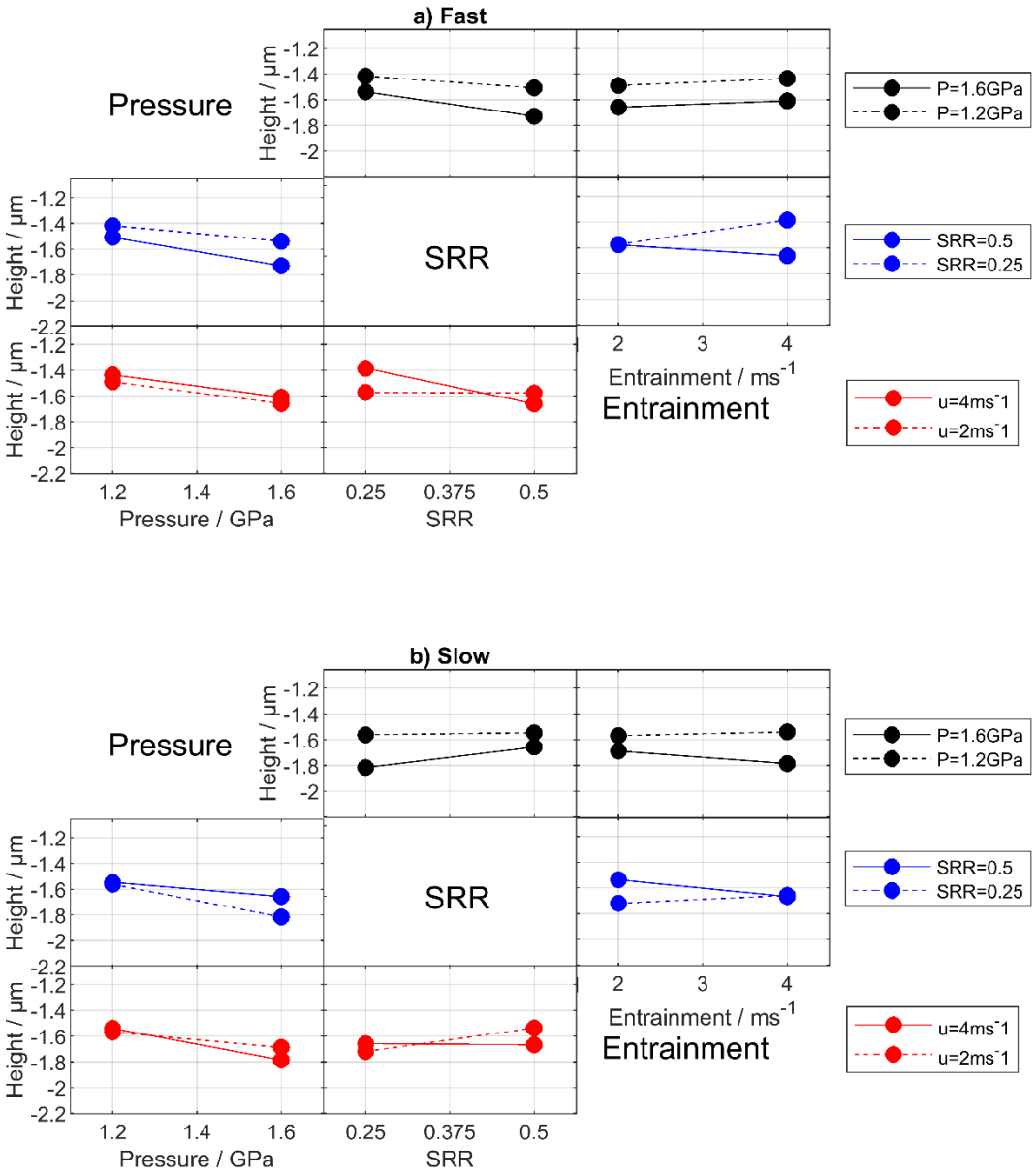

Figure 5.12.5 Two-factor interaction plots for D5 on the a) fast and b) slow surfaces.

Figure 5.12.6 shows two-factor pressure*SRR interaction plots at low and high entrainment. In Figure 5.12.6a and b the same two-factor pressure*SRR interaction can be seen at both high and low entrainment, albeit with a change in angle due to

the SRR*entrainment interaction. This shows that there is minimal three-factor interaction occurring on the fast surface.

On the slow surface the two-factor pressure*SRR interaction does change with entrainment - increasing SRR causing shallower micropits at low pressure and entrainment, but deepening micropits at low pressure and high entrainment. The angle between the two lines is therefore changed, indicating the presence of a three-factor interaction.

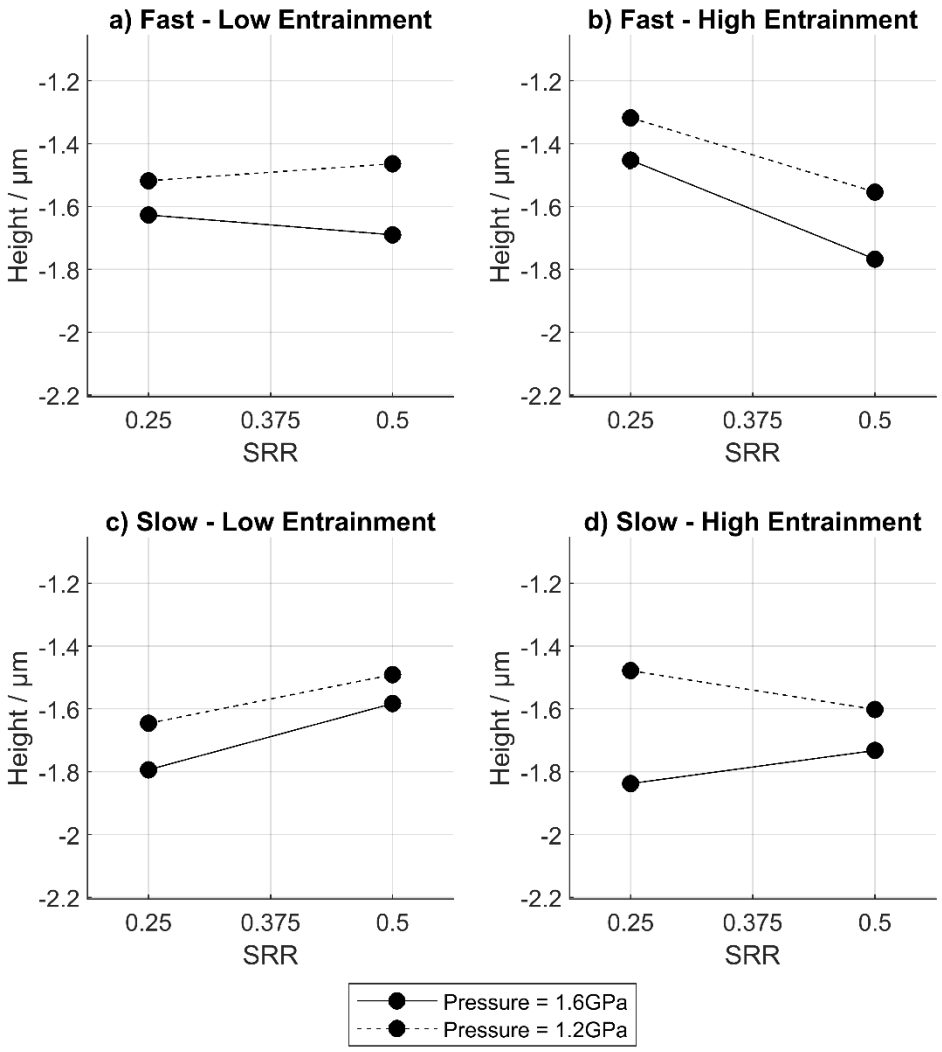

*Figure 5.12.6 Two-factor interaction plots for pressure*SRR on each surface at low and high entrainment, for three-factor interaction analysis of D5.*

The influences of main factors and interaction effects are shown below in Table 5.12.2.

Table 5.12.2 Effects of main factors and interactions on D5.

Factor / Interaction	Fast Surface			Slow Surface		
	Low average / µm	High Average / µm	Effect / Δµm	Low average / µm	High Average / µm	Effect / Δµm
Pressure	-1.463	-1.634	-0.171	-1.554	-1.737	-0.183
SRR	-1.479	-1.619	-0.140	-1.689	-1.602	0.087
Entrainment	-1.575	-1.523	0.052	-1.628	-1.663	-0.034
Pressure*SRR	-1.524	-1.573	-0.049	-1.681	-1.610	0.071
Pressure*Entrainment	-1.547	-1.550	-0.003	-1.614	-1.677	-0.063
SRR*Entrainment	-1.481	-1.616	-0.136	-1.597	-1.693	-0.096
Pressure*SRR*Entrainment	-1.544	-1.554	-0.010	-1.624	-1.667	-0.043

5.12.3 Volume Removed

The volume removed due to micropitting was calculated for each end of test disk surface using the method outlined in Section 3.7. To allow for the differing size of contact areas between the high and low pressure setting, the volume removed was expressed per unit area. The main effects of each factor on volume removed are shown in Figure 5.12.7.

On the fast surface, the influence of each factor on the volume removed was remarkably like that seen for the percentage pitted at end of test discussed in Section 5.12.1. Pressure provided the largest influencing factor, closely followed by SRR – in both cases the higher setting resulting in a greater volume removed. On the fast surface increased entrainment velocity reduced the volume removed through micropitting. No plots for the fast disk main effects passed through or near the centrepoint result.

On the slow surface, pressure was again the most significant effect and acted to increase the volume removed by micropitting. This pressure effect was larger than seen on the fast surface. The SRR and entrainment effects on the slow surface were both extremely small in magnitude and appeared to influence the volume removed in the opposite direction to that seen on the fast surface. For both SRR and entrainment on the slow surface the data at high and low entrainment overlapped entirely, likely indicating negligible influence on the slow surface.

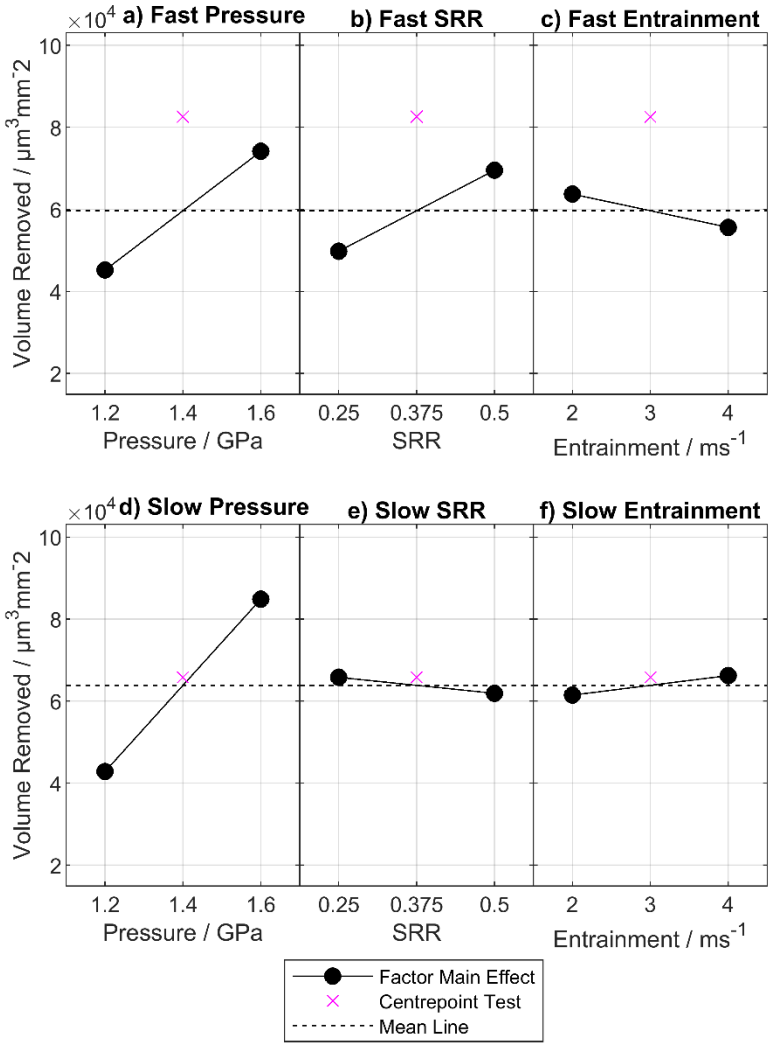

Figure 5.12.7 Main effects for the volume removed through micropitting at the end of test.

The two-factor interaction plots for the volume removed are shown in Figure 5.12.8. Again, there were significant differences between the interactions seen on the fast and slow surfaces.

On both surfaces the pressure*SRR interaction was significant, however the nature of the interaction was substantially different. On the fast surface both SRR and pressure had more significant influence when the other variable was at its low setting, but in all cases increasing SRR or pressure continued to increase the volume removed. On the slow surface, pressure had a stronger volume-removal effect when the SRR was low - however if SRR was increased, in the high pressure condition the volume removed decreased.

Pressure*entrainment and SRR*entrainment interactions on the fast surface were minimal, as can be seen in the parallel and near-parallel lines on Figure 5.12.8a. Interactions were present on the slow surface however. For the pressure*entrainment interaction, pressure had a stronger influence on volume removed under high entrainment conditions. Under low pressure conditions, increasing entrainment reduced the volume removed. Conversely increased entrainment resulted in a larger volume removed when pressure was high.

The SRR*entrainment interaction on the slow surface showed a possible inconsistent main variable effect where the volume removed decreased significantly only in the condition of low entrainment and high sliding. This can result in a false contribution to a main effect.

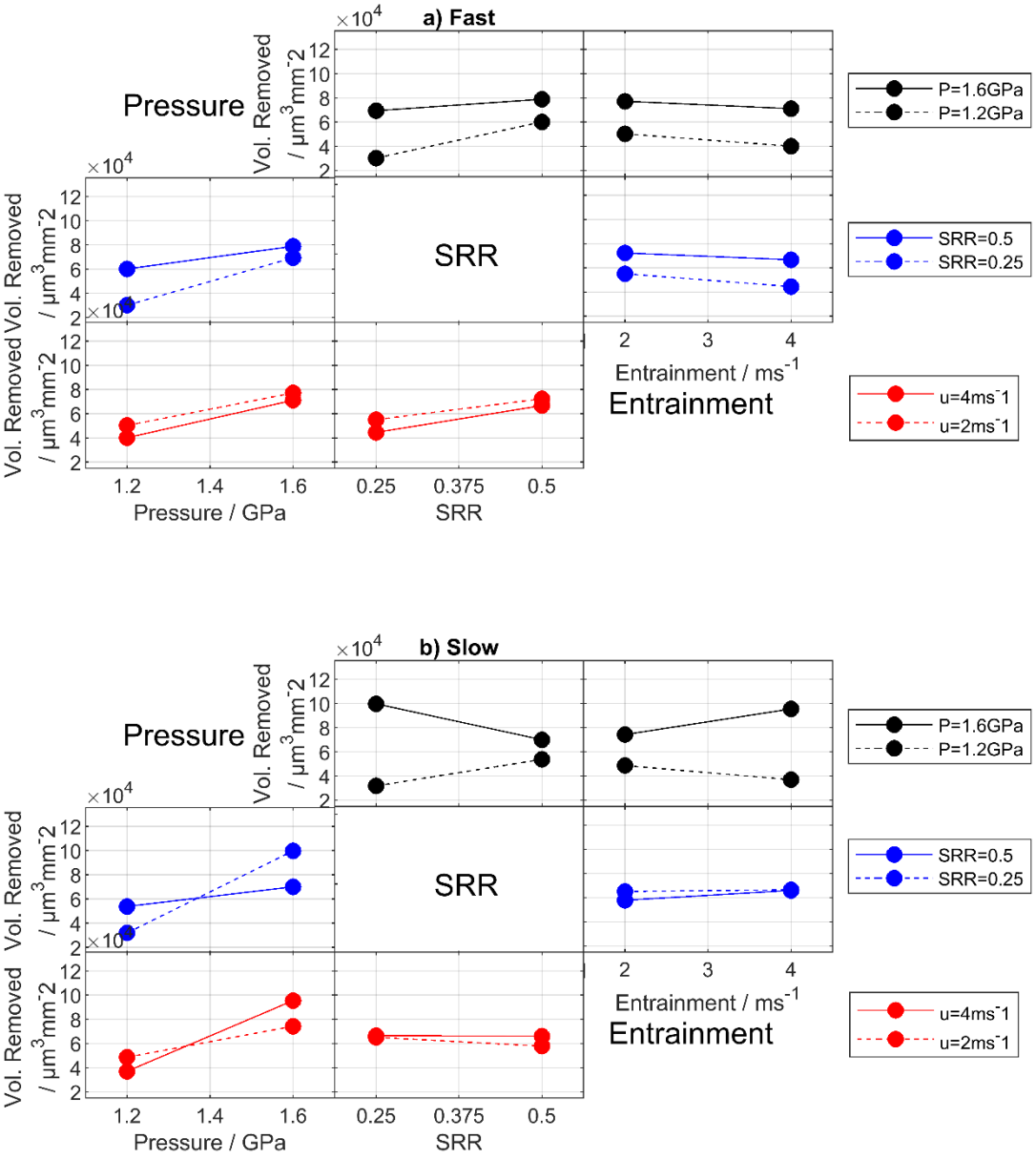

Figure 5.12.8 Two-factor interaction plots for volume removed at end of test on the a) fast and b) slow surfaces.

Figure 5.12.9 indicates the presence of clear three-factor interactions on both surfaces regarding the volume removed. On the fast surface, no two-factor pressure*SRR interaction was present in the low entrainment condition, however

under high entrainment SRR ceased to have an influence at high pressure and the low pressure – low SRR condition resulted in considerably less volume removed.

On the slow surface, the gradient of the low pressure line changed very substantially, also showing the low pressure – low SRR condition to be very mild. The three-factor interaction plots shown here are again very similar to those seen for the percentage of surface micropitted at the end of the test.

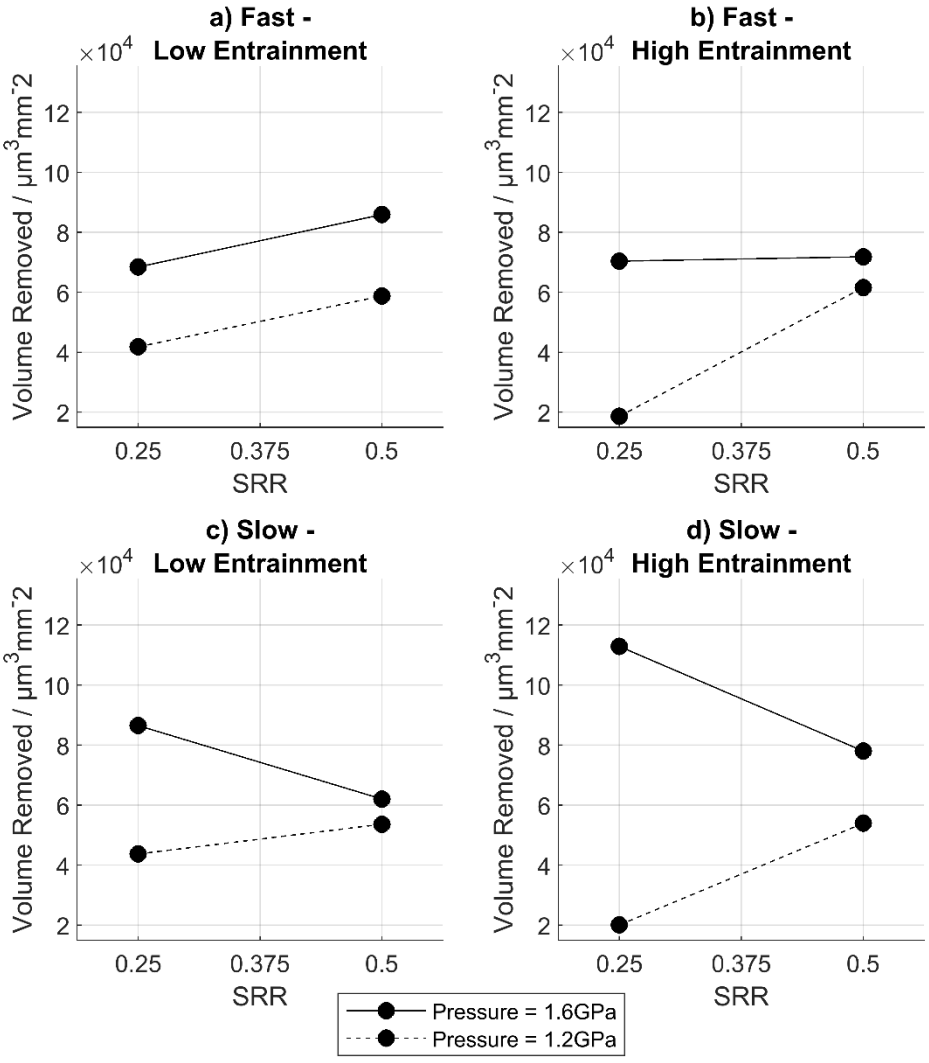

*Figure 5.12.9 Two-factor interaction plots for pressure*SRR on each surface at low and high entrainment, for three-factor interaction analysis of volume removed.*

The Influences of each factor and interaction effect on the volume removed from the surface are shown in Table 5.12.3.

Table 5.12.3 Effects of main factors and interactions on volume removed at end of test.

Factor / Interaction	Fast Surface			Slow Surface		
	Low average / μm^3 mm^{-2}	High Average / μm^3 mm^{-2}	Effect / $\Delta \mu m^3$ mm^{-2}	Low average / μm^3 mm^{-2}	High Average / μm^3 mm^{-2}	Effect / $\Delta \mu m^3$ mm^{-2}
Pressure	45,176	74,127	28,951	42,815	84,849	42,034
SRR	49,791	69,512	19,721	65,778	61,887	-3,891
Entrainment	63,709	55,594	-8,115	61,454	66,210	4,756
Pressure*SRR	64,773	54,530	-10,243	76,732	50,932	-25,800
Pressure*Entrainment	58,626	60,677	2,051	55,618	72,046	16,428
SRR*Entrainment	58,406	60,897	2,491	62,133	65,531	3,398
Pressure*SRR*Entrainment	54,399	64,904	10,505	59,530	68,135	8,605

5.12.4 Cycles to Reach 3% Micropitted

The largest integer percentage micropitted area value that all tests in this programme surpassed was 3%, and hence the number of fast disk cycles required for each surface to reach this value was recorded. This value will henceforth be referred to as N3. This was an approximate number of cycles due to the limited number of surface replications that could be made and scanned, and it was assumed that micropitting occurred at a constant rate between each surface measurement.

The main effects of each factor on N3 are shown in Figure 5.12.10.Pressure was again the strongest factor on the slow surface, however on the fast surface pressure had the smallest effect of the three variables with SRR showing the strongest influence.

On both surfaces pressure acted to decrease N3, as did the SRR for the fast surface. SRR had minimal effect on the slow surface however. Entrainment increased the number of cycles needed to reach 3% micropitted on both surfaces, exhibiting a protective influence. None of the lines for any parameters passed through the centrepoint results on either surface.

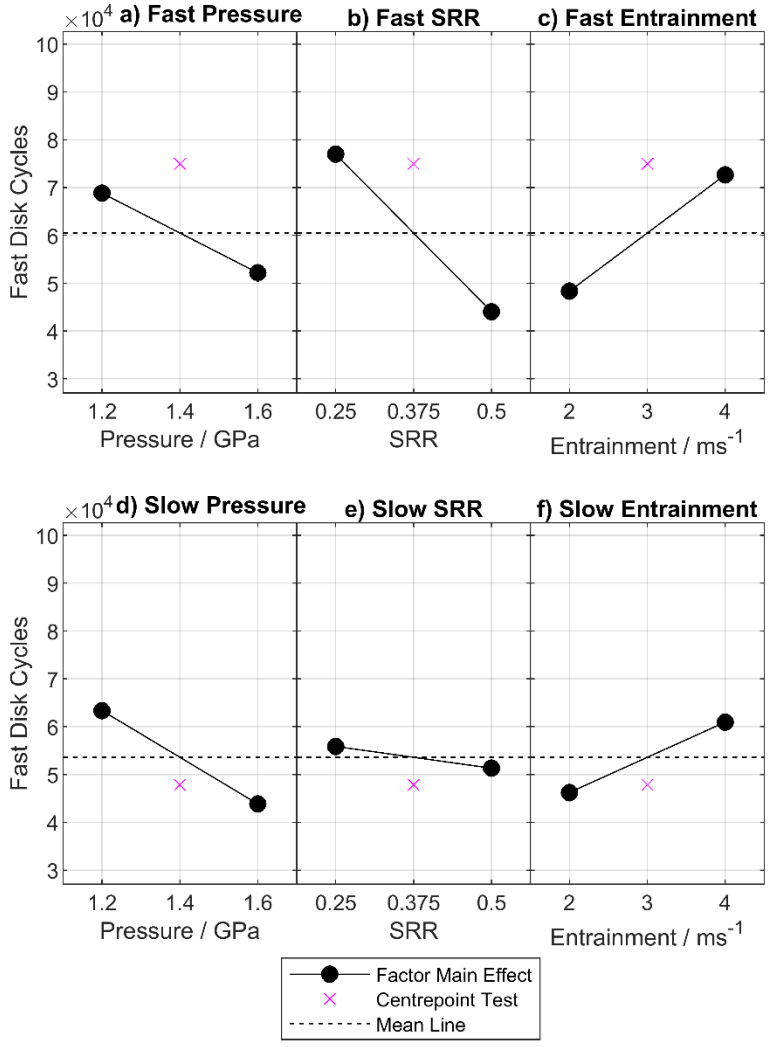

Figure 5.12.10 Main effects for the number of fast disk cycles to reach 3% micropitted.

Interaction plots for N3 are shown in Figure 5.12.11.

Pressure and SRR interacted on the fast and slow surfaces, in both cases pressure having the strongest influence at low sliding and vice versa. Pressure*entrainment did not exhibit an interaction on the fast surface, but on the slow surface showed an inconsistent effect where N3 was significantly increased in the case of high sliding and low pressure. This should be kept in consideration when interpreting however as both variables considered are continuous it is highly unlikely that the issues of inconsistent effects (i.e. an effect happening in one specific case only) apply here. The more likely effect is that the trend continues outside of the bounds investigated, or that a threshold was crossed where the effect of a variable begins to grow more significantly.

An SRR*entrainment interaction was present on both surfaces, with SRR having a stronger influence on the outcome when entrainment was high, and entrainment having a stronger influence when SRR was low.

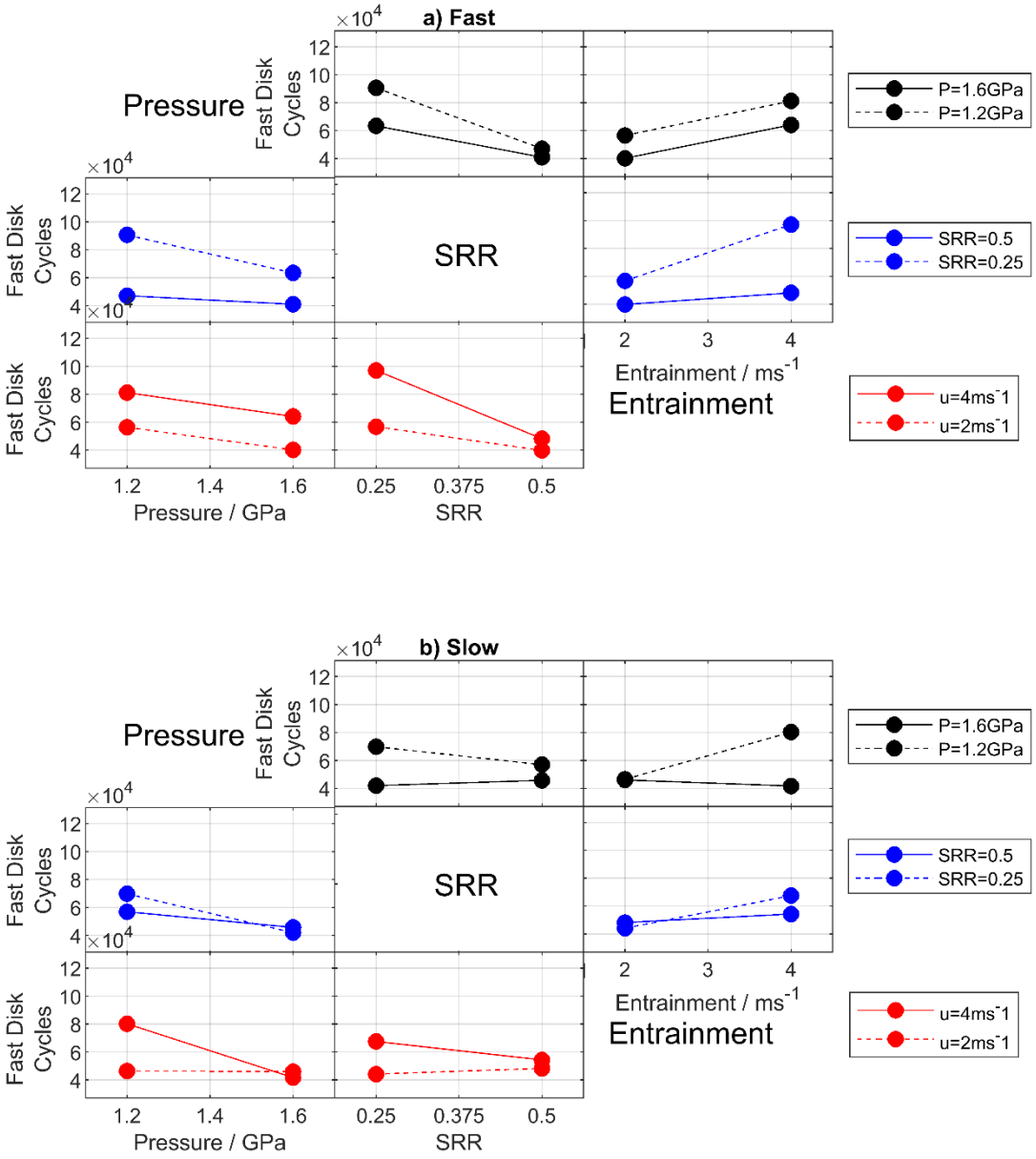

Figure 5.12.11 Two-factor interaction plots for N3 on the a) fast and b) slow surfaces.

As evidenced by Figure 5.12.12, three-factor interactions were present on both surfaces. On the fast surface a strong two-factor effect could be seen between pressure and SRR in the low entrainment condition, but in the high entrainment condition the angle between the two lines decreased as their gradients and heights

changed. On the slow surface, a very strong interaction effect at low entrainment was completely removed at high entrainment, where the two lines are near-parallel.

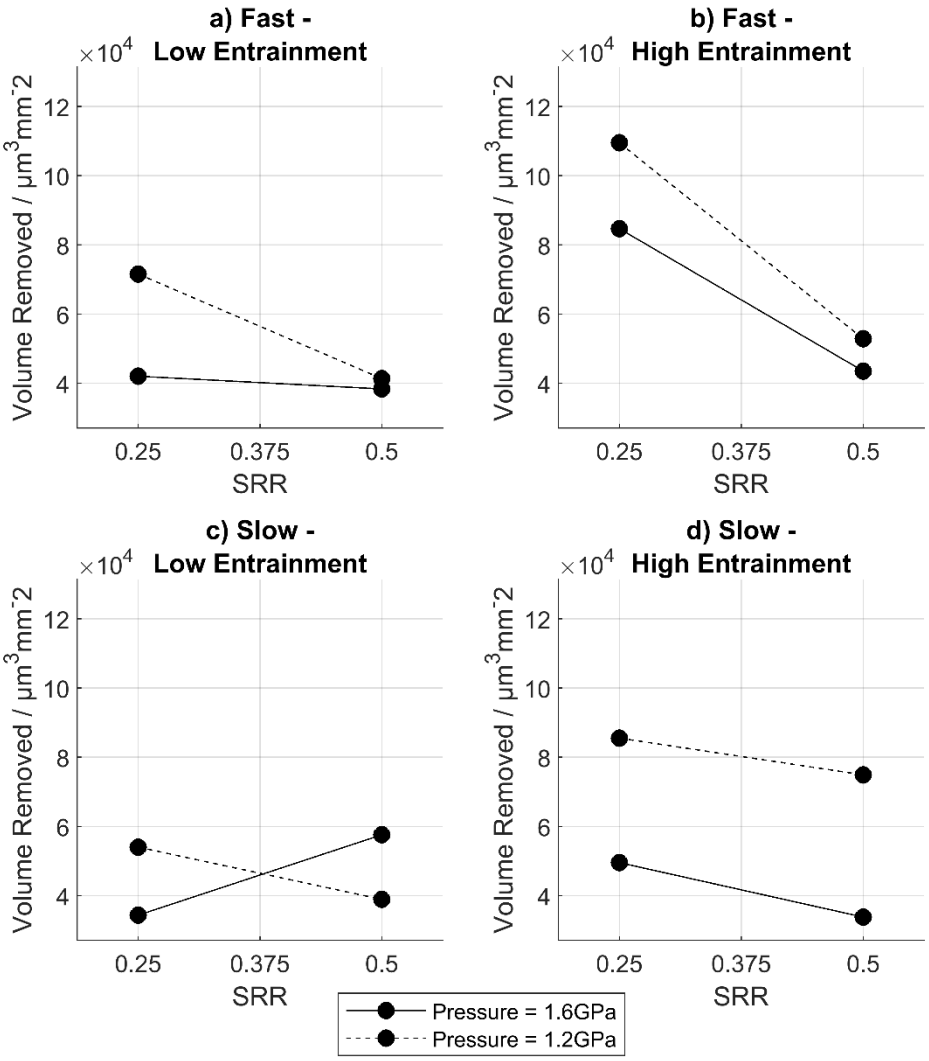

*Figure 5.12.12 Two-factor interaction plots for pressure*SRR on each surface at low and high entrainment, for three-factor interaction analysis of N3.*

The influences of each factor and interaction on N3 are shown in Table 5.12.4.

Table 5.12.4 Effects of main factors and interactions on N3.

Factor / Interaction	Fast Surface			Slow Surface		
	Low average / FD Cycles	High Average / FD Cycles	Effect / Δ FD Cycles	Low average / FD Cycles	High Average / FD Cycles	Effect / Δ FD Cycles
Pressure	68,826	52,150	-16,676	63,350	43,829	-19,521
SRR	76,964	44,012	-32,952	55,863	51,316	-4,547
Entrainment	48,323	72,652	24,329	46,227	60,952	14,726
Pressure*SRR	55,227	65,748	10,521	49,439	57,739	8,300
Pressure*Entrainment	60,694	60,281	-413	63,098	44,081	-19,017
SRR*Entrainment	68,481	52,494	-15,987	57,898	49,281	-8,617
Pressure*SRR*Entrainment	59,104	61,871	2,767	48,155	59,024	10,869

5.12.5 Micropitting Rate During Load Stages 9 and 10

At the conclusion of load stage 8, micropitting on all surfaces had decreased to a lower rate than during the initial stages of the test. The percentage increase in micropitting per disk cycle was calculated assuming a constant rate of micropitting between the surface replicas measured at the conclusions of load stages 8 and 10. This was chosen for use as a parameter for the factorial analysis over the micropitting rate between load stages 10 and 12 as there is no influence from the transition from replica to disk measurements.

The main effects of each factor are shown in Figure 5.12.13. On both surfaces pressure had the largest effect of all variables, with higher pressure acting to increase the rate of micropitting. This effect was larger on the slow surface than the fast.

A small rate-increasing effect from SRR was seen on the fast surface, while for the slow surface SRR exhibited less than half the influence of the fast. Additionally, inspection of the high and low slow surface SRR results showed the range of the low SRR result entirely encompassed the range of the high, in addition to the similar

mean results. While a small decrease in micropitting rate was seen for increasing entrainment on the fast surface, closer inspection showed significant overlap between the data at high and low settings – reinforcing that this may be a weaker entrainment effect than shown by the mean values here. Entrainment had negligible effect on the slow surface.

For all variables on both surfaces, the lines did not pass through the centrepoint result.

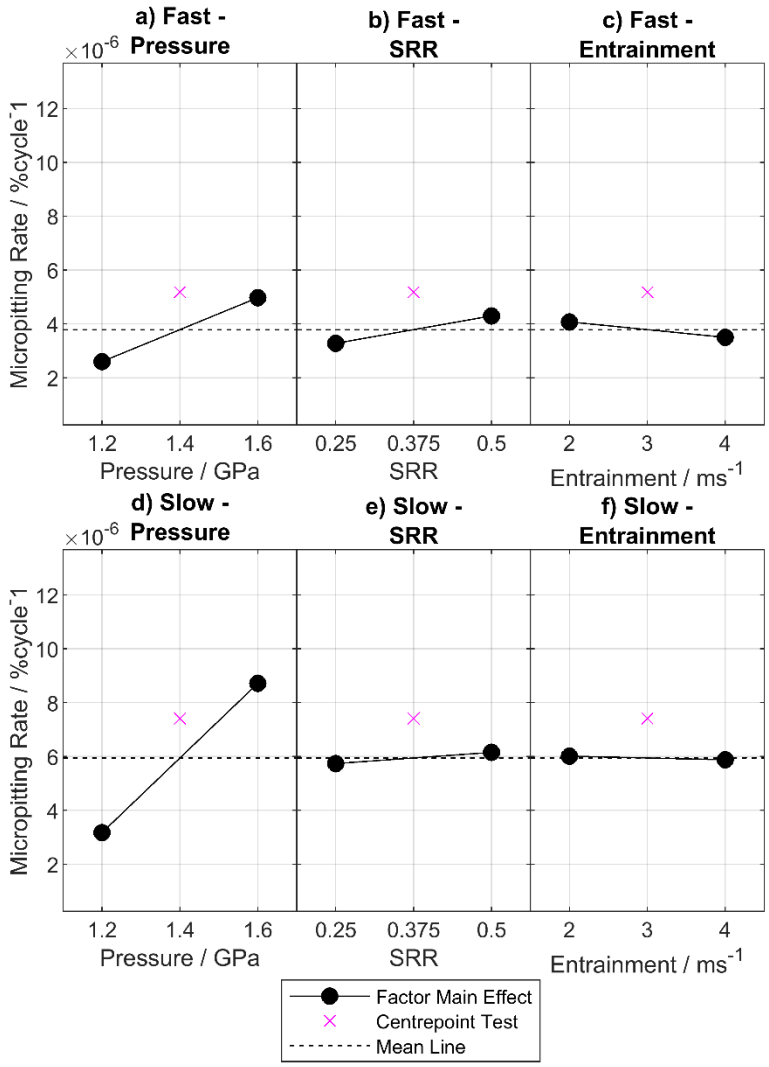

Figure 5.12.13 Main effects for the rate of micropitting during load stages 9 and 10.

Similar effects were seen on both surfaces for all the interactions shown in Figure 5.12.14. For the pressure*SRR interaction on both surfaces, increasing SRR was seen to increase the rate when pressure was low but had the opposite effect under high pressure conditions. Additionally, pressure was shown to have a greater influence when SRR was low.

In the case of the pressure*entrainment interaction precisely the opposite effect was seen, where at low pressure increasing entrainment lowered the rate of micropitting, while at high pressure it increased it. In this case pressure had a larger effect when the entrainment was high than when it was low.

For the SRR*entrainment interaction on the fast disk the micropitting rate was largely unaffected by entrainment at low sliding, but the low entrainment – high sliding combination caused an increase in micropitting rate. On the slow surface, the same increase at low entrainment – high sliding was seen, however the micropitting rate was also seen to decrease in the low entrainment – low sliding condition.

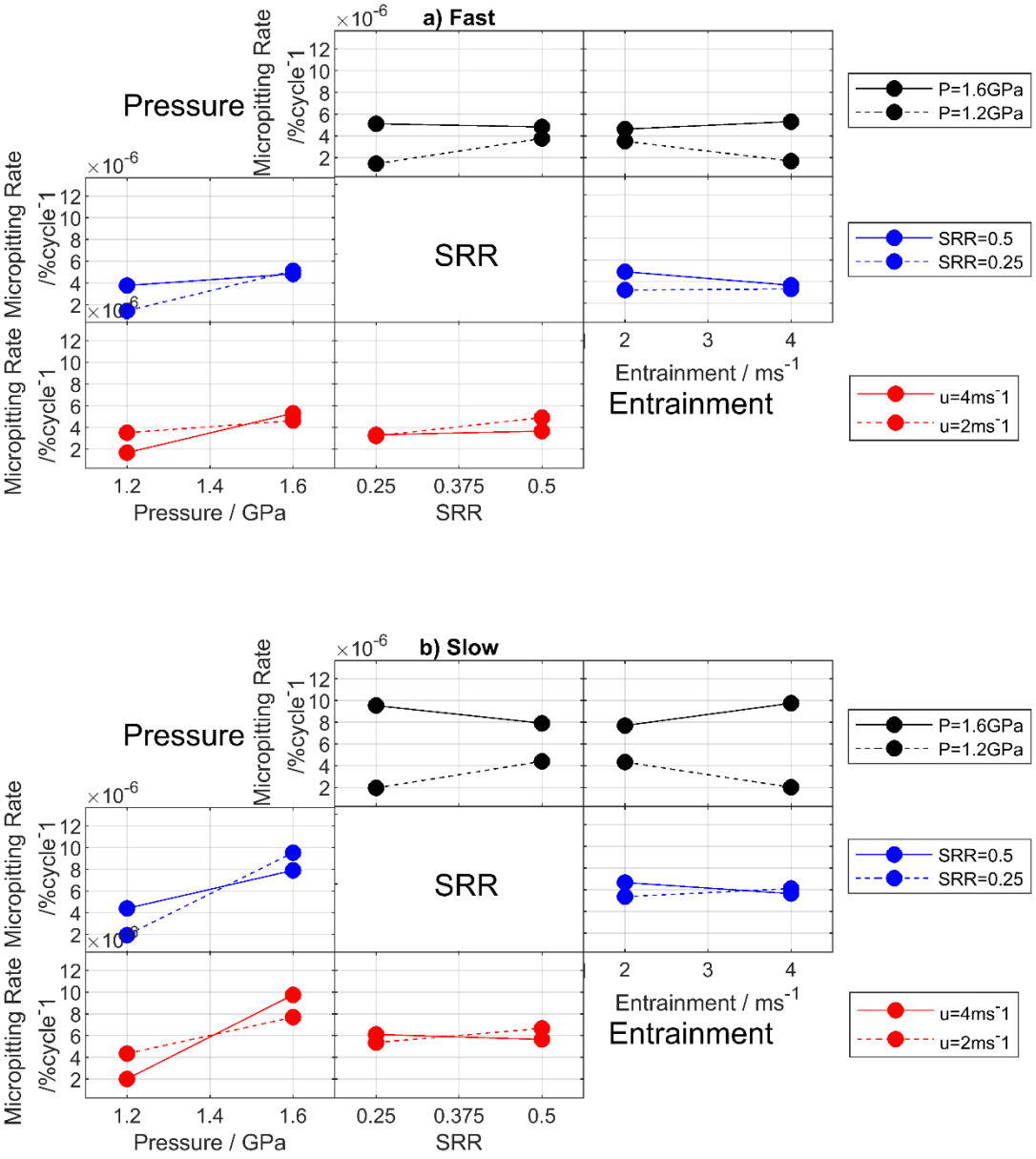

Figure 5.12.14 Two-factor interaction plots for micropitting rate during load stages 9 and 10 for the a) fast and b) slow surfaces.

Again, clear three-factor interactions were present on both surfaces as can be seen in Figure 5.12.15. On the fast surface, the near-parallel lines of the Pressure*SRR interaction show that those variables barely interacted in the low entrainment

condition, while a significant interaction was developed in the high entrainment condition.

On the slow surface an interaction was certainly present under the low entrainment condition, however when high entrainment was applied the effect of pressure widened the gap between the two lines and the effect of SRR at high pressure was changed to a pronounced rate-decreasing effect.

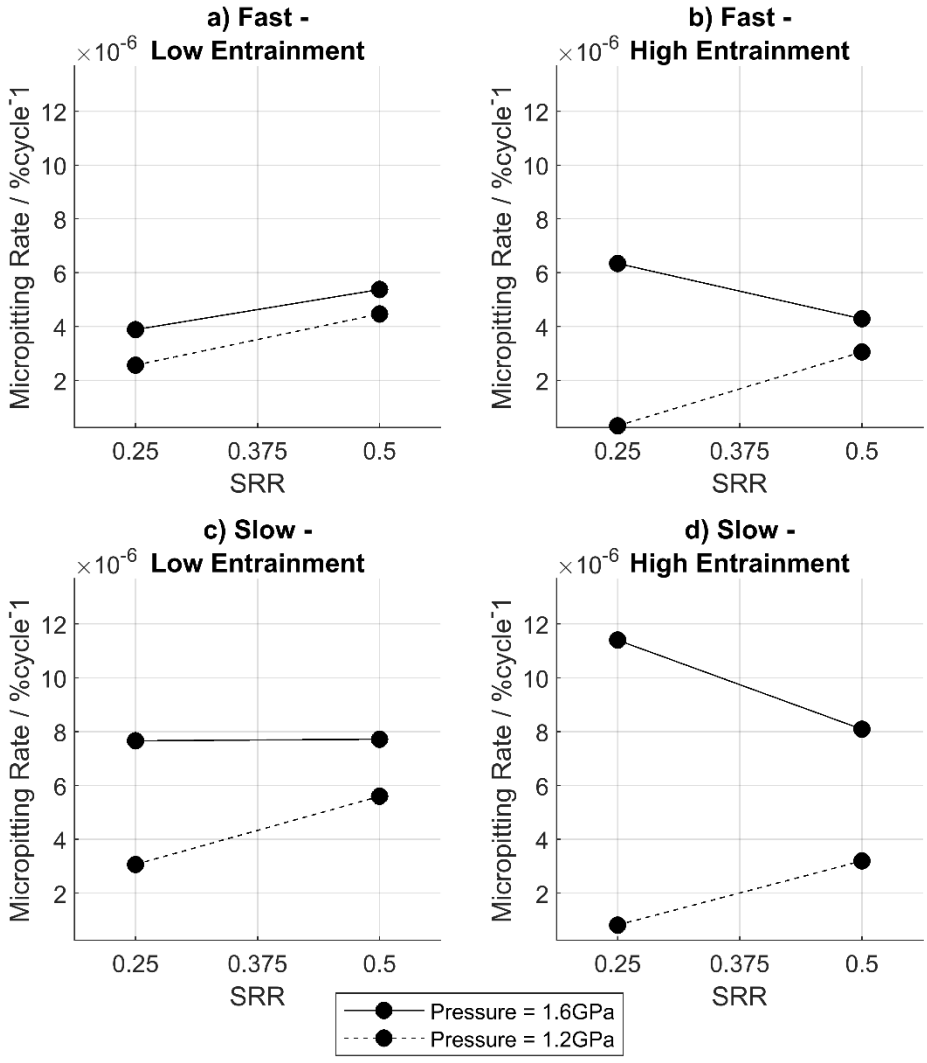

*Figure 5.12.15 Two-factor interaction plots for pressure*SRR on each surface at low and high entrainment, for three-factor interaction analysis of micropitting rate during load stages 9 and 10.*

The influences of main factors and their interactions on the micropitting rate during load stages 9 and 10 are summarised in Table 5.12.5 below:

Table 5.12.5 Effects of main factors and interactions on micropitting rate during load stages 9 and 10

	Fast Surface			Slow Surface		
Factor / Interaction	Low average / 10^{-6} %cycle^{-1}	High Average / 10^{-6} %cycle^{-1}	Effect / Δ 10^{-6} %cycle^{-1}	Low average / 10^{-6} %cycle^{-1}	High Average / 10^{-6} %cycle^{-1}	Effect / Δ 10^{-6} %cycle^{-1}
Pressure	2.60	4.97	2.37	3.17	8.72	5.55
SRR	3.28	4.30	1.02	5.74	6.15	0.42
Entrainment	4.07	3.50	-0.58	6.01	5.88	-0.14
Pressure*SRR	4.44	3.13	-1.30	6.97	4.93	-2.04
Pressure*Entrainment	3.16	4.42	1.26	4.85	7.04	2.19
SRR*Entrainment	4.13	3.45	-0.68	6.39	5.51	-0.88
Pressure*SRR*Entrainment	3.24	4.33	1.10	5.54	6.35	0.81

5.12.6 Early Stage Micropitting

On all surfaces a peak rate of micropitting was reached early in the test. Typically, this peak rate occurred during load stages 3 and 4. A complication of the replication methods used in this work is that the replica material could be unreliable, and a small number of replicas which appeared to be of sufficient quality by microscope inspection had to be discarded when areal scans revealed defects. One such discarded surface was the load stage 4 replica for the fast surface in Test 8, thus preventing the peak micropitting rate being employed in the factorial analysis of the fast surface.

A useful alternative to use of the peak rate of micropitting would be to use the percentage of surface micropitted at the close of load stage 5, i.e. at $1x10^5$ fast disk cycles. As this is early in the test and just after the peak value would have

occurred this provides another means of assessing the aggressiveness of early stage micropitting behaviour. Unfortunately, this approach could not be used for the slow surface as the slow surface replica at load stage 5 of Test 2 was discarded due to poor quality.

Therefore, to evaluate the aggressiveness of micropitting in the very early stages, the fast and slow surfaces shall necessarily be investigated separately in this section.

Fast Surface: Percentage Micropitted after $1x10^5$ Fast Disk Cycles

Similarly to the N3 analysis, which for many of the tests concerned the earlier stages, pressure was the least dominant of the three main factors on the fast surface in this analysis, as can be seen in Figure 5.12.16a. All three variables did show a strong influence on the percentage micropitted however, with SRR exhibiting the largest influence, closely followed by the entrainment. The centrepoint result did not fall on the straight line between high and low settings of any main factors.

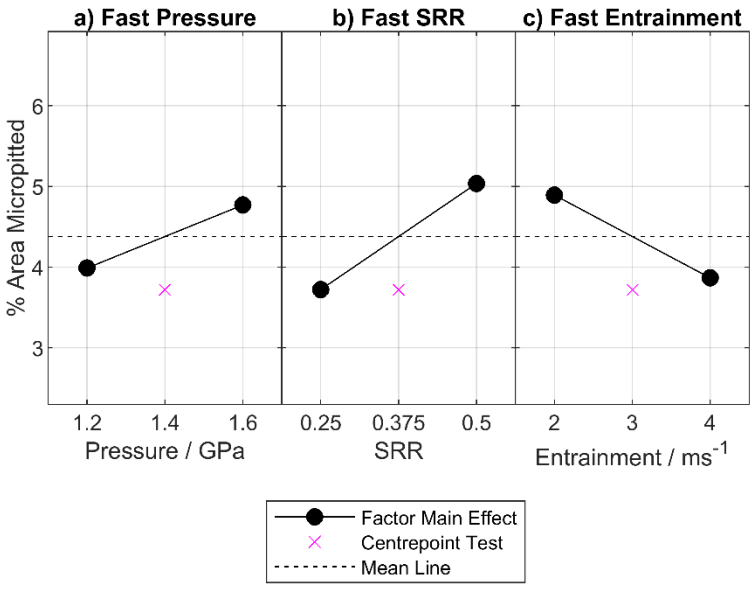

Figure 5.12.16 Main factor effects on the percentage micropitted on the fast surface after 1x10^5 fast disk cycles.

The two-factor interaction effects on the early stage micropitting of the fast disk are shown in Figure 5.12.17. Interestingly, there are no strong interaction effects in evidence, with all lines being near parallel.

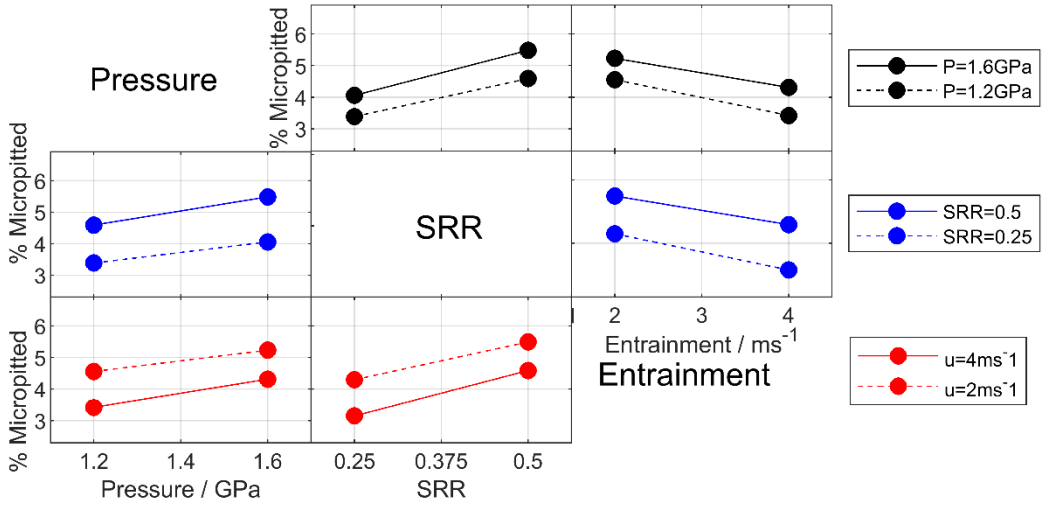

Figure 5.12.17 Two-factor interaction plots for percentage of fast disk micropitted after 1x10^5 fast disk cycles

In Figure 5.12.18 only a small change in the two-factor interaction between SRR and pressure can be seen with changes in entrainment. The lack of strong two-factor interactions in Figure 5.12.17 makes three-factor interactions inherently much less likely. The most probable explanation is that the very small apparent three-factor changes here are due to the natural variation in micropitting around a disk circumference or that would be expected in repeated tests.

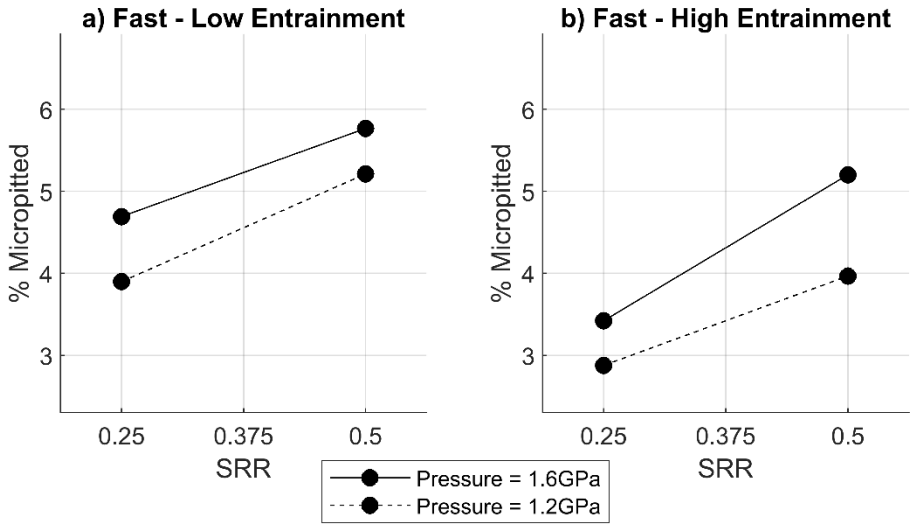

*Figure 5.12.18 Two-factor interaction plots for pressure*SRR on the fast surface at high and low entrainment.*

The results of the factorial analysis for early stage micropitting on the fast surface are summarised in Table 5.12.6 below.

Table 5.12.6 Effects of main factors and interaction effects on percentage of fast surface micropitted after 1x10^5 fast disk cycles.

Factor / Interaction	Fast Surface		
	Low average / %	High Average / %	Effect / Δ%
Pressure	3.99	4.77	0.78
SRR	3.72	5.04	1.32
Entrainment	4.89	3.87	-1.03
Pressure*SRR	4.32	4.44	0.11
Pressure*Entrainment	4.33	4.43	0.11
SRR*Entrainment	4.32	4.44	0.12
Pressure*SRR*Entrainment	4.50	4.26	-0.23

Slow Surface: Peak Micropitting Rate

The main factor effects on peak micropitting rate for the slow surface can be seen in Figure 5.12.19. These plots show that the SRR had the largest influence on early stage micropitting rate followed by pressure, with entrainment having the least influence, although still an appreciable effect.

There is a very pronounced difference between the main effects on micropitting rate seen here and those seen for the slow surface during load stages 9 and 10, as investigated in Section 5.12.5. During the later stages only the pressure had a significant main effect, which is not the case here.

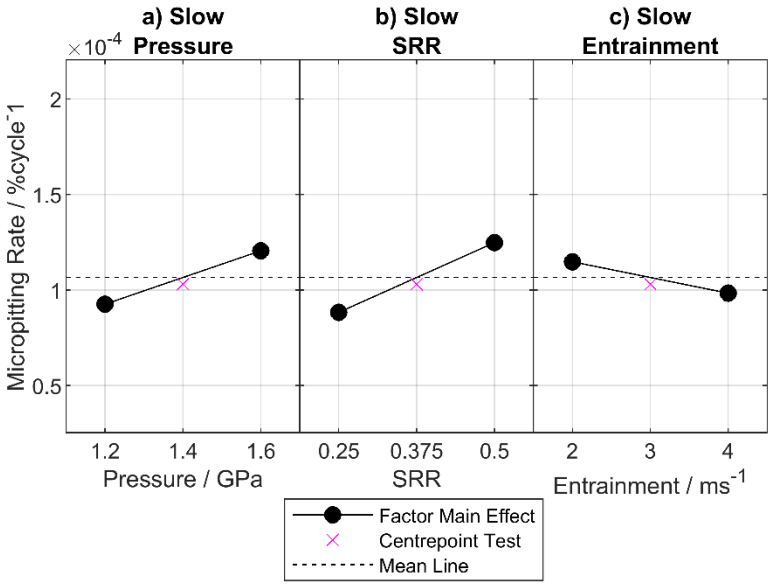

Figure 5.12.19 Main effects for the peak rate of micropitting on the slow surface.

Figure 5.12.20 Shows plots of the two-factor interaction effects on peak micropitting rate of the slow surface. Interaction effects were present for all pairs of main factors. Pressure and SRR had the weakest interaction, with each having a larger influence on micropitting rate when the other was at its low setting.

The Pressure*Entrainment interaction was significant and showed that high pressure gave a slightly higher micropitting rate at high entrainment, but that high entrainment was able to protect the surface more effectively at low pressure. At low entrainment pressure had minimal influence, but under high entrainment conditions, the effect of changing pressure was much more pronounced.

The interaction between SRR and entrainment showed that entrainment had minimal influence at high SRR, but that high entrainment could protect the surface more effectively under low sliding conditions. The effect of SRR was much more pronounced under high entrainment conditions.

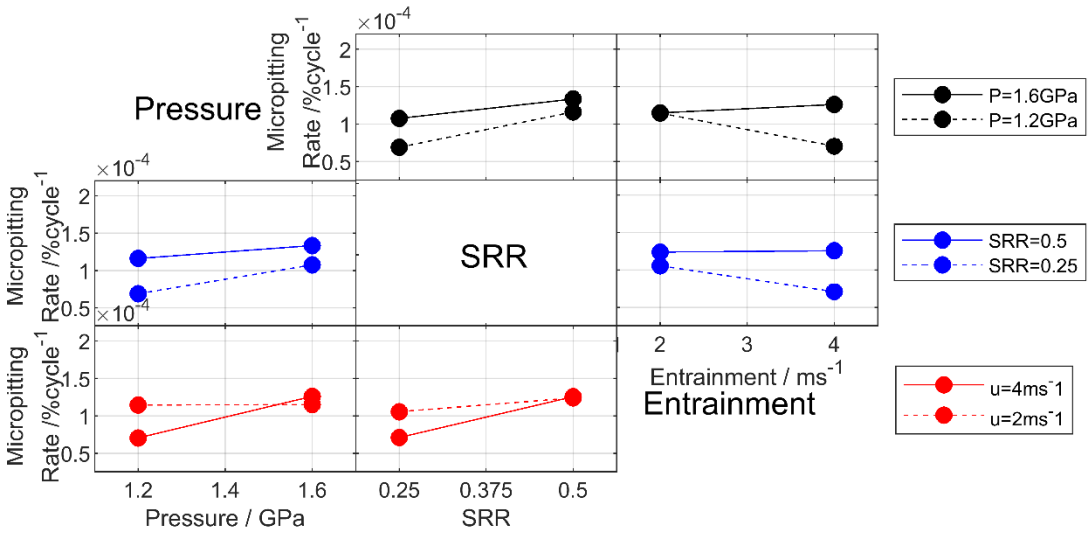

Figure 5.12.20 Two-factor interaction plots for the peak rate of micropitting on the slow surface.

The changes in the Pressure*SRR two-factor interaction with changing entrainment are shown in Figure 5.12.21. The nature of the interaction changed completely with entrainment - the low entrainment interaction showing micropitting rate decreasing with SRR when pressure is high, while the high entrainment interaction shows the micropitting rate increasing with SRR at high pressure with the increase at low pressure being much smaller. This is clear evidence of a strong three-factor interaction.

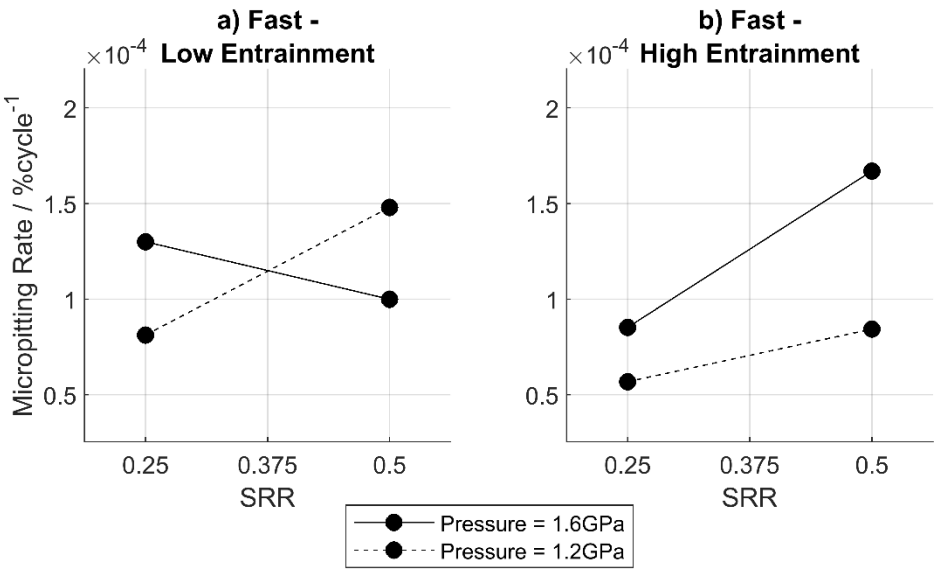

*Figure 5.12.21 Two-factor interaction plots for pressure*SRR on each surface at low and high entrainment, for three-factor interaction analysis of peak micropitting rate on the slow surface.*

The strengths of the main and interaction effects of the factors in the experimental programme can be seen in Table 5.12.7. Interestingly the strongest overall effect recorded was the three-factor interaction between all variables, with the strongest individual effect being due to SRR, and the strongest two-factor interaction being pressure*entrainment.

Table 5.12.7 Effects of main factors and interactions on the peak micropitting rate on the slow surface

Factor / Interaction	Slow Surface		
	Low average /10^{-6} %cycle^{-1}	High Average /10^{-6} %cycle^{-1}	Effect / $\Delta 10^{-6}$ %cycle^{-1}
Pressure	92.58	120.52	27.95
SRR	88.30	124.80	36.50
Entrainment	114.78	98.33	-16.46
Pressure*SRR	111.87	101.23	-10.64
Pressure*Entrainment	92.75	120.35	27.60
SRR*Entrainment	97.48	115.62	18.15
Pressure*SRR*Entrainment	125.45	87.65	-37.80

5.12.7 Modelling Micropitting Response

For all parameters investigated the centrepoint values for the fast surface did not coincide with the straight line between the mean values of any of the main or interaction effects – this is indicative of nonlinear behaviour. This is contrasted by the slow surface centrepoint results, which indicated linear or near-linear behaviour for all parameters except the load stage 9-10 micropitting rate and N3 parameters. Ideally repeats of the centrepoint test would allow this to be confirmed, however this was not possible within the time limits of the project.

The standard two-level factorial model discussed in Section 3.9 inherently assumes linear behaviour for each main or interaction effect which, as discussed, may not be the case for both surfaces. In order to allow simple models of the results to be constructed (and hence aid in the visualisation of this complex three-dimensional problem) this standard approach was still assumed to be valid, and the coefficients in the model equations are shown in Table 5.12.8. Appendix 3 shows plots of these surface models illustrating the dynamic relationship between the three variables.

Table 5.12.8 Coefficients in the factorial response models for each output of the micropitting tests.

Model	Surface	μ	ß1	ß2	ß3	ß12	ß13	ß23	ß123
% micropitted	**Fast**	11.38	2.18	1.53	-0.87	-1.08	0.47	0.19	1.12
	Slow	12.68	3.43	-0.05	-0.27	-2.29	1.27	0.55	0.54
D5	**Fast**	-1.549	-0.085	-0.070	0.025	-0.025	0.000	-0.070	-0.005
	Slow	-1.645	-0.090	0.045	-0.015	0.035	-0.030	-0.050	-0.020
Volume Removed	**Fast**	59651	14475.5	9860.5	-4057.5	-5121.5	1025.5	1245.5	5252.5
	Slow	63832	21017	-1945.5	2378	-12900.0	8214.0	1699	4302.5
N3	**Fast**	60488	-8338	-16476	12164.5	5260.5	-206.5	-7993.5	1383.5
	Slow	53589	-9760.5	-2273.5	7363	4150.0	-9508.5	-4308.5	5434.5
Load stage 9 - 10 micropitting Rate	**Fast**	3.79E-06	1.15E-06	5.10E-07	-2.90E-07	-6.50E-07	6.30E-07	-3.40E-07	5.50E-07
	Slow	5.95E-06	2.78E-06	2.10E-07	-7.00E-08	-1.02E-06	1.10E-06	-4.40E-07	4.05E-07
% pitted at $1x10^5$ cycles	**Fast**	4.38	0.39	0.66	-0.52	0.06	0.06	0.06	-0.12
Peak micropitting rate	**Slow**	1.07E-04	1.40E-05	1.83E-05	-8.23E-06	-5.32E-06	1.38E-05	9.08E-06	-1.89E-05

5.13 Discussion – Micropitting Investigation

5.13.1 An Appraisal of the Two-Dimensional Analysis Approach

In each test, the percentage of the surface micropitted was evaluated by both the areal analysis and two-dimensional analysis approaches, however the results of the two approaches gave very different evaluations of the extent of micropitting on the surface. Typically, the two-dimensional approach detected a smaller percentage of the surface to be micropitted than the areal approach in the earlier stages of the test, before going on to significantly exceed the amount of micropitting evaluated by the areal approach.

In the early stages this is most likely the result of underestimation by the two-dimensional analysis method. While the areal method can be guaranteed to scan all micropits within the measurement area due to the small x and y spacing, the two-dimensional approach has a y-spacing two orders of magnitude larger. As a result, in the early stages of the test where there are fewer micropits on the surface the likelihood of a two-dimensional profile trace passing through a micropit is significantly reduced. This is only slightly mitigated by the fact that, due to the low y-direction resolution, each pit that is detected in the two-dimensional analysis represents a pit $\frac{2}{9}b$ wide, which is much greater than the width of a true pit.

In the later stages, there are more micropits present on the surface, so the likelihood of finding a pit is much higher. Additionally, the ±80 μm relocation error determined in Section 3.1.8 results in slightly different locations being traversed each time, while points which passed through micropits previously (at different locations) must remain irrevocably designated as micropitted. This, combined with each point representing 0.5 μm x $\frac{2}{9}b$ area of the surface, leads to an overestimation later in the test.

The areal analysis was therefore used for the factorial analyses in Section 5.11, as it was not subject to the limitations observed for the two-dimensional approach above, and could be visually checked for accuracy by overlaying the detection.

5.13.2 Influence of Wear and Running-in on Micropitting

The surfaces in both Tests 1 and 2 showed signs of mild wear that developed during the running-in process – a continuous central band on the surfaces of Test 1, and patched islands on the surfaces of Test 2. In both cases these worn areas exhibited considerable micropitting resistance, with only a handful of micropits forming within these regions while aggressive micropitting took place on the rest of the surface.

These tests are therefore very interesting examples of the competition between wear and micropitting that was discussed extensively in Section 1.4.3. As both the worn and unworn areas exist within the same contact conditions, the only differences that could exist between the two regions are changes in surface roughness and texture, changes in local microstructure, or localised changes in lubricant properties due to temperature variation across the contact width.

As was discussed in Section 4.2 the mean radius of curvature of asperities in the worn areas of both surfaces was significantly larger than in the unworn areas after running-in, during which the wear appeared. On average the post-run-in values in the worn areas being 1.39 and 1.34 times the unworn values on the fast and slow surfaces respectively. Comparison between the mean radius of curvature in worn sections versus unworn profiles showed that worn sections had 1.38 and 2.06 times the mean radius of curvature on the fast and slow surfaces respectively.

While on the fast surface of Test 1 the mean roughness parameter values inside the worn area were typically less severe than those outside the worn area, this was not the case for the same parameters on the slow surface (see Table 5.13.1).

Table 5.13.1 Mean roughness parameter values inside and outside of the worn area on the Test 1 surfaces.

	Fast		Slow	
Parameter	**Unworn Area**	**Worn area**	**Unworn Area**	**Worn area**
Rp / µm	0.63	0.58	0.59	0.58
Rv / µm	2.29	2.12	2.14	2.19
Rz / µm	2.92	2.70	2.73	2.78
Rc / µm	1.11	1.00	0.99	1.01
Rt / µm	3.75	3.52	3.37	3.57
Ra / µm	0.36	0.30	0.31	0.31
Rq / µm	0.49	0.42	0.42	0.44
Rsk	-1.74	-1.87	-1.73	-1.86
Rku	6.99	8.21	7.53	7.96

The abundance of data collected for both running-in and micropitting for each test allowed the influence of all running-in parameters used in this work to be investigated for any relationship to micropitting. Each micropitting parameter was plotted against each running-in parameter's initial value, value after running-in, change in value and percentage change in value. In all cases no clear relationship could be seen – as an example, the plots for percentage pitted vs mean radius of curvature of asperities are shown in Figure 5.13.1. A table showing R^2 values for least squares linear fits to all data sets is shown in Appendix 4, to aid in this illustration.

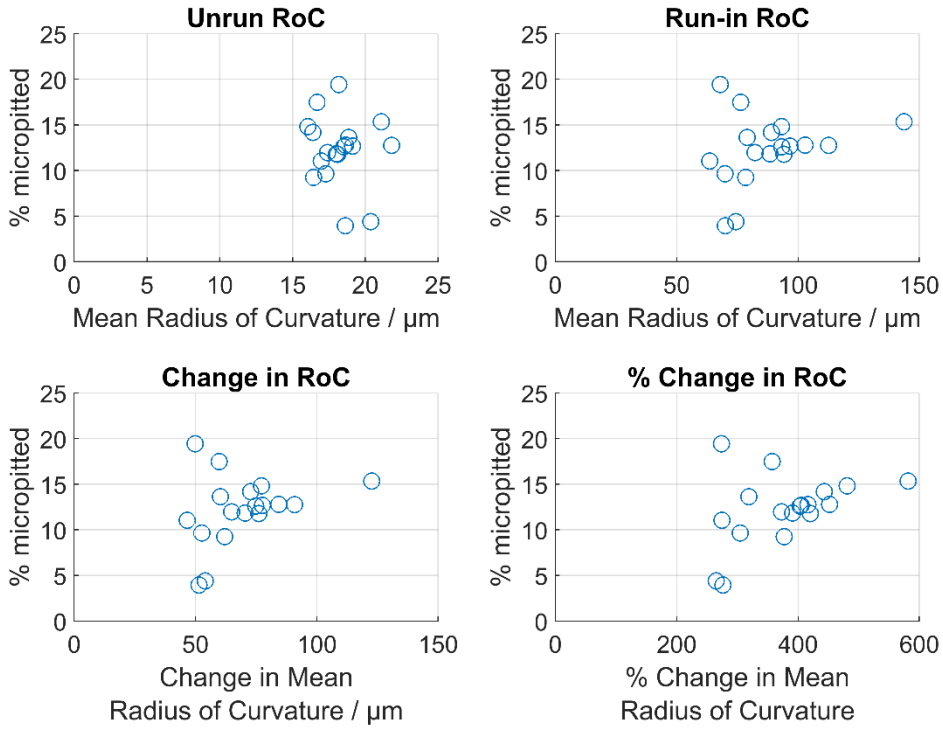

Figure 5.13.1 Percentage of surface micropitted at end of test plotted for each surface plotted against the unrun and run-in values for radius of curvature of asperities, and also against magnitude and percentage change.

Additionally, Rq/radius of curvature of asperities was evaluated after running-in for each surface and compared to the percentage of surface micropitted. This aimed to test the hypothesis out forward by Cao *et al* (2019) that smaller values of this parameter lead to improved fatigue resistance. As can be seen in Figure 5.13.2, no correlation was found between this parameter and the extent of micropitting on the surface.

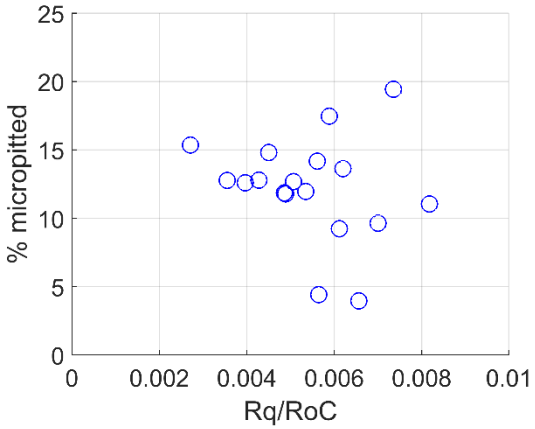

Figure 5.13.2 Comparison of the Rq / radius of curvature of asperities parameter versus % of surface micropitted at end of test

This is a far from conclusive appraisal of the influence of running-in on micropitting however, as there is not a 'level playing field' on which these parameters are being analysed – in each case the different conditions that produced this variation in running-in persist throughout the test and continue to influence the result. What this verifies is that the factors investigated continue to have an influence beyond their modification of the surface during running-in, and it is not the case that the modification or run-in values of the surface alone are the true influencing factors on micropitting.

Previous works discussed in Section 1.4.3 such as Benjayati *et al* (2003) and Lainé *et al* (2008) were able to assess the fatigue behaviour of differently run-in and worn surfaces under otherwise identical contact conditions through the action of the ZDDP additive. These works showed that surfaces where the surface texture was better preserved by the additive suffered greater micropitting than those that were allowed to wear. The behaviour seen in Tests 1 and 2 serves to verify this finding where there is no difference in lubricant additives.

A proposal for future investigation of this would be to conduct a twin disk micropitting study varying the concentration of ZDDP during the running-in stage to modify the running-in and wear behaviour, but to maintain the same concentration and contact conditions during the micropitting test. If the roughness parameters used in this work, including radius of curvature of asperities, were evaluated after running-in or wear, the influence of these surface textural parameters on micropitting could be fully assessed. This would test the hypothesis, formed from analysis of the wear patches in Tests 1 and 2, that radius of curvature of asperities was the dominant factor in changing micropitting behaviour between worn and unworn sections in the same tests.

5.13.3 Influence of Pressure, SRR and Entrainment on Micropitting

The results of the experimental programme completed in this work show the effects of pressure, SRR, and entrainment velocity to involve a complex combination of main effects and multiple-factor interactions. Contact pressure was found to be the dominant main factor effect in terms of the percentage of surface micropitted at the end of test, volume removed, micropit depth and late-stage micropitting rate. In all cases increased pressure led to increased micropitting or micropit severity.

Pressure also showed an influence on earlier-stage micropitting parameters such as N3, where it acted to reduce the number of cycles required to reach 3% micropitted area, and the peak micropitting rate and percentage micropitted at $1x10^5$ fast disk cycles parameters.

For the D5 parameter, the influence of pressure was similar in magnitude on both surfaces. As pressure increases the depth of the maximum shear stresses induced from asperity contact also increases, the magnitude of this being independent of the speed of the surface in question. It is likely that changes in the depths of

stresses with load is related to this increase, although without complex finite-element modelling of contact between representative asperities and crack growth mechanisms this cannot be confirmed.

For other parameters the influence of pressure was stronger on the slow surface than the fast. The reason for this is not entirely clear. The magnitude of stresses on both surfaces would be expected to remain comparable between the two surfaces as pressure increases, and increases in the number of asperity contacts due to pressure (such as through thinning lubricant films due to increased contact friction) would again be expected to affect both surfaces in the same way. It may be that different mechanisms are more dominant on the faster or slower surface – for example it is known that cracks propagate in the opposite direction to traction, making crack pressurisation a feasible mechanism for the slow surface only. Given the current information however, this can only be speculated at.

SRR and entrainment exhibited more complex influences on the micropitting behaviour of the surfaces. For the early stage micropitting parameters – percentage of surface micropitted at $1x10^5$ fast disk cycles for the fast surface, and peak micropitting rate for the slow – SRR and entrainment had a significant influence for both surfaces. In both cases, SRR increased micropitting, while entrainment acted to oppose micropitting. For the other semi-early-stage micropitting parameter N3, all but the slow surface SRR effect (which was minimal) retained the effects seen for the early micropitting parameters.

Parameters which concerned end- or late-test measures (such as the percentage of surface micropitted at the end of test, or the measures of pit depth and volume) SRR and entrainment effects only remained for the fast surface. On the slow surface, SRR and entrainment effects were minimal, with large overlap between the outputs at high and low settings.

The work of Kadiric and Rycerz (2016) found the sliding distance, via the effect of increased stress cycles on asperities, was the cause of a micropitting-increasing SRR effect. As both the slow and fast surfaces must necessarily slide the same distance in a twin-disk test, this would provide the same SRR effect for both surfaces, hence cannot apply in this case. Additionally, while the number of regions contacted on the opposing disk changes with SRR, each surface encounters more locations (which one would expect to induce more fatigue, due to the reduced ability to adapt to the local loading for each configuration) at the low SRR setting than the high.

The influence of entrainment on contact conditions is much simpler than that of SRR; by far the most significant consequence of entrainment is the thickness of the lubricant film generated at the inlet to the contact. The presence of entrainment effects on the early-test parameters for both surfaces suggests that the initiation of fatigue cracks and the rapid production of micropits have a relationship to direct asperity contact which a thicker lubricant film is able to relieve. This relationship is maintained through the test for the fast surface, however continued micropitting through the remainder of the test on the slow surface appears to be significantly less dependent on film thickness. Again this points to the possibility of differences in the mechanisms or prevalence of mechanisms operating on each surface to grow cracks and produce micropits.

Finally, these micropitting tests showed that the influences of contact conditions on micropitting are not restricted to single main factor effects and go beyond the two-factor interactions seen in previous works. The experiments conducted here confirmed the presence of complex three-factor interactions between variables and highlighted the necessity of considering the interconnected behaviours of pressure, speed, and sliding in gear operation.

5.14 Summary - Micropitting

This investigation was able to successfully use an experimental design process to establish the effect of contact conditions on micropitting behaviours, and was able to identify influences from both individual variables and interaction effects. Pressure was shown to be the dominant effect on parameters evaluated at the end of test, such as micropitted area, volume removed, and the depth of the deepest micropitted points – and always acted to increase the severity of micropitting. It also was a diving effect on micropitting rate later in the test.

Inconsistent behaviours were observed in the other two main variables, with SRR driving early-stage micropitting for both fast and slow surfaces, but only maintaining micropitting-increasing effects later in the test for the fast surface. Similarly, entrainment opposed micropitting on both surfaces in the early test but this opposition was only maintained for the fast surface as the tests continued.

Two-factor interactions were observed consistently, illustrating that interaction effects cannot be considered negligible with respect to micropitting (as they have been in previous works).Typically interactions with entrainment led to increased micropitting when both factors concerned were set high or low together – this may be related to wear-micropitting competition. Putting SRR and pressure high or low together reduced micropitting. Three-factor effects were also observed for a number of parameters.

By obtaining data on the influence of contact conditions on micropitting without confounding effects experienced in previous works, this experimental work has been able to identify the presence of effects that were previously assumed to be negligible, and to avoid interference from interactions when considering single-factor effects. By adding new understanding to the process of micropitting, this

work can contribute to improving design for the prevention of micropitting in the future. Additionally, the experimental programme and interpretation applied here presents a new model and structure for rigorous scientific investigation of multi-factor problems.

6 Simulation of Micropitting Fatigue Using Real Surface Profiles

6.1 Introduction

As part of this work, the EHL contact simulations and fatigue analysis discussed in Chapter 2 were applied to simulate the contact and fatigue conditions applied in each test of the experimental programme. This chapter discusses the processes employed to ensure representative conditions for the contact simulation, before then presenting and discussing the results of the fatigue simulations performed.

The processes of selection of the counterface for simulations, averaging results from multiple locations, and profile updating constitute novel developments as part of this work, in addition to the comparison against experimental results for a full test programme.

6.2 Process for Running Simulations

6.2.1 Determining appropriate input conditions

To obtain film thickness values for each region of the contact, an elliptical smooth point contact simulation was performed for each test. The entrainment velocity, SRR, and applied load (in newtons) were input to this simulation as applied in-test, alongside test disk geometry and material properties.

The correct lubricant properties are vital to achieving an accurate simulation, but frictional heating effects within the contact mean that the temperature at the inlet (governing the formation of the lubricant film) quickly rises above the 80°C oil supply temperature, thereby changing lubricant viscosity properties. Thermocouples beneath the surface of each disk provided temperature readings in-test, and values for η (lubricant dynamic viscosity) and α (pressure-viscosity coefficient) corresponding to the average of the two stabilised disk temperatures were input to achieve representative conditions. Figure 6.2.1 shows an example of the calculated film thickness for a smooth elliptical point contact.

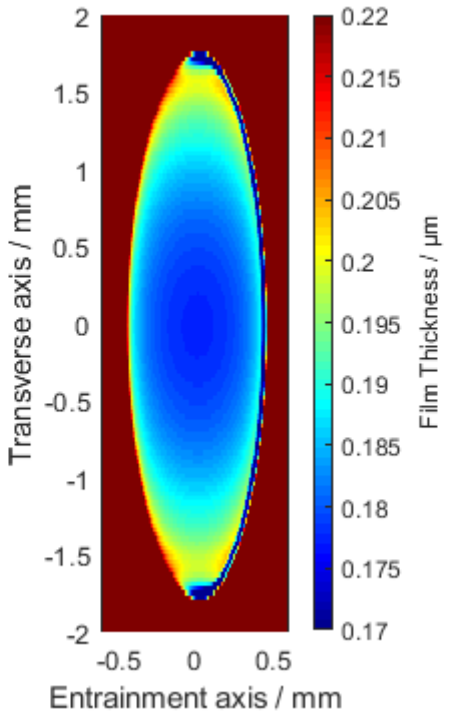

Figure 6.2.1 Colour plot of smooth elliptical point contact film thickness.

The aim of these smooth elliptical point contact simulations was to ensure representative conditions in the eventual rough line contact simulations. As it is impossible for a line contact to exactly replicate a position in a point contact either the contact dimension, maximum Hertzian contact pressure, or radius of relative curvature must deviate from that in the point contact. It was decided to maintain the maximum pressure and contact dimension in each simulation and allow the radius of relative curvature to differ as necessary. The required radius of relative curvature in the line contacts was found to be 18.23 mm for all simulations, while the true radius of relative curvature in the entrainment direction of the point contact was 19.05 mm.

A smooth line contact for the desired position was then performed. Again, due to the inherent differences between point and line contacts, the film thickness calculated for the line contact did not always match that calculated for the point contact. This would alter the specific film thickness when roughness was applied and thus change the individual loading of and direct contact between asperities, which are driving influences for fatigue.

To adjust the film thickness to match that of the point contact simulation, the temperature in the line contact was modified through the lubricant η and α properties. The final values used were those which gave the same central film thickness as found at the corresponding axial position of the point contact simulation.

These conditions were then applied to rough surface line contact simulations, which thus had equivalent pressure, contact dimension, surface speeds and smooth film thickness to the desired axial position of the true contact.

6.2.2 Selection of profile sections

The profiles for the rough line contact simulations were obtained from contact profilometer measurements of the disks in-situ at the conclusion of load stage 2 ($6x10^3$ fast disk cycles). Using profiles obtained after running-in ensured that the true surface modification from running-in was applied in the simulation, which has a significant influence on the fatigue of the surface. Representative profile sections of length $2a$ were then extracted from the measured profiles, and 100 lengths of this representative profile were joined sequentially to make a repeating profile. These profile sections were manually selected based on the following criteria:

- They should not contain any abnormally large valley or asperity features that are not reflective of the typical features through the rest of the profile
- They should not have a notably higher or lower (by eye) density of asperities or peaks than seen on average through the rest of the profile
- They should start and end in valley features below the mean line, such that profile repeats connect without introducing abnormal features or discontinuities

For simulation of Test 1, the selected profiles were taken from outside of the central worn band, although the simulation was still performed using centreline conditions.

Initial simulation work found that different profile sections taken from the same axial position could vary in fatigue behaviour even against a common opposing surface profile. The same was true if the opposing surface profile was changed but the profile for which fatigue was evaluated remained the same. Notably, variation was also observed when the same two profiles were analysed with a range of relative offsets. This illustrated that the calculated fatigue is dependent on the interactions between individual features on each surface, and different configurations can force features into severe direct contact or spare them from direct contact entirely.

For example, Figure 6.2.2a shows 5 sets of predictions for the fatigue of the fast surface. Each of these results from the same rough surface simulation, but with offsets applied to the window of fatigue analysis (which evaluates the damage experienced by a 2a length of the repeated profile during one pass through the contact) in multiples of 400 timesteps. This offset was chosen as the number of timesteps required for a 2a length of fast surface to pass through the surface. As such the fast surface appeared in the analysis window in the same way in each analysis, but with the slow surface offset by $\frac{2}{5}a$ each time (due to the 0.5 SRR applied).

Figure 6.2.2b and c show the fast surface damage contours for the +400 timestep and no offset conditions respectively. The same fast surface asperities can be clearly identified in each contour plot but the damage sustained differs vastly - purely due to the alignment with the opposing surface. As the profiles for both surfaces are repeating 2a segments, all the same features on each surface are present in the contact under each offset condition.

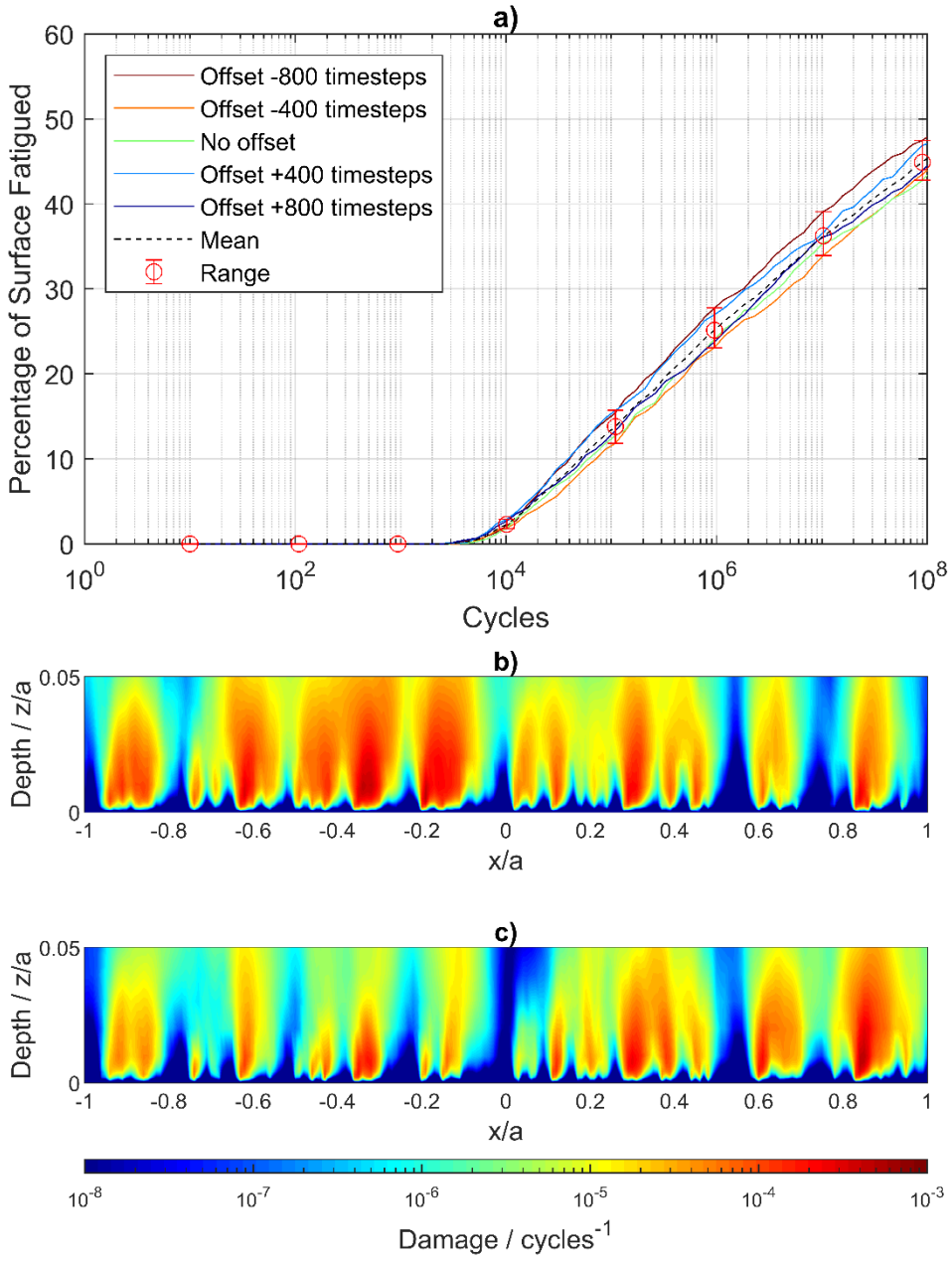

Figure 6.2.2 a) Fast surface percentage fatigued predictions for the same two surfaces in 5 different alignments, alongside fatigue damage contour plots showing the fatigue damage sustained through a single pass through the contact for b) +400 timestep offset and c) no offset conditions.

As well as the relative alignment, the specific geometry of individual features can have a significant influence on the fatigue behaviour, however it is difficult to classify the

aggressiveness of features when selecting profile sections. To achieve a representative prediction for fatigue, five profile sections each were extracted from the fast and slow surfaces at the given axial position. For both fast and slow surface fatigue simulations, one of these profiles was chosen at random as an 'evaluation profile' – the profile for which fatigue will be calculated. This was then run against each of the five opposing surface profiles and predicted percentage of material failed at increasing numbers of load cycles was calculated for each simulation. If, when used as a counterface for the other surface, the selected evaluation profile induced the highest or lowest amount of fatigue (or was otherwise removed from the mean line), the evaluation profile was replaced by the profile for which the predicted fatigue was closest to the mean.

Selection of a representative profile section was performed using the percentage of data points predicted to have failed considering all points from the surface to a given depth. Figure 6.2.3 illustrates this, showing the range of results obtained for material failed from the surface to a depth of 0.004a for a set of 5 simulations. As can be seen in Figure 6.2.3 and Figure 6.2.4, curves of the average fatigue can be drawn to represent the percentage of material failed between the surface and any layer of interest.

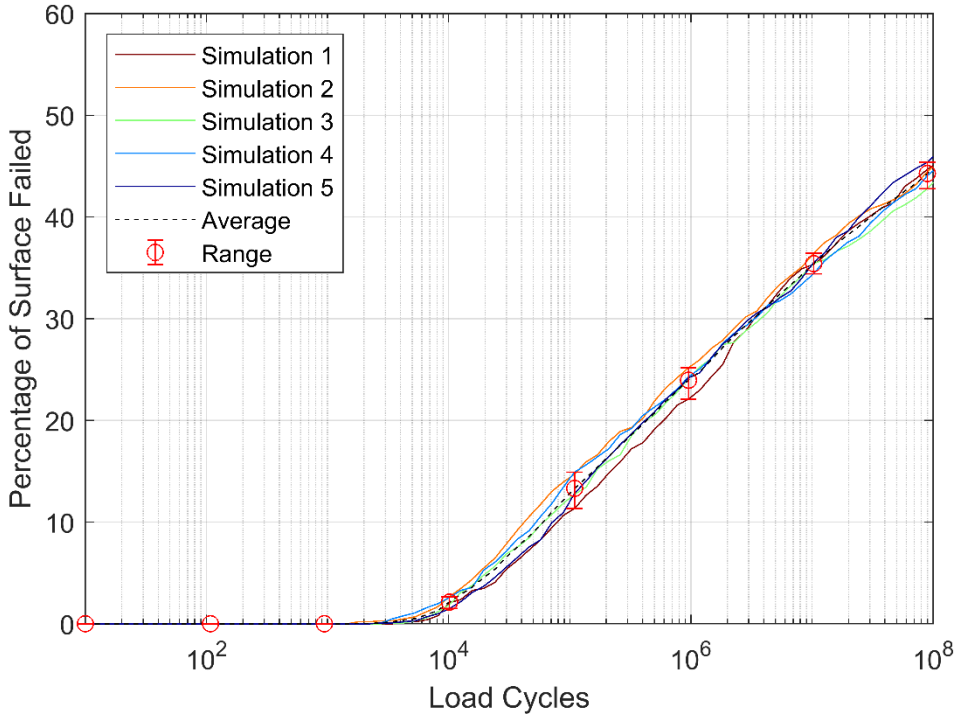

Figure 6.2.3 Proportion of data points fatigued from the surface to a depth of 0.004a for 5 simulations of the same fast surface section against different slow surface sections.

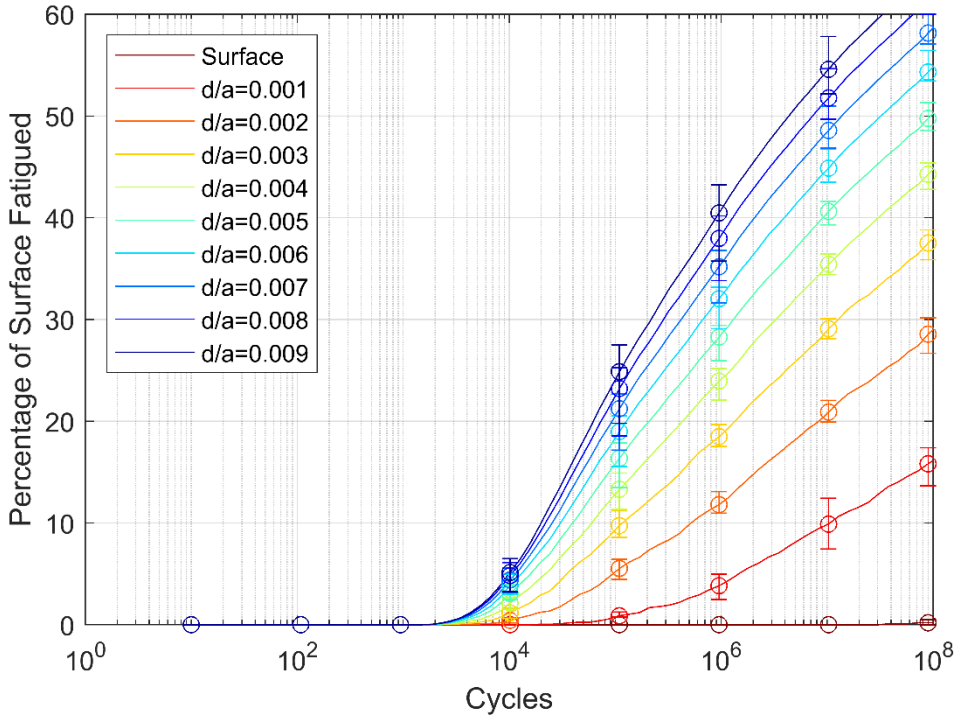

Figure 6.2.4 Average proportion of surface fatigued up to different depths. Error bars indicate the range of values in the 5 simulations from which the average is calculated.

6.2.3 Determining Fatigue Damage

The outputs from the transient rough line EHL contact simulation were used as inputs for the fatigue analysis. Specifically, the transient surface loading [$p(t)$, $\tau(t)$] experienced by a $2a$ length during a single pass through the contact area. This data was used to perform a plane strain stress analysis. This was developed and incorporated into the simulation program by Qiao (2005).

The stress history for each position analysed in the material was then input to a program that applied the Fatemi-Socie fatigue criterion to the material. This provides a value for fatigue damage sustained at each point in the material in a single pass of the contact. When the fatigue damage for a point reaches unity, a fatigue crack is predicted to have been initiated and hence the material at that point is deemed to have failed. As damage is cumulative, by multiplying the damage at each point by a given number of cycles the damage after that number of traversals through the contact area can be predicted.

In the approach adopted for this work, the percentage failed after n cycles was calculated as in Equation 6.2-1, where all points from the surface to a specified layer are considered.

$$\%\, failed = \frac{No.\ points\ failed}{Total\ no. points} \times 100 \qquad \text{Equation 6.2-1}$$

6.2.4 Profile Changes due to Fatigue

The simulation used in the current work did not have the capacity to update the roughness profiles inside the simulation as the result of fatigue. An argument can be made, therefore, that as soon as any fatigue occurs on the profile the distribution of load (and thus the stress experienced) becomes inaccurate, with the degree of inaccuracy increasing as more of the profile becomes fatigued.

To investigate the influence of this a second group of simulations was performed. Profile sections corresponding to the same location as the evaluation profile sections used previously were also obtained at later load stages in the test. This means that the same surface sections were available throughout the test. Simulations were then run using the profiles at load stages 2, 3, 4, 5, 6, 8, 10, and 12. The damage accumulation with loading cycles was calculated by updating to the corresponding damage matrix for the current stage. For example, the damage at $3x10^4$ fast disk load cycles (D_{30k}) would be calculated as below, where d_{LS2} and d_{LS3} are the damage sustained through one cycle of the contact for the load stage 2 and 3 profiles respectively.

$$D_{30k} = (2 \times 10^4) d_{LS2} + (3 \times 10^4 - 2 \times 10^4) d_{LS3}$$

This worked well, although 'jumps' were seen in percentage failed as the profiles updated due to the sudden redistribution of the load. In order to achieve a more gradual redistribution, the damage between profile updates was transitioned using linear interpolation of the damage per cycle at each mesh point. This was recalculated at each of the logarithmically spaced intervals, and then a constant damage per cycle corresponding to the final profile was used after 2 million cycles.

6.3 Fatigue Analysis – Run-in Profiles Only

6.3.1 Percentage of Material Failed

For each set of simulations, the mean percentage of data points that fatigued from the surface to a given depth *d* was calculated for increasing load cycles, as can be seen in Figure 6.3.1 below. The error bars for each depth indicate the range of values in the simulation results. The corresponding experimental result is shown in black. The results for all nine sets of simulations for both the fast and slow surfaces are shown in Appendix 5.

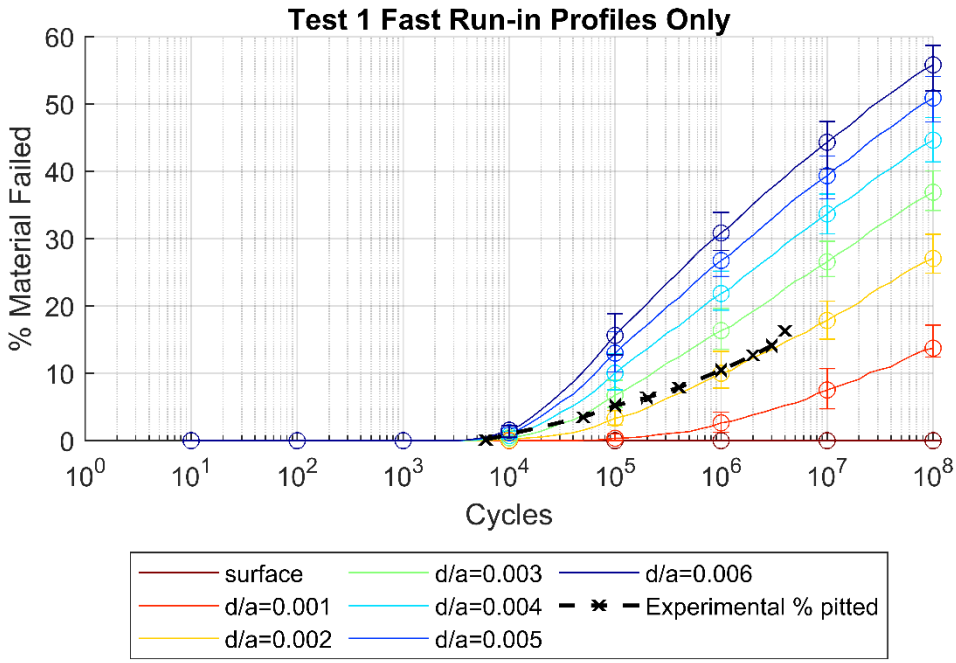

Figure 6.3.1 The simulation result for the fast surface of Test 1, using run-in profiles only.

In order to analyse the Fast surface results, it was necessary to decide which depth should be used for comparison. The experimental values typically followed the shape of the curves given by the simulation results. For the fast surface, the experimental results for Tests 1 and 2 fitted closely to the simulation curves for a depth of 0.002*a*, while Tests 5 and 7 fitted more closely to values for a=0.001*a*. The remaining results were located in-between the two depths. Also, Tests 1 and 2 initially began micropitting much closer to the 0.003*a* or 0.004*a* fatigue simulation lines, although this was not maintained beyond the first (Test 2) or second (Test 1) measurement of micropitted area.

On the slow surface, the experimental results for Tests 1, 3, and 6 were closest to the 0.003*a* depth analysis, while Tests 8 and 5 were more closely represented by the 0.001*a* analysis. The remaining tests remained closest to the 0.002*a* analysis. The depth of 0.002*a* was therefore selected as the analysis depth, being the most representative for both surfaces.

The predicted percentage of surface micropitted at the conclusion of each test for the depth of 0.002*a* was recorded for both the fast and slow surfaces, as can be seen in Table 6.3.1 below.

Table 6.3.1 Predicted % of material failed to a depth of 0.002a using run-in profiles only

	Fast Surface		Slow Surface	
Test	Fast Disk Cycles at end of test	Fast Surface% micropitted at 2million FD cycs	Slow Disk Cycles at end of test	Slow Surface % micropitted at 2 million FD cycs
Test 1	2.00×10^6	12.3	1.20×10^6	13.9
Test 2	2.00×10^6	14.7	1.20×10^6	11.8
Test 3	2.00×10^6	17.0	1.56×10^6	11.7
Test 4	2.00×10^6	14.9	1.20×10^6	14.5
Test 5	2.00×10^6	12.1	1.56×10^6	12.7
Test 6	2.00×10^6	12.7	1.56×10^6	14.4
Test 7	2.00×10^6	15.0	1.56×10^6	14.8
Test 8	2.00×10^6	13.1	1.20×10^6	14.1
Centrepoint	2.00×10^6	14.4	1.37×10^6	12.4

A factorial analysis was conducted using this data. The main effects on predicted percentage of surface failed are shown in Figure 6.3.2. On the fast surface negligible main effects were seen for both pressure and SRR, while increased entrainment was predicted to have a strong protective effect on the surface, reducing the predicted fatigue.

On the slow surface, a small fatigue-reducing effect was predicted for pressure, which is contrary to effects seen on micropitted surfaces in experiments. SRR was again predicted to have a negligible influence on the surface, and while a small apparent fatigue-increasing effect could be seen for entrainment data at high and low settings overlapped completely, suggesting that this may not be a significant influence.

On both surfaces the centrepoint test result was located away from the lines for the main factor effects, indicating the presence of nonlinear behaviour.

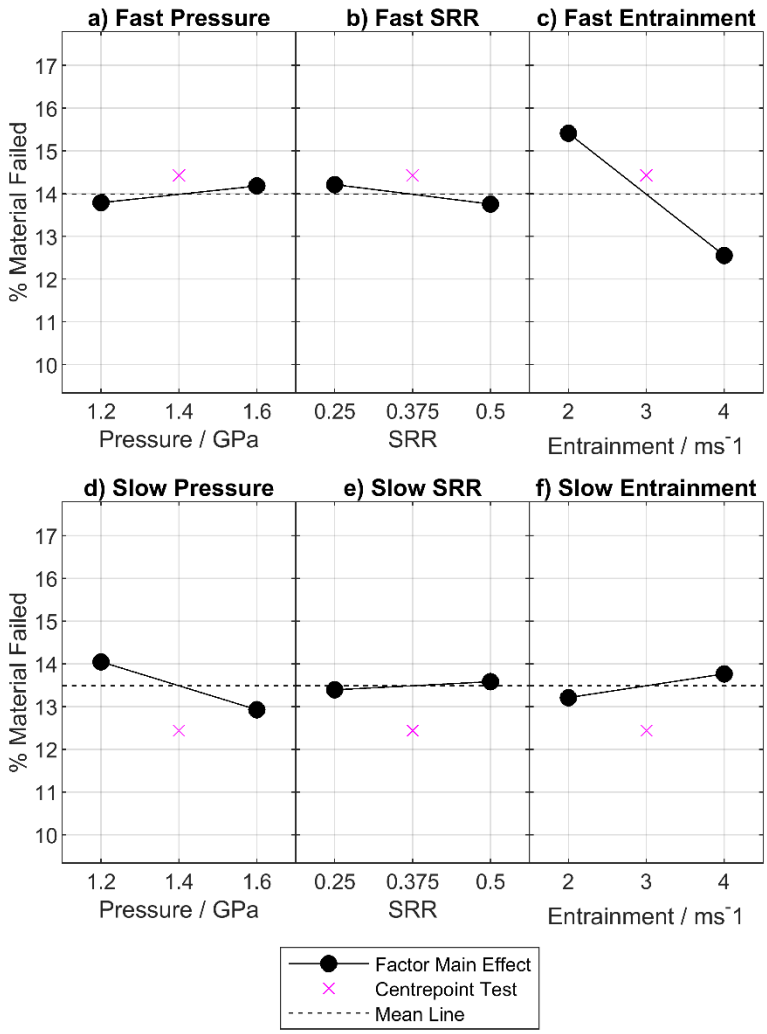

Figure 6.3.2 Main Effects of pressure, SRR, and Entrainment on predicted percentage of material failed to a depth of 0.002a using run-in profiles only.

The two-factor interactions for these simulations can be seen in Figure 6.3.3. On the fast surface, weak two-factor interaction effects can be seen for each of the three pairs of variables, however they did not correspond to the two-factor interactions seen for any of the micropitting experiment parameters.

On the slow surface, the two-factor interactions involving SRR were effectively negligible in both cases - however a much stronger two-factor interaction could be seen between pressure and entrainment. In this interaction higher entrainment appeared to worsen fatigue at high pressure but protect the surface at low pressure. Increasing pressure was

predicted to have a strong fatigue-decreasing effect at low entrainment, while having a mild fatigue-increasing effect where entrainment was high.

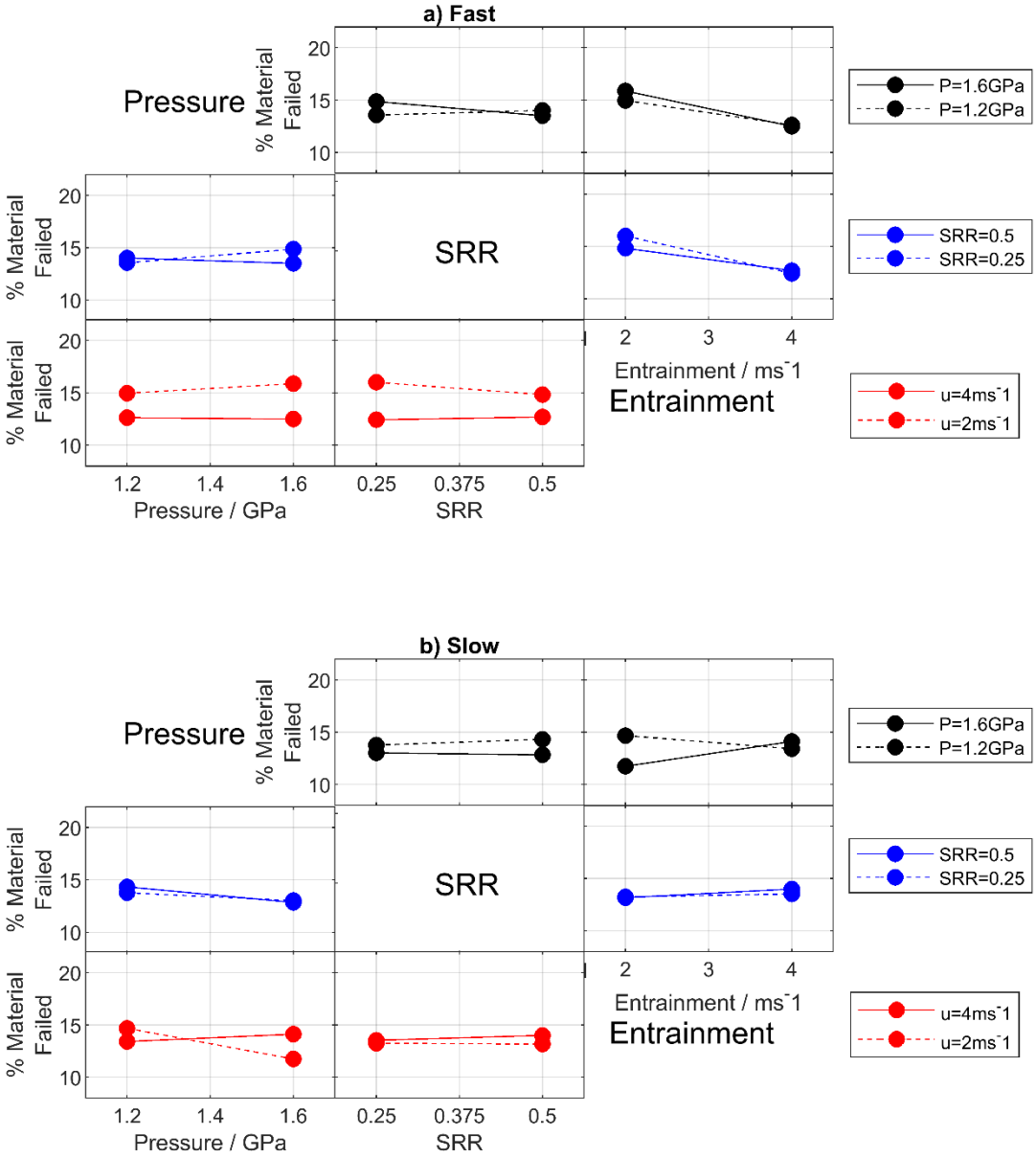

Figure 6.3.3 Two-factor interactions for the predicted percentage of material failed to a depth of 0.002a using run-in profiles only.

The corresponding three-factor interaction effects are illustrated in Figure 6.3.4. The changing interaction between pressure and SRR and high and low entrainment states indicates a three-factor interaction effect is present on both surfaces. This interaction is

much weaker on the fast surface, as indicated by the smaller change in the angle between the two lines.

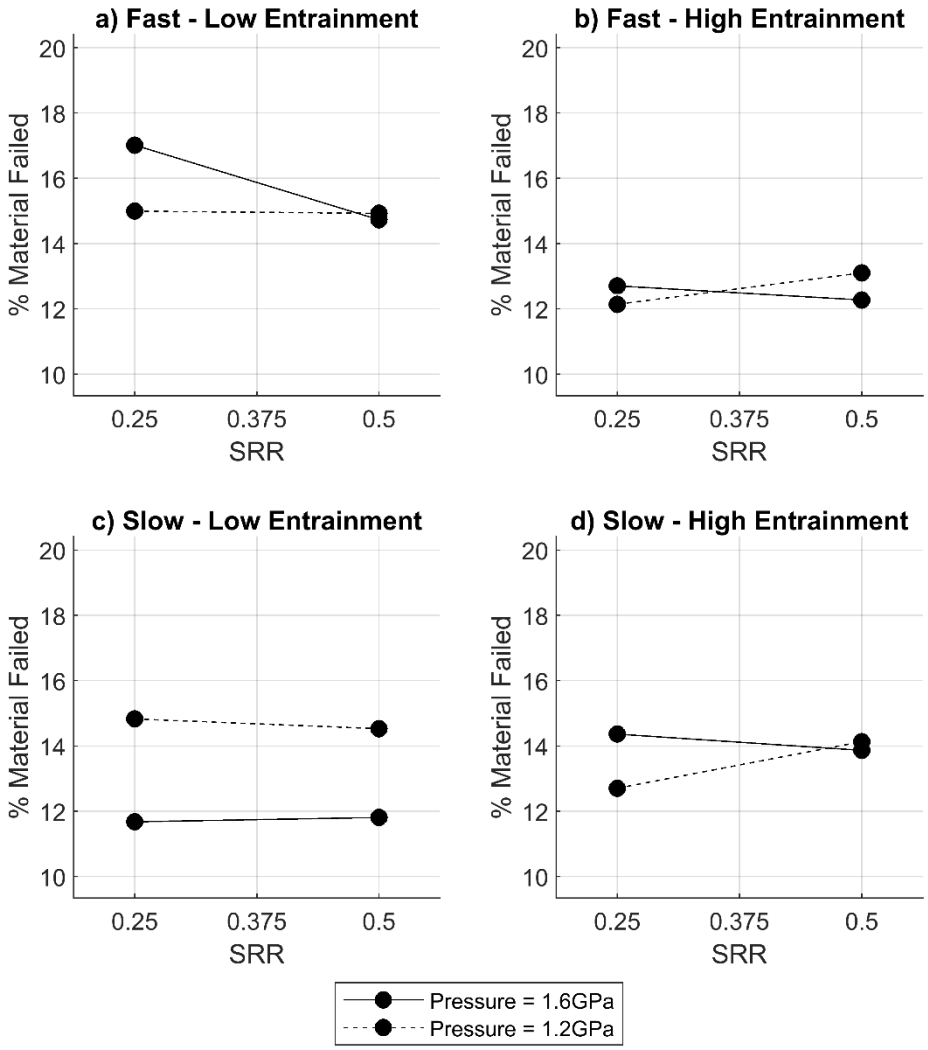

*Figure 6.3.4 Two-factor interaction plots for pressure*SRR on each surface at low and high entrainment, for three-factor interaction analysis of predicted percentage of material failed to a depth of 0.002a using run-in profiles only.*

The predicted effects of the main factors and their interactions are shown in Table 6.3.2.

Table 6.3.2 Effects of main factors and interactions on the predicted percentage of material failed to a depth of 0.002a for simulations using run-in profiles only.

Factor / interaction	Fast Surface			Slow Surface		
	Low average / %	High average / %	Effect / Δ%	Low average / %	High average / %	Effect / Δ%
Pressure	13.79	14.18	0.39	14.05	12.93	-1.12
SRR	14.21	13.76	-0.46	13.39	13.58	0.19
Entrainment	15.41	12.55	-2.86	13.21	13.76	0.56
Pressure*SRR	14.44	13.53	-0.90	13.67	13.30	-0.37
Pressure*Entrainment	14.25	13.72	-0.52	12.58	14.39	1.82
SRR*Entrainment	13.62	14.35	0.72	13.35	13.62	0.27
Pressure*SRR*Entrainment	14.09	13.88	-0.21	13.19	13.78	0.59

It is clear from analysis of the percentage of material failed at the depth of 0.002*a* that the influence of the factors and interactions on predicted fatigue did not correspond to the effects seen for the analysis of micropitting fatigue in the experimental work.

6.3.2 Equivalent Depth

In the figures of experimental and simulation results shown in Appendix 5, while the shapes of the experimental results curve typically approximated that of the fatigue prediction, the depth to which the experimental curve corresponded varied by test. This raised the possibility that the critical depth at which failure occurs is changed by the contact conditions – as the pressure is known to influence the depth of maximum shear stress for the whole contact, there is a strong possibility of this influence on an asperity scale. In this case the appropriate depth for analysis would need to be determined by the user as a function of the contact conditions.

In order to investigate this variation in what will be referred to here as the '*equivalent depth*' – the depth from the surface over which a material failed analysis would match the experimental curve - the process outlined below was followed.

Firstly, the predicted values of percentage of material failed were recorded at the number of cycles corresponding to the conclusion of each test, for each layer from the surface to 0.006*a*. A least-squares second-order polynomial was then fitted to the data, as can be seen in Figure 6.3.5. The equivalent depth was then simply calculated by solving for the depth at which the predicted material failed was equal to the end-of-test experimental value.

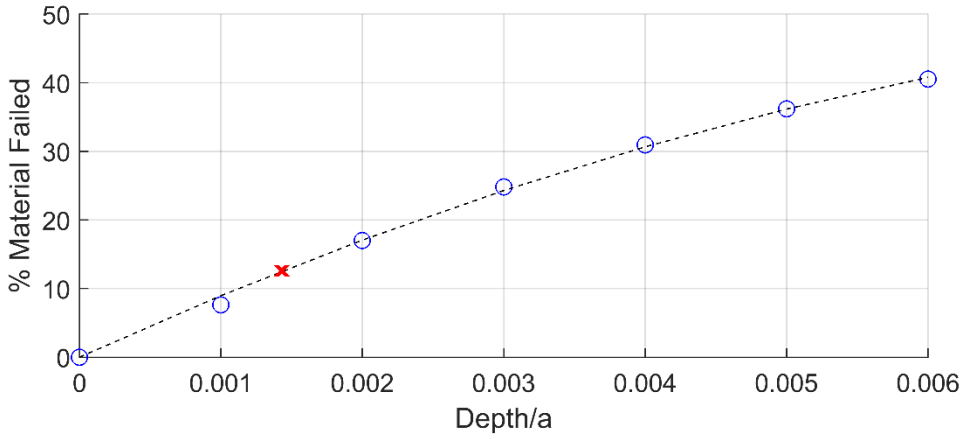

Figure 6.3.5 Predicted percentage of material failed at each depth for Test 3 fast disk, shown by blue circles. Dashed line shows the best fit polynomial, red cross indicates the experimental percentage failed at end of Test 3 at its calculated equivalent depth.

The main effects of each factor on the equivalent depth are shown in Figure 6.3.7. For the fast surface both pressure and SRR showed strong effects to increase the equivalent depth. Entrainment however had negligible influence on the equivalent depth.

On the slow surface a strong depth-increasing effect was seen for pressure, however unlike the fast surface the SRR effect was negligible. A small entrainment effect appeared to be present, however overlap of data at high and low entrainment settings raises doubt about its significance.

The distance of the centrepoint test from the fast surface effects is suggestive of highly nonlinear behaviour in the response. Meanwhile, the centrepoint result was much closer to

the lines for the slow surface results, indicating a response that may still have some nonlinearity but is much closer to linear behaviour.

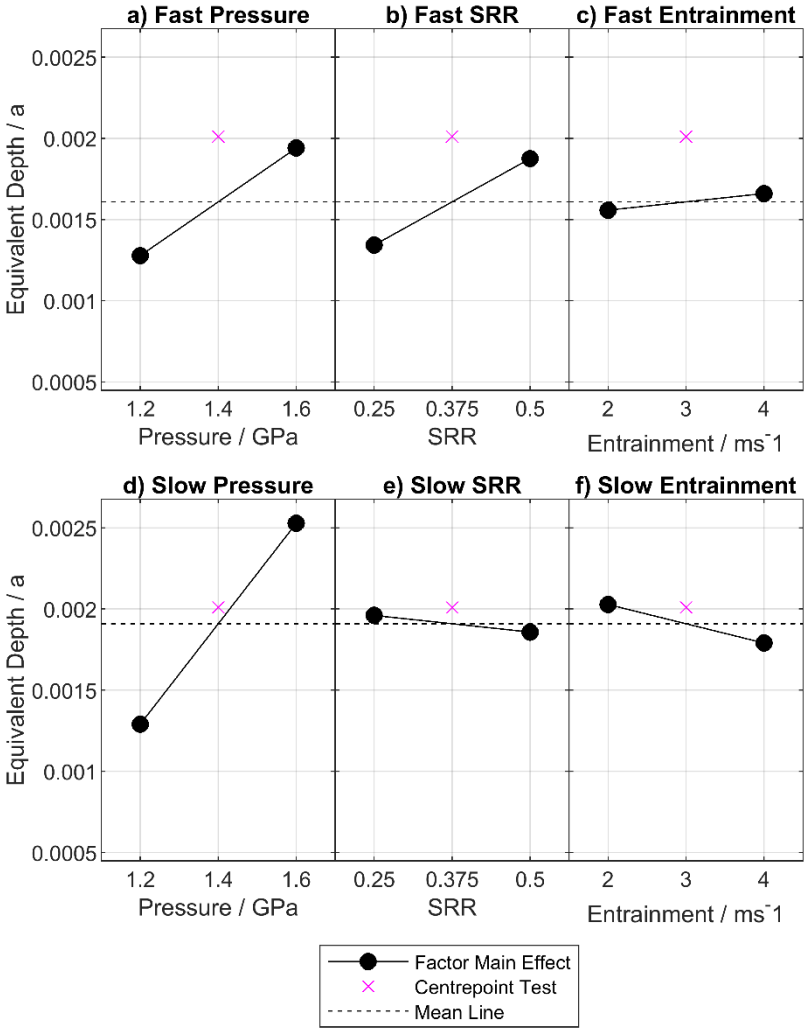

Figure 6.3.6 Main Effects of pressure, SRR, and Entrainment on equivalent depth at end of test, for simulations using run-in profiles only.

Interaction effects were present for the fast and slow surfaces, as shown in Figure 6.3.7. On the fast surface pressure and SRR interacted, each showing a stronger depth-increasing influence when the other was at its low setting. Pressure and entrainment also interacted, pressure increasing depth more strongly at high entrainment, and entrainment influencing the equivalent depth in differing directions dependent on pressure. SRR and entrainment did not interact.

For the slow surface it was instead pressure and entrainment that did not show significant interaction. A much stronger interaction between pressure and SRR was present, with SRR influencing in differing directions at high and low pressure. Entrainment and SRR showed an inconsistent effect where a deeper equivalent depth resulted only when both were set low. This inconsistent effect likely produced the weak entrainment effect seen previously.

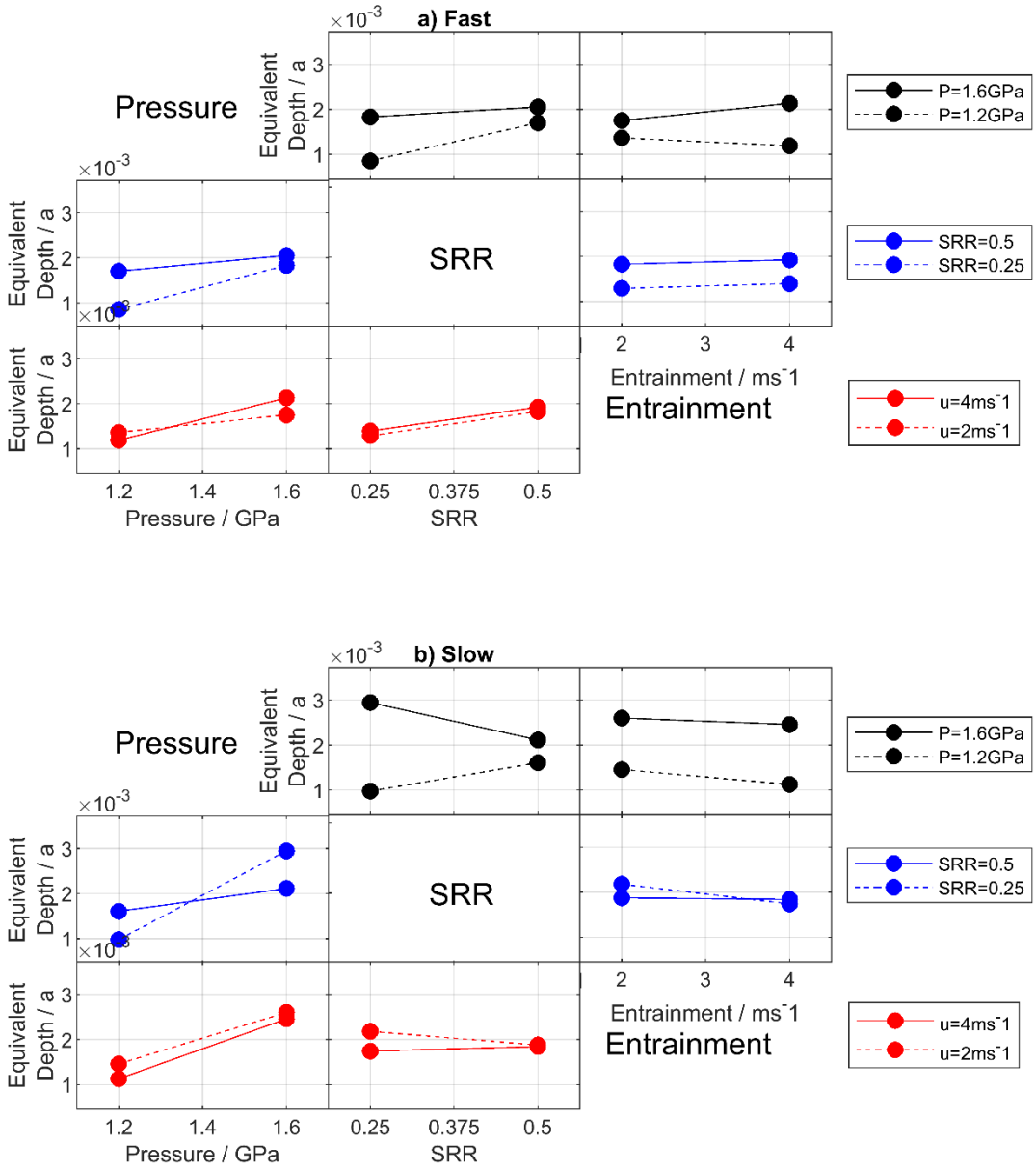

Figure 6.3.7 Two-factor interactions for the equivalent depth at the end of test, for simulations using the run-in profiles only.

Figure 6.3.8 shows significant change in the interaction between pressure and SRR for the fast surface, and hence a strong three-factor interaction. Conversely the angle between the two lines did not change significantly for the slow surface, indicating a negligible three-factor interaction.

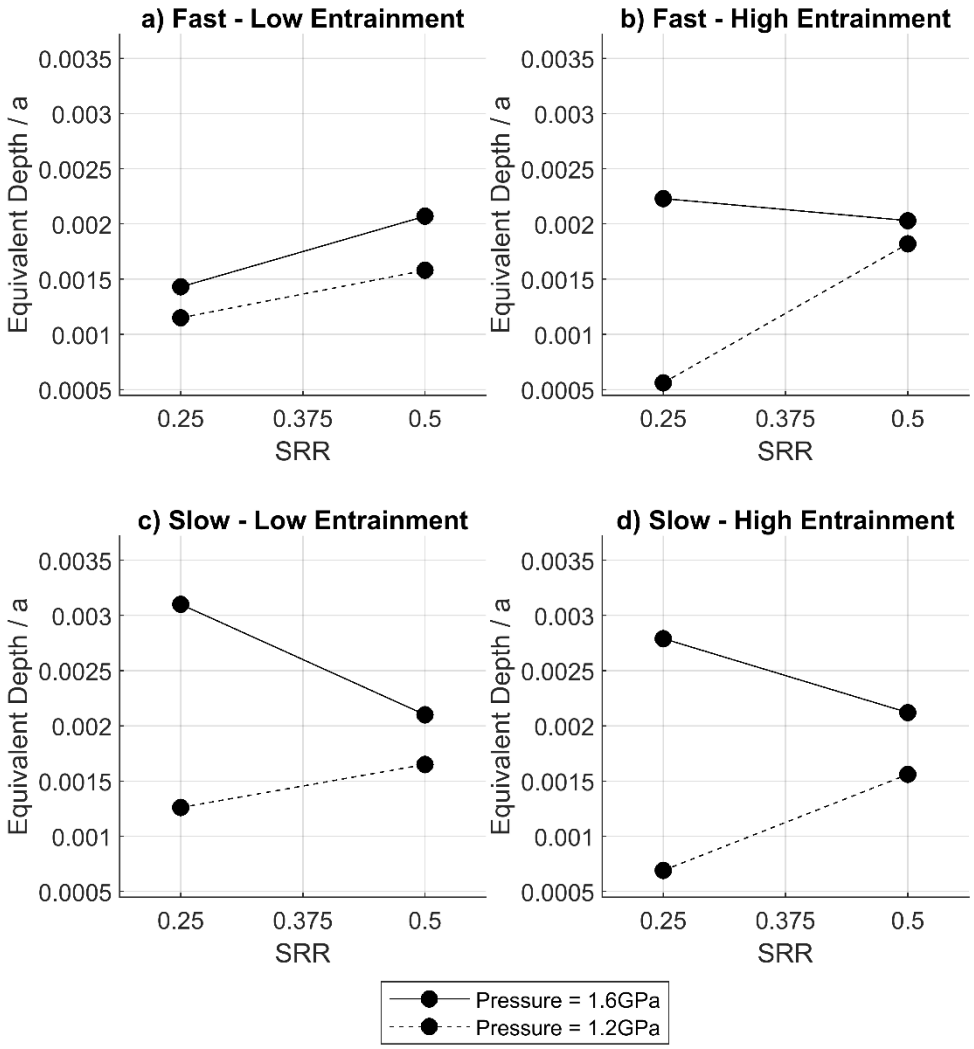

*Figure 6.3.8 Two-factor interaction plots for pressure*SRR at low and high entrainment, illustrating three-factor interactions for equivalent depth at end of test using run-in profiles only.*

The strengths of effects on equivalent depth are shown overleaf in Table 6.3.3.

Table 6.3.3 Effects of main factors and interactions on the equivalent depth at end of test.

Factor / Interaction	Fast			Slow		
	Low average / *a*	High average / *a*	Effect / Δ*a*	Low average / *a*	High average / *a*	Effect / Δ*a*
Pressure	0.00128	0.00194	0.00066	0.00129	0.00253	0.00124
SRR	0.00134	0.00188	0.00053	0.00196	0.00186	-0.00010
Entrainment	0.00156	0.00166	0.00010	0.00203	0.00179	-0.00024
Pressure*SRR	0.00177	0.00145	-0.00031	0.00228	0.00154	-0.00073
Pressure*Entrainment	0.00147	0.00175	0.00028	0.00186	0.00196	0.00009
SRR*Entrainment	0.00161	0.00161	0.00000	0.00181	0.00201	0.00020
Pressure*SRR*Entrainment	0.00140	0.00182	0.00042	0.00189	0.00193	0.00004

Considering that the true surface undergoes changes and redistributions of load as micropitting takes place (which are not captured in these simulations using run-in profiles) it is valuable to make a comparison of the equivalent depth result at the end of test with the same analysis at an earlier stage. As such, an analysis of equivalent depth was conducted for the conclusion of load stage 6 ($2x10^5$ fast disk cycles).

Figure 6.3.9 shows the influence of the main factors on the equivalent depth at this stage. For the fast surface, pressure and SRR again showed a strong depth-increasing effect, while entrainment showed minimal influence. The effect of pressure was slightly smaller in magnitude than seen for the evaluation at the end of the test.

On the slow surface, pressure was the strongest influence as before, although again slightly smaller than at the end of test. SRR once again showed no main effect, while entrainment exhibited a depth-reducing effect.

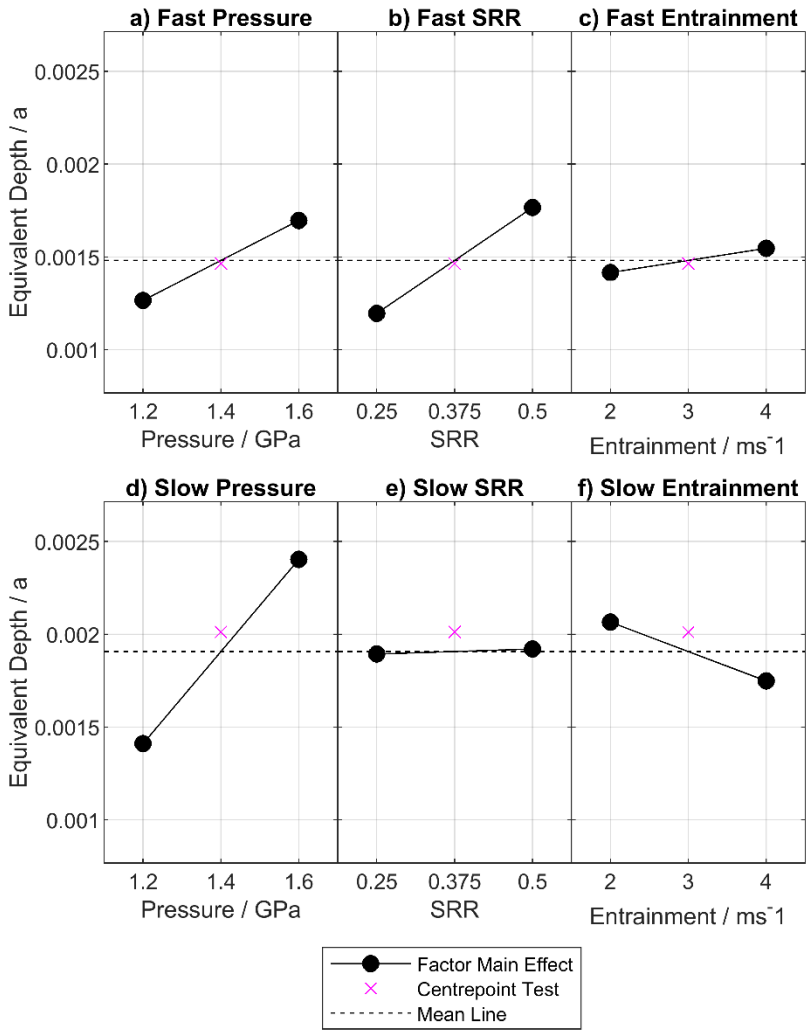

Figure 6.3.9 Main Effects of pressure, SRR, and Entrainment on equivalent depth at the conclusion of load stage 6 for simulations using run-in profiles only.

The two-factor interactions for equivalent depth at the end of load stage 6 are shown in Figure 6.3.10. On the fast surface the pressure*SRR interaction appears to have a different influence at this earlier stage, the two lines diverging as pressure or SRR increased. The interaction between pressure and entrainment was unchanged from the end of test interactions, however entrainment and SRR (which did not interact at the end of test) did show an interaction in this case. On the slow surface the same interactions were present as at the end of test, although with a reduced magnitude in all cases.

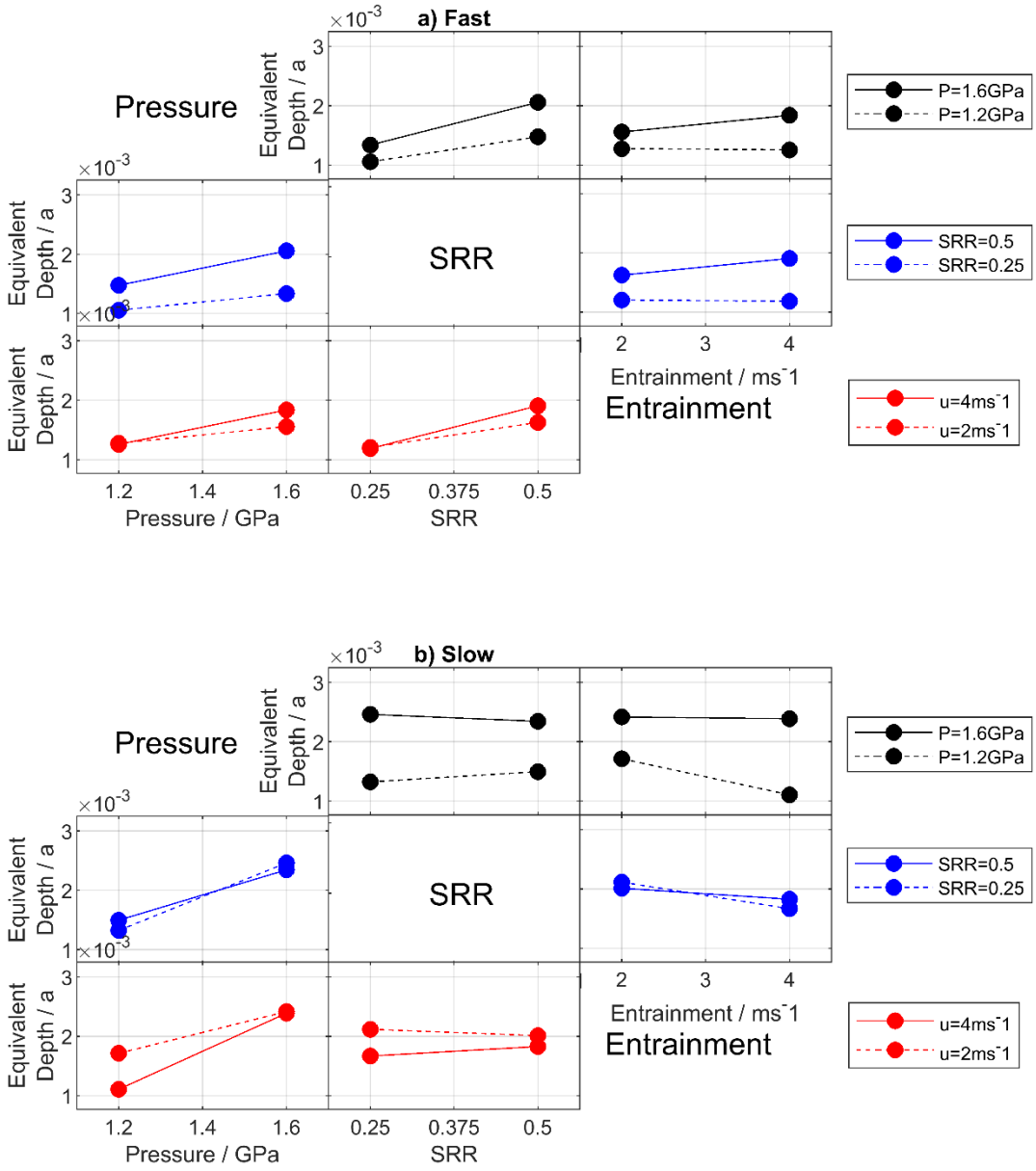

Figure 6.3.10 Two-factor interactions for the equivalent depth at the conclusion of load stage 6, for simulations using the run-in profiles only.

Figure 6.3.11 illustrates three-factor effects present for the equivalent depth at load stage 6. This shows that three-factor effects were present on the slow surface but not the fast, the opposite of that found for the equivalent depth at the end of test.

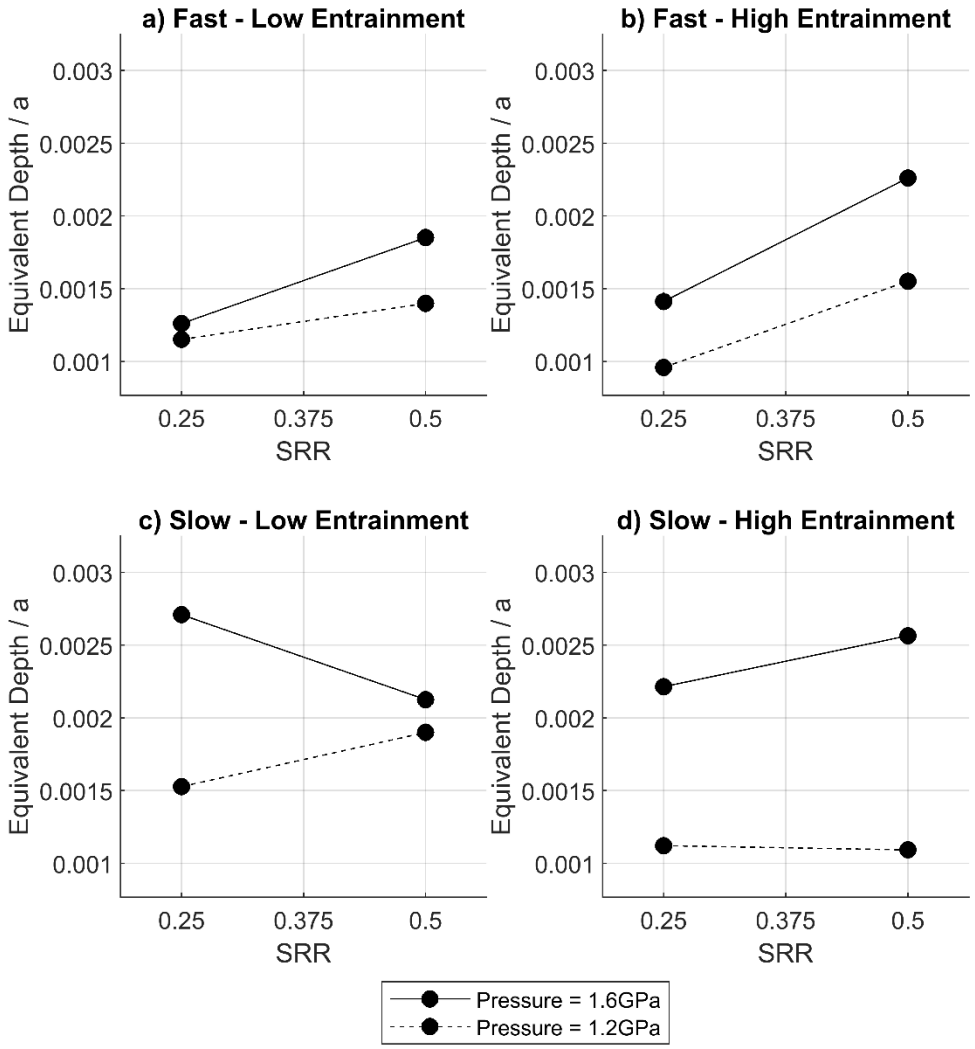

*Figure 6.3.11 Two-factor interaction plots for pressure*SRR at low and high entrainment, illustrating three-factor interactions for equivalent depth at the conclusion of load stage 6 using run-in profiles only.*

The effects on equivalent depth at the conclusion of load stage 6 are summarised in Table 6.3.4 below.

Table 6.3.4 Effects of main factors and interactions on the equivalent depth at the conclusion of load stage 6.

	Fast			Slow		
Factor / Interaction	Low average / a	High average /a	Effect / Δa	Low average / a	High average /a	Effect / Δa
Pressure	0.00127	0.00170	0.00043	0.00141	0.00240	0.00099
SRR	0.00120	0.00177	0.00057	0.00189	0.00192	0.00003
Entrainment	0.00142	0.00155	0.00013	0.00207	0.00175	-0.00032
Pressure*SRR	0.00141	0.00156	0.00015	0.00198	0.00183	-0.00014
Pressure*Entrainment	0.00141	0.00156	0.00015	0.00176	0.00205	0.00029
SRR*Entrainment	0.00141	0.00156	0.00015	0.00184	0.00197	0.00013
Pressure*SRR*Entrainment	0.00147	0.00149	0.00002	0.00207	0.00174	-0.00033

6.3.3 Discussion – Run-in profile simulations

These simulations provide an opportunity to compare directly to the preceding experimental work. Clearly, the initial analysis of percentage of material failed in Section 6.3.1 did not show agreement with the experimental results. Only a strong fatigue-decreasing effect from entrainment was common between the simulations and experimental results on the fast surface – although the strength of the entrainment effect on simulation results was found to be 64% larger than the effect of entrainment on the percentage of fast surface micropitted at the end of test in the experiments. For the slow surface it was only the negligible SRR effect and strong interaction between pressure and entrainment that bore resemblance to the experimental data – although this interaction effect in the simulation was weaker, only 75% the strength of the experimental effect.

The observation that the experimental result followed different depth curves in each test raised the possibility that simply analysing up to the same depth for all tests – even if that depth were normalised by the contact dimension a – may ignore fundamental differences between the contacts that must be accounted for if useful information is to be obtained. For example, contacts between protruding asperities effectively act as miniature EHL

contacts, independent of the larger contact and bearing a disproportionate share of the load. The locations of peak shear stresses beneath these asperities (on which the fatigue simulation is based) change based on the individual asperity contacts rather than the larger contact.

The equivalent depth analyses were able to show that the depth most appropriate for analysis of the simulation was dependent primarily on the pressure and SRR for the fast surface, and pressure on the slow surface. It also showed that both surfaces were affected by two- and three-factor interaction effects of varying strength.

If the analysis at a constant depth is taken to represent the change in the simulation result due to the input conditions, and the analysis of equivalent depth is taken to represent a change in the way in which the simulation outputs should be interpreted due to the inputs, then this can provide insight into the experimental results. In this combined approach, all three main factors influence fatigue on the fast surface, pressure and SRR increasing fatigue while entrainment reduces it. On the slow surface pressure alone would show a significant fatigue-increasing effect. The analyses also indicated smaller fatigue-reducing influences from entrainment may be present on the slow surface but would benefit from further testing to confirm this. Interaction effects, present in both analyses, are much more complex to combine and assess their resulting influence.

In terms of main effects, this result is in agreement with the experimental work regarding the difference between fast and slow surface responses to main effects, and the lack of slow surface dependence on SRR and entrainment velocity. This provides support to the hypothesis that initiation of micropitting fatigue behaviour is dominated by stress cycling on asperity features in the contacts investigated in this work – or at the very least that this approach may be applied to form a basis for micropitting fatigue prediction.

In order to further test the approach used here, factorial models such as those shown in Appendix 6 can be constructed from the equivalent depth analysis. If a separate experimental test were then performed, it would be possible to test the model's ability to predict the appropriate depth for simulation analysis. The centrepoint test results did however suggest the possibility of some nonlinearity in the responses for both the predicted percentage of material failed and equivalent depth analyses, hence it may prove necessary to perform additional tests to define higher order responses to the factors. This is beyond the scope of the current work.

6.4 Fatigue Analysis – Updating Profiles

As detailed in Section 6.2.4 an additional series of simulations were performed using profiles at the same location at different points in the test. These were then used to update the damage matrices at the appropriate number of cycles during damage accumulation. Otherwise, the same damage criteria and means of calculating the percentage of material failed were applied. Figure 6.4.1 shows an example of the simulation results for Fast surface of Test 1. As only one fast and one slow location (at several points through the test) were used in these simulations, error bars indicating range are not present. The full selection of simulation results for fast and slow surfaces with updating profiles can be seen in Appendix 7.

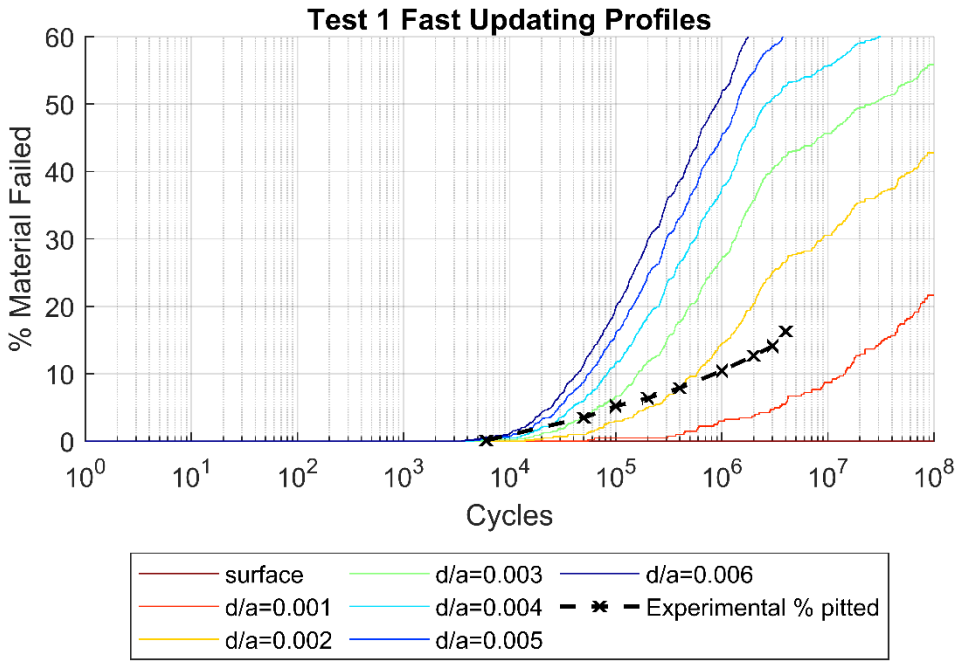

Figure 6.4.1 Results for the Test 1 fast surface simulation using updating profiles.

First considering the results for the fast surface, the experimental results of Tests 1 and 2 fitted more poorly to the simulation predictions when the profiles were updated than when only the run-in profiles were used. Conversely, the experimental results of Test 6 and the Centrepoint Test both exhibited an upturn late in the test that was not predicted using run-in profiles only, however when updating profiles this upturn was effectively captured. For the remaining tests however both methods produced predictions that fitted well to the data.

Considering the slow surface, the influence of the profile updating process was similar. Predictions from the profile updating approach fitted more poorly than the simple run-in profile approach for Tests 1 and 4 (Test 2 in this case fitted well for both methods), but an improved fit was seen for Tests 6 and 8 which each turned upwards late in the test. The remaining tests again showed similar curves by both methods.

Those tests whose outcomes were better predicted shared the quality of a late-stage upturn in micropitting, while for tests whose predictions fit more poorly to the shape of the

experimental curves this upturn was predicted but did not occur. It is important therefore, to understand what causes this upturn in the predicted result - as it seems to be key to both improved and less accurate predictions alike.

A possible explanation may be found by examining contour plots of the damage incurred per cycle for each updated surface in a test.

Beginning with the Test 6 slow surface (shown in Figure 6.4.2) clear occasions can be seen where, after apparently disappearing, a damage concentration reappears in the same location. More than this, patterns of damage concentrations are seen to reappear together. The red and blue lines on the right-hand side of Figure 6.4.2 show matching patterns of damage which disappear and then reappear later in the test.

Other simulations in which the upturn was predicted but did not occur, such as the Test 4 slow surface simulation shown in Figure 6.4.3, and the Test 2 fast surface simulation shown in Figure 6.4.4 also show configurations of damage contours that appear, disappear, and reappear through the course of the test.

In those tests which gave very similar simulation curve shapes for both the profile updating and run-in profile only simulations, such as the Test 8 Fast disk test shown in Figure 6.4.5, less variation in the damage contours was seen through the test. Where the damage contours did vary, this was typically seen for the less aggressive asperities in the surface with milder damage induced per cycle.

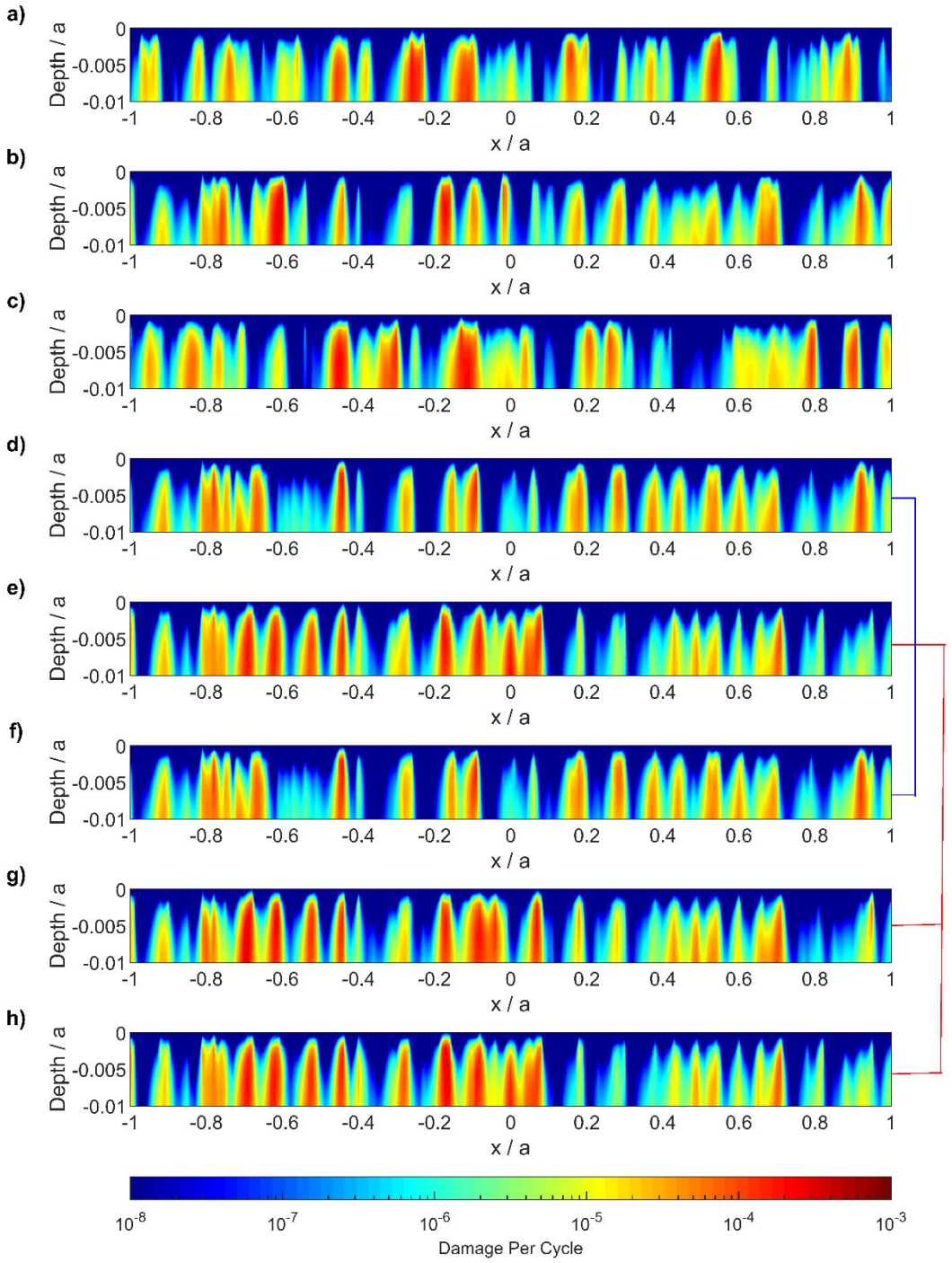

Figure 6.4.2 Contours for damage sustained during a single pass through the contact for each profile of the Test 6 slow surface in the profile updating simulation. Profiles updated at (in equivalent FD cycles) a) start of test (run-in profile), b)2x10^4, c)5x10^4, d)1x10^5, e)2x10^5, f)4x10^5, g) 1x10^6, h) 2x10^6.

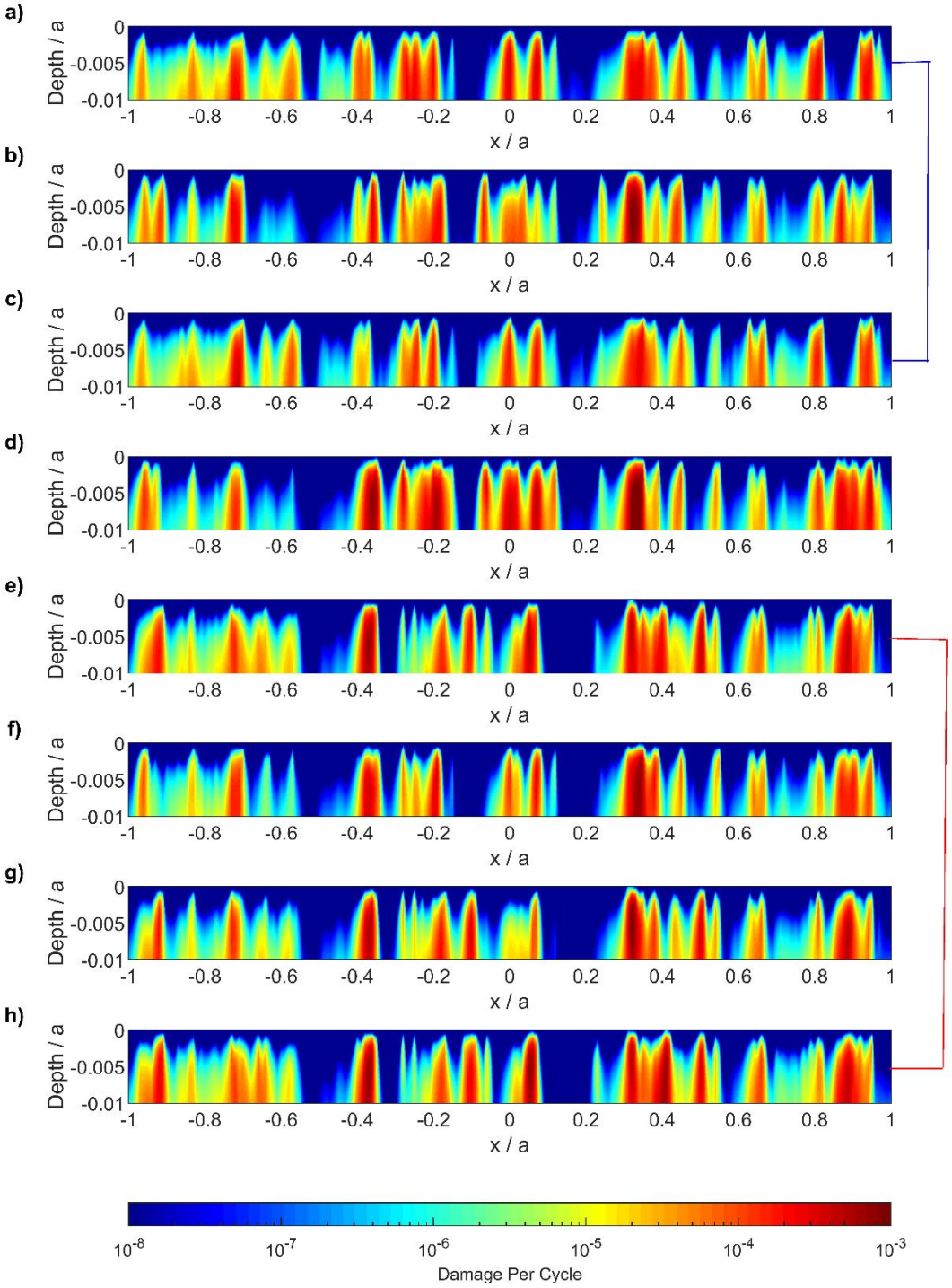

Figure 6.4.3 Contours for damage sustained during a single pass through the contact for each profile of the Test 4 slow surface in the profile updating simulation. Profiles updated at (in equivalent FD cycles) a) start of test (run-in profile), b)2x10^4, c)5x10^4, d)1x10^5, e)2x10^5, f)4x10^5, g) 1x10^6, h) 2x10^6.

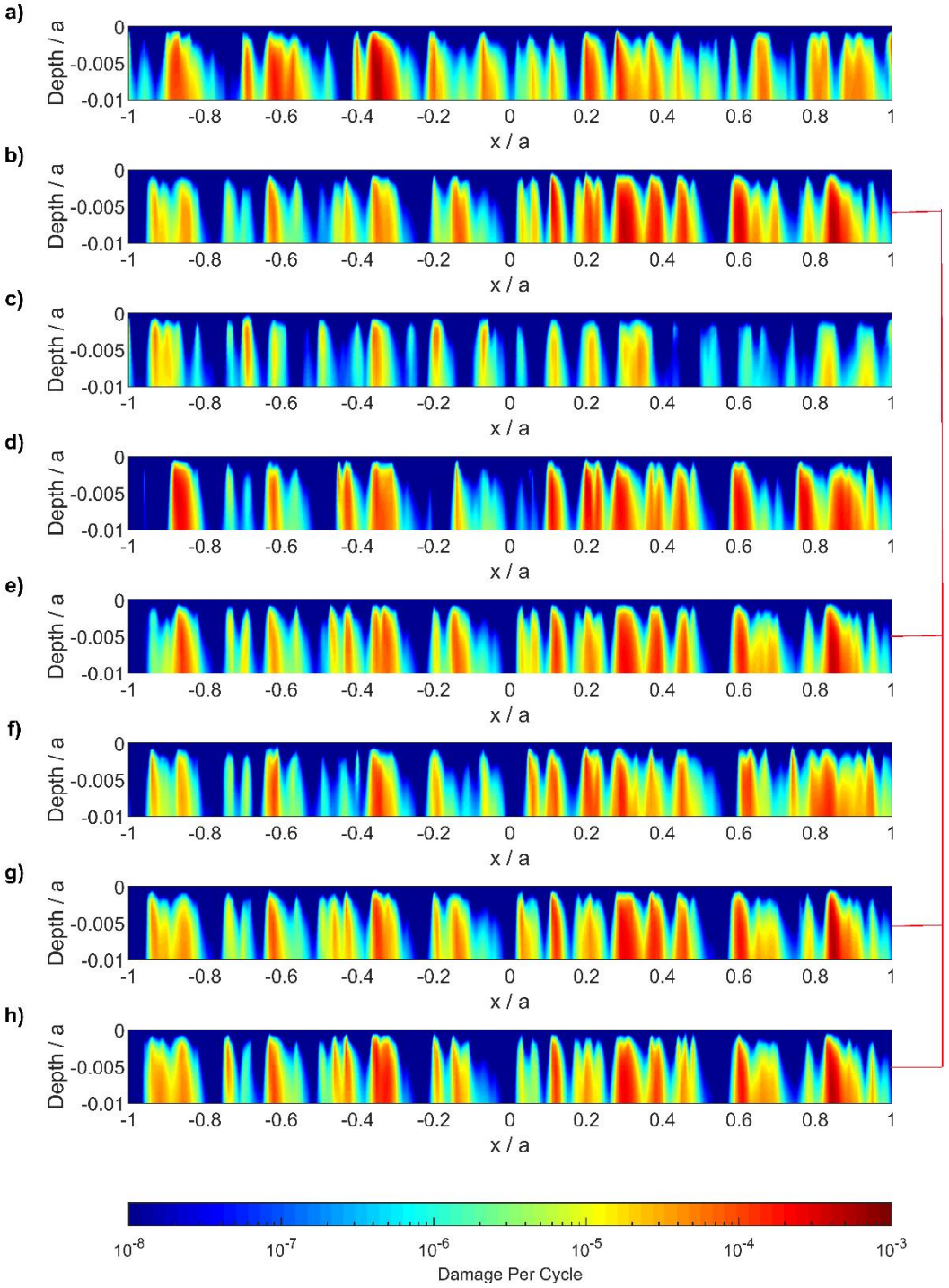

Figure 6.4.4 Contours for damage sustained during a single pass through the contact for each profile of the Test 2 fast surface in the profile updating simulation. Profiles updated at (in FD cycles) a) start of test (run-in profile), b)2x10^4, c)5x10^4, d)1x10^5, e)2x10^5, f)4x10^5, g) 1x10^6, h) 2x10^6.

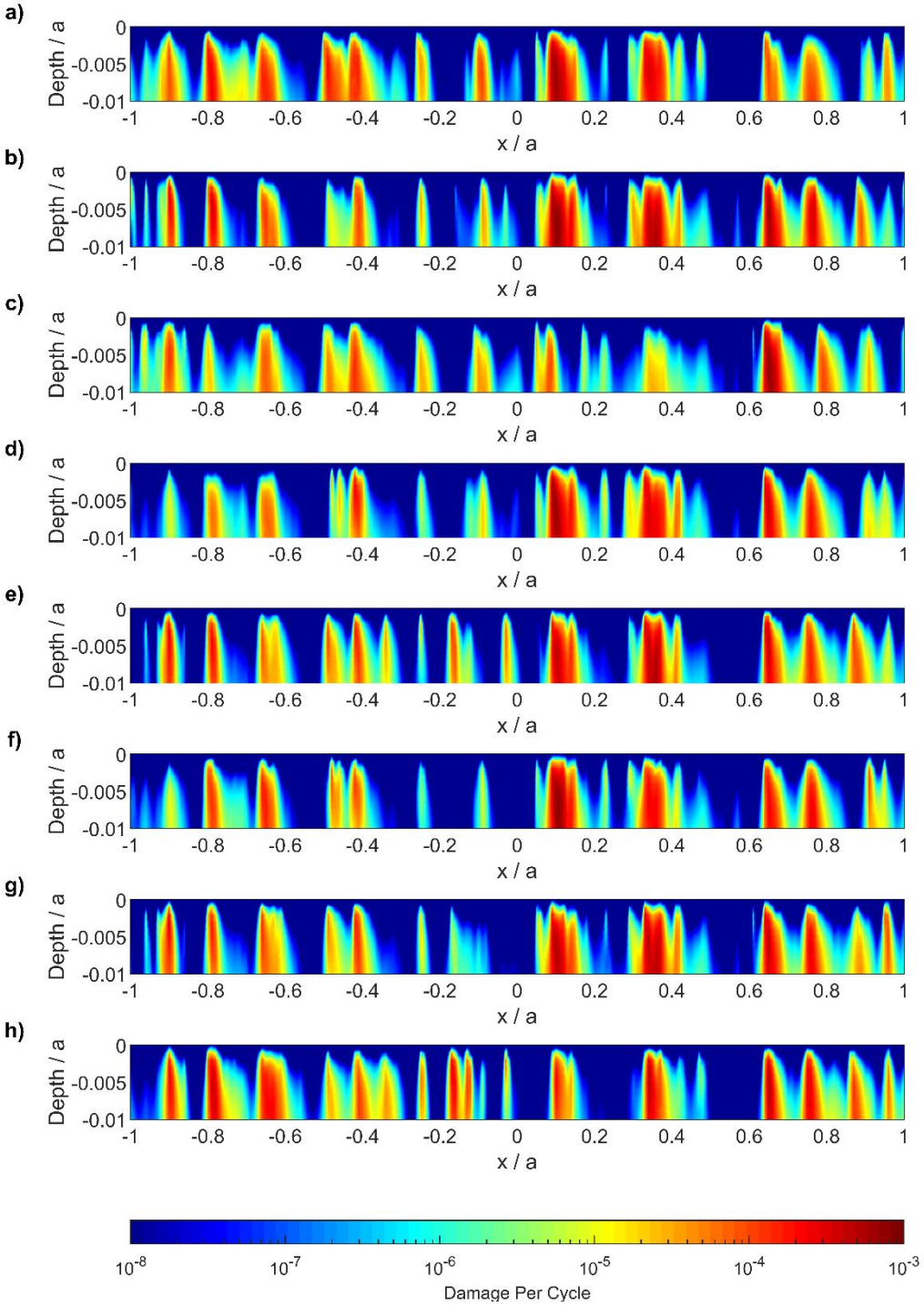

Figure 6.4.5 Contours for damage sustained during a single pass through the contact for each profile of the Test 8 fast surface in the profile updating simulation. Profiles updated at (in FD cycles) a) start of test (run-in profile), b)2x10^4, c)5x10^4, d)1x10^5, e)2x10^5, f)4x10^5, g) 1x10^6, h) 2x10^6.

It is unsurprising that those simulations which gave similar predictions between the run-in profile only and updating profile approaches showed largely similar patterns of damage concentrations as the profiles were updated. Simulations which either showed more or less appropriate predicted curves shared the common property of aggressive damage concentrations changing and often reappearing through time.

The aim of performing profile updating simulations was of course to capture the redistribution of load and resulting changes in stress as the surface changed. The profiles used in these updates however were subject to the relocation error limitations discussed at length in Section 3.1.8. As a consequence, the measured profiles did not pass through exactly the same region of surface at each measuring stage, and traversed different micropits and wear locations, resulting in differing distributions of load. By increasing the number of configurations of asperities bearing load through the simulation, the opportunity for different locations to fatigue is increased. For some locations only a few thousand or tens of thousands of cycles may be required for fatigue to occur.

In some instances, this led to a more representative appraisal of the fatigue - in other cases however, this led to over-prediction of fatigue. The issue is of course that the measuring error cannot be controlled or tailored by the experimenter and is an unreliable influence on the surface loading. To further build on this approach, it is recommended that future work aims to develop an approach to update profiles within the simulation based upon the calculated fatigue, beginning with run-in profiles and modifying their geometry directly. An approach such as this could maintain the benefits of accounting for the changing surface geometry, while avoiding the potential risks of profile relocation error.

6.5 Summary – Fatigue Simulations

The fatigue simulations performed here were able to yield very interesting results and shows the potential for several further avenues of exploration. The results of simulations with run-in profiles were found to show little resemblance to the experimental results as can be seen in Figure 6.5.1.

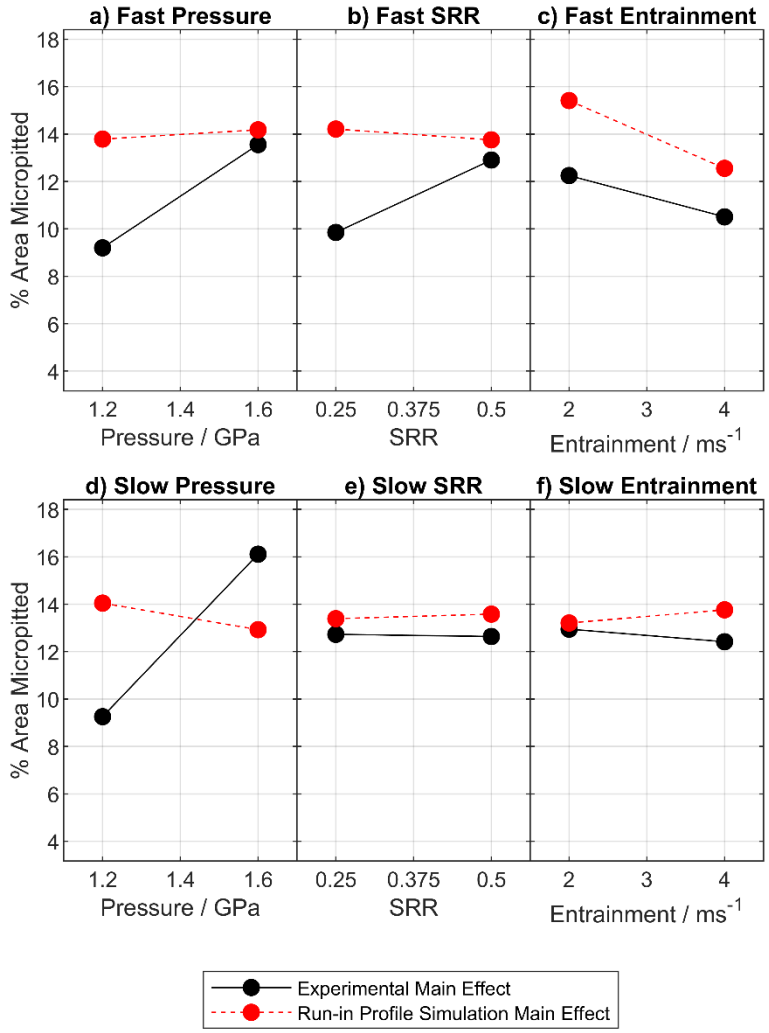

Figure 6.5.1 Effects on percentage pitted at end of test for the experimental results (black) compared to simulation with run-in profiles.

Closer inspection of the results revealed that using the same depth into the material for analysis of all tests may not be appropriate, and so an investigation was conducted into determining the required depth for analysis in different conditions.

This showed promise, but will require further experimental data and corresponding simulations to fully investigate.

Analysis of results when profiles were updated through the simulation showed that updating profiles can produce a better reflection of experimental results, however that updating using real in-test data can introduce measurement error. A possible improvement for future work would be to develop means of updating profiles within the simulation process.

7 Scanning Electron Microscopy of Disk Microstructure

7.1 Introduction

As was discussed in Section 1.4.2 microstructural changes in the near surface of the steel are fundamental to some proposed mechanisms for micropitting in gear contacts. Observations of microstructural changes are key to answering the question of whether the transformations observed in works such as Oila (2005) and L'hostis *et al.* (2017) act as a cause of micropitting or arise due to the conditions present at crack locations.

The unexpected micropitting behaviour observed in Test 1 (Section 5.2) provided an opportunity to compare the microstructure in regions of the same disks which exhibited very different micropitting behaviour. It was hoped that comparisons of the microstructural changes and crack formations in these different areas of the surface could help to grow understanding the process of micropitting.

7.2 Preparation of Samples

Two 10 mm wide sections as shown in Figure 7.2.1 were cut from each disk. One section from each disk was then cut again through the contact centreline B-B, while

the other was cut through the centre of the micropitted region at C-C, approximately 1.5 mm from the centreline.

All cuts were made using Wire Electrical Discharge Machining (Wire-EDM), which is readily available at Cardiff. Investigations undertaken previously by Griffiths (2018) found that Wire-EDM has minimal influence on the properties of gear steel (after polishing and sample preparation) and is comparable to water jet cutting. For each cut the machine operator was instructed to minimise temperature exposure as much as possible.

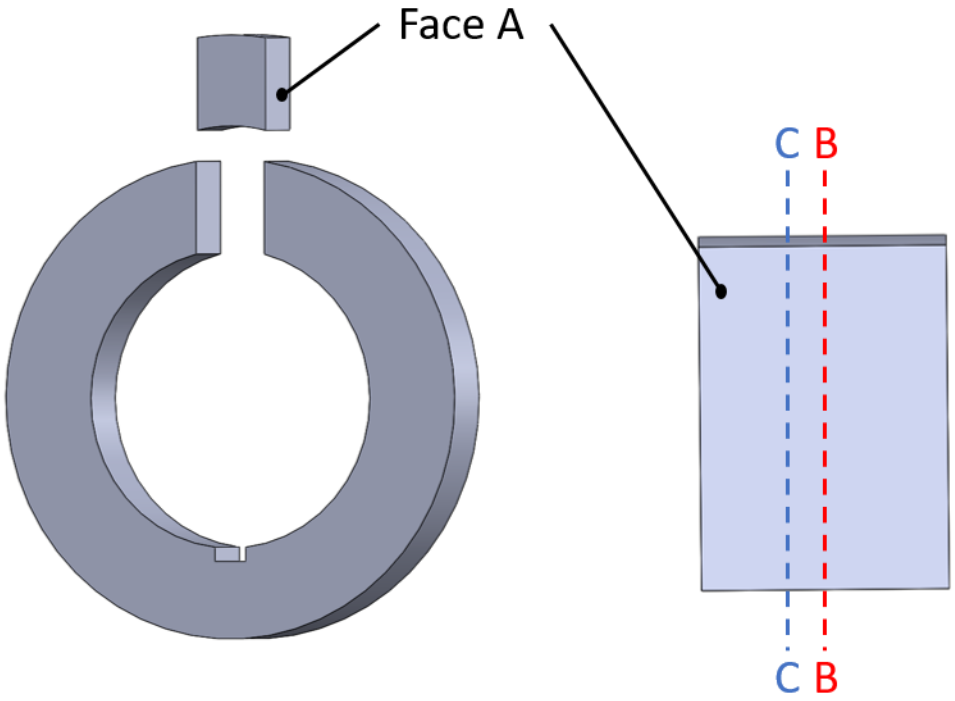

Figure 7.2.1 The process of sectioning the disk to allow inspection of the subsurface at a given axial location.

Each sample was then encased in epoxy resin with a conductive filler, the face of interest facing outward. This face was then ground and polished using progressively finer polishing plates on a Struers Knuth-Rotor-3 polishing machine. The final stage used a polishing cloth (on the same polishing machine) with a solution containing

0.05 μm alumina abrasive particles to leave a scratch-free finish under optical microscope inspection.

Each polished surface was then etched using a 2% nital solution applied to the surface using a cotton wool pad. When the sample began to lose its mirror-like appearance, the etchant was washed off using distilled water.

7.3 Steel microstructure and transformations

The case hardened EN36 steel used in these tests has a case microstructure comprised of plate martensite, retained austenite, carbides, and non-metallic inclusions (Oila 2003). Under etching with 2% nital the martensite is attacked more aggressively than the retained austenite, leaving the austenite with the appearance of islands amidst darker martensite plates. The carbides resemble small spheroids dotted through the surface irregularly.

It is well understood that the retained austenite in this microstructure is unstable and given sufficient energy will transform to martensite. Furthermore, the energy required to induce this transformation is reduced when the material is subject to shear stresses - which are significant in the near surface of a gear contact. This transformation is discussed in great detail by Morris *et al*. (2018) who created a model to predict the decomposition of retained austenite in rolling contact fatigue.

As was discussed in Section 1.4.2 the formation of a Dark Etching Region (DER) in the region of maximum shear stress is a much more well-known phenomenon in bearings, but has been reported in the near surface of gears, both in isolated semi-circular regions and continuous bands (Oila *et al*. 2005). The dark etching region is named as such because after etching the microstructure in this region appears dark when viewed with an optical microscope. The DER arises from the transformation of martensite to ferrite, therefore containing a microstructure of ferrite and finely

dispersed residual martensite. As found by Swahn *et al*. (1976), areas containing no residual martensite become light etching. Some retained austenite may remain within the dark etching region as it develops, but as the transformation of martensite to ferrite continues the energy required for the decomposition of the residual austenite decreases. As a result, the DER may progress to contain no retained austenite (Morris *et al*. 2018).

In bearings a further microstructural change has been observed within the DER after large numbers of cycles – the appearance of White Etching Bands (WEBs). These bands occur first at 30 and later 80 degrees to the surface and are composed of ferrite, bordered (in the case of the 30-degree bands) by carbide particles. While these are regularly observed phenomena in bearings, they are rarely observed in gears.

The final microstructural change commonly observed is the Plastic Deformation Region (PDR). These regions are comprised of very fine ferrite grains with distributed carbon content. Typically, these features are observed alongside surface cracks, often between the crack and the surface.

7.4 Observations from Test 1 Analysis

7.4.1 Non-micropitted sections

As would be expected, far fewer cracks were seen in the centreline regions when compared to the heavily micropitted regions.

Only one crack was observed in the central regions, growing into the slow surface at the typical 30° angle seen in surface fatigue. This is shown in Figure 7.4.1. Notable in this figure is the refined microstructure that can be seen both above and immediately below the crack. This is unusual as cracks are usually seen at the boundary of the two microstructures, either propagating due to the stress

concentration at the boundary or acting as the cause of the refined microstructure between the crack and the surface. In all instances of angled surface cracks, including those in the heavily micropitted area, cracks were seen to grow against the direction of tractional force on the disk surface. This is in agreement with the conventional understanding of crack growth.

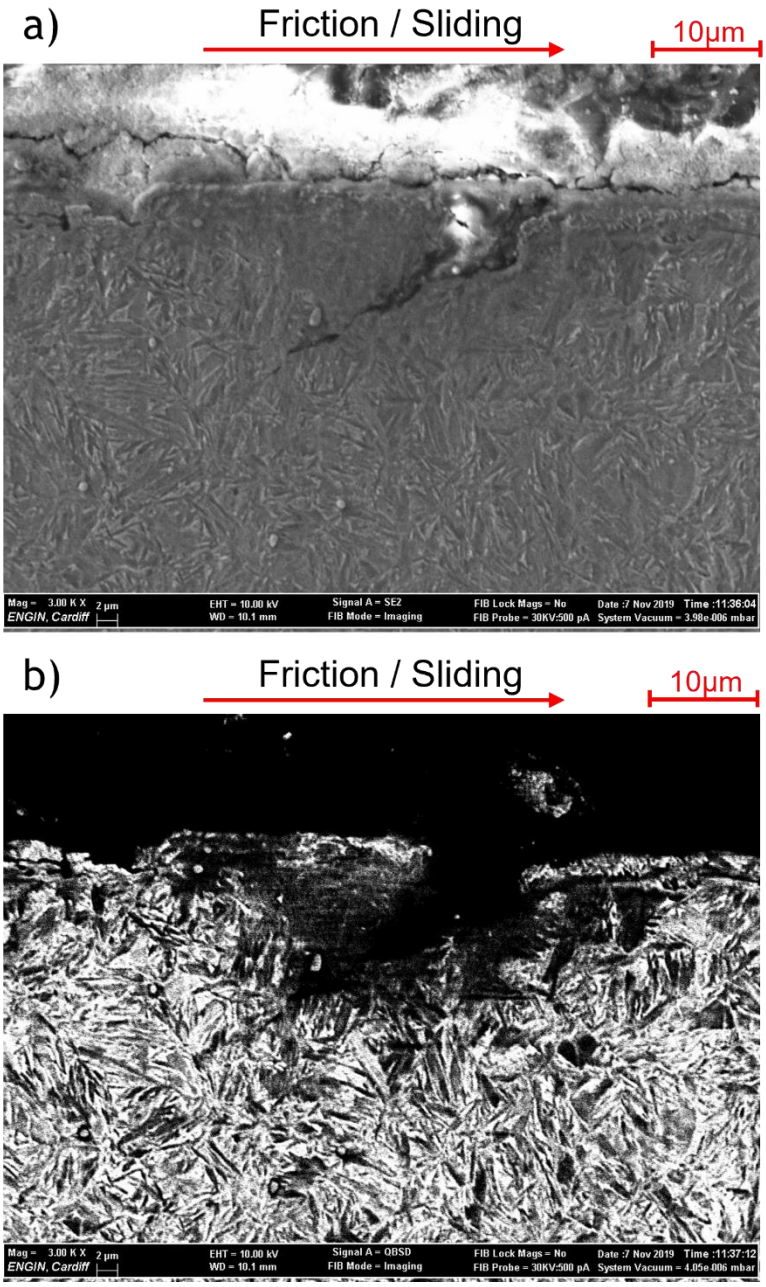

Figure 7.4.1 a) SEM image of a surface-initiated crack b) back-scattered electron image of the same.

The most frequently observed features in the centreline region were flattened, table-like features as can be seen in Figure 7.4.2. Cracks could grow from either side of these features, or in many cases from both sides simultaneously. This lack of consistency in the crack growth direction can be taken as an indication that the fluid entrapment mechanisms widely proposed for micropit crack growth do not apply in this case, as fluid entrapment is highly influenced by direction. The growth of the cracks parallel to the surface as opposed to a 30° to 35° angle also discounts this mechanism. Instead, the sharp-edged shoulders that can be seen on the features would certainly lead to high stress concentrations, which are the most probable cause for the initiation and growth of the observed cracks.

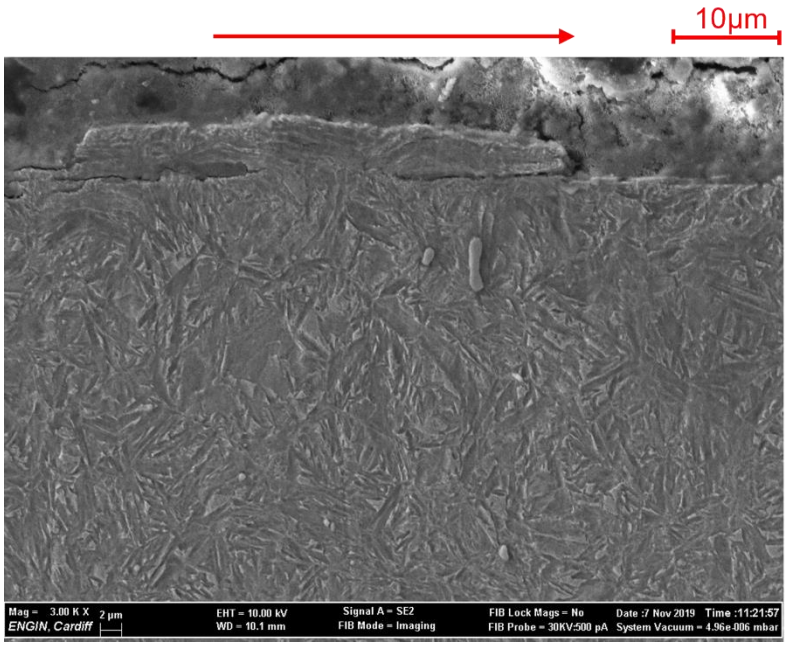

Figure 7.4.2 Flattened, table-like surface feature from the centreline of the slow surface. Cracks can be seen growing from both sides in parallel to the surface, as was seen in all instances of these features.

The origin of these features is also of interest, as their sharp shoulders and flattened tops are not characteristic of features resulting from the surface grinding process. As discussed extensively in Section 4.2 the asperity features in the centreline

regions of this test were very aggressively flattened. It was proposed that this was the result of wear as opposed to plastic deformation, and this analysis provides further support for that hypothesis.

Transformed microstructure was seen in the near surface of both the fast and slow centreline sections, either as discrete semi-circular regions or long subsurface bands. The depth varied from a few microns to tens of microns with more complete transformation nearer the surface. An example can be seen in Figure 7.4.3, the semi-circular region on the left clearly beneath an asperity peak.

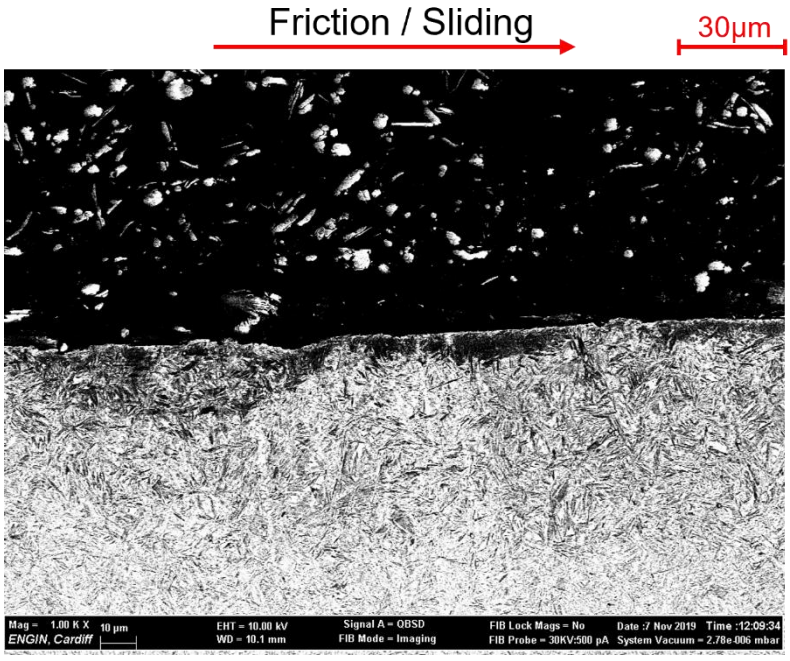

Figure 7.4.3 Back-scattered electron image showing regions of transformed microstructure in the near surface of the slow disk centreline.

The formation of these areas of transformed material closely matches the descriptions of the DER as observed in gear contacts by Oila (2003). The metallic structure in the DER appears to have a significantly reduced proportion of austenite but continues to contain martensite. Previous works have shown the remainder to be a ferritic phase arising from decayed martensite and containing excess carbon

unable to dissolve in the ferrite phase (Swahn *et al*. 1976). No white etching bands were observed.

More aggressively changed regions of microstructure were seen on the fast disk. These bore a strong resemblance to the PDRs previously seen by Oila *et al*. (2005). Figure 7.4.4 shows back-scattered electron images in which the different microstructural regions are clearly contrasted. In both images the plastic deformation region contains a much finer microstructure than the surrounding material, and the lack of distinctive needle shaped grains indicates that the structure in this region is no longer martensitic. Notably, no cracks were observed between these regions and their neighbouring microstructures.

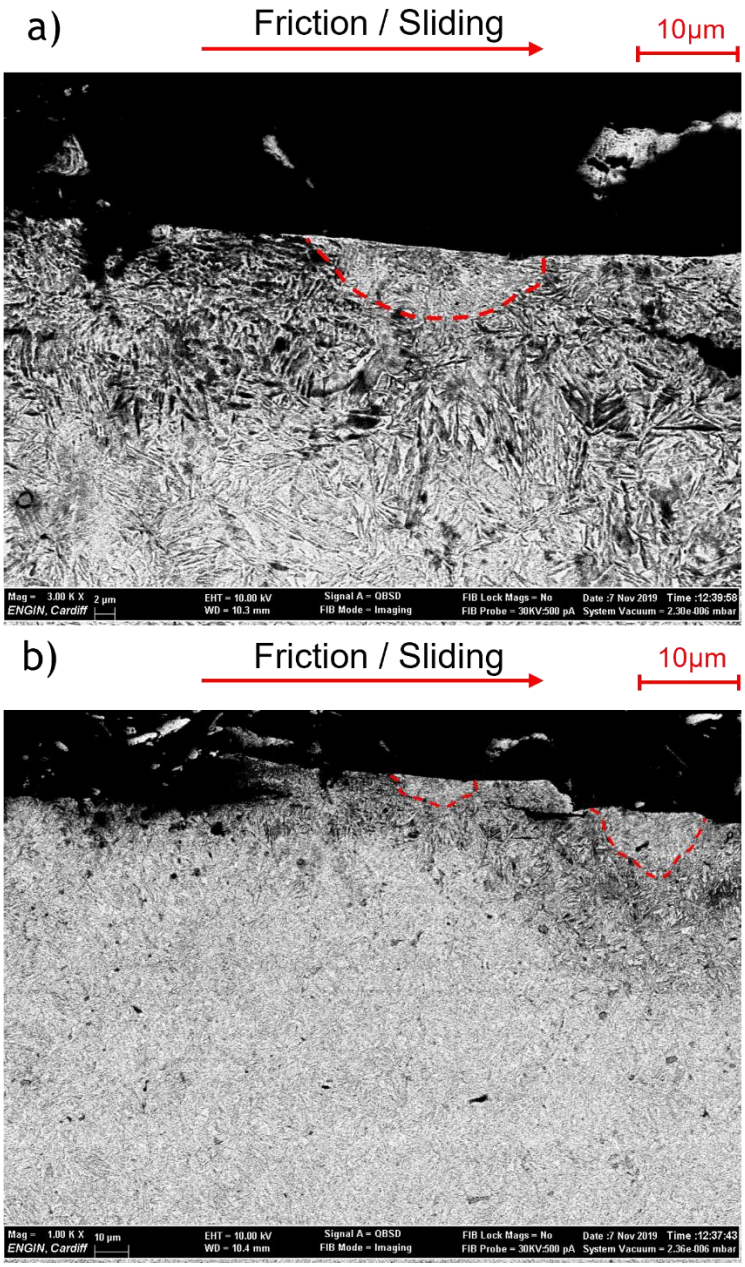

Figure 7.4.4 Two PDRs seen in the fast disk centreline region. In both the PDR is located within a larger area of transformed microstructure, but in b) one PDR is located within a 'tabletop' feature.

7.4.2 Heavily micropitted sections

DERs could be seen on both surfaces, but far more extensively in the fast disk section. In the back-scattered electron images in Figure 7.4.5, these predominantly

appeared as long bands of transformed material extending up to 70 μm beneath the surface.

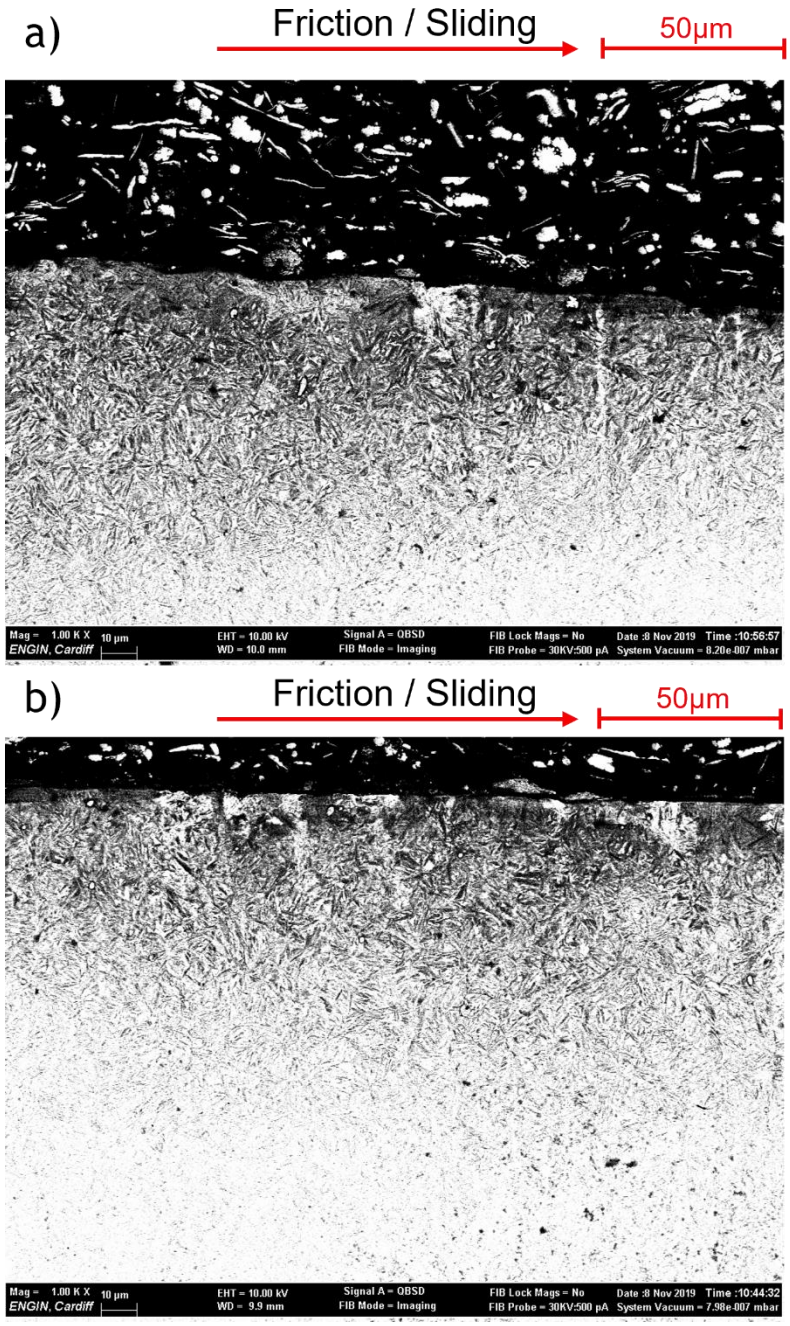

Figure 7.4.5 DERs beneath in the fast disk surface in the pitted region.

Some of these regions the near surface contained extensive networks of subsurface cracks, such as in Figure 7.4.6. This was an exclusive feature of the fast surface seen at approximately six locations on the fast surface, but none on the slow surface

(although the small sample size must be kept in mind). The cracks at this location were at their largest and most concentrated in the near surface area on the right-hand side of the image and occurred throughout the region indicated by the red lines. Considering the back-scattered electron image b) these cracks occurred only within regions where the microstructure was most completely transformed.

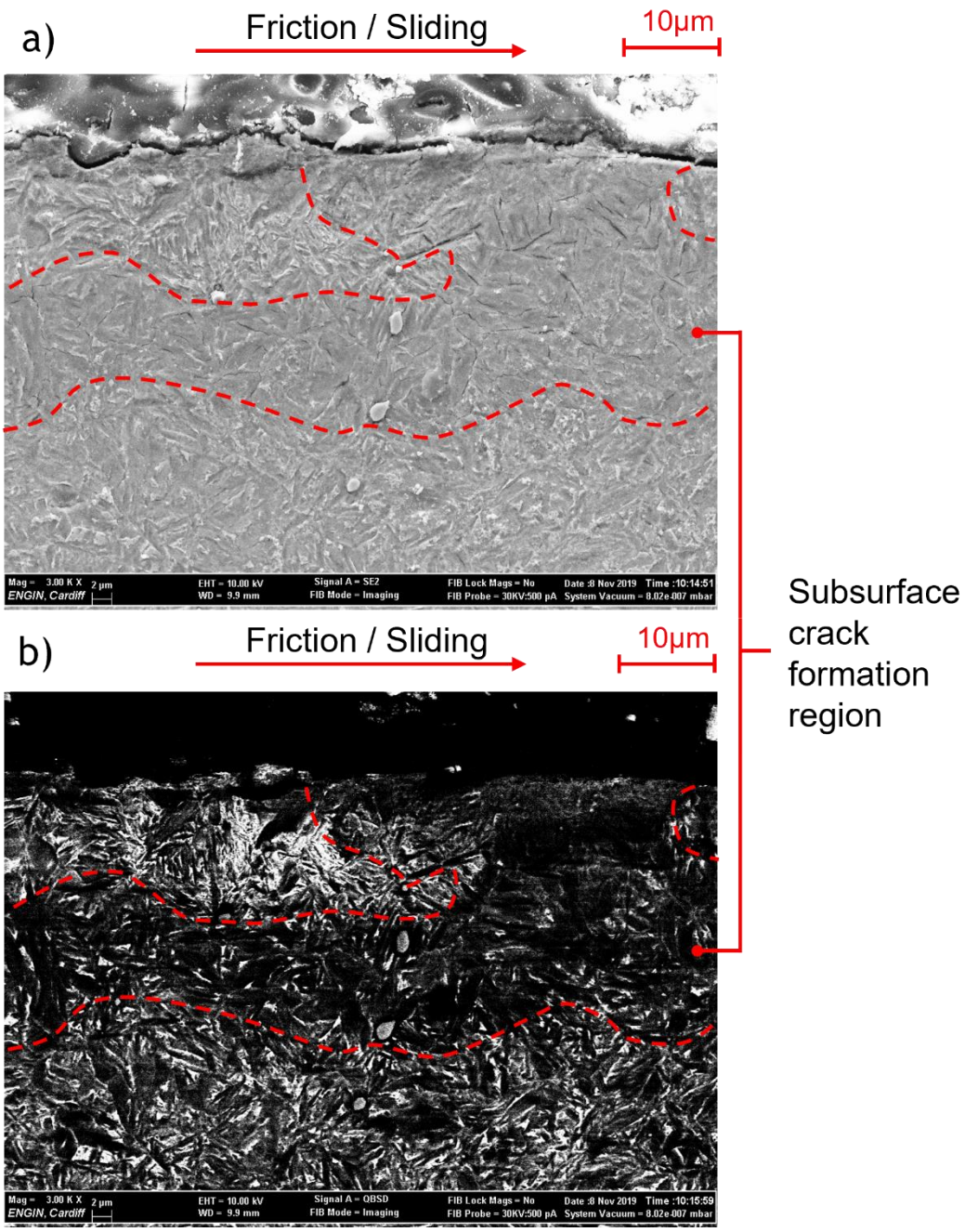

Figure 7.4.6 a) SEM and b) electron back-scatter image of fast surface microstructure containing a network of subsurface cracks. Dotted red lines illustrate the region in which subsurface cracks were seen.

It is possible that the subsurface cracks seen in these areas of the fast disk microstructure may have a role in the removal of material from the surface. Figure 7.4.7 shows an area with a network of subsurface cracks and a plastically deformed

roughness feature protruding from the surface. As is particularly clear in the close-up image b), some of these subsurface cracks formed along the boundary between the PDR resulting from the roughness feature and the surrounding material. Only a small amount of further growth from these cracks would be required to remove this roughness feature from the disk surface.

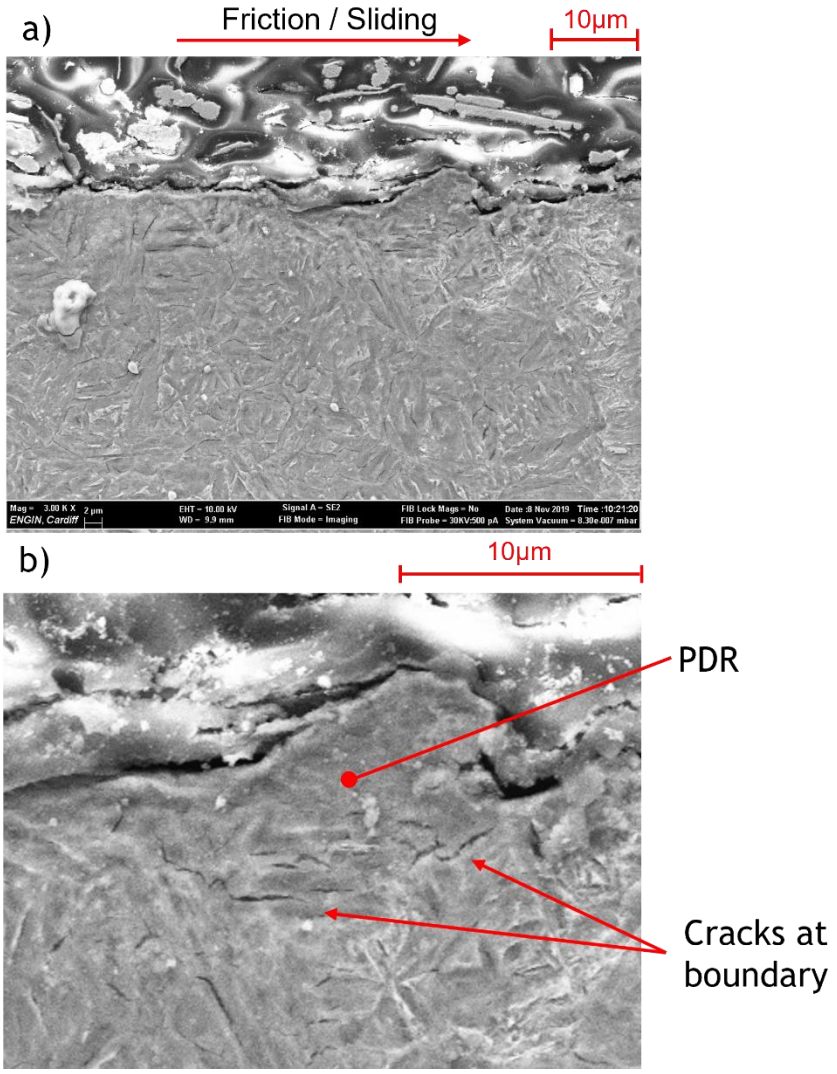

Figure 7.4.7 Microstructural cracks at PDR boundary.

The angled surface cracks growing in the opposite direction to traction which are characteristic of micropitting fatigue were seen in the micropitted area of both surfaces, although much more frequently on the fast surface. In all instances the

material between the crack and the surface showed the refined microstructure typical of extensive plastic deformation. Figure 7.4.8 shows examples of this taken from the slow surface. In Figure 7.4.8b it appears that the cracks are progressing around the boundary of a larger PDR.

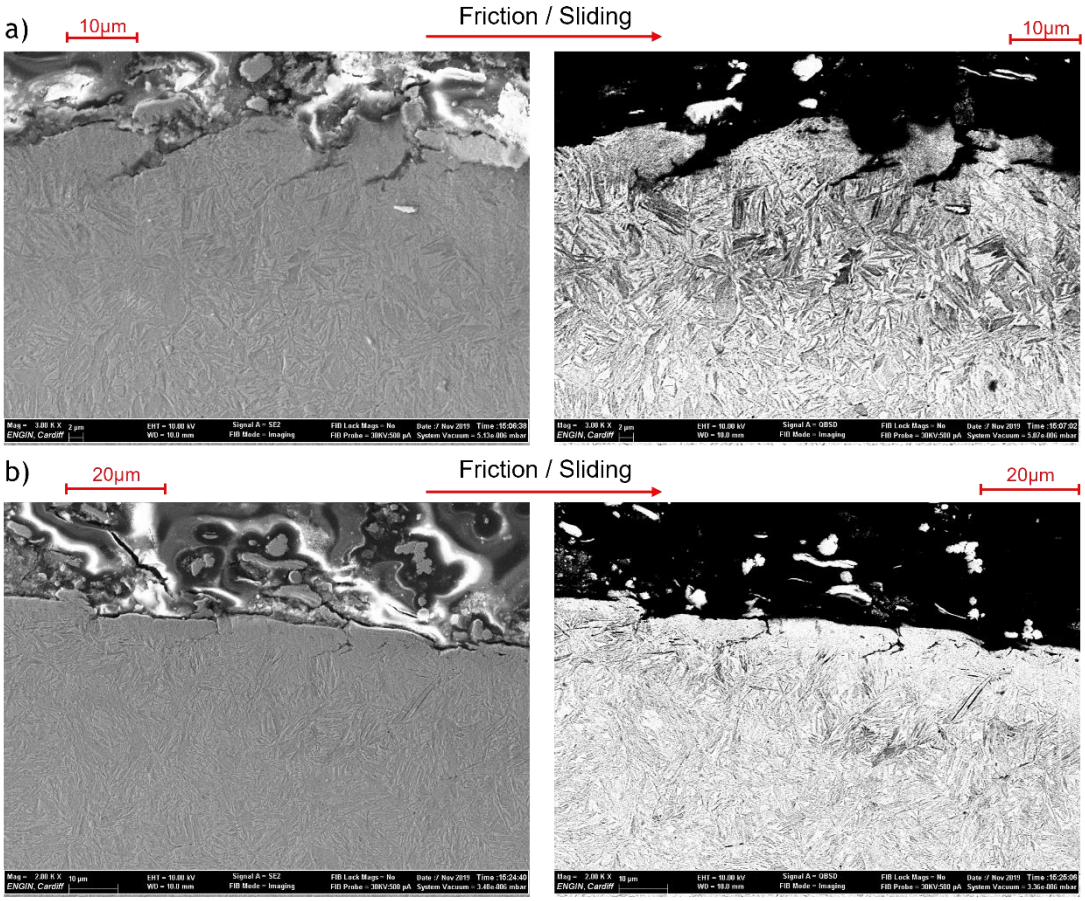

Figure 7.4.8 Secondary electron (left) and corresponding back-scattered electron images (right) showing surface cracks in the slow surface with PDRs between the cracks and surface.

7.5 Discussion and Summary

The inspection of the Test 1 disk sections using SEM was able to show interesting microstructural features induced through the running process. The central regions, which were subjected to wear processes, exhibited very few of the 30° - 45° surface

cracks typical of micropitting. This is unsurprising as the levels of micropitting in these regions were extremely low.

Clear signs of wear were seen in frequent tabletop features, indicative of aggressive abrasive wear or 'smearing' of asperity material across a wider area. These features were accompanied by cracks growing from both sides, parallel to the surface.

Microstructural transformations were seen in both the central regions and heavily micropitted edge regions. Large areas of microstructure within tens of microns of the surface showed apparent reductions in austenite content, and in more severe cases the apparent removal of needle-like martensite grains. This is indicative of DERs, formed by the transformation of austenite to martensite, and martensite to ferrite. These areas of microstructure appeared both in localised semi-elliptical regions as well as long bands. Solely within the fast surface heavily micropitted regions, more complete transformation of the microstructure in DERs was accompanied by the formation of subsurface cracks, possibly at former grain boundary locations.

Plastic deformation regions (areas where extreme stresses induce a highly refined microstructure at the surface) were also seen in both regions. In the centreline, these regions were seen repeatedly without cracks associated with them.

In the heavily micropitted regions PDRs were typically seen between the crack and the free surface. As such this work largely supports the findings of Oila *et al*. (2005) that micropitting cracks are typically located at the boundaries of PDRs. It is necessary to note however, that while all observed surface cracks did have associated PDRs, it does not necessarily follow that cracks are initiated at the boundaries of PDRs. This may be the case in some instances, however in others it is possible that stress concentrations around the crack produce the PDR. It is of

interest that the depths of plastic deformation regions correspond to the depths commonly observed for micropits, up to a maximum of around 10 μm, however it cannot yet be confirmed whether this is a determining factor in the depth of micropits.

8 Discussion and Conclusions

In this final chapter the findings of the project as a whole are discussed, the novel contributions made in this work highlighted, and final conclusions summarised. The work then concludes with recommendations for future work.

8.1 Discussion

8.1.1 Differences Between Fast and Slow Surface Effects

Both the running-in and micropitting portions of the experimental work showed significant differences between the behaviours of the fast and slow surfaces. Specifically, minimal influence of SRR on the slow surface during running-in, and minimal influence of both SRR and entrainment on the slow surface during micropitting. The nature of these differences was discussed at length in each of the corresponding chapters, however the question of how these differences arise remains.

While many works have investigated micropitting behaviour using twin-disk and three-roller type tests, few of these works specify whether the surfaces they have analysed are the faster or slower of the surfaces. Whilst both have been investigated here, there is a necessity to pick a surface on which to base one's measuring intervals, or else double the time required for an already lengthy test by pausing for separate fast and slow surface measurements. As such all measuring points in this work were chosen based on fast disk revolutions.

This does of course mean that slow disks at a lower SRR undergo more revolutions under less severe conditions and those at a higher SRR undergo fewer revolutions while subjected to more harsh conditions. This almost certainly has some amount of influence on the result, but was accepted as a necessary evil in the experimental design. Attention should however be drawn to the fact that the effect of SRR for most parameters on the slow surface for both running-in (which is indisputably completed and stabilised in far fewer than the 6000

fast disk revolutions allowed to it) and micropitting was essentially zero - i.e. the effects of load cycles or contact severity for the SRR intervals would have had to exactly cancel out. This is made even less likely when it is recalled that, for many of the variables examined, the centrepoint test result indicated a linear effect. Keeping this in mind, it is sensible to search for other explanations for this difference.

Considering the results chronologically, running-in will be discussed first. A lack of strong slow-surface SRR effects was observed for all but one of the parameters investigated during running-in, the sole exception being the radius of curvature of asperities for which a radius-increasing effect was seen for both surfaces. This indicates that any differences in action on each surface is regardless of whether asperities are outliers in height or more representative in size.

As the SRR was increased, asperities on both surfaces experienced a higher number of asperity contacts per cycle. This increase was greater for the slow surface on a per-cycle basis, however Equation 8.1-1 shows that the number of asperity contacts *n* for a single slow or fast surface asperity during a test is the same unless there is a difference in the mean distance between asperity peaks *Rsm* (*u* is disk velocity, and *a* is the Hertzian half-dimension in the entrainment direction). The range of *Rsm* across all disks was 6.4 μm with a mean of 341 μm, hence the number of direct asperity loading cycles was of the same order on each disk for all tests. Therefore, difference in direct asperity contact cycles cannot account for the low influence of SRR on the slow surface. Additionally, we know that for every instance of asperity contact the load and duration must be equal upon each surface.

$$n_f = \frac{2a\left(1-\frac{u_s}{u_f}\right)}{Rsm_s} \times FDCycles; \qquad n_s = \frac{2a\left(\frac{u_f}{u_s}-1\right)}{Rsm_f} \times FDCycles \times \left(\frac{u_s}{u_f}\right) \qquad \text{Equation 8.1-1}$$

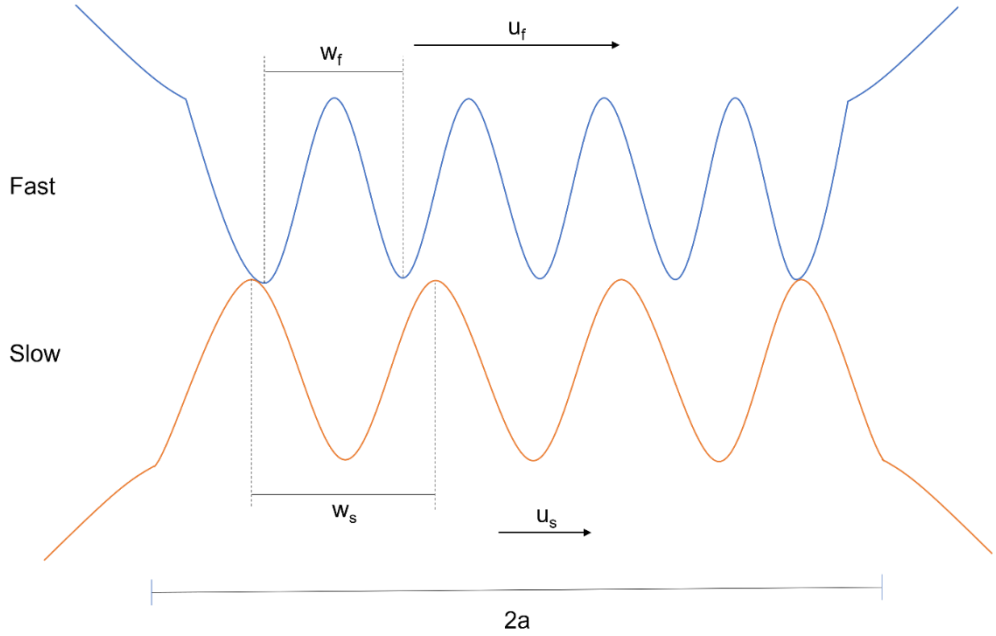

Figure 8.1.1 Illustration of distance between asperity peaks (difference in w between surfaces exaggerated)

For completeness, it is worthwhile noting that while the relationship between surface speeds and disk cycles in the twin-disk rig automatically maintains an equal asperity loading experience for both surfaces (assuming the Rsm is equal for both), this is not the case in gears. Sliding is greatest between gear teeth when the tip and root areas of a tooth pair are in contact. The tooth making contact in its dedendum (root) area has the lower tangential velocity of the pair. Asperities in the root of both surfaces therefore experience the greatest number of direct contacts for each tooth per tooth meshing cycle. The relative number of tooth meshing cycles experienced by each of the two gears is given by the gear ratio. The pinion gear will have the greatest number of tooth meshing cycles and the pinion root area will therefore accumulate the greatest number of direct contacts. This explains why the pinion root is the most susceptible to micropitting.

It is known that the heat generated in EHL contacts is not equally shared between the two surfaces, but instead a greater proportion is given to the faster moving surface as a function of the sliding velocity (Clarke *et al*. 2006). It is highly unlikely however, that differences in

temperature at the conditions tested here could produce sufficient difference in material properties to account for the behaviour observed. It is worth noting that the highest temperatures in tests did reach levels at which some extreme pressure / anti-wear additives can begin to become unstable (around 120°C and above (Frene et al. 1990)) and therefore might become less effective. Alternatively, some additives such as ZDDP form more effectively on the surface at 100°C and above, and hence more effective anti-wear properties might be in effect for tests which exhibited a greater temperature rise. These effects would however only cause difference in results between tests, as opposed to differently influencing disks within the same test.

The cause of differences in effects for each surface during running-in is therefore currently unknown and requires further examination.

Regarding differences between surfaces during the micropitting phase of the test, one possibility suggested in the micropitting results chapter was that micropitting differences may result from differing crack propagation mechanisms on each surface. The analysis of Test 1 surface sections using SEM confirmed that the crack growth direction on both surfaces was against the direction of traction on the surface. This does support the possibility that crack pressurisation and fluid entrapment mechanisms may be present on the slow surface but not on the fast, as fluid would be forced out of fast surface cracks as the material enters the contact as illustrated in Figure 8.1.2.

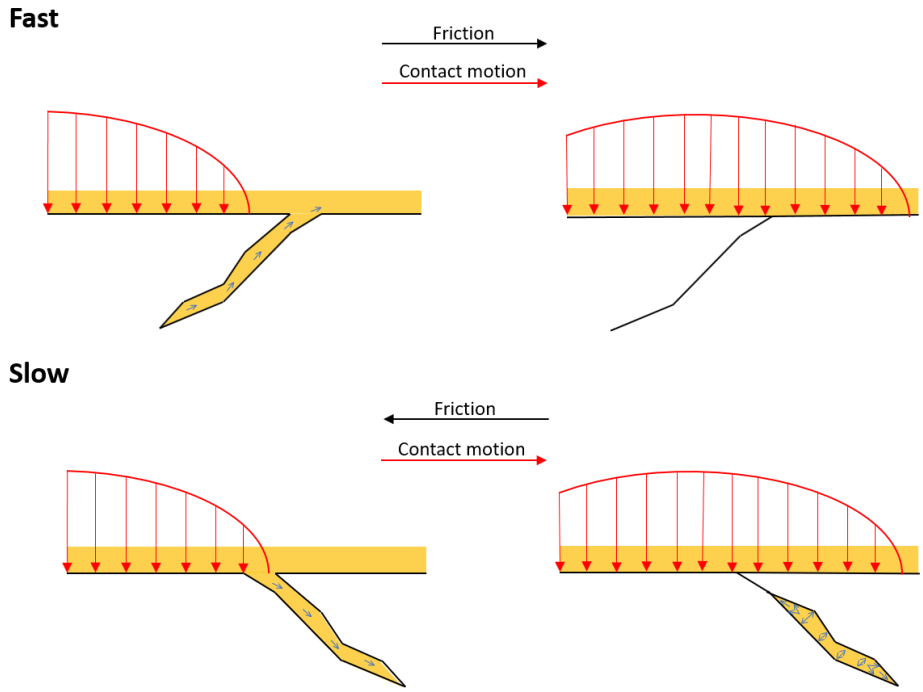

Figure 8.1.2 By crack pressurisation and hydraulic entrapment theory the approaching contact forces the fluid out of the crack on the fast surface. On the slow surface the fluid is first forced into the crack before the mouth closes and the trapped fluid is pressurised.

The fact that differences in the influence of SRR can also be seen during running-in, which occurs before any locations have reached a crack propagation stage, does suggest that this may not be exclusively due to differences in hydraulic action on cracks. Another observation made during SEM inspection of the heavily micropitted regions of Test 1 was that some regions of transformed microstructure on the fast surface developed subsurface microstructural cracks which were not observed for the slow disk (see Figure 7.4.6). Some of these were observed forming at boundaries of deformed asperities and are a plausible mechanism for micropitting on the fast surface. Being present in the areas of most aggressively transformed microstructure, it is likely that these cracks arose as a consequence of plastic deformation and stress cycling, which is in keeping with running-in differences. The limited sample size should be kept in mind however, and while six instances were observed for the fast disk with none observed for the slow disk, a more comprehensive study with a larger sample size is required to conclusively confirm this behaviour.

Further contributing to the possible causes, the fatigue simulations performed in Chapter 6 were able to predict the observed micropitting behaviours provided an appropriate depth of analysis was selected. These fatigue simulations contain no consideration of cracks in the surface or microstructure and are based upon a prediction of stress cycles to failure. This may simply show that this method provides an appropriate approximation for prediction by adapting depth of analysis, but could also be interpreted to suggest that classical fatigue crack initiation and propagation is in action.

In summary, the causes of the differences in the reaction to entrainment and SRR behaviour during the experimental programme are not known, and can only be speculated at with the present information. With regards to micropitting, the cause of this behaviour is likely related either to the relative dominance of different mechanisms on each surface, or to the presence or absence of a single mechanism with a strong directional dependence. The cause of differences that emerged during running-in are yet more difficult to discern, and require further investigation.

8.1.2 Progress against Objectives

In Section 1.5 three primary objectives for this work were defined. The first and second of these objectives were to investigate the influence of operating conditions on early-stage micropitting and running-in respectively. These objectives were achieved through the application of a three-variable full-factorial experimental programme, and through the development of tools and methodologies to improve existing methods to do this.

The results of this work showed that the influences of Pressure, SRR and entrainment velocity on micropitting behaviour are complex, and replete with two-and three-factor interaction effects in addition to the influences of the individual factors. The individual results of these are covered in their respective chapters, and will be summarised in Section 8.2.1.

The third objective of this work was to compare the results of these experiments with computational simulations of fatigue. This was again a successfully completed objective, however it is more difficult to gauge the success of the implied objective of assessing whether the simulation method was able to accurately predict the results of early-stage micropitting fatigue tests. As the simulation method is used to output a number of results corresponding to different depths into the material, user decisions are required to interpret the data.

Qualitative inspection of the prediction curves showed that, in most cases, the shapes of the predicted curve for percentage of material failed closely matched that for the experimentally determined percentage of surface failed. In those cases for which this was not the case, updating the profiles during the analysis to reflect load redistribution between asperities was able to improve this.

Quantitatively, it was seen that simply picking an individual depth of analysis for each simulation output did not reflect the true test behaviour – however it was also seen that the most appropriate depth for analysis may be influenced by the contact conditions.

Models were constructed for the appropriate depth of analysis based on the change in Pressure, SRR and Entrainment, assuming linear effects. To fully investigate whether this model can be used to inform the analysis of simulations, this must be tested using further experimentation and simulations, and falls outside the scope of this work. Nonetheless this allows for the possibility that models may be constructed to convert the continuous output assessed at a number of depths to a single output at a calculated representative depth.

8.1.3 How Robust is This Work?

In any work it is vital to consider the robustness of the findings; in what ways they are subject to error, and in what ways they are improvements over previous works.

One clear limitation of the experimental work presented here is the lack of test repeats in the experimental programme. An ideal test plan would include repetitions of each test, which is of course not practical here, or would compromise with repeats of the centrepoint test to estimate the error or variability inherent within the running-in and micropitting experiments. This did not prove achievable within the timeframe allowed.

By taking 2d-profile measurements at multiple offset locations across the contact width, some variation in results due to error or measurement resolution was mitigated, however this did not apply to areal scans and other areas of this experimental programme.

Of note also is that the changes in features being measured were in a number of cases not much greater than the resolution of the measuring equipment (0.016μm). This was a limitation that had to be accepted to allow measurement in-situ on the rig, and particularly applies to the evaluation of running in - but also impacts the stationary profilometer used for areal scans. This necessitates an understanding that the effects in some instances in this work may be slightly smaller or larger than observed – for the smallest effects recorded this could result in them having negligible influence.

Practises such as Analysis of Variance (ANOVA), often applied to factorial experiments with larger sample sizes to evaluate the statistical significance of results versus error, could therefore not be applied in this case. Previous fractional factorial investigations of micropitting have also suffered from an inability to perform test repeats (Oila and Bull 2005; Li and Kahraman 2013), hence this is a common complication of extensive and time-consuming rolling contact fatigue experimental programmes.

Similarly, only one location was measured on each disk per test, which does allow for the possibility of variation in micropitting or running-in around the disk circumference to influence the final results. For running-in, it is less important that the measured location was a representation of the average disk section than that it was consistently relocated and

the change in roughness parameters at that location was accurately appraised. In terms of the surface prior to the initiation of micropitting, the two-dimensional profile relocation was sufficiently accurate to fulfil this purpose effectively.

In the case of the micropitting phase of the experiments, the use of only one measuring location was a necessity due to the limitations of the technology available. The areal profilometer scans obtained for surfaces required between sixteen and twenty-four hours per scan, and using only one position per disk the experimental programme required 162 scans to be completed. Adding to this the needs for post-processing and analysis, additional measuring locations would not have been feasible.

The likelihood of significant variation around the disk circumference is low however, as the full circumference of each disk was ground simultaneously in one process to impart a consistent surface finish around the whole disk. Application and removal of load at each stage was performed at random locations, and test conditions were of course applied universally across the disks. Visual inspection of each disk in all cases showed uniform appearance around the full disk circumference. The risk of non-representative measurement locations was also mitigated using comparatively large measurement areas compared to other works – in all cases areal scans covered an area of 6 mm x contact width.

Several significant improvements were made over previous works however. Firstly, the potential error in relocation of two-dimensional profiles was quantified, and it was established that this methodology was susceptible to significant over- or under-estimation of micropitting fatigue. The use of replica materials enabled surface scans of sizeable areas of the disk surface to be used throughout the test, and the full three-dimensional nature of micropitting on the surface to be captured.

The full utilisation of these areal scans was made possible by the development of a novel algorithm to detect micropits in ground surfaces. This development made significant

improvements in accuracy over approaches utilised by other researchers, such as manual classification (Li and Kahraman 2013), simple height thresholding (Roy *et al*. 2018; Vrcek *et al*. 2019), or combinations of thresholding and diameter criteria (Prajapati and Tiwari 2019). As such the correct shape of micropits was detected in full, other wear mechanisms and surface marks could be discounted, and large areas could be utilised without prohibitively time-consuming analysis.

Finally, previous works which used statistical Design of Experiment approaches to assess micropitting (Oila and Bull 2005; Li and Kahraman 2013) were limited to fractional factorial designs in which main factors were confounded/aliased with three-factor interactions, and two-factor interactions were confounded/aliased with four-factor interactions. This is an inherent limitation of this approach and was acceptable for their purposes of conducting an initial investigation of many variables. By employing a full factorial experimental design the current work was able to remove confounding entirely from the experimental structure, and has shown that the three-factor interactions with which main factors were confounded were in many cases non-trivial. This also provides a marked improvement in the robustness of the experimental findings in this work.

8.2 Novelty

This research work has made several novel contributions to the field, which are outlined here.

- A novel algorithm was devised to detect micropits in ground surfaces in a comparatively large area of surface. This offered several improvements over existing methods of micropit detection and allowed direct comparison between areal analysis of micropitting, and analysis using two-dimensional profiles.
- A full-factorial experimental programme was completed for running-in and micropitting in gear contacts at a range of pressure, SRR, and entrainment velocities

representative of those found in gear contacts. The full-factorial experiment had a higher resolution than previously performed fractional-factorial experiments into micropitting, and to the author's knowledge provides the first full-factorial analysis of change in surface characteristics of ground gear-type surfaces during running-in. For both running-in and micropitting, complex two- and three-factor interactions were observed, illustrating the importance of the approach taken in this work.

- Simulations were performed using real rough surface profiles, and comparisons were made between the experimental micropitting results and the Cardiff University fatigue simulation method, applying the Fatemi-Socie fatigue criterion at a range of contact conditions. This was a new analysis helping to validate and suggest areas for improvement of the Cardiff university model.
- SEM measurements were made to investigate the microstructural changes present beneath a surface that exhibited both heavy micropitting and micropit-preventing wear.
- A full-factorial experimental model was applied across two experimental investigations and a programme of simulations. A defined structure was devised to analyse data with a rigorous, methodical approach. This can serve as a model for similar investigations of multi-factor problems in future works.

8.2.1 Conclusions

The conclusions of this work are summarised below:

Running-in

- Pressure is a strong influence on all surface parameters analysed. In all instances pressure is seen to increase the magnitude of change in surface roughness parameters through the running-in period. Pressure is the strongest influence on slow surface running-in, and the influence of pressure is greater on the slow surface than on the fast.

- The influence of SRR through running-in differs on the fast and slow surfaces. SRR is a driving influence to increase change during running-in on the fast surface, with a similar magnitude to the influence of pressure for the range of variation adopted for the parameters. On the slow surface SRR exhibited minimal influence in almost all instances. For both surfaces SRR was the strongest influence on the radius of curvature of asperities.
- Increased entrainment velocity provides a protective effect through running-in and opposes modification of the surface (and of surface parameters) through the production of a thicker lubricant film.
- Two-factor effects are present for all parameters investigated. Pressure*Entrainment and SRR*Entrainment interactions increase the change observed when the component factors were both at high or low settings for all parameters other than radius of curvature. Pressure*SRR interaction effects vary across the parameters studied.
- Three-factor effects are present for all investigated parameters, although often markedly stronger on one surface than the other.

Micropitting

- Pressure is the strongest factor influencing the micropitted area, micropit depth, volume removed through micropitting, and rate of micropitting once fatigue has become established. For the slow surface it is also the strongest influence on the number of cycles to reach 3% micropitted. In all cases, pressure acts to increase micropitting on the surface. As such, pressure is a strong influence on the late stage micropitting, but a weaker influence during the initiation of micropitting for both surfaces.
- SRR is the strongest main factor influencing early stage micropitting for both surfaces, promoting micropitting behaviour. On the faster surface SRR remains a

strong influence on micropitting throughout operation. For the slower surface the effect of SRR decreases markedly after the micropitting initiation stage.

- Entrainment provides a moderate opposition to micropitting during the early micropitting initiation stages for both surfaces. On the fast surface, entrainment continues to provide a moderate opposition to the micropitted area, and a weak opposition to micropit depth and volume. For the slow surface the effect of entrainment is considerably weaker.
- Two-factor effects are present for all micropitting parameters.
    - Pressure*SRR interactions show a micropitting-reducing effect for both surfaces
    - Pressure*Entrainment interactions increase micropitting on both surfaces, but are considerably stronger on the slow surface.
    - SRR*Entrainment interactions typically increase micropitting on both surfaces
- Three-factor interactions are present on both surfaces. These oppose micropitting initially, but increase the late-stage micropitting rate and end of test micropitting, pit depth, and volume parameters.
- Microstructural change is present in the near-surface of micropitted test disks, in line with observations of dark etching regions. White etching bands were not observed. Areas of severe microstructural change on the fast surface were seen to contain microstructural cracking which may promote micropitting.
- Plastic deformation regions were observed both in isolation and at the boundaries of cracks.

Simulations

- A fatigue simulation using the Fatemi-Socie critical plane approach with real rough surface profiles can provide an estimation of micropitting growth across a range of contact conditions, provided an appropriate depth is selected for evaluation.

- Updating profiles as fatigue occurs can improve the fidelity of fatigue predictions through appropriate redistribution of load, however updating with real profiles can introduce experimental profile relocation errors to the simulation predictions.

8.3 Future Work

The work conducted here has raised several questions that could be addressed in future projects.

One such investigation would test the hypothesis that the appropriate depth of analysis for fatigue simulations is dependent on operating conditions. This would require an additional micropitting test such as those conducted in this work to be performed alongside a corresponding fatigue simulation. By applying the factorial model for equivalent depth devised here, the predicted required depth for analysis could be calculated and compared to the true in-test value.

The simulation work carried out by updating with profiles measured in-test illustrated the possibility of improved results from updating the load distribution, but also highlighted the limitations of using profiles subject to relocation error. Incorporating a process into the simulation to generate an updated profile from predicted failures has the potential to maintain the benefits of profile updating while removing the influence of measurement error. This would require a loop to be constructed where the EHL simulation is run, followed by the fatigue analysis, to a set number of cycles. A third process to modify the profiles from any predicted failures would then be required, before inputting the modified profiles back to the fatigue simulation. This profile modification stage would be an ideal application for machine learning, as there is ample data available to form a database showing the change in profile as asperities under a range of conditions undergo micropitting – and this approach may be simpler than attempting to predict mathematically.

Finally, the experimental results concerning the difference in SRR between the fast and slow surfaces were both unexpected and interesting. These would benefit from further experimentation. Within the factorial experiment there are four pairs of experiments in which the pressure and entrainment conditions remain the same, while the SRR changes. Selecting one or more of these pairs and adding additional SRR data points above, below, and between these settings of SRR would allow better understanding of how the SRR relationship on each disk changes the micropitting and running-in responses.

This list is by no means exhaustive and further opportunities to explore the experimental, computational, and metallurgical implications of this work are abundant.

9 References

Ahlroos, T. et al. 2009. Twin disc micropitting tests. *Tribology International* 42(10), pp. 1460–1466. doi: 10.1016/j.triboint.2009.05.023.

Alanou, M.P. 2005. *Study of Parameters Influencing Surface Distress of Gears*. Cardiff University.

AL-Mayali, M.F. et al. 2018. Experimental and Numerical Study of Micropitting Initiation in Real Rough Surfaces in a Micro-elastohydrodynamic Lubrication Regime. *Tribology Letters* 66(4). Available at: http://link.springer.com/10.1007/s11249-018-1110-2 [Accessed: 28 November 2018].

Ariura, Y.A. et al. 1983. An Investigation of Surface Failure of Surface Hardened Gears by Scanning Electron Microscopy Observations. *Wear* 87(1983), pp. 305–316.

Bannantine, J. and Socie, D. 1992. A Multiaxial Fatigue Life Estimation Technique. In: Mitchell, M. and Landgraf, R. eds. *Advances in Fatigue Lifetime Predictive Techniques*. 100 Barr Harbor Drive, PO Box C700, West Conshohocken, PA 19428-2959: ASTM International, pp. 249-249–27. Available at: http://www.astm.org/doiLink.cgi?STP24163S [Accessed: 29 June 2021].

Benjayati, C. et al. 2003. An Experimental study of micropitting using a new miniature test rig.pdf. In: *Transient Processes in Tribology*. Tribology Series, 43. Lyon, France: Elsevier

Bergseth, E. et al. 2012. Effect of Gear Surface and Lubricant Interaction on Mild Wear. *Tribology Letters* 48(2), pp. 183–200. doi: 10.1007/s11249-012-0004-y.

Bishop, I.F. and Snidle, R.W. 1984. An investigation of alternative methods of quantifying running-in of surfaces. Warrendale, PA: Society of Automotive Engineers

Blau, P.J. 2005. On the nature of running-in. *Tribology International* 38(11–12), pp. 1007–1012. doi: 10.1016/j.triboint.2005.07.020.

Bowden, F.P. and Tabor, D. 1939. The area of contact between stationary and between moving surfaces. *Proceedings of the Royal Society A* 169(938), pp. 391–413.

Bower, A.F. 1988. The Influence of Crack Face Friction and Trapped Fluid on Surface Initiated Rolling Contact Fatigue Cracks. *Journal of Tribology* 110(4), p. 704. doi: 10.1115/1.3261717.

Box, G.E.P. et al. 1978. *Statistics for Experimenters: An Introduction to Design, Data Analysis and Model Building*. Wiley.

Britton, R.D. et al. 2000. Effect of surface finish on gear tooth friction. *Journal of tribology* 122(1), pp. 354–360.

Brizmer, V. et al. 2013. Micropitting Performance of Oil Additives in Lubricated Rolling Contacts. *Tribology Transactions* 56(5), pp. 739–748. doi: 10.1080/10402004.2013.790097.

Brown, M.W. and Miller, K.J. 1973. A Theory for Fatigue Failure under Multiaxial Stress-Strain Conditions. 187(65/73), p. 27.

BSI 1996. Wrought Steels for Mechanical and Allied Engineering Purposes - Part 1: General inspection and testing procedures and specific requirements for carbon, carbon manganese, alloy and stainless steels. BS 970-1: 1996

Bush, J.J. et al. 1961. Microstructural and Residual Stress Changes in Hardened Steel Due to Rolling Contact. *Transactions of the ASM* 54, pp. 390–412.

Cabanettes, F. and Rosén, B.-G. 2014. Topography changes observation during running-in of rolling contacts. *Wear* 315(1–2), pp. 78–86. doi: 10.1016/j.wear.2014.04.009.

Cao, H. et al. 2019. Comparison of rolling contact fatigue life between elastohydrodynamic lubricated point contacts pre and post running-in treatment. *Tribology International* , p. 106089. doi: 10.1016/j.triboint.2019.106089.

Cen, H. et al. 2018. Effect of slide to roll ratio on the micropitting behaviour in rolling-sliding contacts lubricated with ZDDP-containing lubricants. *Tribology International* 122, pp. 210–217. doi: 10.1016/j.triboint.2018.02.038.

Chittenden, R.J. et al. 1985. A Theoretical Analysis of the Isothermal Elastohydrodynamic Lubrication of Concentrated Contacts. II. General Case, with Lubricant Entrainment along Either Principal Axis of the Hertzian Contact Ellipse or at Some Intermediate Angle. *Proceedings of the Royal Society A: Mathematical, Physical and Engineering Sciences* 397(1813), pp. 271–294. doi: 10.1098/rspa.1985.0015.

Clarke, A. et al. 2006. Heat Partition in Rolling/Sliding Elastohydrodynamic Contacts. *Journal of Tribology* 128(1), p. 67. doi: 10.1115/1.2125867.

Clarke, A. et al. 2016a. Running-in and micropitting behaviour of steel surfaces under mixed lubrication conditions. *Tribology International* 101, pp. 59–68. doi: 10.1016/j.triboint.2016.03.007.

Clarke, A. et al. 2016b. Understanding micropitting in gears. *Proceedings of the Institution of Mechanical Engineers, Part C: Journal of Mechanical Engineering Science* 230(7–8), pp. 1276–1289. doi: 10.1177/0954406215606934.

Conry, T.F. et al. 1987. A Reynolds-Eyring Equation for Elastohydrodynamic Lubrication in Line Contacts. *Transactions of the ASME* 109(October 1987), pp. 648–654.

Courtney-Pratt, J.S. and Tudor, G.K. 1946. An Analysis of the Lubrication between the Piston Rings and Cylinder Wall of a Running Engine. *Proceedings of the Institution of Mechanical Engineers* 155(1), pp. 293–299. doi: 10.1243/PIME_PROC_1946_155_048_02.

Crook, A.W. 1957. Simulated Gear-Tooth Contacts: Some Experiments upon Their Lubrication and Subsurface Deformations. *Proceedings of the Institution of Mechanical Engineers* 171(1), pp. 187–214.

Crump, M.J.C. et al. 2019. *Answering Questions with Data: Introductory Statistics for Psychology Students*. Available at: https://doi.org/10.17605/OSF.IO/JZE52 [Accessed: 6 January 2021].

Dang Van, K. et al. 1989. Criterion for high cycle fatigue failure under multiaxial loading. In: *Biaxial and Multiaxial Fatigue*. London: Mechanical Engineering Publications, pp. 459–478.

Davies, C.N. 2005. *Effects of non-newtonian rheology on the line contact elastohydrodynamic lubrication problem*. Cardiff: Cardiff University.

D'Errico, F. 2011. Micropitting Damage Mechanism on Hardened and Tempered, Nitrided, and Carburizing Steels. *Materials and Manufacturing Processes* 26(1), pp. 7–13. doi: 10.1080/10426910903388424.

Downing, S. and Socie, D. 1982. Simple rainflow counting algorithms. *International Journal of Fatigue* 4(1), pp. 31–40. doi: 10.1016/0142-1123(82)90018-4.

Dowson, D. 1998. *History of Tribology*. Second. London: Professional Engineering Publishing.

Dowson, D. and Higginson, G.R. 1977. *Elasto-Hydrodynamic Lubrication*. Pergamon.

Epstein, D. et al. 2003. Effect of Surface Topography on Contact Fatigue in Mixed Lubrication. *Tribology Transactions* 46(4), pp. 506–513. doi: 10.1080/10402000308982657.

Errichello, R.L. 2012. Morphology of Micropitting. *Gear Technology* (November/December), pp. 74–81.

Evans, H.P. and Hughes, T.G. 2000. Evaluation of deflection in semi-infnite bodies by a differential method. 214, p. 22.

Fatemi, A. and Socie, D.F. 1988. A Critical Plane Approach to Multiaxial Fatigue Damage Including Out-of-Phase Loading. *Fatigue & Fracture of Engineering Materials and Structures* 11(3), pp. 149–165. doi: 10.1111/j.1460-2695.1988.tb01169.x.

Findley, W.N. 1959. A Theory for the Effect of Mean Stress on Fatigue of Metals Under Combined Torsion and Axial Load or Bending. *Journal of Engineering for Industry* 81(4), pp. 301–305. doi: 10.1115/1.4008327.

Frene, J. et al. 1990. Hydrodynamic Lubrication: Bearings and Thrust Bearings. In: *Tribology Series*. 33. Elsevier, pp. 27–46. Available at: https://linkinghub.elsevier.com/retrieve/pii/S0167892297800594 [Accessed: 12 June 2022].

George, A.F. 1979. A comparative study of surface replicas. *Wear* 57(1), pp. 51–61. doi: 10.1016/0043-1648(79)90139-X.

Griffiths, D. 2018. *Analysis of High Strength Steels in a Transmission Gear*. Cardiff: Cardiff University.

Guangteng, G. et al. 1999. Contact Resistance Measurements in Mixed Lubrication. In: *The advancing frontier of engineering tribology : proceedings of the 1999 STLE/ASME H.S. Cheng Tribology Surveillance*. Society of Tribologists and Lubrication Engineers, pp. 64–70.

Holmes, M.J.A. 2002. *Transient Analysis of the Point Contact Elastohydrodynamic Problem Using Coupled Methods*. PhD, Cardiff: Cardiff University.

Holmes, M.J.A. et al. 2003. Transient elastohydrodynamic point contact analysis using a new coupled differential deflection method Part 2: Results. *Proceedings of the Institution of Mechanical Engineers, Part J: Journal of Engineering Tribology* 217(4), pp. 305–322. doi: 10.1243/135065003768618650.

Holmes, M.J.A. et al. 2005. Analysis of Mixed Lubrication Effects in Simulated Gear Tooth Contacts. *Journal of Tribology* 127(1), p. 61. doi: 10.1115/1.1828452.

Hutt, S. et al. 2018. Generation of Acoustic Emission from the running-in and subsequent micropitting of a mixed-elastohydrodynamic contact. *Tribology International* 119, pp. 270–280. doi: 10.1016/j.triboint.2017.11.011.

Hutt, S. 2018. *The Acoustic Emission from Mixed Elastohydrodynamic Lubrication*. PhD Thesis, Cardiff: Cardiff University.

Ioannides, E. and Harris, T.A. 1985. A new fatigue life model for rolling bearings. *Journal of Tribology* 107(3), pp. 367–377.

Ishibashi, A. and Tanaka, S. 1981. Effects of Hunting Gear Ratio Upon Surface Durability of Gear Teeth. *Journal of Mechanical Design* 103(4), pp. 227–235.

ISO 2014. ISO-TR 15144-1-2014 Calculation of micropitting load capacity of cylindrical spur and helical gears Part 1: Introduction and basic principles.

Jones, A.B. 1947. Metallographic Observations of Ball Bearing Fatigue Phenomena. In: Administrative Committee on Simulated Service Testing ed. *Symposium on Testing of Bearings*. 100 Barr Harbor Drive, PO Box C700, West Conshohocken, PA 19428-2959: ASTM International, pp. 35-35–18. Available at: http://www.astm.org/doiLink.cgi?STP42598S [Accessed: 19 March 2018].

Kadiric, A. and Rycerz, P. 2016. Influence of Contact Conditions on the Onset of Micropitting in Rolling-Sliding Contacts Pertinent to Gear Applications. *AGMA Technical Paper 16FTM21, AGMA, Virginia, USA*

Keller, J. et al. 2017. Investigating Bearing Failures in Wind Turbine Drivetrains. Boulder, Colorado, USA. Available at: http://windtechconferences.org/wp-content/uploads/2017/10/Keller-Jonathan-Abstract-for-Invited-Talk.pdf [Accessed: 12 December 2017].

Kelly, D.A. et al. 1998. Aspects of thrust cone tribology: Part 1: Effects of slide to roll ratio on surface failure mechanisms in twin-disc tests. *Proceedings of the Institution of Mechanical Engineers, Part J: Journal of Engineering Tribology* 212(1), pp. 55–72.

Kotzalas, M.N. and Doll, G.L. 2010. Tribological advancements for reliable wind turbine performance. *Philosophical Transactions of the Royal Society A: Mathematical, Physical and Engineering Sciences* 368(1929), pp. 4829–4850. doi: 10.1098/rsta.2010.0194.

Krantz, T. 2005. *The influence of roughness on gear surface fatigue*. U.S. Army Research Laboratory, Glenn Research Center, Cleveland, Ohio.

Krantz, T.L. et al. 2001. Surface Fatigue Lives of Case-Carburized Gears With an Improved Surface Finish. *Journal of Tribology* 123(4), p. 709. doi: 10.1115/1.1387036.

Krantz, T.L. 2015. On the Correlation of Specific Film Thickness and Gear Pitting Life. *Gear Technology* (January/February 2015), pp. 52–62.

Lainé, E. et al. 2008. Effect of lubricants on micropitting and wear. *Tribology International* 41(11), pp. 1049–1055. doi: 10.1016/j.triboint.2008.03.016.

Lee, Y.-L. and Tjhung, T. 2012. Rainflow Cycle Counting Techniques. In: *Metal Fatigue Analysis Handbook*. Elsevier, pp. 89–114. Available at: https://linkinghub.elsevier.com/retrieve/pii/B9780123852045000033 [Accessed: 3 March 2020].

L'Hostis, B. et al. 2017. Influence of lubricant formulation on rolling contact fatigue of gears – interaction of lubricant additives with fatigue cracks. *Wear* 382–383, pp. 113–122. doi: 10.1016/j.wear.2017.04.025.

Li, S. and Kahraman, A. 2013. Micro-pitting fatigue lives of lubricated point contacts: Experiments and model validation. *International Journal of Fatigue* 48, pp. 9–18. doi: 10.1016/j.ijfatigue.2012.12.003.

Littmann, W.E. and Widner, R.L. 1966. Propagation of contact fatigue from surface and subsurface origins. *Journal of Basic Engineering* 88(3), pp. 624–635.

Liu, H. et al. 2020. Study on gear contact fatigue failure competition mechanism considering tooth wear evolution. *Tribology International* 147, p. 106277. doi: 10.1016/j.triboint.2020.106277.

Lord, J. and Larsson, R. 2008. Film-forming capability in rough surface EHL investigated using contact resistance. *Tribology International* 41(9–10), pp. 831–838. doi: 10.1016/j.triboint.2007.11.006.

Lugt, P.M. et al. 2001. Influence of surface topography on friction, film breakdown and running-in in the mixed lubrication regime. *Proceedings of the Institution of Mechanical Engineers, Part J: Journal of Engineering Tribology* 215(6), pp. 519–533.

Mallipeddi, D. et al. 2017. Influence of running-in on surface characteristics of efficiency tested ground gears. *Tribology International* 115, pp. 45–58. doi: 10.1016/j.triboint.2017.05.018.

Martins, R. et al. 2011. Evolution of tooth flank roughness during gear micropitting tests. Seabra, J. ed. *Industrial Lubrication and Tribology* 63(1), pp. 34–45. doi: 10.1108/00368791111101821.

Matake, T. 1977. An explanation on fatigue limit under combined stress. *Bulletin of the JSME* 20(141), pp. 257–263.

Merritt, H.E. 1935. Worm Gear Performance. *Proceedings of the Institution of Mechanical Engineers* 129(1), pp. 127–194. doi: 10.1243/PIME_PROC_1935_129_011_02.

Montgomery, D.C. 2009. *Design and Analysis of Experiments*. 8th ed. Singapore: Wiley.

Moorthy, V. and Shaw, B.A. 2012. Contact fatigue performance of helical gears with surface coatings. *Wear* 276–277, pp. 130–140. doi: 10.1016/j.wear.2011.12.011.

Moorthy, V. and Shaw, B.A. 2013. An observation on the initiation of micro-pitting damage in as-ground and coated gears during contact fatigue. *Wear* 297(1–2), pp. 878–884. doi: 10.1016/j.wear.2012.11.001.

Morales-Espejel, G.E. et al. 2018. Prediction of micropitting damage in gear teeth contacts considering the concurrent effects of surface fatigue and mild wear. *Wear* 398–399, pp. 99–115. doi: 10.1016/j.wear.2017.11.016.

Morales-Espejel, G.E. 2020. Thermal damage and fatigue estimation in heavily loaded lubricated rolling/sliding contacts with Micro-Geometry. *Proceedings of the Institution of Mechanical Engineers, Part J: Journal of Engineering Tribology* , p. 135065012097259. doi: 10.1177/1350650120972591.

Morales-Espejel, G.E. and Brizmer, V. 2011. Micropitting Modelling in Rolling–Sliding Contacts: Application to Rolling Bearings. *Tribology Transactions* 54(4), pp. 625–643. doi: 10.1080/10402004.2011.587633.

Morris, D. et al. 2018. A novel approach for modeling retained austenite transformations during rolling contact fatigue. *Fatigue & Fracture of Engineering Materials & Structures* 41(4), pp. 831–843. doi: 10.1111/ffe.12731.

NIST/SEMATECH 2013. *NIST-SEMATECH e-Handbook of Statistical Methods*. NIST. Available at: https://www.itl.nist.gov/div898/handbook/index.htm [Accessed: 6 January 2021].

Oila, A. 2003. *Micropitting and Related Phenomena in Case Carburised Gears*. Newcastle: University of Newcastle upon Tyne.

Oila, A. et al. 2005. Martensite decay in micropitted gears. *Proceedings of the Institution of Mechanical Engineers, Part J: Journal of Engineering Tribology* 219(2), pp. 77–83. doi: 10.1243/135065005X9790.

Oila, A. and Bull, S.J. 2005. Assessment of the factors influencing micropitting in rolling/sliding contacts. *Wear* 258(10), pp. 1510–1524. doi: 10.1016/j.wear.2004.10.012.

Olver, A.V. 2002. Gear lubrication—a review. *Proceedings of the Institution of Mechanical Engineers, Part J: Journal of Engineering Tribology* 216(5), pp. 255–267.

Olver, A.V. et al. 2004. Direct observations of a micropit in an elastohydrodynamic contact. *Wear* 256(1–2), pp. 168–175. doi: 10.1016/S0043-1648(03)00374-0.

Olver, A.V. 2005. The Mechanism of Rolling Contact Fatigue: An Update. *Proceedings of the Institution of Mechanical Engineers, Part J: Journal of Engineering Tribology* 219(5), pp. 313–330. doi: 10.1243/135065005X9808.

Østvik, R. and Christensen, H. 1968. Changes in Surface Topography with Running-In. *Proceedings of the Institution of Mechanical Engineers, Conference Proceedings* 183(16), pp. 57–65. doi: 10.1243/PIME_CONF_1968_183_279_02.

Patching, M.J. et al. 1995. Conditions for Scuffing Failure of Ground and Superfinished Steel Disks at High Sliding Speeds Using a Gas Turbine Engine Oil. *Journal of Tribology* 117(3), p. 482. doi: 10.1115/1.2831279.

Prajapati, D.K. and Tiwari, M. 2019. Assessment of Topography Parameters During Running-In and Subsequent Rolling Contact Fatigue Tests. *Journal of Tribology* 141(5), p. 051401. doi: 10.1115/1.4042676.

Prajapati, D.K. and Tiwari, M. 2020. Experimental analysis of contact fatigue damage using fractal methodologies. *Wear* 450–451, p. 203262. doi: 10.1016/j.wear.2020.203262.

Qiao, H. 2005. *Prediction of contact fatigue for the rough surface elastohydrodynamic lubrication line contact problem*. Cardiff: Cardiff University.

Qiao, H. et al. 2008. Comparison of fatigue model results for rough surface elastohydrodynamic lubrication. *Proceedings of the Institution of Mechanical Engineers, Part J: Journal of Engineering Tribology* 222(3), pp. 381–393. doi: 10.1243/13506501JET347.

Rabaso, P. et al. 2013. Rolling Contact Fatigue: Experimental Study of the Influence of Sliding, Load, and Material Properties on the Resistance to Micropitting of Steel Discs. *Tribology Transactions* 56(2), pp. 203–214. doi: 10.1080/10402004.2012.737504.

Reynolds, O. 1886. On the Theory of Lubrication and its Application to Mr. Beauchamp Tower's Experiments, including an Experimental Determination of the Viscosity of Olive Oil. *Phil. Trans. R. Soc. Lond.* 177, pp. 157–234.

Roberts, D.P. 2017. *Analysis of gear running-in experimental data*. Cardiff: Cardiff University.

Roy, S. et al. 2018. Correlation between evolution of surface roughness parameters and micropitting of carburized steel under boundary lubrication condition. *Surface and Coatings Technology* 350, pp. 445–452. doi: 10.1016/j.surfcoat.2018.05.083.

Sharif, K.J. et al. 2012. Modelling of elastohydrodynamic lubrication and fatigue of rough surfaces: The effect of lambda ratio. *Proc IMechE Part J: J Engineering Tribology* 226(12), pp. 1039–1050.

Shaw, B. et al. 2003. The role of residual stress on the fatigue strength of high performance gearing. *International Journal of Fatigue* 25(9–11), pp. 1279–1283. doi: 10.1016/j.ijfatigue.2003.08.014.

Singh, H. et al. 2016. Fatigue resistant carbon coatings for rolling/sliding contacts. *Tribology International* 98, pp. 172–178. doi: 10.1016/j.triboint.2016.02.008.

Socie, D. 1992. Rainflow Cycle Counting : A Historical Perspective. In: *The Rainflow Method in Fatigue*. Elsevier, pp. 3–10. Available at: https://linkinghub.elsevier.com/retrieve/pii/B9780750605045500096 [Accessed: 3 March 2020].

Sosa, M. et al. 2015. In situ surface characterization of running-in of involute gears. *Wear* 340–341, pp. 41–46. doi: 10.1016/j.wear.2015.03.008.

Sosa, M. et al. 2016. In situ running-in analysis of ground gears. *Wear* 352–353, pp. 122–129. doi: 10.1016/j.wear.2016.01.021.

Stachowiak, G.W. and Batchelor, A.W. 1993. *Engineering Tribology*. Amsterdam: Elsevier.

Swahn, H. et al. 1976. Martensite decay during rolling contact fatigue in ball bearings. *Metallurgical Transactions A* 7(8), pp. 1099–1110. doi: 10.1007/BF02656592.

Tallian, T.E. 1967. On Competing Failure Modes in Rolling Contact. *A S L E Transactions* 10(4), pp. 418–439. doi: 10.1080/05698196708972201.

Timoshenko, S.P. and Goodier, J.N. 1970. *Theory of Elasticity*. 3rd ed. Singapore: McGraw-Hill.

Vrcek, A. et al. 2019. Micro-pitting and wear assessment of engine oils operating under boundary lubrication conditions. *Tribology International* 129, pp. 338–346. doi: 10.1016/j.triboint.2018.08.032.

Wang, W. et al. 2000. Experimental study of the real time change in surface roughness during running-in for PEHL contacts. *Wear* 244(1), pp. 140–146.

Warhadpande, A. et al. 2013. Microstructural Alterations in Bearing Steels under Rolling Contact Fatigue Part 1—Historical Overview. *Tribology Transactions* 56(3), pp. 349–358. doi: 10.1080/10402004.2012.754073.

Way, S. 1935. Pitting due to Rolling Contact.pdf. *Journal of Applied Mechanics* 2, p. A-49-A-58.

Webster, M.N. and Norbart, C.J.J. 1995. An Experimental Investigation of Micropitting Using a Roller Disk Machine. *Tribology Transactions* 38(4), pp. 883–893.

Weeks, I.J. 2015. *An Experimental Investigation into the Mixed Lubrication of Steel Surfaces*. Cardiff: Cardiff University.

Wellauer, E.J. and Holloway, G.A. 1976. Application of EHD oil film theory to industrial gear drives. *Journal of Engineering for Industry* 98(2), pp. 626–631.

Zaretsky, E.V. 1987. Fatigue Criterion to System Design, Life and Reliability.pdf. *Journal of Propulsion and Power* 39(2), pp. 76–83.

Zhang, J. and Shaw, B. 2016. Performance of gears with WC/C coating. In: *Power Transmissions: Proceedings of the International Conference on Power Transmissions 2016 (ICPT 2016), Chongqing, P.R. China, 27-30 October 2016*. Chongqing, P.R. China: Taylor & Francis, pp. 357–360.

Zhou, Y. et al. 2019a. A Micropitting Study Considering Rough Sliding and Mild Wear. *Coatings* 9(639)

Zhou, Y. et al. 2019b. The effect of contact severity on micropitting: Simulation and experiments. *Tribology International* 138, pp. 463–472. doi: 10.1016/j.triboint.2019.06.020.

Appendix 1. Running in Factorial

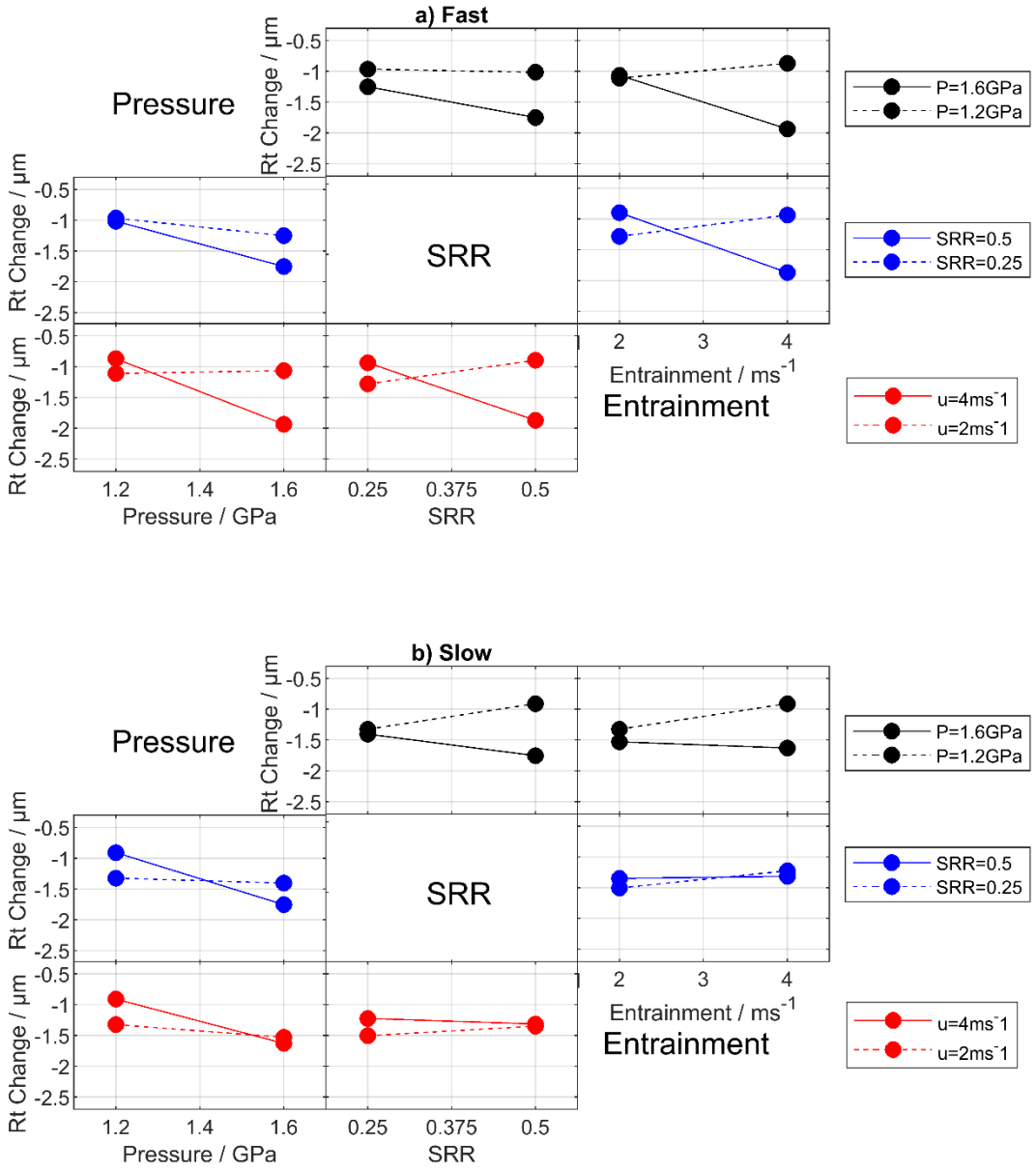

Figure 8.3.1 Two-factor interaction effect plots for the effects of pressure, SRR, and entrainment on Rt.

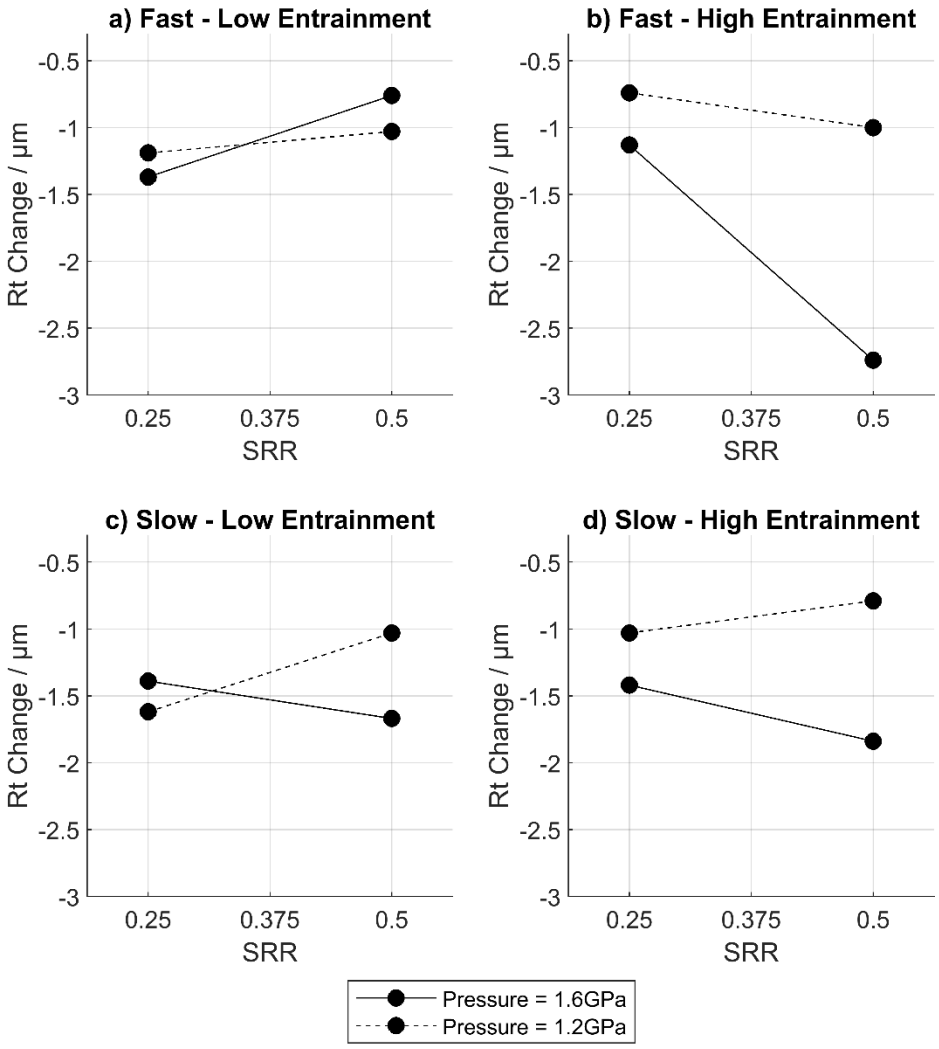

*Figure 8.3.2 Two-factor interaction effect plots for pressure*SRR at low and high entrainment for Rt.*

Table 8.3.1 Main and interaction effect strengths for Rt

Factor / Interaction	Fast Surface change in Rt			Slow Surface change in Rt		
	Low average / µm	High Average / µm	Effect / µm	Low average / µm	High Average / µm	Effect / µm
Pressure	-0.990	-1.500	-0.510	-1.118	-1.580	-0.463
SRR	-1.108	-1.383	-0.275	-1.365	-1.333	0.033
Entrainment	-1.088	-1.403	-0.315	-1.428	-1.270	0.158
Pressure*SRR	-1.133	-1.358	-0.225	-1.158	-1.540	-0.383
Pressure*Entrainment	-0.968	-1.523	-0.555	-1.220	-1.478	-0.258
SRR*Entrainment	-0.915	-1.575	-0.660	-1.288	-1.410	-0.123
Pressure*SRR*Entrainment	-1.470	-1.020	0.450	-1.323	-1.375	-0.053

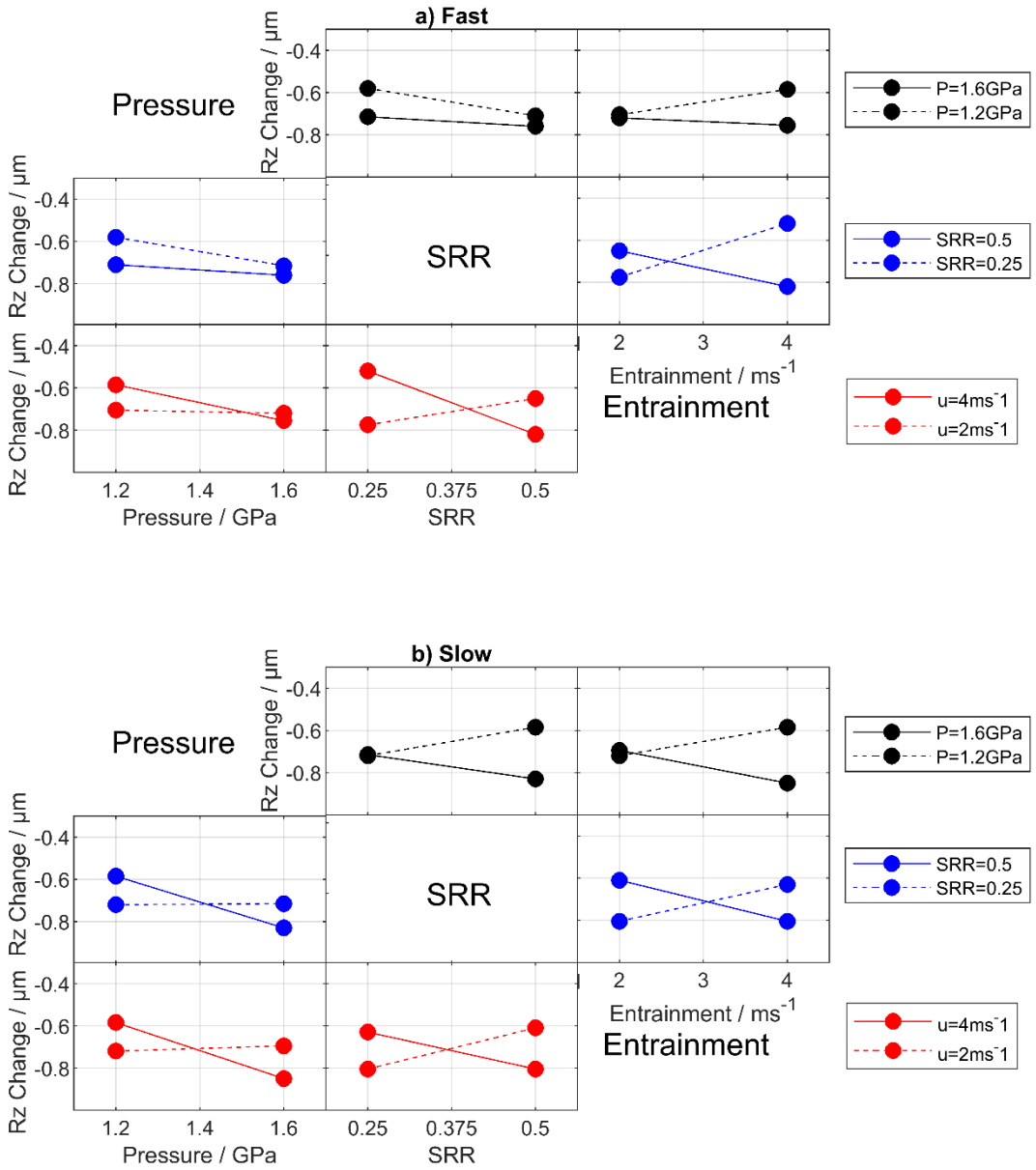

Figure 8.3.3 Two-factor interaction effect plots for the effects of pressure, SRR, and entrainment on Rz.

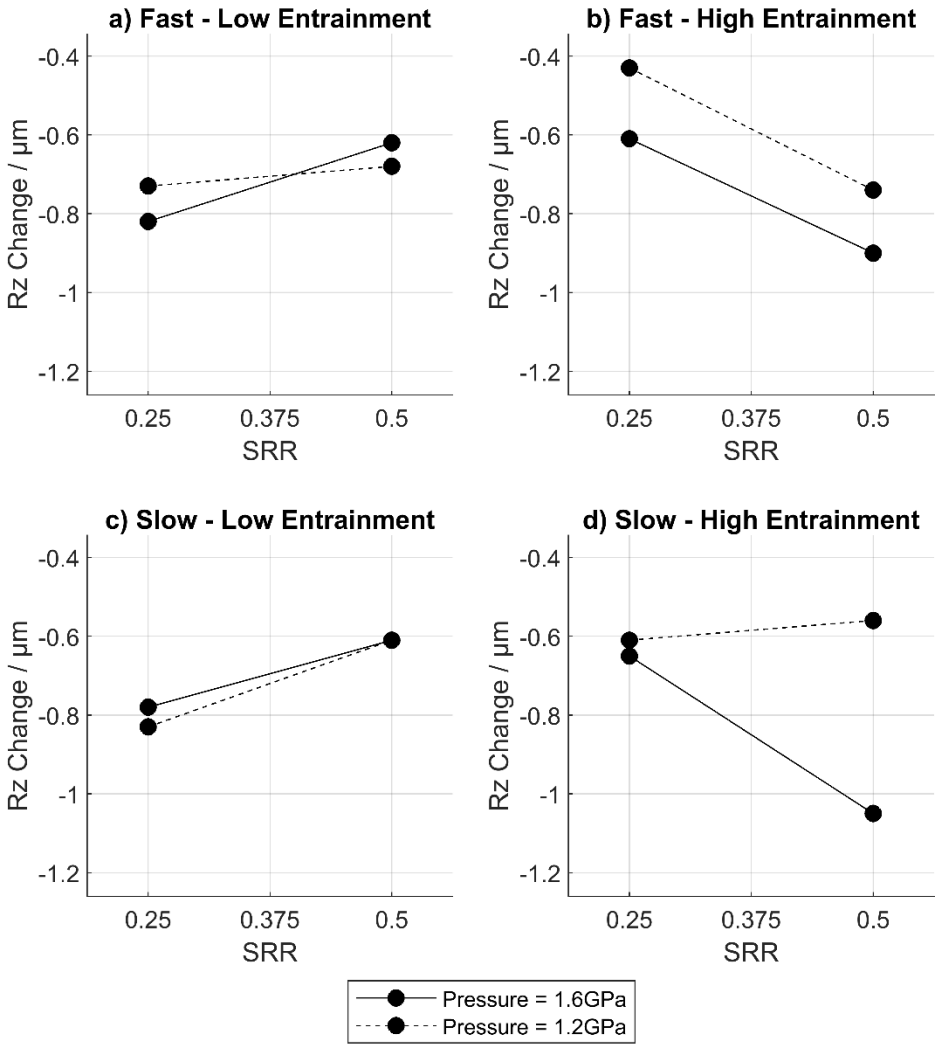

*Figure 8.3.4 Two-factor interaction effect plots for pressure*SRR at low and high entrainment for Rz.*

Appendix 2. Running-in Factorial Response Models

In each of the figures shown here, the upper row for each surface (a-c and g-i) shows the response where the third factor (the factor not shown on the axes in question) is high, while the lower row (d-f and j-l) shows the response where the third factor is low. Coefficients for each model are shown in Table 8.3.2.

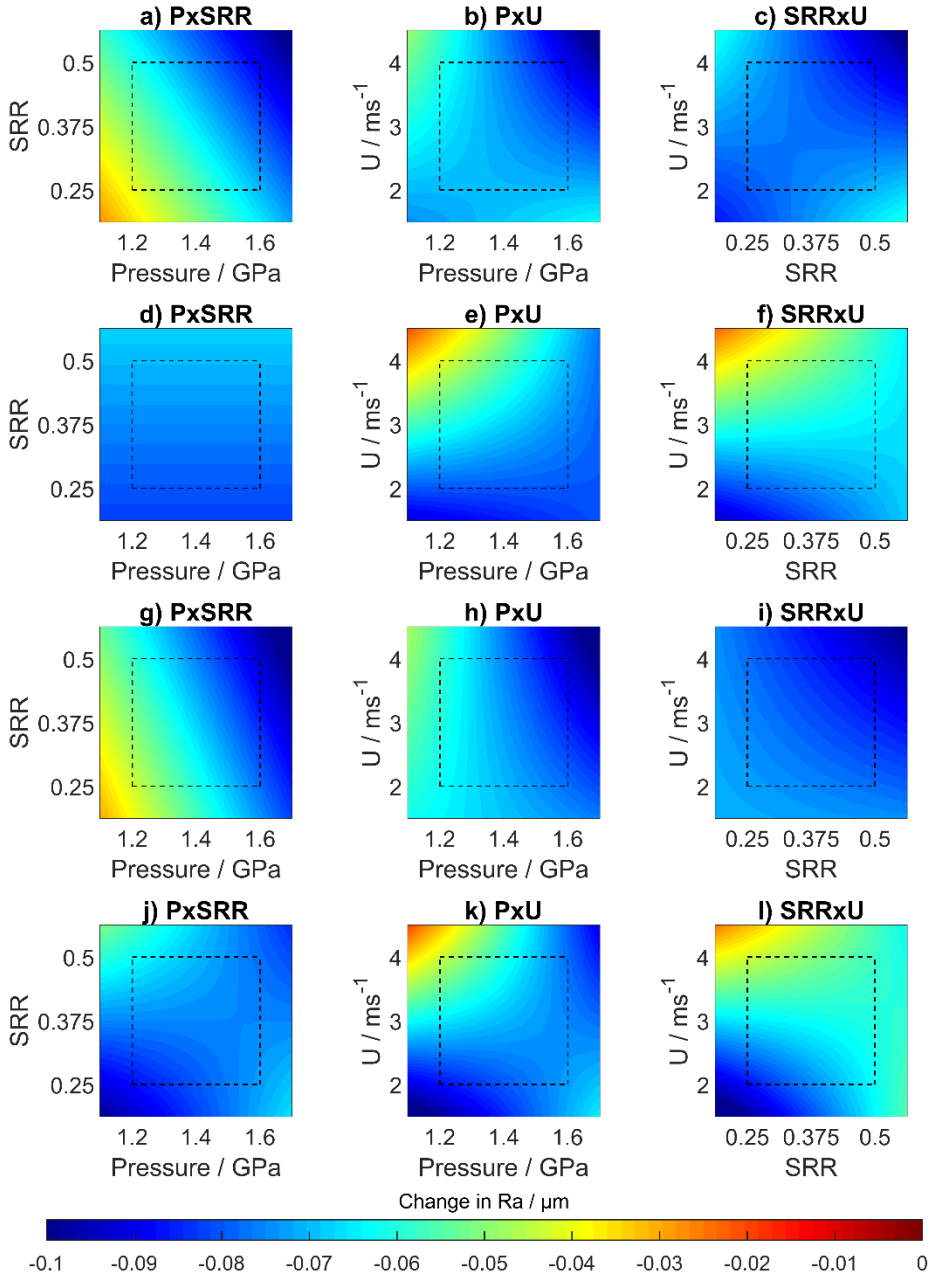

Figure 8.3.5 Factorial response models for change in Ra through running in for the fast (a-f) and slow (g-l) surfaces.

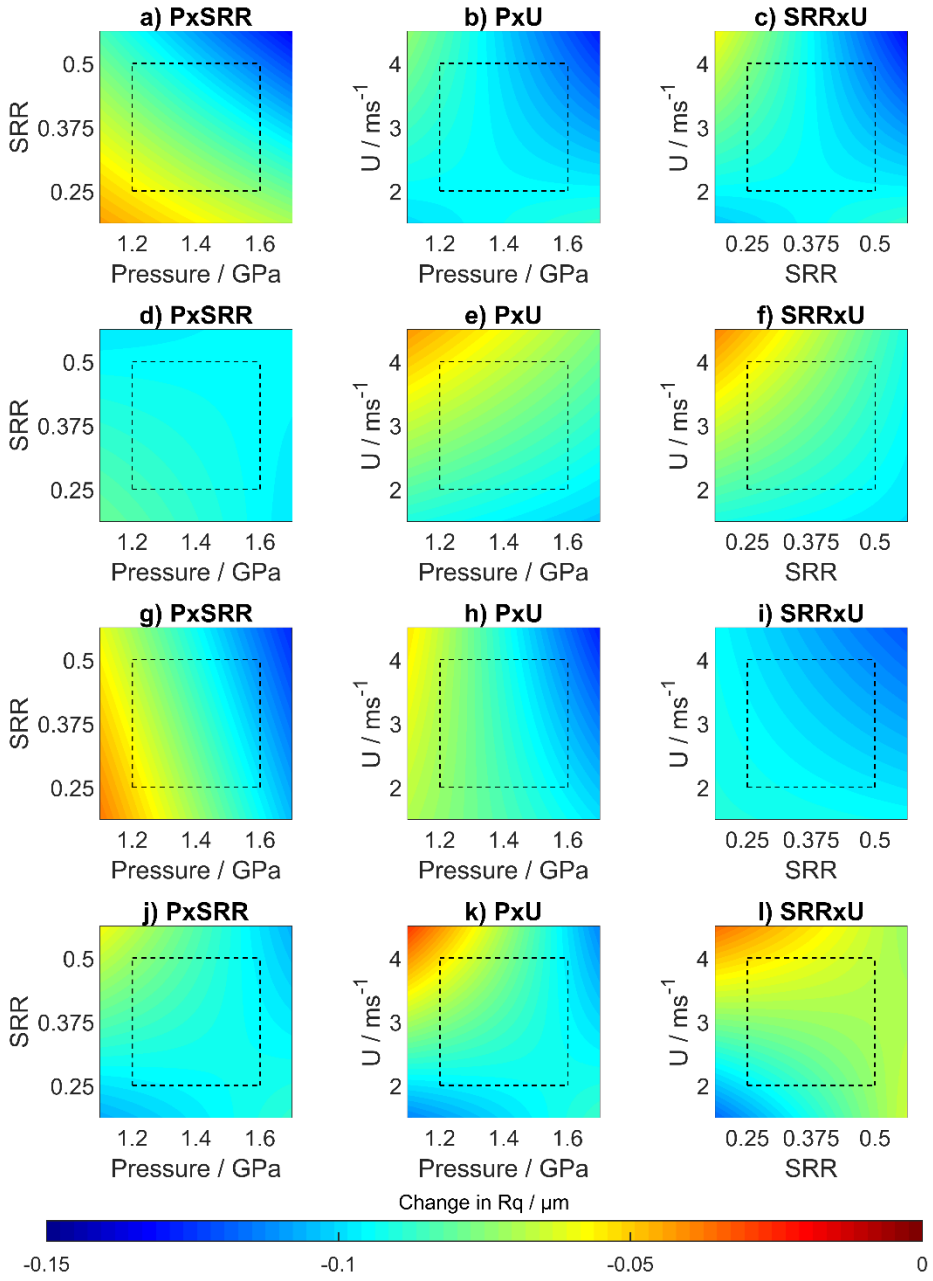

Figure 8.3.6 Factorial response models for change in Rq through running in for the fast (a-f) and slow (g-l) surfaces.

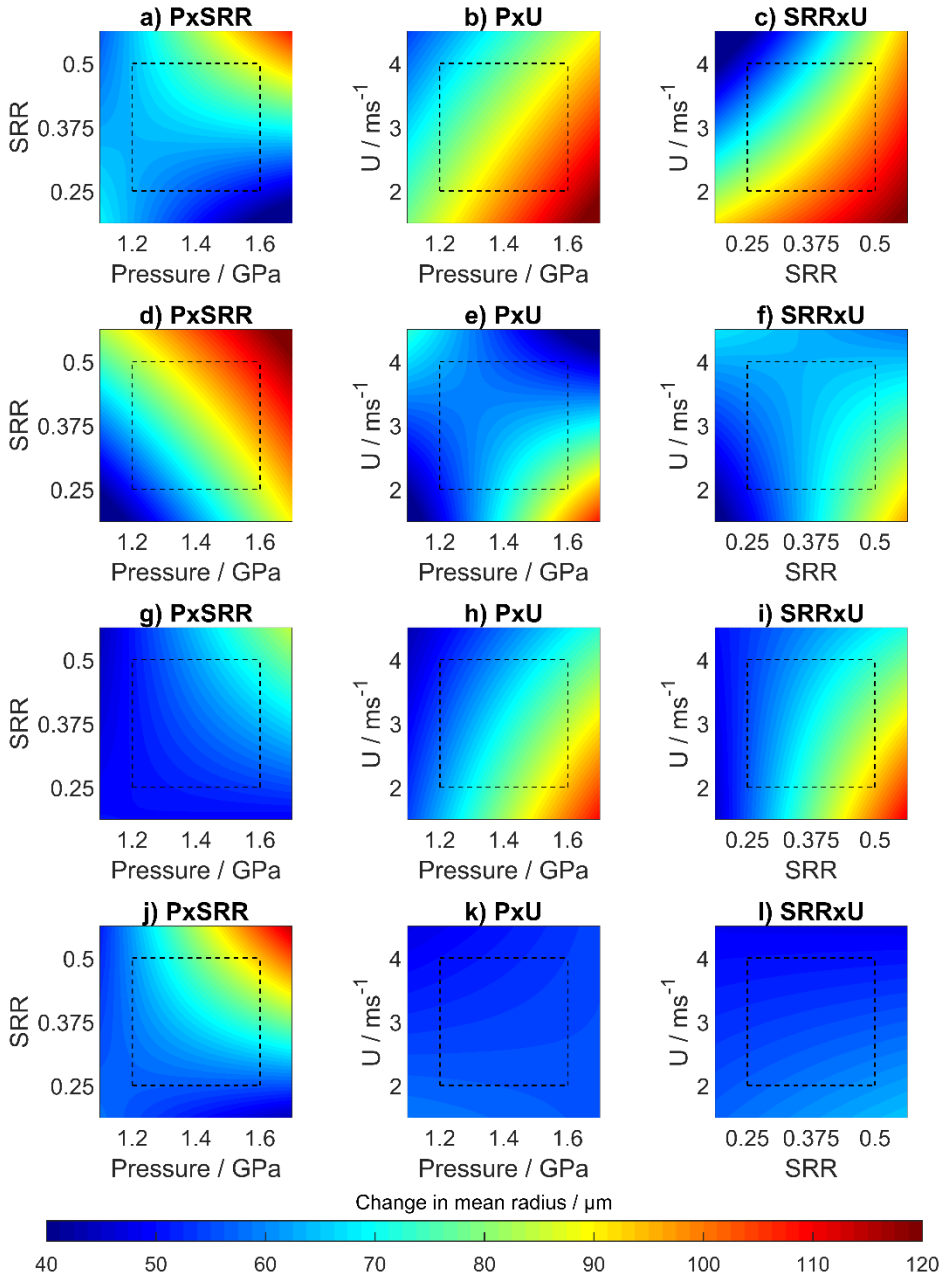

Figure 8.3.7 Factorial response models for change in mean radius of curvature of asperities through running in for the fast (a-f) and slow (g-l) surfaces.

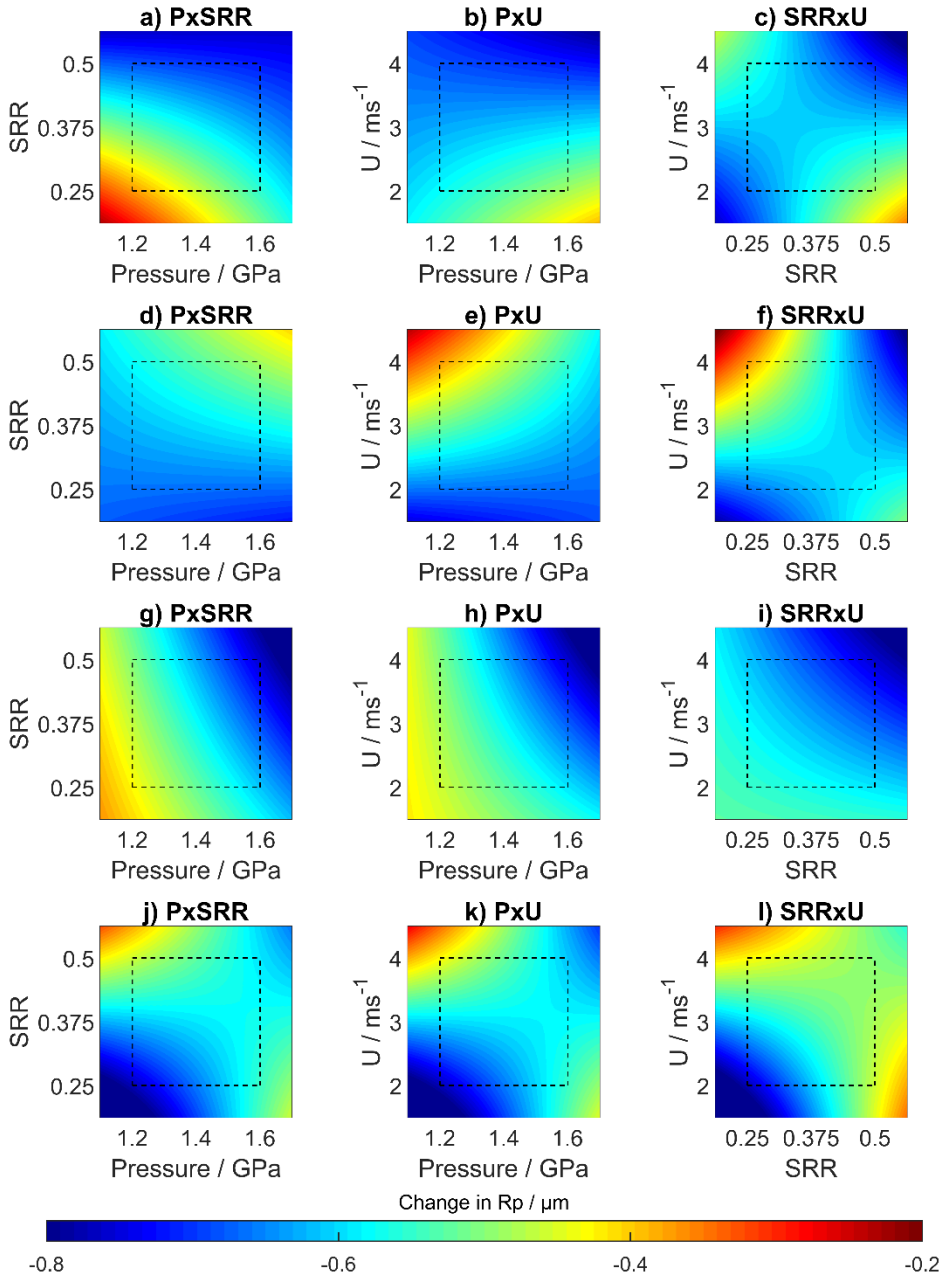

Figure 8.3.8 Factorial response models for change in Rp through running in for the fast (a-f) and slow (g-l) surfaces.

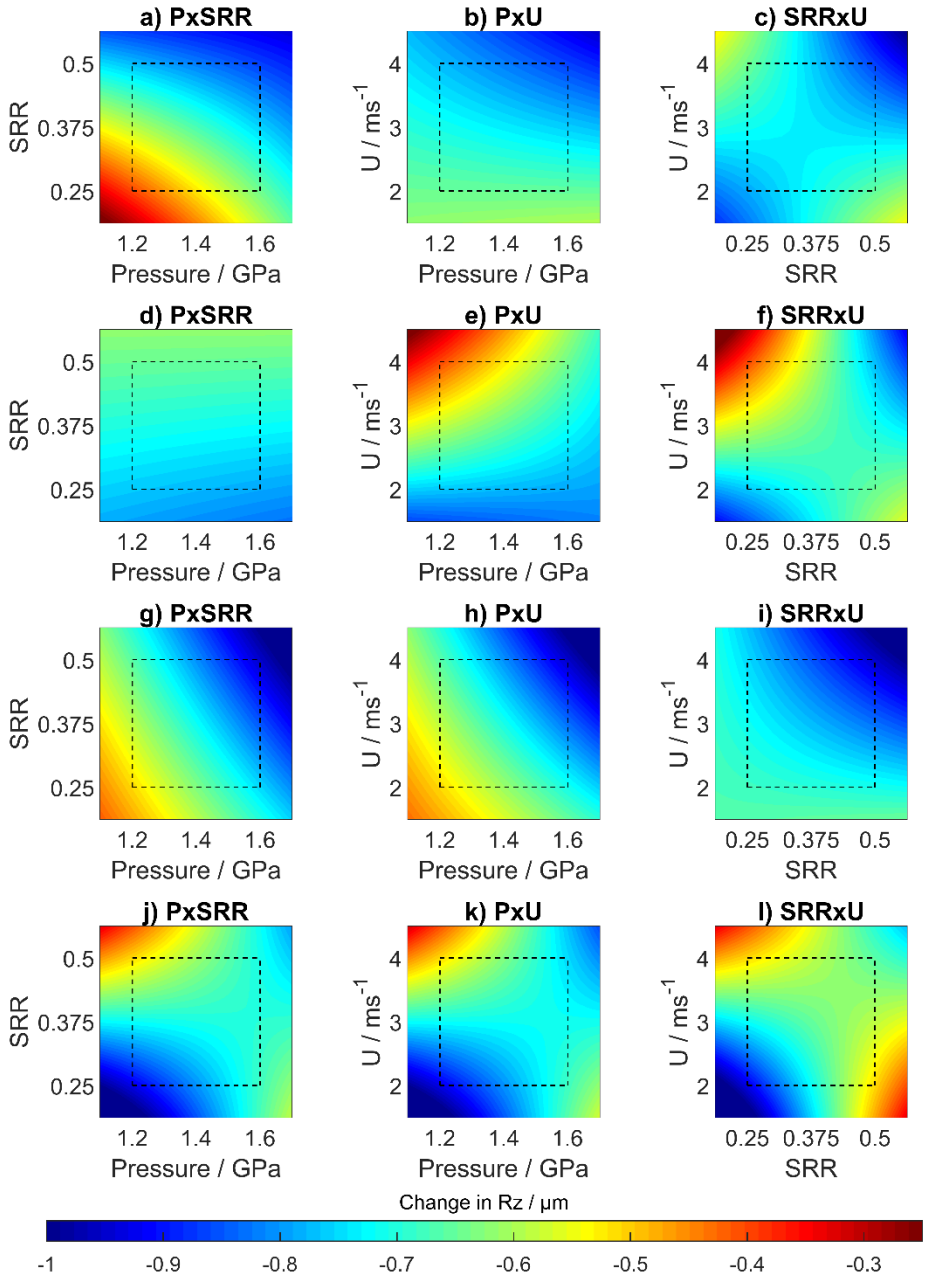

Figure 8.3.9 Factorial response models for change in Rz through running in for the fast (a-f) and slow (g-l) surfaces.

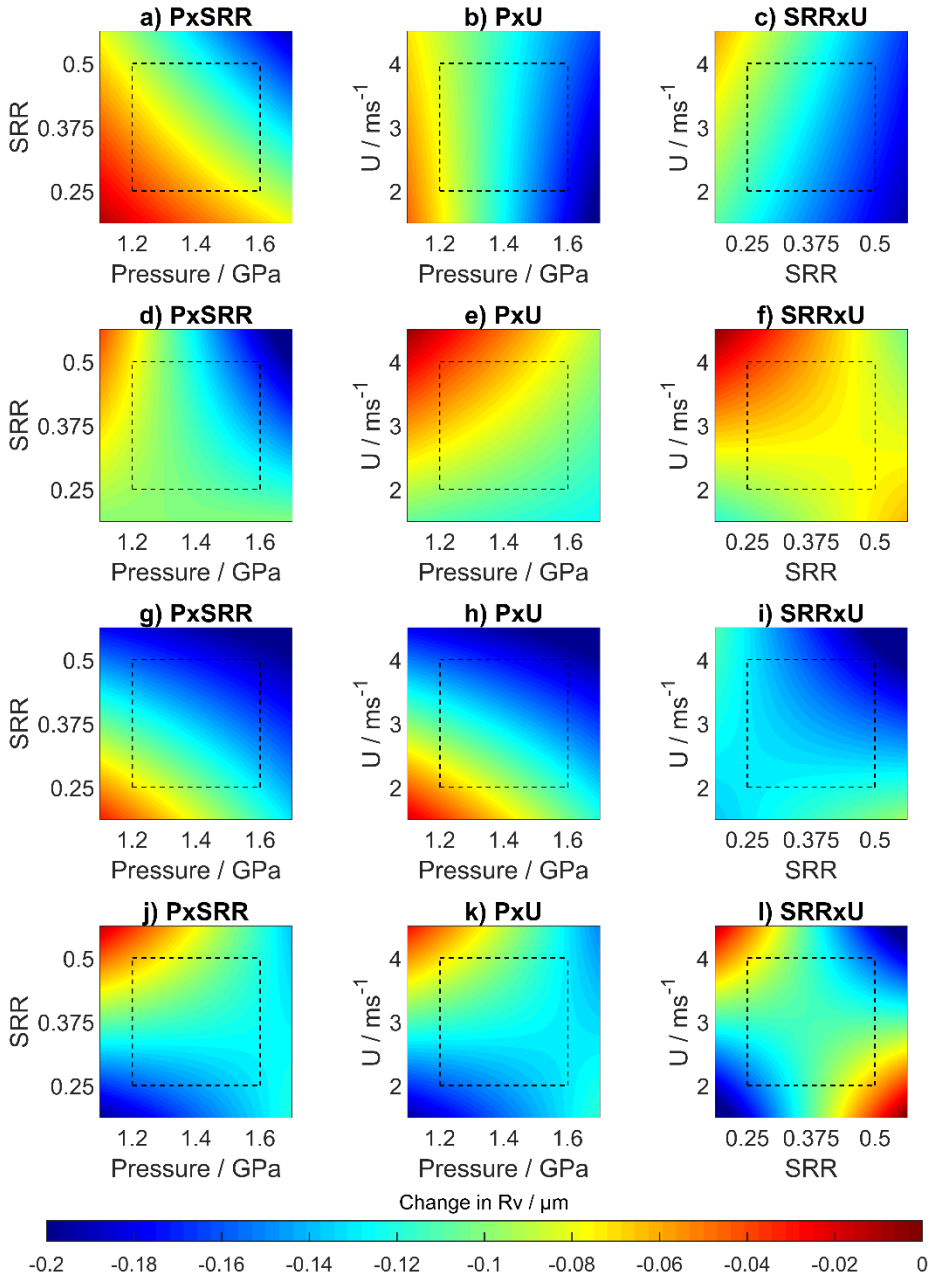

Figure 8.3.10 Factorial response models for change in Rv through running in for the fast (a-f) and slow (g-l) surfaces.

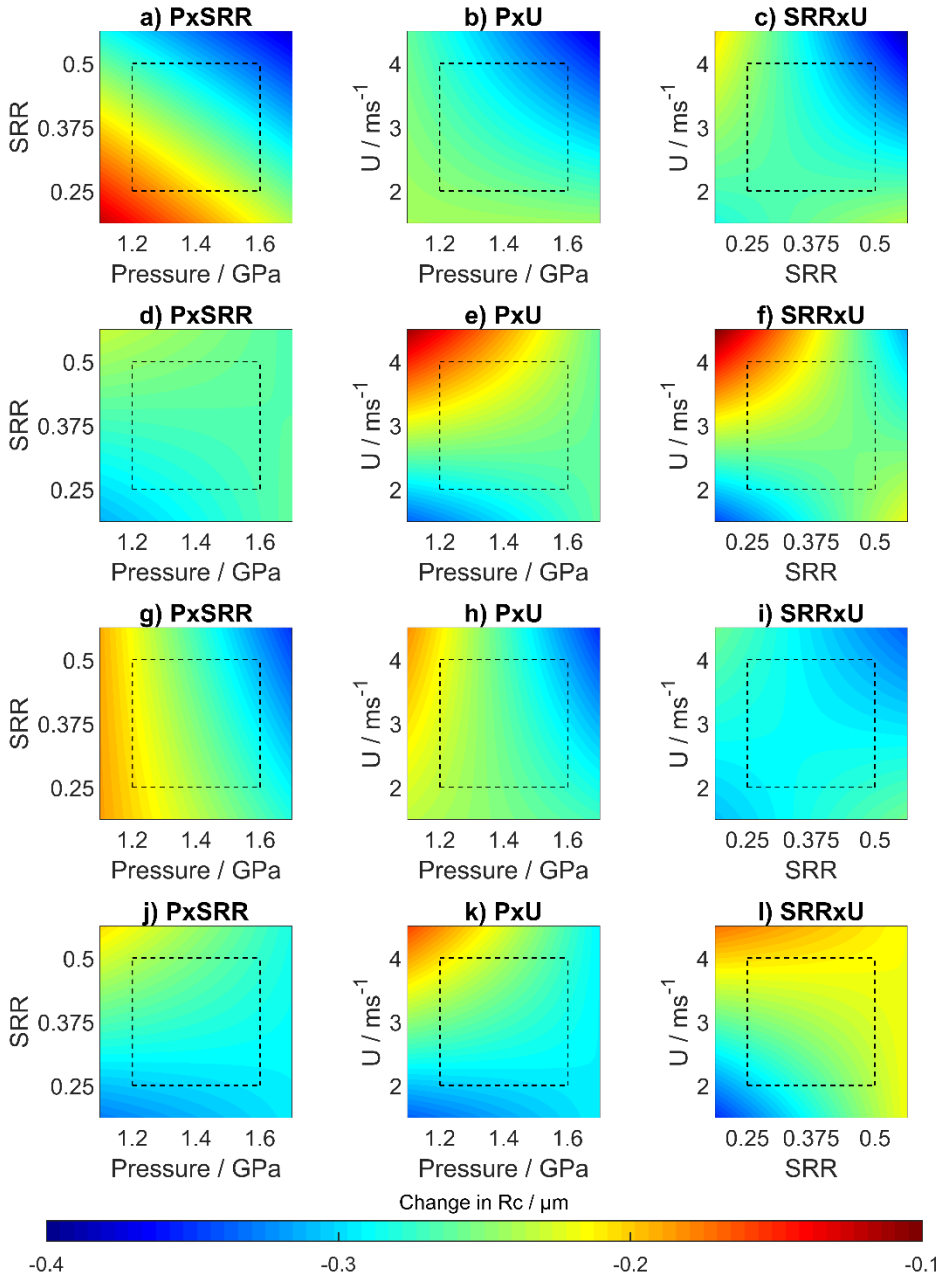

Figure 8.3.11 Factorial response models for change in Rc through running in for the fast (a-f) and slow (g-l) surfaces.

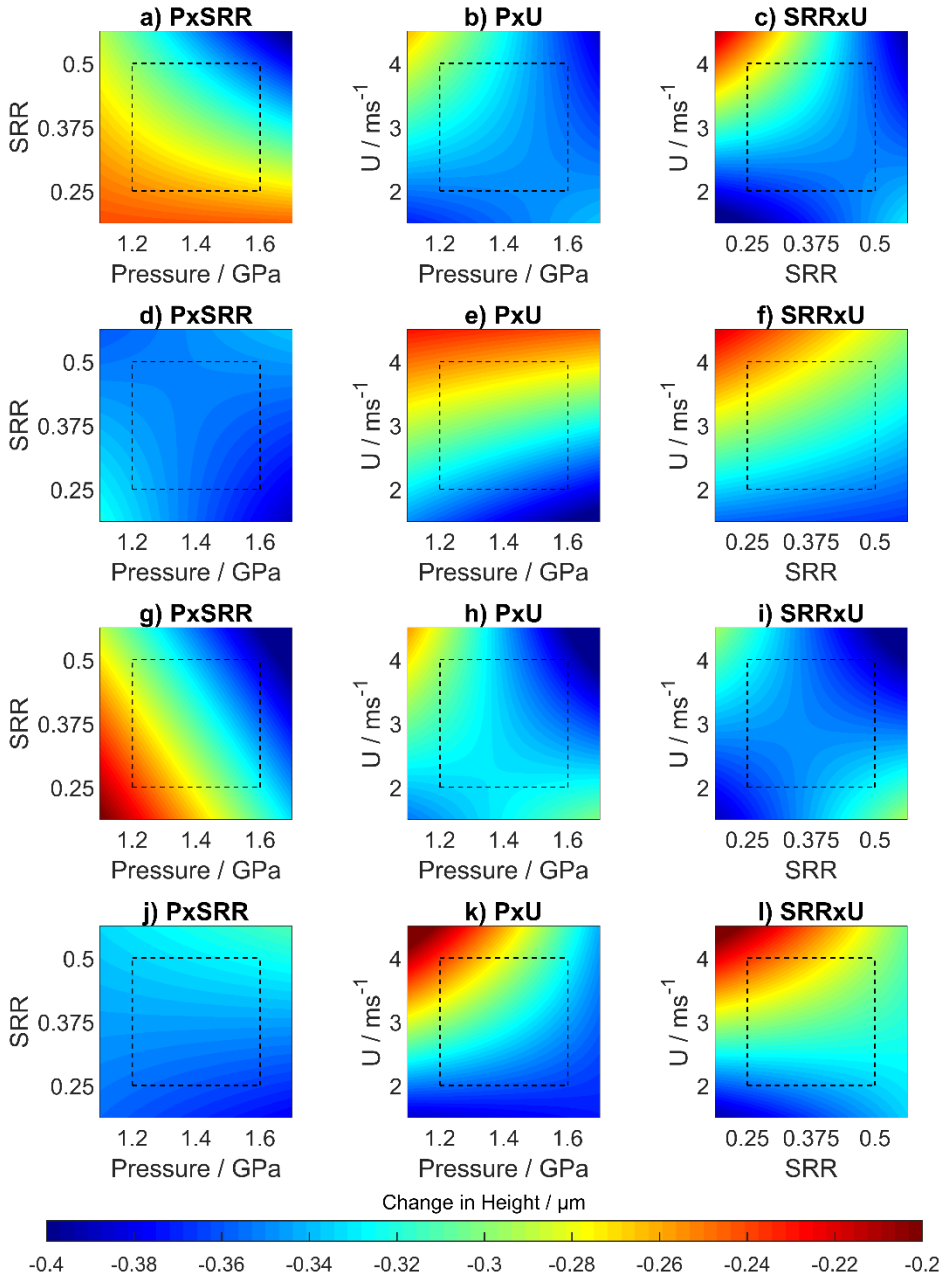

Figure 8.3.12 Factorial response models for change in mean asperity height above the mean line through running in for the fast (a-f) and slow (g-l) surfaces.

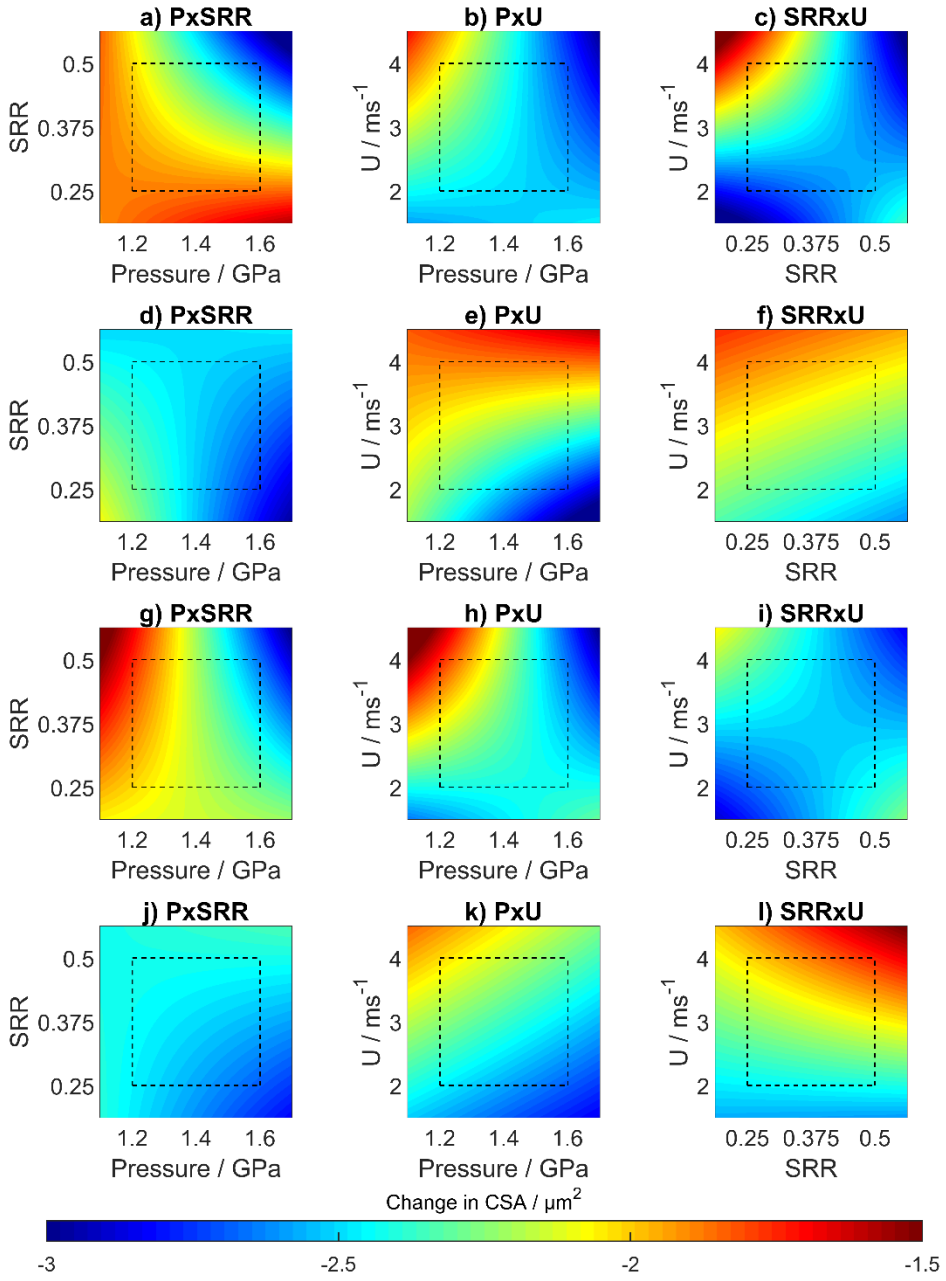

Figure 8.3.13 Factorial response models for change in mean cross-sectional area of asperities above the mean line through running in for the fast (a-f) and slow (g-l) surfaces.

Table 8.3.2 Coefficients in the factorial response models for the outputs of the running in tests.

Model	Surface	μ	ß1	ß2	ß3	ß12	ß13	ß23	ß123
Ra	**Fast**	-0.070	-0.008	-0.003	0.005	0.000	-0.008	-0.008	0.000
	Slow	-0.071	-0.009	-0.001	0.004	-0.004	-0.009	-0.006	0.004
Rq	**Fast**	-0.088	-0.008	-0.010	0.005	0.000	-0.005	-0.008	-0.003
	Slow	-0.086	-0.014	-0.001	0.004	-0.004	-0.009	-0.006	0.004
Radius of Curvature	**Fast**	74.391	9.399	12.286	-8.081	4.024	-6.844	-1.796	5.839
	Slow	61.961	7.414	7.906	-5.051	6.709	-0.824	-2.916	-1.991
Rp	**Fast**	-0.589	-0.016	-0.026	0.009	0.031	-0.039	-0.094	0.006
	Slow	-0.584	-0.044	0.006	0.009	-0.054	-0.066	-0.061	0.036
Rz	**Fast**	-0.691	-0.046	-0.044	0.021	0.021	-0.039	-0.106	0.016
	Slow	-0.713	-0.060	0.005	-0.005	-0.063	-0.073	-0.093	0.050
Rv	**Fast**	-0.103	-0.030	-0.020	0.013	-0.013	0.000	-0.010	0.008
	Slow	-0.128	-0.015	-0.005	-0.010	-0.008	-0.008	-0.033	0.015
Rc	**Fast**	-0.261	-0.016	-0.019	0.006	-0.004	-0.019	-0.032	0.006
	Slow	-0.265	-0.025	0.005	0.013	-0.010	-0.018	-0.018	0.003
Mean Asperity Cross-Sectional Area	**Fast**	-2.315	-0.155	-0.120	0.193	-0.040	-0.013	-0.133	-0.143
	Slow	-2.338	-0.178	0.028	0.160	-0.053	-0.120	-0.050	-0.110
Mean Asperity Height	**Fast**	-0.324	-0.014	-0.016	0.029	-0.001	-0.006	-0.019	-0.011
	Slow	-0.328	-0.023	-0.008	0.018	0.003	-0.023	-0.023	-0.003

Appendix 3. Micropitting Factorial response Models

In each of the figures shown here, the upper row for each surface (a-c and g-i) shows the response where the third factor (the factor not shown on the axes in question) is high, while the lower row (d-f and j-l) shows the response where the third factor is low.

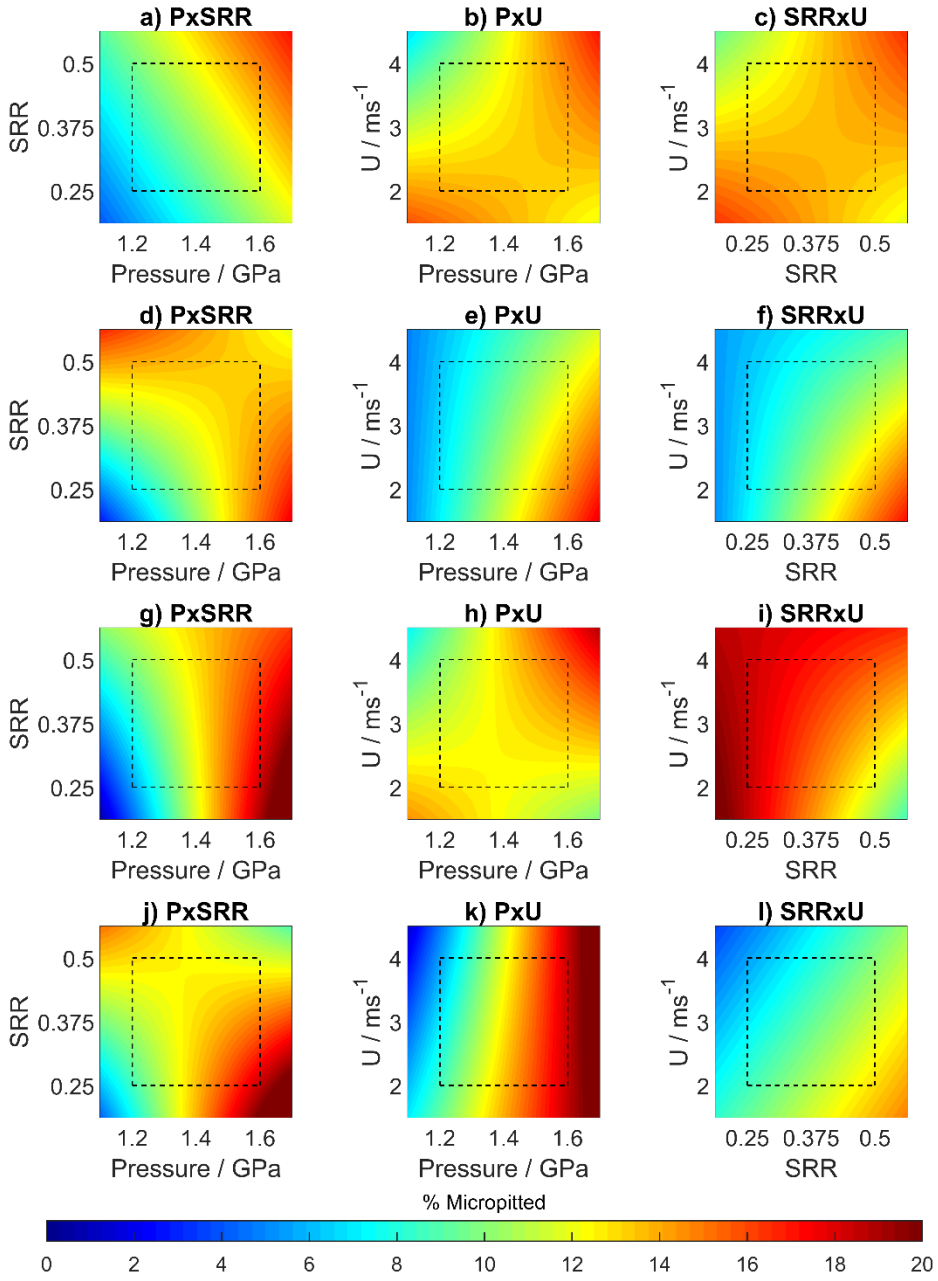

Figure 8.3.14 Factorial response models for percentage of surface pitted for the fast (a-f) and slow (g-l) surfaces.

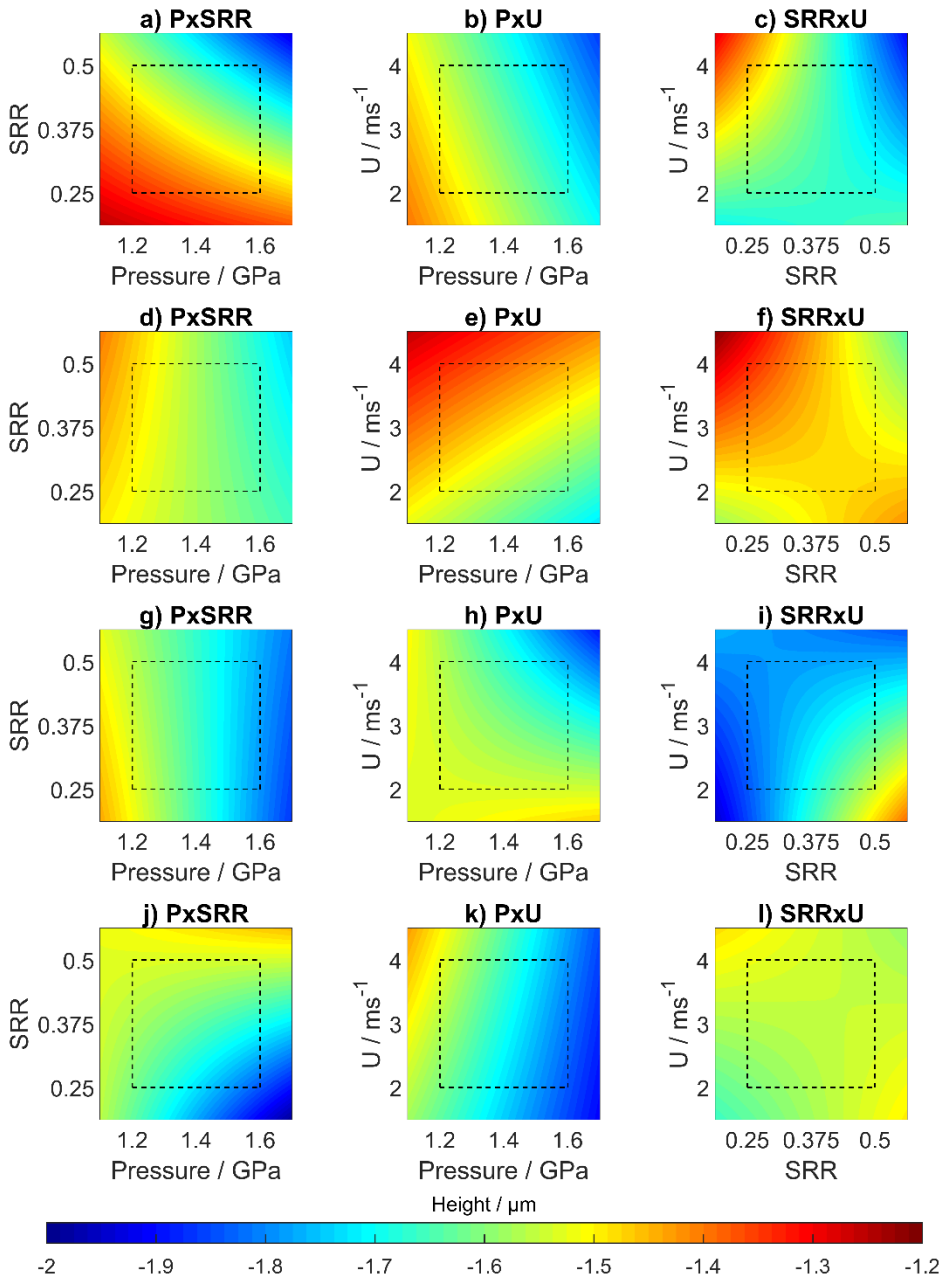

Figure 8.3.15 Factorial response models for the height of the deepest 5% of micropitted points (D5) for the fast (a-f) and slow (g-l) surfaces.

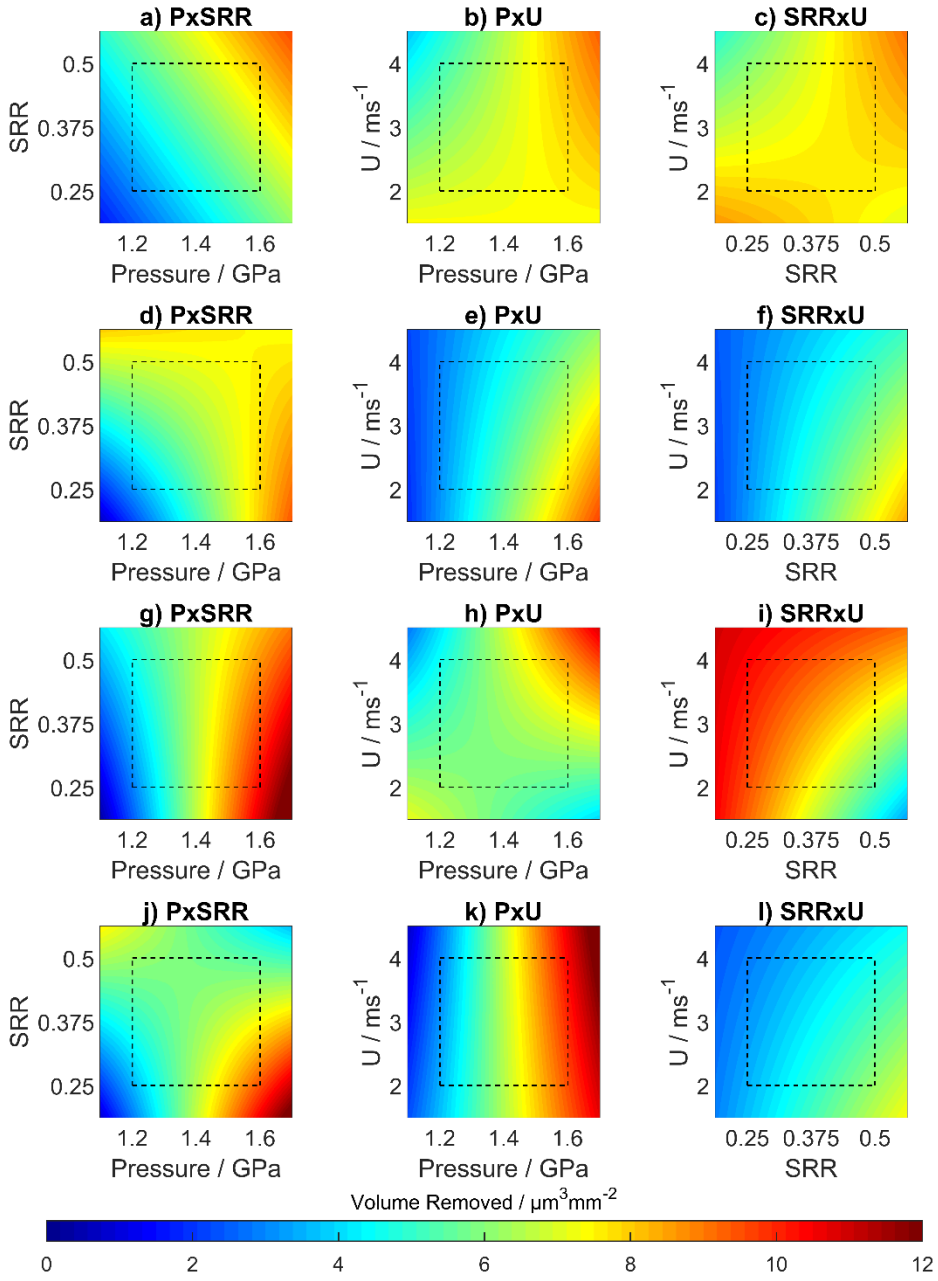

Figure 8.3.16 Factorial response models for volume removed through micropitting for the fast (a-f) and slow (g-l) surfaces.

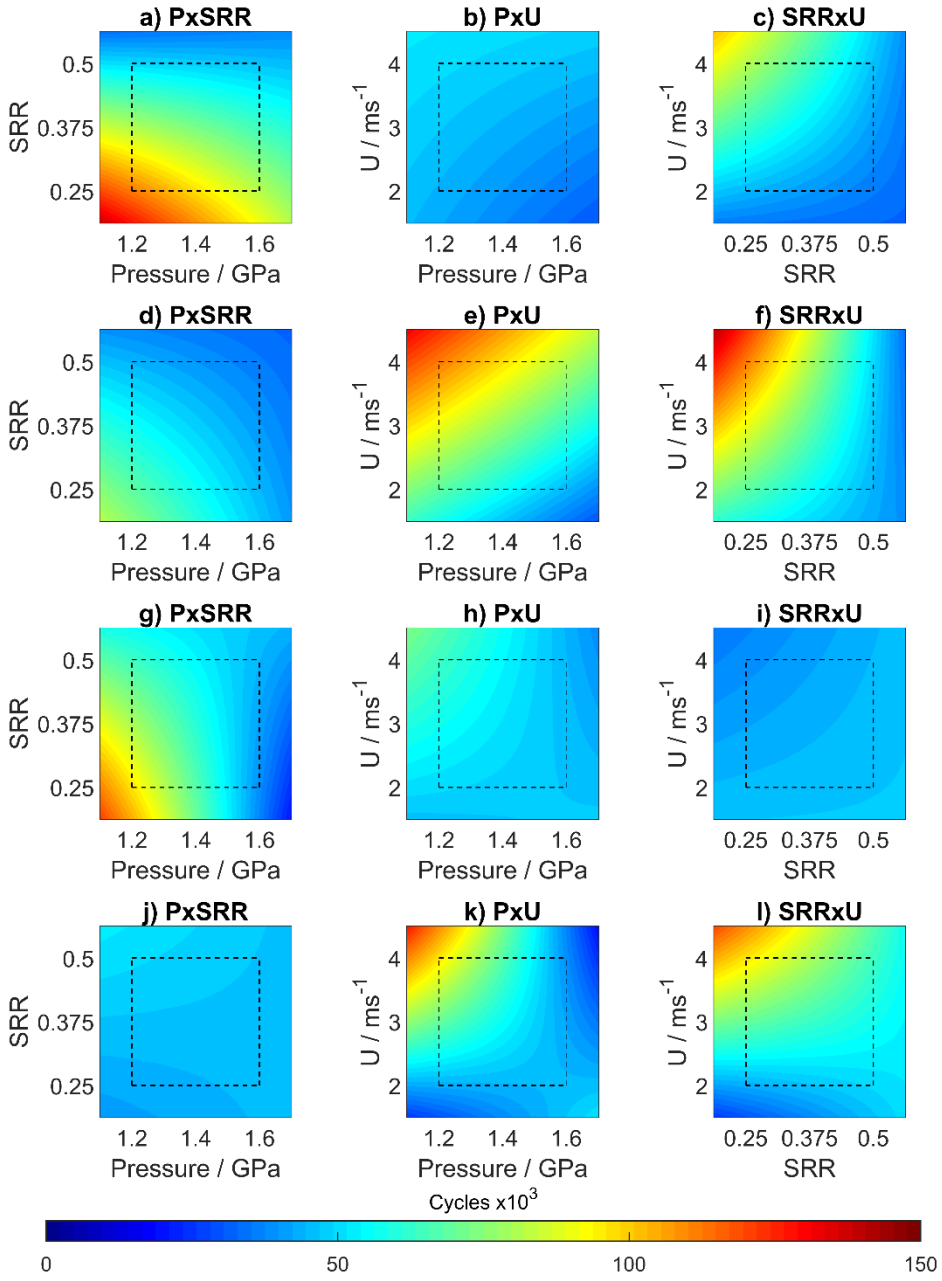

Figure 8.3.17 Factorial response models for number of fast disk cycles to reach 3% micropitted for the fast (a-f) and slow (g-l) surfaces.

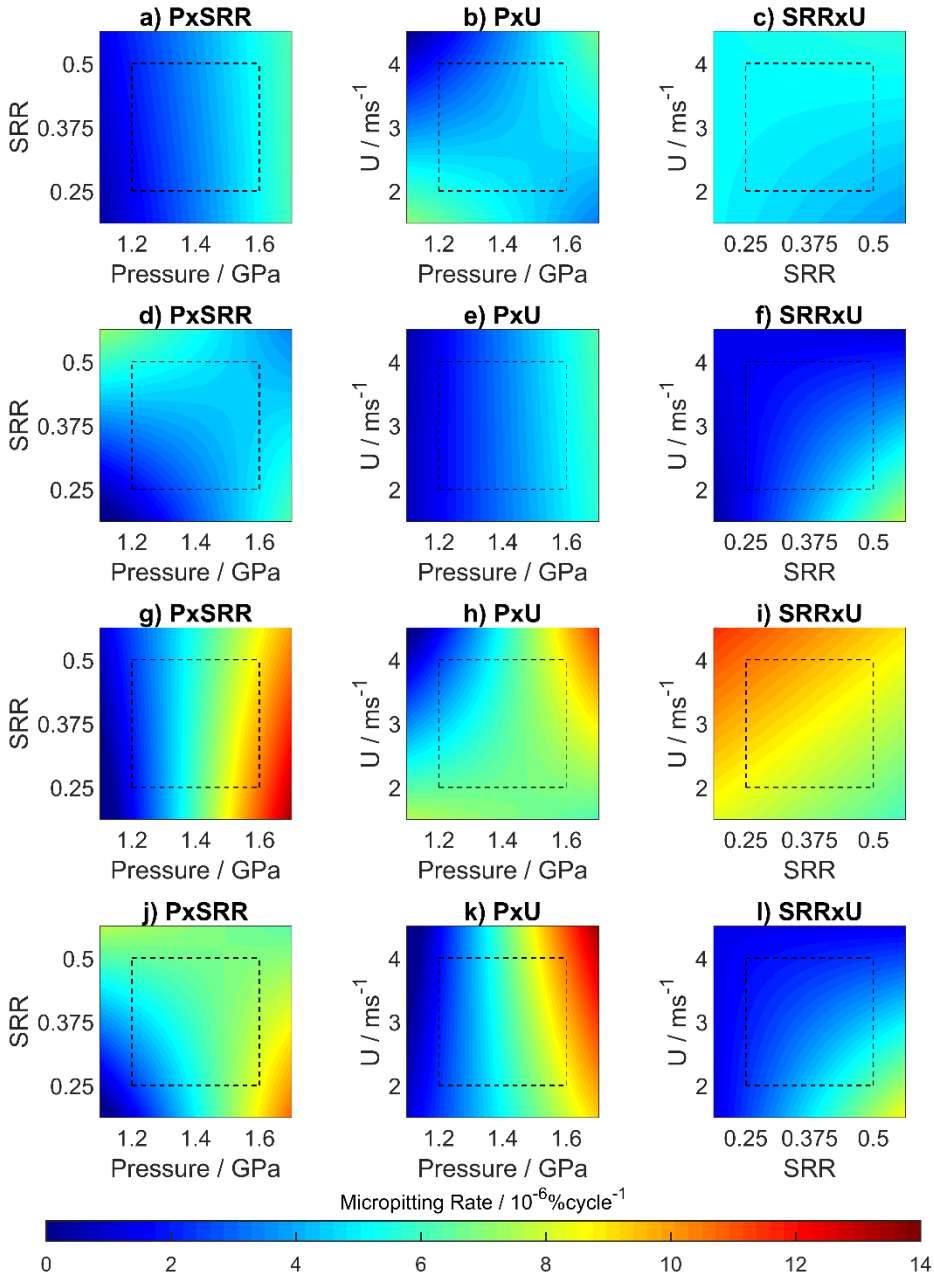

Figure 8.3.18 Factorial response models for rate of micropitting during load stages 9 and 10 for the fast (a-f) and slow (g-l) surfaces.

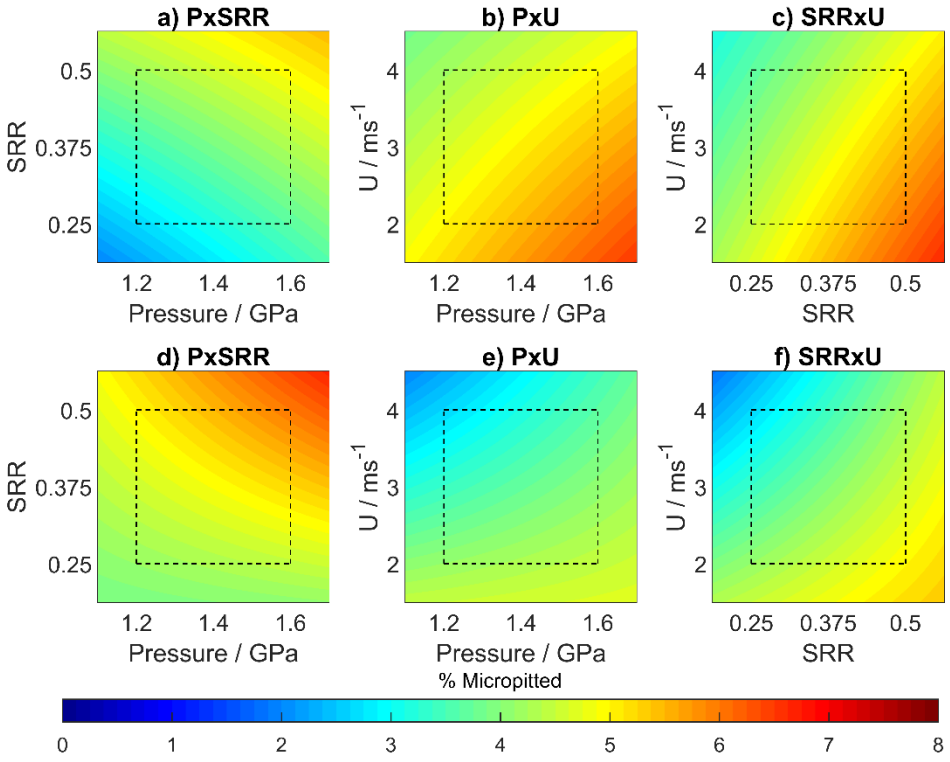

Figure 8.3.19 Factorial response models for the percentage of fast disk surface micropitted at 100k fast disk cycles. In the upper row the factor not shown on the axes is at its high setting, while in the lower row that factor is low.

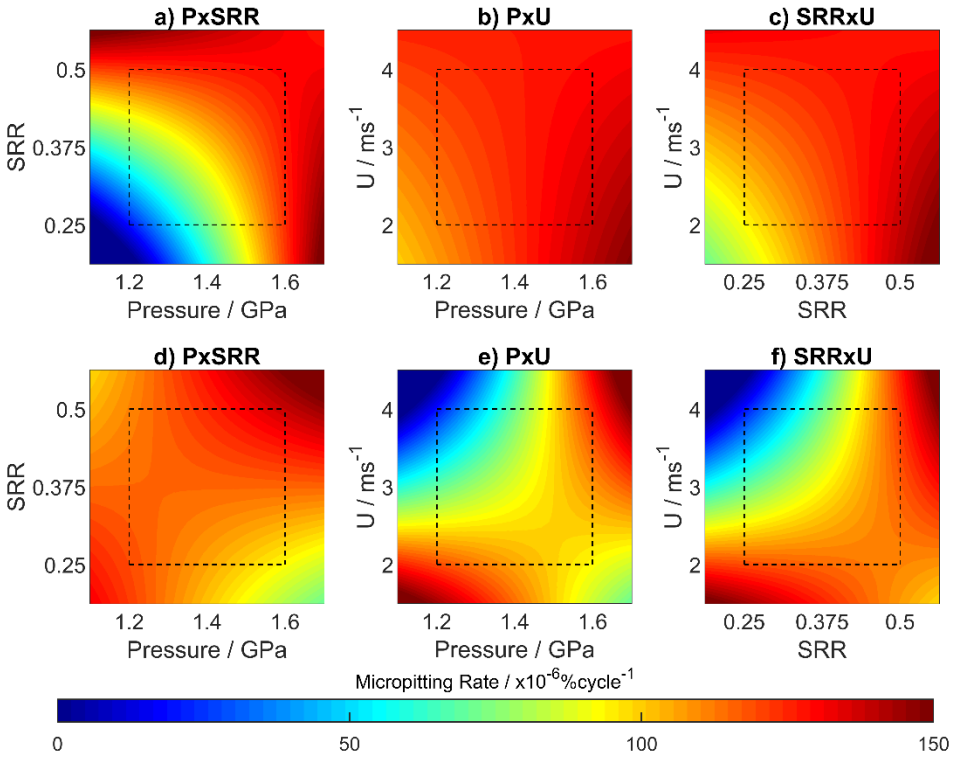

Figure 8.3.20 Factorial response models for the peak rate of micropitting on the slow surface. In the upper row the factor not shown on the axes is at its high setting, while in the lower row that factor is low.

Appendix 4. R^2 values for micropitting outputs to roughness parameters

Table 8.3.3 R^2 values for linear fits of micropitting parameters against running in parameters for all micropitting outputs that apply to both surfaces.

Output	Comparison	CSA	Asperity height	Radius of Curvature	Ra	Rc	Rku	Rp	Rq	Rsk	Rt	Rv	Rz
% Micropitted at Load stage 12	Unrun Value	0.011	0.041	0.022	0.071	0.092	0.060	0.024	0.094	0.098	0.046	0.114	0.107
	Value after running-in	0.118	0.217	0.081	0.000	0.005	0.075	0.078	0.001	0.123	0.000	0.083	0.043
	Change through running-in	0.420	0.451	0.097	0.309	0.274	0.089	0.101	0.467	0.110	0.098	0.215	0.153
	% change through running in	0.312	0.361	0.159	0.225	0.231	0.125	0.134	0.340	0.002	0.151	0.187	0.112
Volume Removed	Unrun Value	0.017	0.030	0.010	0.068	0.098	0.090	0.021	0.095	0.129	0.075	0.140	0.125
	Value after running-in	0.091	0.196	0.097	0.000	0.006	0.095	0.084	0.002	0.148	0.002	0.103	0.057
	Change through running-in	0.379	0.390	0.112	0.262	0.286	0.093	0.100	0.431	0.114	0.130	0.241	0.161
	% change through running in	0.268	0.320	0.167	0.187	0.234	0.114	0.133	0.307	0.004	0.167	0.199	0.106
D5	Unrun Value	0.003	0.030	0.040	0.109	0.220	0.235	0.080	0.155	0.259	0.267	0.291	0.286
	Value after running-in	0.157	0.250	0.036	0.002	0.020	0.210	0.157	0.013	0.288	0.042	0.206	0.117
	Change through running-in	0.441	0.471	0.047	0.361	0.561	0.161	0.260	0.473	0.208	0.374	0.578	0.409
	% change through running in	0.337	0.373	0.103	0.235	0.406	0.145	0.294	0.289	0.019	0.399	0.444	0.256

N3	Unrun Value	0.167	0.035	0.008	0.022	0.003	0.106	0.009	0.001	0.058	0.009	0.039	0.036
	Value after running-in	0.592	0.630	0.195	0.210	0.136	0.148	0.422	0.139	0.156	0.004	0.016	0.004
	Change through running-in	0.467	0.548	0.221	0.505	0.317	0.197	0.255	0.715	0.336	0.067	0.254	0.300
	% change through running in	0.645	0.674	0.321	0.569	0.502	0.255	0.420	0.751	0.083	0.154	0.291	0.410
Peak Micropitting Rate	Unrun Value	0.273	0.027	0.064	0.025	0.006	0.110	0.000	0.001	0.083	0.003	0.061	0.039
	Value after running-in	0.377	0.284	0.025	0.147	0.063	0.193	0.289	0.085	0.163	0.006	0.035	0.001
	Change through running-in	0.097	0.217	0.036	0.273	0.088	0.307	0.119	0.424	0.269	0.014	0.223	0.161
	% change through running in	0.277	0.286	0.110	0.331	0.160	0.369	0.218	0.435	0.001	0.044	0.159	0.155

Appendix 5. Run-in Profile Simulation Results

The Figures in this section show the results of the fatigue simulations performed with only run-in profiles, alongside the corresponding experimental result. The fast surface results are shown first, followed by those for the slow surface.

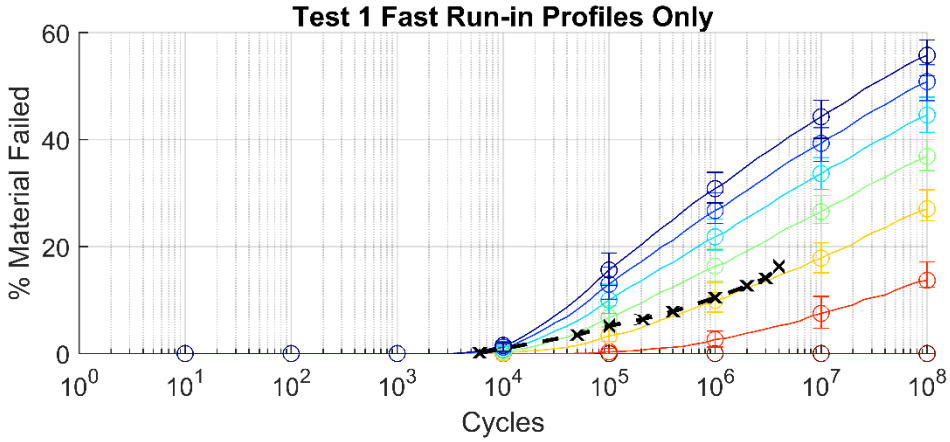

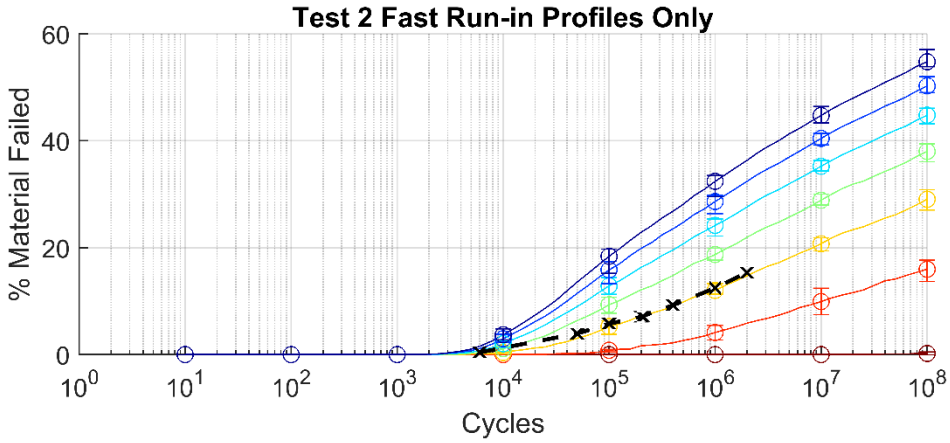

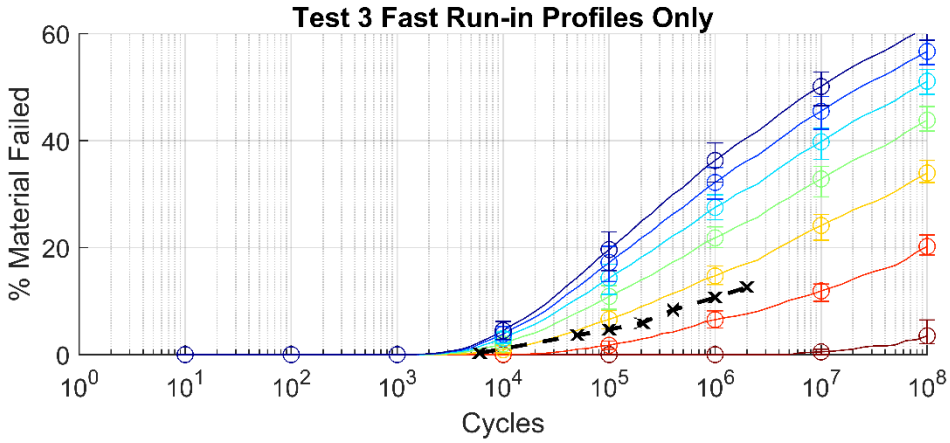

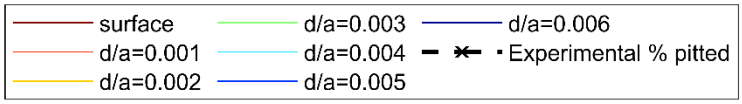

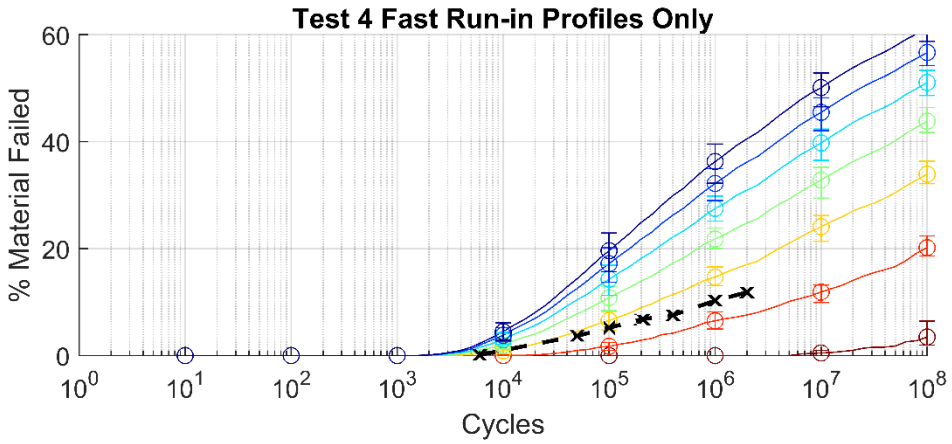
Test 4 Fast Run-in Profiles Only
% Material Failed
Cycles

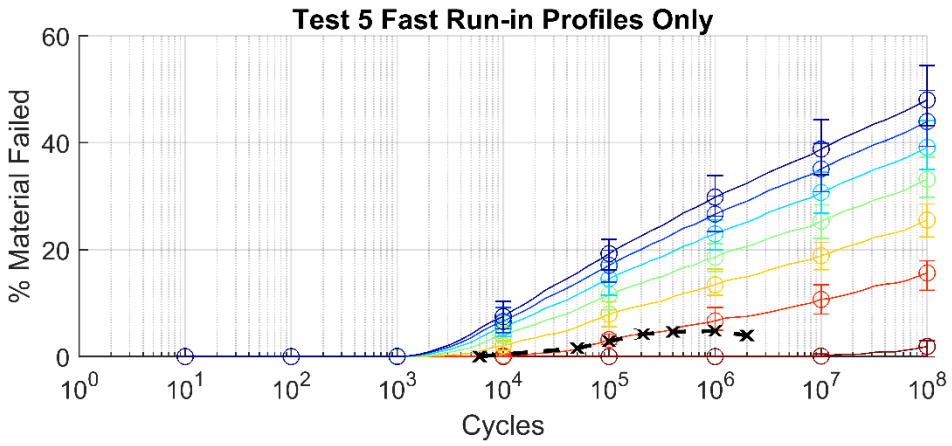
Test 5 Fast Run-in Profiles Only
% Material Failed
Cycles

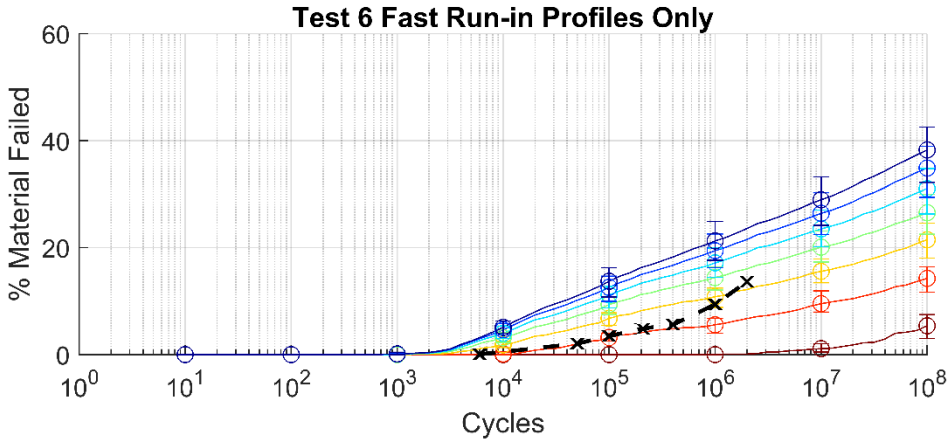
Test 6 Fast Run-in Profiles Only
% Material Failed
Cycles

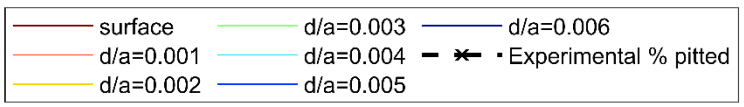
surface
d/a=0.001
d/a=0.002
d/a=0.003
d/a=0.004
d/a=0.005
d/a=0.006
Experimental % pitted

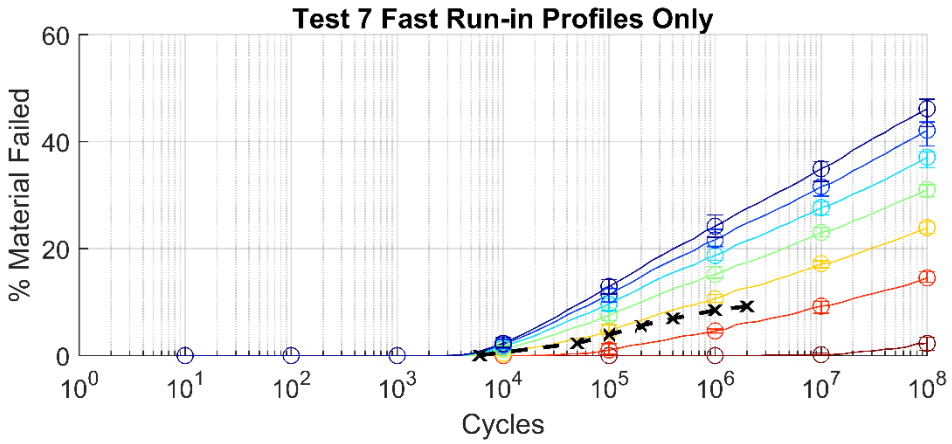
Test 7 Fast Run-in Profiles Only
% Material Failed
Cycles

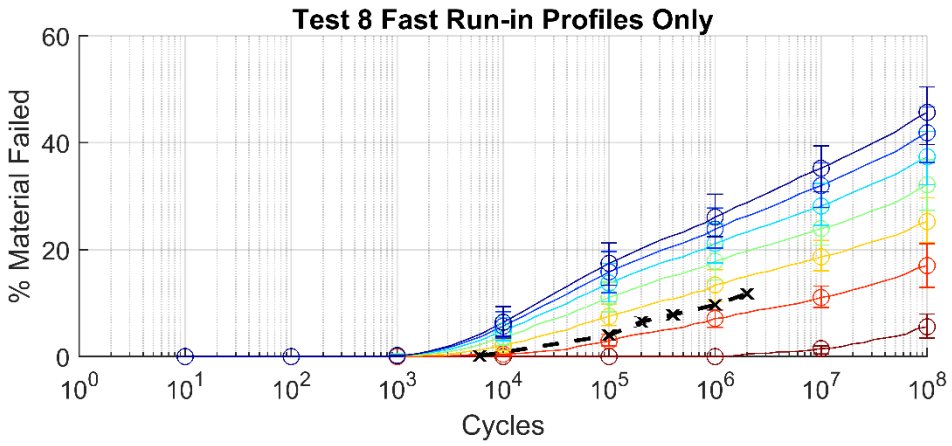
Test 8 Fast Run-in Profiles Only
% Material Failed
Cycles

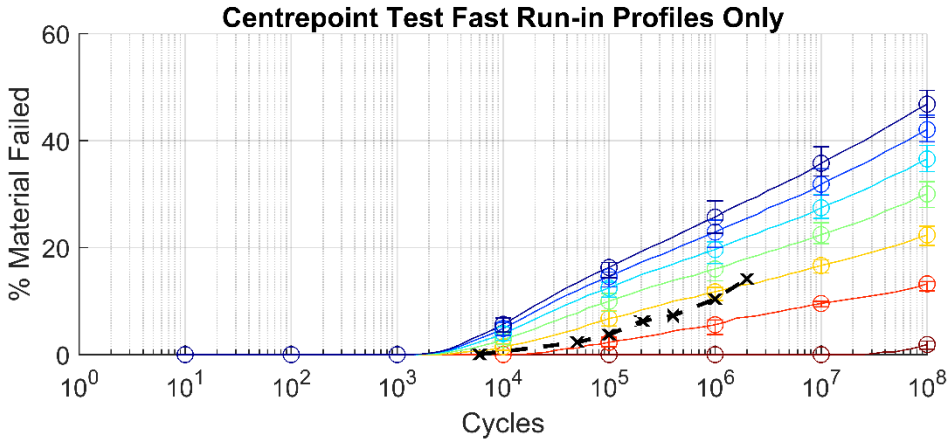
Centrepoint Test Fast Run-in Profiles Only
% Material Failed
Cycles

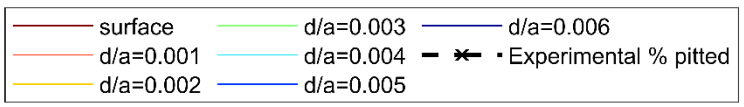
surface
d/a=0.001
d/a=0.002
d/a=0.003
d/a=0.004
d/a=0.005
d/a=0.006
Experimental % pitted

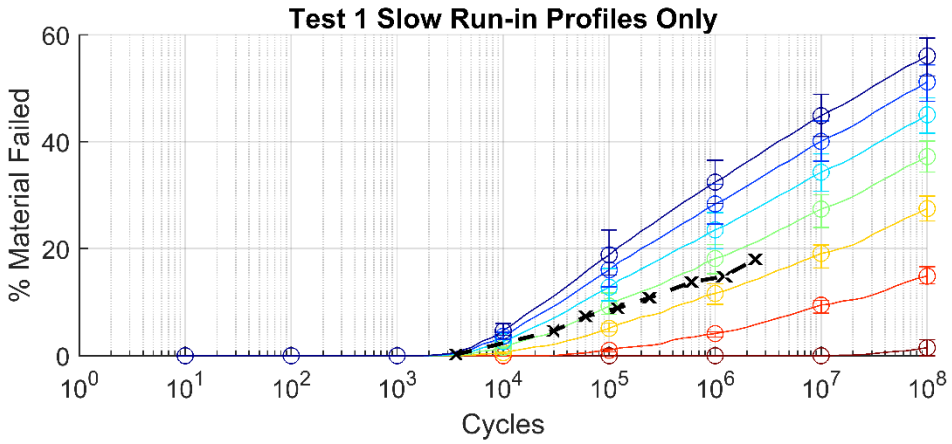
Test 1 Slow Run-in Profiles Only
% Material Failed
Cycles

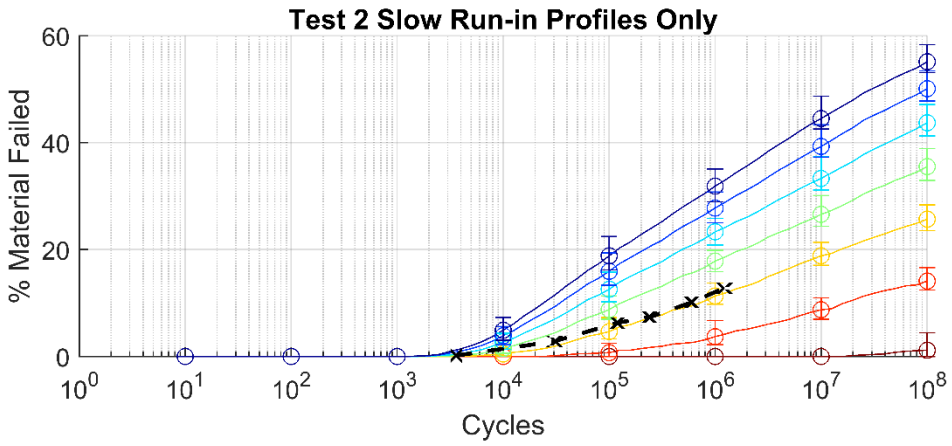
Test 2 Slow Run-in Profiles Only
% Material Failed
Cycles

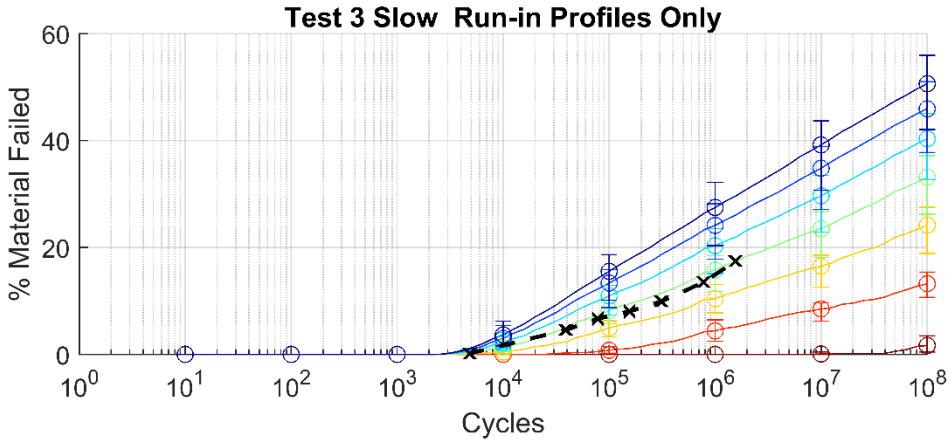
Test 3 Slow Run-in Profiles Only
% Material Failed
Cycles

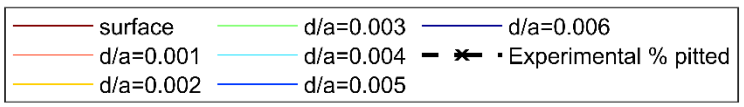
surface
d/a=0.001
d/a=0.002
d/a=0.003
d/a=0.004
d/a=0.005
d/a=0.006
Experimental % pitted

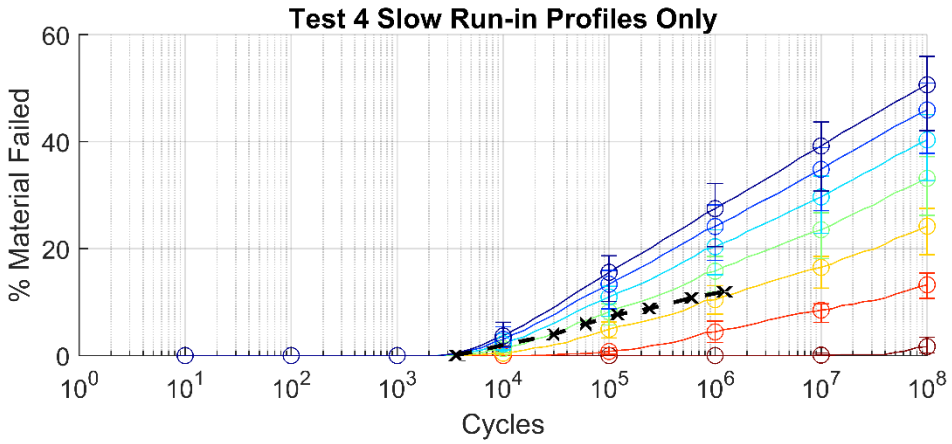
Test 4 Slow Run-in Profiles Only
% Material Failed
Cycles

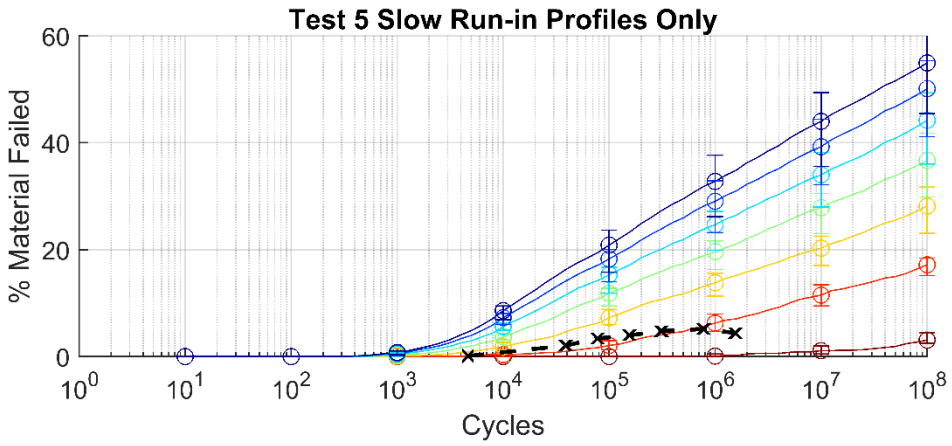
Test 5 Slow Run-in Profiles Only
% Material Failed
Cycles

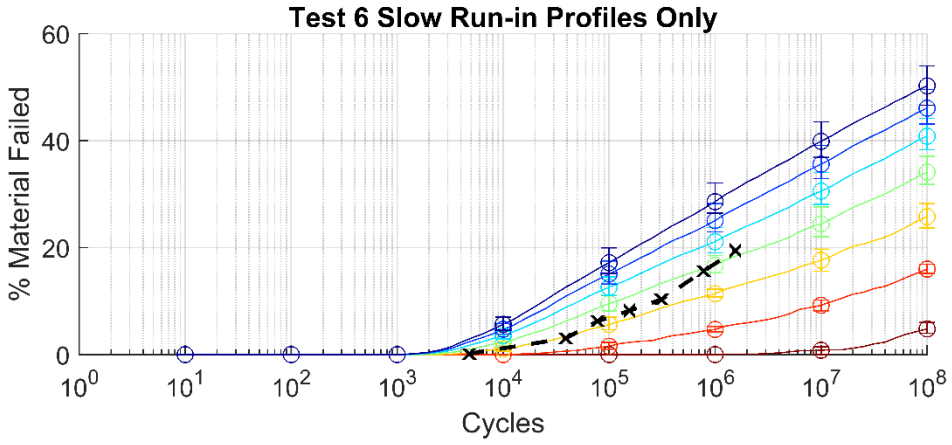
Test 6 Slow Run-in Profiles Only
% Material Failed
Cycles

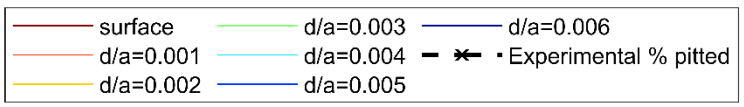
surface
d/a=0.001
d/a=0.002
d/a=0.003
d/a=0.004
d/a=0.005
d/a=0.006
Experimental % pitted

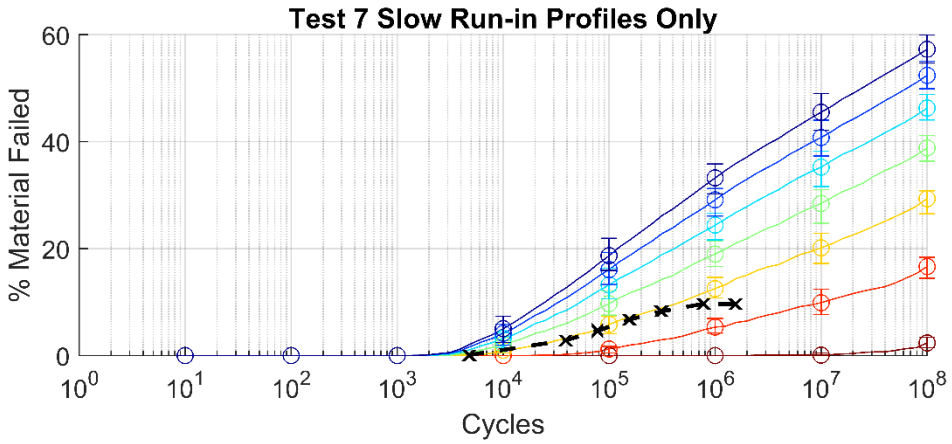
Test 7 Slow Run-in Profiles Only
% Material Failed
Cycles

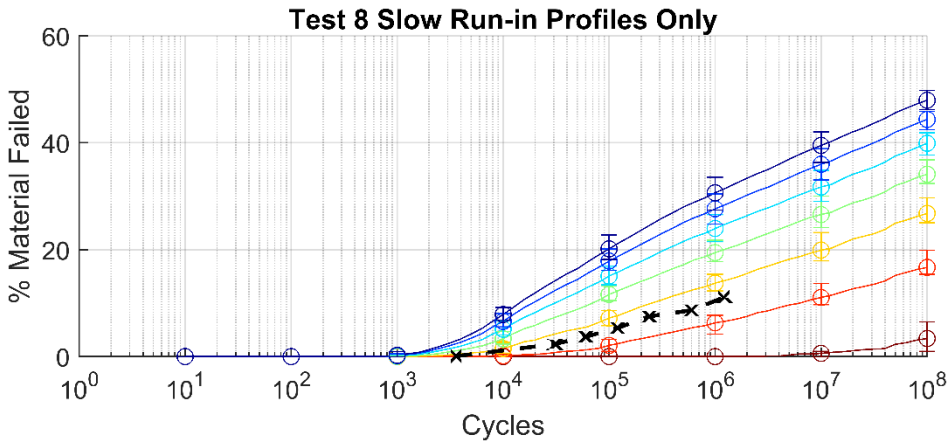
Test 8 Slow Run-in Profiles Only
% Material Failed
Cycles

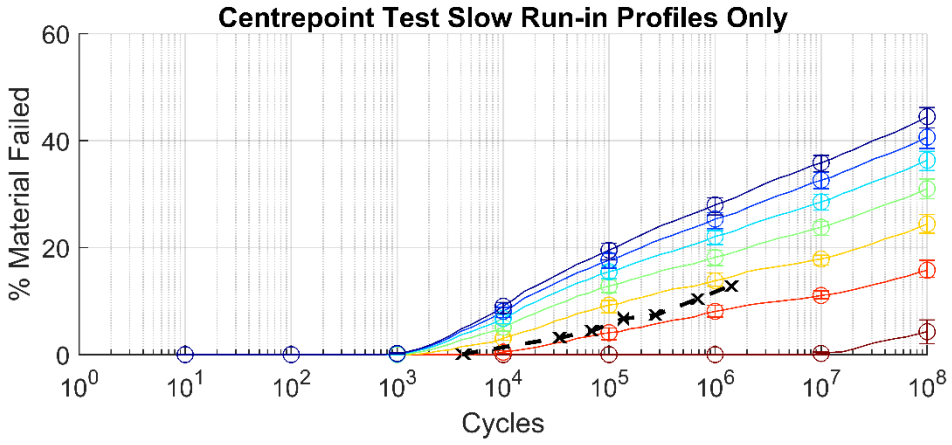
Centrepoint Test Slow Run-in Profiles Only
% Material Failed
Cycles

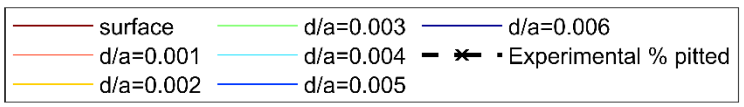
surface
d/a=0.001
d/a=0.002
d/a=0.003
d/a=0.004
d/a=0.005
d/a=0.006
Experimental % pitted

Appendix 6. Factorial Response Models for Simulations Using Run-in Profiles

As in Appendix 2, In each of the figures shown here, the upper row for each surface (a-c and g-i) shows the response where the third factor (the factor not shown on the axes in question) is high, while the lower row (d-f and j-l) shows the response where the third factor is low.

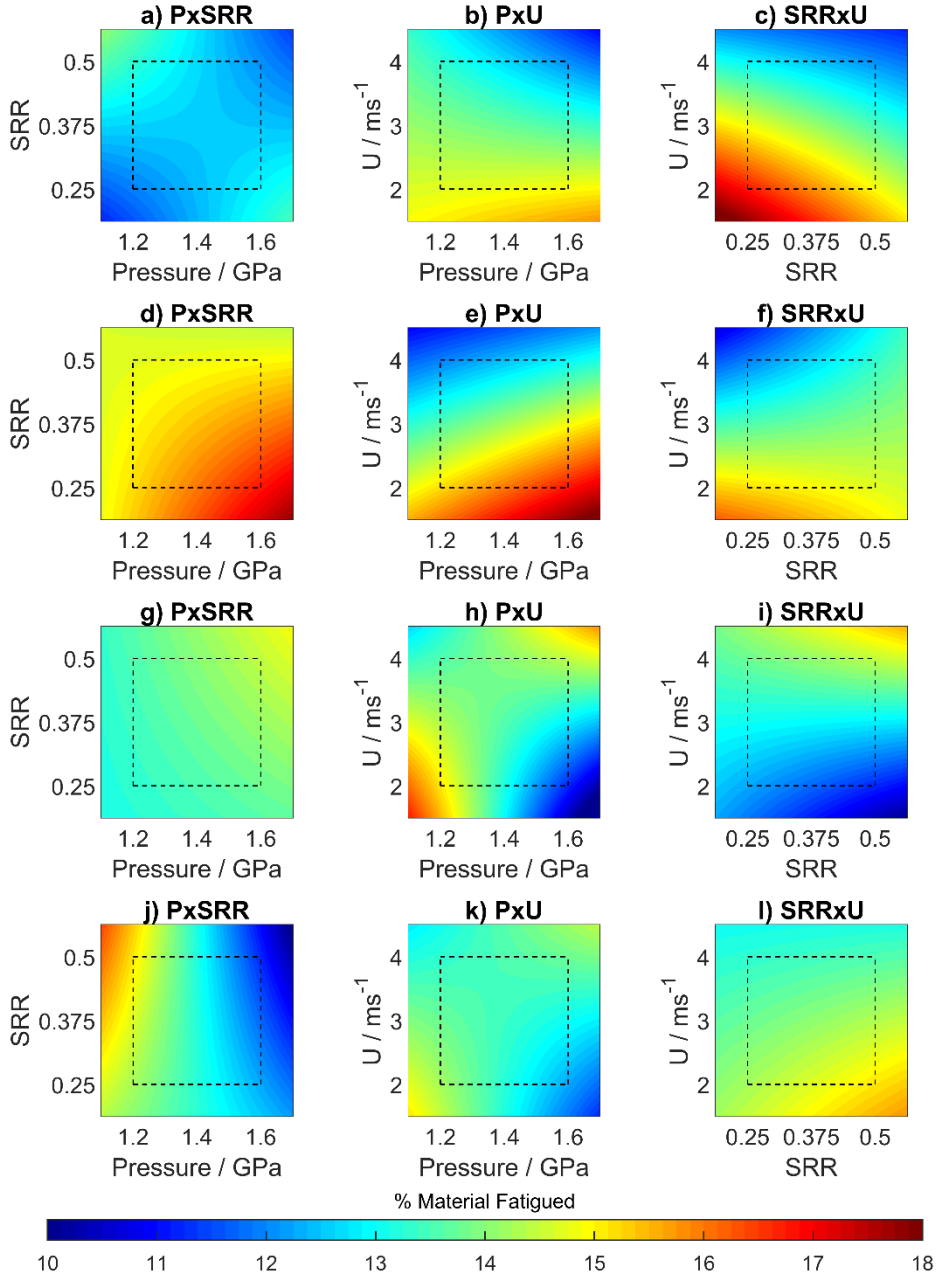

Figure 8.3.21 Factorial response model of percentage of material failed to a depth of 0.002a for Fast (a-f) and slow (g-l) surface simulations using run-in profiles only.

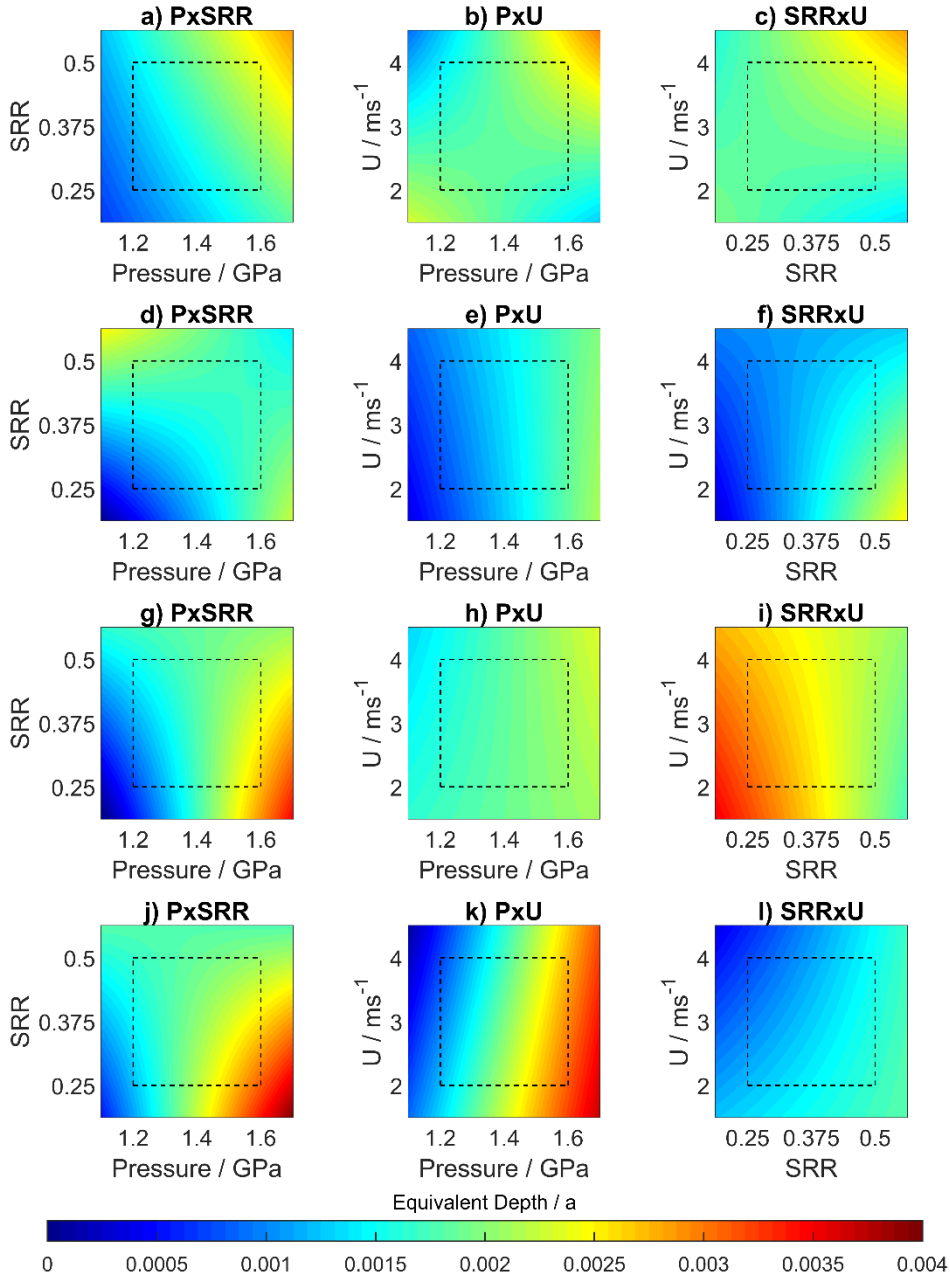

Figure 8.3.22 Factorial response model of equivalent depth at end of test for Fast (a-f) and slow (g-l) surface simulations using run-in profiles only.

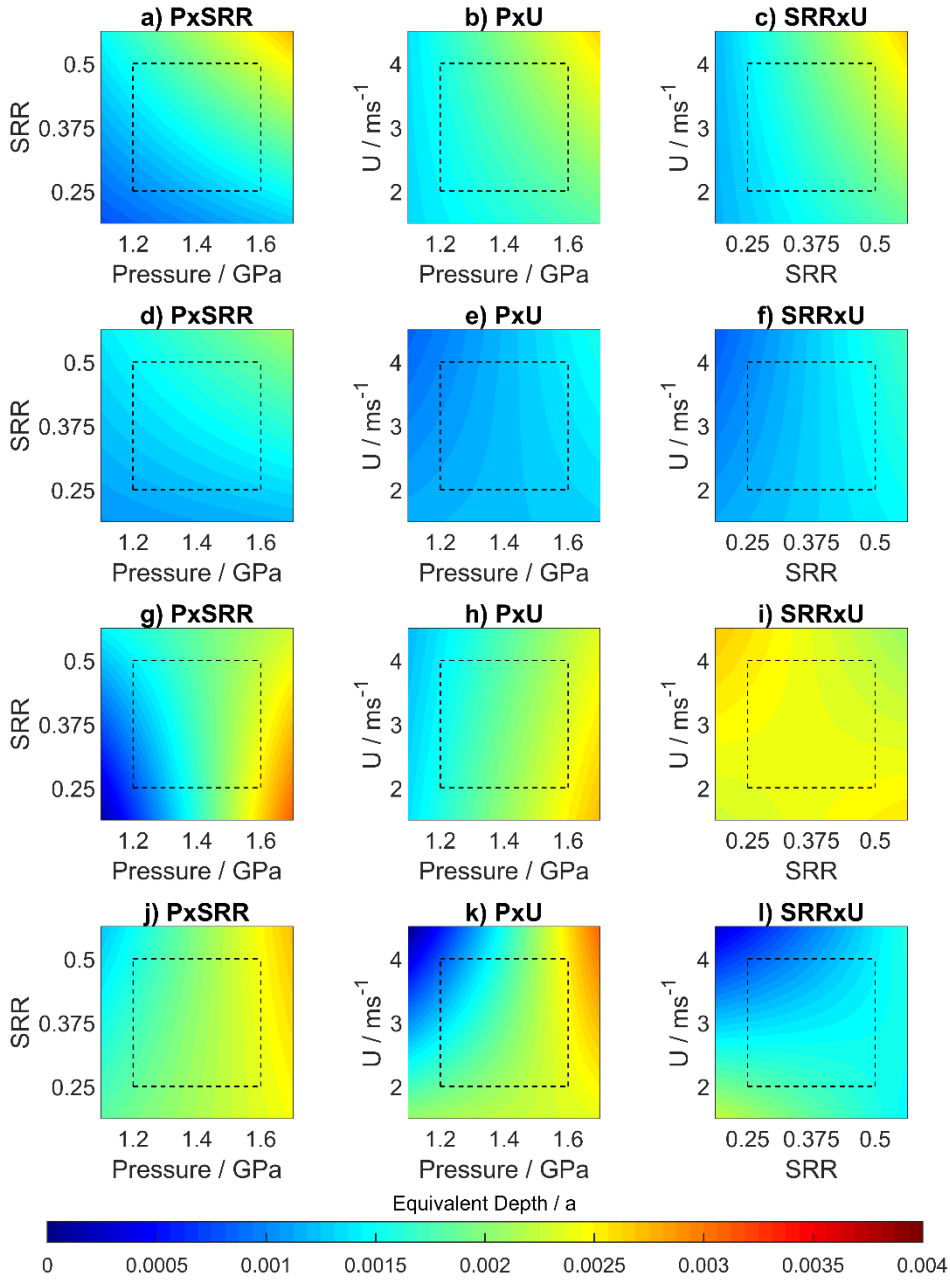

Figure 8.3.23 Factorial response model of equivalent depth at the conclusion of load stage 6 for Fast (a-f) and slow (g-l) surface simulations using run-in profiles only.

Appendix 7. Updating Profile Simulation Results

The Figures in this section show the results of the fatigue simulations performed with updating profiles, alongside the corresponding experimental result. The fast surface results are shown first, followed by those for the slow surface.

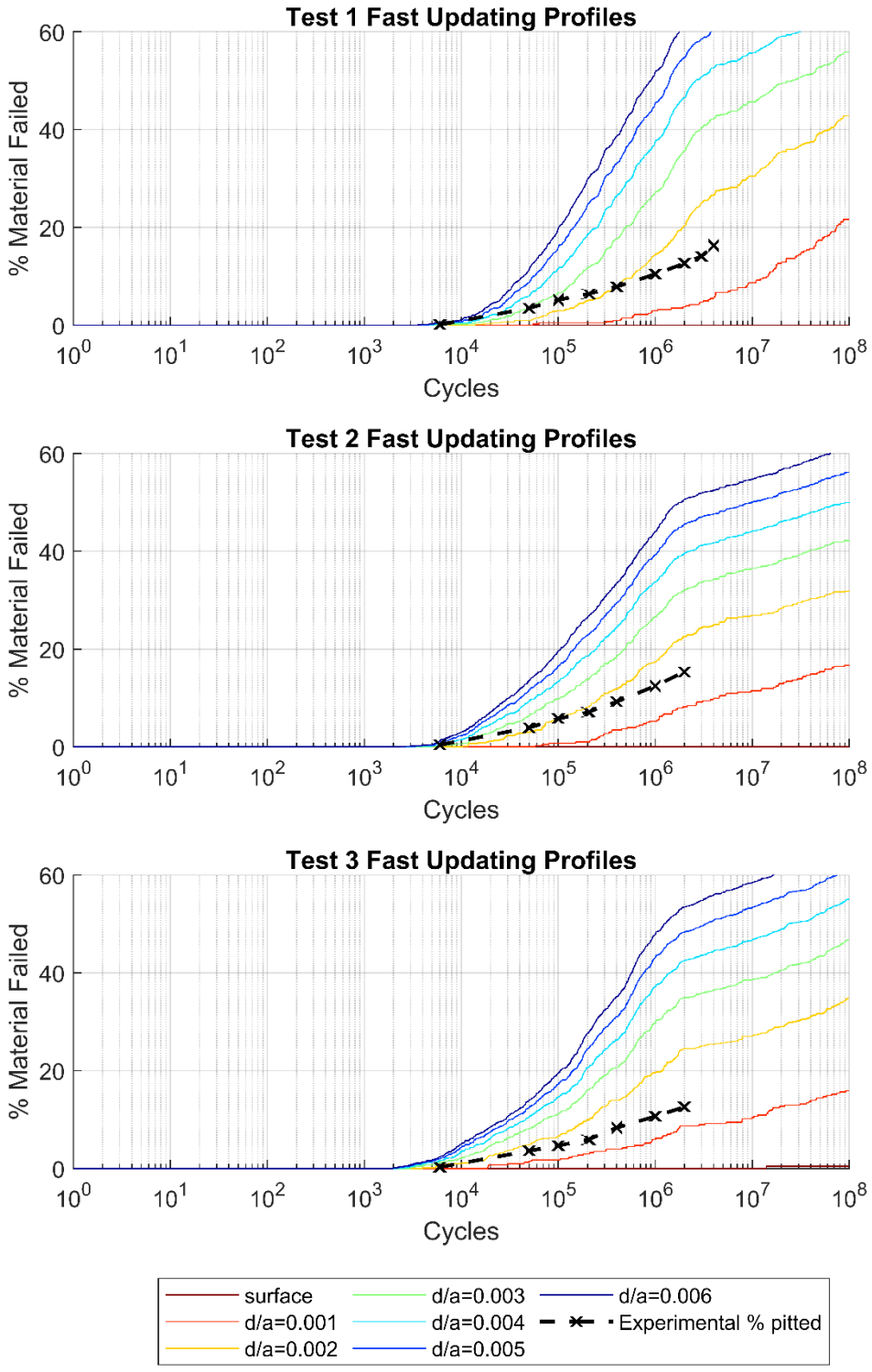

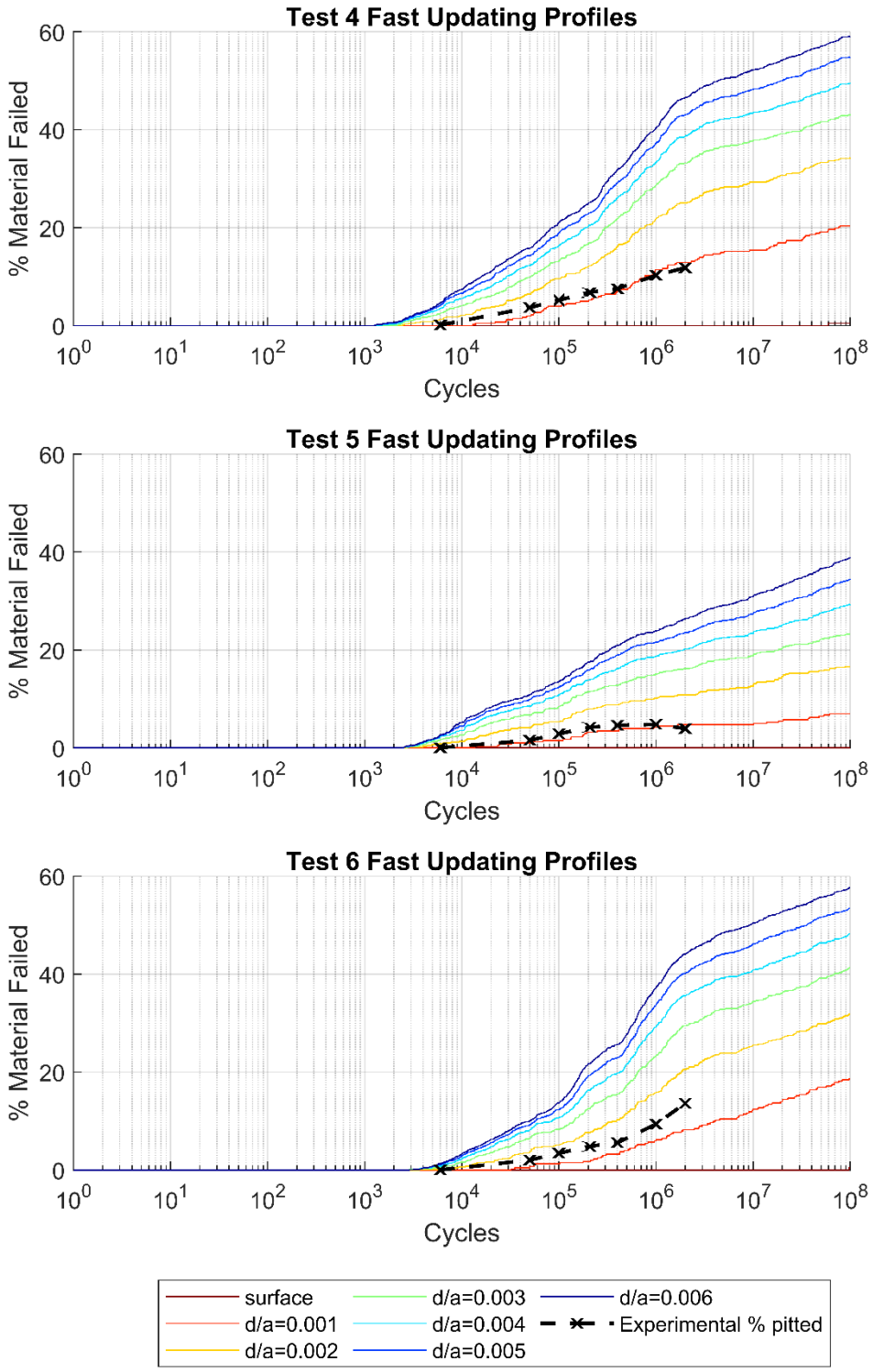
Test 4 Fast Updating Profiles
% Material Failed
Cycles
Test 5 Fast Updating Profiles
% Material Failed
Cycles
Test 6 Fast Updating Profiles
% Material Failed
Cycles
surface
d/a=0.001
d/a=0.002
d/a=0.003
d/a=0.004
d/a=0.005
d/a=0.006
Experimental % pitted

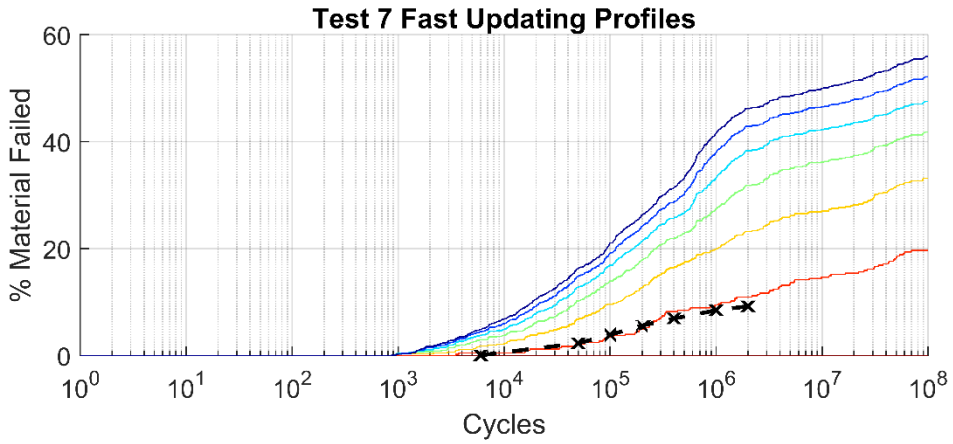
Test 7 Fast Updating Profiles
% Material Failed
Cycles
0
20
40
60
10^0
10^1
10^2
10^3
10^4
10^5
10^6
10^7
10^8

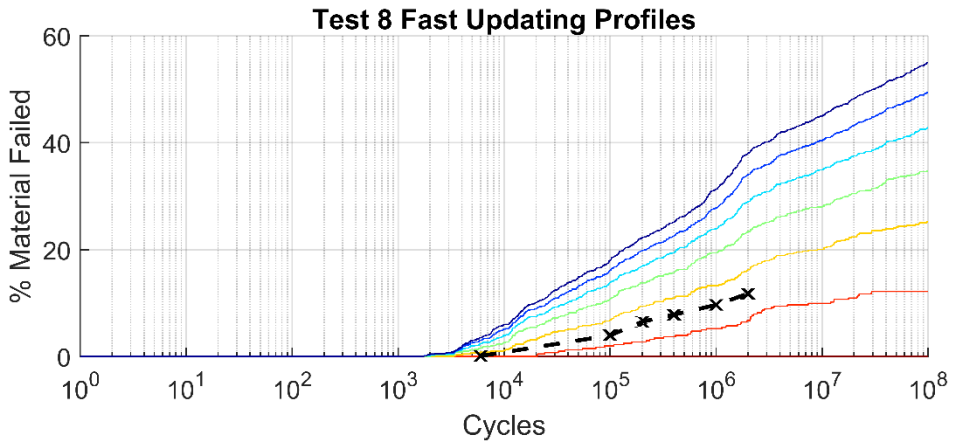
Test 8 Fast Updating Profiles
% Material Failed
Cycles
0
20
40
60
10^0
10^1
10^2
10^3
10^4
10^5
10^6
10^7
10^8

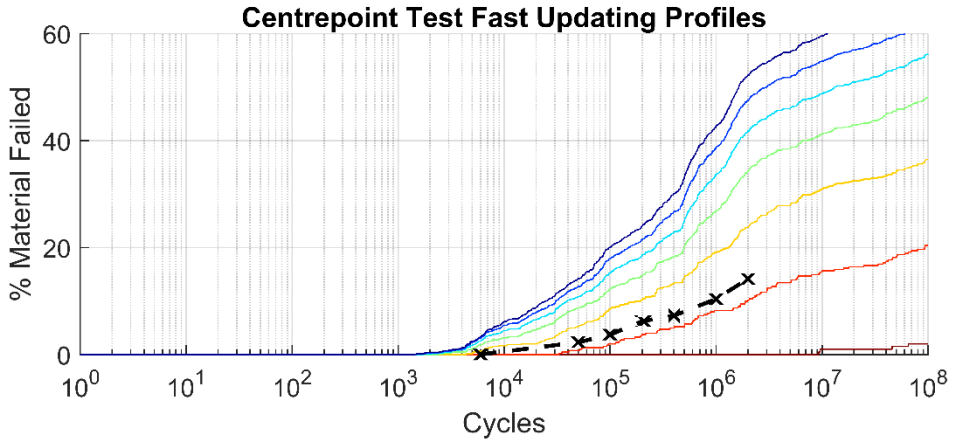
Centrepoint Test Fast Updating Profiles
% Material Failed
Cycles
0
20
40
60
10^0
10^1
10^2
10^3
10^4
10^5
10^6
10^7
10^8

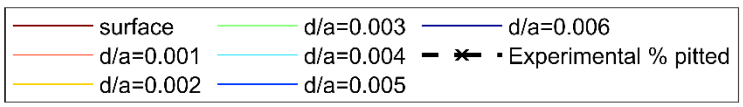
surface
d/a=0.001
d/a=0.002
d/a=0.003
d/a=0.004
d/a=0.005
d/a=0.006
Experimental % pitted

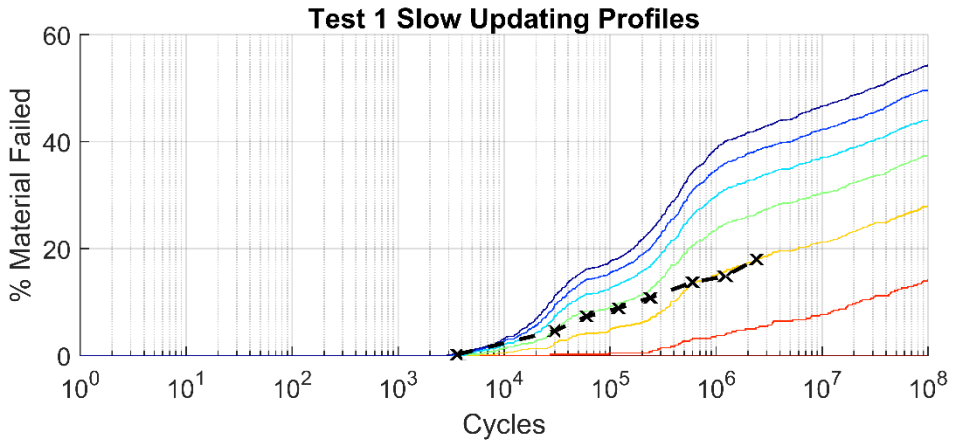
Test 1 Slow Updating Profiles
% Material Failed
Cycles
0
20
40
60
10^0
10^1
10^2
10^3
10^4
10^5
10^6
10^7
10^8

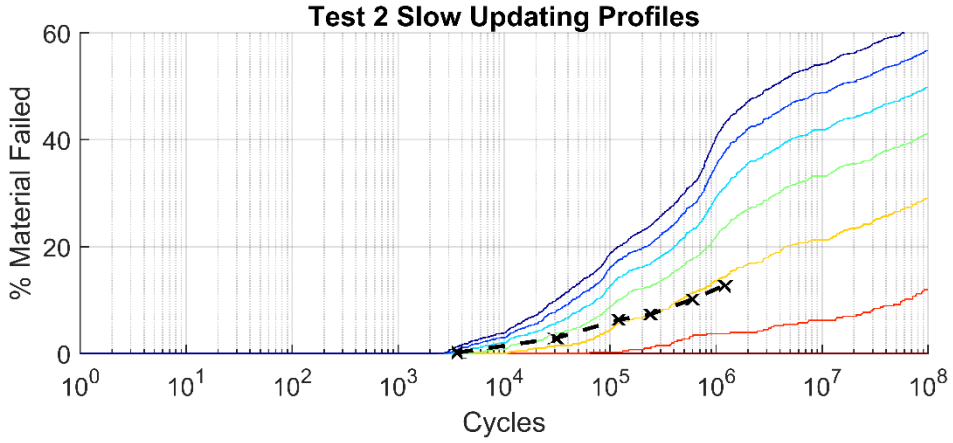
Test 2 Slow Updating Profiles
% Material Failed
Cycles
0
20
40
60
10^0
10^1
10^2
10^3
10^4
10^5
10^6
10^7
10^8

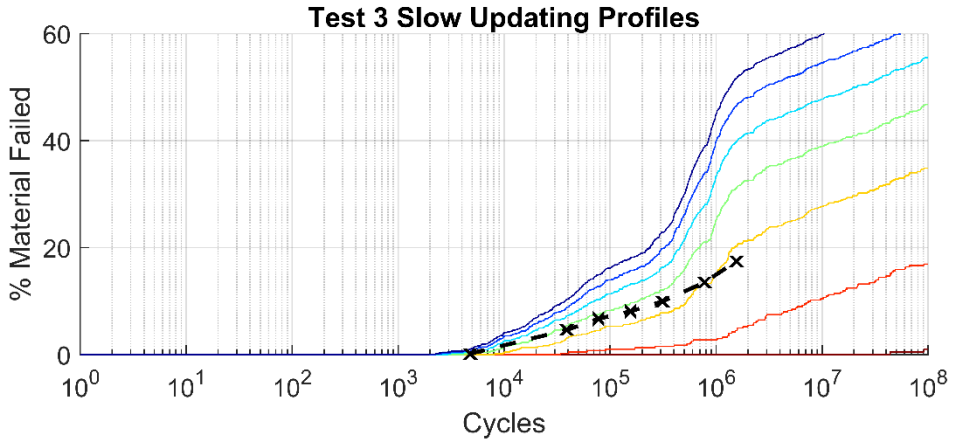
Test 3 Slow Updating Profiles
% Material Failed
Cycles
0
20
40
60
10^0
10^1
10^2
10^3
10^4
10^5
10^6
10^7
10^8

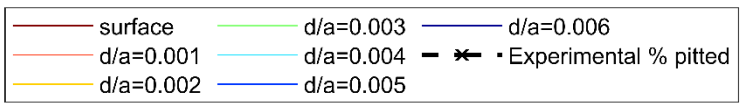
surface
d/a=0.001
d/a=0.002
d/a=0.003
d/a=0.004
d/a=0.005
d/a=0.006
Experimental % pitted

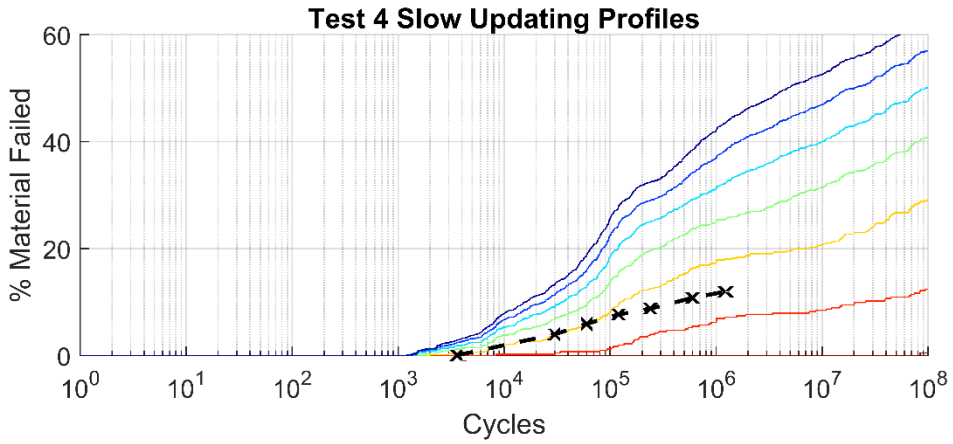
Test 4 Slow Updating Profiles
% Material Failed
Cycles
0
20
40
60
10^0
10^1
10^2
10^3
10^4
10^5
10^6
10^7
10^8

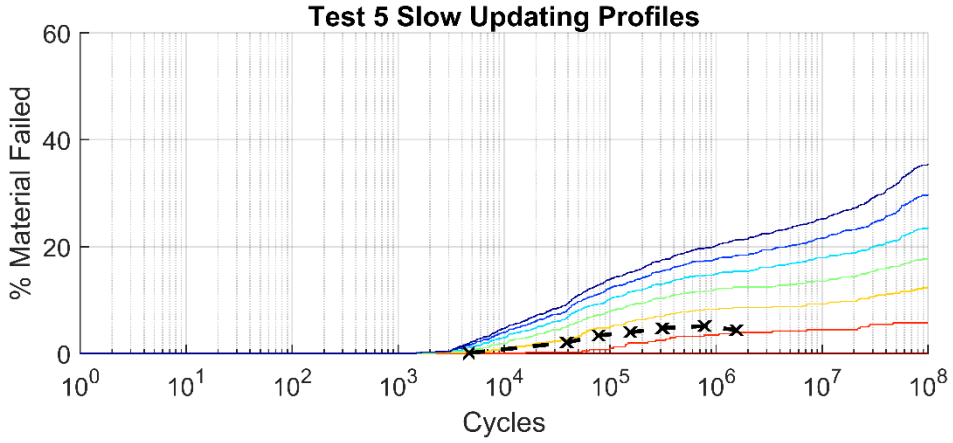
Test 5 Slow Updating Profiles
% Material Failed
Cycles
0
20
40
60
10^0
10^1
10^2
10^3
10^4
10^5
10^6
10^7
10^8

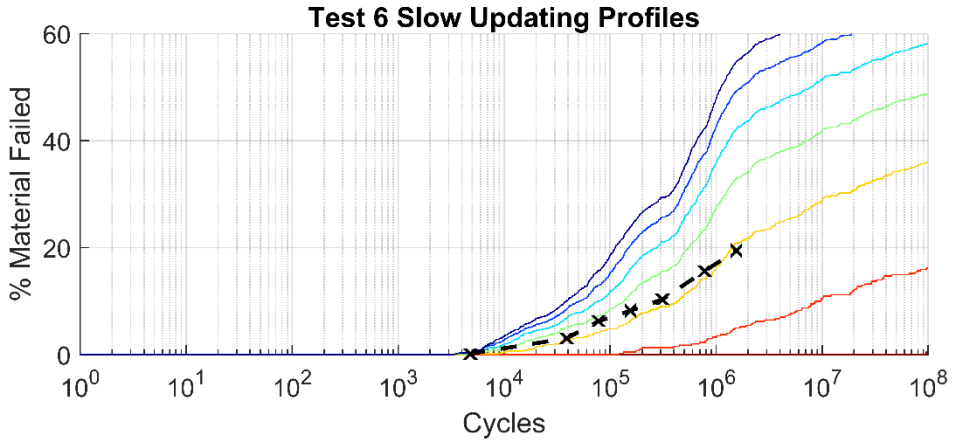
Test 6 Slow Updating Profiles
% Material Failed
Cycles
0
20
40
60
10^0
10^1
10^2
10^3
10^4
10^5
10^6
10^7
10^8

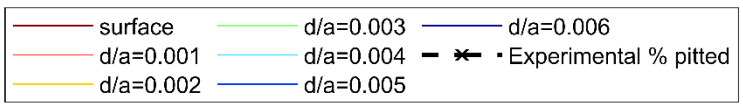
surface
d/a=0.001
d/a=0.002
d/a=0.003
d/a=0.004
d/a=0.005
d/a=0.006
Experimental % pitted

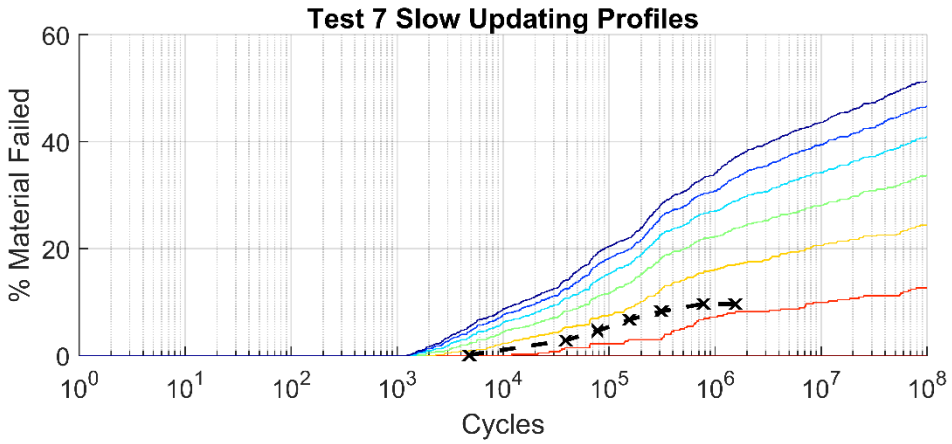
Test 7 Slow Updating Profiles
% Material Failed
Cycles

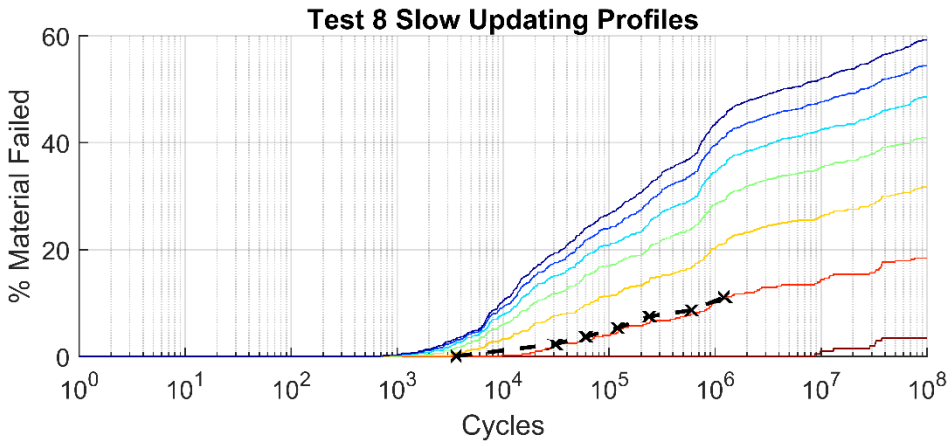
Test 8 Slow Updating Profiles
% Material Failed
Cycles

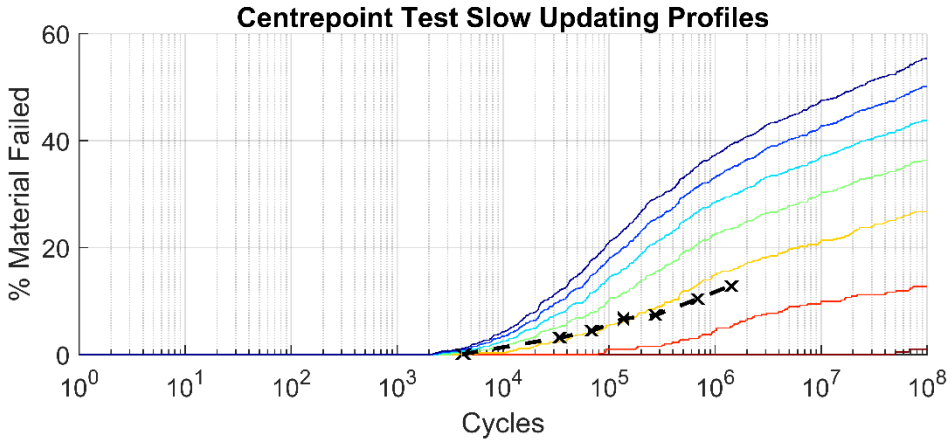
Centrepoint Test Slow Updating Profiles
% Material Failed
Cycles

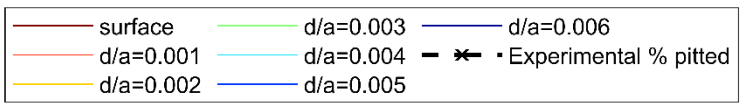
surface
d/a=0.001
d/a=0.002
d/a=0.003
d/a=0.004
d/a=0.005
d/a=0.006
Experimental % pitted